

International Conference on Dynamics of Composite Structures



June 2-4, 2015
Arles, France

Proceedings



To browse the proceedings, use the **authors index** or the **search box** with CTRL-F (PC) or Command ()-F (Macintosh).



Copyright ©2015 by the authors. Distribution of all material contained in this document is permitted under the terms of the Creative Commons license Attribution-NonCommercial-NoDerivatives 4.0 International (CC-by-nc-nd 4.0).

Authors Index

Abbadi, Zouhir.....	175
Abdelmalek, Zine.....	113
Ablitzer, Frederic.....	360
Ablitzer, Frédéric.....	64, 353
Alouani, Antoine.....	5
Arbaoui, Jamal.....	16
Arfaoui, Makrem.....	105
Atalla, Noureddine.....	269
Baho, Omar.....	205
Baleh, Rachid.....	176
Barbarulo, Andrea.....	66
Bareille, Olivier.....	105, 120, 129, 165, 240, 284
Ben Abda, Amel.....	101
Ben Abdallah, Jalel.....	105
Ben Souf, Mohamed Amine.....	129
Benamar, Rhali.....	120, 205, 250
Bermúdez, María Dolores.....	185
Blairon, Nicolas.....	284
Borello, Gerard.....	91
Bouazzouni, Amar.....	211
Bouhaddi, Noureddine.....	1
Boumrar, Akli.....	211
Boussu, François.....	197
Bouvet, Christophe.....	280
Braguy, Cyril.....	284
Brocail, Julien.....	360
Butaud, Pauline.....	231
Bézier, Guillaume.....	66
Bös, Joachim.....	293
Carrión-Vilches, Francisco José.....	185
Cattabiani, Alessandro.....	66
Chazot, Jean-Daniel.....	26
Cherif, Raef.....	269
Chevalier, Caroline.....	197
Chevallier, Gaël.....	231
Christen, Jean-Loup.....	165
Chronopoulos, Dimitrios.....	129, 140
Claeys, Claus.....	54

Cogan, Scott.....	191
Collet, Manuel.....	140, 240
Coutellier, Daniel.....	197
Dahmane, Merzak.....	211
Dau, Frédéric.....	280
De Luca, Patrick.....	332
Deckers, Elke.....	54
Desmet, Wim.....	54
Dessolier, Thibaut.....	83
Deü, Jean-François.....	150
Dimitrijevic, Zoran.....	240
Droz, Christophe.....	46, 260
Dupont, Jean-Baptiste.....	1
El Malki, Aboulghit.....	16
Faderl, Norbert.....	197
Fan, Yu.....	240
Foltête, Emmanuel.....	191, 231
Fouinneteau, Michel.....	164
Gagliardini, Laurent.....	175
Garcia Pérez, Pablo.....	280
Gaudin, Arnaud.....	175
Gautier, François.....	70, 175
Genevaux, Jean-Michel.....	360
Gumula, Teresa.....	185
Guyader, Jean-Louis.....	64
Haddar, Mohamed.....	129
Hamdi, Adel.....	105, 113
Hamdi, Mohamed-Ali.....	26
Harras, Bilal.....	120, 205, 250
Hassin, Jérémie.....	221
Hereil, Pierre-Louis.....	221
Ichchou, Mohamed.....	46, 105, 113, 120, 129, 140, 165, 205, 240, 260, 284
Jaber, Mariam.....	293
Jalel, Benabdallah.....	113
Jäiem, Emna.....	101
Jridi, Nidhal.....	105
Kerisit, Christophe.....	197
Khalfallah, Sinda.....	101

Kraiem, Omar.....	307
Lachat, Rémy.....	83
Lacome, Jean-Luc.....	221
Ladeveze, Pierre.....	325
Lainé, Jean-Pierre.....	46, 260
Laligant, Etienne.....	284
Lascoup, Bertrand.....	353
Le Plenier, Cyprien.....	154
Leerungruang, S.....	140
Legallo, Vincent.....	74
Legay, Antoine.....	150
Li Hao, Olivier.....	325
Limido, Jérôme.....	221
Lépine, Paul.....	191
Magniez, Julien.....	26
Makrem, Arfaoui.....	113
Mejdi, Abderrazak.....	343
Melz, Tobias.....	293
Meyer, Yann.....	83
Millithaler, Pierre.....	1
Mitrou, Giannoula.....	36
Moulay Abdelali, Hanane.....	250
Muller, Stéphane.....	5
Nobou Dassi, Martial.....	175
Ouisse, Morvan.....	1, 165, 231
Ourahmoune, Reda Elhak.....	314
Parent, Marie-Océane.....	191
Peres, Patrick.....	280
Petitjean, Benoît.....	74
Pezerat, Charles.....	64, 70, 175, 353
Pfaab, Kilian.....	221
Picart, Pascal.....	70
Poittevin, Julien.....	70
Puillet, Christian.....	221
Renaud, Franck.....	231
Renno, Jamil.....	36
Riou, Hervé.....	66, 325
Rouleau, Lucie.....	150

Sadoulet-Reboul, Emeline.....	1
Salvia, Michelle.....	105, 314
Schmitt, Nicolas.....	307
Schneeweiss, Helmut.....	293
Tarfaoui, Mostapha.....	16
Tayeb, Adel.....	113
Trameçon, Alain.....	332
Troclet, Bernard.....	26, 66, 165
Tufano, Anna Rita.....	284
Wareing, Andrew.....	269
Wassereau, Thibault.....	64
Zergoune, Zakaria.....	120
Zhao, Han.....	307
Zine, Abdelmalek.....	101
Zoghaib, Lionel.....	74
Zouari, Sahar.....	360



IDENTIFICATION OF EQUIVALENT ANISOTROPIC MATERIAL PROPERTIES OF 3D-HETEROGENEOUS STRUCTURES

P. Millithaler^{1,2,*}, É. Sadoulet-Reboul², M. Ouisse², J.-B. Dupont¹ and N. Bouhaddi²

¹Vibratec,

28 chemin du petit bois, BP36, F-69131 Écully Cedex, France
Email: pierre.millithaler@vibratec.fr, jean-baptiste.dupont@vibratec.fr

²Femto-S.T. Institute - Applied Mechanics, UMR CNRS 6174

24 chemin de l'Épitaphe, 25000 Besançon, France
Email: emeline.sadoulet-reboul@univ-fcomte.fr, morvan.ouisse@femto-st.fr,
nouredine.bouhaddi@univ-fcomte.fr

ABSTRACT

Finite-element models of heterogeneous structures often need to be simplified by the means of representative equivalent homogeneous materials in order to simulate their mechanical behaviours with a reasonably low number of degrees of freedom. In this paper, a novel method of 3D-equivalent material identification is proposed for finite element anisotropic structures and for models subjected to preloads and friction. Taking into account friction properties as well as compression preloads resulting from the manufacturing process, an equivalent finite-element model for the magnetic core of an electric machine stator is created. The simulated modal basis is then compared to experimental ovalisation modes measured on a real stator, and shows good accuracy. These results offer interesting perspectives for dynamic simulations of heterogeneous structures such as industrial electric machines, for which predicting the acoustic behaviours is a key issue for the automotive industry.

1 INTRODUCTION

Relatively common in finite-element simulations involving composite structures, so-called “homogenisation” methods are developed in order to model heterogeneous structures such as laminates or honeycomb plates. For dynamic simulations on industrial electric machine stators, 3D-homogenisation methods for laminated structures may be required as they are built on multi-layered cores. Some vibration and finite-element modelling analyses have been detailed in the literature (such as the works [1, 2]). The current simulation procedures on electric motor stators have the drawback of relying on delicate measurements on costly prototypes.

This is why a new method is proposed, in order to create homogeneous materials whose elasticity matrices approximate the phenomena existing in the initial heterogeneous structures, and take into account boundary conditions and external perturbations as well. A numerical-experimental application on the finite-element model of the magnetic core of an electric machine stator is proposed, accounting for heterogeneities induced by weld beads as well as the influence of inter-lamina friction and prestress on the elastic behaviour. In the following sections, the development of the algorithm for the identification of elastic properties in the case of triclinic materials will be presented, and followed by applications.

2 IDENTIFICATION METHOD FOR ANISOTROPIC MATERIALS

The identification process must be made on a sample representing the periodicity of the structure to be homogenised. Taking the influence of perturbations on the elastic properties is a necessary prerequisite that the finite-element solver used for the identification on the sample must manage. In order to model friction properties, the elements have to be separated: the interface nodes are doubled and coincident (as illustrated in the ellipses on Figure 1), and each of them only belongs to one of the two elements. Then, creating a superelement (with translational degrees of freedom) at the outer nodes is an efficient way to output a stiffness matrix and merge the nodes at the interface.

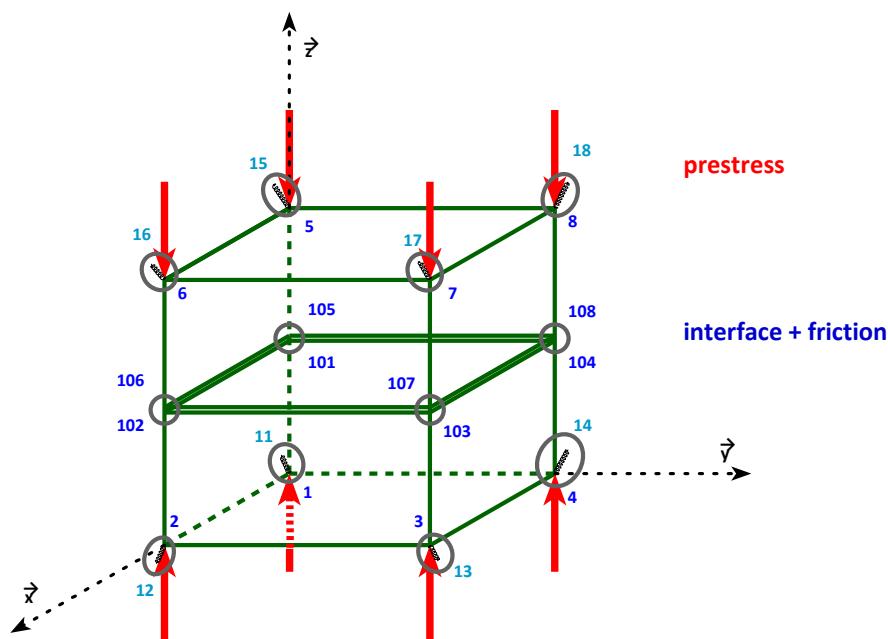


Figure 1: Example of finite element sample

The 21 independent coefficients of a triclinic elasticity matrix C or the associated com-

pliance matrix $S = C^{-1}$ have to be identified independently. The idea of the method is to recompose Hooke's law $\varepsilon = S\sigma$ with 21 independent static simulations on the sample, which are computed in only a few seconds with any commercial finite-element solver.

3 EQUIVALENT FINITE-ELEMENT MODEL OF AN ELECTRIC MOTOR STATOR WITH FRICTIONAL AND PRESTRESS EFFECTS

The finite-element model of an industrial "12-8" switched-reluctance motor is used for this application. An illustration of the model is given on Figure 2. The stator consists in a stack of several hundreds of steel sheets separated from each other by varnish. During its manufacturing process, weld beads are applied on the lateral side of the stack, while the magnetic core is placed under a press. When the pressure is released, the stack is held in one piece by the weld beads, while in the rest of the structure, the only bond between the sheets are bound together is the varnish. This is a source of heterogeneities in the behaviour of the entire structure. Therefore, each colour zone of the model on Figure 2 corresponds to a specific material identification, and therefore to distinct equivalent material properties. The finite-element model as well as the material properties are expressed in the cylindrical coordinate system $\{r, \theta, z\}$.

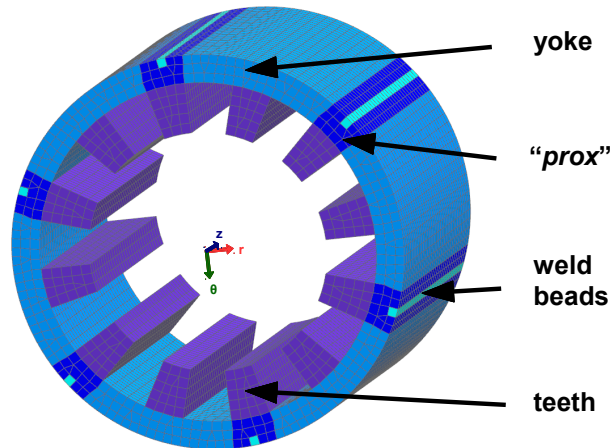


Figure 2: Magnetic core's finite-element model (axis along z)

The compression prestress are computed from the value of 2,500 kg applied on the structure during its manufacturing process, accounting for the distance of the considered zone to the weld beads. At the interface, the contact properties are described by a Coulomb dry friction is of coefficient $\mu = 0.9$. Applying the identification method on each zone then yields the elasticity matrices

$$\tilde{C}^{yoke} = \begin{bmatrix} 227 & 65 & 29 & 6 \cdot 10^{-4} & -1 \cdot 10^{-5} & 2 \cdot 10^{-8} \\ & 227 & 29 & 6 \cdot 10^{-4} & -1 \cdot 10^{-5} & 5 \cdot 10^{-8} \\ & & 90 & 2 \cdot 10^{-3} & -4 \cdot 10^{-5} & 1 \cdot 10^{-8} \\ & & & 45 & 3 \cdot 10^{-3} & 4 \cdot 10^{-1} \\ \text{sym.} & & & & 45 & 4 \cdot 10^{-1} \\ & & & & & 78.1 \end{bmatrix} \cdot 10^9 \quad (1)$$

and

$$\tilde{\mathbf{C}}^{\text{teeth}} = \begin{bmatrix} 233 & 69 & 43 & 2 \cdot 10^{-7} & -2 \cdot 10^{-7} & 3 \cdot 10^{-8} \\ & 233 & 44 & 2 \cdot 10^{-7} & -2 \cdot 10^{-7} & 1 \cdot 10^{-8} \\ & & 14 & 2 \cdot 10^{-7} & -2 \cdot 10^{-7} & 2 \cdot 10^{-8} \\ & & & 3.3 & 2 \cdot 10^{-4} & 1 \cdot 10^{-1} \\ \text{sym.} & & & & 3.3 & 1 \cdot 10^{-1} \\ & & & & & 55 \end{bmatrix} \cdot 10^9 \quad (2)$$

and the orthotropic material properties for the zone “prox”: $\tilde{E}_r = \tilde{E}_\theta = 205 \text{ GPa}$, $\tilde{E}_z = 157 \text{ GPa}$, $\tilde{G}_{z\theta} = \tilde{G}_{zr} = 51.2 \text{ GPa}$, $\tilde{G}_{r\theta} = 82.1 \text{ GPa}$, and $\tilde{\nu}_{\theta z} = \tilde{\nu}_{rz} = \tilde{\nu}_{r\theta} = 0.25$. The weld beads are modelled with isotropic steel, such as $E = 207 \text{ GPa}$ and $\nu = 0.29$. The same density $7,750 \text{ kg} \cdot \text{m}^{-3}$ is applied to the entire structure.

A modal basis is simulated in real domain between 0 and 10,000 Hz from the entire magnetic core’s finite-element model. This simulated modal basis is compared with a set of purely radial modes (of spatial orders 2, 3, 4, 5 and 0), extracted from frequency response functions measured with an impact hammer on the corresponding real stator’s magnetic core. These modes are sometimes referred to as “cylinder” or “ovalisation” modes, and are critical for the acoustic behaviour of the entire stator [2]; being able to predict them accurately is thus of particular interest. Finally, the average of absolute frequency discrepancies between simulated and measured modes is 2.83%, while the average MAC-value (expressing the similarities between paired mode shapes) is at 71.9%. Therefore, these results show that the equivalent finite-element model is able to predict the measured ovalisation modes with good accuracy, and without need of expensive updating procedures.

4 CONCLUSION

In this paper, a novel method for identifying equivalent materials to anisotropic structures was proposed. It has been shown that the method is also able to identify equivalent elasticity matrices for an electric machine stator subjected to friction and prestress, and its effectiveness has been validated with experimental data. Additionally, this identification method can be applied to superelements, unlike existing homogenization techniques, and can therefore convert stiffness matrices into equivalent elasticity matrices.

REFERENCES

- [1] L. Humbert, P. Pellerey, and S. Cristaudo. Electromagnetic and structural coupled simulation to investigate nvh behavior of an electrical automotive powertrain. *SAE International*, (12SNVH-0002):1–12, 2012.
- [2] J.-B. Dupont, P. Bouvet, and L. Humbert. Vibroacoustic simulation of an electric motor: methodology and focus on the structural fem representativity. In *International Conference on Electrical Machines*, pages 1–7, Marseille, September 2012.



APPLICATION OF NON-PARAMETRIC UNCERTAINTIES METHOD ON LAUNCHERS MECHANICAL SPECIFICATIONS

S. Muller¹, A. Alouani^{1,3}

¹AIRBUS Defence and Space, Department Mechanical Engineering
66 route de Verneuil, F-78133, Les Mureaux Cedex, France

Email: stephane.muller@astrium.eads.net, antoine.alouani2@astrium.eads.net

ABSTRACT

The launch vehicles are subject to severe dynamic loads at lift-off and during flight ascent. Moreover, a major part of European launch vehicles are of composite construction. Thus, a robust design requires a proper consideration of uncertainties in excitations and materials. A non-parametric methodology was experienced on the condensed finite element models of parts of the ARIANE 5 launcher with the objective of releasing less dimensioning but still justified mechanical specifications to get used by the launcher sub-contractors. Such methodology allows introducing different level of uncertainties on parts of the launcher depending on the complexity of elements and their impact on the dynamic phenomenon targeted. The article details the methodology implementation already achieved on ARIANE 5 on the solid rocket booster pressure oscillation load case which is one of the driving load case regarding the amplitude of the low frequency vibrations on the launcher.

1 INTRODUCTION

A launcher FEM is the result of the assembly of numerous sub-structures FEM provided by sub-contractors. Uncertainties at launcher level cover not only scattering of materials and modeling but include also discrepancies introduced by operational conditions of use (with different boundaries conditions than the ones used to set-up and validate the sub-structure FEM) and by connections modeling between sub-structures. Mastering of uncertainties in structural dynamics is hence a challenge that can be handled through a various set of methodologies. [1] gives a global overview of the research field that can be subdivided, on an engineering perspective, into “microscale” schemes dealing with physical properties of FE elements and “macroscale” schemes dealing with mass, stiffness, damping matrices properties of a FE sub-component.

- Microscale (parametric) methods are adapted to small models but require prohibitive CPU times when applied to large FE models like in a launcher modeling case. Furthermore, they take only into account physical parameter uncertainties.
- Macroscale (non-parametric) methods are introducing uncertainties at a macroscopic level of analysis, e.g. on matrices of super-elements of the assembled FEM. The main methods include Gaussian orthogonal ensemble, non-parametric approaches and matrix scaling.

These approaches, coupled with simulation methods (Monte-Carlo, Factorial Design) are much less CPU demanding and allow introducing macroscopic perturbation covering more than physical properties uncertainties. The main drawback is that the link between tuning factors and design parameters is not as straightforward as for the local methods. The interpretation of the level of uncertainties and its physical likelihood is less direct. A first trade-off between the methods led us introducing uncertainties in the launcher FEM through global approaches, e.g. matrix scaling and non-parametric techniques. Aside CPU time considerations, these methods are also well adapted to the launcher dynamic modeling based on assembly of different Craig-Bampton condensed FEM from sub-contractors that can only be scattered through their mass, stiffness and damping matrices, native FEM being rarely accessible at launcher system level.

1.1 Matrix scaling

The matrix scaling consists in introducing perturbations into mass, damping and stiffness condensed matrices $[M], [K], [C]$ used in the structural dynamics equation (1) with scalar operators $\delta_M, \delta_C, \delta_K$ associated to a probability distribution. Mechanical uncertainties are then characterized by random matrices $[\tilde{M}], [\tilde{C}], [\tilde{K}]$ (2).

$$[\tilde{M}]\{\ddot{X}\} + [\tilde{C}]\{\dot{X}\} + [\tilde{K}]\{X\} = \{F_{ext}\} \quad (1)$$

$$[\tilde{M}] = \delta_M \cdot [M], [\tilde{C}] = \delta_C \cdot [C], [\tilde{K}] = \delta_K \cdot [K] \quad (2)$$

We applied this technique for simple sub-structures presenting uniform characteristics (isotropy of material and/or geometry) where the risk of non-physical likelihood introduced by the scaling is limited.



Figure 1: ARIANE 5 payload structure

In the ARIANE 5 launcher case, elements like payload adaptors (Figure 1) are relevant for such a technique. As a result, the matrix scaling is also suited for models condensed statically via the Guyan method.

1.2 Random matrices

This technique [3] is a generalization of the matrix scaling applied on FEM super-elements with stochastic matrices applied on mass, damping and stiffness matrices (3) instead of scalar operator. The random matrices are then defined by:

$$[\tilde{M}] = [L_M]^T \cdot [G_M] \cdot [L_M], \quad [\tilde{C}] = [L_C]^T \cdot [G_C] \cdot [L_C], \quad [\tilde{K}] = [L_K]^T \cdot [G_K] \cdot [L_K] \quad (3)$$

Where $[G_{M,C,K}]$ are stochastic initiation matrices and $[L_{M,C,K}]$ are the mass, damping and stiffness matrices expressed by the Cholesky factorization (4).

$$[X] = [L_X]^T \cdot [L_X] \text{ with } X = M, C, \text{ or } K \quad (4)$$

Guaranteeing the random matrices being physically admissible, meaning that they give admissible solutions of (1), requires the stochastic initiation matrix $[G]$ verifying the following conditions [3], called the available objective information:

- Random matrices $[G]$ are defined in the probability space $(\mathcal{A}, \mathcal{T}, \mathcal{P})$ with values in $\mathbb{M}_n^+(\mathbb{R})$
- The mean values of these random matrices must be equal to $[I]$ so that $\varepsilon([\tilde{M}, \tilde{K}, \tilde{C}]) = [M, K, C]$
- $\varepsilon(\| [G]^{-1} \|_F^2) < \infty$, where $\| \cdot \|_F$ is the Frobenious norm in order to guarantee that the matrix inverse always exists,

Nevertheless, the amount of uncertainty introduced in the model via this technique can still be assessed thanks to a scalar quantity. This so called uncertainty tuning parameter δ applied on $[M], [C]$ or $[K]$ is defined by (5):

$$\delta = \sqrt{\frac{\| [G] - [I] \|_F^2}{\| [I] \|_F^2}} \quad (5)$$

As a result, an infinite amount of stochastic matrices $[G]$ corresponding to the same level of global uncertainty can be generated. This parameter δ would thus be an equivalent of the standard deviation of a scalar uncertainty: infinity of random values can be generated for a given standard deviation in accordance with a defined distribution law. The distribution law associated to those matrices [3] has been defined in order to respect the available objective information and to minimize the entropy introduced in the system:

$$P_{[G]}([G]) = 1_{\mathbb{M}^+(\mathbb{R})}([G]) \cdot C_G \cdot \det([G])^{(n+1)\frac{(1-\delta^2)}{2\delta^2}} \cdot e^{-\frac{n+1}{2\delta^2}tr([G])} \quad (6)$$

Where:

- $\det([G])$ is the determinant of the $[G]$ matrix,
- $tr([G])$ its trace, n its dimension,
- $1_{\mathbb{M}^+(\mathbb{R})}$ is a function equal to 1 as the matrix belongs to $\mathbb{M}^+(\mathbb{R})$, and zero otherwise,
- C_G is a positive normative constant, detailed in [3].

Unlike the matrix scaling method where the uncertainties are introduced uniformly on the FE matrices of each super-element, the non-parametric methodology allows introducing local and independent uncertainty factors.

2 A STUDY CASE –ARIANE5 SOLID ROCKET BOOSTERS FIRST ACOUSTIC MODE LOAD CASE

2.1 Load case characteristics

One of the main mechanical load case encountered in ARIANE 5 flight is the first Solid Rocket Boosters (SRBs) acoustic mode load case [2]. This load case is characterized by sine bursts excitations generated by both SRBs (Figure 2) and gives significant vibration responses on all parts of the launcher.

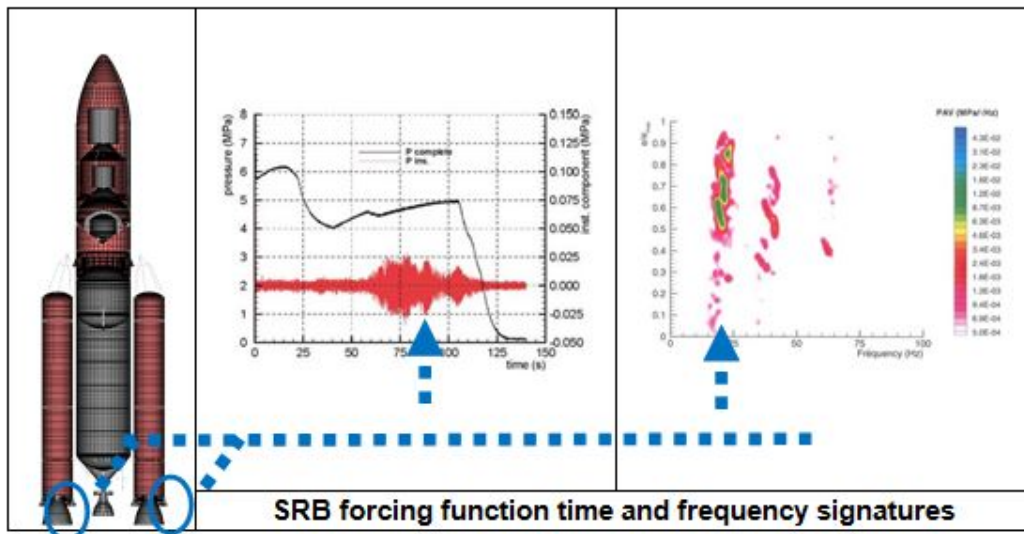


Figure 2: ARIANE 5 SRBs first acoustic mode load case

The flight analyses show that the vibrations levels are generated mostly by global modes of the launcher (bending modes, tank modes) that are dynamically driven by global mechanical characteristics of launcher sub-components. It is then well suited for the non-parametric uncertainties methodology applied on mechanical consistent ensembles (stages, skirt...). In consequence, we cut the launcher FEM into super-elements (Figure 3) on which uncertainties could be applied.

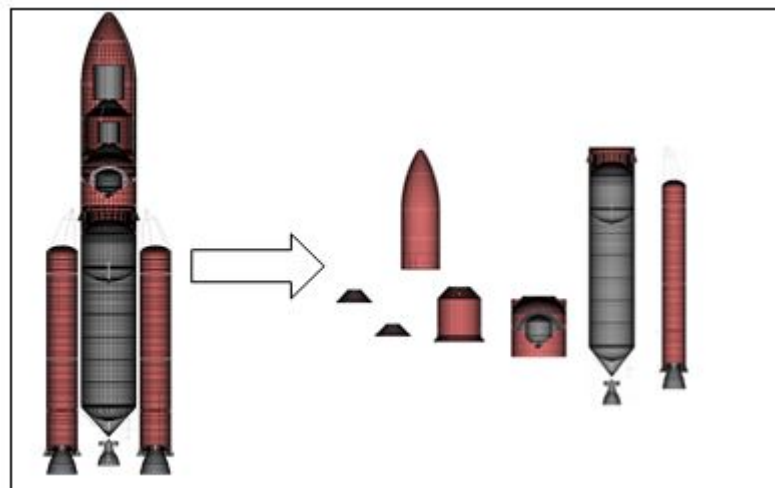


Figure 3: Launcher cutting into elementary mechanical models

This includes Craig-Bampton (non-parametric uncertainties) and Guyan (matrix scaling) condensation schemes as well as explicit modeling (matrix scaling) for some simple elements. As the relevant values of uncertainty tuning parameters δ on the different launcher parts cannot be fixed thanks to physical considerations, an inverse problem has to be solved. The aim is then to find values for these parameters able to predict responses consistent with what has been observed in flight and also with a certain degree of conservatism in order to have a robust simulation tool. The identification of uncertainties factor to get applied on super-elements to reach a relevant coverage of predictions requires metrics in both frequency and time domain. ARIANE 5 load case predictions are indeed performed in these two spaces with a global objective of releasing 99% envelope vibration levels.

2.2 Time domain (A_t) & frequency domain (A_f) sensitivity metrics

In the time domain, the metric is defined as the scalar ratio between maximum values of 99% envelope and nominal prediction (7).

$$A_t = \frac{\max_t(\gamma_{99\%}(t))}{\max_t(\gamma_{nominal}(t))} \tag{7}$$

In the frequency domain, the metric is defined by the weighted sum of the mean amplification ratios at resonance calculated on the different peaks computed through shock spectra responses (8).

$$A_f = \sum_{i=1}^{N_{peak}} C_i \cdot \frac{\int_{f_1^{nom}(i)}^{f_2^{nom}(i)} \gamma_{99\%}(f) df}{\int_{f_1^{nom}(i)}^{f_2^{nom}(i)} \gamma_{nominal}(f) df} \quad \text{with } C_i = \frac{\max_{f \in [f_1^{nom}(i), f_2^{nom}(i)]} (\gamma_{99\%}(f))}{\sum_1^{N_{peak}} \max_{f \in [f_1^{nom}(i), f_2^{nom}(i)]} (\gamma_{99\%}(f))} \tag{8}$$

The 99% envelopes are assessed through quantiles computations based on the several thousands of simulations representing one single uncertainty case where different super-elements are scattered with a specific value of uncertainty parameter δ (Figure 4).

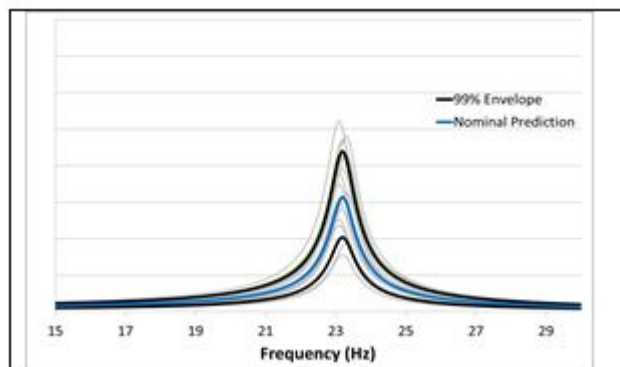


Figure 4: Nominal and 99% predictions

2.3 Calibration of δ_M and δ_K

As a first step, unitary sensitivity studies were performed to identify driving uncertainty factors w.r.t dynamic responses of the launcher. Each super-element was scattered separately considering four values of tuning factor δ_M and δ_K selected between 10% and 40%, represented each time by about 2000 draws of different stochastic matrices [G] introducing the required global

degree of uncertainty on the related launcher part. Each assembled model was then used for a vibration prediction corresponding to the SRBs first acoustic mode load case in both frequency and time domains Using coverage metrics A_t and A_f , sensibility plots were computed on every launcher's point of interest corresponding to sensor locations in order to compare the results with the flight data. Families were identified based on their visual similarity of behavior and their spatial location on the launcher. Similar footprints were identified on spatial location families on the launcher which allowed defining spatially correlated zone regarding the load case dynamic responses on spatial zones. An example is given for the blue delimited zone on the Figure 5.

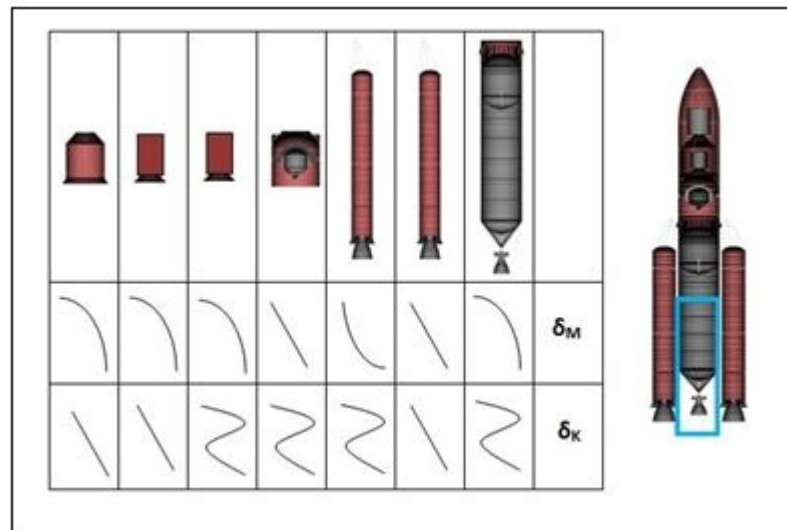


Figure 5: Sensibility footprints vs. mechanical models within a spatial family

The family segmentation gave similar results when performed in time and frequency domains, which looks logical as the physic of the load case is unique behind the time or frequency approaches. Hence, the non-parametric methodology allows putting uncertainties on a FEM on a limited spatial zone. This opens a large spectrum of possible tuning consistent with uncertainties of one or several super-elements. Nevertheless, the single footprints, if useful to have a first trend of the relative importance of uncertainties applied on super-elements, are not adapted to multi-variable uncertainties tuning; this requires setting-up multi-dimensional surfaces whose exhaustive computation would be still too demanding regarding CPU time. To overcome this drawback, an optimized factorial design coupled with relevant simplifications was set-up in order to estimate reliably the response surfaces approximating the responses amplification as a function of the various uncertainties within an acceptable amount of computations.

3 SURFACE RESPONSES FACTORIAL DESIGN APPROACH

3.1 Modeling of factorial design

The aim of the factorial design is to have an analytical formulation as accurate as possible in order to predict quickly the launcher responses for any set of uncertainties applied on its structures without generating the 2000 stochastic matrices or computing the corresponding responses with the FEM. The surface response was addressed through a Taylor development of the computed sensitivity metrics (9).

$$A_{v/f}(X_i, X_j, X_k, X_l, X_m) = \alpha_0 + \sum_i \alpha_i X_i + \sum_{(i,j), i \leq j} \alpha_{ij} X_i X_j + \dots + \sum_{(i,j,k,l,m), i \leq j \leq k \leq l \leq m} \alpha_{ijklm} X_i X_j X_k X_l X_m + \epsilon \quad (9)$$

With:

- A_{vf} : the time/frequency coverage of the response in one point of the scattered launcher with respect to the nominal response (no uncertainty in the model)
- X_i : centered uncertainty level (mass/stiffness) applied to the super-element i ,

$$X_i = \frac{\delta_i - 0.2}{0.2}$$
- α_i : response surface coefficients to be identified
- ε : residue

The $N = 14$ dimension corresponds to the number of super-elements considered for the non-parametric method, e.g. stiffness and mass uncertainties tuning factors applied on 7 super-elements. The polynomial form is in accordance with sensibility footprints that didn't put in evidence any steep variations but rather continuous evolutions. The factorial design setting-up is based on the selection of optimal sets of values for input parameters (X_i, X_j, X_k, X_l, X_m) allowing the minimization of the residual factors $\varepsilon\{\varepsilon_i\}$ for P realization with $P \leq N$. The identification problem of the response surface coefficients can thus be defined by the linear system (10).

$$\begin{Bmatrix} y_1 \\ \vdots \\ y_N \end{Bmatrix} = [X] \times \begin{Bmatrix} \alpha_i \\ \vdots \\ \alpha_P \end{Bmatrix} + \begin{Bmatrix} \varepsilon_i \\ \vdots \\ \varepsilon_N \end{Bmatrix}, X \in M^{(N,P)}(\mathfrak{R}) \quad (10)$$

With:

- y : realization vector gathering the results of the experiences attempted
- X : factorial design matrix gathering the selected values of the input parameters and defining the different independent experiences performed to have the realization vector.

Such system is classically solved through a regression method by increasing the number of experiences from P to N and computing most likely parameters $\tilde{\alpha}$ (11).

$$\tilde{\alpha} = (X^T \cdot X)^{-1} \cdot X^T \cdot \{Y\} \quad (11)$$

Nevertheless, with formulation (8), the resolution of the order N exhaustive Taylor development requires to identify a very large number of coefficients (12):

$$\dim = 1 + \sum_{i=1}^N C_i^N + N \cdot (N - i) \cdot C_{i-1}^{N-1} \quad (12)$$

For 14 variables, it is equivalent to 761.856 coefficients, so potentially as many experiences to perform, representing up to more than 3000 years of CPU time. As a result, such a problem cannot be solved now, except by massive parallelization of CPU's. Thus, dimension of the problem was reduced (13) in order to ensure admissible computation time but still maintaining an acceptable accuracy of the response surface. A factorial design approach based on Rechtshaffner formulations [5] was set-up accordingly.

$$y = \alpha_0 + \sum_i \alpha_i X_i + \sum_{i=1}^{N-1} \sum_{j=i+1}^N \alpha_{ij} X_i X_j \quad (13)$$

Relative weights on applied uncertainties can be assessed through $\alpha_{ij,(i,j),i<j}$ (order 2 interaction) and $\alpha_{ij,k,(i,j,k),i<j<k}$ (order 3 interaction) of (9). Their importance is determined by the measurement of the difference in predicted levels with and without this term (Table 1).

$\varepsilon_{ij} = \max_{\delta} \left(\frac{\alpha_{ij} \delta^2}{\alpha_0 + (\alpha_i + \alpha_j) \delta + (\alpha_{ii} + \alpha_{jj}) \delta^2} \right)$ <p>2nd order interaction metric</p>
$\varepsilon_{ijk} = \max_{\delta} \left(\frac{\alpha_{ijk} \delta^3}{\alpha_0 + (\alpha_i + \alpha_j + \alpha_k) \delta + (\alpha_{ij} + \alpha_{ik} + \alpha_{jk}) \delta^2 + (\alpha_{ii} + \alpha_{jj} + \alpha_{kk}) \delta^2} \right)$ <p>3rd order interaction metric</p>

Table 1: Cross-interaction metrics

The Figure 6 presents a typical interaction plot where the ground surface is offset at 15%, meaning that only differences higher than this threshold appear. The stiffness uncertainties cross-interactions are presented, IxJ tag corresponding to the cross interaction between super-elements I and J along the different response locations.

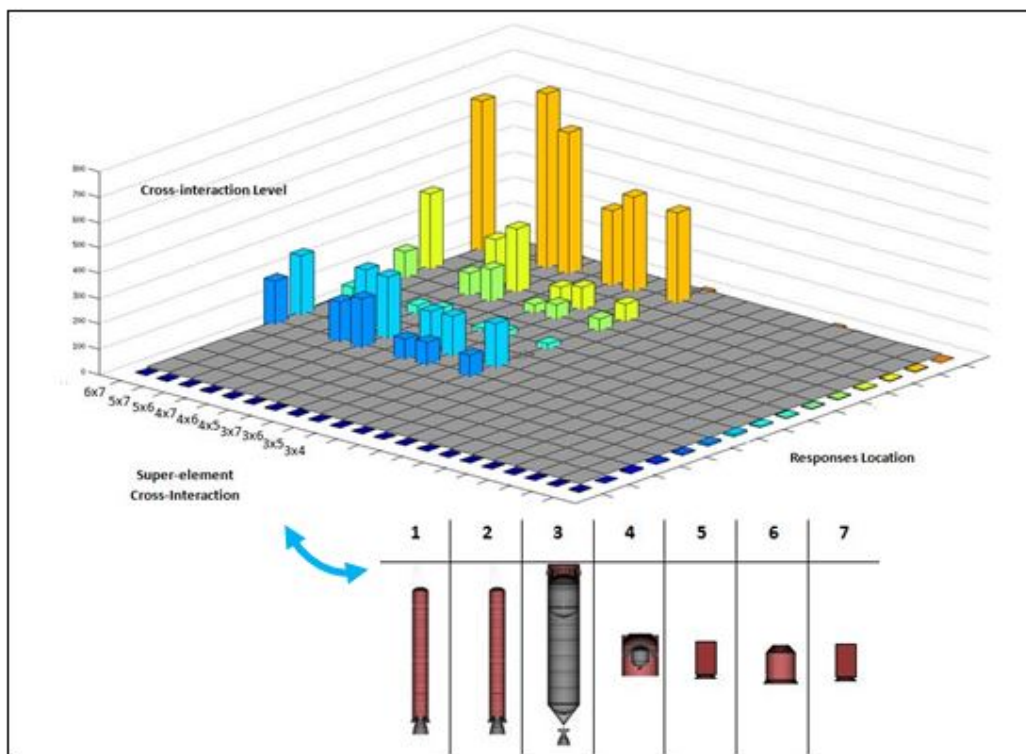


Figure 6: Stiffness cross-interactions between super-elements

The factorial design approach is thus a powerful tool that will be used to set-up a generic uncertainties treatment to be used to release justified and less dimensioning specifications. As a first step, the methodology was used to tune uncertainty factor required to cover flight vibrations by prediction thanks to the polynomial approximation of the launcher responses amplification.

4 CALIBRATION OF UNCERTAINTIES TUNING FACTORS

The weight to be applied on uncertainties tuning factors can be assessed by analysis of flight vibration records using coverage metrics and the analytical behavior of the response amplification of the scattered launcher given by the response surface (13). These populations were then reused to extrapolate tuning factors to get used for releasing 99% envelope vibration levels. Results presented here are a first flight coverage analyses.

4.1 Flight coverage tuning factors

The coverage level is defined (in the frequency domain) by (14).

$$C_F(\delta_j^M, \delta_j^K) = C_F^{nom/vol} \cdot f_F(\delta_j^M, \delta_j^K) \quad (14)$$

- $C_F^{nom/vol}$ is the ratio of nominal (e.g. without uncertainties) predicted responses vs. flight measured ones (Figure 7),
- f_F is the response surface approximating the response amplification of the scattered launcher with respect to the nominal one via the polynomial expression (13).

The frequency analyses of flight records were reached by shock spectra analysis.

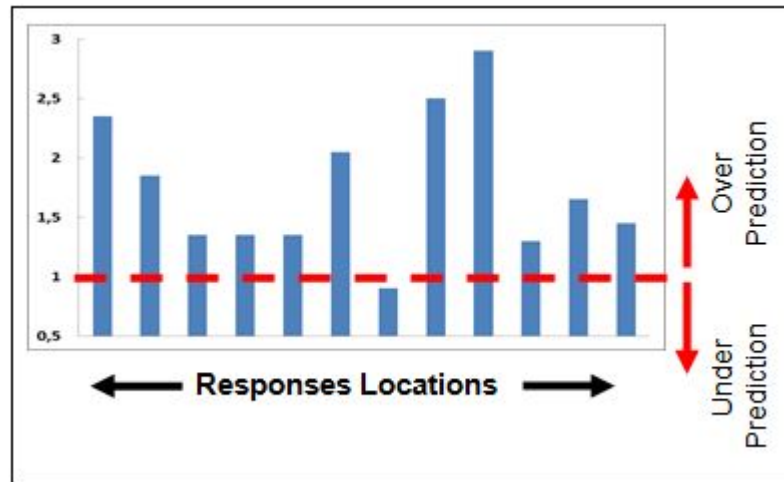


Figure 7: Flight average coverage

A vector objective function (15) was defined on the uncertainty vector $\delta = (\delta_1^M, \dots, \delta_7^M, \delta_1^K, \dots, \delta_7^K)$ and optimization algorithms were used to find tuning parameters allowing prediction being as close as possible as flight observations.

$$\overrightarrow{F_{obj}}(\delta) = \{C_F \cdot f_F(\delta) - 1\} \quad (15)$$

The optimizations were realized through Monte-Carlo simulations that demonstrated a convergence of uncertainties tuning parameters into limited intervals.

The table 2 illustrates the results for stiffness uncertainties.

Monte-Carlo populations	Number of solutions	Tuning parameters intervals					
		SE-1&2	SE-3	SE-4	SE-5	SE-6	SE-7
50 k	0	-	-	-	-	-	-
500 k	3	0.3316	0.0034	0.0168	0.0974	0.0135	0.1459
		0.4129	0.0396	0.0392	0.3594	0.0199	0.1900
5000 k	81	0.3024	0.0002	0.0000	0.0033	0.0003	0.1409
		0.4343	0.0556	0.0621	0.4240	0.0717	0.2027

Table 2: Optimized uncertainties tuning parameters

The solution domain corresponding to a flight event is only a small sub-domain of the 7th dimension space (stiffness uncertainties considered here) but is not singular, meaning that different tuning factors were found admissible regarding the objective function and physical likelihood. Moreover, it has been numerically assessed that the solution sub-domain was continuous: for a specific solution vector δ_0 , the vectors $\delta_0 + d\delta$ with $|d\delta| \ll |\delta_0|$ belong also to solutions sub domain. Different convergence algorithms were tested to verify the robustness of the solution domain and find one specific set of uncertainties optimizing the flight coverage by the scatter launcher assembly. They confirmed the tuned domains, without noticeable reduction. These optimums identified thanks to the polynomial approximation of the launcher behavior have been checked by re-computing directly the responses of the corresponding scattered launcher with the finite element model and the related scattered matrices of its sub-structures. Those final direct computations (not the polynomial prediction) for two optimized uncertainties sets are presented in Figure 8 and compared with the nominal simulation by showing the response amplification of 12 observation points with respect to the flight measurements. The unity coverage diagram (plotted in blue) represents the target level of amplification for the optimization process and also the threshold that should not be underpassed.

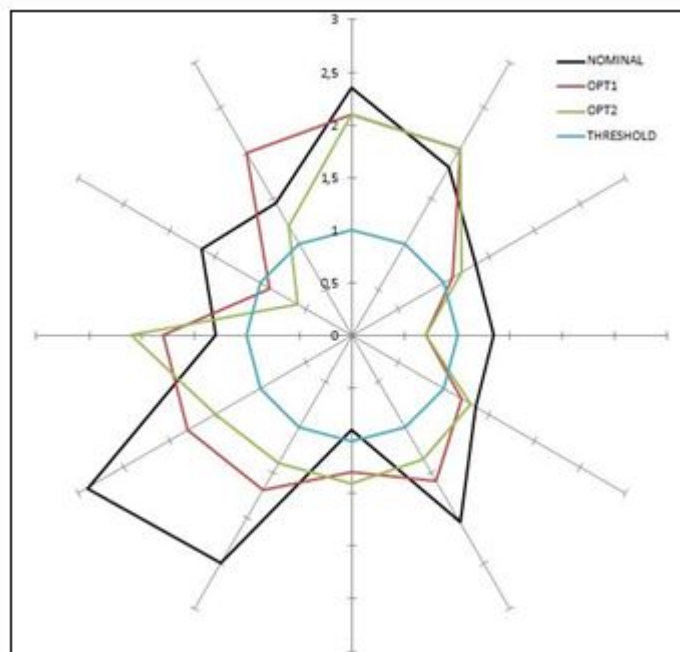


Figure 8: Optimization flight coverage results

The optimal tunings are giving a closer coverage flight than nominal simulation. They are demonstrating that predictions closer to flight can be achieved through application of non-parametric uncertainties technique to super-elements.

5 CONCLUSION

The application of non-parametric uncertainties propagation through factorial design on an ARIANE5 dimensioning load case proved to be fruitful. With a relatively limited time computation, it is possible to analyze unitary and cross-interaction of mass and stiffness characteristics of the main sub-part of the launcher. Using flight measurement feedback allows quantifying and justifying uncertainties set to be applied on the different sub-structures flight by flight.

ACKNOWLEDGEMENTS

This work was performed with the support of CNES R&T Launcher program.

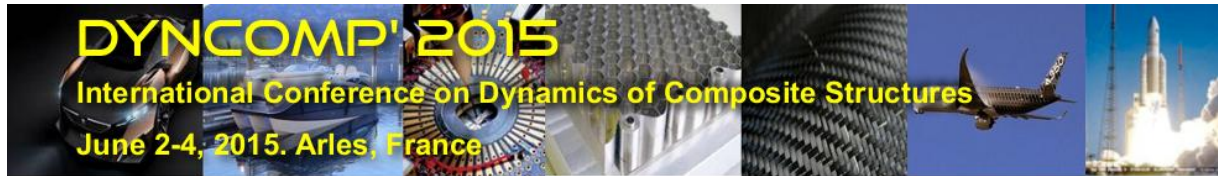
REFERENCES

- [1] C.S. Manohar and R.A. Ibrahim. *Progress in Structural Dynamics with Stochastic Parameter Variations: 1987-1998*, Applied Mechanics Review Vol. 52 – Iss. 5, 177-197, 1999
- [2] Y. Fabignon, J. Dupays, G. Avalon, F. Vuillot, N. Lupaglazoff, G. Casalis and M. Prévost. *Instabilities and Pressure Oscillations in Solid Rocket Motors*, Aerospace Science and Technology 7 : 191-200, 2003
- [3] C. Soize. *Random matrix theory and non-parametric model of random uncertainties in vibration analysis*, Journal of Sound and Vibration, 263 : 893 – 916, 2003.
- [4] J. Goupy. *Modélisation par les plans d'expériences*, Techniques de l'Ingénieur, traité Mesures et contrôle, 2000
- [5] R. L. Rechtshaffner. *Saturated fraction of 2nd and 3rd factorial design*, Technometrics, Vol. 9 – No. 4, 1967

COPYRIGHT NOTICE

Copyright ©2015 by the authors. Distribution of all material contained in this paper is permitted under the terms of the Creative Commons license Attribution-NonCommercial-NoDerivatives 4.0 International (CC-by-nc-nd 4.0).





EXPERIMENTAL AND NUMERICAL STUDY OF THE DYNAMICAL BEHAVIOR OF E-GLASS/VINYLESTER COMPOSITES SUBJECTED TO IN-PLANE AND OUT-OF-PLANE HIGH STRAIN RATE COMPRESSIVE LOADING

J. ARBAOUI^{1*}, M. TARFAOUI¹ and A. EL MALKI¹

¹ENSTA-Bretagne, MSN/LBMS/DFMS, 2 rue François Verny 29806 Brest, France

Email: jamal.arbaoui@ensta-bretagne.fr, mostapha.tarfaoui@ensta-bretagne.fr,
aboulghit.el_malki_alaoui@ensta-bretagne.fr

ABSTRACT

Split Hopkinson Pressure Bar (SHPB) is one of the most important and recognized apparatus used for characterizing the dynamic behavior of materials. In the first part, the results from a series of SHPB tests on the woven composites are presented in this paper. These tests were done in two configurations: in-plane and out-of-plan compression test. It is observed that the failure strength varies with the different loading directions. The results indicate that the stress-strain curves, maximum compressive stresses and strains evolve as strain rate changes. In the second part of this study, numerical models without damage are developed to investigate the validity of assumptions of compression Split-Hopkinson Pressure Bar technique. Abaqus software was used for the numerical simulation. The results obtained by numerical investigation (finite elements) of SHPB are compared with the in-plane and out-of-plan compression test of a woven composite. A good correlation was noted between the experimental and numerical results which allows validate the numerical approach used.

1 INTRODUCTION

Composite materials exhibit favorable mechanical properties over metallic materials and hence are increasingly considered for high technology applications, particularly in the naval field. Some of these applications are in structures subjected to dynamic loads. Since behavior of composites is known to depend on the rate of loading, knowledge of the constitutive behavior and dynamic strength (which is usually higher than the static value) is highly desirable for designers of structures intended to withstand dynamic loads [1]. Dynamic behavior of materials in the range of 100–10000 s⁻¹ strain rates has been widely studied by the Split Hopkinson's Pressure Bars (SHPB) [2]. Griffiths and Martin [3] investigated the dynamic behavior of unidirectional carbon fiber composites at high strain rates to determine how the material behavior is dependent on fiber volume fraction and fiber orientation. Chen et al. [4] investigated the effect of strain rate on the compressive and tensile behavior of a 0/90 carbon fiber reinforced resin matrix composite. Hosur et al. [5] tested the compressive properties of carbon/epoxy laminated composites at three different strain rates of 82, 164 and 817 s⁻¹ along in-plane directions. Elanchezhian et al. [6] studied the effect of varying strain rates and temperatures on the Mechanical behavior of glass and carbon fiber reinforced composites. Sierakowski et al. [7] investigated steel/epoxy composites in compression up to 1000 s⁻¹. Jenq and Sheu [8] examined the high strain rate behavior of stitched and unstitched glass/epoxy composites. Tarfaoui et al. [9, 10] tested the mechanical behaviors of angle-ply (0°, ±20°, ±30°, ±45°, ±60°, ±70° and 90°) plain weave composite laminates subjected to in-plane and out-of-plane high strain rate compressive loading. The stress-strain curves of the composite laminates showed that the material is strongly sensitive to fiber orientation and loading direction. El-Habak [11] studied the mechanical behavior of woven glass fiber reinforced composites at failure strain rates ranging from 100 to 1000 s⁻¹. He studied the effect of sizing of the fiber, and two different resin systems: epoxy and vinylester. He found that, while sizing did not influence the high strain rate behavior, composites made of vinylester matrix yielded higher strength. Woldenbet and Vinson [12] studied the effect of specimen geometry in high strain rate testing of graphite/epoxy laminates. Harding [13] studied two woven glass/ epoxy material systems in compression up to 860 s⁻¹ using cylindrical and thin strip specimens. The results for both specimen geometries indicated a significant increase in the initial modulus, strength and strain to failure with increasing strain rate.

In the present work, in-plane and out-of-plane compression behavior of an E-glass fiber reinforced vinylester composite at high strain rates was determined. Composite were prepared in 0°/90° orientation by using infusion process, tested in Split Hopkinson Pressure Bar apparatus, and modeled with explicit commercial finite element code Abaqus [14].

2 EXPERIMENTAL PROCEDURE

The woven E-glass/vinylester laminate composites samples used in our experiment were provided by EADS Composites and were manufactured for the naval applications. The sample has 52 layers with a vinylester resin matrix DION 9102. Each layer is a plain weave construction (50% weft yarns per 50% warp yarns) made of E-glass fabric, which create orthotropic mechanical properties in the three orthogonal directions. The thickness of the samples is 10.0 mm and their density is 1.85 g/cm³. The overall fiber volume fraction is 49% for the composite. The physical and mechanical properties of the vinylester resin and E-glass fibers are shown in Table 1. For dynamic tests, the cubic specimens with side length 10.0 mm for out-of-plane and 13.0 mm for in-plane loading tests, are considered, respectively. The specimen and loading direction, in-plane, and out-of-plane are presented in Figure 1. The faces

of the specimens were polished with 1000-grit sandpaper to ensure parallel loading edges. To avoid uncertainties related to size effects, the specimens in all the tests are of the same geometry.

Characteristic	E-glass fiber	Vinylester resin
Density (kg/m^3)	2540	1050
Young modulus in tension (MPa)	74000	80
Shear modulus (GPa)	33.3	1.24
Poisson Coefficient	0.22	0.35
Tensile strength (MPa)	2400	80
Compressive strength (MPa)	1450	115

Table 1. Characteristics of the E-glass fiber and the vinyl ester resin

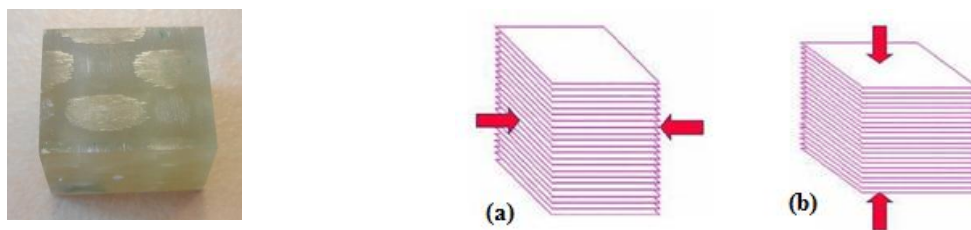


Figure 1. Specimen and loading direction, (a) in-plane and (b) out-of-plane

3 EXPERIMENTAL RESULTS

In these dynamic compression tests, a cubic sample of size $13 \text{ mm} \times 13 \text{ mm} \times 10 \text{ mm}$, is placed between the two bars, of the same diameter of 20 mm. The striker, incident and transmitted bars have a length of 400 mm, 1985 mm and 1845 mm, respectively. These bars are correctly aligned and are able to slide freely in the frame of the apparatus. The composite specimen is not attached to the bar in order to prevent the perturbation of measurement due to additional interfaces, Figure 2.

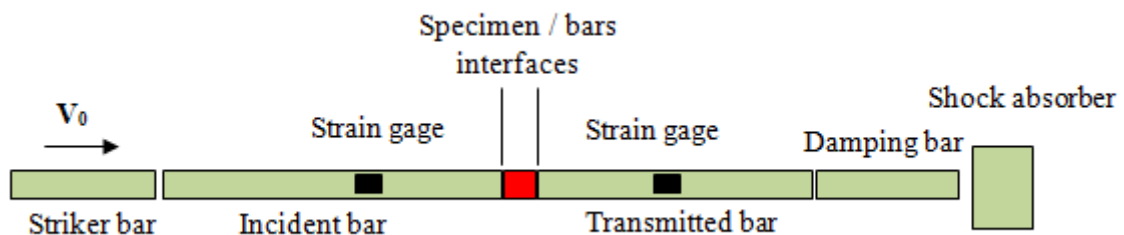


Figure 2. Schematic of compression SHPB set-up.

Before conducting the dynamic tests on the Hopkinson bar, it is necessary to ensure that these tests can be reproduced. With this objective in mind, for each loading direction, a minimum of two tests were carried out at the same impact pressure in order to analyze the tests reproducibility. As Figure 3 shows, it is noted that the tests are repeatable and this was checked for each test. For in-plane and out-of-plane tests, results for compressive strain rate between 293 s^{-1} and 1902 s^{-1} are obtained using SHPB.

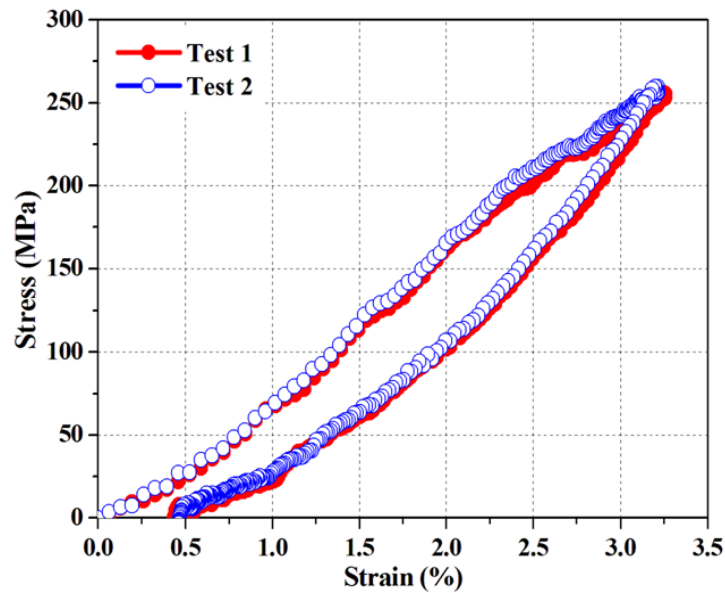


Figure 3. Test reproducibility, $P=0.1$ MPa – $V=8.29$ m/s

3.1 In-plane test

3.1.1 Mechanical behavior

The laminate specimens $[0/90]_{26}$ were subjected to in-plane loading with nine different impact pressures of the striker bar on the incident bar: 0.5, 0.7, 1, 1.2, 1.5, 1.7, 2, 2.2 and 2.5 bar (50, 70, 100, 120, 150, 170, 200, 220 and 250 ($\times 10^{-3}$ MPa)). The typical strain rate-time obtained from tests on the Hopkinson bar is shown in Figure 4. The strain rate evolution is sensitive to the entry pressure P in the chamber of compressed air and the loading direction. In the first phase, the strain rate increases rapidly, then decreases and remains fairly constant for an impact pressure from 0.5 to 1.7 bar. Indeed, the increase in impact pressure shows that the strain rate is not constant in the second phase. The presence of a second peak is the principal characteristic of these curves, which characterizes the onset of macroscopic damage [9, 10]. The critical pressure responsible for the appearance of second peak is between 1.7-2 bar. For non-damaging tests, the fall of strain rate reaches negative values, which correspond to the springback in the sample. Figure 5 shows the stress/strain for nine strain rates of 224, 339, 439, 454, 545, 603, 656, 700 and 882 s^{-1} which correspond respectively to 0.5, 0.7, 1, 1.2, 1.5, 1.7, 2, 2.2 and 2.5 bar impact pressure. Dynamic compressive behavior of the composite is strongly influenced by the strain rate. The stress-strain behavior in each case was similar during the linear elastic behavior, whereas the stress increased with the increasing strain rate. For non-damaging tests, we observed that the sample tends to take again its initial state, with presence of plastic deformation. On the other side, for damaging tests, the sample continues to deform. Also, a brittle behavior is noted, which is controlled by matrix failure. The nonlinearity of the stress-strain curves is different and corresponds to different damaging modes. From Figure 5, the Young modulus, maximum compressive stress and failure strain have been obtained and listed in Table 2. For in-plane loading, the dynamic stiffness $E_{dynamic}$ remains almost constant and the maximum stress σ_{max} increases with the impact pressure until a pressure threshold is reached from which the tendency is reversed; i.e. they decrease with the increase of impact pressure. The thermal softening due to inelastic heat dissipation and damage may explain this

behavior. Similar behavior has been reported by Tarfaoui [15] for SHPB testing of Glasse/Epoxy laminated composites.

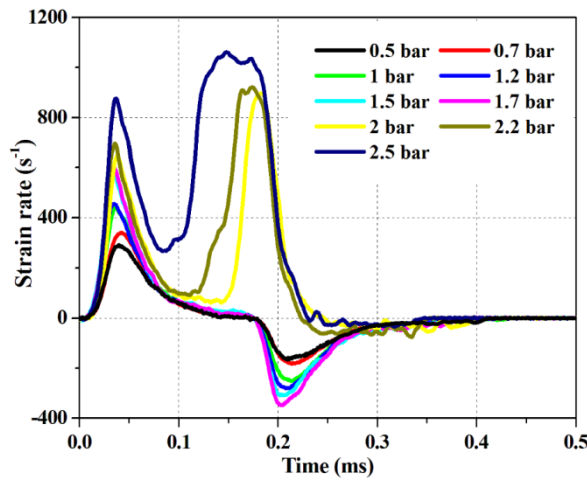


Figure 4. The strain rate–time curves of the specimen under in-plane loading

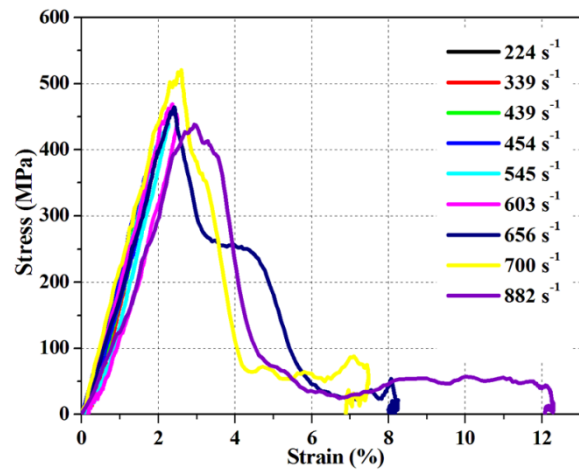


Figure 5. The stress–strain curves of the specimen under in-plane loading

Strain rate (s ⁻¹)	Young modulus (GPa)	Maximum stress (MPa)	Maximum strain (%)
293	21.01	207.58	1.1
339	21.67	297.30	1.7
439	21.27	355.92	1.9
454	21.91	390.38	2.1
545	21.31	436.62	2.4
614	21.10	475.91	2.6
903	19.94	481.34	2.8
922	21.58	519.71	2.8
1061	16.49	445.43	3.5

Table 2. Mechanical properties of the woven composites subjected to in-plane loading

3.2 Out-of-plane test

3.2.1 Mechanical behavior

The out-of-plane dynamic compression response of the materials was also investigated. Figure6 give the evolution of the strain rate of [0°/90°]₂₆ samples for seven impact pressure. This figure shows the same likely than to in-plane tests. For undamaging tests, the fall of strain rate passes by negative values, which correspond to the springback in the sample. On the other hand, the appearance of a second peak characterizes the onset of macroscopic damage. The critical impact pressure at which the second peak appears is between 5.17-5.25 bar (respectively 1813-1902 s⁻¹). The compressive stress-strain curves at strain rate from 659 to 1902 s⁻¹ for the composites are presented in Figure7. From this figure, the Young modulus, maximum stress and failure strain have been obtained and listed in Table 3. It is observed also an increase of the mechanical properties, stress and strain, with the increase of the strain rate. However, the elastic modulus seems not to change before the appearance of the damage.

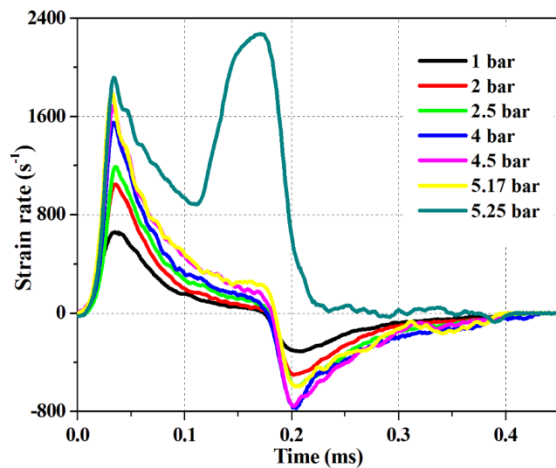


Figure 6. The strain rate–time curves of the specimen under out-of-plane loading

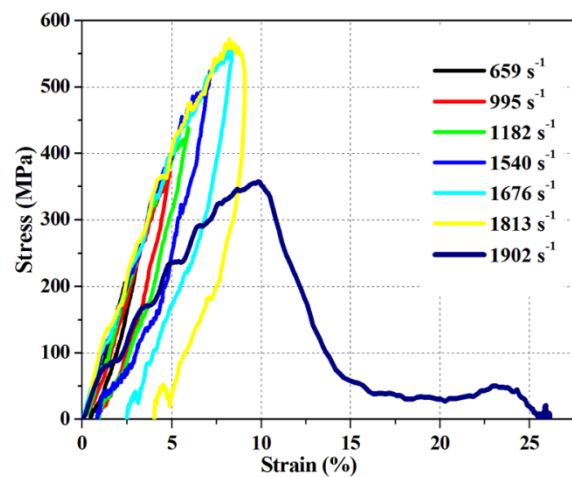


Figure 7. The stress–strain curves of the specimen under out-of-plane loading

Strain rate (s^{-1})	Young modulus (GPa)	Maximum stress (MPa)	Maximum strain (%)
659	8.64	263.80	2.56
995	8.74	381.56	5.54
1012	8.27	386.09	5.85
1182	8.11	435.22	6.67
1540	7.95	518.00	8.20
1676	7.55	551.99	9.80
1813	7.50	565.74	9.60
1902	4.05	357.43	11.00

Table 3. Mechanical properties of the woven composites subjected to out-of-plane loading

4 NUMERICAL SIMULATION

4.1 FE model

Split Hopkinson Pressure Bar tests were modeled to study the stress wave propagation and dynamic deformation of the composite materials. Commercially available finite element software ABAQUS was used throughout the numerical studies. Considering the arrangement showed in Figure 2 and taking into account the dimensions of the equipment available in the Ship Structures Mechanics Laboratory of the ENSTA Bretagne, both incident and transmitted bar were modeled with a diameter of 20 mm and a length of 1985 mm and 1948 mm, respectively. Likewise, the striker had 400 mm in length and the same diameter. The incident, transmitted and the striker bars were modeled as an isotropic elastic material. Meanwhile the specimen was a common size of $13 \times 13 \times 10 \text{ mm}^3$ and was modeled with an orthotropic elastic material. This composite specimen is made up of 52 stacked plies $[0^\circ/90^\circ]$ with a ply thickness of 0.195 mm. An assembly containing all parts (bars, striker and specimen) was modeled using three-dimensional solid 8-node linear brick elements, with reduced integration and hourglass control (C3D8R in ABAQUS library). The incident, transmitted and the striker bars had uniform mesh into 104192, 97870 and 21890 elements, respectively. The specimen is meshed into 8788 elements. Mesh configuration of the composite specimen appears in Figure 8, while in turn Figure 9 presents a detail of the full model assembly. At the interfaces of different parts of the SHPB setup, a surface to surface contact is defined to simulate the interaction at these interfaces, allowing for compressive loads to be transferred between the

slave nodes and the master segments. Material properties used in the finite element code are shown in Table 4 and Table 5. The skins with a negligible thickness acting as gauges were placed on incident and transmitted bars, with the purpose to determine the incident, transmitted and reflected waves. These skins were modeled using the mesh with membrane elements M3D4R (A 4-node quadrilateral membrane, reduced integration, hourglass control). Initial velocity conditions were applied to the whole striker volume (all nodes), whose value exactly corresponded to the actual one, e.g. $V=5$ m/s. Initial boundary conditions were applied to the striker and the bars such that only movement in one direction was allowed. The different physical parameters (loads, velocities, strains...) can be determined by the numerical model and compared with experimental results:

- The loads " F_i " and " F_t " are determined at the incident and transmitted bar in contact with the specimen, the loads are deduced from the values of stress applied at the nodes of each of the elements.
- The incident velocity " V_i " and transmitted velocity " V_t " of the bar are deduced at the surface of contact between the incident and transmitted bars with the specimen, Figure. 10.

Material	Density (Kg/m ³)	Young's modulus (GPa)	Poisson's ratio	Elastic wave speed, (m/s)
Steel (Maraging)	7819	183.9	0.32	4849.70

Table 4: Material properties of bar materials used in numerical study

E_1 (MPa)	E_2 (MPa)	E_3 (MPa)	ν_{11}	ν_{23}	ν_{13}	G_{12} (MPa)	G_{13} (MPa)	G_{23} (MPa)
23711	23711	9000	0.151	0.2	0.2	4498	1456	1456

Table 5: Material properties of the composite

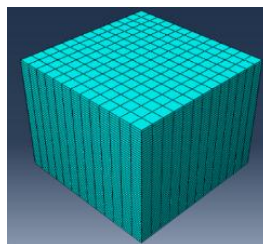


Figure 8. Mesh configuration of composite specimen

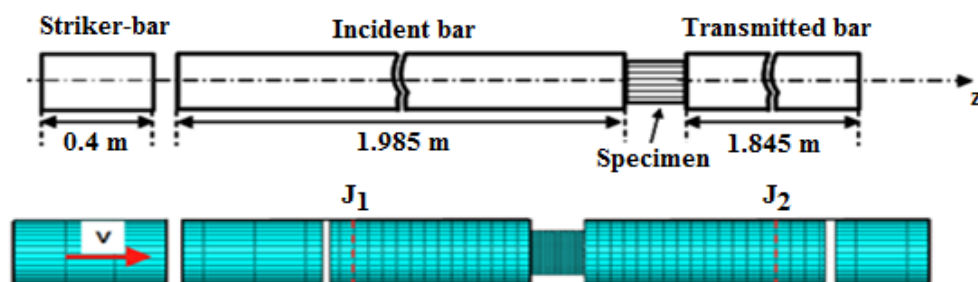


Figure 9. Numerical model of SHPB apparatus

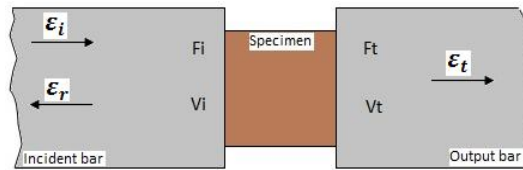


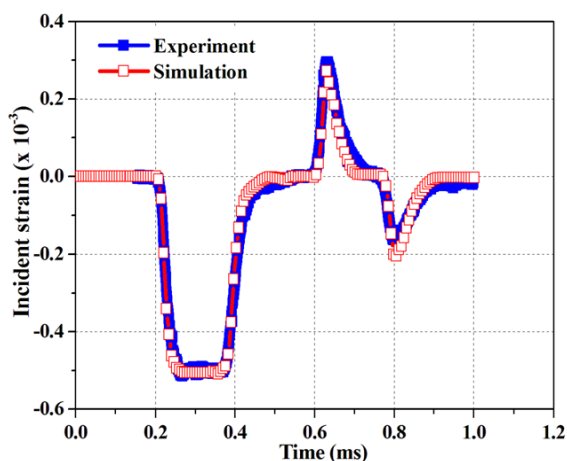
Figure 10. Correlation parameters of the model

4.2 Results of Numerical Study

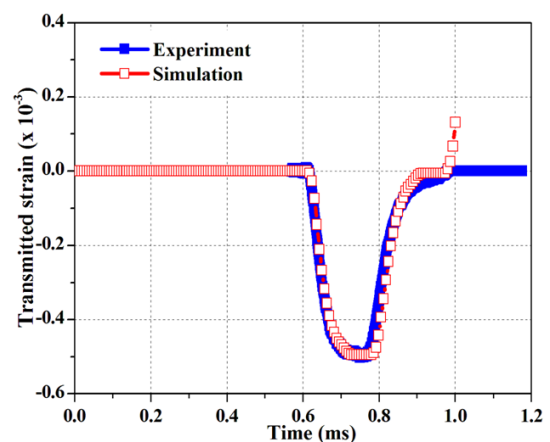
SHPB experiments conducted with composite were numerically modeled using ABAQUS finite element software. The SHPB experiments done with composite subjected to in-plane and out-of-plane were compared with the numerical study which is presented in Figure 11. In this figure, blue curve represents the SHPB experiment of the composite while red curve represents the result of numerical study and both curves were shifted in time domain to simplify distinguishing. In general, a good agreement between the measured results and finite element results is observed for in-plane loading direction.

For in-plane simulations, the strain of incident and reflected compression wave measured by the gauge J_1 , gives a good estimate of the experimental results. This also applies for incident and transmitted velocity. Indeed, the numerical velocity is taken at the incident surface of the bar in contact with the sample. The evolution of the incident and transmitted loads, given at two interfaces of the bars in contact with the sample are well simulated. We have the same rise and fall of the load, but we haven't the same level of the maximum load. At the experimental and numerical results we find a slight general difference which may be related to the experimental conditions:

- the geometry of the samples is not perfectly cubic,
- the parallelism of the faces in contact with the bars,



(a) Incident strain



(b) Transmitted strain

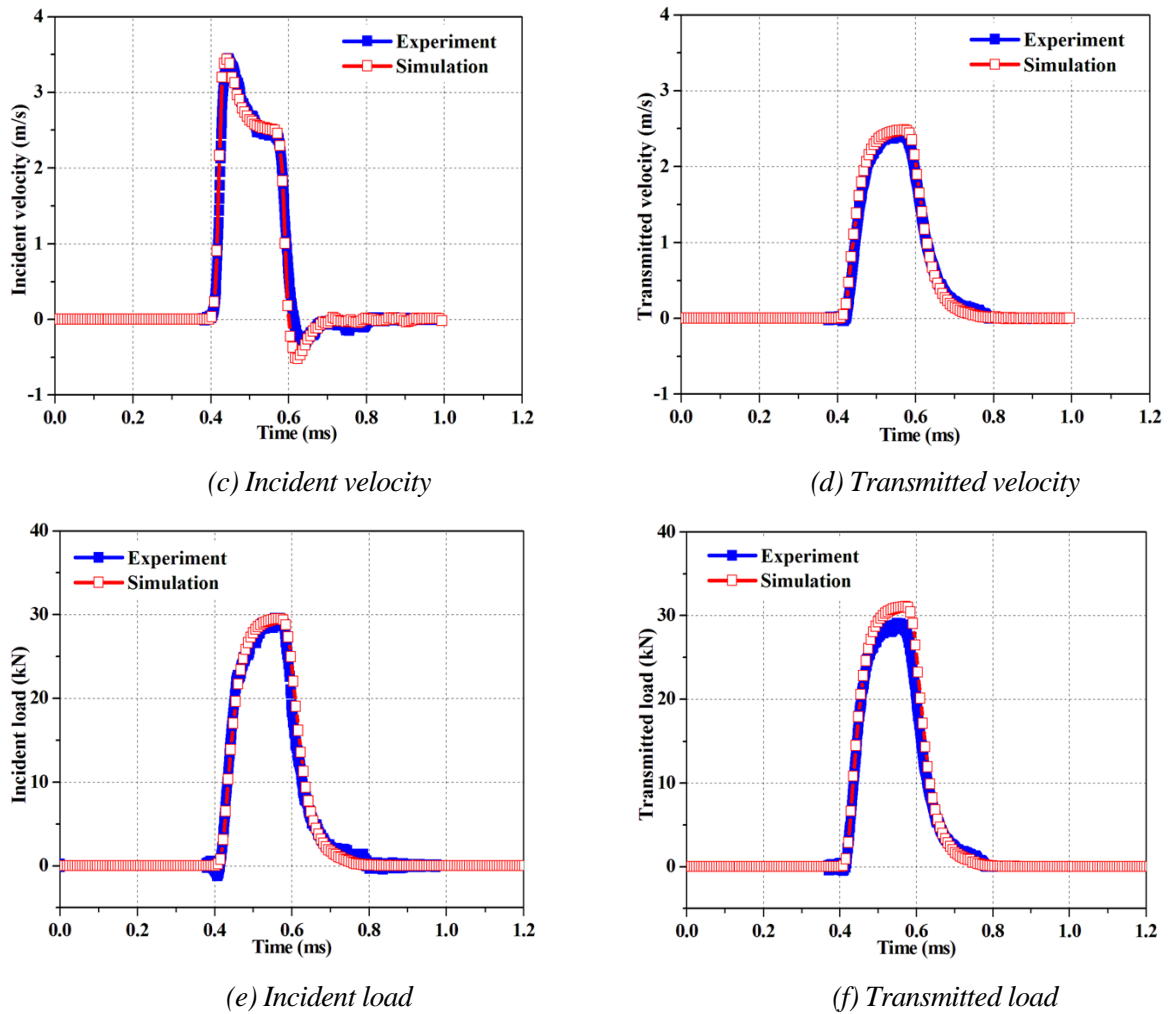


Figure 11. Experimental and numerical results, in-plane test, $P=0.5$ bar.

5 CONCLUSION

A Split Hopkinson pressure bar was used to conduct high compressive strain rate experiments. Samples were subjected to in-plane (IP) and out-of-plane (OP) tests. The first observation can be made, for IP and OP tests, is that materials show a strength dependency on loading direction and impact pressure. Moreover, the stress-strain curves manifest significant influence of the strain rate on the composite mechanical behavior. The maximal stresses achieved depend on the strain rate; the higher the strain rate, the higher the stress level. The maximal stresses obtained both during dynamic compression tests are higher for the composite subjected to out-of-plane loading. Damage appears only for specific impact pressure on the samples: 1.7 - 2 bar for in-plane loading and 5.17 - 5.25 bar for out-of-plane loading.

In the second part of this study, a three-dimensional numerical model of the SHPB test including the incident bar, transmitter bar, the projectile and the specimen was developed. The dynamic compression response was simulated using ABAQUS structural analysis software. Numerical models without damage were developed and successfully predicted the elastic behavior of the materials. The results predicted by the numerical simulation are consistent with observed experimental results with a slight difference, which may be related to the experimental conditions: the geometry of the samples is not perfectly cubic, the parallelism of

the facets in contact with the bars.... This study is to be completed by developing the model which takes into account the damage.

ACKNOWLEDGEMENTS

The Authors of this paper gratefully acknowledge the financial support of the DGA, France (MRIS project).

REFERENCES

- [1] L. Ninan, J. Tsai, C.T. Sun. Use of split Hopkinson pressure bar for testing off-axis composites, *International Journal of Impact Engineering*.25: 291-313, 2001
- [2] H. Kolsky, An investigation of the mechanical properties of materials at very high rates of loading, *Proc. phys. Society*. 62: 676-700, 1949.
- [3] L.J. Griffiths, D.J. Martin. A study of the dynamic behaviour of a carbon–fibre composite using the split Hopkinson pressure bar, *Journal of Physics*.7:2329–41, 1974.
- [4] X. Chen, X. Li, Z. Zhi, Y. Guo, N. Ouyang. The compressive and tensile behavior of a 0/90 C fiber woven composite at high strain rates, *Carbon*.61: 97–104, 2013.
- [5] M.V. Hosur, J. Alexandre, U.K. Vaidya., S. Jeelani.High Strain Rate Compression Response of Carbon/Epoxy Laminate Composites.*Journal of Composite Structures*, 52: 405-417, 2001.
- [6] C.E. Lanchezhian, B. Vijaya Ramnath, J. Hemalatha. Mechanical behaviour of glass and carbon fibre reinforced composites at varying strain rates and temperatures, *Procedia Materials Science*. 6 : 1405–1418, 2014.
- [7] R.L. Sierakowski, G.E. Nevill, C.A. Ross, E.R. Jones. Dynamic Compressive Strength and Failure of Steel Reinforced Epoxy Composites.*Journal of Composite Materials*, 5: 362-377, 1971.
- [8] S.T. Jenq, S.L. Sheu, High Strain Rate Compressional Behavior of Stitched and Unstitched Composite Laminates with Radial Constraint, *Composite structure*. 25: 427-438, 1993.
- [9] M. Tarfaoui, S. Choukri, A. Neme.Effect of fibre orientation on mechanical properties of the laminated polymer composites subjected to out-of-plane high strain rate compressive loadings, *Composite Science and Technology*. 68 : 477-485, 2008.
- [10] M. Tarfaoui, S. Choukri, A. Neme.Damage kinetics of glass/epoxy composite materials under dynamic compression, *Journal of Composite Materials*. 43: 1137-1154, 2009.
- [11] A.M.A. El-Habak. Mechanical behaviour of woven glass fibre-reinforced composites under impact compression load.*Composites*, 22 : 129–134, 2001.
- [12] E. Woldenbet, J.R. Vinson. Effect of specimen geometry in high strain rate testing of graphite/epoxy composites, *In: Proceedings of the 38th AIAA/ASME/ASCE/AHS/ASC Struc Struc Dyn and Matl Conf*. 2 : 927-934, 1997.
- [13] J. Harding. Effect of strain rate and specimen geometry on the compressive strength of woven glass-reinforced epoxy laminates.*Composites*, 24 : 323–432 , 1993.
- [14] Abaqus 6.12: Analysis User's Manual.
- [15] M. Tarfaoui, Experimental investigation of dynamic compression and damage kinetics of Glass/Epoxy laminated composites under high strain rate compression, *Advances in Composites materials-Ecodesign and Analysis*, 16 : 359-382, 2011.



A MIXED “BIOT-SHELL” ANALYTICAL MODEL FOR THE CALCULATION OF SOUND TRANSMISSION THROUGH SANDWICH CYLINDERS WITH POROELASTIC CORES

Julien Magniez^{1*}, Mohamed Ali Hamdi¹, Jean-Daniel Chazot¹ and Bernard Troclet²

¹Laboratoire Roberval UMR 7337

Université de Technologie de Compiègne, CS 60319, 60203 Compiègne cedex, FRANCE

Email: julien.magniez@utc.fr, mohamed-ali.hamdi@utc.fr, jean-daniel.chazot@utc.fr

²Airbus Defence & Space

51-61 Route de Verneuil, BP 3002, 78133 Les Mureaux Cedex, FRANCE

Email: bernard.troclet@astrium.eads.net

ABSTRACT

In this work, the sound transmission through a sandwich cylinder with a poroelastic core is studied analytically. The cylinder is composed of two orthotropic skins, modeled with a shell theory, and a poroelastic core modeled with the full 3D Biot's theory. Thus, a mixed “Biot-Shell” analytical model is presented in this paper. First, the motion of the sandwich cylinder obtained with this mixed “Biot-Shell” model is presented. Then, the model is used to calculate the sound transmission in the case of an excitation by an external oblique plane wave. A very good agreement is found when the results are compared to those obtained with a finite element model. Finally, some results are presented and the Transmission Loss (TL) is studied in different configurations. The main conclusion obtained from the results is that the poroelastic coating can significantly improve the TL of a cylindrical structure in mid- and high frequencies.

1 INTRODUCTION

Multilayer cylinders are widely used in aeronautics and aerospace industries. Generally designed to be as light as possible, these structures must also take into account the problem of inner noise transmission. Indeed, protection against noise is still necessary in such applications, whether it is for the passengers comfort or the payload protection. Thus, an optimization tool is necessary to reduce the total weight of the structure while increasing its acoustic efficiency. Consequently, fast analytical models have to be developed in order to predict accurately the sound transmission through these cylindrical structures.

In these applications, poroelastic materials are commonly used to reduce significantly the noise transmitted inside the compartment. Many studies have been made to model the behavior of these porous materials, and literature reveals a large number of publications on this subject. However, the state of the art shows that there are two main approaches to model them. The first way is to model them as equivalent fluids [1]. In these models, the viscous and thermal effects due to the skeleton are considered, but the skeleton elasticity is neglected. The second way is to use Biot's model [2, 3]. In the case of Biot's model, the motion of the skeleton is taken into account through the elastodynamic equations. This basic model considers the porous material as a superposition of two coupled solid and fluid phases. It is more adapted to model the dynamic behavior of poroelastic materials.

In this paper, the sound transmission through a sandwich cylinder having a poroelastic core modeled with Biot's theory is studied analytically. The two skins of the sandwich structure are orthotropic and modeled with a shell model. Thus, a mixed "Biot-Shell" analytical model is presented in this paper. In section 2, the motion of the sandwich cylinder obtained with this mixed "Biot-Shell" model is presented. The transfer matrix of the poroelastic core is used to couple the two skins. In section 3, the model is used to calculate the sound transmission when the cylinder is excited by an external oblique plane wave. In section 4, numerical results obtained with the proposed model are presented. As firstly shown, a very good agreement is found when the results are compared to those obtained with a finite element model. Then, the Transmission Loss (TL) is studied in different configurations. Finally, the main conclusions are presented in section 5.

2 VIBRATIONS OF THE SANDWICH CYLINDER

The sandwich structure and the notations used in the following are presented in detail in Figure 1. Note that layers 1 and 3 refer to the inner and outer skins respectively, and that layer 2 designates the poroelastic core.

2.1 Motion of the orthotropic skins

For each skin i ($i = 1, 3$) the displacement field is given by the First-order Shear Deformation Theory (FSDT):

$$u^i(z, \theta, \xi) = u_0^i(z, \theta) + \xi \psi_z^i(z, \theta), \quad (1a)$$

$$v^i(z, \theta, \xi) = v_0^i(z, \theta) + \xi \psi_\theta^i(z, \theta), \quad (1b)$$

$$w^i(z, \theta, \xi) = w_0^i(z, \theta), \quad (1c)$$

where u_0^i , v_0^i and w_0^i are the displacements at $\xi = 0$ of the layer i in the axial, circumferential and radial directions, respectively, and ψ_z^i and ψ_θ^i are the rotations of the normal to the median surface of each layer i . Note that the ξ -axis origin is at the median surface of the cylinder (see Figure 1).

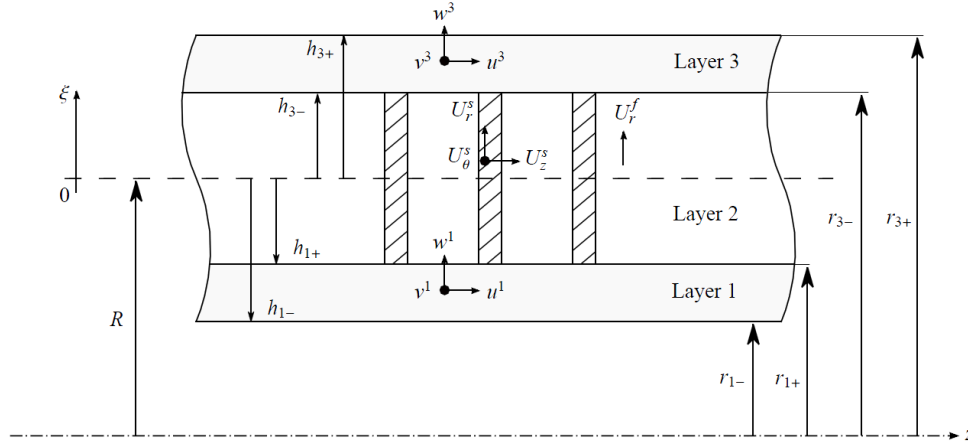


Figure 1. Sandwich structure and notations.

For each skin, five equilibrium equations are written in terms of displacements as (see [4, 5] for more details):

$$\mathbf{L}^i \mathbf{u}^i + \mathbf{M}^i \ddot{\mathbf{u}}^i = \mathbf{q}^i, \quad (2)$$

with \mathbf{u}^i the displacement-rotation vector and \mathbf{q}^i the force-moment vector given by:

$$\mathbf{u}^i = [u_0^i, v_0^i, w_0^i, \psi_z^i, \psi_\theta^i]^T \quad \text{and} \quad \mathbf{q}^i = [q_z^i, q_\theta^i, q_r^i, m_z^i, m_\theta^i]^T. \quad (3)$$

Moreover, \mathbf{L}^i is the stiffness operator and \mathbf{M}^i is the mass matrix, which are not given here for sake of conciseness but can be found in reference [5].

2.2 Transfer matrix of the poroelastic core

Biot's theory is used to describe the motion of the poroelastic core. The classical Biot's equations involve the solid phase (skeleton) displacement field \mathbf{U}^s and the fluid phase displacement field \mathbf{U}^f [1, 2]. However, it has been shown by Atalla *et al.* [6] that Biot's equations can be rewritten in order to introduce the interstitial pressure p instead of the fluid displacement field \mathbf{U}^f . This mixed (\mathbf{U}^s, p) formulation has the great advantage of reducing the number of degrees of freedom per node from 6 to 4 in a finite element implementation. Moreover, according to Hamdi *et al.* [7], the mixed formulation presented by Atalla *et al.* [6] can be reformulated in order to involve explicitly the total stress tensor in the poroelastic medium. In this way, the associated weak integral formulation has the great advantage of leading to natural coupling conditions at the interface between two adjacent layers [7, 8]. The combination between the method given by Atalla *et al.* [6] and the formulation proposed by Hamdi *et al.* [7] leads to the following mixed Biot's equations, written in terms of the solid phase displacement field \mathbf{U}^s and the interstitial pressure p :

$$\tilde{\rho}\omega^2 \mathbf{U}^s + \nabla \cdot (\hat{\boldsymbol{\sigma}}^s - \alpha \phi p \mathbf{I}) + \beta \nabla(\phi p) = 0, \quad (4)$$

$$\nabla \cdot \left(\frac{1}{\tilde{\rho}_{22}\omega^2} \nabla(\phi p) - \beta \mathbf{U}^s \right) + \frac{\phi p}{\tilde{R}} + \alpha \nabla \cdot \mathbf{U}^s = 0, \quad (5)$$

where ϕ is the porosity, $\hat{\boldsymbol{\sigma}}^s$ the stress tensor of the skeleton *in vacuo*, and \mathbf{I} the identity matrix. The terms $\alpha = 1 + \frac{\tilde{Q}}{\tilde{R}}$ and $\beta = 1 + \frac{\tilde{\rho}_{12}}{\tilde{\rho}_{22}}$ are two coupling factors between the skeleton and the interstitial fluid. Moreover, the effective densities $\tilde{\rho}$, $\tilde{\rho}_{12}$, and $\tilde{\rho}_{22}$ and the elastic coefficients \tilde{Q} and \tilde{R} can be found in reference [1]. Note however that the time convention $e^{-j\omega t}$ is taken here with an angular frequency ω .

By using the stress-displacement relation $\hat{\sigma}^s = \lambda (\nabla \cdot \mathbf{U}^s) \mathbf{I} + \mu (\nabla \mathbf{U}^s + (\nabla \mathbf{U}^s)^T)$, the first mixed Biot's equation (4) becomes:

$$\tilde{\rho}\omega^2 \mathbf{U}^s + (\lambda + 2\mu)\nabla(\nabla \cdot \mathbf{U}^s) - \tilde{\gamma}\nabla(\phi p) - \mu\nabla \wedge \nabla \wedge \mathbf{U}^s = 0, \quad (6)$$

where λ and μ are the Lamé coefficient of the skeleton *in vacuo* and $\tilde{\gamma} = \alpha - \beta$. To solve this equation, the following Helmholtz decomposition is used for the solid displacement:

$$\mathbf{U}^s = \nabla(\varphi_1^s + \varphi_2^s) + \nabla \wedge \boldsymbol{\psi}^s, \quad (7)$$

where φ_1^s and φ_2^s are the scalar potentials related to the two longitudinal waves, and $\boldsymbol{\psi}^s$ the vector potential related to the shear wave in the poroelastic medium. Substituting the decomposition (7) into Biot's equations (6) and (5) gives, all calculations done, three wave equations fulfilled by each of the potentials:

$$\Delta\varphi_1^s + \frac{\omega^2}{c_1^2}\varphi_1^s = 0, \quad \Delta\varphi_2^s + \frac{\omega^2}{c_2^2}\varphi_2^s = 0 \quad \text{and} \quad \Delta\boldsymbol{\psi}^s + \frac{\omega^2}{c_3^2}\boldsymbol{\psi}^s = 0, \quad (8)$$

where Δ is the Laplacian operator, c_1 and c_2 the celerity of the two longitudinal waves and c_3 the celerity of the shear wave. The details of c_1 , c_2 and c_3 can be found in reference [1]. The substitution of (7) into (6) also gives a relation between the interstitial pressure and the scalar potentials:

$$p = \frac{1}{\tilde{\gamma}\phi} \left((\lambda + 2\mu)\Delta(\varphi_1^s + \varphi_2^s) + \tilde{\rho}\omega^2(\varphi_1^s + \varphi_2^s) \right). \quad (9)$$

The general solutions of the wave equations given in (8) are expanded in cylindrical harmonics. By substituting these solutions into equation (7), the following solid displacement field is obtained:

$$U_r^s(r, \theta, z, t) = \sum_{n=0}^{\infty} U_r^{s,n}(r) \cos(n\theta) e^{jk_z z - j\omega t}, \quad (10a)$$

$$U_\theta^s(r, \theta, z, t) = \sum_{n=0}^{\infty} U_\theta^{s,n}(r) \sin(n\theta) e^{jk_z z - j\omega t}, \quad (10b)$$

$$U_z^s(r, \theta, z, t) = \sum_{n=0}^{\infty} jU_z^{s,n}(r) \cos(n\theta) e^{jk_z z - j\omega t}, \quad (10c)$$

where n designates the circumferential order and k_z the axial wavenumber. Moreover, U_r^s , U_θ^s and U_z^s are the radial, circumferential and axial components respectively. The fluid displacement \mathbf{U}^f is also related to the scalar and vector potentials with

$$\mathbf{U}^f = \nabla(\mu_1\varphi_1^s + \mu_2\varphi_2^s) + \nabla \wedge \mu_3\boldsymbol{\psi}^s, \quad (11)$$

where the amplitude ratios μ_1 , μ_2 and μ_3 can be found in reference [1]. The radial component is thus also expanded in cylindrical harmonics as follows:

$$U_r^f(r, \theta, z, t) = \sum_{n=0}^{\infty} U_r^{f,n}(r) \cos(n\theta) e^{jk_z z - j\omega t}. \quad (12)$$

The stress components are also needed to characterize the poroelastic medium. The total stress tensor in the poroelastic medium $\boldsymbol{\sigma}^t$ is the sum of a tensor related to the solid phase $\hat{\boldsymbol{\sigma}}^s$ and a tensor related to the fluid phase $\hat{\boldsymbol{\sigma}}^f$:

$$\boldsymbol{\sigma}^t = \hat{\boldsymbol{\sigma}}^s + \hat{\boldsymbol{\sigma}}^f, \quad (13)$$

where the notation $\hat{\sigma}^f = -\alpha\phi p\mathbf{I}$ has been introduced. The solid phase stress tensor is obtained by using the stress-displacement relation. This yields:

$$\hat{\sigma}_{rr}^s(r, \theta, z, t) = \sum_{n=0}^{\infty} \hat{\sigma}_{rr}^{s,n}(r) \cos(n\theta) e^{jk_z z - j\omega t}, \quad (14a)$$

$$\hat{\sigma}_{r\theta}^s(r, \theta, z, t) = \sum_{n=0}^{\infty} \hat{\sigma}_{r\theta}^{s,n}(r) \sin(n\theta) e^{jk_z z - j\omega t}, \quad (14b)$$

$$\hat{\sigma}_{rz}^s(r, \theta, z, t) = \sum_{n=0}^{\infty} j\hat{\sigma}_{rz}^{s,n}(r) \cos(n\theta) e^{jk_z z - j\omega t}. \quad (14c)$$

The tensor $\hat{\sigma}^f$ is obtained by using the expression of p given in equation (9). The scalar potentials φ_1^s and φ_2^s being defined in cylindrical coordinates, this tensor is also expanded in cylindrical harmonics. This yields for $\hat{\sigma}_{rr}^f$:

$$\hat{\sigma}_{rr}^f(r, \theta, z, t) = \sum_{n=0}^{\infty} \hat{\sigma}_{rr}^{f,n}(r) \cos(n\theta) e^{jk_z z - j\omega t}. \quad (15)$$

The modal transfer matrix method is now used to relate the displacements and stresses at each interface of the poroelastic core. The modal amplitudes at the interfaces $r = r_{1+}$ and $r = r_{3-}$ of the core are hence related with:

$$\hat{\mathbf{S}}(r_{1+}) = \hat{\mathbf{T}}\hat{\mathbf{S}}(r_{3-}), \quad (16)$$

where $\hat{\mathbf{S}}(r) = [U_z^{s,n}(r), U_\theta^{s,n}(r), U_r^{s,n}(r), U_r^{f,n}(r), \hat{\sigma}_{rz}^{s,n}(r), \hat{\sigma}_{r\theta}^{s,n}(r), \hat{\sigma}_{rr}^{s,n}(r), \hat{\sigma}_{rr}^{f,n}(r)]^T$ is the modal amplitude vector, and $\hat{\mathbf{T}}$ is the 8×8 modal transfer matrix. Equation (16) can be rewritten in order to express the stresses components in terms of the displacements components. This yields:

$$\hat{\sigma}_n^{1-3} = \hat{\mathbf{k}} \hat{\mathbf{U}}_n^{1-3}, \quad (17)$$

with

$$\hat{\sigma}_n^{1-3} = [\hat{\sigma}_{rz}^{s,n}(r_{1+}), \hat{\sigma}_{r\theta}^{s,n}(r_{1+}), \hat{\sigma}_{rr}^{s,n}(r_{1+}), \hat{\sigma}_{rr}^{f,n}(r_{1+}), -\hat{\sigma}_{rz}^{s,n}(r_{3-}), -\hat{\sigma}_{r\theta}^{s,n}(r_{3-}), -\hat{\sigma}_{rr}^{s,n}(r_{3-}), -\hat{\sigma}_{rr}^{f,n}(r_{3-})]^T, \quad (18)$$

and

$$\hat{\mathbf{U}}_n^{1-3} = [U_z^{s,n}(r_{1+}), U_\theta^{s,n}(r_{1+}), U_r^{s,n}(r_{1+}), U_r^{f,n}(r_{1+}), U_z^{s,n}(r_{3-}), U_\theta^{s,n}(r_{3-}), U_r^{s,n}(r_{3-}), U_r^{f,n}(r_{3-})]^T. \quad (19)$$

The matrix $\hat{\mathbf{k}}$ is homogeneous to a stiffness matrix and is build from the components of the modal transfer matrix $\hat{\mathbf{T}}$.

2.3 Coupling conditions

(i) The continuity of the displacements must be satisfied at the core-skin interfaces. At $r = r_{1+}$ (interface between layers 1 and 2) this condition writes:

$$U_z^s(r_{1+}, \theta, z) = u^1(z, \theta, h_{1+}) = u_0^1(z, \theta) + h_{1+}\psi_z^1(z, \theta), \quad (20a)$$

$$U_\theta^s(r_{1+}, \theta, z) = v^1(z, \theta, h_{1+}) = v_0^1(z, \theta) + h_{1+}\psi_\theta^1(z, \theta), \quad (20b)$$

$$U_r^s(r_{1+}, \theta, z) = w^1(z, \theta, h_{1+}) = w_0^1(z, \theta), \quad (20c)$$

$$U_r^f(r_{1+}, \theta, z) = w^1(z, \theta, h_{1+}) = w_0^1(z, \theta), \quad (20d)$$

while at $r = r_{3-}$ (interface between layers 2 and 3) it writes:

$$U_z^s(r_{3-}, \theta, z) = u^3(z, \theta, h_{3-}) = u_0^3(z, \theta) + h_{3-}\psi_z^3(z, \theta), \quad (21a)$$

$$U_\theta^s(r_{3-}, \theta, z) = v^3(z, \theta, h_{3-}) = v_0^3(z, \theta) + h_{3-}\psi_\theta^3(z, \theta), \quad (21b)$$

$$U_r^s(r_{3-}, \theta, z) = w^3(z, \theta, h_{3-}) = w_0^3(z, \theta), \quad (21c)$$

$$U_r^f(r_{3-}, \theta, z) = w^3(z, \theta, h_{3-}) = w_0^3(z, \theta). \quad (21d)$$

(ii) Instead of using the stress continuity explicitly, the forces \mathbf{q}^i appearing in the right-hand side of the skins equations (2) will be split as the sum of the generalized reaction forces $\hat{\mathbf{q}}_{core}^i$ applied by the poroelastic core on the skin i , and of the external forces \mathbf{q}_{ext}^i :

$$\mathbf{L}^i \mathbf{u}^i + \mathbf{M}^i \ddot{\mathbf{u}}^i = \hat{\mathbf{q}}_{core}^i + \mathbf{q}_{ext}^i. \quad (22)$$

The generalized core reaction forces given here are obtained by using the stress components of the poroelastic core in Eqs. (14) and (15) such as:

$$\hat{\mathbf{q}}_{core}^1 = \begin{bmatrix} \hat{\sigma}_{rz}^s(r_{1+}, \theta, z, t) \\ \hat{\sigma}_{r\theta}^s(r_{1+}, \theta, z, t) \\ \hat{\sigma}_{rr}^s(r_{1+}, \theta, z, t) + \hat{\sigma}_{rr}^f(r_{1+}, \theta, z, t) \\ h_{1+}\hat{\sigma}_{rz}^s(r_{1+}, \theta, z, t) \\ h_{1+}\hat{\sigma}_{r\theta}^s(r_{1+}, \theta, z, t) \end{bmatrix} \text{ and } \hat{\mathbf{q}}_{core}^3 = - \begin{bmatrix} \hat{\sigma}_{rz}^s(r_{3-}, \theta, z, t) \\ \hat{\sigma}_{r\theta}^s(r_{3-}, \theta, z, t) \\ \hat{\sigma}_{rr}^s(r_{3-}, \theta, z, t) + \hat{\sigma}_{rr}^f(r_{3-}, \theta, z, t) \\ h_{3-}\hat{\sigma}_{rz}^s(r_{3-}, \theta, z, t) \\ h_{3-}\hat{\sigma}_{r\theta}^s(r_{3-}, \theta, z, t) \end{bmatrix}. \quad (23)$$

and while the external forces \mathbf{q}_{ext}^i write:

$$\mathbf{q}_{ext}^i = [f_{z,ext}^i, f_{\theta,ext}^i, f_{r,ext}^i, m_{z,ext}^i, m_{\theta,ext}^i]^T, \quad (24)$$

with $f_{z,ext}^i$, $f_{\theta,ext}^i$ and $f_{r,ext}^i$ the external forces per unit area, and $m_{z,ext}^i$ and $m_{\theta,ext}^i$ the external moments per unit area.

2.4 Global dynamic equilibrium

The two equations of motion of the skins are firstly grouped into a single system:

$$\begin{bmatrix} \mathbf{L}^1 & \mathbf{0} \\ \mathbf{0} & \mathbf{L}^3 \end{bmatrix} \begin{bmatrix} \mathbf{u}^1 \\ \mathbf{u}^3 \end{bmatrix} + \begin{bmatrix} \mathbf{M}^1 & \mathbf{0} \\ \mathbf{0} & \mathbf{M}^3 \end{bmatrix} \begin{bmatrix} \ddot{\mathbf{u}}^1 \\ \ddot{\mathbf{u}}^3 \end{bmatrix} = \begin{bmatrix} \hat{\mathbf{q}}_{core}^1 \\ \hat{\mathbf{q}}_{core}^3 \end{bmatrix} + \begin{bmatrix} \mathbf{q}_{ext}^1 \\ \mathbf{q}_{ext}^3 \end{bmatrix}, \quad (25)$$

and, as in section 2.2 for the core displacement, the skins displacements and the external forces are expanded in cylindrical harmonics:

$$\begin{bmatrix} u_0^i \\ v_0^i \\ w_0^i \\ \psi_z^i \\ \psi_\theta^i \end{bmatrix} = \sum_{n=0}^{\infty} \begin{bmatrix} j u_{0n}^i \cos(n\theta) \\ v_{0n}^i \sin(n\theta) \\ w_{0n}^i \cos(n\theta) \\ j \psi_{zn}^i \cos(n\theta) \\ \psi_{\theta n}^i \sin(n\theta) \end{bmatrix} e^{jk_z z - j\omega t} \text{ and } \begin{bmatrix} f_{z,ext}^i \\ f_{\theta,ext}^i \\ f_{r,ext}^i \\ m_{z,ext}^i \\ m_{\theta,ext}^i \end{bmatrix} = \sum_{n=0}^{\infty} \begin{bmatrix} j f_{zn,ext}^i \cos(n\theta) \\ f_{\theta n,ext}^i \sin(n\theta) \\ f_{rn,ext}^i \cos(n\theta) \\ j m_{zn,ext}^i \cos(n\theta) \\ m_{\theta n,ext}^i \sin(n\theta) \end{bmatrix} e^{jk_z z - j\omega t}. \quad (26)$$

Using the expressions of the skins displacements and of the external forces given in equation (26), equation of motion (25) can be rewritten for each circumferential mode n as follows:

$$\begin{bmatrix} \mathbf{K}^1 & \mathbf{0} \\ \mathbf{0} & \mathbf{K}^3 \end{bmatrix} \begin{bmatrix} \mathbf{u}_n^1 \\ \mathbf{u}_n^3 \end{bmatrix} - \omega^2 \begin{bmatrix} \mathbf{M}^1 & \mathbf{0} \\ \mathbf{0} & \mathbf{M}^3 \end{bmatrix} \begin{bmatrix} \mathbf{u}_n^1 \\ \mathbf{u}_n^3 \end{bmatrix} = \begin{bmatrix} \hat{\mathbf{q}}_{n,core}^1 \\ \hat{\mathbf{q}}_{n,core}^3 \end{bmatrix} + \begin{bmatrix} \mathbf{q}_{n,ext}^1 \\ \mathbf{q}_{n,ext}^3 \end{bmatrix}, \quad (27)$$

where \mathbf{u}_n^i is the displacement-rotation amplitude vector:

$$\mathbf{u}_n^i = [u_{0n}^i, v_{0n}^i, w_{0n}^i, \psi_{zn}^i, \psi_{\theta n}^i]^T, \quad (28)$$

$\hat{\mathbf{q}}_{n,core}^i$ is the generalized reaction amplitude vector:

$$\hat{\mathbf{q}}_{n,core}^1 = \begin{bmatrix} \hat{\sigma}_{rz}^{s,n}(r_{1+}) \\ \hat{\sigma}_{r\theta}^{s,n}(r_{1+}) \\ \hat{\sigma}_{rr}^{s,n}(r_{1+}) + \hat{\sigma}_{rr}^{f,n}(r_{1+}) \\ h_{1+} \hat{\sigma}_{rz}^{s,n}(r_{1+}) \\ h_{1+} \hat{\sigma}_{r\theta}^{s,n}(r_{1+}) \end{bmatrix} \quad \text{and} \quad \hat{\mathbf{q}}_{n,core}^3 = - \begin{bmatrix} \hat{\sigma}_{rz}^{s,n}(r_{3-}) \\ \hat{\sigma}_{r\theta}^{s,n}(r_{3-}) \\ \hat{\sigma}_{rr}^{s,n}(r_{3-}) + \hat{\sigma}_{rr}^{f,n}(r_{3-}) \\ h_{3-} \hat{\sigma}_{rz}^{s,n}(r_{3-}) \\ h_{3-} \hat{\sigma}_{r\theta}^{s,n}(r_{3-}) \end{bmatrix}, \quad (29)$$

$\mathbf{q}_{n,ext}^i$ is the external force amplitude vector:

$$\mathbf{q}_{n,ext}^i = [f_{zn,ext}^i, f_{\theta n,ext}^i, f_{rn,ext}^i, m_{zn,ext}^i, m_{\theta n,ext}^i]^T, \quad (30)$$

and \mathbf{K}^i is the stiffness matrix given in reference [5].

The generalized reaction amplitude vectors $\hat{\mathbf{q}}_{n,core}^1$ and $\hat{\mathbf{q}}_{n,core}^3$ appearing in the right-hand side of Eq. (27) can be written in terms of the skins displacements, using equations (17), (20) and (21). The resulting generalized reaction amplitude vectors write hence:

$$\begin{bmatrix} \hat{\mathbf{q}}_{n,core}^1 \\ \hat{\mathbf{q}}_{n,core}^3 \end{bmatrix} = \begin{bmatrix} \hat{\mathbf{K}}_{11}^2 & \hat{\mathbf{K}}_{13}^2 \\ \hat{\mathbf{K}}_{31}^2 & \hat{\mathbf{K}}_{33}^2 \end{bmatrix} \begin{bmatrix} \mathbf{u}_n^1 \\ \mathbf{u}_n^3 \end{bmatrix}, \quad (31)$$

and after substitution of this equation in (27), we finally obtain:

$$\begin{bmatrix} \mathbf{K}^1 - \hat{\mathbf{K}}_{11}^2 & -\hat{\mathbf{K}}_{13}^2 \\ -\hat{\mathbf{K}}_{31}^2 & \mathbf{K}^3 - \hat{\mathbf{K}}_{33}^2 \end{bmatrix} \begin{bmatrix} \mathbf{u}_n^1 \\ \mathbf{u}_n^3 \end{bmatrix} - \omega^2 \begin{bmatrix} \mathbf{M}^1 & \mathbf{0} \\ \mathbf{0} & \mathbf{M}^3 \end{bmatrix} \begin{bmatrix} \mathbf{u}_n^1 \\ \mathbf{u}_n^3 \end{bmatrix} = \begin{bmatrix} \mathbf{q}_{n,ext}^1 \\ \mathbf{q}_{n,ext}^3 \end{bmatrix}. \quad (32)$$

Equation (32) describes the motion of the entire structure excited by external forces. This equation clearly shows the coupling between the inner and the outer skin with the impedance matrix of the poroelastic core $\hat{\mathbf{K}}^2(\omega)$.

3 VIBROACOUSTIC PROBLEM

3.1 Global vibroacoustic system

In this paper, the cylinder is excited by an external oblique plane wave. For this kind of excitation, the external forces acting on the structure are the following:

$$\mathbf{q}_{ext}^1 = [0, 0, p_2(r_{1-}, \theta, z, t), 0, 0]^T \quad \text{and} \quad \mathbf{q}_{ext}^3 = [0, 0, -p_1(r_{3+}, \theta, z, t), 0, 0]^T, \quad (33)$$

where p_1 and p_2 are the acoustic pressures in the external medium and in the cavity respectively. In reference [5] it is shown that for this kind of excitation, the external force amplitude vectors $\mathbf{q}_{n,ext}^i$ can be written in terms of the skins displacement amplitude vectors \mathbf{u}_n^i in the following form:

$$\begin{bmatrix} \mathbf{q}_{n,ext}^1 \\ \mathbf{q}_{n,ext}^3 \end{bmatrix} = \begin{bmatrix} \mathbf{Z}^1 & \mathbf{0} \\ \mathbf{0} & \mathbf{Z}^3 \end{bmatrix} \begin{bmatrix} \mathbf{u}_n^1 \\ \mathbf{u}_n^3 \end{bmatrix} + \begin{bmatrix} \mathbf{0} \\ \mathbf{p}_n^b \end{bmatrix}, \quad (34)$$

where \mathbf{p}_n^b is the blocked-wall vector expressed in terms of the blocked-wall pressure p^b . Moreover, \mathbf{Z}^1 and \mathbf{Z}^3 are impedance matrices expressed in terms of Z_{1n} and Z_{2n} , the radiation impedance of the external and internal surfaces of the cylinder respectively. The expressions of \mathbf{p}_n^b , \mathbf{Z}^1 and \mathbf{Z}^3 are given in reference [5]. Finally, the global vibroacoustic system is obtained by substituting (34) into (32):

$$\begin{bmatrix} \mathbf{K}^1 - \hat{\mathbf{K}}_{11}^2 - \mathbf{Z}^1 & -\hat{\mathbf{K}}_{13}^2 \\ -\hat{\mathbf{K}}_{31}^2 & \mathbf{K}^3 - \hat{\mathbf{K}}_{33}^2 - \mathbf{Z}^3 \end{bmatrix} \begin{bmatrix} \mathbf{u}_n^1 \\ \mathbf{u}_n^3 \end{bmatrix} - \omega^2 \begin{bmatrix} \mathbf{M}^1 & \mathbf{0} \\ \mathbf{0} & \mathbf{M}^3 \end{bmatrix} \begin{bmatrix} \mathbf{u}_n^1 \\ \mathbf{u}_n^3 \end{bmatrix} = \begin{bmatrix} \mathbf{0} \\ \mathbf{p}_n^b \end{bmatrix}. \quad (35)$$

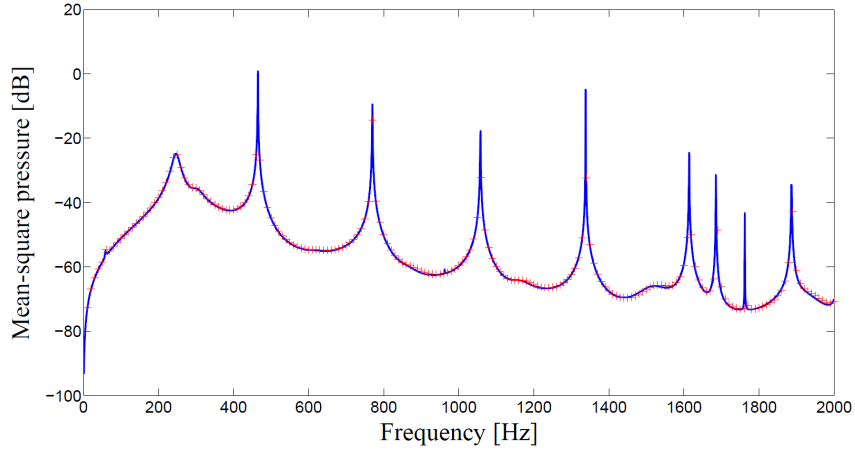


Figure 2: Comparison of the mean-square pressure obtained with the present mixed “Biot-Shell” analytical model and with a finite element model for a sandwich cylinder excited by a plane wave ($\gamma = 0^\circ$). (—) Mixed “Biot-Shell” analytical model, (+) finite element model.

3.2 Transmission Loss calculation

The Transmission Loss (TL) is used to characterize the sound transmission. The TL is defined by:

$$TL = 10 \log \frac{W^I}{W^T}, \quad (36)$$

where W^I and W^T are the incident and transmitted powers, respectively. All calculations done, the TL is found in the following form (see reference [5] for more details):

$$TL = -10 \log \sum_{n=0}^{\infty} \frac{\text{Re} \{ Z_{2n} w_{0n}^1 \cdot (-j\omega w_{0n}^1)^* \} r_{1-\rho_1 c_{01}} \pi}{r_{3+p_0^2 \varepsilon_n \cos \gamma}}, \quad (37)$$

where γ is the incidence angle with respect to the normal of the cylinder. Moreover, p_0 is the amplitude of the incident wave, ε_n is the Neumann factor ($\varepsilon_n = 1$ if $n = 0$, $\varepsilon_n = 2$ if $n \neq 0$), ρ_1 and c_{01} are the density and the speed of sound in the external fluid, and $\text{Re}\{\cdot\}$ and $*$ are the real part and the complex conjugate, respectively. The displacement amplitude w_{0n}^1 is obtained by solving the global vibroacoustic system (35) for each circumferential mode n .

4 RESULTS

4.1 Analytical model validation

In this section, the mixed “Biot-Shell” analytical model is validated with a finite element model. The problem studied here is the acoustic transmission through an infinite cylinder. To simulate the axially infinite extent, a 2-dimensional finite element model in the $(r-\theta)$ plane is used, and the external plane wave is applied at normal incidence with respect to the cylinder axis ($\gamma = 0^\circ$). The model is meshed with linear triangular elements, and an absorbent Perfectly Matched Layer (PML) is also used to impose a non-reflection boundary condition. Note that a resonant cavity is considered in the finite element model. This condition is therefore also applied in the analytical model. Finally, the mean-square pressure $\langle p_{int}^2 \rangle$ in the internal cylindrical cavity is used herein to compare the two methods.

Figure 2 presents the mean-square pressure obtained with the two methods, in the case of a sandwich cylinder having aluminum skins of 5 mm and a foam core of 20 mm, whose properties are given in reference [9]. A very good agreement is obtained between the mixed

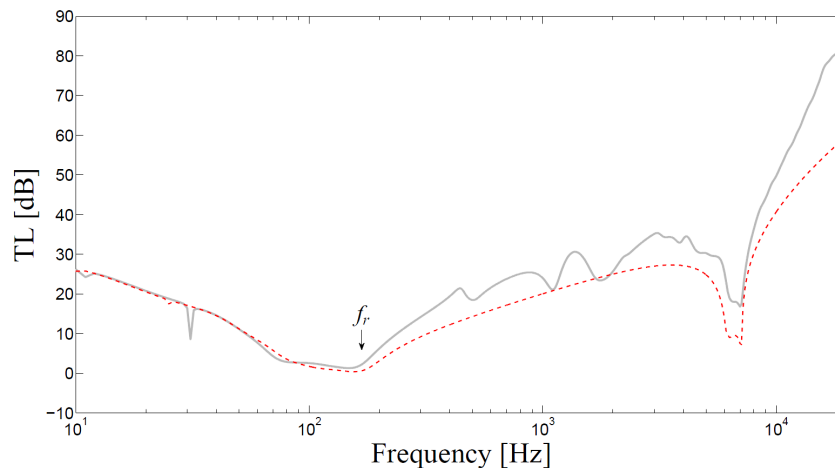


Figure 3: Effect of the poroelastic material on the TL of a cylinder excited by a plane wave ($\gamma = 45^\circ$). (- -) Single shell, (—) shell + poroelastic coating (two-layer configuration).

“Biot-Shell” analytical model and the finite element model. Other configurations have also been tested and have given similar results. The analytical model is hence validated. Note also that the computation time of the analytical model is very low compared to the finite element model.

4.2 Poroelastic material effects

The mixed “Biot-Shell” analytical model is now used to study the influence of the poroelastic material on sound transmission. To do this, two configurations are studied. The first one is the single shell configuration, where a single orthotropic shell is considered. The second one is the two-layer configuration, where a poroelastic coating is added to the shell used in the first configuration. The orthotropic shell being the same in both cases, this allows us to directly study the influence of the poroelastic material on sound transmission. Note that the calculation is made for an aerospace configuration ($r_{3+} = 2.164$ m, shell thickness of 2 mm and poroelastic thickness of 50 mm). The results are presented in Figure 3.

In view of this figure, the ring frequency f_r separates two domains. Below the ring frequency, in very low frequencies ($f < 60$ Hz), adding a poroelastic material does not reduce sound transmission and the TL is not improved. Indeed, for $f < f_r$, the structure vibrates with a global behavior and sound transmission is primarily governed by the rigid shell. Nevertheless, the poroelastic layer shifts the frequencies of the structural resonances. However, it is found that around the ring frequency, adding a poroelastic layer improves the TL. Indeed, a gain from 1 to 2 dB is observed in this frequency zone. This interesting result is explained by the fact that the poroelastic layer adds damping to the structure, which is mainly due to the thermal and viscous dissipation. Since the TL is dependent of the damping at the ring frequency, this explains why the results are improved with the poroelastic layer.

Observing now the results above the ring frequency, we see that the TL is significantly improved with the poroelastic material. Three factors can explain this phenomenon. First, the poroelastic material adds weight to the structure. This allows the TL to be increased, mainly in the mass-controlled zone (between 175 Hz and 6000 Hz). Then, the poroelastic material adds damping to the structure. Thus, it reduces the TL at its dips (between 6000 Hz and 7500 Hz in particular). Last but not least, the poroelastic material has a high power of absorption of acoustic waves, and its efficiency is greater when the frequency increases. This explains the improving of the TL in the mid- and high frequencies with the poroelastic coating.

Finally, since the mass of the poroelastic layer is low, adding this type of material is a very interesting solution to reduce the sound transmission through cylindrical structures.

5 CONCLUSION

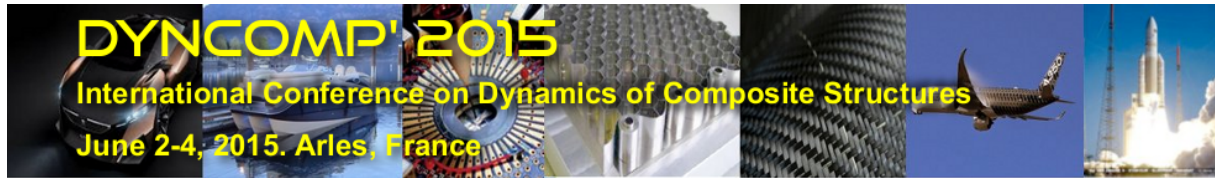
In this paper, a mixed “Biot-Shell” analytical model has been presented. Its main advantage is to allow fast analytical calculations of sound transmission through orthotropic shells having a poroelastic coating, taking into account the elasticity effects of the poroelastic material.

Two important effects of the poroelastic layer were highlighted from the results obtained with the proposed model. The first one is to reduce significantly the sound transmission above the ring frequency, and the second one is to reduce the transmission around the ring frequency. The mass added by a poroelastic material being quite low, this is a very interesting solution to reduce sound transmission through a cylindrical structure.

In conclusion, the mixed “Biot-Shell” analytical model proposed in this paper is very well adapted to describe the behavior of an orthotropic cylinder having a poroelastic coating, since all the physical phenomena are taken into account in the poroelastic layer with Biot’s model.

REFERENCES

- [1] J.-F. Allard and N. Atalla. *Propagation of sound in porous media: modelling sound absorbing materials, second edition*. Wiley, 2009.
- [2] M. A. Biot. Theory of propagation of elastic waves in a fluid-saturated porous solid. I. Low-frequency range. *J. Acoust. Soc. Am.*, 28(2):168–178, 1956.
- [3] M. A. Biot. Theory of propagation of elastic waves in a fluid-saturated porous solid. II. Higher frequency range. *J. Acoust. Soc. Am.*, 28(2):179–191, 1956.
- [4] M. S. Qatu. *Vibration of laminated shells and plates*. Elsevier Academic Press, Oxford, 2004.
- [5] J. Magniez, J.-D. Chazot, M. A. Hamdi, and B. Troclet. A mixed 3D-Shell analytical model for the prediction of sound transmission through sandwich cylinders. *J. Sound Vib.*, 333(19):4750–4770, 2014.
- [6] N. Atalla, R. Panneton, and P. Debergue. A mixed displacement-pressure formulation for poroelastic materials. *J. Acoust. Soc. Am.*, 104(3):1444–1452, 1998.
- [7] M. A. Hamdi, L. Mebarek, A. Omrani, and N. Atalla. An efficient formulation for the analysis of acoustic and elastic waves propagation in porous-elastic materials. In *Proceedings of ISMA 25, International Conference on Noise and Vibration Engineering*, 2000.
- [8] N. Atalla, M. A. Hamdi, and R. Panneton. Enhanced weak integral formulation for the mixed (u, p) poroelastic equations. *J. Acoust. Soc. Am.*, 109(6):3065–3068, 2001.
- [9] J. Kanfoud, M. A. Hamdi, F.-X. Becot, and L. Jaouen. Development of an analytical solution of modified Biot’s equations for the optimization of lightweight acoustic protection. *J. Acoust. Soc. Am.*, 125(2):863–872, 2009.



SCATTERING PROPERTIES OF JOINTS IN COMPOSITE PLATES

Giannoula Mitrou[†], Jamil Renno[‡]

Institute of Sound and Vibration Research
University of Southampton, Southampton SO17 1BJ, UK
Email: g.mitrou@soton.ac.uk

ABSTRACT

The aim of this work is to demonstrate how the wave and finite element (WFE) method can be used for the prediction of the scattering of waves in joined flat panels that are homogeneous in two directions but that could be arbitrarily complicated through the thickness. The WFE method is based on analysing the FE model of, typically, a rectangular segment of the plate through its thickness. This FE model can be obtained using standard FE libraries and commercial or in-house packages can be equally exploited with the only restriction being that the nodes and the corresponding degrees of freedom are identically arranged at each edge. The FE model of the segment is post-processed using periodic structure theory to formulate an eigen-problem whose solution includes complete information of the wave characteristics of the plate. For joined panels, the wave behaviour of each panel is obtained using the WFE method and the joint is modelled using standard FE with a matching number of nodes at the interface with each panel. Then, continuity and equilibrium conditions are enforced at the interfaces. Coupling the WFE and FE models can be utilised to deduce the scattering of waves through the joint. Furthermore, the flow of power can be investigated at different frequencies and in various incidence directions.

[†]Corresponding, presenting author.

[‡]Currently at Plant Integrity Department, Doosan Babcock, Porterfield Road, Renfrew PA4 8HR, email: jamil.renno@doosan.com

1 INTRODUCTION

The prediction of disturbance transmission, energy transport and acoustic radiation from composite structures is of great importance for many applications. Composite plates are generally used for buildings, bridges, vehicles and many other structures. A typical composite plate can comprise many layers of different properties and orientations. Details about the mechanics of laminated composite plates can be found in [1]. Developing analytical models that describe the dynamic behaviour of such plates can be a very difficult task. Although layer-wise theories can be used, the resulting governing equations can be cumbersome and the dispersion equations can be of very high order or transcendental. As an alternative, numerical techniques such as the finite element (FE) method are often used; however, FE models become impractically large at high frequencies.

In recent years, the wave and finite element (WFE) method has been proposed and developed to model the wave behaviour of complicated media that is homogeneous in one or two directions. One of the early works on this method can be found in [4]. This method has also been further applied to study thin plates [5, 6], laminated plates [7], fluid-filled pipes [8, 9], cylindrical structures [10, 11] and to predict the free [7] and forced [12] response.

For simple cases, the scattering properties of joints can be obtained by analytical solutions, see [2, 3]. Whereas, in case of more complicated structures, such as plate/beam junctions [13], bolted joints [14] and curved beams [15], wave approaches can be used to find the reflection and transmission coefficients. The hybrid FE/WFE approach for the computation of the scattering properties of joints in structures comprised of waveguides is introduced in [16].

The aim of this paper is to calculate the scattering properties of the joint in case of two-dimensional structures by using the hybrid FE/WFE method. In section 2 the WFE method in plates is presented. The scattering properties of waves in plates is discussed in section 3. Section 4 includes some numerical results about the dispersion curves and the power flow at different frequencies and incidence directions. Conclusions are drawn in section 5.

2 WFE METHOD IN TWO-DIMENSIONAL STRUCTURES

In this section, the WFE method for two-dimensional structures is briefly reviewed [5]. Time-harmonic motion of the form $\exp[i(\omega t - k_x x - k_y y)]$ is assumed where $k_x = k \cos \theta$ and $k_y = k \sin \theta$ are the components of the wavenumber k in the x and y directions, i.e., the wave is travelling in the θ direction. The wavenumbers might be: real for propagating waves in the absence of damping, pure imaginary for evanescent waves or complex for oscillating, decaying waves. Consider a solid which is homogeneous in both the x and y directions, but whose

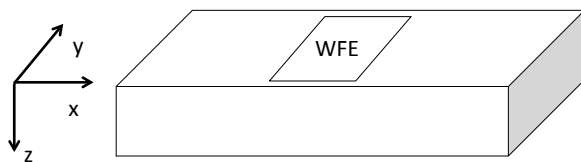


Figure 1: Segment for the WFE modelling of the plate.

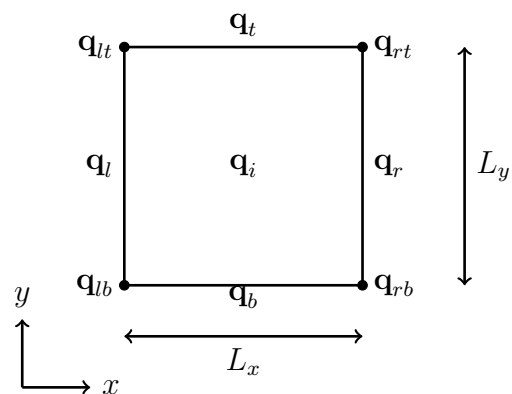


Figure 2: Rectangular segment.

properties may vary arbitrarily through its thickness in the z -direction, see Figure 1. The WFE method starts with a FE model of a small rectangular segment in the (x,y) plane of the plate with sides of lengths L_x and L_y as in Figure 2. This segment is meshed through the thickness using any number of elements: the only condition is that the nodes and degrees of freedom (dofs) are identically arranged on the opposite sides of the segment. Consequently, in case of laminated panels any number of layers and any stacking sequence can be considered.

The vector of dofs \mathbf{q} is partitioned as

$$\mathbf{q} = [\mathbf{q}_{lb}^T \quad \mathbf{q}_{rb}^T \quad \mathbf{q}_{lt}^T \quad \mathbf{q}_{rt}^T \quad \mathbf{q}_b^T \quad \mathbf{q}_r^T \quad \mathbf{q}_t^T \quad \mathbf{q}_l^T \quad \mathbf{q}_i^T]^T.$$

The vector of nodal forces \mathbf{f} is partitioned in a similar manner. For time harmonic motion at frequency ω and in absence of external forces, the governing equation of the segment is $\mathbf{D}\mathbf{q} = \mathbf{f}$, where $\mathbf{D} = (\mathbf{K} + i\omega\mathbf{C} - \omega^2\mathbf{M})$ is the stiffness matrix and \mathbf{K} , \mathbf{C} , and \mathbf{M} are the stiffness, viscous damping and mass matrices, respectively. Under the free passage of a wave whose component in the y direction is k_y , a transformation matrix \mathbf{R} relates the full vector of dofs to a reduced set of dofs as

$$\mathbf{q} = \mathbf{R}\mathbf{q}_{red}, \quad \text{where} \quad \mathbf{q}_{red} = \begin{Bmatrix} \mathbf{q}_{lb} \\ \mathbf{q}_l \\ \mathbf{q}_{rb} \\ \mathbf{q}_r \\ \mathbf{q}_b \\ \mathbf{q}_i \end{Bmatrix} = \begin{Bmatrix} \mathbf{q}_L \\ \mathbf{q}_R \\ \mathbf{q}_O \end{Bmatrix}.$$

The transformation matrix \mathbf{R} depends on the propagation constant $\lambda_y = \exp(-ik_y L_y)$ and is given as

$$\mathbf{R} \cong \mathbf{R}(\lambda_y) = \begin{bmatrix} \mathbf{I} & \mathbf{0} & \mathbf{0} & \mathbf{0} & \mathbf{0} & \mathbf{0} \\ \mathbf{0} & \mathbf{0} & \mathbf{I} & \mathbf{0} & \mathbf{0} & \mathbf{0} \\ \lambda_y \mathbf{I} & \mathbf{0} & \mathbf{0} & \mathbf{0} & \mathbf{0} & \mathbf{0} \\ \mathbf{0} & \mathbf{0} & \lambda_y \mathbf{I} & \mathbf{0} & \mathbf{0} & \mathbf{0} \\ \mathbf{0} & \mathbf{0} & \mathbf{0} & \mathbf{0} & \mathbf{I} & \mathbf{0} \\ \mathbf{0} & \mathbf{0} & \mathbf{0} & \mathbf{I} & \mathbf{0} & \mathbf{0} \\ \mathbf{0} & \mathbf{0} & \mathbf{0} & \mathbf{0} & \lambda_y \mathbf{I} & \mathbf{0} \\ \mathbf{0} & \mathbf{I} & \mathbf{0} & \mathbf{0} & \mathbf{0} & \mathbf{0} \\ \mathbf{0} & \mathbf{0} & \mathbf{0} & \mathbf{0} & \mathbf{0} & \mathbf{I} \end{bmatrix}.$$

Hence, the governing equation can be written in terms of the reduced dofs as

$$\mathbf{R}^H (\mathbf{K} + i\omega\mathbf{C} - \omega^2\mathbf{M}) \mathbf{R} \mathbf{q}_{red} = \mathbf{f}_{red}, \quad (1)$$

where H is the Hermitian matrix operator and

$$\mathbf{f}_{red} := \mathbf{R}^H \mathbf{f} = \begin{Bmatrix} \mathbf{f}_{lb} + \lambda_y^{-1} \mathbf{f}_{lt} \\ \mathbf{f}_l \\ \mathbf{f}_{rb} + \lambda_y^{-1} \mathbf{f}_{rt} \\ \mathbf{f}_r \\ \mathbf{f}_b + \lambda_y^{-1} \mathbf{f}_t \\ \mathbf{f}_i \end{Bmatrix} = \begin{Bmatrix} \mathbf{f}_L \\ \mathbf{f}_R \\ \mathbf{f}_O \end{Bmatrix}.$$

Since the internal nodal forces are zero, $\mathbf{f}_i = \mathbf{0}$, and due to the equilibrium conditions at the bottom edge of the segment $\mathbf{f}_b + \lambda_y^{-1} \mathbf{f}_t = \mathbf{0}$ then $\mathbf{f}_O = \mathbf{0}$. Thus, Equation 1 can be expressed as $\tilde{\mathbf{D}}\mathbf{q}_{red} = \mathbf{f}_{red}$, where $\tilde{\mathbf{D}} = \mathbf{R}^H [\mathbf{K} + i\omega\mathbf{C} - \omega^2\mathbf{M}] \mathbf{R}$; this can be rearranged into

$$\begin{bmatrix} \tilde{\mathbf{D}}_{LL} & \tilde{\mathbf{D}}_{LR} & \tilde{\mathbf{D}}_{LO} \\ \tilde{\mathbf{D}}_{RL} & \tilde{\mathbf{D}}_{RR} & \tilde{\mathbf{D}}_{RO} \\ \tilde{\mathbf{D}}_{OL} & \tilde{\mathbf{D}}_{OR} & \tilde{\mathbf{D}}_{OO} \end{bmatrix} \begin{Bmatrix} \mathbf{q}_L \\ \mathbf{q}_R \\ \mathbf{q}_O \end{Bmatrix} = \begin{Bmatrix} \mathbf{f}_L \\ \mathbf{f}_R \\ \mathbf{0} \end{Bmatrix}. \quad (2)$$

The dofs in \mathbf{q}_O can be eliminated, and the following form is obtained

$$\begin{bmatrix} \mathbf{D}_{LL} & \mathbf{D}_{LR} \\ \mathbf{D}_{RL} & \mathbf{D}_{RR} \end{bmatrix} \begin{Bmatrix} \mathbf{q}_L \\ \mathbf{q}_R \end{Bmatrix} = \begin{Bmatrix} \mathbf{f}_L \\ \mathbf{f}_R \end{Bmatrix}. \quad (3)$$

This formulation of the governing equation corresponds to the one-dimensional formulation of the WFE method introduced in [7]. The propagation constant in the x -direction $\lambda_x = \exp(-ik_x L_x)$ can be found by stating the periodicity and equilibrium conditions between the left and right edges of the segment

$$\mathbf{q}_R = \lambda_x \mathbf{q}_L \quad \text{and} \quad \lambda_x \mathbf{f}_L + \mathbf{f}_R = \mathbf{0} \quad (4)$$

and by formulating the eigenvalue problem

$$\mathbf{T} \begin{Bmatrix} \mathbf{q}_L \\ \mathbf{f}_L \end{Bmatrix} = \lambda_x \begin{Bmatrix} \mathbf{q}_L \\ \mathbf{f}_L \end{Bmatrix}, \quad \text{where} \quad \mathbf{T} = \begin{bmatrix} -\mathbf{D}_{LR}^{-1} \mathbf{D}_{LL} & \mathbf{D}_{LR}^{-1} \\ -\mathbf{D}_{RL} + \mathbf{D}_{RR} \mathbf{D}_{LR}^{-1} \mathbf{D}_{LL} & -\mathbf{D}_{RR} \mathbf{D}_{LR}^{-1} \end{bmatrix} \quad (5)$$

is the transfer matrix. A number of better-conditioned eigenproblems can be formulated [17]. Regardless of the eigenproblem used, its solution yield the WFE estimate of the wavenumber k_x and the wavemode shapes, which form the wave basis. The eigenvalues and the associated eigenvectors of the transfer matrix occur in pairs (λ_x^+, ϕ^+) and (λ_x^-, ϕ^-) , which represent a pair of positive- and negative-going waves [17, 18]. From the computed waves, by applying the criterion $|k_x L_x| < 1$, only the propagating waves and the slowly decaying waves are retained at each frequency. Reducing the wave basis will: (a) reduce the size of the model and (b) improve the conditioning of the system [19].

With the positive- and negative-going waves identified and the eigenvectors partitioned to demonstrate the influence of the nodal dofs and forces the vectors \mathbf{q} and \mathbf{f} can be written in terms of the wave amplitudes \mathbf{a}^\pm , i.e.,

$$\mathbf{q} = \Phi_q^+ \mathbf{a}^+ + \Phi_q^- \mathbf{a}^- \quad , \quad \mathbf{f} = \Phi_f^+ \mathbf{a}^+ + \Phi_f^- \mathbf{a}^- \quad (6)$$

These matrices define a transformation between the physical domain, where the motion is described in terms of \mathbf{q} and \mathbf{f} , and the wave domain, where the motion is described in terms of waves of amplitudes \mathbf{a}^\pm that travel in the positive and negative x -directions, respectively.

The knowledge of the wavemodes can be further used to find the time-averaged power of the waves as

$$\Pi = \frac{1}{2} \mathbf{a}^H \mathbf{P} \mathbf{a} \quad ,$$

where $\mathbf{a} = [(\mathbf{a}^+)^T (\mathbf{a}^-)^T]^T$ and \mathbf{P} is the power matrix that can be expressed as

$$\mathbf{P} = \frac{i\omega}{2} \left\{ \begin{bmatrix} (\Phi_q^+)^H \Phi_f^+ & (\Phi_q^+)^H \Phi_f^- \\ (\Phi_q^-)^H \Phi_f^+ & (\Phi_q^-)^H \Phi_f^- \end{bmatrix} - \begin{bmatrix} (\Phi_f^+)^H \Phi_q^+ & (\Phi_f^+)^H \Phi_q^- \\ (\Phi_f^-)^H \Phi_q^+ & (\Phi_f^-)^H \Phi_q^- \end{bmatrix} \right\}. \quad (7)$$

The power matrix is Hermitian and thus the time averaged power Π is always real.

3 REFLECTION AND TRANSMISSION COEFFICIENTS OF JOINTS

Structures can include discontinuities such as boundaries, line junctions or joints of finite dimensions, whose scattering properties are of a great importance for the structural vibration analysis.

Consider a straight line junction between two plates, see Figure 3. Waves in ‘‘Plate 1’’ of amplitudes \mathbf{a}^+ are incident on the joint and they give rise to reflected waves of amplitudes

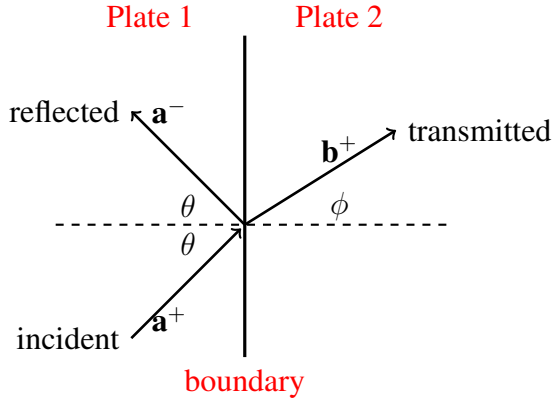


Figure 3: Reflection and transmission on a joint.

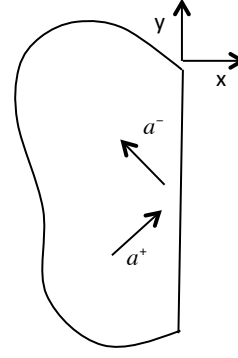


Figure 4: Simply supported plate.

$\mathbf{a}^- = \mathbf{r}_{11}\mathbf{a}^+$ and transmitted waves in “Plate 2” of amplitudes $\mathbf{b}^+ = \mathbf{t}_{12}\mathbf{a}^-$, where \mathbf{r}_{11} and \mathbf{t}_{12} are the matrices of the reflection and transmission coefficients of the joint. These define the scattering matrix \mathbf{s} of the joint, whose partitions relate the amplitudes of the incident and scattered waves.

Denoting by j the wavemodes and by a_j the wave amplitude, from Equation 7, the power flow of the j -th wave is given by $P_{jj}|a_j|^2$. For an incoming wave denoted by j and by using the indices i and k for reflected and transmitted waves, respectively, the reflection and transmission coefficients are computed by

$$\mathcal{R} = [R_{ij}] = \left[|r_{ij}|^2 \frac{P_{ii}}{P_{jj}} \right] \quad \text{and} \quad \mathcal{T} = [T_{kj}] = \left[|t_{kj}|^2 \frac{P_{kk}}{P_{jj}} \right]. \quad (8)$$

For lossless systems the reflection and transmission coefficients should sum to unity.

3.1 Reflection at a boundary

Consider an isotropic plate which lies in the region $x \leq 0$ with an edge along the line $x = 0$ as shown in Figure 4. Waves with amplitude \mathbf{a}^- are incident upon the boundary and generate only reflected waves. Any boundary condition in terms of the nodal dofs and nodal forces can be written as $\mathbf{A}\mathbf{f} + \mathbf{B}\mathbf{q} = \mathbf{0}$. The dofs and the internal forces can be further projected onto the wave domain using Equation 6, yielding

$$\mathbf{A}(\Phi_{\mathbf{f}}^+ \mathbf{a}^+ + \Phi_{\mathbf{f}}^- \mathbf{a}^-) + \mathbf{B}(\Phi_{\mathbf{q}}^+ \mathbf{a}^+ + \Phi_{\mathbf{q}}^- \mathbf{a}^-) = \mathbf{0}. \quad (9)$$

The incident and reflected waves are related by the reflection matrix which follows as

$$\mathbf{r} = - [\mathbf{A}\Phi_{\mathbf{f}}^+ + \mathbf{B}\Phi_{\mathbf{q}}^+]^{-1} [\mathbf{A}\Phi_{\mathbf{f}}^- + \mathbf{B}\Phi_{\mathbf{q}}^-]. \quad (10)$$

3.2 FE/WFE method for a joint of finite dimensions

Analytical results for the scattering coefficients exist for few simple cases, e.g. the reflection coefficients of waves in a simply supported or fixed edge of an isotropic plate. For more complicated structures and joints of finite dimension the hybrid FE/WFE approach is proposed. Details about the FE/WFE approach in case of joined waveguides can be found in [6, 16].

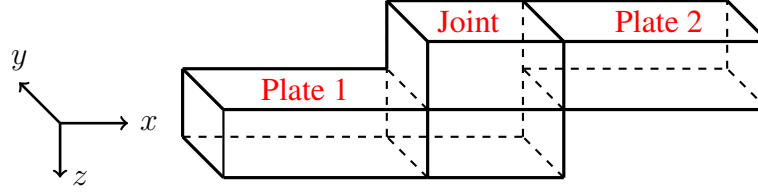


Figure 5: Schematic of two bonded plates. The overlapping region of the two plates is considered the joint.

Consider two plates and a joint as they are illustrated in Figure 5. The FE/WFE approach relies on modelling the plates by using the WFE method, as it was described in section 2, and on modelling the joint by using standard FE methods. A segment of the joint is modelled using standard FE; the stiffness and mass matrices \mathbf{K} and \mathbf{M} of a segment of the joint are used to formulate the dynamic stiffness matrix of the joint $\mathbf{D} = \mathbf{K} - \omega^2 \mathbf{M}$. In principle, the scattering properties of a joint can be found by applying equations of equilibrium and continuity at the interface nodes between the joints and the plates. For this aim, it is assumed that the interfaces have compatible meshes. The time harmonic behaviour of the joint is described through

$$\mathbf{D} \begin{Bmatrix} \mathbf{Q}_i \\ \mathbf{Q}_n \end{Bmatrix} \equiv \begin{bmatrix} \tilde{\mathbf{D}}_{ii} & \tilde{\mathbf{D}}_{in} \\ \tilde{\mathbf{D}}_{ni} & \tilde{\mathbf{D}}_{nn} \end{bmatrix} \begin{Bmatrix} \mathbf{Q}_i \\ \mathbf{Q}_n \end{Bmatrix} = \begin{Bmatrix} \mathbf{F}_i \\ \mathbf{F}_n \end{Bmatrix}, \quad (11)$$

where \mathbf{Q} and \mathbf{F} are vectors of dofs and of internal nodal forces. Since no external forces are applied at the non-interface nodes, i.e., $\mathbf{F}_n = \mathbf{0}$, then Equation 11 reduces to

$$\mathbf{D}_{ii} \mathbf{Q}_i = \mathbf{F}_i \quad \text{where} \quad \mathbf{D}_{ii} = \tilde{\mathbf{D}}_{ii} - \tilde{\mathbf{D}}_{in} \tilde{\mathbf{D}}_{nn}^{-1} \tilde{\mathbf{D}}_{ni}, \quad \text{and} \quad \mathbf{Q}_n = -\tilde{\mathbf{D}}_{nn}^{-1} \tilde{\mathbf{D}}_{ni} \mathbf{Q}_i. \quad (12)$$

By applying the periodicity conditions, the nodal dofs and forces at the interface are expressed in terms of the dofs and forces of the plate. Equation 12 can be expressed in the wave domain and the scattering matrix, which relates the incoming and outgoing waves with $\mathbf{a}^- = \mathbf{s} \mathbf{a}^+$, is finally given by

$$\mathbf{s} = - [\mathbf{D}_{ii} \Phi_q^- - \Phi_f^-]^{-1} [-\Phi_f^+ + \mathbf{D}_{ii} \Phi_q^+]. \quad (13)$$

4 NUMERICAL RESULTS

In this section, numerical examples are presented to demonstrate the developed method. The first example is of a plate with a simply supported edge. The next one is about two bonded plates with the same properties and the last one is of two joined laminated plates. In the following, all properties and dimensions are in SI units.

4.1 Isotropic plate with simply supported edge

For the first example a plate in the $(x-y)$ plane with simply supported edge and three dofs has been chosen, see Figure 4. The plate has thickness $h = 3 \times 10^{-3}$ and material properties given by the values $\rho = 2700$, $E = 0.71 \times 10^{11}$ and $\nu = 0.28$. The boundary conditions are: the displacement in the z direction is zero and the bending moment along the x axis is zero. The wavenumbers are analytically known [2, 3] and the numerical computations can validate the WFE model, Figure 6a.

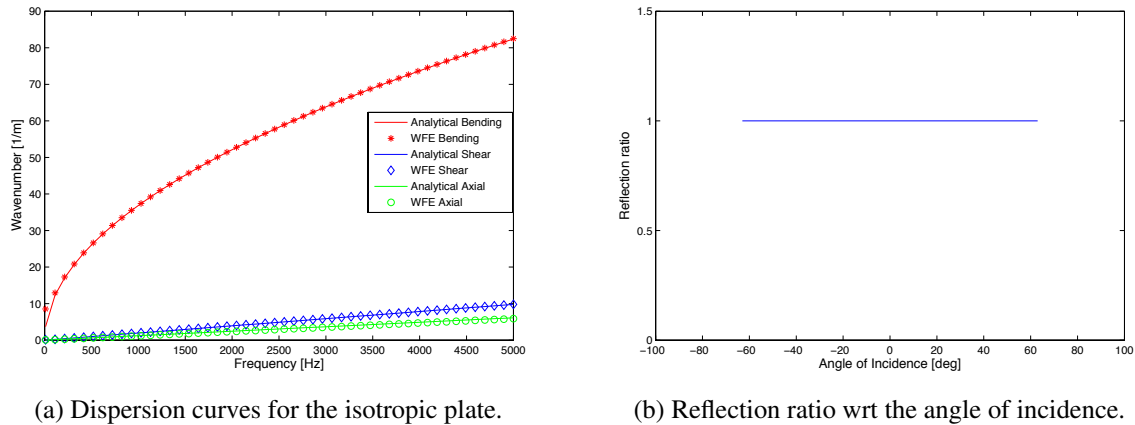


Figure 6: Isotropic plate with simply supported edge.

Due to the boundary there exist only reflected power and the analytic value of the reflection ratio is equal to one. Computing the reflection matrix in terms of the wavemodes by using Equation 10 the reflection ratio with respect to the angle of incidence is shown in Figure 6b.

4.2 Identical bonded plates

The structure in the second example comprises of two joined identical isotropic plates with the same material properties as in the example of subsection 4.1 and a joint as shown in Figure 5. The hybrid FE/WFE model as described in subsection 3.2 allows the computation of the reflection and transmission coefficients of the joint. For motion along the x -axis, i.e., $\theta = 0^\circ$ and for different frequencies, the power ratio between two bending-type waves is equally distributed between reflection and transmission as shown in Figure 7a.

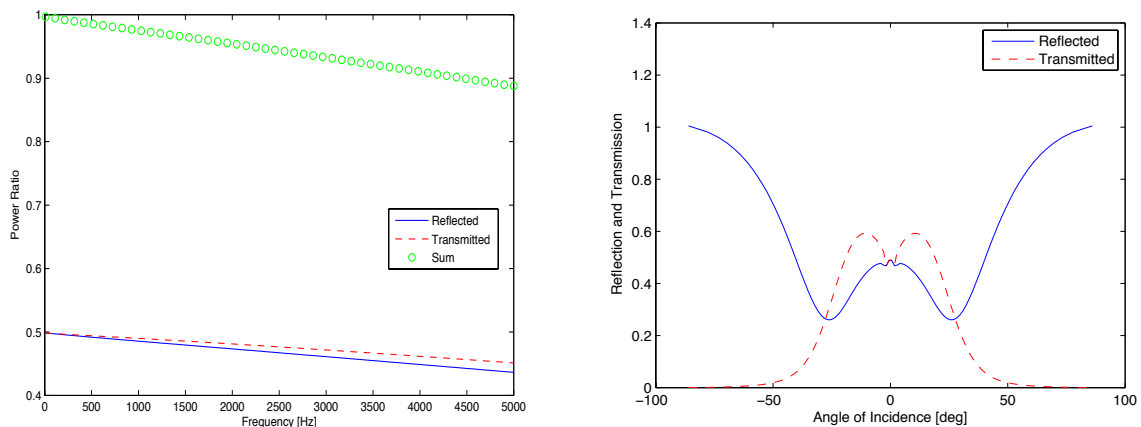


Figure 7: Power reflection and transmission coefficients between two bending-type waves in case of identical bonded isotropic plates.

One can also investigate the influence of the angle of incidence, θ , on the reflection and transmission. Figure 7b shows the power reflection and transmission coefficients for bending-to-bending reflection and transmission at 1 kHz with respect to the incidence angle range $(-90^\circ, 90^\circ)$. For propagation angle $\theta = 0^\circ$ the reflection and transmission ratios are

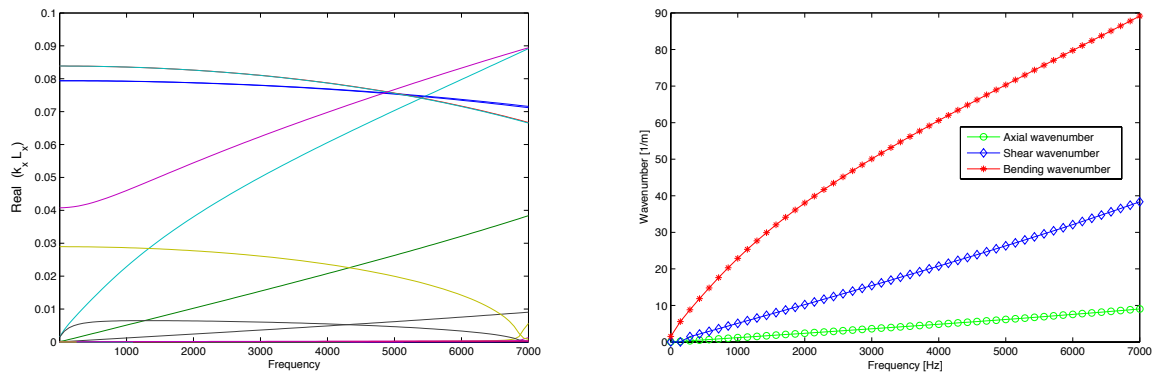
equal (≈ 0.5). While the propagation angle is increasing, the reflection ratio is increasing too. At an incidence angle $\theta \approx 90^\circ$, which corresponds to wave propagation in the y -direction, the reflection ratio is equal to one and the transmission ratio is zero.

4.3 Bonded plates made of composite materials

The plates in the third example are two laminated plates that have the same thickness and properties, and are attached to each other by an adhesive with properties $E = 2.95 \times 10^9$, $\rho = 1100$ and $\nu = 0.286$. Each plate comprises a light, soft foam core sandwiched between two skins. Each skin is made of four layers of graphite epoxy whose material properties along the axes x' , y' and z' of orthotropy are $E_{x'} = 144.48 \times 10^9$ and $E_{y'} = E_{z'} = 9.63 \times 10^9$; the shear moduli are $G_{x'y'} = G_{x'z'} = G_{y'z'} = 4.128 \times 10^9$; Poisson's ratios are $\nu_{x'y'} = \nu_{z'y'} = 0.02$ and $\nu_{x'z'} = 0.3$; the density is $\rho = 1389$ and the material loss factor is $\eta = 0.01$.

The layout of the inner (i.e., bottom) skin is $[0/90/90/0]$ degrees and that of the outer (i.e., top) skin is $[90/0/0/90]$ degrees, and each skin is 4×10^{-3} thick (with each laminate being 1mm thick). The core is a polymethacrylamide ROHACELL foam which is isotropic with modulus of elasticity $E = 0.18 \times 10^9$, density $\rho = 1100$ and Poisson's ratio $\nu = 0.286$. For the WFE modelling, SOLID45 elements of ANSYS were meshed through the thickness of each plate.

In Figure 8a the numerically computed values of the wavenumbers of all retained waves are plotted. In this figure one can distinguish the wavenumbers which correspond to the standard waves (i.e., axial, shear and bending). These are also separately shown in Figure 8b. Moreover, there can also be observed and more complicated waves. These are expected to cut-on (i.e. become propagating waves) at higher frequencies as Figure 8a shows. Since there are no known analytical values for these wavenumbers, WFE method is a valuable tool to evaluate the wave characteristics of the plates.

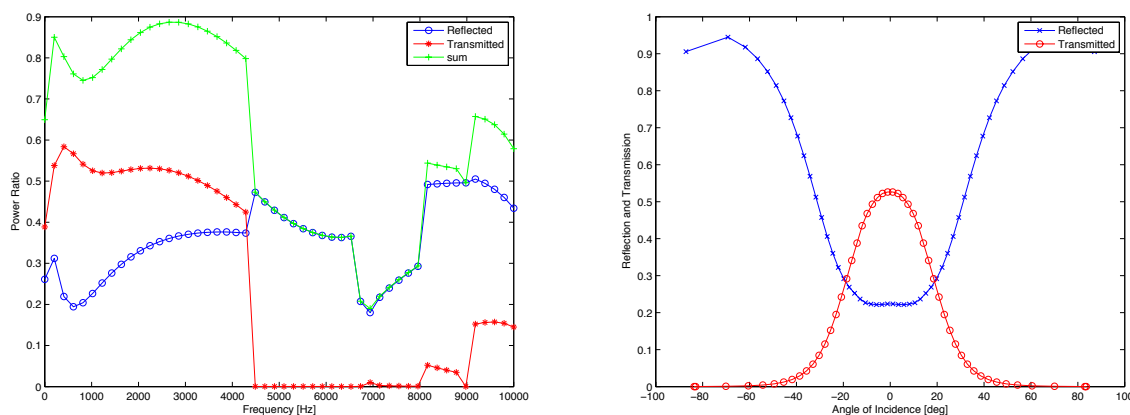


(a) The wavenumbers of all the retained waves after the filtering. (b) The axial, shear and bending wavenumbers of the waves.

Figure 8: Dispersion curves for the laminated plate in case of propagation angle $\theta = 0$.

Concerning the reflection and transmission coefficients between two bending type waves one can see from Figure 9a that for propagation along the x -axis and lower frequencies, the transmission ratio is higher than the reflection ratio. On the other hand, for higher frequencies there is almost no transmitted power. At low frequencies, the sandwiched behave similar to orthotropic plates with a “near” equi-partition between reflected and transmitted power. As the frequency increases, the role of the joint becomes more apparent and it acts as an impedance which causes the bending waves to reflect into the “source” plate. The discontinuities that are observed above 4.5 kHz can be attributed to wavemode conversions where the waves cannot be

purely classified. Similar results are observed for the power ratios at 1kHz for a varying angle of incidence, see Figure 9b. In particular, the transmitted power is decreasing while the angle of propagation is getting bigger and for an angle $\theta > 45^\circ$ there are only reflected waves.



(a) Power reflection and transmission coefficients between two bending-type waves for $\theta = 0^\circ$.

(b) Power reflection and transmission coefficients between two bending-type waves at 1 kHz.

Figure 9: Power reflection and transmission coefficients between two bending-type waves in case of bonded laminates.

5 CONCLUSION

In this paper the WFE method for two dimensional structures has been implemented not only for isotropic plates but also for laminates. The scattering matrix of the joints, when joined plates are considered has also been computed by means of the hybrid FE/WFE approach. Combining the wave characteristics of the plates with the scattering properties of joint, the power reflection and transmission ratios are estimated. The findings of this paper provide valuable knowledge regarding the propagation of waves in the structures under consideration, especially for the cases where analytical results are not known or too difficult to be found.

REFERENCES

- [1] J.N. Reddy. *Mechanics of Laminated Composite Plates: Theory and Analysis*. CRC Press, 1996.
- [2] K. F. Graff. *Wave Motion in Elastic Solids*. Dover Publications Inc., New York, 1975.
- [3] L. Cremer, M. Heckel, and B. A. T. Petersson. *Structure-Borne Sound*. Springer, third edition, 2005.
- [4] Y A Abdel-Rahman. *Matrix Analysis of Wave Propagation in Periodic Systems*. PhD thesis, 1979.
- [5] B. R. Mace and E. Manconi. Modelling wave propagation in two-dimensional structures using finite element analysis. *Journal of Sound and Vibration*, 318(4-5):884 – 902, 2008.
- [6] J. M. Renno and B. R. Mace. Calculating the forced response of two-dimensional homogeneous media using the wave and finite element method. *Journal of Sound and Vibration*, 330(24):5913–5927, 2011.

- [7] B. R. Mace, D. Duhamel, M. J. Brennan, and L. Hinke. Finite element prediction of wave motion in structural waveguides. *Journal of the Acoustical Society of America*, 117(5):2835 – 2843, 2005.
- [8] M. Maess, N. Wagner, and L. Gaul. Dispersion curves of fluid filled elastic pipes by standard fe models and eigenpath analysis. *Journal of Sound and Vibration*, 296(1-2):264 – 276, 2006.
- [9] J.-M. Mencik and M.N. Ichchou. Wave finite elements in guided elastodynamics with internal fluid. *International Journal of Solids and Structures*, 44(7-8):2148 – 2167, 2007.
- [10] Elisabetta Manconi and Brian R. Mace. Wave characterization of cylindrical and curved panels using a finite element method. *Journal of the Acoustical Society of America*, 125(1):154 – 163, 2009.
- [11] Jamil M. Renno and Brian R. Mace. Calculating the forced response of cylinders and cylindrical shells using the wave and finite element method. *Journal of Sound and Vibration*, 333(21):5340 – 5355, 2014.
- [12] D. Duhamel, B. R. Mace, and M. J. Brennan. Finite element analysis of the vibrations of waveguides and periodic structures. *Journal of Sound and Vibration*, 294(1-2):205 – 220, 2006.
- [13] R. S. Langley and K. Heron. Elastic wave transmission through plate/beam junctions. *Journal of Sound and Vibration*, 143:241–253, 1990.
- [14] I. Bosmans and T. Nightingale. Modeling vibrational energy transmission at bolted junctions between a plate and a stiffening rib. *Journal of Acoustical Society of America*, 109(3):999–1010, 2001.
- [15] S.J. Walsh and R.G. White. Vibrational power transmission in curved beams. *Journal of Sound and Vibration*, 233(3):455 – 488, 2000.
- [16] J. M. Renno and B. R. Mace. Calculation of reflection and transmission coefficients of joints using a hybrid finite element/wave and finite element approach. *Journal of Sound and Vibration*, 332(9):2149–2164, April 2013.
- [17] W.X. Zhong and F.W. Williams. On the direct solution of wave propagation for repetitive structures. *Journal of Sound and Vibration*, 181(3):485 – 485, 1995.
- [18] W.X. Zhong, F.W. Williams, and A. Y. T. Leung. Symplectic analysis for periodical electro-magnetic waveguides. *Journal of Sound and Vibration*, 267(2):227 – 244, 2003.
- [19] Y. Waki, B. R. Mace, and M. J. Brennan. Numerical issues concerning the wave and finite element method for free and forced vibrations of waveguides. *Journal of Sound and Vibration*, 327(1-2):92–108, 2009.



SCATTERING OF HIGH-ORDER GUIDED WAVES IN SANDWICH PLATES

Droz C.^{1,2*}, J.-P. Lainé² and M.N. Ichchou²

¹Airbus Helicopters
Aéroport Inter. Marseille-Provence, 13725 Marignane Cedex, FRANCE

²Ecole Centrale de Lyon
36 Avenue Guy de Collongue, 69134 Ecully Cedex, FRANCE
Email: christophe.droz@ec-lyon.fr

ABSTRACT

In this paper, the propagation of high-order waves in a sandwich plate made of transverse isotropic honeycomb core surrounded by fiber-reinforced skins is investigated. These waves are created under pulse train excitation. The wave scattering effects are studied using time-response analysis in the composite waveguide and compared to the WFEM predictions. Furthermore, these high-order waves have low spatial attenuation in broadband frequency range and can be used as an alternative to several SHM techniques based on first-order wave propagation. It may ultimately encompass some of the drawbacks encountered when dealing with boundary conditions in 2D-waveguides or provide accurate wave-based inspection techniques for heterogeneous or composite beams.

1 INTRODUCTION

For the last decades, numerical and experimental methods were extensively investigated to provide efficient and accurate Structural Health Monitoring (SHM) and Non Destructive Evaluation (NDE) techniques for automotive and aerospace industry [1]. Most of the aforementioned methods consist in evaluating the dispersion characteristics of a reduced number of propagating (or guided) waves in a given structure since they can propagate long distances with weak spatial attenuation. In this context, numerous numerical methods were developed in order to predict the wave dispersion characteristics in composite waveguides. Waveguides are structures, such as beams, pipes, sandwich panels or layered shells, whose dimensions lead to a set of privileged directions for the propagation of the mechanical energy. The Wave Finite Element Method (WFEM) uses Bloch's theorem [2] to provide significant reduction of the modelling effort for such analyses, since it combines the Periodic Structures Theory (PST) with commercial finite element packages [3, 4]. Therefore, wave dispersion characteristics of a waveguide whose cross-section is modelled with FEM can be derived by solving a small quadratic eigenvalue problem [5].

Although wave-based methods are extensively employed in the offshore and aerospace industries for inspecting defects and cracks in 1D and 2D waveguides, these approaches are often involving first-order waves, such as the flexural, or Lamb waves for beams, plates, laminated or sandwich panels, and torsional waves in pipelines inspection. However, when composite or large-scaled 1D waveguides are considered, first-order waves can be prone to coupling effects, or unaffected by localized defects. In this case higher-order, or localized waves may be used instead. Therefore, the specific dispersion characteristics of these waves have to be taken into consideration. In this paper, the propagation of high-order plane waves in a sandwich plate made of transverse isotropic honeycomb core surrounded by fiber-reinforced skins is investigated. These waves are created under pulse sinusoidal excitation. The wave scattering effects are studied using time-response analysis in the composite plate and compared to the WFEM predictions. Furthermore, these high-order waves have low spatial attenuation in broadband frequency range and can be used as an alternative to several SHM techniques based on first-order wave propagation. It may ultimately encompass some of the drawbacks encountered when dealing with boundary conditions in 2D-waveguides or provide accurate wave-based inspection techniques for heterogeneous or composite beams.

2 WAVE FINITE ELEMENT METHOD (WFEM)

A waveguide is considered as a straight elastic structure made of N of identical substructures of same length d , connected along the direction x . The state vector is described in figure 1. Nodal displacements and forces are denoted \mathbf{q} and \mathbf{f} , where the subscripts 'L' and 'R' describe the cell's left and right faces. Both edges have the same number n of degrees of freedom. Mesh compatibility is assumed between the cells. The governing equation in a cell at frequency ω is written :

$$(-\omega^2\mathbf{M} + \mathbf{K})\mathbf{q} = \mathbf{f} \quad (1)$$

where \mathbf{M}, \mathbf{K} are the mass and complex stiffness matrices, respectively. A dynamic condensation of the inner DOFs can be required if the structure is periodic. The governing equation can be written by reordering the DOFs :

$$\begin{bmatrix} \mathbf{K}_{LL} & \mathbf{K}_{LR} \\ \mathbf{K}_{RL} & \mathbf{K}_{RR} \end{bmatrix} - \omega^2 \begin{bmatrix} \mathbf{M}_{LL} & \mathbf{M}_{LR} \\ \mathbf{M}_{RL} & \mathbf{M}_{RR} \end{bmatrix} \begin{Bmatrix} \mathbf{q}_L \\ \mathbf{q}_R \end{Bmatrix} = \begin{Bmatrix} \mathbf{f}_L \\ \mathbf{f}_R \end{Bmatrix} \quad (2)$$

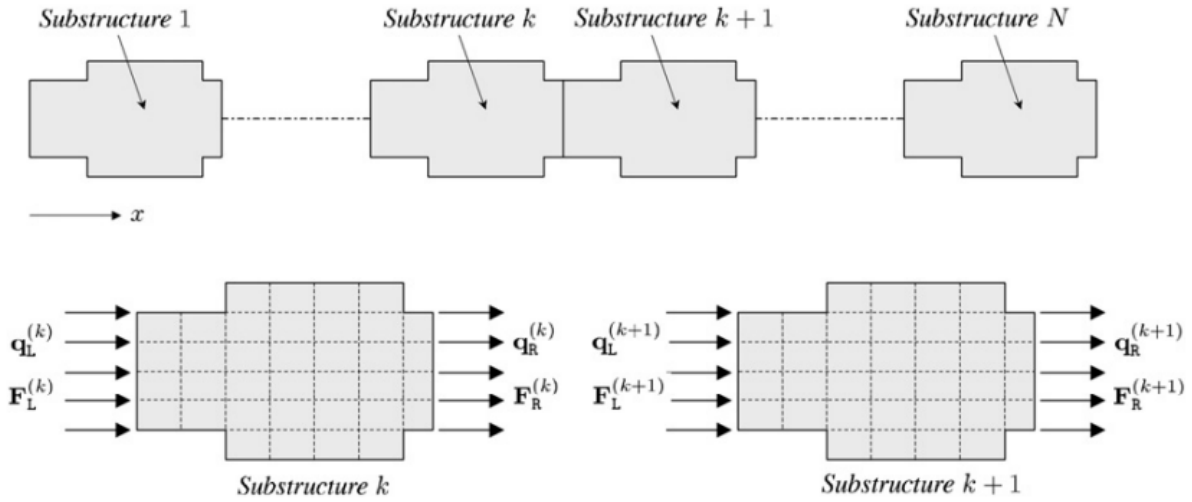


Figure 1. Illustration of a waveguide and the state vector of a unit cell.

where \mathbf{M}_{ii} and \mathbf{K}_{ii} are symmetric, $\mathbf{M}_{LR}^t = \mathbf{M}_{RL}$ and $\mathbf{K}_{LR}^t = \mathbf{K}_{RL}$. $\lambda = e^{-jkd}$ is the propagation constant, describing wave propagation over the cell length d and k is the associated wavenumber, considering force equilibrium

$$\lambda \mathbf{f}_L + \mathbf{f}_R = 0 \quad (3)$$

in a cell and Bloch's theorem:

$$\mathbf{q}_R = \lambda \mathbf{q}_L \quad (4)$$

into Eq. (2), it yields the following spectral eigenproblem :

$$\mathbf{S}(\lambda, \omega) = (\lambda \mathbf{D}_{LR} + (\mathbf{D}_{LL} + \mathbf{D}_{RR}) + \frac{1}{\lambda} \mathbf{D}_{RL}) \Phi = \mathbf{0} \quad (5)$$

where the solutions Φ stand for the wave shape associated with the displacements \mathbf{q}_L of the waveguide's cell. In damped waveguides, complex wavenumbers are associated to decaying waves. Defining the state vector : $\Phi = [(\Phi_q)^t, (\Phi_f)^t]^t$, the spectral problem can be written using the symplectic transfer matrix \mathbf{T} .

$$\mathbf{T}\Phi = \begin{bmatrix} \mathbf{D}_{LR}^{-1} \mathbf{D}_{LL} & \mathbf{D}_{LR}^{-1} \\ \mathbf{D}_{RL} - \mathbf{D}_{RR} \mathbf{D}_{LR}^{-1} \mathbf{D}_{LL} & -\mathbf{D}_{RR} \mathbf{D}_{LR}^{-1} \end{bmatrix} \begin{Bmatrix} \Phi_q \\ \Phi_f \end{Bmatrix} = \lambda \begin{Bmatrix} \Phi_q \\ \Phi_f \end{Bmatrix} \quad (6)$$

Here, the waves associated with positive wavenumber are travelling in the positive x-direction and the negative wavenumbers describe propagation in the negative x-direction. The dynamical behaviour of the global system can be expressed by expanding amplitudes of incident and reflected waves on a basis of eigenvectors. If the structure is undamped, solutions are divided into propagative waves, whose wavenumbers are real, and evanescent waves for which wavenumbers are imaginary. In dissipative case, complex wavenumbers are associated to decaying waves.

3 DISPERSION CHARACTERISTICS OF A SANDWICH PLATE

3.1 Description of the composite waveguide

The rectangular sandwich waveguide is composed of a 8 mm thick homogenised honeycomb core surrounded by 1 mm thick fiber-reinforced skins. The 400 mm width cross-section is modelled using 360 linear block elements having 8-nodes and 3 degrees of freedom (DOF) per

node. The waveguide is described in figure 2, a structural loss factor $\eta = 0.01$ is assumed and a detailed description of the materials is given in tables 1 and 2.

Material	Density (kg.m^{-1})	Young Modulus (Pa)	Shear Modulus (Pa)
Nomex	24	$E_x = 5 \times 10^6$ $E_y = 5 \times 10^6$ $E_z = 46.6 \times 10^6$	$G_{xy} = 1 \times 10^6$ $G_{xz} = 10.13 \times 10^6$ $G_{yz} = 10.13 \times 10^6$

Table 1. Material properties of honeycomb core

Material	Density (kg.m^{-1})	Young Modulus (Pa)	Shear Modulus (Pa)
TC skin	1451	$E_x = 81 \times 10^9$ $E_y = 81 \times 10^9$ $E_z = 3.35 \times 10^9$	$G_{xy} = 2.5 \times 10^9$ $G_{xz} = 2.8 \times 10^9$ $G_{yz} = 2.8 \times 10^9$

Table 2. Material properties of fiber-reinforced skins

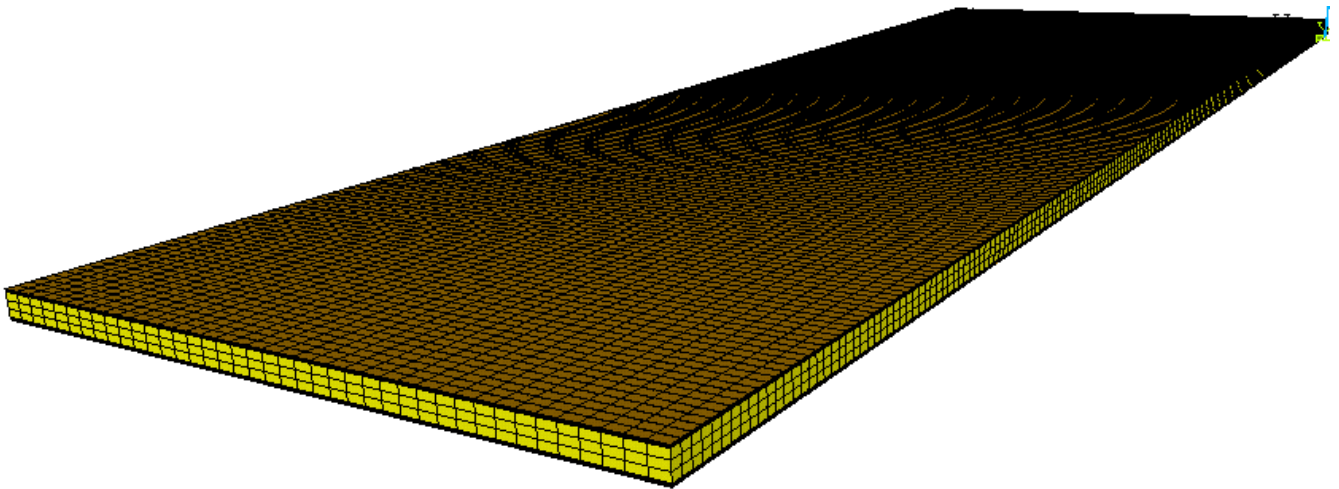


Figure 2. Finite element model of sandwich plate involving finite width.

3.2 Propagating waves and shapes

The wavenumbers associated with the propagating waves in the sandwich waveguide are shown in figure 3. The continuous lines (—) describe first-order waves while dashed lines (- - -) represent high-order propagating waves, associated with deformed cross-sections. It can be noticed that numerous high-order waves are propagating in this structure, in addition to the four first-order waves (transverse and in-plane flexural, torsional and longitudinal waves). The cross-sectional deformed shapes associated with these first-order waves are shown in figure 4. In the considered structure, high-order waves are associated with sinusoidal deformation of the waveguide's cross-section. Their shapes are described in figure 5. The spatial attenuations of the propagating waves in the frequency range $[0, 4000]$ Hz are shown in figure 6. The wave amplitudes are given after a one meter propagation in the main direction. Although high-order waves share the same asymptotic group velocity of the first-order flexural and torsional waves, their spatial attenuations exhibit different behaviour close to each of their cut-on frequencies.

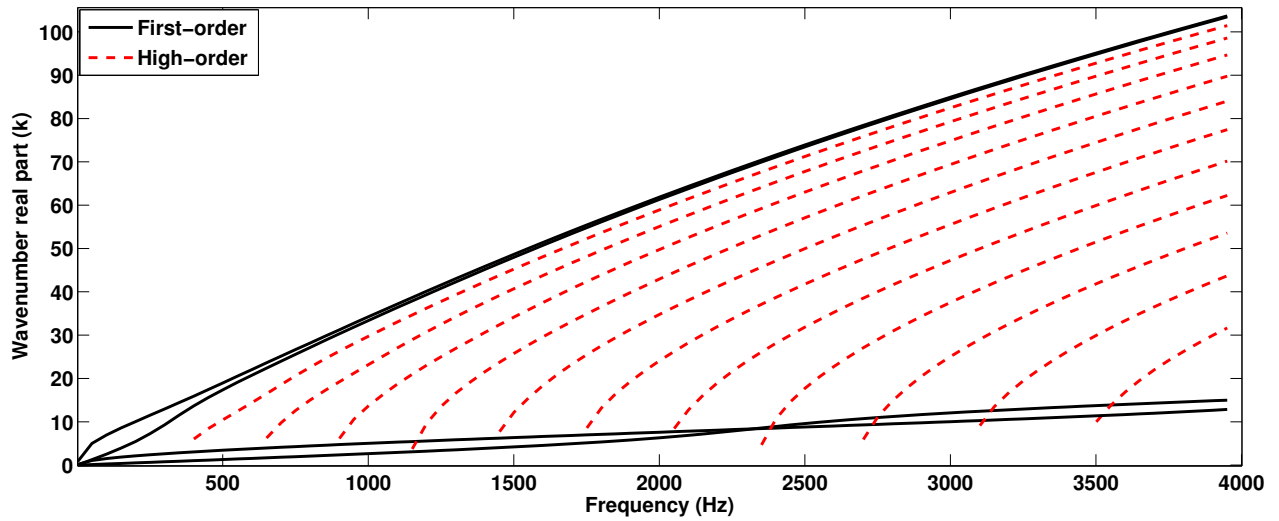


Figure 3. Real part of the wavenumbers associated with propagating, positive-going waves.

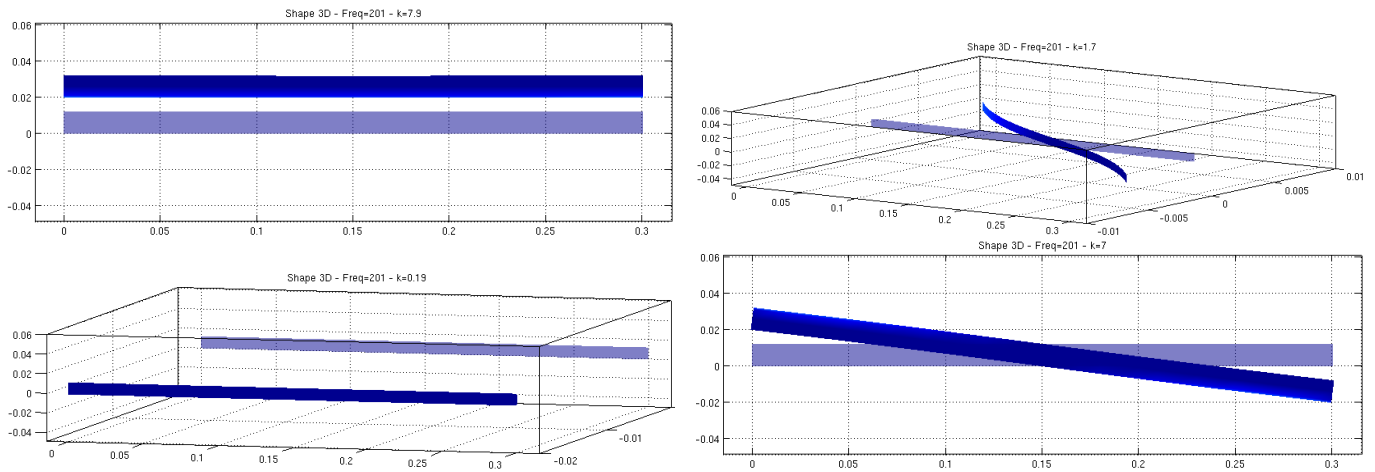


Figure 4. Deformed shapes associated with the first-order propagating waves.

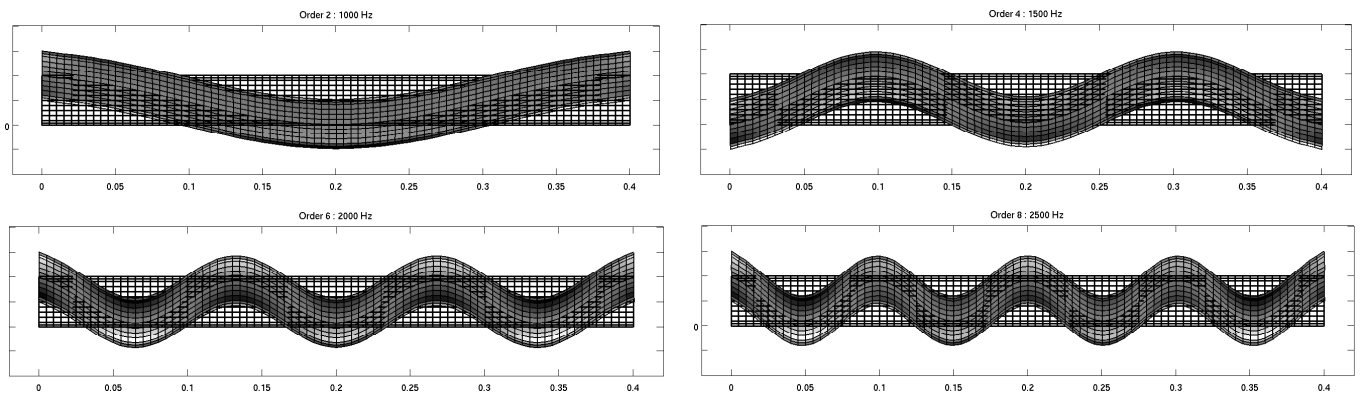


Figure 5. Deformed shapes associated with high-order propagating waves.

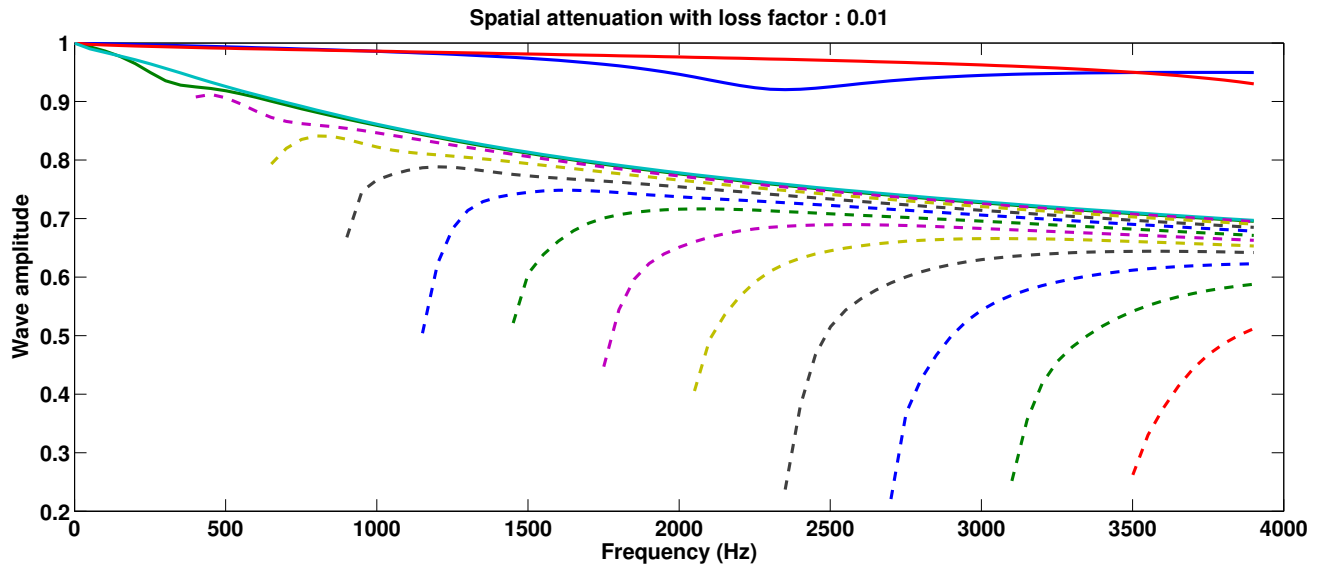


Figure 6: Amplitudes of the propagating waves in the sandwich waveguide after 1 meter propagation.

4 TIME ANALYSIS USING WAVE APPROPRIATION

This work is concerned with the propagation of the aforementioned high-order waves in a sandwich plate of finite dimensions. Therefore, the actuation of the waves described in figure 5 is proposed using localized vertical displacements. The shape appropriation is shown in figure 7 for the 4th order flexural wave.

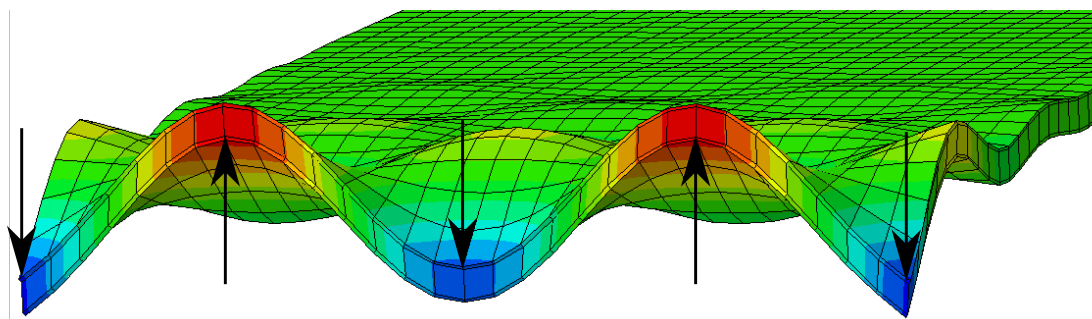


Figure 7. Shape appropriation of the 4th-order flexural wave.

The transient response under pulse train excitation (see figure 8) is determined using time-explicit simulation. The frequency spectrum of the pulse is described in figure 9. A reduced dispersion of the pulse train can be obtained by narrowing the frequency spectrum bandwidth. It can be done by increasing the number of periods in the pulse train. In figure 10, the time response of the waveguide is described under a 2nd-order wave at 1k Hz . Noteworthy, the wave pulse propagates without coupling effects and a slight dispersion. It can be explained since the frequency spectrum involves different group velocities for a given wave. Therefore, it seems advantageous to generate waves at higher frequencies. Similarly, the propagation of the 4th-order wave is shown for a 2k Hz pulse involving 8 periods is shown in figure 11.

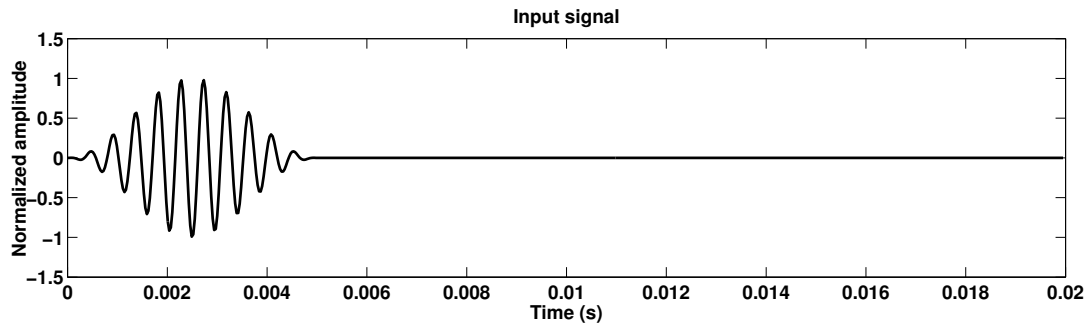


Figure 8. Time signal of the pulse.

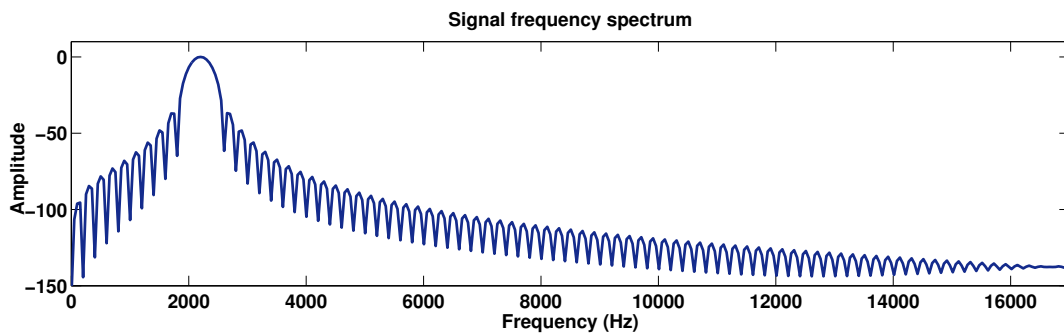


Figure 9. Frequency spectrum of the pulse.

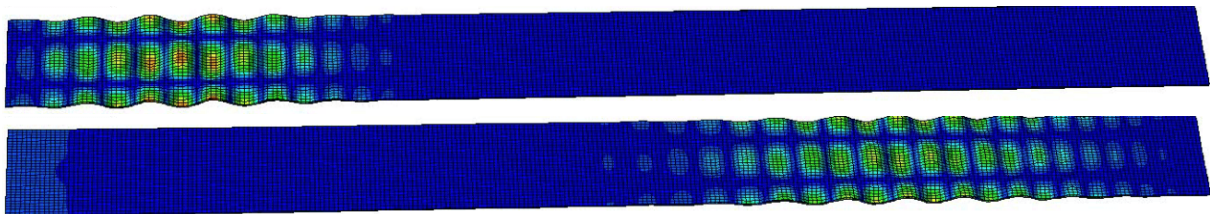


Figure 10. Propagation and dispersion of a 2nd-order wave generated at 1k Hz.

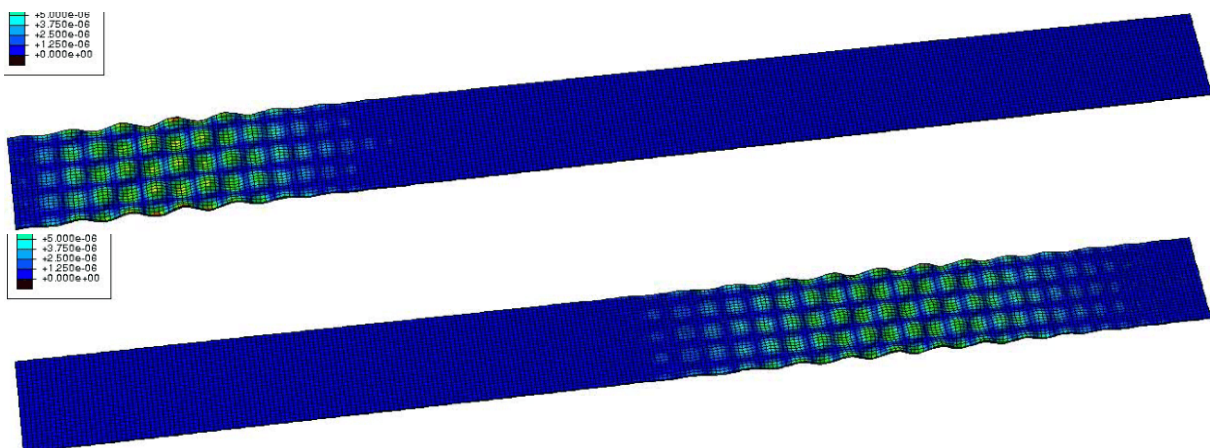


Figure 11. Propagation and dispersion of a 4th-order wave generated at 2k Hz.

5 DISCUSSIONS

This paper is concerned with the time response of a sandwich waveguide to high-order waves, generated by appropriation of their propagating wave shapes. First, the wave dispersion characteristics are determined using the WFEM. Then, the wave amplitudes are compared for first- and high-order waves after 1 meter of propagation in the considered waveguide, assuming a constant structural loss factor $\eta = 0.01$. Noteworthy, the wave attenuation is higher close to the cut-on frequencies, meaning that higher frequencies should be considered for actuating high-order propagating waves. The waves shapes being associated with sinusoidal mode shapes of the cross section, a reduced number of punctual displacements is required for producing the wave appropriation. The time response is determined for two different wave types at 1k Hz and 2k Hz. A good generation of the wave pulse is produced with a weak dispersion and no wave conversion. Therefore, it is shown that a high-order wave involving deformed cross-section can be easily actuated and propagates with dispersion characteristics predicted by the WFEM. Furthermore, these waves are expected to provide further information on defects or structural perturbations in composite, heterogeneous or large-scaled waveguides involving localized or high-order waves.

ACKNOWLEDGEMENTS

The authors would like to gratefully acknowledge Airbus Helicopters for their financial support.

REFERENCES

- [1] Victor Giurgiutiu. *Structural health monitoring: with piezoelectric wafer active sensors*. Academic Press, 2007.
- [2] Felix Bloch. Über die quantenmechanik der elektronen in kristallgittern. *Zeitschrift für physik*, 52(7-8):555–600, 1929.
- [3] D. Duhamel, B. R. Mace, and M. J. Brennan. Finite element analysis of the vibration of waveguides and periodic structures. *J. Sound Vib.*, 294:205–220, 2006.
- [4] J. M. Mencik and M. N. Ichchou. Multi-mode propagation and diffusion in structures through finite elements. *Eur. J. Mech. A–Solid*, 24(5):877–898, 2005.
- [5] C. Droz, J.-P. Lainé, M.N. Ichchou, and G. Inquiété. A reduced formulation for the free-wave propagation analysis in composite structures. *Compos. Struct.*, 113:134–144, 2014.



A WAVE BASED UNIT CELL METHOD TO PREDICT ABSORPTION AND TRANSMISSION COEFFICIENTS OF POROELASTIC MATERIALS CONTAINING PERIODIC INCLUSIONS

E. Deckers¹, C. Claeys^{1*} and W. Desmet¹

¹ KU Leuven, Dept. of Mechanical Engineering
Celestijnenlaan 300B box 2420, 3001 Heverlee (Leuven), BELGIUM
Email: elke.deckers@kuleuven.be, claus.claeys@kuleuven.be, wim.desmet@kuleuven.be

ABSTRACT

This paper presents an efficient Wave Based modelling procedure to predict the absorption and transmission coefficient of infinite poroelastic materials containing a periodic grid of inclusions. As compared to standard numerical prediction schemes it offers the following advantages: (1) contrarily to Transfer Matrix Methods the layers do not need to be homogeneous, (2) contrarily to multipole methods, the inclusions do not need to be circular, (3) contrarily to element based prediction techniques, unbounded domains can easily be accounted for. Moreover, the procedure allows more easily for optimisation routines since it is a meshless and computationally more efficient technique. The Wave Based Method is an indirect Trefftz approach; it approximates the dynamic fields using a weighted sum of exact solutions of the governing differential equations. The Multi-Level Wave Based Method, which allows to describe the dynamic field of a cavity containing an inclusion, is extended in two ways: (1) Bloch-Floquet conditions are imposed on the boundaries to take into account the periodicity of the complete structure and (2) novel unbounded acoustic wave functions are presented that fulfil the acoustic Helmholtz equation, the Sommerfeld radiation condition and the Bloch-Floquet conditions. The implementation of the method is validated with the multipole method.

1 INTRODUCTION

In many industrial applications poroelastic materials are applied as efficient noise reduction measures. These materials show to be most effective in the mid to high frequency range where the acoustic wavelengths are of the same order of magnitude as the thickness of the material. In the past decades, much research effort is spent in order to increase the absorption of the material in the low frequency range. Often multilayered structures are applied in order to prohibit wave propagation, combining different kinds of porous and viscous materials combined with air gaps. Although effective, this approach may lead to heavier and more bulky solutions. Another approach consists in studying inhomogeneous materials, such as double porosity materials [1] or poroelastic materials containing inclusions [2]. This paper focuses on the numerical modelling of the latter.

An efficient Wave Based modelling procedure is presented to predict the absorption and transmission coefficient of laterally infinite poroelastic materials containing a periodic grid of inclusions. The Wave Based Method (WBM) [3, 4] is an indirect Trefftz approach; it approximates the dynamic fields using a weighted sum of exact solutions of the governing differential equation(s). It can be applied to any dynamic problem of which mathematical description of the governing physics can be cast into a (number of) Helmholtz equation(s). The unknowns are the contribution factors of the wave functions. A sufficient condition for the WBM to converge is that the considered problem domains are convex. Non-convex domains need to be partitioned into a (preferably small) number of subdomains. When considering geometries containing inclusions, it is clear that the standard WBM cannot easily be applied as it would lead to many subdomains. For circular inclusions it would even be impossible. To overcome these constraints, the Multi-Level WBM (ML-WBM) has been developed [5]. The bounded domain and each of the inclusions are considered in a different 'level' as if the others are not present. Their approximation sets are then combined using a weighted residual approach.

When considering an acoustic plane wave impinging on an infinite 2D poroelastic material with periodic inclusions, the response of the entire structure is characterized by the response of a unit cell. The theorem of Bloch states that the relative amplitude change and phase shift of a wave propagating through an infinite periodic structure, is the same across each cell; as a result the response of any unit cell can be expressed in terms of the response of a reference unit cell multiplied by an exponential term that defines the amplitude and the phase shift as the wave propagates from the reference cell to neighbouring cells.

In this paper, the ML-WBM is extended in two ways: (1) Bloch-Floquet conditions are imposed on the boundaries to take into account the periodicity of the complete structure and (2) novel unbounded acoustic wave functions are presented that fulfil the acoustic Helmholtz equation as well as the Sommerfeld radiation condition and Bloch-Floquet conditions. As compared to standard numerical prediction schemes it offers the following advantages: (1) contrarily to Transfer Matrix Methods the layers do not need to be homogeneous, (2) contrarily to multipole methods, the inclusions do not need to be circular, (3) contrarily to element based prediction techniques, unbounded domains can easily be accounted for. Moreover, the procedure is meshless such that it more easily allows for optimization routines.

The implementation of the method is validated with the multipole method. Two examples show the effect of different types of inclusions on the absorption as well as the transmission coefficient.

2 PROBLEM DESCRIPTION

The mathematical problem setting of a general 2D periodic coupled (semi-) infinite acoustic-poroelastic steady-state problem containing rigid circular inclusions, as shown in Figure 1 is

given in this section. A time-harmonic motion with $e^{j\omega t}$ -dependence is assumed.

The problem domain Ω can be divided into two non-overlapping domains Ω_a and Ω_e , containing air and a poroelastic medium, described as an equivalent fluid, respectively. A plane wave is impinging on the poroelastic structure, incident at an angle θ . The thickness of the poroelastic structure is denoted L_y and the heterogeneities are periodic in the x -direction with period L_x . In the application cases of this paper, the inclusions are considered rigid (i.e. Neumann boundary conditions) and circular. In a completely similar way, other boundary conditions can be introduced. Moreover, the Multi-Level WBM allows to study different inclusion geometries as well; there is no restriction to circular geometries.

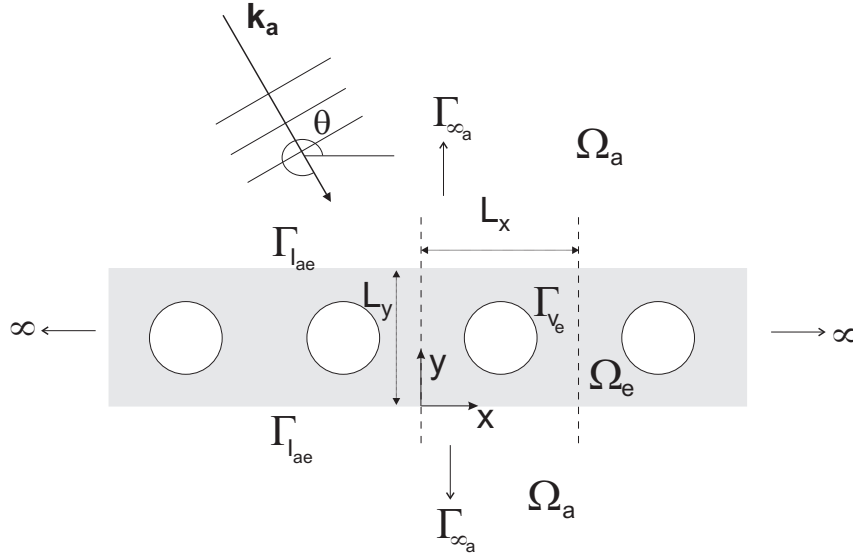


Figure 1: Problem description of a 2D infinite poroelastic structure with periodic circular inclusions, coupled to two infinite acoustic domains.

It is assumed that the poroelastic material has a rigid frame and can be modelled as an equivalent fluid medium, with a complex effective density ρ_e and effective compressibility K_e , following the same expressions as in [2]. The steady-state pressure $p_e(\mathbf{r})$, inside the medium Ω_e , is governed by the Helmholtz equation. Also the acoustic pressure, $p_a(\mathbf{r})$, in medium Ω_a is governed by the Helmholtz equation. Consequently, the steady state pressure $p_\bullet(\mathbf{r})$, with $\bullet = a$ for the acoustic and $\bullet = e$ for the equivalent fluid case is given by:

$$\mathbf{r} \in \Omega_\bullet : \nabla^2 p_\bullet(\mathbf{r}) + k_\bullet^2 p_\bullet(\mathbf{r}) = \mathcal{F}_\bullet(\mathbf{r}), \quad (1)$$

where, ∇^2 is the Laplacian operator, $k_\bullet = \omega/c_\bullet$ is the wave number of medium Ω_\bullet . The fluid is excited by a source defined by $\mathcal{F}_\bullet(\mathbf{r})$.

Due to the geometrical periodicity and the plane wave nature of the excitation, the resulting dynamic fields have to be periodic in the x -direction as well. The dynamic fields in all cells can be related to the one of a single cell using the Bloch-Floquet relation [6]:

$$\forall N \in \mathbb{Z} : p_\bullet(x + NL_x, y) = p_\bullet(x, y) e^{-jk_{ax}NL_x}, \quad (2)$$

where $k_{ax} = k_a \cos \theta$.

In this paper, only Sommerfeld, Neumann boundary conditions and coupling conditions between an equivalent fluid and an acoustic domains are considered. On the exterior acoustic boundary at infinity, Γ_{∞_a} , the former the condition applies:

$$\mathbf{r} \in \Gamma_{\infty_a} : R_{\infty_a}(\mathbf{r}) = \lim_{|\mathbf{r}| \rightarrow \infty} \left(\sqrt{|\mathbf{r}|} \left(\frac{\partial p_a(\mathbf{r})}{\partial |\mathbf{r}|} + jk_a p_a(\mathbf{r}) \right) \right) = 0. \quad (3)$$

On the rigid boundaries determined by the inclusions, Γ_{v_e} the following residual applies:

$$\mathbf{r} \in \Gamma_{v_e} : R_{v_e}(\mathbf{r}) = \mathcal{L}_{v_e}(p_e(\mathbf{r})) - \bar{v}_{e,n} = 0, \tag{4}$$

with $\bar{v}_{e,n}$ the prescribed value for the normal velocity, being 0 m/s for a rigid boundary. The velocity operator is defined as:

$$\mathcal{L}_{v_\bullet}(\ast) = \frac{j}{\rho_\bullet \omega} \frac{\partial \ast}{\partial \gamma_{\mathbf{n}}}, \tag{5}$$

with $\gamma_{\mathbf{n}}$ the normal direction to the boundary, pointing outwards.

On the interfaces $\Gamma_{I_{ae}}$ between the acoustic and the poroelastic medium, the continuity of pressure and velocity are imposed:

$$\mathbf{r} \in \Gamma_{I_{ae}} : \begin{cases} R_{I_{p_{ae}}}(\mathbf{r}) = p_a(\mathbf{r}) - p_e(\mathbf{r}) = 0, \\ R_{I_{v_{ae}}}(\mathbf{r}) = \mathcal{L}_{v_a}(p_a(\mathbf{r})) + \mathcal{L}_{v_e}(p_e(\mathbf{r})) = 0. \end{cases} \tag{6}$$

The governing Helmholtz equations in the different domains (1), the periodicity conditions (2), the applied boundary conditions (3)-(4) and interface conditions (6) define a unique pressure field.

3 MULTI-LEVEL WAVE BASED METHOD

The main idea of the WBM Multi-Level approach [5] is to consider the different inclusions and the bounded domain as different ‘levels’ of the problem. Each level considers the scattering of one specific object, or the dynamic wave field within the bounded domain as if the other inclusions and/or the bounded domain were not present. The total solution field can then be obtained by combining the different levels together in a weighted residual approach, using the superposition principle. The concept is explained for the simple acoustic problem in Figure 2 showing a bounded problem domain with one circular inclusion. For a complete discussion, the reader is referred to [5].

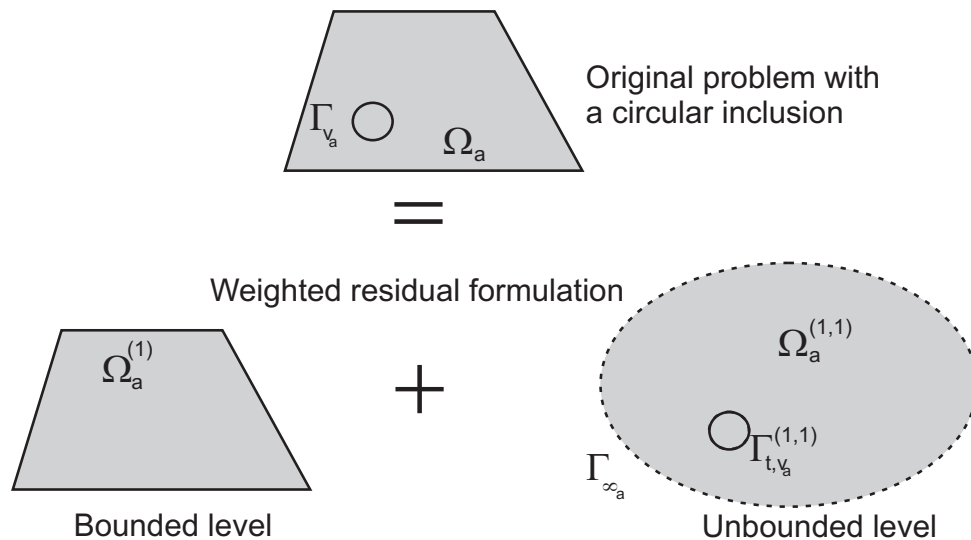


Figure 2: Graphical representation of the Multi-Level modelling concept for bounded problems.

The Multi-Level WBM approach consists of four steps that are briefly revisited for this simple problem setting:

1. *Division of the original problem into levels*

In a first step the original problem is divided into a number of levels: the first level includes the bounded problem as if there were no inclusions present. If the bounded domain is non-convex, it is further partitioned into convex subdomains (not needed in this case). This bounded subdomain is indicated $\Omega_a^{(1)}$ where subscript (1) indicates the index of the bounded subdomain. The other level considers the scattering due the inclusion as if the bounded domain was not present. The truncation circle $\Gamma_{t,v_a}^{(1,1)}$ circumscribes the inclusion (it this case it is coinciding with the actual boundary). The first subscript digit indicates the index of the bounded subdomain to which the inclusion belongs, the second indicates the index of the unbounded level. In this specific case only Neumann boundary conditions are applied on the truncation surface. The unbounded acoustic subdomain exterior to $\Gamma_{t,v_a}^{(1,1)}$ is denoted $\Omega_a^{(1,1)}$.

2. *Selection of wave functions for the different levels:*

For each subdomain belonging to a level, a suitable wave function set is selected to describe its dynamic field. Following the WBM procedure [4, 5], the acoustic pressure is approximated by a solution expansion $\hat{p}_a^{(\bullet)}(\mathbf{r})$:

$$p_a^{(\bullet)}(\mathbf{r}) \simeq \hat{p}_a^{(\bullet)}(\mathbf{r}) = \sum_{w=1}^{n_{a,w}^{(\bullet)}} p_{a,w}^{(\bullet)} \Phi_{a,w}^{(\bullet)}(\mathbf{r}) + \hat{p}_{a,q}(\mathbf{r}) = \mathbf{\Phi}_a^{(\bullet)}(\mathbf{r}) \mathbf{p}_{a,w}^{(\bullet)} + \hat{p}_{a,q}(\mathbf{r}). \quad (7)$$

The wave function contributions $p_{a,w}^{(\bullet)}$ are the weighting factors for each of the selected wave functions $\Phi_{a,w}^{(\bullet)}$. All weighting factors together form the vector of degrees of freedom $\mathbf{p}_{a,w}^{(1)}$. The corresponding *a priori* defined wave functions are collected in the row vector $\mathbf{\Phi}_a^{(1)}$. The particular solution $\hat{p}_{a,q}(\mathbf{r})$ accounts for the effect of source terms, resulting from an inhomogeneous Helmholtz equation (1). For this particular example, this term vanishes. For this example, \bullet can be replaced by 1 for the bounded domain or 1,1 for the unbounded domain.

For the 2D bounded subdomain, two types of wave functions are distinguished, the so-called r- and s-set:

$$\sum_{w=1}^{n_{a,w}^{(1)}} p_{a,w}^{(1)} \Phi_{a,w}^{(1)}(\mathbf{r}) = \sum_{w_r=1}^{n_{a,w_r}^{(1)}} p_{a,w_r}^{(1)} \Phi_{a,w_r}^{(1)}(\mathbf{r}) + \sum_{w_s=1}^{n_{a,w_s}^{(1)}} p_{a,w_s}^{(1)} \Phi_{a,w_s}^{(1)}(\mathbf{r}) \quad (8)$$

with $n_{a,w}^{(\alpha)} = n_{a,w_r}^{(1)} + n_{a,w_s}^{(1)}$. These wave functions are defined as:

$$\Phi_{a,w}^{(1)}(x, y) = \begin{cases} \Phi_{a,w_r}^{(1)}(x, y) = \cos(k_{a,xw_r}^{(1)} x) e^{-jk_{a,yw_r}^{(1)} y} \\ \Phi_{a,w_s}^{(1)}(x, y) = e^{-jk_{a,xw_s}^{(1)} x} \cos(k_{a,yw_s}^{(1)} y) \end{cases} \quad (9)$$

Desmet [3] has shown that the following selection of wave number components leads to a converging wave function set:

$$\begin{aligned} (k_{a,xw_r}^{(1)}, k_{a,yw_r}^{(1)}) &= \left(\frac{w_{1a}^{(1)} \pi}{L_{x_a}^{(1)}}, \pm \sqrt{k_a^2 - (k_{a,xw_r}^{(1)})^2} \right) \\ (k_{a,xw_s}^{(1)}, k_{a,yw_s}^{(1)}) &= \left(\pm \sqrt{k_a^2 - (k_{a,yw_s}^{(1)})^2}, \frac{w_{2a}^{(1)} \pi}{L_{y_a}^{(1)}} \right) \end{aligned} \quad (10)$$

with $w_{1_a}^{(1)}$ and $w_{2_a}^{(1)} = 0, 1, 2, \dots$. The dimensions $L_{x_a}^{(1)}$ and $L_{y_a}^{(1)}$ represent the dimensions of the (smallest) bounding rectangle, circumscribing the considered subdomain $\Omega_a^{(1)}$.

The wave functions for the unbounded domain $\Omega_a^{(1,1)}$ are chosen to explicitly comply with not only the Helmholtz equation, but also with the Sommerfeld radiation condition at Γ_{∞_a} . The following wave function set for unbounded domains exterior to a circular truncation curve with radius R_{t_a} is used, distinguishing between a c- and an s-set:

$$\Phi_{a,w}^{(1,1)}(r, \theta) = \begin{cases} \Phi_{a,w_c}^{(1,1)}(r, \theta) = H_{w_{1_a}^{(1,1)}}^{(2)}(k_a r) \cos(w_{1_a}^{(1,1)} \theta) \\ \Phi_{a,w_s}^{(1,1)}(r, \theta) = H_{w_{2_a}^{(1,1)}}^{(2)}(k_a r) \sin(w_{2_a}^{(1,1)} \theta) \end{cases} \quad (11)$$

with $w_{1_a}^{(1,1)} = 0, 1, 2, \dots$ and $w_{2_a}^{(1,1)} = 1, 2, 3, \dots$ and $H_n^{(2)}(\bullet)$ is the n -th order Hankel function of the second kind. As for bounded domains, the series of functions (11) needs to be truncated in order to be used in a numerical scheme. A similar truncation rule as for the bounded domains is used and determines the highest orders $w_{1_a, max}$ and $w_{2_a, max}$ of the Hankel functions used in the exterior wave function expansion [7]. We denote $\hat{p}_a^{(1,1)}(\mathbf{r})$ the field variable of the unbounded acoustic subdomain $\Omega_a^{(1,1)}$.

The pressure field $\hat{p}_a^{(1')}(\mathbf{r})$ in the compound subdomain $\Omega_a^{(1')} = \Omega_a^{(1)} \cap \Omega_a^{(1,1)}$ can be written as:

$$\mathbf{r} \in \Omega_a^{(1')} : \quad \hat{p}_a^{(1')}(\mathbf{r}) = \hat{p}_a^{(1)}(\mathbf{r}) + \hat{p}_a^{(1,1)}(\mathbf{r}). \quad (12)$$

3. Construction of the system of equations:

The residuals on boundaries and interfaces are minimised using a weighted Galerkin approach and using the compound wave function set for subdomains $\Omega_a^{(1')}$. Different test functions are selected for the different boundaries. The only prerequisite to have valid test functions is that they need to be able to represent an arbitrary field on that specific boundary. As unbounded wave functions can accurately represent any field on the truncation surface they are associated to, they are used as weighting functions on that truncation boundary. A similar reasoning is followed for the bounded wave functions defined for $\Omega_a^{(1)}$: they can be used as weighting functions on the boundaries defining the bounded level.

4. Solution and post-processing:

The system matrices can be solved for the unknown contribution factors of all wave functions. In a post-processing step, the response field can be evaluated.

4 WBM FOR PERIODIC STRUCTURES

As pointed out in Section 2 it is sufficient to study the response in one unit cell to be able to reconstruct the response in any point of the system. The bounded, poroelastic part of the problem domain can be modelled using the Multi-Level WBM using the equivalent fluid properties to determine the wave number components in the pressure expansions. The next subsections discuss the application of the periodicity conditions and the wave functions in the semi-unbounded periodic acoustic domains.

4.1 Bloch-Floquet boundary conditions in the multilevel WBM framework

The wave functions used in the Multi-Level WBM framework do not fulfil the periodicity condition, equation (2). The advantage of using the WBM is, however, that there is no restriction

to circular inclusions as compared to the multipole method. Geometrically not too complex inclusions can be dealt with using the regular multilevel WBM.

The Bloch-Floquet periodicity conditions have to be embedded in the WBM in a weak sense. The following residuals are minimised on the left (Γ_{BFL_e}) and right boundary (Γ_{BFR_e}) of the poroelastic unit cell:

$$\mathbf{r} \in \Gamma_{BFL_e} : R_{BFL_e}(\mathbf{r}) = p(\mathbf{r}) - p(\mathbf{r}^1) e^{jk_{ax}L_x} = 0, \quad (13)$$

$$\mathbf{r} \in \Gamma_{BFR_e} : R_{BFR_e}(\mathbf{r}) = \mathcal{L}_{v_e}(p(\mathbf{r})) + \mathcal{L}_{v_e}(p(\mathbf{r}^1)) e^{-jk_{ax}L_x} = 0, \quad (14)$$

in which $\mathbf{r}^1 \in \Gamma_{BFL_e}$ and $\mathbf{r}^r \in \Gamma_{BFR_e}$.

4.2 Semi-unbounded Bloch-Floquet acoustic wave functions

A novel wave function set is needed in the semi-unbounded acoustic domains to avoid integration on infinite boundaries. Again, the pressure field can be approximated by a weighted set of wave functions, equation (7). Wave functions are selected that fulfil the Helmholtz equation, the Sommerfeld radiation condition and the Bloch-Floquet periodicity condition. The wave functions $\Phi_{a,w}^{(\alpha)}(\mathbf{r})$ for a semi-unbounded periodic domain are a plane wave expansion:

$$\Phi_{a,w}^{(\alpha)}(\mathbf{r}(x, y)) = e^{-j(k_{BFx,w}x + k_{BFy,w}y)}. \quad (15)$$

The wave number components $k_{BFx,w}$ are selected such that the periodicity condition is fulfilled:

$$k_{BFx,w}^{(\alpha)} = k_{ax} + \frac{2m\pi}{L_x}, \quad (16)$$

with $m \in \mathbb{Z}$. In order to fulfil the Helmholtz equation, the wave numbers $k_{BFy,w}$ are selected as:

$$k_{BFy,w}(\alpha) = \pm \sqrt{k_a^2 - \left(k_{BFx,w}^{(\alpha)}\right)^2}, \quad (17)$$

and the sign of the root is selected such that the waves are purely outgoing and consequently the Sommerfeld condition is fulfilled.

A plane wave source is exciting the system. For this source, the particular term yields:

$$\hat{p}_{a,q}(\mathbf{r}) = A e^{-j\mathbf{k}_a \cdot \mathbf{r}}, \quad (18)$$

with A the plane wave amplitude, $\mathbf{k}_a = (k_{ax}, k_{ay}) = (k_a \cos \theta, k_a \sin \theta)$ the wave vector and θ the propagation angle, see also Figure 1.

4.3 Reflection, transmission and absorption coefficient evaluation

Due to the plane wave nature of the wave functions in the semi-unbounded periodic acoustic domains, the hemispherical reflection and transmission coefficients, \mathcal{R} and \mathcal{T} , can be calculated as:

$$\mathcal{R} = \sum_w \frac{\Re(k_{BFy,w}^{(1)}) \|p_{a,w}^{(1)}\|^2}{k_{ay} \|A\|^2}, \quad (19)$$

$$\mathcal{T} = \sum_w \frac{\Re(k_{BFy,w}^{(2)}) \|p_{a,w}^{(2)}\|^2}{k_{ay} \|A\|^2}. \quad (20)$$

The absorption coefficient \mathcal{A} can be evaluated via:

$$\mathcal{A} = 1 - \mathcal{R} - \mathcal{T}. \quad (21)$$

5 NUMERICAL VALIDATION

The validation case considers the problem setting shown in Figure 3. The dimensions, the frequency range as well as the material properties are based on values available from literature [8].

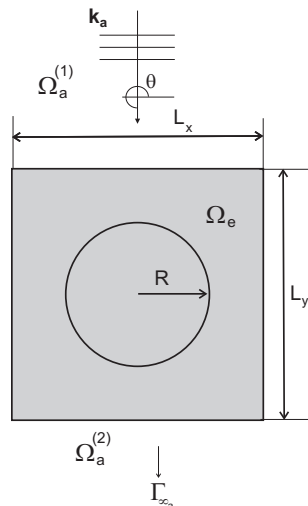


Figure 3: Acoustic-Poroelastic-Acoustic unit cell problem geometry with a circular rigid inclusion.

The angle of incidence is $3\pi/2$. The radius of the rigid inclusion R is taken to be 2.5 mm. The thickness L_y of the foam and the distance L_x in between the inclusions are both 1 cm.

Figure 4 shows the absorption, reflection, and transmission coefficient of the periodic medium, with and without periodic rigid circular inclusions, calculated with the WBM and the multipole method for frequencies between 1 kHz and 300 kHz. A perfect match between the WBM and the MPM is seen, confirming the validity of the former.

It is seen that the reflection coefficient is clearly increased due to the addition of the inclusions. Some of the incoming energy is reflected on the rigid inclusion instead of travelling through the material. The absorption coefficient is increased around the modified plate modes, leading to an entrapment of energy. Except around these frequencies, the absorption coefficient is not altered to a large extent. The increased reflection and absorption coefficient obviously have a beneficial effect on the obtained transmission coefficient.

6 CONCLUDING REMARKS

This paper discusses the extension of the Multi-Level Wave Based Method to predict the absorption, reflection and transmission coefficients of poroelastic structures with periodic inclusions. In this paper, as a first step, only circular inclusions are considered, although this is no limitation for the method. The poroelastic material is modelled as an equivalent fluid. Bloch-Floquet periodicity conditions are imposed in a weak sense, minimising residuals on the boundary conditions. A novel wave function set is applied for the acoustic semi-infinite domains; each wave function fulfills the acoustic Helmholtz equation, the Sommerfeld radiation condition and the periodicity conditions. The method has been applied for a simple sound transmission problem and the results obtained are confirmed by a multipole implementation. In a next step, the method will be applied in optimisation studies as the procedure is meshless and there is no restriction towards circular inclusions.

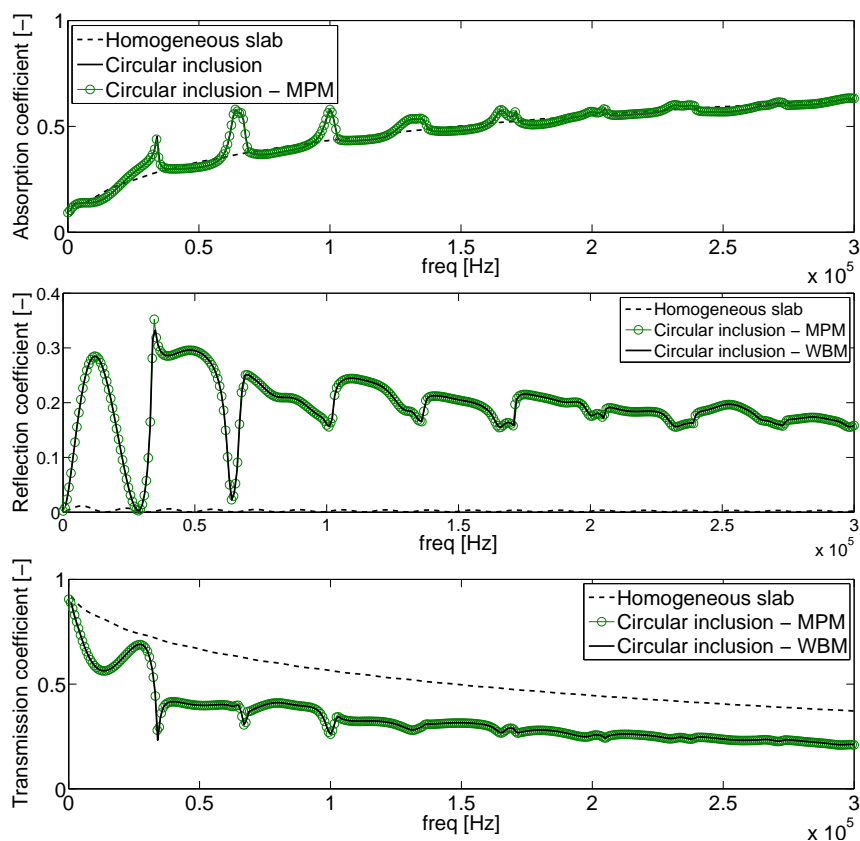


Figure 4: Absorption coefficient (top), reflection coefficient (middle) and transmission coefficient (bottom) for the polyurethane foam with and without circular inclusions.

ACKNOWLEDGEMENTS

Elke Deckers is a Postdoctoral Fellow of the Fund for Scientific Research-Flanders (F.W.O.), Belgium. The Research Fund KU Leuven is gratefully acknowledged for its support. The authors would also like to thank Jean-Philippe Groby of the Laboratoire d'Acoustique de l'Université du Maine to provide the results obtained by the multipole Method.

REFERENCES

- [1] C. Boutin and F.-X. Bécot. Theory and experiments on poro-acoustics with inner resonators. *Wave Motion*, 54:76–99, 2015.
- [2] J.-P. Groby, A. Duclos, O. Dazel, L. Boeckx, and L. Kelders. Enhancing absorption coefficient of a backed rigid frame porous layer by embedding circular periodic inclusions. *J. Acoust. Soc. Am.*, 130:3771–3780, 2011.
- [3] W. Desmet. *A wave based prediction technique for coupled vibro-acoustic analysis*. KULeuven, division PMA, PhD. thesis 98D12, 1998.
- [4] E. Deckers, O. Atak, L. Coox, R. D'Amico, H. Devriendt, S. Jonckheere, K. Koo, B. Pluymers, D. Vandepitte, and W. Desmet. The Wave Based Method: an overview of 15 years of research. *Wave Motion*, 51:550–565, 2014.
- [5] B. Van Genechten, K. Vergote, D. Vandepitte, and W. Desmet. A Multi-Level Wave Based numerical modelling framework for the steady-state dynamic analysis of bounded

- Helmholtz problems with multiple inclusions. *Comput. Methods Appl. Mech. Engrg.*, 199:1881–1905, 2010.
- [6] F. Bloch. Über die Quantenmechanik der Elektronen in Kristallgittern. *Zeitschrift für Physik A Hadrons and Nuclei*, 52:555–600, 1929.
- [7] B. Bergen, B. Pluymers, B. Van Genechten, D. Vandepitte, and W. Desmet. A Trefftz based method for solving Helmholtz problems in semi-infinite domains. *Engineering Analysis with Boundary Elements*, 36:30–38, 2012.
- [8] J.-P. Groby, A. Wirgin, L. De Ryck, W. Lauriks, R.P Gilbert, and Y.S. Xu. Acoustic response of a rigid-frame porous medium plate with a periodic set of inclusions. *J. Acoust. Soc. Am.*, 126:685–693, 2009.

COPYRIGHT NOTICE

Copyright ©2015 by the authors. Distribution of all material contained in this paper is permitted under the terms of the Creative Commons license Attribution-NonCommercial-NoDerivatives 4.0 International (CC-by-nc-nd 4.0).





IMPROVEMENTS OF FORCE ANALYSIS TECHNIQUE FOR FLAW DETECTION ON COMPOSITE MATERIALS

T. Wassereau^{1*}, C. Pézerat², J.-L. Guyader³ and F. Ablitzer²

¹Institut de Recherche Technologique Jules Verne
Chemin du Chaffault, 44340 Bouguenais, FRANCE
Email: thibault.wassereau@irt-jules-verne.fr

²Laboratoire d'Acoustique de l'Université du Maine
Avenue Olivier Messiaen, 72085 Le Mans, FRANCE
Email: charles.pezerat@univ-lemans.fr and frederic.ablitzer@univ-lemans.fr

³Laboratoire Vibrations et Acoustique
25bis avenue Jean Capelle, 69621 Villeurbanne, FRANCE
Email: jean-louis.guyader@insa-lyon.fr

ABSTRACT

In the light of fossil energy dry, the transportation industries are looking on lighter materials to be applied on their vehicles, in order to reduce their energy consumptions. Composite materials perfectly meet the needs of these industries by offering light weight and high resistance. Although these materials still lack of comprehension regarding their dynamic behavior and the visualization of typical flaws like delamination or tears. Moreover considering wide structures like a plane wing makes usual ultrasonic methods uncomfortable because of complex implementation and the amount of time needed. The goal of our work is to develop a fast vibratory method that could detect flaws on large composite structures with an improvement of the Force Analysis Technique. In a second time if necessary a sharper scanning could be done with ultrasonic methods around the defect region.

Created around 1994 the Force Analysis Technique allows detection of vibratory source by using the equation of motion. Its local aspect confers it a strong point since the boundary conditions are not necessary. Around 2012 an important enhancement of the Force Analysis Technique was brought by applying it out of the vibratory sources, giving access to local cartography of Young modulus and structural damping. The latest improvement deals with non-destructive testing for flaw detection on composite materials, through the analysis of its materials parameters (Young modulus, structural damping and/or shear modulus) in space domain and in frequency domain.

Our first development concerns composite beams. In order to best consider such material we used Timoshenko's beam theory which involves shearing effect unlike the mostly spread Euler-Bernoulli beam theory. By applying the equation of motion out of controlled vibratory sources one can deduce the local material parameters. If a flaw is present in the scanned area, a strong

singularity should appear on the cartographies. Furthermore defects are linked to physical consequence making our method able to deduce the kind of flaw: for instance a delamination might only appear as a variation of the shear modulus, a local lack of viscosity would be seen solely on the cartography of structural damping, etc.

The presentation will deal with a general explanation of our method, and results obtained from various kind of flaws existing on composite beams and will also highlight the advantages of considering Timoshenko theory instead of the Euler-Bernoulli's one. Then we'll draw some conclusions about feasibility of our procedure and opportunities to apply it on more complex composite structures.

1 INTRODUCTION

The increased use of composite shell structures has fostered interest towards virtual testing of vibrational behavior of orthotropic shell structures. In literature there are many methods optimized to investigate a vibrational problem in a specific frequency range. [1] reports a detailed description of these approaches. The present work focuses on the mid-frequency range extending the applicability of the Variational Theory of Complex Rays (VTCR) [2] to orthotropic shell structures. This method approximates the vibrational problem solution as a sum of shape functions that identically satisfy equilibrium equations and addresses boundary conditions in weak form. This approach allows *a priori* independent approximations among subdomains granting flexibility and robustness. VTCR has been already implemented in shallow shell theory [3] and for orthotropic plates [4].

The present work extends the VTCR to orthotropic shell structures. First, the general shell-VTCR theory is presented and corrections are introduced for orthotropic shells. After that, a relevant numerical example is investigated to validate the strategy.

2 SHELL - VTCR

We will refer to the notation introduced in [5] where the general shell theory is described. Since the VTCR is a Trefftz method, the solution is searched in a function set that satisfies equilibrium equations. Boundary and corner residuals are addressed in weak form $\mathbf{B} = \mathbf{l}$ where \mathbf{B} is the bilinear form, \mathbf{l} is the linear form being VTCR a Galerkin method. [3] reports a more detailed version of the weak variational formulation.

Since VTCR is a Trefftz method, any kind of shape function f_{SF_i} , proved that satisfies equilibrium equations, can be chosen as solution in subdomain Ω_i . In the present work plane waves are used

$$f_{SF}(\mathbf{x}_{reli}) \approx \sum_{l=1}^n a_{li} \hat{\mathbf{c}}_{li} e^{j \mathbf{k}_{li} \mathbf{x}_{rel}}, \quad (1)$$

where a_{qi} are amplitude coefficients determined by the weak form, \mathbf{k}_{li} is the wave vector, $\hat{\mathbf{c}}_{li}$ unit direction vector, and \mathbf{x}_{reli} is the relative position vector in curvilinear coordinates $\{\alpha_i, \beta_i\}$. Without loss of generality, the wave vector can be divided into the wavenumber k_{li} and the unit direction vector of the wave vector $\hat{\mathbf{k}}_{li}$

$$\mathbf{k}_i(l) = \mathbf{k}_{li} = k_{li} \hat{\mathbf{k}}_{li}. \quad (2)$$

k_{li} and $\hat{\mathbf{c}}_{li}$ are chosen so that equilibrium equations are identically satisfied. The discretization is performed on $\hat{\mathbf{k}}_{li}$. Two kinds of plane waves are needed: evanescent and propagative. The difference lies on $\hat{\mathbf{k}}_{li}$. It is

$$\hat{\mathbf{k}}_{li} = \mathbf{L}_i \mathbf{O}_i \mathbf{T}_{li} \cdot \mathbf{p} \quad (3)$$

$$\mathbf{T}_{li} = \begin{bmatrix} \cos(\theta_{li}) & -\sin(\theta_{li}) \\ \sin(\theta_{li}) & \cos(\theta_{li}) \end{bmatrix}, \quad \mathbf{O}_i = \sqrt{D_{\alpha i} D_{\beta i}} \begin{bmatrix} D_{\alpha i}^{-1/4} & 0 \\ 0 & D_{\beta i}^{-1/4} \end{bmatrix}, \quad \mathbf{L}_i = \begin{bmatrix} L_{\alpha i} & 0 \\ 0 & L_{\beta i} \end{bmatrix} \quad (4)$$

where $\mathbf{p} = [1, 0]'$ for propagative waves and $\mathbf{p} = [\cosh(\phi_{mi}), j \sinh(\phi_{mi})]'$ for evanescent waves, $L_{\alpha i}$ and $L_{\beta i}$ are Lamé parameters, θ_{li} is the discretization angle over the unit circle, and ϕ_{mi} is a real parameter that controls between the oscillatory and the evanescent part of the evanescent wave. Figure 1 reports their qualitative behavior. \mathbf{L}_i and \mathbf{O}_i are correction matrices for orthotropic materials.



Figure 1: Qualitative behavior of the propagative and evanescent waves described in Section 2.

3 NUMERICAL RESULTS

Figure 2 illustrates geometry of a complex frame structure and the amplitude magnitude of the VTCR solution. Three sub-domains are connected by the same edge. The first two are cylinder parts while the last one is a plate. All boundaries are clamped but left edge where an out-of-plane oscillatory distributed load $\mathbf{p} = [1, 0, 0]'e^{i\omega t}$ N/m is applied. For the sake of simplicity thicknesses are constant $h_1 = h_2 = h_3 = 3\text{mm}$ as well as the damping factor $\eta = 0.001$. Table 1 reports material properties as well as frequency.

f	3700	Hz
$E_{\theta 1} = E_{\theta 2} = E_{z 3}$	125	GPa
$E_{y 1} = E_{y 2} = E_{y 3}$	60	GPa
$G_{\theta y 1} = G_{\theta y 2} = G_{z y 3}i$	18	GPa
$\nu_{\theta y 1} = \nu_{\theta y 2} = \nu_{z y 3}$	0.3	
$\rho_1 = \rho_2 = \rho_3$	2000	Kg/m ³

Table 1: Orthotropic material properties and frequency examined of the numerical example described in Section 3.

The VTCR implemented in MATLAB[®] is compared with a FEM reference generated by ABAQUS[®]. The two programs are run on the same workstation and performances compared. The error based on kinetic energy is

$$err = \frac{|E_K(\mathbf{u}_{FEM}) - E_K(\mathbf{u}_{VTCR})|}{E_K(\mathbf{u}_{FEM})}. \quad (5)$$

In this case the error is $\approx 8\%$ due to small theory differences. Computational costs are illustrated in Table 2. FEM mesh must be very refined to counteract the pollution effect [6]. For this reason, VTCR greatly outperforms FEM in terms of time and memory consumption.

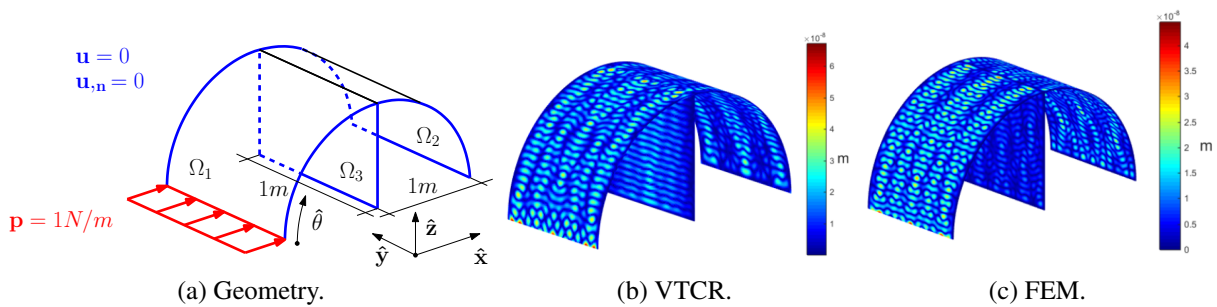


Figure 2: Geometry, VTCR and FEM solutions of the frame structure described in Section 3..

	Time consumption	Memory consumption
FEM	1153 [s]	10 [Gb]
VTCR	4 [s]	70 [Kb]

Table 2: Performances comparison of the numerical example described in Section 3

4 CONCLUSIONS

Corrections for orthotropic materials were introduced in the general shell-VTCR theory. Since at mid-frequency FEM suffers of pollution error, FEM mesh must be very refined. For this reason, VTCR greatly outperforms FEM at mid-frequency.

ACKNOWLEDGEMENTS

The authors gratefully acknowledge the “Centre National d’Études Spatiales (CNES)” and “Airbus Defense and Space”

REFERENCES

- [1] W Desmet, B Pluymers, A Onur, and O Atak. *methodologies for mid-frequency analysis in vibration and acoustics*. Marie Curie Initial Training Network (ITN), Leuven, 2012.
- [2] P Ladevèze, L Arnaud, P Rouch, and C Blanzé. The variational theory of complex rays for the calculation of medium-frequency vibrations. *Engineering Computations*, 18(1/2):193–214, 2001.
- [3] Alessandro Cattabiani, Hervé Riou, Andrea Barbarulo, Pierre Ladevèze, Guillaume Bézier, and Bernard Troclet. The Variational Theory of Complex Rays applied to the shallow shell theory (accepted for publication). *Computers & Structures*, 2015.
- [4] L Kovalevsky, P Ladevèze, H Riou, and M Bonnet. The variational theory of complex rays for three-dimensional helmholtz problems. *Journal of Computational Acoustics*, pages 1–25, 2012.
- [5] E Ventsel and T Krauthammer. *Thin plates and shells: theory: analysis, and applications*. CRC press, Basel, 2001.
- [6] A Deraemaeker. Dispersion and pollution of the FEM solution for the Helmholtz equation in one, two and three dimensions. *International Journal for Numerical Methods in Engineering*, 46(4):471–499, 1999.

COPYRIGHT NOTICE

Copyright ©2015 by the authors. Distribution of all material contained in this paper is permitted under the terms of the Creative Commons license Attribution-NonCommercial-NoDerivatives 4.0 International (CC-by-nc-nd 4.0).





CONTACT-LESS FULL-FIELD OPTICAL MEASUREMENT METHOD TO ANALYZE VIBRATIONS OF STRUCTURES

J. POITTEVIN^{1*}, P. PICART², F. GAUTIER² and C. PEZERAT²

¹Institute in Research and Technology Jules Verne
ENSIM, Rue Aristote, Le Mans, FRANCE
Email: julien.poittevin@irt-jules-verne.fr

²LUNAM, LAUM CNRS UMR 6613
Universit du Maine, Le Mans, FRANCE
Email: pascal.picart@univ-lemans.fr, francois.gautier@univ-lemans.fr,
charles.pezerat@univ-lemans.fr

ABSTRACT

Structural vibrations can be measured with optical digital holography. Such a method provides measurements with a very high spatial resolution and is a contactless technique. This method is based on the interference between a reference laser beam and the field diffracted by the studied object. Using a high speed camera, it can also be implemented in the time domain to investigate non-stationary problems. Recent investigation shows the high-speed digital holography is comparable with classical laser vibrometry.

Acoustic Black Hole (ABH) effect is a innovative method to reduce the structural vibration. The vibratory field inside an ABH is characterized by a strong variation of the wavelength with space and an increase of the amplitude of the vibratory field at the extremity. In this paper, we present an experimental investigation of the vibratory field inside an Acoustic Black Hole on a beam.

1 INTRODUCTION

In the domains of acoustics, vibro-acoustics, vibrations of structures or flow-induced vibrations, both accelerometer and laser-vibrometry are the most favorite instruments for dynamic measurements. Accelerometer is robust and cheap but is a pointwise only a punctual sensor and is intrusive. Laser-vibrometry uses a laser beam to probe a dynamic object provides non-contact, high accuracy and high temporal resolution measurements. In order to get full-field data, a laser-scanning mechanism is required. This operation needs long time and the dynamic specimen under interest must be quite stationary (i.e. highly controlled excitation). Full-field evaluation can be obtained with holographic and speckle interferometry [1]. Vibration analysis with optical holographic interferometry began with the works of Powell and Stetson [2] who first established the principle of time-averaging. However, the stationary regime is a particular case for investigating the structure vibration behavior, and the characterization of structures under operational or real functioning conditions requires analysis in the time domain. Then, providing a real-time follow-up of the vibration amplitude, whatever the excitation condition, is a challenge for full-field optical metrology [3]. As examples, problems that can not be addressed by a stationary approach are: vibrations of panels induced by hydro or aero-acoustic sources, structural vibrations induced by squeak and rattle noise. We would like to take the opportunity of the DYNCOMP'15 meeting to discuss about the vibration field measurement of a structure supplying an Acoustic Black Hole.

2 PRINCIPLE : FROM HOLOGRAMS TO DISPLACEMENT FIELD

Basically, digital holography consists in recording an interference pattern using a sensor arranged as a matrix of pixels. In the set-up (Fig.1.a), the structure under interest is illuminated by a laser beam, which is then scattered by the object surface.

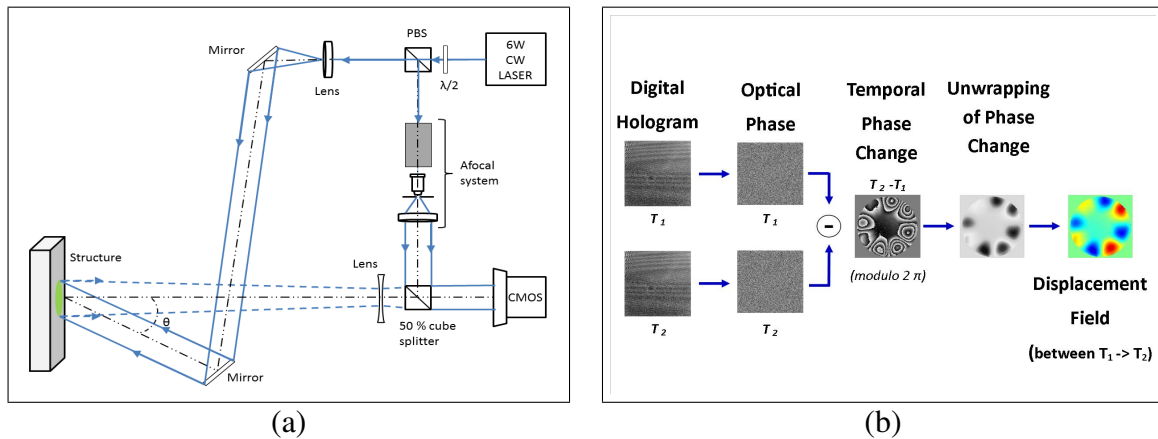


Figure 1. (a) Optical set-up and (b) Illustration of digital hologram post-processing

A hologram H is a quadratic sum of the both reference wave and object wave, and is expressed as

$$H(x, y, t) = |R(x, y) + O(x, y, t)|^2, \quad (1)$$

where $R(x, y)$ is defined as the reference plane wave. The object wave $O(x, y, t)$ is proportional to the object shape, and is described by

$$O(X, Y, t) = A_O \exp(j(\varphi_o(X, Y, t) + \psi_o(X, Y))), \quad (2)$$

where A_O is the optical wave magnitude, $\psi_o(X, Y)$ is the optical surface phase and $\varphi_o(X, Y, t)$ represents the optical phase induced by the vibration field, in the object plane. The recorded hologram includes complex information related to the amplitude and phase. The phase is proportional to the optical path i.e. the distance between the object and the sensor. With two successive phase maps (Fig.1.b), a phase difference can be calculated. This phase is calculated through an inverse tangent function and is then obtained modulo 2π . It exhibits 'numerical fringes' that can be interpreted as contour lines of the vibration. These numerical fringes need to be unwrapped to obtain a continuous phase map being directly proportional to the displacement field.

3 ACOUSTIC BLACK HOLE EFFECT MEASUREMENT

The Acoustic Black Hole effect is an innovative method to reduce the structural vibration. The ABH effect takes advantage of flexural waves properties in plates of variable thickness : Mironov [4] shows that if the thickness of the plate decreases sufficiently smoothly to zero close to the edge, waves slow down and stop without being reflected. Different works [5] have shown the complex behavior of the ABH extremity. We propose to take the advantage of the optical method with contactless and full field measurement, to analyze these local complex vibratory field. The optical setup is presented in Fig.2.a. In this study, a beam supplied a ABH extremity is placed vertically and is suspended to a shaker (Fig.2.b), and is excited by a linear sweep-sine from 20Hz to 10kHz.

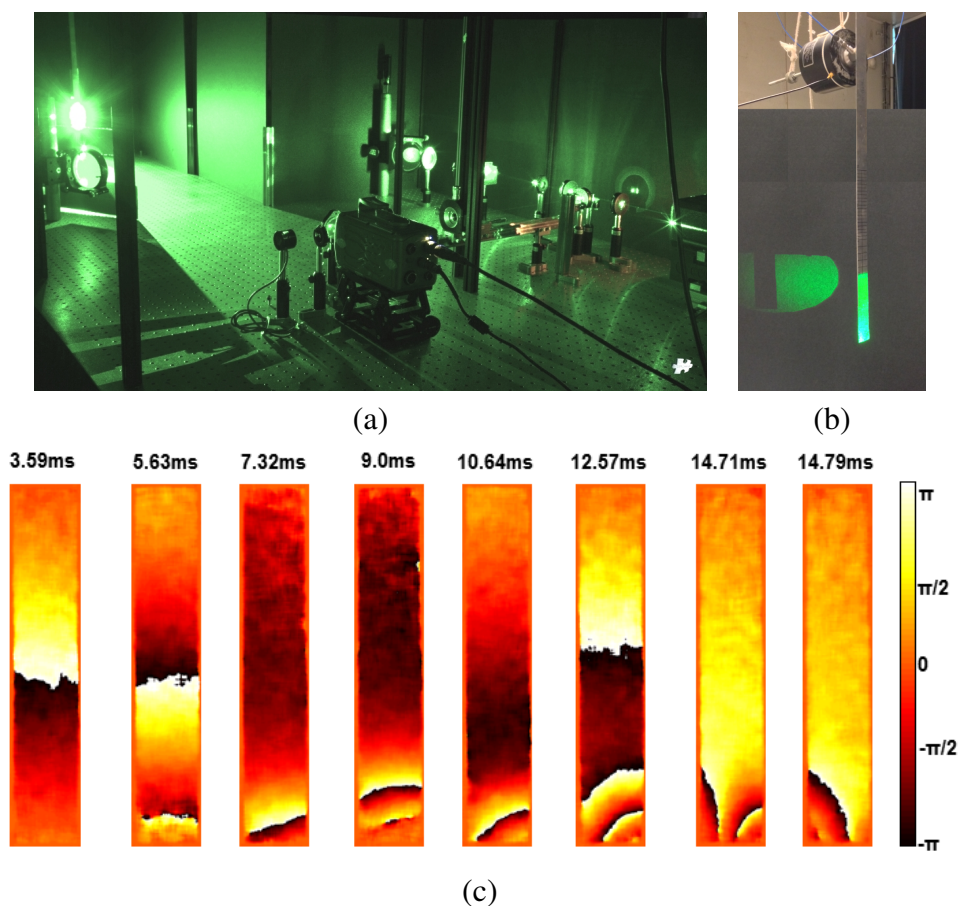


Figure 2: (a) Experimental set-up, (b) Picture of beam with ABH suspended to a shaker and (c) Displacement map vs time evolution, result obtained with 512 x 128 pixels, and a time delay between each map at $125\ \mu\text{s}$

The observation area is 10cm x 2cm, corresponding to the lower extremity of the beam. Fig.2.c shows the phase change ($\text{mod}.2\pi$) recorded at different instants of the sequence with high-speed digital holography. The incoming 1D wave front can clearly be seen on the first pictures. A wave conversion can then be observed since the field presents a 2D component. This wave conversion may be due either to non plane incidence on the edge or to slight imperfections at the ABH tip.

4 CONCLUSION

This paper present with few words the principle of this new metrological tools for vibration analysis. High-speed digital holography give the possibility to a synchronous recording, of spatial and temporal information of vibration field. This method allows to observe the complex vibratory field on the edge of the beam supplying an ABH.

5 ACKNOWLEDGMENT

This study is part of the Chair program VIBROLEG (Vibroacoustics of Lightweight structures) supported by IRT Jules Verne (French Institute in Research and Technology in Advanced Manufacturing Technologies for Composite, Metallic and Hybrid Structures). The authors wish to associate the industrial and academic partners of this project; respectively Airbus, Alstom Power, Bureau Veritas, CETIM, Daher, DCNS Research, STX and University of Maine in France.

REFERENCES

- [1] T. Kreis. Holographic interferometry: Principles and methods. 1996.
- [2] R.L Powell and K.A Stetson. Interferometric vibration analysis by wavefront reconstruction. *JOSA*, 55(12):1593–1597, 1965.
- [3] J. Poittevin, P. Picart, F. Faure, F. Gautier, and C. Pezerat. Multi-point vibrometer based on high-speed digital in-line holography. *Applied optics*, submitted.
- [4] MA Mironov. Propagation of a flexural wave in a plate whose thickness decreases smoothly to zero in a finite interval, 1988.
- [5] V. Denis. *Vibration damping in beams using the acoustic black hole effect*. PhD thesis, Université du Maine, 2014.

COPYRIGHT NOTICE

Copyright ©2015 by the authors. Distribution of all material contained in this paper is permitted under the terms of the Creative Commons license Attribution-NonCommercial-NoDerivatives 4.0 International (CC-by-nc-nd 4.0).





“DAMPING COMPOSITE CARRYING STRUCTURES FOR FUTURE LAUNCHERS”

Vincent LE GALLO¹, B. PETITJEAN², L. ZOGHAIB²

¹AIRBUSDefence&Space
Route de Verneuil
78133 Les Mureaux, FRANCE
Email: vincent.le-gallo@astrium.eads.net

²AIRBUS Group Innovations
12 rue Pasteur
92150 Suresnes, FRANCE
Email: benoit.petitjean@airbus.com, lionel.zoghaib@airbus.com

ABSTRACT

Satellites, as payloads of launch vehicles, are connected to the launcher by composite supporting structures. These structures are responsible for the transmission of dynamic excitations generated during the different launch phases, leading to a vibration environment around satellites potentially not friendly to be mastered. One simple way to reduce the payload dynamic environments is to isolate it from the rest of the launcher, by a soft mounting, and/or to damp the vibrations coming from the launcher.

On ARIANE launchers, both strategies are investigated in order to increase the payload comfort, based on Launcher system requirements:

- *passive isolation devices to isolate the payload from Solid Rocket Boosters thrust oscillations: this kind of devices can be efficient but introduces some unusual complexities to be managed at launcher level due to the required flexibility,*
- *damping carrying structures to damp launcher vibrations at the resonance, by integrating damping viscoelastic layers with moderate softness into composite carrying structures.*

In this paper, we focus on the damping carrying structures, with a presentation of the concept and an evaluation of associated benefits and drawbacks.

1 INTRODUCTION

The dynamic environment generated by launchers on satellites is often significant and can sometimes lead to potential problems. One simple way to reduce the payload dynamic environments is to isolate it from the launcher, by a soft mounting, and/or to damp the vibrations coming from the launcher. On ARIANE launchers, both strategies are studied.

For A5 Midlife Evolution (A5ME), a Passive Isolation Device (PID) has been developed to isolate the payloads from the Solid Rocket Boosters thrust oscillations, in order to improve payload comfort. This kind of solution has demonstrated a good efficiency but introduced some unusual complexities to be managed at launcher level due to the significant flexibility of the PID necessary to isolate.

For future launchers, with potential applications to ARIANE 6 in case of need, another solution is currently investigated in an R&T context. It consists to damp the launcher's vibrations by integrating damping viscoelastic material into composite carrying structures. The main idea is to add locally in the carrying structures (for example a payload adaptor or an inter-stage structure) some layers with moderate softness and high damping in order to attenuate the transmission of vibrations to the payload at the resonance. A prototype of such damping adaptor is currently developed in order to be tested on a full-scale demonstrator. The application of this technology is also studied to isolate the whole upper stage of a launcher, based on the same concept.

This paper gives the main requirements in terms of stiffness and damping, describes the concept retained, following a trade-off on damping materials, and then gives a preliminary status in terms of efficiency from analyses. Also, main advantages and drawbacks of this solution are highlighted for future launcher application.

2 LAUNCHER NEEDS AND REQUIREMENTS

2.1 Launcher needs

A launcher is a complex system presenting sometimes antagonist needs. For example, structural mass must be reduced to increase performance, but keeping sufficient stiffness to avoid controllability problems. This compromise leads to low damped structures and high transmissibility of vibrations. Moreover, Solid Rocket Boosters (SRB), used for the first phase of flight (first stage), generate high levels of vibration, at low frequencies, which are transmitted to payload and can be amplified in case of dynamic coupling at the resonance, due to the low level of structural damping, confirmed by flight analyses [1].

In order to mitigate this problem, an isolation device has been introduced on ARIANE 5 between the boosters and the central stage. This solution reduces very significantly the transmissibility of dynamic loads to the payload. However, residual vibrations can still cause troubles and must be managed. It is why a special damping device called "SARO" [2] has been introduced on the upper stage of A5E/CA, and a PID has been developed for A5ME (concept derived from a shock attenuation device called SASSA [3]), in both cases to reduce lateral vibrations of the payload.

For future launchers, AIRBUS investigates alternative solutions in order to limit system impacts and to reduce the added mass by a functionalization of carrying structures. As an example, two types of structures are studied, more dedicated to longitudinal isolation needs:

- A damping payload adaptor,
- A damping launcher inter-stage structure.

The first structure is a prototype dedicated to demonstrate the efficiency of the concept by dynamic tests on-ground. The second one constitutes the main industrial potential target: indeed, the main idea is not to improve only payload comfort but also to reduce the dynamic environment of the whole upper stage of a launcher, including the payload of course but with less sensitivity to its characteristics in this case (low payload mass compare to upper stage one).

2.2 Launcher requirements

From preliminary future launchers studies, the main objective is to maximize the attenuation of SRB vibrations during the first phase of flight essentially in axial direction, and to minimize also launcher impacts associated to lateral motion (e.g. launcher controllability and payload relative displacements). Consequently, a set of functional requirements has been determined at launcher level, expressed in terms of suspension modes characteristics targets:

- Minimum lateral frequency: sufficiently high to avoid problems of controllability, but sufficiently low to reduce lateral vibrations (by isolation)
- Maximum longitudinal frequency: sufficiently low to reduce longitudinal vibrations (by isolation)
- Minimum damping: sufficiently high to attenuate excitability of the suspension modes and to increase the damping of first launcher modes to improve launcher controllability, but not too much in order to avoid complexities at system level and increase shock transmissibility.

It remains that this set of requirement is quite over-constrained, leading more or less to an optimal solution.

In order to verify the strength and the functional performances of the product, thermo-mechanical environment (ranges and cycles) has been specified.

3 TRADE-OFF ON DAMPING MATERIALS

3.1 General material trade-off analysis

A trade-off has been initially performed in order to investigate existing solutions to increase structural damping on stiff structures. It is well-known that there is a natural antagonism between damping and rigidity, illustrated by the diagram here below: polymers offers excellent damping but associated to low stiffness, contrary to metallic materials which have high stiffness and low damping.

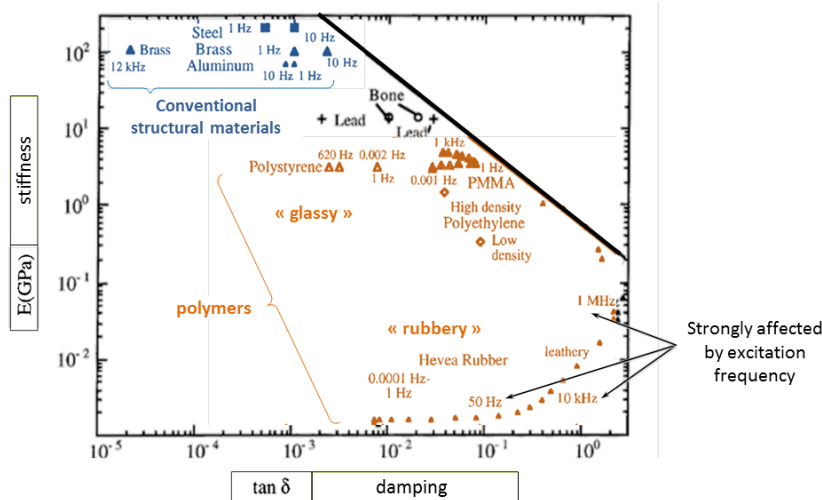


Figure 1. Generic properties of materials (stiffness-damping compromise)

Main conclusions of this trade-off were that:

- for short term applications with high TRL required, only the introduction of elastomeric layers in a structure (metallic or composite) could be envisaged
- for long term applications, a dedicated R&D program is foreseen in order to design functionalized materials, by innovative architectures constituted for example of polymers embedded at subscales in a special core of composite materials.

This paper deals only with the first short term applications.

Another problematic is the sensitivity of elastomers to thermo-mechanical environments, self-heating, ageing, creeping, etc. In order to minimize associated dispersions, a dedicated set of requirements have been written to identify the most promising elastomer.

Also, the bonding of the elastomer on metallic or composite parts constitutes a special challenge with respect to industrial constraints for manufacturing of large space structures.

3.2 Elastomer characterization

Elastomer selection was the result of a first set of optimisation loops (see next section), where the material properties played a first order role. The achievement of static and dynamic performance of the damping adaptor lead to the definition of a set of material specifications, regarding mechanical strength but also dynamic behaviour.

Once a suitable elastomeric material was selected, a series of elementary tests was performed by LRCCP laboratory on dedicated samples in shear and compression. Combination of static and dynamic loads was applied, in order to define hyperelastic and viscoelastic laws. In addition, the effect of cycle numbers was also investigated in order to verify the acceptability of self-heating effect (e.g. slight decrease in stiffness with time), an important topic in order to guarantee stiffness stability during flight:

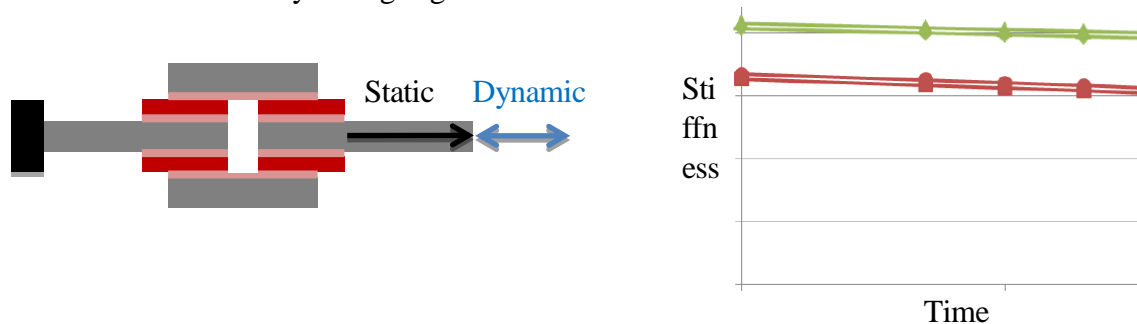


Figure 2. Shear sample test for elastomer characterization

This fine characterisation of elastomer behaviour allowed the final tuning of the damping adaptor, described in the next section.

Finally, elastomer bonding on composite materials is being investigated in order to identify the most efficient manufacturing process with respect to industrial constraints.

4 PRELIMINARY DESIGNS

4.1 Damping Payload Adaptor

The payload adaptor in launch vehicles is the intermediate structure connecting the payload (satellite) to the launcher structure. It is generally constituted of truncated conical shapes, and quite a few variants exist, meeting different sets of requirements. The following picture shows the overall geometry of payload adaptor:

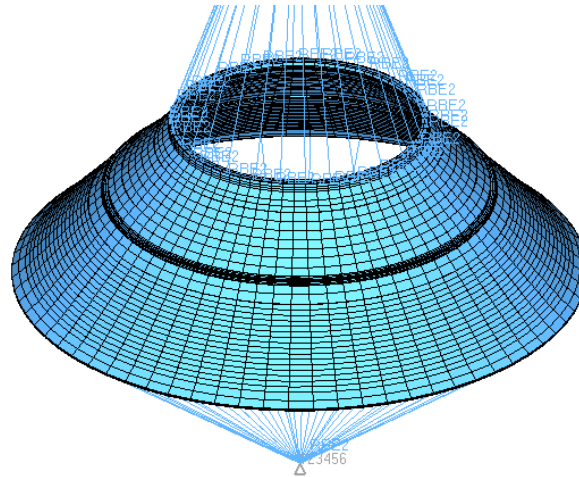


Figure 3. Global geometry of a typical payload adaptor structure

For the definition of a damping adaptor, a first decision was made to keep the upper interface (interface to payload) and the lower interface (interface to launcher) unchanged, making future integration easier. Some adaptors have an intermediate structure allowing flexibility in the longitudinal direction for adaptation to various payload geometries. This intermediate location was chosen as a potential candidate for the implementation of a “damping layer”.

The correct representation of the local stiffness and damping of a thin elastomer layer requires the use of volume elements instead of the usual shell elements used for everyday modelling practice. An automatic mesh generator was developed in order to change very quickly the section of the adaptor and to explore many design options in a quick and efficient way. Some of the concepts explored in the study are displayed in the next figure:

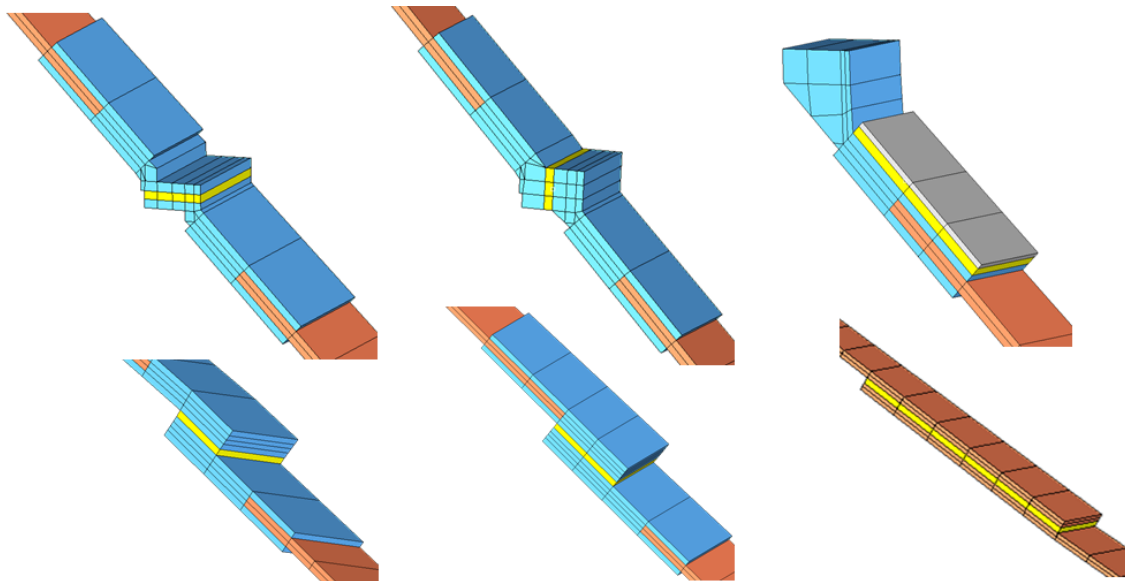


Figure 4. Illustration of possible elastomeric layer introduction

In this figure, blue elements correspond to metallic parts, pink ones to composite materials, and yellow ones to the rubber layer to be optimised. As visible in the figure, many options were compared, with various layer locations, inclination, and so on... It turns out that the dynamic behaviour of the overall system { launch vehicle+adaptor+payload } is very sensitive to the detailed design of the rubber layer.

Then the optimisation itself was based on a compromise between:

- The dynamic targets set in section 2 (expressed in terms of modal frequencies)
- The damping performance which is evaluated by the computation of frequency response functions for various excitations
- Static requirements for strength analyses

This design loop becomes even more complex where the nature of the elastomeric material is taken into account, together with its thickness in each configuration. The following graph shows the calculated longitudinal and lateral transmissibility obtained for a number of possible designs.

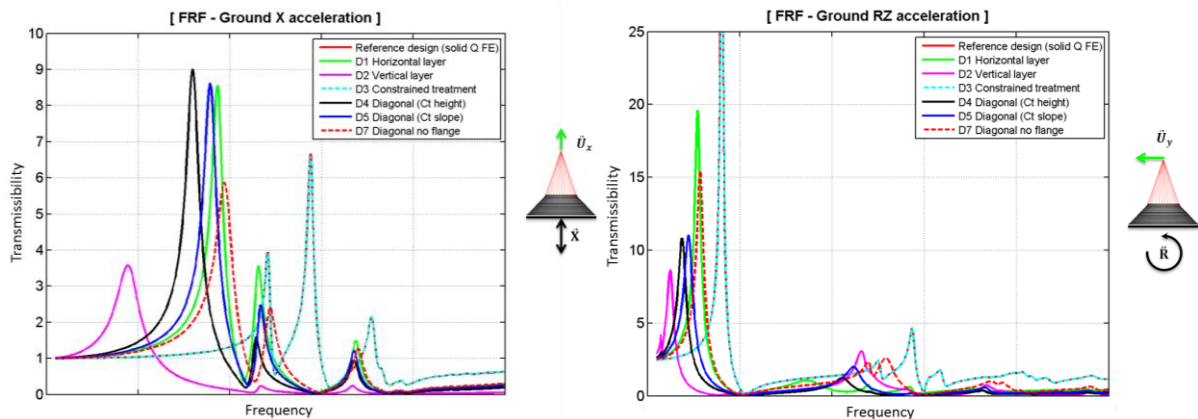


Figure 5. Acceleration transmissibility from damping payload adaptor (basis to top)

The modal frequency shifts are very large, and the comparison must be made simultaneously for longitudinal and lateral directions. Since the requirement for longitudinal frequency is to lower it and the requirement for the lateral frequency is to keep it above a given threshold, the two graphs show that it is difficult to have a discriminating action on each of them.

After this global and very large optimisation process, best solution was chosen and some fine tuning was carried out: in fact, there are even other degrees of freedom to use, for example the distribution of rubber elements along the circumferential direction. A complete layer is not the only option.

4.2 Damping Launcher Inter-stage Structure

The same approach was extended in order to evaluate the potential of this damping layer concept to control vibration transmission for an entire launcher upper stage. Of course the requirements in terms of space and mass were quite different.

The optimisation and design process was carried out on a simplified model of a future launcher, not known with a high precision at the time of the study. The location of the possible viscoelastic layer was chosen to be in between the main launcher body and the upper stage, where a truncated conical structure is present. This conical structure connects a smaller diameter in the main body to a larger one in the upper stage.

In the following figure, the dynamic effect of such an inter-stage layer is computed in terms of acceleration transmissibility in a wide frequency range. The stiffness effect (lowering of typical lateral and longitudinal frequencies) together with the damping effect are clearly visible, in comparison to the reference stiff design.

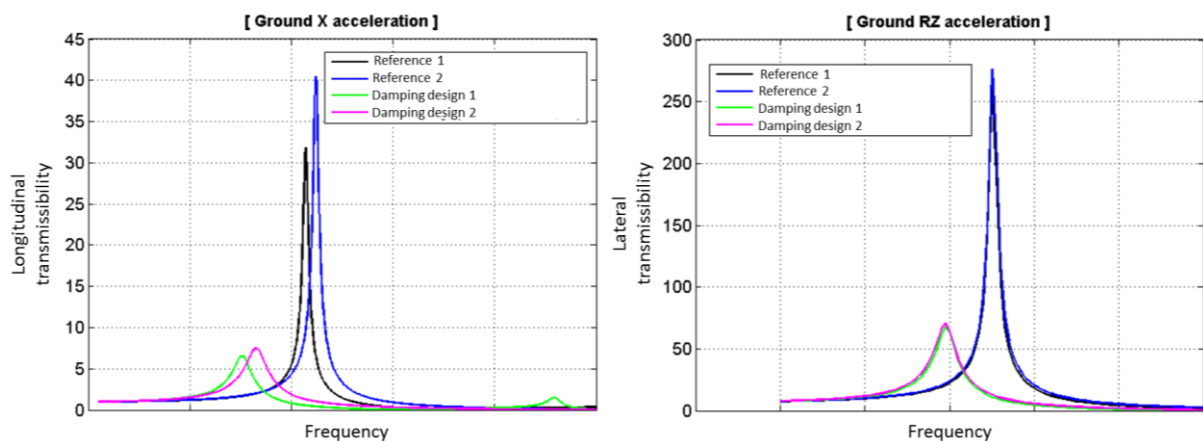


Figure 6. Acceleration transmissibility from damping launcher inter-stage structure (basis to top)

This, together with the static evaluation based on existing elastomeric material mechanical property data, proved that the introduction of an elastomeric layer between main launcher body and upper stage could have the required effect on payload comfort. Of course, given the structure size and weight, manufacturing process issues would still need to be solved.

5 PROTOTYPE, TESTS& PERSPECTIVES

In order to increase the maturity of damping structures for space applications, the manufacturing of a full-scale prototype of damping payload adaptor is foreseen. The objective is to perform dynamic tests on a representative payload mounted on such carrying structure exposed to flight-representative environments: transient excitation for lift-off, random excitation for buffeting at transonic and sine excitation for SRB thrust oscillations.

The achievement of those demonstrator tests will allow the validation of dynamic simulations and improve the maturity of this technology (TRL 6 expected). This step is needed in order to convince programs to integrate such promising damping structures, for example at the inter-stage of a new launcher.

6 CONCLUDING REMARKS

In order to reduce the transmission of vibrations generated by a launcher to the satellites, the solutions already developed for ARIANE 5 launchers are to add isolation devices, located at boosters and/or near payload attachments, or damping device. Both of these solutions are efficient but increase launcher system complexity due to softening (lower modal frequencies) and/or non-linearity induced.

An alternative solution, presented in this paper, consists in increasing the damping of carrying structures, limiting softening and non-linearity effects as far as possible. Based on a trade-off study on damping structures and materials, it remains that the simplest and efficient way could be to integrate elastomeric layers inside composite (or metallic) structures, based on mature materials.

Two examples of design were proposed and studied: a damping payload adaptor and a damping inter-stage structure. A suitable elastomer material was identified and characterized by sample tests. Preliminary static and dynamic analyses have demonstrated the potential of such technology to transmit the flight loads correctly, reducing the transmission of the dynamic environment by a promising factor (> 4) compared to current structures. Also, such technology correctly located on a launcher could improve both launcher and payload comfort, without significant system impacts.

However, the manufacturing process (especially the elastomer bonding on large space structures) remains to be matured in order to demonstrate the industrial feasibility. It is why a second step is foreseen to manufacture a full-scale prototype of damping payload adaptor, to be tested on-ground with flight-representative dynamic environments. This step is needed to reach a sufficient pre-industrial maturity level (TRL 6), in order to be onboard in new launcher developments.

REFERENCES

- [1] V. Le Gallo, M. Goursat, and L. Gonidou. "Damping Characterization & Flight Identification". 57th International Astronautic Congress. Valencia. 2006.
- [2] V. Le Gallo and T. Romeuf. "ARIANE 5 new upper composite including a non-linear damper: prediction of the dynamic behaviour and validation during on-ground tests & flights". 6th International Symposium on Launcher Technologies. Munich. 2005.
- [3] P. Camarasa and S. Kiryenko. "SASSA". European Conference on Spacecraft Structures, Materials and Mechanical Testing. Toulouse. 2009.

[4] Petitjean B., Jaumouillé V., Saad P., “Modelling non-linear effects in elastomer components, including uncertainties”, Proceedings of ISMA2010, Leuven, Belgium, 20-22 September 2010

[5] Petitjean B., Hernandez O., Zoghaib L., “Vibration Control of Composite Structures, Issues and Challenges”, Proceedings of the DYNACOMP Conference, Arcachon, France, May 2012

COPYRIGHT NOTICE

Copyright ©2015 by the authors. Distribution of all material contained in this paper is permitted under the terms of the Creative Commons license Attribution-NonCommercial-NoDerivatives 4.0 International (CC-by-nc-nd 4.0).





FIBERS-BASED COMPOSITE STRUCTURES WITH INTEGRATED PIEZO-CERAMICS DESIGN APPROACH OF SMART DEVICES

T. Dessolier¹, R. Lachat¹ and Y. Meyer^{1*}

¹IRTES-M3M, UTBM, 90010 Belfort Cedex, France
Email: thibault.dessolier@utbm.fr, remy.lachat@utbm.fr

*Corresponding author's email :
yann.meyer@utbm.fr

ABSTRACT

Currently, in different industrial fields as transport or aerospace, a research effort is lead concerning structural weight reduction. One of the most promising solutions is the use of composite structures and, in particular, the fibers-based composite structures. In the same time, there is an intensification of the operational dynamic environment and an increase of durability requirements. One way to manage this point is to design and manufacture adaptive composite structures. To integrate new functionalities inside mechanical structures, it is necessary to develop a real fully distributed set of transducers and to include them at the heart of composite materials that is to say during the manufacturing process.

In this paper, a design approach based on engineering system theory is developed for fibers-based composite structures including several piezoceramic transducers, electrically independent. These structures are manufactured in our laboratory. Several characterization needs are identified so as to well-design these complex structures. An experimental non-destructive procedure based on the analysis of anti-resonance and resonance frequencies of the transducers is proposed for determining the initial material coefficients of interest. Moreover, an experimental process is identified to obtain the global mechanical parameters of the fibers-based composites we produced.

1 INTRODUCTION

Currently, in different industrial fields as transport or aerospace, a research effort is lead concerning structural weight lightening [1, 2]. One of the most promising solutions is the use of composite structures [3] and, in particular, the fibers-based composite structures [4], due to their high stiffness, their low mass density and their low damping factor. In the same time, there is an intensification of the operational dynamic environment and an increase of durability requirements [5]. These different expectations seem to be contradictory. One way to manage this point is to design and manufacture integrated smart composite structures. These structures have to be able to modify their mechanical properties with respect to their environment (e.g. active vibration control), to interact with other structures (e.g. mechatronic) or with human beings (e.g. fatigue management).

To integrate new functionalities inside mechanical structures (in particular, for large structures) for active vibration control, mechatronic, energy harvesting or fatigue management, it is necessary to develop a real fully distributed set of transducers and to include them at the heart of composite materials that is to say during the manufacturing process. To reach this goal, it is absolutely necessary to limit the cost of the numerous transducing elements, the electric connections or the control tests with respect to the global system cost and, in the same time, to well-know the electromechanical behavior of the smart structure in order to well-design the system controller. The classical approach using an identification process applied to the final structures is not relevant for large distributed transducers networks or for mass production.

The paper is organized as follows. Section 2 gives the technical requirements to design and manufacture adaptive composite structures. The core elements for all the smart structures are listed. The specific requirements due to the approach selected are detailed. The design approach is introduced in section 3. In section 4, the experimental characterization needs, essential for the design step, are presented. Two set of results are given for the characterization of piezoceramics and of an in-house glass fibers-based material. Finally, concluding remarks are discussed.

2 TECHNICAL REQUIREMENTS

2.1 Core elements

To design an adaptive mechanical structure, some elements are essential. First of all, transducers have to be implemented. Different physical principles can be used. In our laboratory, the developments are based on the use of piezoelectric transducers. Their main advantage is their large operating frequency range. It can be compatible with the automotive applications ([6 Hz 250 Hz]) or with the equipments for aircraft ([6 Hz 3000 Hz]). A controller and a control strategy have to be selected. Basically, there are two main possible choices: a centralized controller and a decentralized controller. In a centralized control strategy, one electric component is designated as the master controller. It creates the actuators input signal by using the sensors signals and so it is responsible for managing the actuators. In a decentralized control strategy, the paradigm is different. The sensor output signal is locally managed by a component and the control signal is only injected on the actuators close to this sensor. The local behavior modifications allow to obtain an overall controlled behavior. A control electronics is also needed. Electrical conductors are necessary to connect all the transducers, electrically independent, with the control electronics and the electric power supply. Of course, all the added elements have to allow the manufacturing of planar or specific shaped structures with a limited thickness modification.

2.2 Approach developed

Conventionally, the transducers, in particular the piezoelectric ones, are glued onto the structure to be controlled and the electronics is located out of the structure. Our approach is significantly different. We wish to design, build and optimize composite structures based on matter fibers with a large distributed and integrated piezoceramic network. The idea is to protect the transducing elements and their electric connections and to industrially develop end products in plug-and-play mode. Furthermore, the integration of transducing elements at the heart of the material is the first step to develop, through the integration of micro and nano structures, programmable or controllable matter.

To integrate these new functionalities at the heart of composite structures (in particular, for large structures), it is necessary to develop a real fully distributed set of transducers and to include them during the manufacturing process. To reach this goal, several major constraints and manufacturing requirements were identified. It is necessary to:

- *Electrically connect a large number of transducers* so as to act on the whole structure.
- *Make electrically-independent each transducer.* This is a particular issue for the development of carbon fibers-based composite structures which are naturally conductive.
- *Limit the thickness variations due to the piezoelectric inclusions.* These inclusions inside the material will inevitably modify locally the thickness of the structure. This fact may be limited by the use of thin piezoceramics (about $200\ \mu\text{m}$). However, the electric connection by conventional welding is not possible because of the resulting overthickness. A special connection technique was specifically developed.
- *Achieve specific shaped structures* (for instance, bi-concave structures) so as to adapt to a wide range of applications (for instance, the vibration control of a car fender or the vibration isolation of an aeronautical launcher cap).

To address these constraints and requirements, a manufacturing specific method has been developed. In particular, this method uses the composite manufacturing features either by infusion technique, used in particular to manufacture large structures, or by the RTM (Resin Transfer Moulding) technique, used to manufacture mechanical parts with tight tolerances. Examples of structures manufactured in our laboratory with these processes are depicted in figures 1, 2, 3 and 4.



Figure 1: Beam manufactured with carbon fibers including four piezoceramic transducers

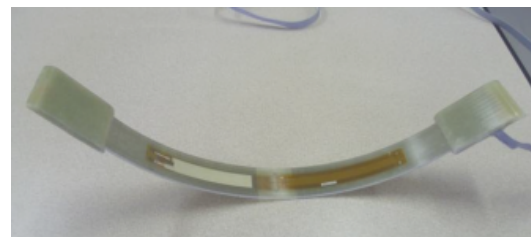


Figure 2: Curved beam manufactured with glass fibers including two PVDF transducers and two MFC transducers

3 DESIGN APPROACH

The development of the manufacturing process is still ongoing. In parallel, a design approach is also developed. Of course, the idea is to be able to design these complex structures that is

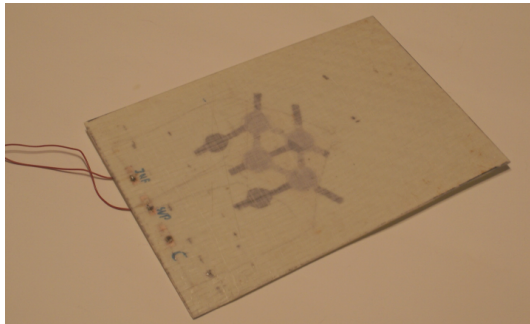


Figure 3: Plate manufactured with glass fibers including eight piezoceramic transducers



Figure 4: Kart center fairing manufactured with vegetable fibers including nine piezoceramic transducers

to say to be able to predict the final behavior of the structure in a predesign step. For this, the system engineering tools are exploited. First of all, the Product Breakdown Structure (PBS) is built. A simplified version of this PBS is given in figure 5. The product is broken down in sub-systems and in components. This process is iterative and is repeated for different depth levels. This process is stopped when the components are indivisible, are commercial off-the-shelf components or can be designed by only one development team in the project team. Once the down tree obtained, it is necessary to establish the system architecture. The different elements of the product tree are organized with respect to their interfaces. Thus, the interfaces between the components are defined. The major issue of a complex system design is not the individual design of the components, in general managed by one project team. The major issue is to design the components interacting with their environment and with the other components. To summarize, the key point of a good complex system design is to manage and well-design the interfaces between the components. Figure 6 is an example of a simplified system architecture established for an adaptive composite structure.

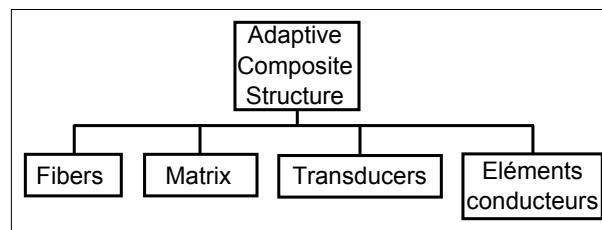


Figure 5. Simplified Product Breakdown Structure of an adaptive composite structure

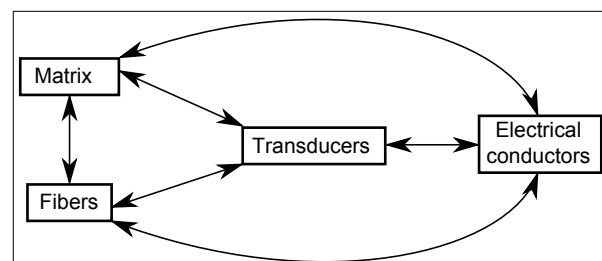


Figure 6. Simplified system architecture of an adaptive composite structure (Interfaces management)

4 EXPERIMENTAL CHARACTERIZATION NEEDS

Based on the design approach selected, it is possible to establish the essential experimental characterizations. It is absolutely necessary to well-know the overall system behavior with the integrated piezoceramic transducers so as to properly design the system controller. The classical approach using an identification process applied to the final structures is a priori not relevant for large distributed transducer arrays or for a mass production. Indeed, the idea is to avoid uncertainty and costly and time-consuming works. Our approach is based on an experimental approach upstream by predicting the overall physical parameters of the manufactured composite structure. The system architecture is used to specify the experimental characterization needs and so the procedures to be developed. Consequently, it is necessary to develop :

- *a characterization method of the piezoceramics.* In an industrial point of view, it corresponds to an input control for the piezoceramics. A non-destructive process, based on the vibration analysis of poles and zeros of the transducers, is developed and used for obtaining the coupling coefficients of interest [6].
- *a characterization method of the manufactured composite material.* Once the manufacturing process stabilized, the composite must be fully characterized using a set of tests allowing to have access to materials nominal parameters and their uncertainty. For this, two major methods are exploited. The classical characterization process is based on the use of material testing machines and strain gauges [7, 8]. Another vibration characterization is also used : the resonalyser method [9, 10].
- *a characterization method of the integrated piezoceramics.* The idea is to be able to produce a generic behavior modeling from the input control data so as to assess the drift of material parameters and coupling coefficients, when integrating the piezoceramics inside the material. Specific samples are manufactured. Piezoceramics, perfectly characterized, are encapsulated in a composite structure with tight dimensions around the transducers. The idea is to limit the effects due to the overall structure, the wires length, the electric connections, the cross-talk ...Finally, the same process used as input control is applied to these new samples.
- *a characterization method of the electric interfaces.* The electrical connection process, in particular between the transducers and the electrical conductors, requires to assess the influence of process parameters on the quality of electrical contacts.
- *a characterization method of the cross-talk between the active elements.* It is necessary to evaluate the cross-talk between the transducers so as to establish dedicated design rules. This feature depends on the wires distance and the electric connection technology used.

In the following subsections, the first methods are applied and the results obtained are given.

4.1 Characterization method of the piezoceramics : Application to low-cost thin disks made of piezoceramics

For this study, 40 low-cost piezoceramic samples are measured and analyzed. The material coefficients of these samples are calculated according to the experimental procedure presented in [6].

In table 1, only the average material coefficients and their standard deviation are given. Let the reader note that the mass density, ρ , is measured according to [11] (the minimum quantity

Parameter of interest	Unit	Nominal value	Standard deviation (%)
$2a$	mm	24.7	0
ρ	$Kg.m^{-3}$	7227	0
$2b$	μm	135	5
ε_{33}^T	$F.m^{-1}$	1894	3.9
ε_{33}^S	$F.m^{-1}$	1195	6
k_t	-	0.17	6.2
k_{31}	-	0.34	4.6
k_p	-	0.59	4.9
e_{33}	$C.m^{-2}$	5.00	6.5
e_{31}	$C.m^{-2}$	19.95	6
C_{11}^E	$N.m^{-1}$	$1.01e^{11}$	1.4
C_{12}^E	$N.m^{-1}$	$3.50e^{10}$	2.7
C_{33}^E	$N.m^{-1}$	$8.19e^{10}$	5.2
σ_p	-	0.34	2.8

Table 1. Parameters of interest from the measured data

doesn't permit to compute a standard deviation) and the disk diameter has a very small deviation probably due to the manufacturing process used. The measurements are completed by a mechanical quality factor measurement for the radial mode vibrations with the 3-dB method [11, 12]. The average mechanical quality is 49.4 with a standard deviation of 18.2 %. The standard deviation values show a quite good manufacturing homogeneity despite of a low cost. Let the reader remark a quite low planar coupling coefficient, k_p and, globally, the coupling and piezoelectric coefficients are quite limited. This fact has to be managed by the strategy used for modifying the structure behavior.

4.2 Characterization method of the manufactured composite material : the resonalyser method

The Resonalyser method is a material identification technique following a reverse engineering scheme. Under in-plane stress assumptions, the in-plane elastic properties, given in equation (1), can be determined by a dynamic modulus identification using the resonant frequencies [9, 10]. Basically, this method uses resonance frequencies measured on rectangular plate specimens, so-called Poisson test plates, and two beams samples so as to identify orthotropic material properties. Moreover, an inverse technique is used to update the material properties in a numerical model of the test plates and the beams. The main advantage of this method is the simple apparatus necessary for the measurements and the simple numerical models used.

$$\begin{Bmatrix} \epsilon_{11} \\ \epsilon_{22} \\ \gamma_{12} \end{Bmatrix} = \begin{bmatrix} \frac{1}{E_1} & -\frac{\nu_{12}}{E_2} & 0 \\ -\frac{\nu_{21}}{E_1} & \frac{1}{E_2} & 0 \\ 0 & 0 & \frac{1}{G_{12}} \end{bmatrix} \begin{Bmatrix} \sigma_{11} \\ \sigma_{22} \\ \tau_{12} \end{Bmatrix} \quad (1)$$

This method was applied to an in-house composite material made of glass fibers. The structure has a 2 mm thickness. A fiber rate of around 35 % is obtained. A glass fiber mat is used. Consequently, the final structure is transverse isotropic, that is to say $E_1 = E_2$ and $\nu_{12} = \nu_{21}$. The first results are given in table 2. The repeatability tests are ongoing so as to produce the standard deviation. This part is particularly time-consuming. Let the reader note that the classical formula for the isotropic materials, $G = \frac{E}{2(1+\nu)}$, is in good agreement with the identified parameters.

Parameter of interest	Unit	Nominal value	Standard deviation (%)
ρ	$Kg.m^{-3}$	1630	?
$E_1 = E_2$	GPa	13	?
$\nu_{12} = \nu_{21}$	—	0.2	?
G_{12}	GPa	5.5	?

Table 2: Parameters of interest from the measured data for an in-house glass fibers-based composite material

5 CONCLUDING REMARKS

A design approach of fibers-based composite structures integrating transducers is detailed. The experimental characterization needs are clearly expressed. Two examples of identified data of interest are given for low cost piezoceramics and a glass fibers-based material manufactured in our laboratory.

The next steps of this work are the development and the reliability of the different characterization processes. After this, all the obtained data will be combined to develop a predictive behavioral model. The idea is to provide a pre-design tool for engineers.

ACKNOWLEDGEMENT

This project has been performed in cooperation with the Labex ACTION program (contract ANR-11-LABX-0001-01)

REFERENCES

- [1] Lynette W Cheah. *Cars on a diet: the material and energy impacts of passenger vehicle weight reduction in the US*. PhD thesis, Massachusetts Institute of Technology, 2010.
- [2] Karen Taminger. Technical challenges to reducing subsonic transport weight. In *AIAA Aerospace Sciences Meeting*, 2012.
- [3] Georgios Koronis, Arlindo Silva, and Mihail Fontul. Green composites: a review of adequate materials for automotive applications. *Composites Part B: Engineering*, 44(1):120–127, 2013.
- [4] Sujit Das. Life cycle assessment of carbon fiber-reinforced polymer composites. *The International Journal of Life Cycle Assessment*, 16(3):268–282, 2011.
- [5] Air Resources Board. Preliminary discussion paper - amendments to california's low-emission vehicle regulations for criteria pollutants - lev iii. State of California, 2010.
- [6] Yann Meyer and Remy Lachat. Vibration characterization procedure of piezoelectric ceramic parameters-application to low-cost thin disks made of piezoceramics. In *MATEC Web of Conferences*, volume 20, page 01003. EDP Sciences, 2015.
- [7] ASTM Standard. D638: Standard test method for tensile properties of plastics. *West Conshohocken (PA): ASTM International*, 2010.
- [8] D3039: Standard test method for tensile properties of polymer matrix composite materials. *West Conshohocken (PA): ASTM International*, 2000.

- [9] Tom Lauwagie, H Sol, W Heylen, and G Roebben. Determination of the in-plane elastic properties of the different layers of laminated plates by means of vibration testing and model updating. *Journal of Sound and Vibration*, 274(3):529–546, 2004.
- [10] Ives De Baere, Wim Van Paepegem, Joris Degrieck, H Sol, D Van Hemelrijck, and A Petreli. Comparison of different identification techniques for measurement of quasi-zero poisons ratio of fabric-reinforced laminates. *Composites Part A: Applied Science and Manufacturing*, 38(9):2047–2054, 2007.
- [11] E. N. 50324-2 European standard. *Piezoelectric properties of ceramic materials and components, Part 2: Methods of measurement Low power*. CENELEC European Committee for Electrotechnical Standardization, 2002.
- [12] A. D. Nashif, D. I. G. Jones, and J. P. Henderson. *Vibration damping*. John Wiley, New York, 1985.

COPYRIGHT NOTICE

Copyright ©2015 by the authors. Distribution of all material contained in this paper is permitted under the terms of the Creative Commons license Attribution-NonCommercial-NoDerivatives 4.0 International (CC-by-nc-nd 4.0).





A NEW LAMINATE MODEL FOR BROADBAND FREQUENCY ANALYSIS

G rard Borello

InterAC

10 impasse Borde-Basse, Z.A. La Violette, 31240 L'Union, FRANCE

gerard.borello@interac.fr

ABSTRACT

For predicting vibratory responses of multi-layered panels over a wide frequency range (100-10000 Hz), a new laminate theory has been developed. It overcomes the limit of classical zigzag laminate theory reached when panels start to undertake transverse resonant behavior. This theory mixes the three degrees of freedom (u_0, v_0, w_0) of the thin orthotropic panel, statically equivalent to the layup assembly with the three "blocked" degrees of freedom (u_i, v_i, w_i) of each layer, considered in relative motion to (u_0, v_0, w_0). A panel made of N layers is thus described by $3(N+1)$ displacement variables coupled by a dynamic operator obtained by assembling plate, cylinder or doubly-curved shell thin orthotropic dynamical operators of individual layers depending on geometry. The real coupled operator is first analytically solved for all possible (m, n) quantic numbers to get eigenvalues and eigenmodes from which is derived the modal density of flexural, shear and extensional modes. In a second time, all material properties are made complex and the operator is solved again to predict the frequency band-averaged mean damping loss factor of the assembly from the complex eigenvalues. Examples of modeling aerospace sandwich or sandwich with thin viscoelastic core are discussed against related FEM models. This theory adds a new class of SEA subsystems to SEA+ software, extending its modeling capability in addition to the introduction of an "extended orthotropic" material described by frequency dependent elastic constants.

1 INTRODUCTION

Thin multi-layered elastic shells are components of many industrial products from spacecraft with light honeycomb sandwich panels to car dashboards made of stamped viscoelastic steel sheets. Their equivalent damping properties are needed for controlling the accuracy of statistical Energy Analysis (SEA) prediction of their vibroacoustic behavior as well as their modal density. Due to limitation of the classical laminate theory in the high frequency range (HF), a new method has been developed for deriving the coupled equations of multilayered shells considered as an assembly of 2D thin layers. This theory has been implemented in the SEA+ software and is briefly exposed in this document with some validation results.

2 DYNAMICAL DESCRIPTION OF INDIVIDUAL LAYERS

In HF, each elastic layer will asymptotically oscillate on its uncoupled $\{u_k, v_k, w_k\}$ displacement in respectively x, y and z axis, with (x, y) defining the plane of the layer.

$\{u_k, v_k, w_k\}$ are the local degrees of freedom of a layer k. The elastic behavior of layer neutral fiber is assumed to be orthotropic within (x, y) plane and defined by the following E_{ij} matrix relating torque at neutral fiber to strains.

$$\begin{bmatrix} \sigma_{xx} \\ \sigma_{yy} \\ \sigma_{xy} \\ \sigma_{zz} \\ \sigma_{z\{xy\}} \end{bmatrix} = \begin{bmatrix} E_x & \nu_x E_y & 0 & 0 & 0 \\ \nu_x E_y & E_x & 0 & 0 & 0 \\ 0 & 0 & G_{xy} & 0 & 0 \\ 0 & 0 & 0 & E_z & 0 \\ 0 & 0 & 0 & 0 & G_z \end{bmatrix} \begin{bmatrix} \epsilon_{xx} \\ \epsilon_{yy} \\ \gamma_{xy} \\ \epsilon_{zz} \\ \langle \gamma_{xz}, \gamma_{yz} \rangle \end{bmatrix}$$

The two additional elastic parameters E_z and G_z are added for more flexibility in modeling complex design material. C_{ij} coefficients are relating the corresponding forces applied to neutral fiber to displacement vector $\{u_k, v_k, w_k\}$ and its spatial derivatives by integrating previous stresses defined by E_{ij} over the layer thickness.

The dynamic of a single layer is then described by its local 3x3 dynamic stiffness operator which applies to $\{u_k, v_k, w_k\}$ with expression given here for a flat thin layer:

$$L_k = \begin{bmatrix} C_{11}\partial_{x^2} + C_{66}\partial_{y^2} & (C_{12} + C_{66})\partial_{xy} & 0 \\ (C_{12} + C_{66})\partial_{xy} & C_{66}\partial_{x^2} + C_{22}\partial_{y^2} & 0 \\ 0 & 0 & D_{11}\partial_{x^4} + D_{22}\partial_{y^4} + 2(D_{12} + 2D_{66})\partial_{x^2y^2} \end{bmatrix} \quad (2.1)$$

3 DYNAMICAL DESCRIPTION OF GLOBAL LAYER

When assembling the layers on top of each other, three complementary DoFs are added, $\{u_0, v_0, w_0\}$ for describing the low frequency motion when all layers are vibrating in phase with no relative motion between them as shown in Figure 1.

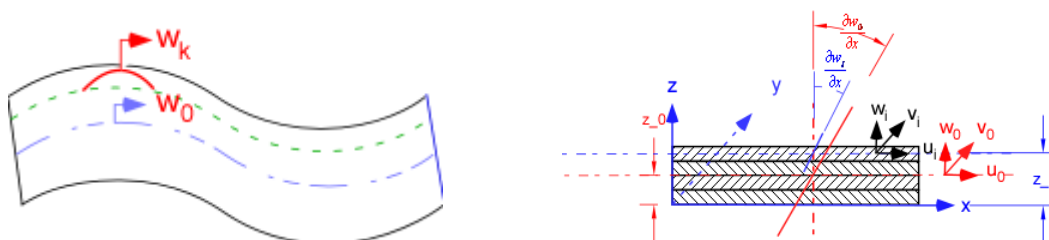


Figure 1. Degree of freedom of the laminate assembly

This global layer is assumed to behave as the equivalent "static" shell with C_{ij} elastic matrix calculated for phased translational and rotational motions of all layers. Given z_k , the relative height of neutral fiber of a layer k vs z_0 , fiber height of layer 0, the actual displacement vector X of a layer k is expressed in the axis of global layer 0 as follows:

$$X = \begin{bmatrix} u(z, x, y, t) \\ v(z, x, y, t) \\ w(z, x, y, t) \end{bmatrix} = \begin{bmatrix} u_0(x, y, t) - z \frac{\partial w_0}{\partial x} \\ v_0(x, y, t) - z \frac{\partial w_0}{\partial y} \\ w_0(x, y, t) \end{bmatrix} H_0(z) + \begin{bmatrix} u_k(x, y, t) - (z - z_k) \frac{\partial w_k}{\partial x} \\ v_k(x, y, t) - (z - z_k) \frac{\partial w_k}{\partial y} \\ w_k(x, y, t) \end{bmatrix} H_{1/2}(z - z_k) = X_0 + X_k$$

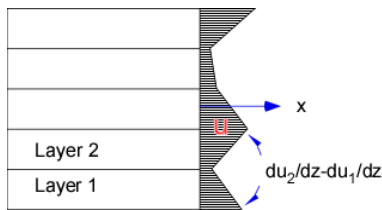
H is the Heaviside function, indicating the motion of each layer is limited to its thickness. Its dynamic stiffness is given by (2.1) using equivalent static $C_{ij(k)}$ coefficients.

4 COUPLING SCHEME OF GLOBAL AND LOCAL LAYERS

When excited by broadband random force, the layers will progressively decouple and will start to have relative motion between them. Assuming all layers will oscillate with common spatial phase function $g\psi$, their vectorial motion is then given by:

$$X = \begin{bmatrix} U \\ V \\ W \end{bmatrix} g(x_0, y_0) \psi(z) e^{j\omega t} \tag{4.1}$$

$\psi(z)$ is assumed continuous along transverse section with continuity of displacement at layer interface but its derivative $\frac{\partial \psi}{\partial z}$ is discontinuous. $\frac{\partial \psi}{\partial z}$ is a distribution with derivative jumps θ_k at layer interfaces.



$\frac{\partial \psi}{\partial z}$ may then be expressed as:

$$\frac{\partial \psi}{\partial z} = \sum_k \theta_k(x, y) (\delta_k(z - z_k)) + \left\{ \frac{\partial \psi}{\partial z}(x, y, z) \right\}$$

{ } means $\frac{\partial \psi}{\partial z}$ is continuous outside discontinuity interval.

Derivative jump is then estimated by $\theta_{k(k-1)} = \frac{\psi(z_k) - \psi(z_{k-1})}{z_k - z_{k-1}}$ which means interlayer forces will

be proportional to the difference of their $\psi(z_k)$ motion amplitude.

The general coupling scheme of global and local layer is sketched in Figure 2 as a generalized mass-spring dynamic system where X are vectors with components $\{u, v, w\}$ and stiffness terms are 3x3 dynamic operators. As well as mass operator, L_k is the dynamic operator of a layer k coupled through springs to global layer described by L_0 . To write down the coupled equations of the system, we have to provide expression of the coupled springs between global and local layers and between local layers.

The spring operator L_{k0} represents the various elastic forces connecting local and global layers.

L_{k0} is split into two additive terms: first term $L_{k0(x,y)}$ is calculated from the strain energy due to the joint work of their respective dynamic operators L_k and L_0 . Effectively, a k-layer when

moving is developing work within the stress field generated by L_0 . The work E is thus computed from $E = \sum_k \int_{I_k} (\sigma_k + \sigma_0)(\epsilon_k - \epsilon_0)^* d\epsilon_k$ representing the relative work of all motions X_k . Second term $L_{k0(z)}$ corresponds to work induced by complementary stresses generated by $\psi(z)$ strain and not accounted in the work related to $L_{k0(x,y)}$. They are introduced as complementary stiffness matrix added to $L_{k0(x,y)}$ as the two types of stresses are acting in parallel.

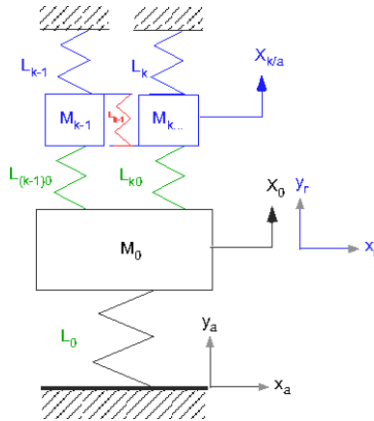


Figure 2. The global-to-local coupling scheme

The coupling between two adjacent layers k and $k-1$ is described by the matrix $L_{k(k-1)}$ of which components are springs acting on the various layer motions. For example, along z -axis, layers may be compressed with a related interface stress σ_{zz} . Assuming a continuous linear compression strain at interfaces A and B, potential energy is given by:

$$U = \frac{1}{2} \left\{ K_{zz-} (w_k - w_{k-1})^2 + K_{zz+} (w_k - w_{k+i})^2 \right\}$$

If the stiffness K_{zz} is calculated between the respective neutral fibers of two adjacent layers, it may be calculated following:

$$K_{zz-} = \frac{K_{zz}^{(k-1)} K_{zz}^{(k)}}{K_{zz}^{(k-1)} + K_{zz}^{(k)}} \quad K_{zz+} = \frac{K_{zz}^{(k+1)} K_{zz}^{(k)}}{K_{zz}^{(k+1)} + K_{zz}^{(k)}} \quad K_{zz}^{(k)} = \beta E_{zz} / t_k$$

The parameter β is depending on chosen $g(x_0, y_0)$ function, K_{zz} being defined as a stiffness per unit m^2 , proportional to $\frac{1}{A} \int_{x,y} g(x, y)$.

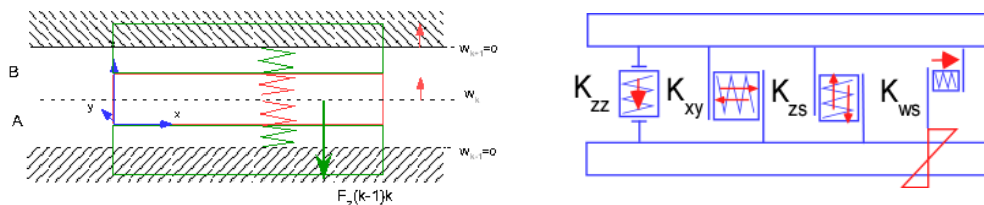


Figure 3. **Left:** Sketch for z -stiffness term derivation of K_{zz} impedance - **Right:** the four coupling impedances introduced in the laminate model

Similarly, there are shear forces at interfaces when rotation $\frac{\partial \psi}{\partial z}$ is non-zero. Four different springs, K_{zz} , K_{xy} , K_{xyz} and K_{ws} are then acting in the motion X_k when all other layers are blocked at their neutral fibers.

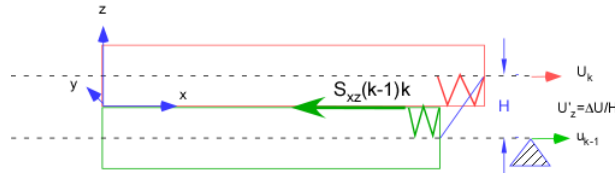
K_{xy} is the shear spring due to rotation $\frac{\partial \psi}{\partial z}$ and calculated as:

$$K_{xy} = \frac{K_{xy}^{(k-1)} K_{xy}^{(k)}}{K_{xy}^{(k-1)} + K_{xy}^{(k)}} \text{ with } K_{xz}^k = \frac{\beta G_{zz}}{t}$$

The related force applied in the plane (x, y) is given by:

$$F_{xy} = -K_{xy} (u_k - u_{k-1})$$

F_{xy} corresponds to the stress σ_{zx} or σ_{zy} and sketched as force $S_{xz(k-1)k}$ in next figure.



K_{xyz} and K_{ws} are respectively due to moment generated by F_{xy} when motion is expressed at neutral fiber. The second derivative of this moment gives two shear forces in the transverse section (x, z) and (y, z) which opposes to inertial force and act of w components and due to the moment of F_{xy} and the moment exerted by the rotation of the section of layer k (K_{ws} stiffness). A last stiffness term is introduced. This stiffness is due to differential rotation $\left(\frac{\partial w_k}{\partial x} - \frac{\partial w_{k-1}}{\partial x} \right)$ inducing shear stress in (x, z) and (y, z) transverse planes, acting on w 's components of motion.

5 SOLVING THE DYNAMICAL MATRIX

From previously defined set of interacting forces, the coupled equations of the multilayered motion are reduced to a set of linear relationships given in matrix form (given for two layers herbelow):

$$\begin{bmatrix} L_0 + L_{10} + L_{20} & -L_{10} & -L_{20} \\ -L_{10} & L_1 + L_{10} + L_{12} & -L_{12} \\ -L_{20} & -L_{12} & L_2 + L_{20} + L_{12} \end{bmatrix} \begin{bmatrix} X_0 \\ X_1 \\ X_2 \end{bmatrix} + \omega^2 \mathbf{M} \mathbf{X} = 0 \quad (5.1)$$

Equations are next expressed in function of the relative local motion of layers k , δX_k .

Given $\delta X_k = X_k - X_0$, (5.1) becomes:

$$\begin{bmatrix} L_0 & -L_{10} & -L_{20} \\ L_1 & L_1 + L_{10} + L_{12} & -L_{12} \\ L_2 & -L_{12} & L_2 + L_{20} + L_{12} \end{bmatrix} \begin{bmatrix} X_0 \\ \delta X_1 \\ \delta X_2 \end{bmatrix} + \omega^2 \tilde{\mathbf{M}} \begin{bmatrix} X_0 \\ \delta X_1 \\ \delta X_2 \end{bmatrix} = 0 \quad (5.2)$$

This matrix makes the dynamic problem easier to solve as the high-valued terms on the diagonal of L_0 are removed leading to more stability in the LF range where L_0 operator is predominant.

In relative motion, the mass matrix is non-diagonal and is given by:

$$\tilde{M} = \begin{bmatrix} M_0 & 0 & \dots & \dots & \dots & 0 \\ M_1 & M_1 & 0 & 0 & \dots & 0 \\ \dots & \dots & \dots & \dots & \dots & 0 \\ M_k & 0 & 0 & M_k & 0 & 0 \\ \dots & \dots & \dots & \dots & \dots & 0 \\ M_N & 0 & 0 & 0 & 0 & M_N \end{bmatrix}$$

To get a fast analytical solution, displacements in the (x, y) plane are constrained to some global shape compatible with boundary conditions such as:

$$g(x, y) = \sin \frac{m\pi x}{L_x} \sin \frac{n\pi y}{L_y} \text{ in case of simply supported edges.}$$

When applying the differential operators to $g(x, y)$, \tilde{L} and \tilde{M} matrices are becoming functions of quantic m and n numbers. For each pair (m, n) , an eigenvalue problem is solved, leading, for N assembled layers, to a system of $3 \times (N+1)$ eigenvalues, λ_{imn} . After extraction, λ_{imn} are sorted into extensional, shear and bending categories by analyzing the relative importance of eigenvector amplitudes in each u, v, w directions.

Finally, the band-averaged modal density and the band-averaged wavenumber are estimated from the set of all discrete λ_{imn} up to some maximal m, n orders limited by the upper frequency of calculation.

The model is made more general by introducing frequency-dependent elastic parameters using *SEA+ Extended Material* definition.

The full dynamic matrix is then solved twice, the first solve giving the primary solution frequency and the second solve providing the final frequency after interpolating elastic matrix at primary solution frequency.

Modal damping loss factor (DLF) is estimated by transforming \tilde{L} matrix into a complex matrix \mathbf{L} using complex C_{ij} matrix of which component related to each layer k are given by:

$$\tilde{C}_{ij_k} = (1 + j\eta_k) C_{ij_k}$$

with η_k the local material damping associated to each layer.

The mean DLF of the assembly is finally delivered in integrated band format of width $\Delta\omega$ and central frequency ω_c :

$$\langle \eta(\omega_c) \rangle_{\Delta\omega} = \frac{1}{N_{\Delta\omega}} \left\{ \sum_i X_i^T \text{Im}\{\mathbf{L}\} X_i / \sum_i X_i^T \text{Re}\{\mathbf{L}\} X_i \right\}$$

where $N_{\Delta\omega}$ is the number of eigenvalues retained in $\Delta\omega$ and X_i eigenvector related to λ_{imn} .

6 APPLICATION TO VARIOUS SYSTEMS

6.1 Consistency of the formulation

The self-consistency of the formulation is checked against the calculation of an arbitrary isotropic thin plate of uniform material but decomposed into different number of layers for unchanged total thickness. A 1 m x 1 m uniform plate of 4-mm aluminum thickness is then modeled as SEA+ dynamic laminate plate with selected thickness distribution defined in next table.

Case	Type	#Layer	t1 (mm)	t2 (mm)	t3 (mm)	t4 (mm)	t5 (mm)	Total t mm
P0	uniform	1	4					4
P1	Laminate	1	4					4
P2	Laminate	2	2	2				4
P3	Laminate	3	1	0.5	2.5			4
P4	Laminate	4	1	1	1	1		4
P5	Laminate	5	1.5	1	0.25	1	0.25	4

Table 1. Consistency test of the formulation modeling same plate with different dynamic laminate settings (P0 is the reference plate result modeled as 4-mm uniform SEA+ plate)

Figure 4 shows all models are given same eigenfrequencies, modal density and mass except out of resonances where modal density is interpolated differently between uniform and laminate modeling.

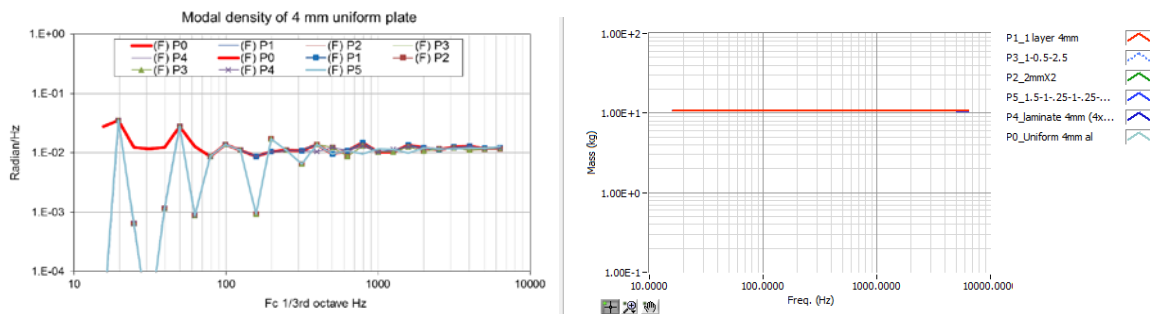


Figure 4. **Left:** modal density of 4mm-Al plate modeled as uniform and as dynamic laminate with different thickness distributions - **Right:** related mass of all plates

6.2 Aerospace sandwich flat plate structure

Case C1 is a 1 x 1 m² flat plate made of sandwich construction with two 1-mm aluminum skins and 10-mm NIDA core with $G = 200$ MPa, $E = 3$ MPa and $\rho_c = 60$ kg/m³.

SEA+ calculation is compared with three FEM simulations with NASTRAN NX solver.

- **C1 "PSOLID1"** FEM model, skins are modeled using 2D-plate elements and glued to the core meshed with 3D-PSOLID elastic elements. PSOLID1 is simply-supported on edge of only one skin.
- **C1 "PSOLID2"** FEM model, same model than PSOLID1 but simply-supported on edges of the two skins.
- **C1 "PCOMP"** FEM model, both skins and core are modeled with 2D PCOMP plate laminate elements within a single 2D-plate and with simply-supported edges.

Real eigenmodes are extracted from FEM models by NASTRAN NX SOL103 solver and imported in SEA+ Virtual SEA solver [1] [2] [3] [4] to calculate related SEA parameters: modal density, wavenumber and mean input mobility. They are then compared to corresponding SEA+ Dynamic Laminate outputs. Figure 5 and Figure 6 show good agreement between SEA and both PCOMP and PSOLID FEM models for modal density and conductance (real part of driving point mobility). Mid to high frequency slopes of both flexural modal density and mobility spectra due to core shear are well-reproduced by SEA+ model. Shifting from PCOMP to PSOLID FEM models increases the first resonance frequencies provided by PCOMP. This is observed in the two selected boundary conditions: constraining one skin, then, two skins to simply-supported on edge, demonstrating the difficulty in predicting deterministic resonance frequencies even on simple systems.

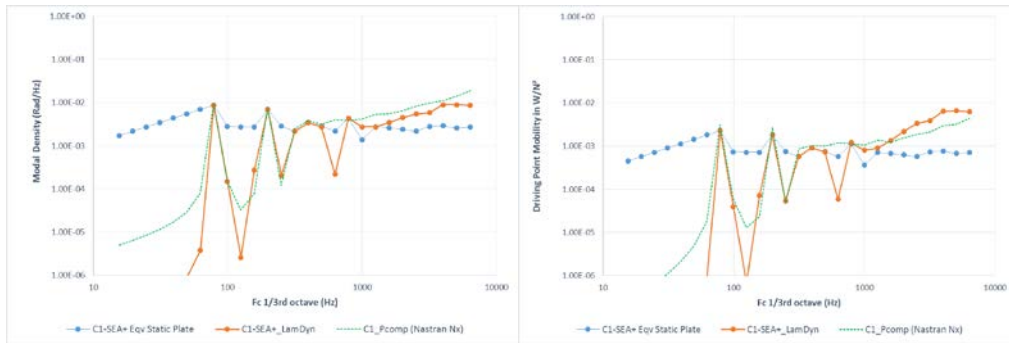


Figure 5. Case C1-Comparisons of (Left) Model density and (Right) conductance using SEA+ Dynamic Laminate (red), PCOMP NASTRAN (dashed green) and SEA+ uniform equivalent static plate (dot blue)

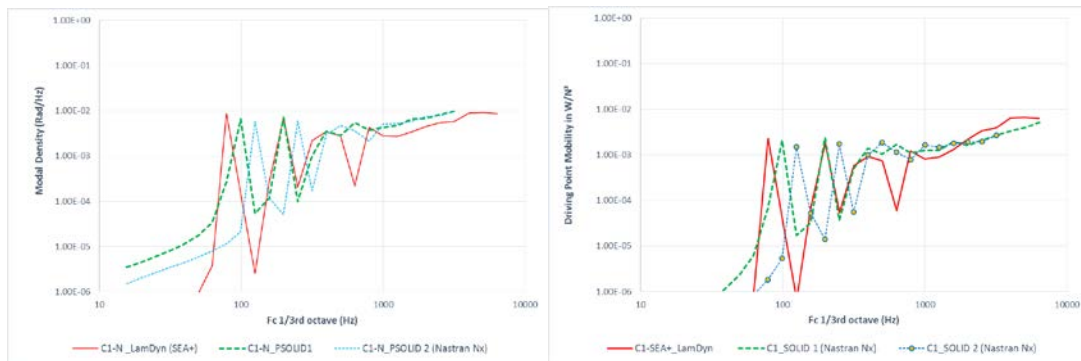


Figure 6. Case C1 - Comparisons of (Left) Model density and (Right) conductance using SEA+ Dynamic Laminate (red) and PSOLID 1 & 2 NASTRAN

6.3 Aerospace sandwich singly-curved structure

Case C2 is a quarter of cylinder in same sandwich than C1. Radius and length are set to 1 m. Again a very good agreement is found between FEM and SEA+ calculation (see Figure 7, Modal density comparison with PSOLID2 model).

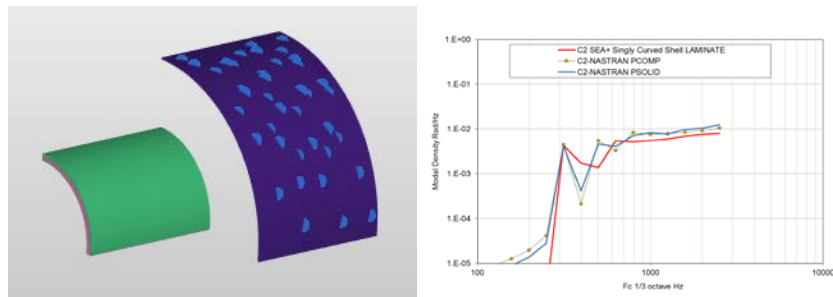


Figure 7. Case C2 - Comparisons of SEA+ and NASTRAN PSOLID2 Model density for a quarter of simply-supported cylinder

6.4 Sandwich steel plate with viscoelastic insertion

Case C3 is also a 3-layered steel panel with very thin film of viscoelastic material bonding together two thin steel plates. A sample from ThyssenKrupp manufacturer was measured to compare with SEA+ simulation. Characteristic used in the modeling are reported in next Table 1.

Manufacturer	Panel size	Skin thickness	Core thickness	Core Young's modulus	Shear modulus	DLF core	Skin Mat.
ThyssenKrupp	0.275m x .2m	0.75 mm	0.04 mm	50 MPa	40 MPa	1	Steel

Table 2. Characteristic of tested samples

Core material intrinsic DLF is taken equal to 1. Skin DLF are fixed arbitrarily to 0.01. Regarding measured data, a set of complex frequency transfer inertances were recorded under impact hammer using InterAC SEA-XP data Acquisition system. Driving point inertances are converted into conductance per 1/3rd octave band. Reverberation time on free-free panels is also analyzed and converted into DLF.

In Figure 8 are reported calculated flexural input conductances for both SEA+ and FEM (here PCOMP model result) and measurement. SEA+ modal density and conductances are also found in good agreement with PCOMP, PSOLID and measurement results. Prediction of DLF is also satisfactory compared to measurement as the impact pulse is very short with low modal density below 1000 Hz. Nevertheless, both Power Injected Method (PIM) and Reverberation time are leading to same measured DLF values in the range 200-2000 Hz.

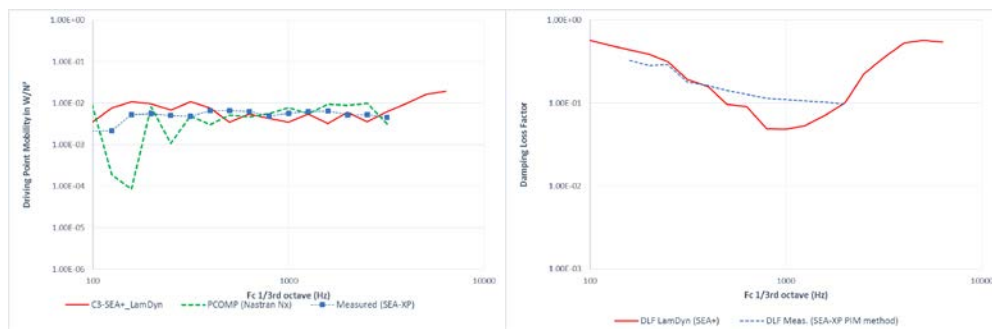


Figure 8. Case C3 - Viscoelastic steel sandwich - **Left:** SEA+ Laminate and NASTRAN PSOLID conductances compared to measurement - **Right:** SEA+ DLF laminate calculation compared to measurement through injected power

6.5 Multilayered window

Case C4 is a window made of five layers. Layers are 8mm-Glass, 9.6mm-PU (Polyurethane), 8mm-Glass, 2mm-PVB (Polyvinyl Butyral) and 3mm-Glass. Window size is 0.76m x 1m. Modal density of corresponding SEA+ laminate model is checked against measured and calculated data in Figure 9 (left). Measured modal density is obtained from FRF measurements performed directly on the built-up window with hammer impact. Measured modal density is obtained from the relationship $N = 4mY$, with m the window mass and Y the real part of driving point FRF. The comparative calculated modal density is extracted from NASTRAN NX FEM model of the window built with PSOLID elements. There is good convergence between the three results taking note that actual window was connected to the mounting frame during the measurement, explaining observed difference at low frequencies between measured and calculated modal densities.

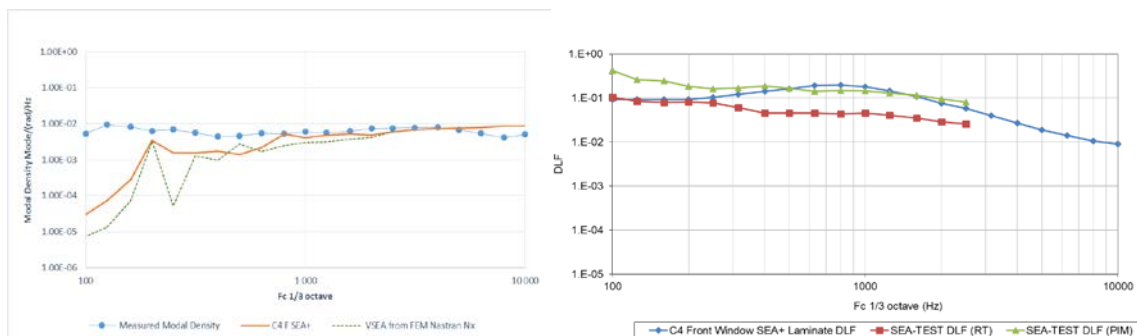


Figure 9. Case C4 - Multilayered window - **Left:** SEA+ and NASTRAN FEM calculated modal density compared with experimental modal density and **Right:** calculated DLF compared with RTIR and PIM measurements

Predicted SEA+ DLF is compared to measured DLF in Figure 9 (right).

Measured DLF is identified in two different ways by Reverberation Time of window Impulse Response (RTIR) and by Power Injected Method (PIM) using SEA-TEST software.

7 CONCLUSIONS

The SEA+ Dynamic Laminate model is based on a new theory which provides fast calculation of SEA parameters. This theory is reducing the 3D dynamic of a multi-layered thin shell to the assembly of series of thin orthotropic layers, each layer being described by a single material and by its asymptotic uncoupled dynamic stiffness. Along transverse direction, the strain shape motion is assumed to behave as static with continuous displacement and rotation and discontinuous second z-derivative at layer interfaces. This theory is then a specific instance of the Zig-Zag theory using local asymptotic motions of individual layers in place of the classical Taylor's series decomposition of the global motion for projecting the actual motion. Dynamic Laminate theory has been extended from plate to singly-curved and doubly-curved systems and released in SEA+ 2015. Comparative calculations with FEM models and with measurements have shown good convergence in all tested configurations which were requiring specific SEA model, now all covered by the Dynamic Laminate construction.

REFERENCES

- [1] G. Borello (InterAC), L. Gagliardini, L. Houillon (PSA), L. Petrinelli (Geci Systems). Virtual SEA: mid-frequency structure-borne noise modeling based on Finite Element Analysis. *SAE Noise and Vibration Conference* – May 6-8, 2003 – Traverse City, Michigan, USA.
- [2] G. Borello, A. Courjal, R. Nguyen Van Lan (InterAC). Combining Finite Element and SEA approach in Vibroacoustic Analysis. *7th French Acoustic Congress* – March 22-25, 2004 – Strasbourg, France.
- [3] G. Borello (InterAC), L. Gagliardini, L. Houillon (PSA), L. Petrinelli (Geci Systems). Virtual SEA-FEA-based Modeling of Structure-Borne Noise. *Sound and Vibration Magazine* – January 2005.
- [4] G. Borello, A. Courjal, R. Nguyen Van Lan (InterAC), Analysing structure borne sound transmission in car body using combined FE/SEA techniques. *SIAT* – January 19-22, 2005 – Pune, India.
- [5] G. Borello (InterAC), J.-L. Kouyoumji (CTBA). Vibroacoustic Analysis of Sound Transmission in Double-glass Timber Windows. *Inter-Noise* – August 7-10, 2005 – Rio de Janeiro, Brazil.
- [6] Luciano Demasi (San Diego University). An invariant Model for any Composite Plate Theory and FEM Applications: the Generalized Unified Formulation. *50th AIAA/ASME/ASCE/AHS/ASC Structures, Structural Dynamics and Material Conference 17th*. 4-7 May 2009, Palm Springs, CA, USA.
- [7] J.-M. Berthelot. Matériaux Composites, comportement mécanique et analyse des structures. *Masson 2^{me} édition*, 1996.

1 INTRODUCTION

Throughout this paper, we consider a bounded domain $B \subset \mathbb{R}^2$ with boundary Υ , occupied by a linear elastic material and we assume that there exists a cavity, namely a bounded domain $\bar{A} \subset B$ with boundary Γ . Let us denote by Ω the domain $B \setminus \bar{A}$. The forward linear elastic problem is therefore given by

$$\begin{cases} \operatorname{div} \sigma(u) = 0 & \text{in } \Omega, \\ \sigma(u) = \lambda \operatorname{tr} \varepsilon(u) I + 2\mu \varepsilon(u) & \text{in } \Omega, \\ \sigma(u) n = 0 & \text{on } \Gamma, \\ \sigma(u) n_\Upsilon = g & \text{on } \Upsilon, \end{cases} \quad (1)$$

where u is the displacement, $\sigma(u)$ is the associated stress tensor, $\varepsilon(u)$ is the linearized strain tensor given by $\varepsilon(u) = \frac{1}{2} (\nabla u + \nabla u^T)$. n_Υ and n are the outward unit normals to the boundary of Ω . The geometric inverse problem under consideration consists so in recovering the cavity A , namely the unknown shape Γ by applying some prescribed load g on Υ and measuring the induced displacement on the same part Υ , i.e

$$\begin{cases} u = f & \text{on } \Upsilon, \\ \sigma(u) n_\Upsilon = g & \text{on } \Upsilon. \end{cases}$$

For a given Ω , let u_D and u_N be the solutions of the following Dirichlet, respectively Neumann problem

$$\begin{cases} \operatorname{div} \sigma(u_D) = 0 & \text{in } \Omega, \\ \sigma(u_D) = \lambda \operatorname{tr} \varepsilon(u_D) I + 2\mu \varepsilon(u_D) & \text{in } \Omega, \\ \sigma(u_D) n = 0 & \text{on } \Gamma, \\ u_D = f & \text{on } \Upsilon, \end{cases} \quad (2)$$

respectively

$$\begin{cases} \operatorname{div} \sigma(u_N) = 0 & \text{in } \Omega, \\ \sigma(u_N) = \lambda \operatorname{tr} \varepsilon(u_N) I + 2\mu \varepsilon(u_N) & \text{in } \Omega, \\ \sigma(u_N) n = 0 & \text{on } \Gamma, \\ \sigma(u_N) n_\Upsilon = g & \text{on } \Upsilon. \end{cases} \quad (3)$$

Thus, the cavities identification problem can be formulated as a shape optimization one (see [1, 2, 4]) as follows

$$\begin{cases} \text{Find } \Omega \text{ such that} \\ J(\Omega) = \min_{\tilde{\Omega} \subset B} J(\tilde{\Omega}), \end{cases} \quad (4)$$

using the constitutive law misfit functional

$$J(\Omega) := \frac{1}{2} \int_{\Omega} (\sigma(u_D) - \sigma(u_N)) : (\varepsilon(u_D) - \varepsilon(u_N)). \quad (5)$$

The main contribution of the present work relies on the use of the error functional (5) that can be interpreted as an energetic least-squares one.

2 SHAPE DERIVATIVE

We consider a hold-all domain $U \supset \bar{\Omega}$ and construct a family of perturbations F_t as follows

$$F_t = id + th,$$

where h is a deformation field belonging to the space

$$Q = \{h \in C^{1,1}(\bar{\Omega})^2; h = 0 \text{ on } \Upsilon\}$$

and t is sufficiently small such that F_t is a diffeomorphism from Ω onto its image. The family of domains $\{\Omega_t\}$ respectively $\{\Gamma_t\}$ are then defined by $\Omega_t := F_t(\Omega)$ respectively $\Gamma_t := F_t(\Gamma)$. The condition $h|_{\Upsilon} = 0$ means that the boundary Υ is a part of the boundary of Ω_t .

Definition 1 *The Eulerian derivative of the functional J at Ω in the direction of an element $h \in Q$ is defined by the quantity, when it exists*

$$J'(\Omega, h) = \lim_{t \rightarrow 0} \frac{J(\Omega_t) - J(\Omega)}{t}.$$

The Eulerian derivative is called shape derivative if $J'(\Omega, h)$ exists for all $h \in Q$ and the mapping $h \mapsto J'(\Omega, h)$ is linear and continuous with respect to the topology of $C^{1,1}(\bar{\Omega})^2$.

Theorem 1 *The mapping $t \mapsto J(\Omega_t)$ is C^1 in a neighborhood of 0 and its derivative at 0 is given by*

$$J'(\Omega, h) = \int_{\Gamma} G(h \cdot n),$$

with

$$G = \frac{1}{2} [(\sigma(u_D) : \varepsilon(u_D)) - (\sigma(u_N) : \varepsilon(u_N))]. \tag{6}$$

3 NUMERICAL RESULTS

An iterative method is proposed to solve the shape optimization problem (4). The last theorem allows to choose like a descent direction of the functional J

$$h \in Q \quad \text{such that} \quad h|_{\Gamma} = -G n,$$

where G is given by (6). To numerically implement this iterative process, we use the level set method [3].

3.1 First case

As a first test, we consider $\Upsilon = \{x; |x| = 0.9\}$. The solution is the circle centered at the origin with radius equal to 0.35. The convergence is obtained after 17 iterations as it is shown in Figure 1.

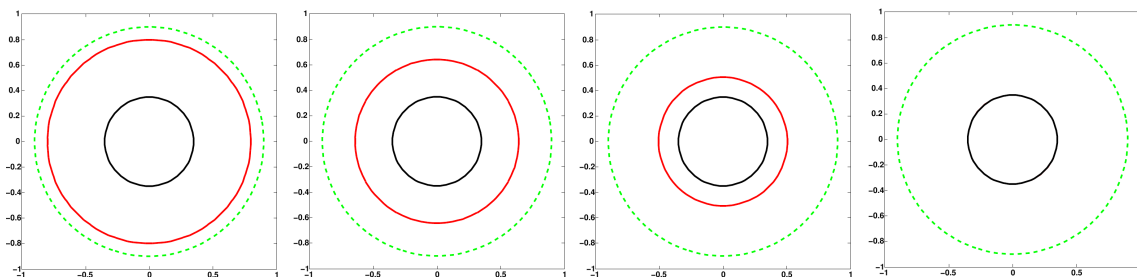


Figure 1: Υ the exterior boundary (the dashed green line), Γ the exact solution (the black line), evolution of the boundary Γ^k (the red line) for $k = 0, 10, 14, 17$ (left to right).

3.2 Second case

In this second case, the cavity to recover is a connected domain, namely the disc of radius equal to 0.3 centered at the origin. However, we consider a disconnected initial guess. Indeed, Γ^0 is the union of the three disjoint circles of radius R equal respectively to 0.14, 0.17 and 0.14 (left to right), centered respectively at $(-0.4, 0)$, $(0, 0)$ and $(0.4, 0)$ as it is shown in Figure 2. The convergence is obtained after 9 iterations.

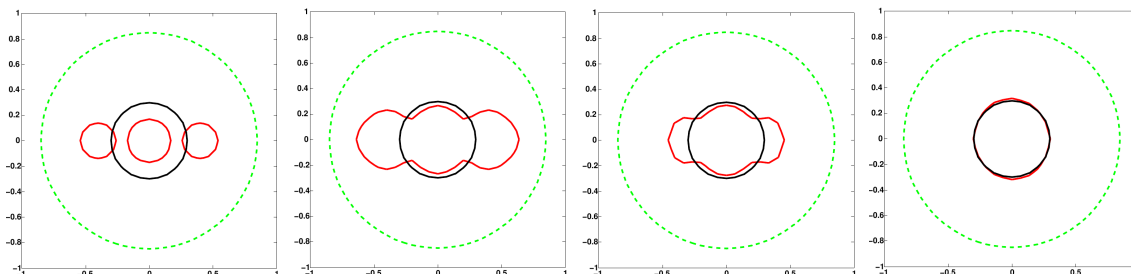


Figure 2: Topology change test: Υ the exterior boundary (the dashed green line), Γ the exact solution (the black line), evolution of the boundary Γ^k (the red line) for $k = 0, 1, 3, 9$ (left to right).

4 CONCLUSION

In this work, a cavities identification problem in linear elasticity was transformed to a shape optimization one by the means of a Dirichlet-Neumann misfit functional. To solve this problem, we made use theoretically of the shape derivative concept and numerically of the level set method. The numerical tests illustrated the efficiency of the proposed approach.

REFERENCES

- [1] A. Ben Abda, F. Bouchon, G. H. Peichl, M. Sayeh, R. Touzani, *A Dirichlet-Neumann cost functional approach for the Bernoulli problem*, (J. Eng. Math. 81(1), 157–176, 2013).
- [2] H. Ben Ameer, M. Burger, B. Hackl, *Level set methods for geometric inverse problems in linear elasticity*, (Inverse Problems 12, 673–696, 2004).
- [3] R. Fedkiw, S. Osher, *Level Set Methods and Dynamic Implicit Surfaces*, (Springer-Verlag, New York, 2003).
- [4] E. Jaiem, S. Khalfallah, *An energy-gap cost functional for cavities identification*, (Submitted, 2014).

COPYRIGHT NOTICE

Copyright ©2015 by the authors. Distribution of all material contained in this paper is permitted under the terms of the Creative Commons license Attribution-NonCommercial-NoDerivatives 4.0 International (CC-by-nc-nd 4.0).





Predeformation and frequency-dependence : Experiment and FE analysis

Nidhal Jridi^{1,2*}, Michelle Salvia², Adel Hamdi¹, Olivier Bareille², Makrem Arfaoui¹,
Mohammed Ichchou², Jalel Ben Abdallah¹

¹Laboratoire de Mécanique Appliquée et Ingénierie LR-11-ES19(LRMAI)
Université de Tunis El Manar, École Nationale d'Ingénieurs de Tunis, LR-11-ES19
BP 37, LE BELVEDERE 1002 TUNIS
Email: jridinidhal@gmail.com

²Laboratoire de Tribologie et Dynamique des Systèmes (LTDS)
CNRS : UMR5513, Ecole Centrale de Lyon
36 Avenue Guy de Collongue, 69134 Ecully Cedex France

ABSTRACT

Elastomers show significant dependence on prestrain and frequency when they are loaded with large static predeformation superimposed by harmonic small amplitude dynamic excitations. In order to investigate these dependencies, quasi statics and dynamic experiments were carried out. Based on the experimental facts, we examined the capacity of the Simo viscoelastic model implemented in the FEA software Abaqus to simulate experimental data with good accuracy. The formulation is in the frequency domain. Therefore, the constitutive equations are linearized in the neighborhood of a predeformed configuration, with the assumption that the linear expression of stress governs the new configuration. Hence, the experimental data at different prestrain levels are compared to the simulation results.

Keywords: elastomers, dynamic material behavior, frequency-dependence, prestrain-dependence, abaqus frequency domain viscoelasticity.

1 INTRODUCTION

Because of their remarkable dissipative properties, elastomers are widely used as damping components in industry. Indeed, they can undergo severe mechanical loading conditions. The load-case of large static predeformation superimposed by small amplitude dynamic excitations can be found in many applications. Experimental investigations of rubber materials show lots of non linear effects. In order to design industrial components, it is of major importance to measure the sensitivity of the dynamic response to the influencing parameters, and be able to predict the impact of those effects on the products.

In the present paper, we examine the capacity of the Simo viscoelastic model implemented in Abaqus software to simulate experimental data with good accuracy, and with respect to the frequency and predeformation-dependence. Hence, the frequency domain viscoelastic model in Abaqus is explored. The input requirement of the model from dynamic tests at several frequencies is detailed. The model assumes that the input requirement to Abaqus is independent of the prestrain in the data. This assumption is examined for a filled rubber material. The material model is used to predict component level response in simulations performed at different prestrain levels for several frequencies. Experimental data at different prestrain levels are compared to the simulation results.

2 EXPERIMENTAL RESULTS

2.1 Static experiments

The experimental investigations are focused on the prestrain and frequency-dependent behaviour of a filled rubber. For this aim, some quasi-static experiments are carried out. To exclude the Mullins effect, which is known as a stress softening of virgin material in the first loading cycles [1], the specimens are preconditioned before testing. Monotonic tests were carried out with an Instron Table Model Testing Machine (model 3345). All tests were performed at room temperature under displacement control, and under the assumption of homogeneous deformations. Tensile tests were performed on H2 specimens. Shear tests were performed on quad-shear test samples [2]. Focusing on the equilibrium stress response, we make use of multistep experiments at different strains with holding time of ten minutes. The resulting stress responses are shown in Figure 1.

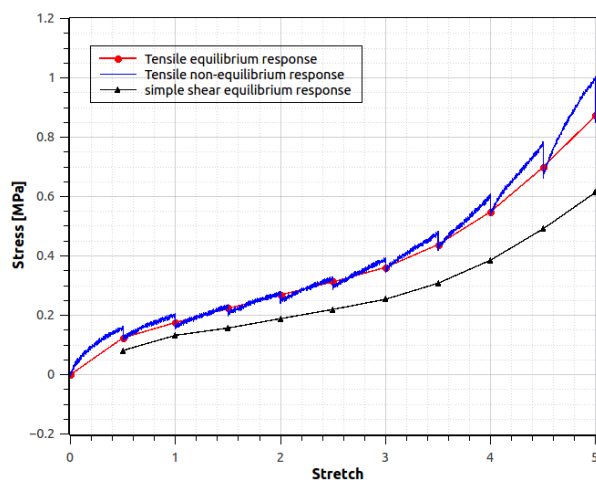


Figure1. Monotonic tests, loading conditions , equilibrium and non equilibrium stress response

2.2 Dynamic experiments

In this section, we discuss experimental observations on shear specimens. The specimens consist on an assembly of 3 stainless steel cylinders with 10 mm of diameter and 10 mm of length between which 2 rubber inserts, of about 2.4 mm thickness and indented from a rubber sheet furnished by the manufacturer, are glued. Dynamic properties were investigated by mean of a Metravib DMA 50N.

The experimental procedure consists in superimposing simple shear prestrain and a sinusoidal strain as:

$$\varepsilon(t) = \varepsilon_0 + \varepsilon_a \sin(\omega t) \quad (1)$$

where ε_0 denotes the prestrain, ε_a denotes the strain amplitude, and ω is the angular frequency.

To consider the frequency-dependent materials behavior, frequency sweeps test with stepwise changing frequency from 0.1 Hz up to 40 Hz at constant predeformation and constant dynamic strain amplitude are used. In order to evaluate the materials response over a wide range of frequency, we used temperature-frequency shifting techniques and generate mastercurves [3][4]. Therefore, we have to investigate the temperature-dependence of the material behavior. The measuring temperature is varied between -100 °C and 100 °C and the reference temperature for the shifting process is set to 23.3 °C. On the basis of these conditions, we were able to shift the measured curves on the logarithmically scaled frequency axis.

The results were evaluated in terms of the shear storage modulus and the shear loss factor. The storage modulus determines that part of stress response which is in phase with the strain. The loss modulus that part of stress response which is in phase with the strain rate. The loss factor is the quotient of the loss modulus by the storage modulus. Figure 2 exhibits the frequency-dependent material behavior. The experimental data shows that the storage modulus increases significantly with increasing frequency. In comparison with this, the loss factor shows a broad maximum in the region of 1 e^{+04} Hz. In the region of lower or higher frequencies, this factor is significantly lowermost. Hence, the loss modulus increases with increasing frequency.

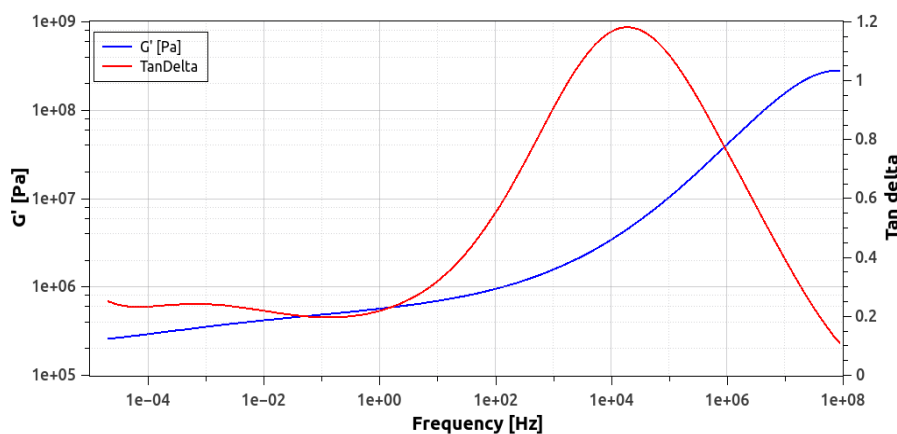


Figure 2. Material's frequency-dependent behavior , shear storage and loss factor

As mentioned before, and in order to determine the influence of the static prestrain on the dynamic materials behavior, frequency sweeps at different levels of static preload were carried

out. The experimental curves show that increasing the static prestrain leads to a lower storage modulus and loss factor. Greater prestrain leads to a lower softening in term of shear storage modulus (Figure 3), the decrease between 0% of prestrain and 10% of prestrain is greater than that between 20% of prestrain and 30% of prestrain. Figure 4 exhibits the same phenomena for the loss factor. Therefore, the softening of the material is non linear.

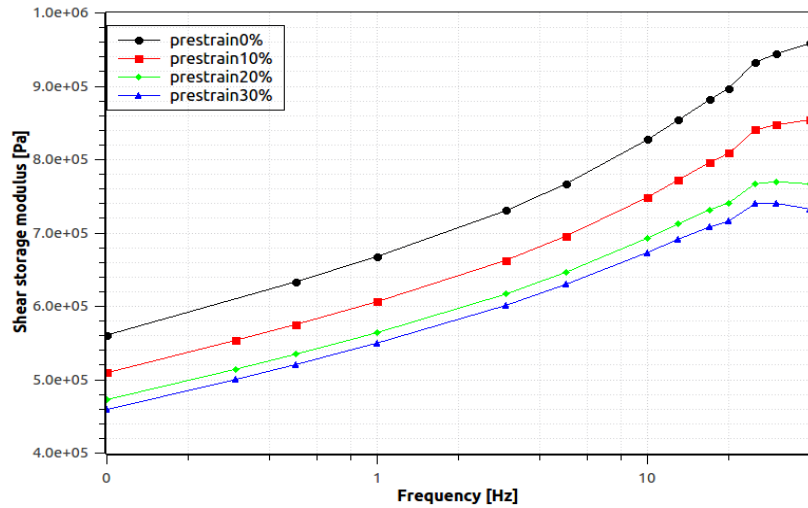


Figure 3. Shear storage modulus at different frequencies and prestrain levels

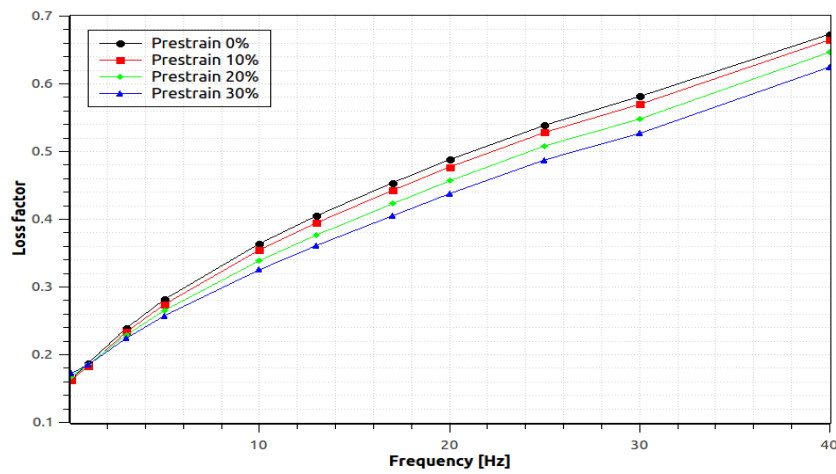


Figure 4. Loss factor at different frequencies and prestrain levels

3 FINITE ELEMENT ANALYSIS IN THE FREQUENCY DOMAIN

3.1 Abaqus FEA finite viscoelasticity model

We call \mathbf{F} the deformation gradient it is defined as $\mathbf{F} = \frac{\partial \mathbf{X}}{\partial \mathbf{x}}$ where \mathbf{x} is the coordinate in the current configuration at \mathbf{X} in the reference configuration. We call J its determinant $J = \det \mathbf{F}$. When a solid is incompressible, every deformation is isochoric, so that: $J = 1$.

The Abaqus FEA model is reminiscent of the Simo model [5]. The finite-strain viscoelasticity theory implemented in Abaqus is a time domain generalization of the hyperelastic constitutive model. Section 4.8.2 of the Abaqus Theory Manual version 6.13 [6] gives the following constitutive relations to model nonlinear viscoelastic effects :

$$\boldsymbol{\sigma}(t) = \boldsymbol{\sigma}_0^D(t) + \text{dev} \left[\int_0^t \dot{G}(s) \mathbf{F}_t^{-1}(t-s) \boldsymbol{\sigma}_0^D(t-s) \mathbf{F}_t^{-T}(t-s) ds \right] - p \mathbf{I} \quad (2)$$

where $\text{dev}(\cdot) = (\cdot) - \frac{1}{3}(\cdot) : \mathbf{I}$ is the deviatoric part of the bracketed term and $\boldsymbol{\sigma}_0^D$ is the instantaneous deviatoric Cauchy stress response (elastic response at very short times). This constitutive relation is for incompressible solids. $-p \mathbf{I}$ is the hydrostatic term, and p is a Lagrange multiplier.

The time dependent shear relaxation function $G(t)$ is defined in terms of a series of exponentials known as the Prony series as:

$$G(t) = G_\infty + \sum_{i=1}^n G_i e^{-\frac{t}{\tau_i}} \quad (3)$$

where G_∞ represents the long term shear modulus, G_i and τ_i are material constants. Using Fourier transforms, the expression for the time dependent shear modulus can be written in the frequency domain as follows:

$$G_s(\omega) = G_0 \left(1 - \sum_0^n g_i \right) + G_0 \sum_0^n \frac{g_i \tau_i^2 \omega^2}{1 + \tau_i^2 \omega^2} \quad (4)$$

$$G_l(\omega) = G_0 \sum_0^n \frac{g_i \tau_i \omega}{1 + \tau_i^2 \omega^2} \quad (5)$$

where $G_s(\omega)$ is the shear storage modulus, $G_l(\omega)$ is the shear loss modulus and ω is the angular frequency. g_i are dimensionless shear relaxation constants and are as:

$$g_i = \frac{G_i}{G_0} \quad (6)$$

The frequency domain viscoelasticity model in Abaqus is defined for a kinematically small perturbation about a predeformed state. The procedure consists on a linearised vibration solution associated with a long-term hyperelastic material behavior. This assumes that the linear

expression for the shear stress still governs the system except that the long-term shear modulus G_∞ depends on the amount of the static prestrain γ_0 as:

$$G_\infty = G_\infty(\gamma_0) \quad (7)$$

Hence, this implies that the frequency-dependent part of the material's response is not affected by the static prestrain level.

3.2 Simulation results

In this section, the frequency domain viscoelastic model defined with the Abaqus step “Direct-solution steady-state dynamic analysis” [7] is studied in order to examine the capacity of the Simo viscoelastic model to simulate experimental data with good accuracy and with attention to frequency and prestrain dependences.

Harmonic excitation data at different prestrain and frequency levels are available. This data contains loss and storage modulus information. Long-term uniaxial data was used to calibrate an hyperelastic material model.

The simulation results for the equilibrium stress response are shown in Figure 5. They reveal a very good matching between the experimental data and the simulated data for both uniaxial tension and pure shear tests.

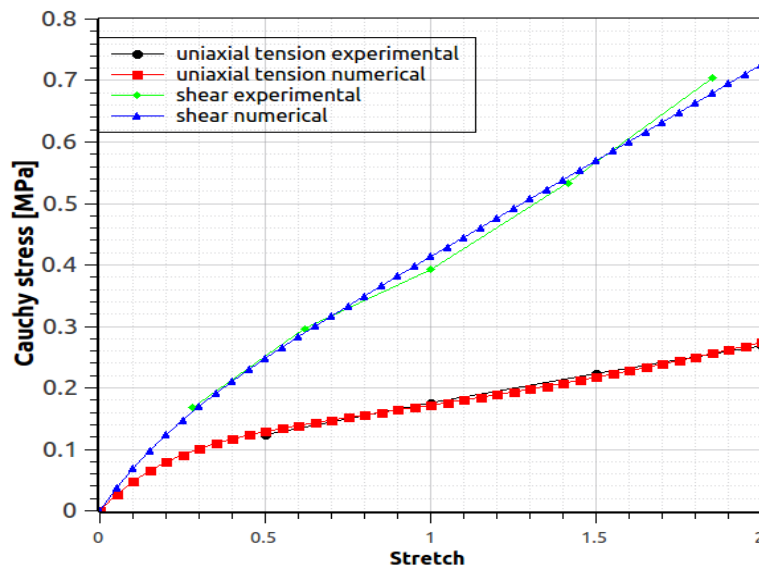


Figure 5. Experimental and simulated data for uniaxial and pure shear tests

With respect to the assumption of linearized vibration about prestrained configuration mentioned previously, harmonic data were introduced in the undeformed state. Hence, a small amplitude dynamic excitation was superimposed to a simulation of the nonlinear base state. Simulation results are graphically shown in Figure 6 and Figure 7. The frequency-dependent behavior is pronounced. Therefore, the results for the dynamic material response with respect to the prestrain-dependency are not accurate: the strain and frequency effects are separated. Thus, the basic

assumption for the frequency domain viscoelasticity used in Abaqus is not reasonable for our investigated filled rubber.

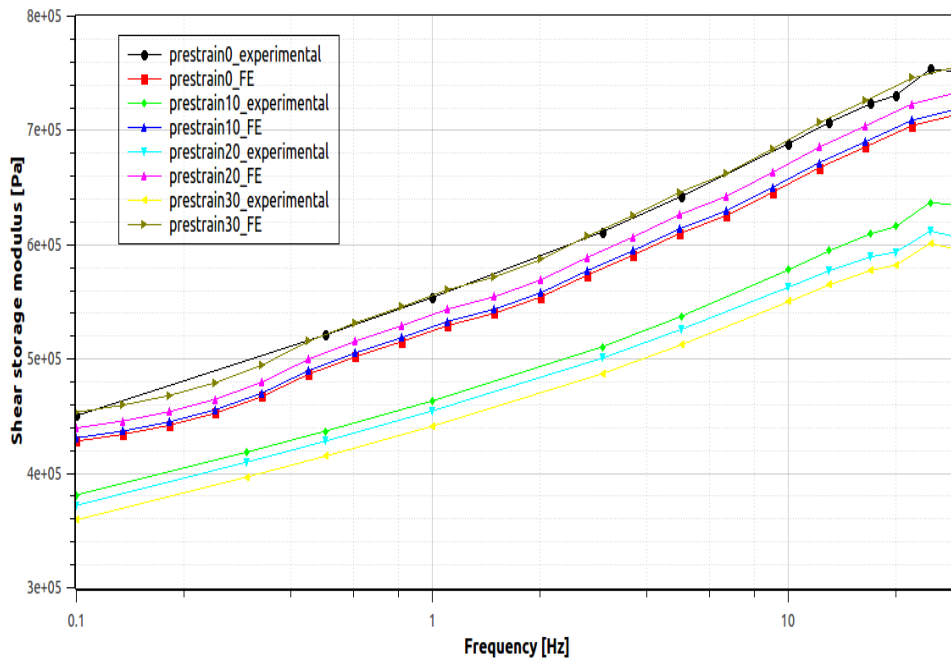


Figure 6. Experimental and simulated shear storage modulus at different frequencies and prestrain levels

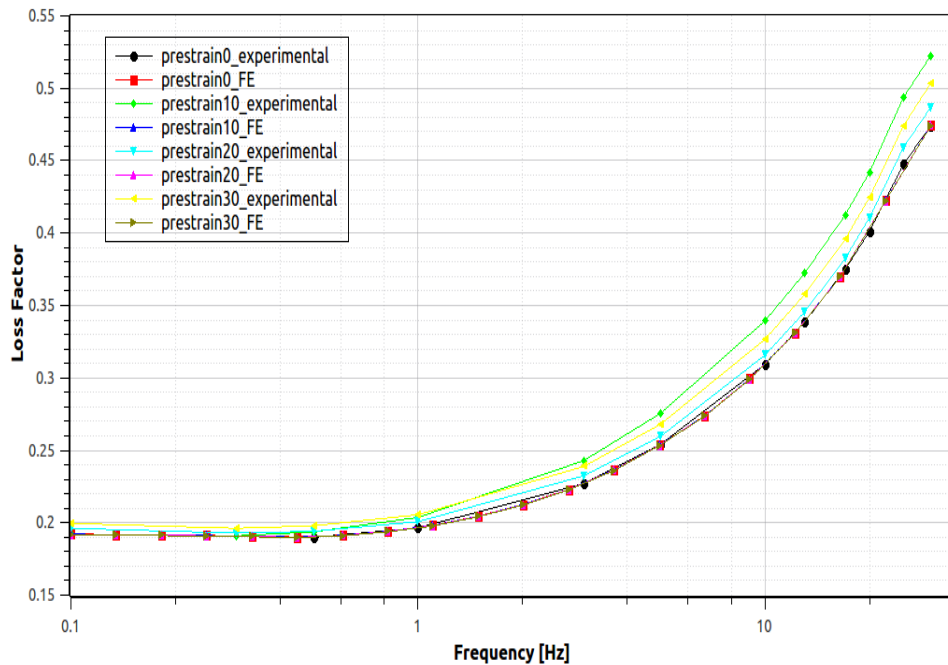


Figure 7. Experimental and simulated loss factor at different frequencies and prestrain levels

CONCLUSION

The experimental investigations of a filled rubber revealed a significant dependence on frequency and prestrain level. The frequency domain viscoelasticity in the FEA software Abaqus is used to simulate those dependencies and reproduce experimental results. This approach is based on the assumption of linearized harmonic excitation about a base state. Simulation results compared to experimental curves show that the frequency-dependent behavior is pronounced, but not the prestrain dependence. Thus, the strain and frequency effects are separated and the mentioned assumption above is non reasonable for the filled rubber material investigated in this paper.

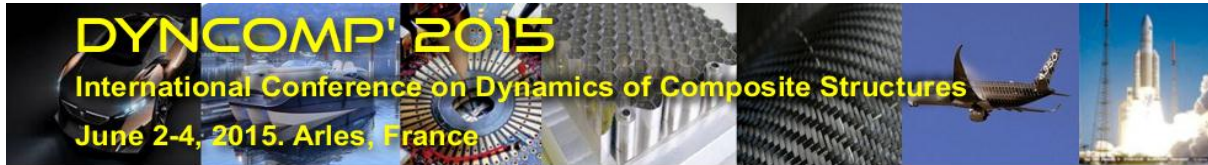
REFERENCES

- [1] L. Mullins, Softening of Rubber by Deformation, Rubber Chemistry and Technology, Volume 42, Issue 1, Pages 339-362, 1969
- [2] D.J.Charlton, J.Yang and K.K. Teh, A review of methods to characterize rubber elastic behavior for use in finite element analysis, Rubber Chemistry and Technology, Volume 67, Issue. 3, Pages 481-503, 1994
- [3] J D Ferry, Viscoelastic Properties of Polymers., John Wiley and sons,New York,1980
- [4] M Klüppel, Evaluation of viscoelastic mastercurves of filled elastomers and applications to fracture mechanics, Journal of physics : Condensed Matter Volume 21, Issue 3, Starting page 035104, 2009
- [5] J.C. Simo, , On a fully three-dimensional finite-strain viscoelastic damage model: Formulation and computational aspects, Computer Methods in Applied Mechanics and Engineering Volume 60, Issue 2, Pages 153–173, 1987
- [6] Abaqus Theory manual section 4.8.2, Abaqus version 6.13
- [7] Abaqus Analysis user's manual section 6.3.4, Abaqus version 6.13

COPYRIGHT NOTICE

Copyright ©2015 by the authors. Distribution of all material contained in this paper is permitted under the terms of the Creative Commons license Attribution-NonCommercial-NoDerivatives 4.0 International (CC-by-nc-nd 4.0).





MODELING AND IDENTIFICATION OF A CLASS OF HYPERVISCOELASTIC MATERIAL BEHAVIOR

Tayeb Adel^{1,2}, Arfaoui Makrem¹, Zine Abdelmalek², Hamdi Adel¹, Benabdallah Jalel¹ and
Ichchou Mohamed²

¹Laboratoire de Mécanique appliquée et Ingénierie
Université de Tunis ElManar, Tunis, TUNISIE

Email: teyebadel@yahoo.fr, makremarfaoui@yahoo.fr, ahamdi.tu@gmail.com,
jalel.benabdallah@enit.rnu.tn

²Laboratoire de Tribologie et Dynamique des Systèmes
Université de Lyon, Lyon, FRANCE

Email: Abdel-Malek.Zine@ec-lyon.fr, mohamed.ichchou@ec-lyon.fr

ABSTRACT

Elastomers are widely used in aerospace, automotive and civil engineering applications thanks to their ability to undergoing high strains in large temperature range. To study the nonlinearities, several models have been developed in the literature. In this work, a nonlinear viscoelastic model at finite strain is developed based upon functional and internal variable approaches and the time strain superposition principle (TSSP). Constitutive equations for the stress are derived such that the second law of thermodynamic, in the form of Clausius-Duhem inequality, is satisfied. Identification of several model' parameters is studied using experimental data of pure shear, simple extension tests on a natural rubber NR and a least square minimization procedure.

Keywords: *nonlinear viscoelasticity, finite strain, time-strain superposition principle, identification, discretization of constitutive equations.*

1 INTRODUCTION

Viscoelastic materials, such as elastomers, are well known by their nonlinear time dependent behaviour and large deformation. In the literature, two main approaches are used to determine constitutive equations for these materials: functional approach and internal variables approach.

The first one consists on expressing the free energy density as a multiple integral functional in terms of the history of deformation (Christensen [1] Pipkin [2]), and then the stress tensor is derived from this functional with respect to the strain tensor, taking into account the whole thermodynamic assumptions. Whereas, the second one consists on expressing the free energy density as a Taylor series in terms of the strain tensor and a set of internal variables (second order tensor akin to the second Piola-Kirchhoff stress tensor Simo [3] Govindjee [5] or the right Cauchy-Green strain tensor Holzapfel [4] Valanis [6] Schapery [7]). The viscoelastic behavior is described with a linear rate equation governing the set of internal variables and the thermodynamic restrictions are expressed by the Clausius-Duhem inequality.

In this study, a model is developed for nonlinear viscoelastic materials undergoing large mechanical process. As a first step, a rheological motivation is investigated. Then, the nonlinear viscoelastic model is introduced using a formulation based upon both functional and internal variables approaches and the time strain superposition principle TSSP (reduced time). Constitutive equations for stress and dissipation are then derived from the thermodynamic principles. Finally, an identification procedure of several model parameters is highlighted using pure shear and simple extension tests on a natural rubber material (NR).

2 NONLINEAR VISCOELASTIC MODEL

2.1 Rheological model

The use of rheological models to describe the mechanical behavior of several materials is very widespread. The advantage of such model is its simplicity to obtain the constitutive equations of a material. It consists on associating elementary rheological models, namely a Hookean element (spring) and a Newtonian fluid element (dashpot). This association could be in series and/or in parallel.

The aim of this section is to develop the viscoelastic model proposed by Simo [3] using a rheological model of Zener. For that, we shall investigate some assumptions in the definition of internal variables. The viscoelastic model is developed using the concept of internal variables; the stress is used as an internal variables and denoted Q .

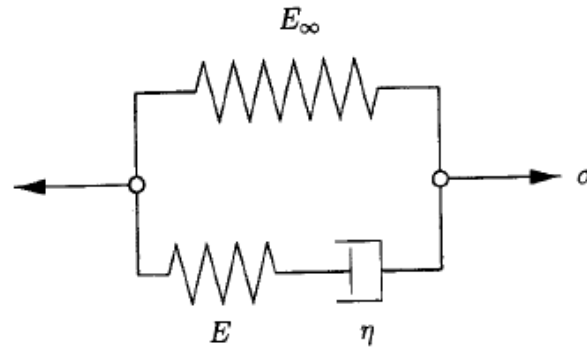


Figure-1: Zener rheological model

In the rheological model, (figure 1), E is the spring constant of the Maxwell branch, η is its dashpot viscosity coefficient and E_∞ is the constant of the spring related to the equilibrium state ε and σ are the total deformation and the stress respectively. The deformation of the dashpot of the Maxwell branch is denoted α and the free energy density is denoted Ψ . Note that this model is governed by the following equations:

$$\sigma = E_\infty \varepsilon + E(\varepsilon - \alpha) \quad (1)$$

$$\eta \dot{\alpha} = E(\varepsilon - \alpha) \quad (2)$$

$$\Psi = \frac{1}{2} E_\infty \varepsilon^2 + \frac{1}{2E} (E\varepsilon - Q)^2 \quad (3)$$

$$\dot{Q} + \frac{1}{\tau} Q = \frac{\gamma}{\tau} \frac{\partial \psi_o}{\partial \varepsilon} \quad (4)$$

In Equations (2) and (4) the dot (.) denotes the derivative of this variable with respect to time. Note that $\gamma = E/E_o$ is a positive constant, E_o is the instantaneous modulus of the material model and $\tau = \eta/E$ is the relaxation time constant. The instantaneous potential mentioned in equation (4) is the instantaneous elastic energy defined as:

$$\psi_o = \frac{1}{2} E_o \varepsilon^2 \quad (5)$$

Considering equations (1), (2), (3), (4) and (5), one can obtain the expression of the Cauchy stress:

$$\sigma = \int_0^t \left((1-\gamma) + \gamma \exp\left(-\frac{t-t'}{\tau}\right) \right) \frac{\partial \psi_o}{\partial \varepsilon} dt' \quad (6)$$

2.2 Nonlinear viscoelastic model with reduced time

The concept of reduced time was introduced essentially to describe thermorheologically simple materials' behavior. For such materials, their behaviors are affected by the history of temperature via a single scalar-valued function called temperature shift function [8] [9]. This concept was generalized to investigate thermorheologically complex materials' behavior by a temperature and stress/ strain dependant shift function (Schapery [10], Matsuoka [11] and McKenna [12]).

In what follows a viscoelastic model with reduced time is proposed.

The free energy density proposed by Simo [3] is considered. Remember that the author postulated a free energy as a Taylor series of the right Cauchy-Green strain tensor and an internal variable $\underline{\underline{Q}}$: overstress or non-equilibrium stress (theory of thermodynamic internal variables). Simo [3] proposed an evolution law of this variable. Our approach consists on resolving this law in order to obtain the expression of the internal variable as an integral of the history of deformation/ stress, and then we replace the variable $\underline{\underline{Q}}$ by its expression in the energy. So, we obtain a free energy density in a functional form, then we follow the approach of Christensen [1] to derive constitutive equations.

The evolution law of the internal variable, the free energy and the reduced time function are postulated as follow:

$$\frac{d\underline{\underline{Q}}}{d\underline{\underline{\xi}}} + \frac{1}{\tau} \underline{\underline{Q}} = \frac{\gamma}{\tau} \left[2 \frac{\partial \psi_o(\underline{\underline{C}})}{\partial \underline{\underline{C}}} \right] \quad (7)$$

$$\underline{\underline{\xi}}(t) = \int_0^t \frac{dt'}{a(\underline{\underline{C}})} \quad (8)$$

$$\Psi = \psi_o(\underline{\underline{C}}) - \frac{1}{2} \underline{\underline{Q}} : \underline{\underline{C}} + \frac{1}{4\mu_o \gamma} \underline{\underline{Q}} : \underline{\underline{Q}} \quad (9)$$

In equation (9) μ_o denotes the initial shear modulus of the material. Considering these equations and using the methodology, described above, one can obtain the constitutive equation of the second Piola-kirchhoff stress tensor:

$$\underline{\underline{S}} = \int_0^{\underline{\underline{\xi}}} G(\underline{\underline{\xi}} - \underline{\underline{\xi}}') \frac{\partial}{\partial \underline{\underline{\xi}}'} \left(2 \frac{\partial \psi_o(\underline{\underline{C}})}{\partial \underline{\underline{C}}} \right) d\underline{\underline{\xi}}' \quad (10)$$

$G(t)$ is a time dependant exponential decay function, known as the relaxation function. The equation of this material characteristic function can be expressed as:

$$G(t) = \gamma_\infty + \sum_i \gamma_i \exp\left(-\frac{t}{\tau_i}\right) \quad (11)$$

3 IDENTIFICATION

The aim of this section is to present the identification procedure of the hyperelastic potential, the relaxation function and the reduced time function.

3.1 Identification of hyperelastic potential and relaxation function

The identification of the hyperelastic potential $\psi_o(\underline{\underline{C}})$ and the relaxation function $G(t)$ equation (11) is provided using ABAQUS software and simple extension tests at equilibrium state; i.e. low strain rates and relaxation at different levels of deformation. In figure 2 these two functions are plotted using experimental data and the one obtained by the identification. Note that the used hyperelastic potential is a third order Ogden law [13]. For such material the hyperelastic potential is expressed as follows:

$$W = \sum_{n=1}^3 \frac{\mu_n}{\alpha_n} (\lambda_1^{\alpha_n} + \lambda_2^{\alpha_n} + \lambda_3^{\alpha_n} - 3) \quad (12)$$

$\lambda_i, i=1..3$ are the principle stretches of the Cauchy-Green strain tensor and α_n and $\mu_n ; n=1..3$ are material's constants to be identified.

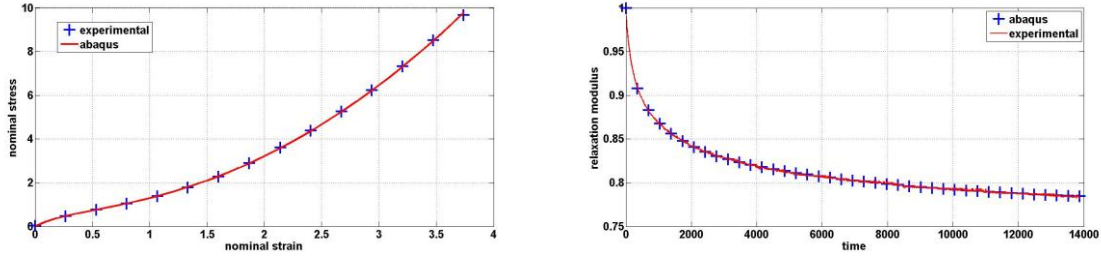


Figure 2: Hyperelastic behavior and relaxation curves

3.2 Identification of reduced time function

In order to satisfy thermodynamic principles via Clausius-Duhem inequality the deformation shift function $a(\underline{\underline{C}})$ should be a nonnegative function of the right Cauchy-Green strain tensor.

Two identification approaches was investigated to determine this function. The first one consists on postulating that this function as a Mooney-Rivlin potential (Equation (13)). Several parameters are then identified using a minimization procedure on the error between experimental and theoretical stress values.

Whereas, the second one consists on expressing the error between theoretical and experimental second Piola-Kirchhoff stresses for pure shear test (15) and simple extension test (14) as a function of the reduced time $\xi(t_i)$ at each experimental time t_i . For a given experimental stress the corresponding reduced time is obtained thanks to a minimization procedure over the absolute error function (equations (14) and (15)) using MATLAB software. Numerical values of the reduced time are obtained for each experimental time. A least square fitting procedure is then used to determine the form of the reduced time function.

$$a(\underline{\underline{C}}) = c_1 (I_1 - 3) + c_2 (I_2 - 3) \quad (13)$$

$$E_{rr}^a(\xi) = \left| \begin{array}{l} \sum_{i=1}^2 \frac{2\mu_i}{\alpha_i} \left(\lambda(\xi)^{-\alpha_i} + \lambda(\xi)^{-\frac{1}{2}\alpha_i-1} \right) + \\ G_0 \int_0^\xi \sum_{i=1}^2 \left(\frac{g_i}{\tau_i} \exp\left(-\frac{\xi - \xi'}{\tau_i}\right) \right) \times \sum_{i=1}^2 \frac{2\mu_i}{\alpha_i} \left(\lambda(\xi')^{-\alpha_i} + \lambda(\xi')^{-\frac{1}{2}\alpha_i-1} \right) d\xi' - S^{\text{exp}} \end{array} \right| \quad (14)$$

$$E_{rr}^a(\xi) = \left| \begin{array}{l} \sum_{i=1}^2 \frac{2\mu_i}{\alpha_i} \left(\lambda(\xi)^{-\alpha_i} + \lambda(\xi)^{-\alpha_i-1} \right) + \\ G_0 \int_0^{\xi} \sum_{i=1}^2 \left(\frac{g_i}{\tau_i} \exp\left(-\frac{\xi - \xi'}{\tau_i}\right) \right) \times \sum_{i=1}^2 \frac{2\mu_i}{\alpha_i} \left(\lambda(\xi')^{-\alpha_i} + \lambda(\xi')^{-\alpha_i-1} \right) d\xi' - S^{\text{exp}} \end{array} \right| \quad (15)$$

4 CONCLUDING REMARKS

In this paper, a nonlinear viscoelastic model for rubber-like materials is presented. It's able to predict the elastomers behavior in the whole range of deformation and for several strain rates. As a first step, a rheological motivation was investigated to build a one dimensional viscoelastic model. Then, a three dimensional model was developed thanks to a combination between two approaches: the functional approach and the internal variable approach. The dependence of the material's properties on the strain was illustrated using a reduced time instead of the real time which is a function of the deformation history.

The identification procedure of several parameters of the model was studied. For the identification of relaxation modulus/hyperelastic potential and reduced time function, experimental data of pure shear and uniaxial extension tests, on a natural rubber NR, was used with a combination of ABAQUS and MATLAB software respectively.

REFERENCES

- [1] R.M Christensen. *Theory of viscoelasticity*. Academic Press, New York, 1982.
- [2] A.C Pipkin. Small finite deformations of viscoelastic solids. *Reviews of modern physics*. : 1034-1041, 1964.
- [3] J.C. Simo. On a fully three-dimensional finite-strain viscoelastic damage model: formulation and computational aspects. *Computer methods in applied engineering* 60 : 153-173, 1987.
- [4] G.A. Holzapfel and J.C. Simo. A new viscoelastic constitutive model for continuous media at finite thermomechanical changes. *International journal of solids and structures* : 33 (20-22) : 3019-3034, 1996
- [5] S. Govindjee and J.C. Simo. Mullins' effect and the strain amplitude dependence of the storage modulus. *International journal of solids and structures* : 29 (14-15): 1737-1751, 1992
- [6] K.C. Valanis. *Irreversible thermodynamics of continuous media, internal variable theory*. Springer, Verlag, Wien, 1972
- [7] R.A. Schapery. An engineering theory of nonlinear viscoelasticity with applications. *International journal of solids and structures*. 2: 407-425, 1966
- [8] N.W. Tschoegl. Time Dependence in Material Properties: An Overview. *Mechanics of Time-Dependent Materials* 6: 53-99, 2002.
- [9] N.W. Tschoegl, W. G. KNAUSS and I. EMRI. The Effect of Temperature and Pressure on the Mechanical Properties of Thermo- and/or Piezorheologically Simple

Polymeric Materials in Thermodynamic Equilibrium-A Critical Review. *Mechanics of Time-Dependent Materials*. 6: 53–99, 2002.

[10] R.A. Schapery. On the characterization of nonlinear viscoelastic materials. *Polymer engineering and science*. 9(4): 295-310, 1969

[11] S. Matsuoka, C. J. Aloisio, and H. E. Bair. Interpretation of shift of relaxation time with deformation in glassy polymers in terms of excess enthalpy. *Journal of Applied Physics*. 44(10): 4265-4268, 1973

[12] P. A. O'CONNELL and G. B. McKFCNNA. Large Deformation Response of Polycarbonate: Time-Temperature Time-Aging Time and Time-Strain Superposition. *Polymer engineering and science*. 37(9): 1485-1495, 1997

[13] R.W. Ogden. Large Deformation Isotropic Elasticity-On the Correlation of Theory and Experiment for Incompressible Rubber-like Solids. *Proceedings of the royal society A*. 326: 565-584, 1972

COPYRIGHT NOTICE

Copyright ©2015 by the authors. Distribution of all material contained in this paper is permitted under the terms of the Creative Commons license Attribution-NonCommercial-NoDerivatives 4.0 International (CC-by-nc-nd 4.0).





A TWO-SCALE APPROACH FOR ASSESSMENT OF THE HONEYCOMB CORE SHEAR EFFECTS ON THE TRANSMISSION LOSS

Z. Zergoune^{1,2*}, M. N. Ichchou¹, O. Bareille¹, B. Harras², and R. Benamar³

¹École Centrale de Lyon / LTDS

36 Avenue Guy de Collongue, 69134 Écully Cedex, France

Email: zergoune.uni@gmail.com, mohamed.ichchou@ec-lyon.fr, olivier.bareille@ec-lyon.fr

²FST de Fès / Laboratoire de Génie mécanique

Route d'Immouzer, BP 2202 Fès, Morocco

Email: harrasbilal@yahoo.fr

³École Mohammadia d'Ingénieurs / Université Mohammed V

BP 765 Agdal, Rabat, Morocco

Email: rhali.benamar@gmail.com

ABSTRACT

The main purpose of the work reported here is to bring out the effects of the different meso-scale parameters of the honeycomb sandwich panel on their vibro-acoustic response using a meso-macro approach. The present approach is developed using a numerical method known as a wave finite element method (WFEM). The WFE method combines the classical finite element method (FEM) and the periodic structure theory (PST). The main advantage of this method is that it takes into consideration the periodicity of the structure, which allows to model typically just one elementary cell instead of the whole structure. Accordingly, the calculations cost is hugely reduced. In addition, this numerical model keeps the meso-scale parameters of the periodic cell. The obtained results are compared with different analytical methods and commercial tool (Ms-NOVA), showing a very good agreement. A vibro-acoustic parametric analysis of the honeycomb panel with composite face-sheets is done. This analysis showed a great influence of the cell size and of the core material on the transmission loss (TL).

1 INTRODUCTION

In the last decade, composite materials are considered as the most successful and the most promising materials to be used in many advanced industrial fields. Aerospace, transportation, and other branches of civil and mechanical engineering are the major beneficiaries of their tremendous growth. Apart from their considerably low ratio of weight to strength, some composites benefit from other desirable properties, such as corrosion and thermal resistance, toughness and low cost. Yet from an acoustic point of view, decreasing the mass, while keeping a high level of stiffness, could have a significant influence on the vibro-acoustic performance of the honeycomb sandwich panel. As a result, this might lead to unsatisfactory noise reduction efficiency.

The prediction of accurate wave dispersion characteristics in a cellular honeycomb core bonded by two laminated orthotropic face-sheets is a key information for computing the vibro-acoustic indicators. Over the last few decades, various analytical methods have been developed to predict the wave dispersion characteristics. Erickson [1] and Clarkson [2] developed methods of estimating the modal density of typical honeycomb sandwich panels with isotropic face-sheets. These methods take into account the effect of shear of the core on the sandwich panel's deflection. Renji et al. [3] introduce the orthotropic bending properties in both directions and include the core's transverse shear stiffness in a new analytical model. However, these analytical methods do not reveal the meso-scale influence on the acoustic transmission of the sandwich structure. Therefore, a numerical method need to be employed.

The numerical method reported here enables to predict the wave propagation characteristics within a sandwich structure which provides a key to decrypt its vibro-acoustical behavior. The method known as WFE combine the classical finite element method and the theory of periodic structures. A vibro-acoustic parametric analysis is then performed on the transmission loss (TL) in order to study the effect of different parameters of the unit cell.

2 OVERVIEW OF THE 2D WFE METHOD

The Wave Finite Element method (WFE method) is applied for predicting the dynamic behavior of a periodic structure. The method includes the reformulation of the equation of motion by using the dynamic stiffness matrix. This matrix involves the mass and stiffness matrices of a periodic cell of the sandwich structure. Structural wave motion of the sandwich structure is expressed in terms of the eigenvalues and the eigenvectors of the dynamic stiffness matrix (DSM) and these eigenvalues and eigenvectors represent the wavenumbers and the wave modes respectively.

The equation of motion for periodic structural waveguides can be expressed as follows

$$D \begin{pmatrix} U_{bd} \\ U_I \end{pmatrix} = \begin{pmatrix} f_{bd} \\ 0 \end{pmatrix}. \quad (1)$$

Where $D = (1 + j\eta) K - \omega^2 M$ is the dynamic stiffness matrix which is obtained from the stiffness and the mass matrices extracted by using a finite element method package like Ansys. U_{bd} and f_{bd} are respectively the displacement and the force of the boundary nodes. While U_I represents the internal nodes.

Using the Floquet-Bloch theory for a periodic rectangular cell and assuming a time-harmonic response, the displacements of each edge can be written as a function of the displace-

ments at one single edge.

$$\Lambda_L(\lambda_x, \lambda_y) D \Lambda_R(\lambda_x, \lambda_y) \begin{pmatrix} U_1 \\ U_L \\ U_B \end{pmatrix} = 0. \quad (2)$$

By introducing the matrices $\Lambda_L(\lambda_x, \lambda_y)$ and $\Lambda_R(\lambda_x, \lambda_y)$ in the equation (1) a polynomial equation of second-order obtained as written in the equation (3)

$$\frac{1}{\lambda_x^2} (A\lambda_x^2 + B\lambda_x + C) \begin{pmatrix} U_1 \\ U_L \\ U_B \end{pmatrix} = 0. \quad (3)$$

Where $\lambda_x = e^{i\mu_x}$, $\lambda_y = e^{i\mu_y}$ and $\mu_x = k_x L_x$, $\mu_y = k_y L_y$ are the propagation constants of a plane harmonic wave in both x- and y-direction respectively. While k_x, k_y are the wavenumbers along the x- and y-direction respectively.

The sound transmission through an infinite sandwich panel can be calculated by knowing the dispersion curve of the bending wave through the plate. For a flat plate impacted by an acoustic plane wave incidence α and ϕ direction, the acoustic transparency is defined as the ratio of transmitted power through the plate to the incident power. It can be calculated as follows:

$$\tau(\alpha, \phi) = \left\{ \left[1 + \eta \frac{\omega m \cos \alpha}{2\rho_0 c_0} \frac{k_0^4 \sin^4 \alpha}{k_{eq,\phi}^4} \right]^2 + \left[\frac{\omega m \cos \alpha}{2\rho_0 c_0} \left(1 - \frac{k_0^4 \sin^4 \alpha}{k_{eq,\phi}^4} \right) \right]^2 \right\}^{-1}. \quad (4)$$

Where the equivalent wavenumber in the equation (4) is written as follows :

$$\frac{1}{k_{eq,\phi}^2} = \frac{\sin^2 \phi}{k_{Bx}^2} + \frac{\cos^2 \phi}{k_{By}^2}. \quad (5)$$

The acoustic transparency diffuse field is calculated by averaging all the possible incidents and directions.

$$\tau = \frac{\int_0^{2\pi} \int_0^{\pi/2} \tau(\alpha, \phi) \sin \alpha \cos \alpha \, d\alpha \, d\phi}{\int_0^{2\pi} \int_0^{\pi/2} \sin \alpha \cos \alpha \, d\alpha \, d\phi}. \quad (6)$$

Finally, the sound transmission loss is given by the following expression :

$$TL = 10 \log\left(\frac{1}{\tau}\right). \quad (7)$$

The parameters to be studied in this vibro-acoustic parametric analysis are the young modulus of the core E , the cell angle θ (the angle between horizontal cell wall and inclined cell wall), the thickness of the walls t , the thickness of the core h_c , and finally the cell size l and h of the periodic cell (see figure 1).

3 RESULTS

A periodic segment of a honeycomb sandwich panel with orthotropic face-sheets is considered hereby (see figure 1) with L_x, L_y its surface's dimensions and $h_t = h_c + h_f$ its total thickness. The geometrical and material properties of the periodic segment were summarized in Table 1. The vibro-acoustic study is performed in a frequency range between 0 Hz and 5000 Hz.

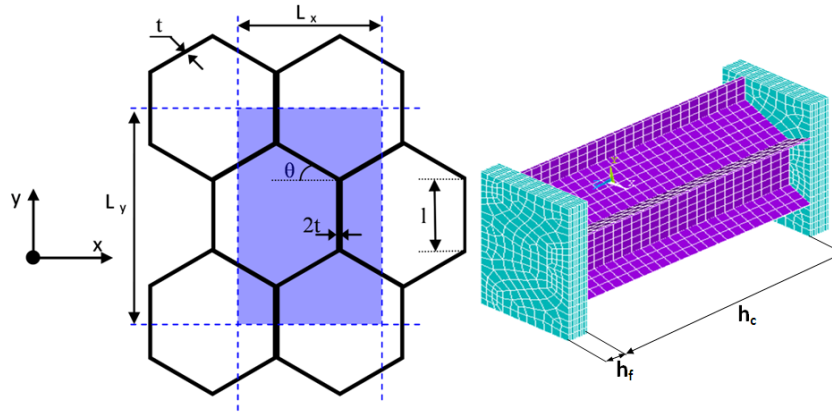


Figure 1. Cell geometrical parameters of the periodic hexagonal cell.

	Core (Nomex material)	Skins (Epoxy resin with carbon yarn)
Material	$E = 5.5 \text{ GPa}$ $\rho = 1240 \text{ kg/m}^3$ $G = 2.07 \text{ GPa}$ $\mu = 0.33$	$E_1 = 133.6 \text{ GPa}$ $E_2 = 7.7 \text{ GPa}$ $E_3 = 7.7 \text{ GPa}$ $G_{12} = 3.1 \text{ GPa}$ $\mu_{12} = \mu_{13} = 0.29$
Geometry	$h_c = 12 \text{ mm}$ $t = 76.2 \mu\text{m}$ $l = h = 2.7 \text{ mm}$ $\theta = 30^\circ$	$h_f = 1 \text{ mm}$ $[0, 45, 90, -45]_s$ $e_{UD} = 125 \mu\text{m}$

Table 1. The material and geometrical parameters of the periodic cell.

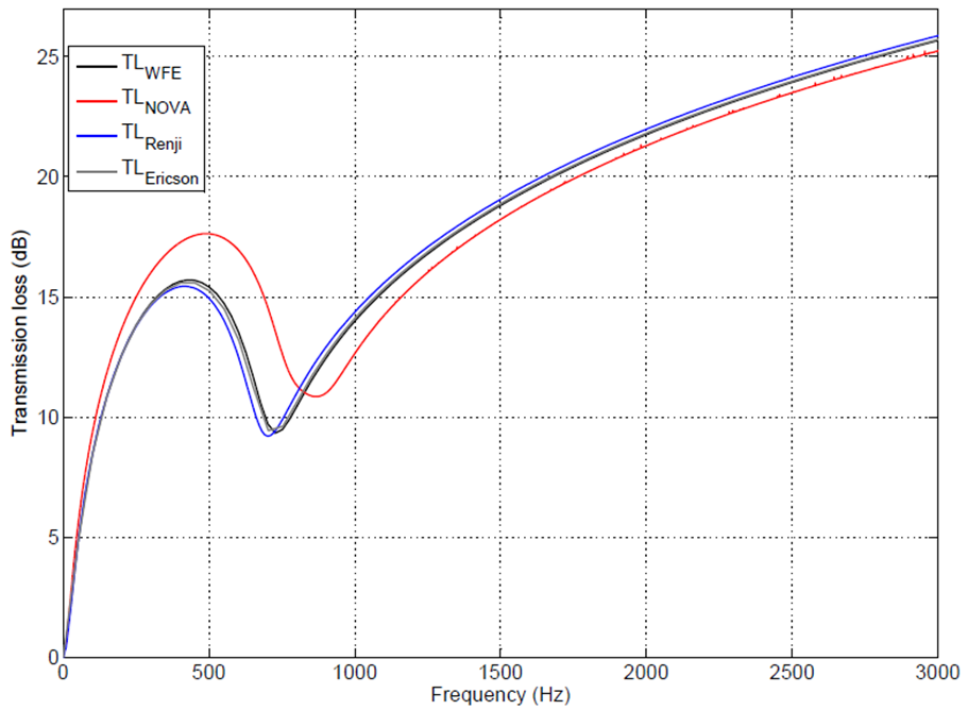


Figure 2. Comparisons of different analytical and numerical models in terms of TL.

Figure 2 present the comparison of the current model with analytical models and commercial tool (Ms-Nova). The comparison of the meso-macro approach with the analytical model shows a good agreement either in the critical frequency or in the rest of the frequency range. However, the comparison with commercial tool exhibits a slight difference, these initial comparisons allow us to validate the present model.

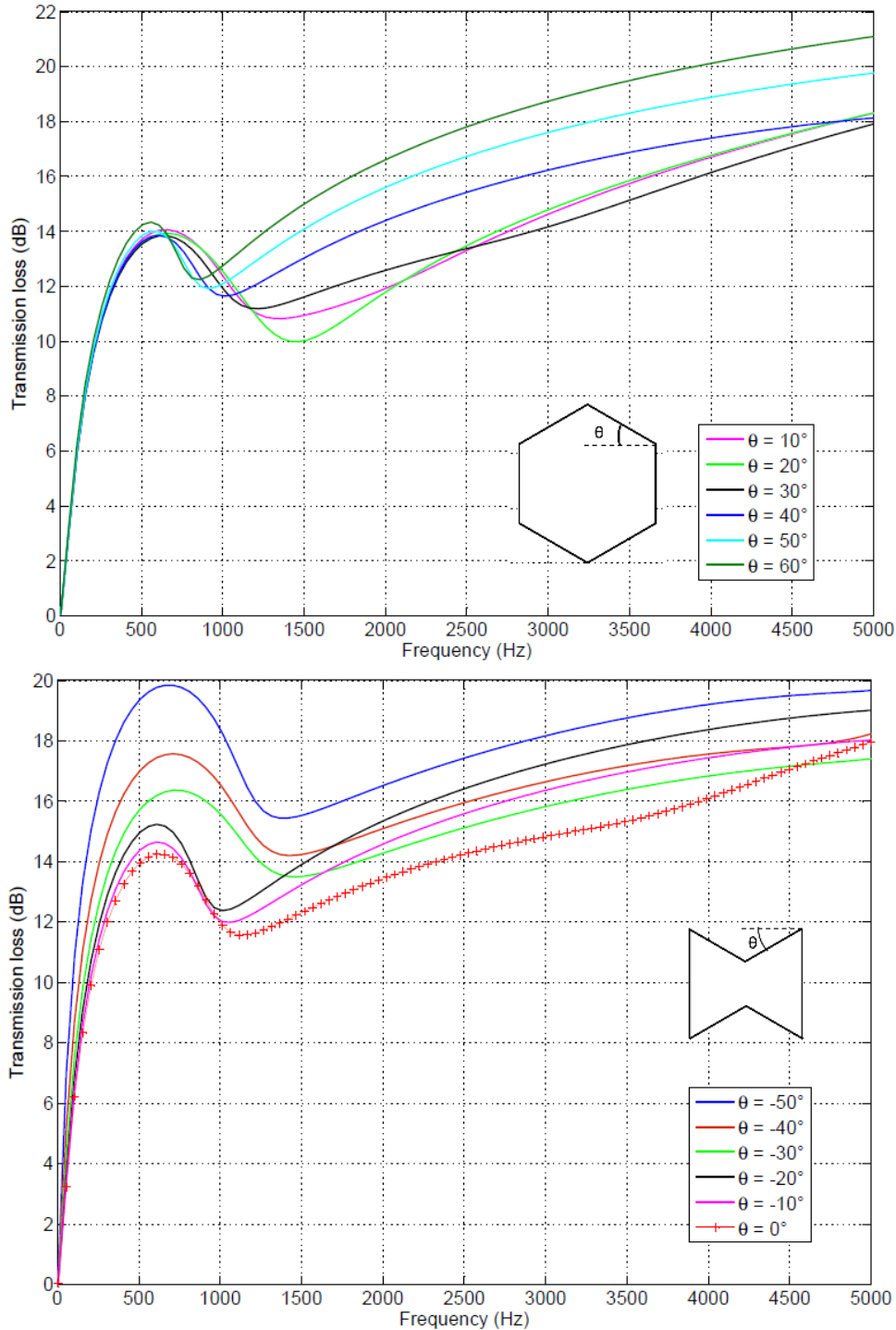


Figure 3. Effect of the cell angle θ on the transmission loss.

The parametric study on the cell angle θ presented in Figure 3 indicates that the cell angle θ generally influences on the sound transmission loss (TL) whether in the low, medium

or high frequency ranges. On the one hand, with the positive cell angle θ , the more the angle increases the more the critical frequency decreases and the sound transmission loss is enhanced throughout the whole frequency band. On the other hand, for the negative cell angle θ , the more the angle decreases the more the sound transmission loss rises as well as the critical frequency is shifted.

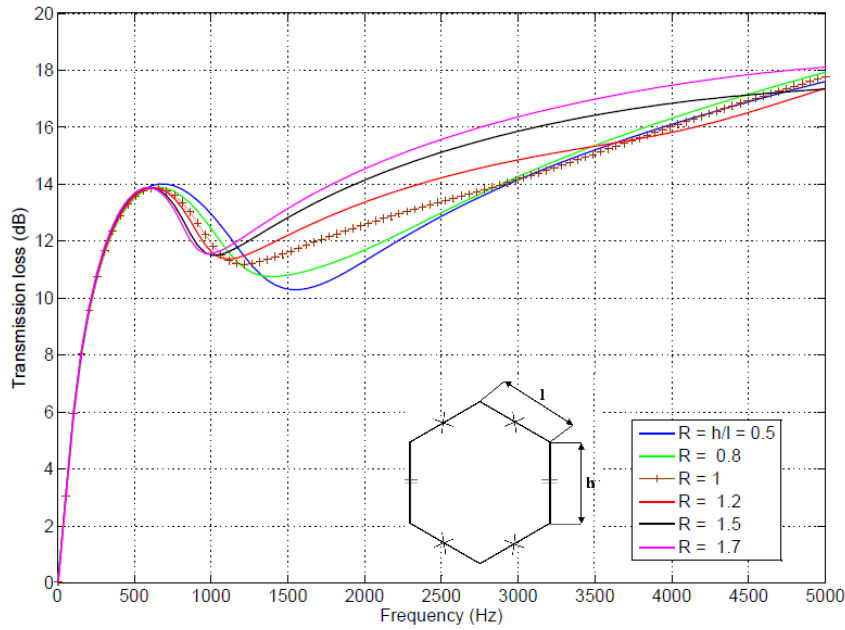


Figure 4. Effect of cell size h and l on the transmission loss.

Figure 4 exhibits the comparison of the different curves of the sound transmission loss while varying the cell size (h and l). The comparison showed that the more the parameter h increases the more the sound transmission loss improves. However, the critical frequency of the sandwich panel decreases.

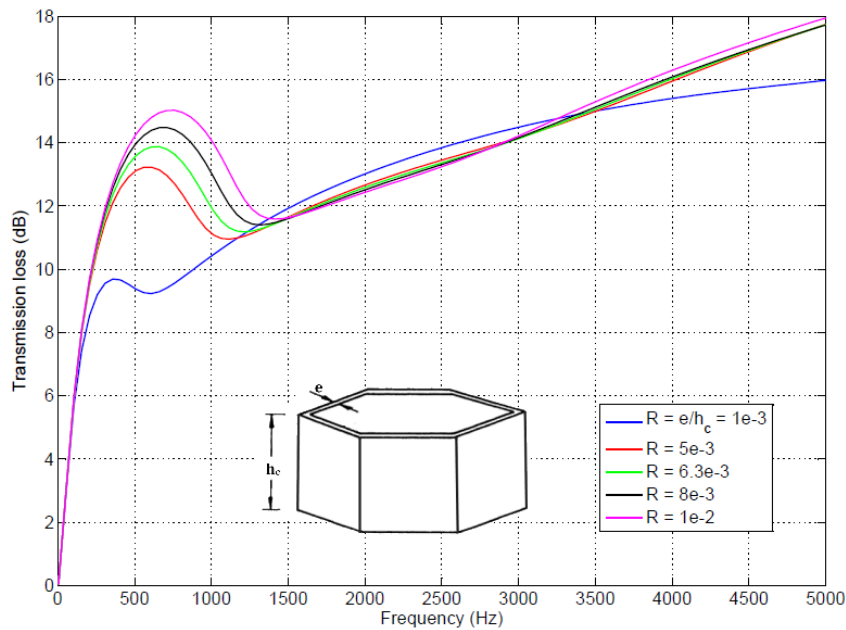


Figure 5: Effect of the thickness of the core h_c and the thickness of the walls e on the transmission loss.

The comparison performed in Figure 5 by changing the ratio of e/h_c , shows that the more the thickness of the core's sandwich panel h_c decreases and the thickness of the walls of the periodic cell e increases, the more the sound transmission loss enhances and the critical frequency shifts.

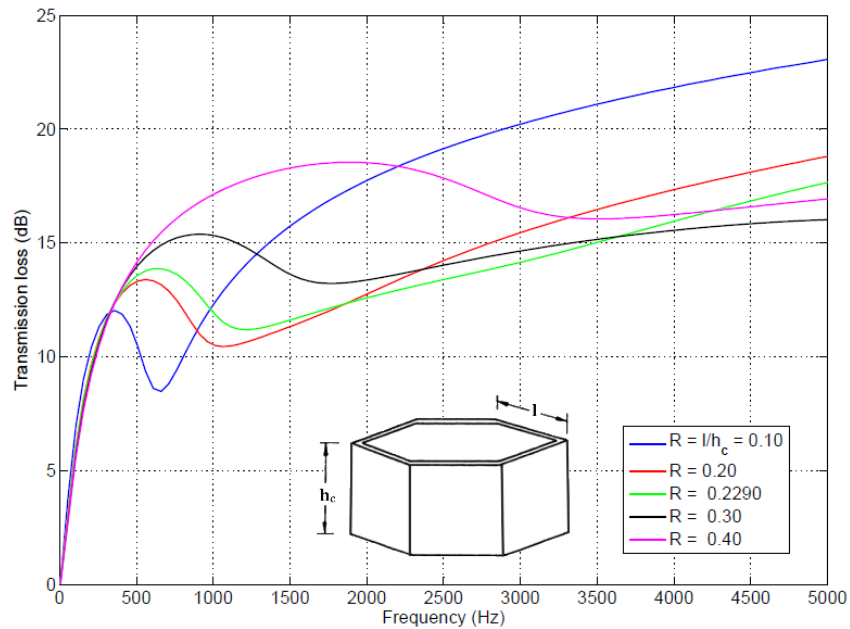


Figure 6. Effect of the cell size l and the thickness of the core h_c on the transmission loss.

The next comparison is carried out between the thickness of the core's sandwich panel h_c and the cell size l . Figure 6 shows that the more the cell size l increases with respect to the thickness h_c the more the critical frequency increases until the transmission loss curve becomes smooth. However, the sound transmission loss curve decreases in the different frequency range.

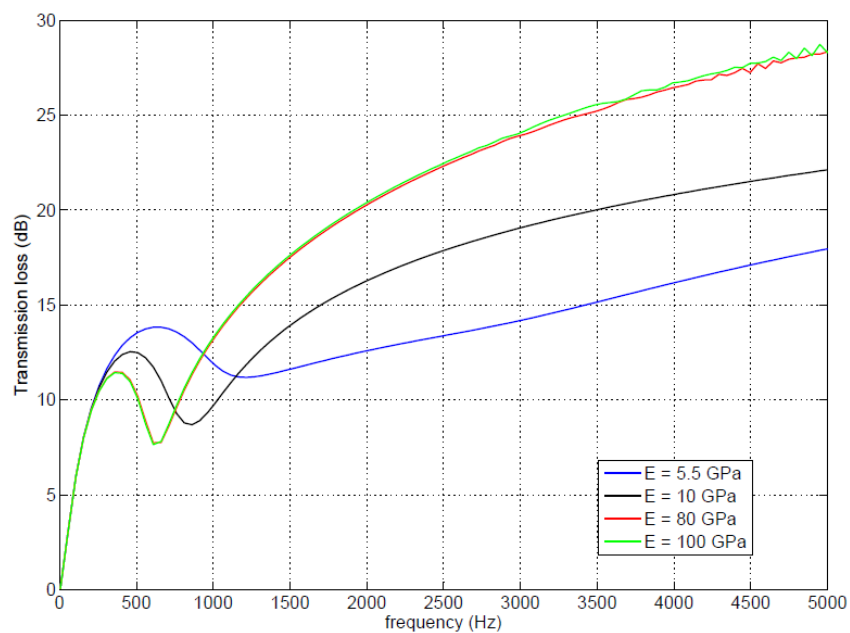


Figure 7. Effect of the young modulus E of the core on the transmission loss.

In Figure 7, a comparison of the sound transmission loss (TL) with respect to the young modulus E of the core is presented. The comparison exhibits that the more the young modulus E increases the more the sound transmission loss enhances up to a certain value at which the sound transmission loss curve will not increase. However, the critical frequency decreases when the young modulus increases.

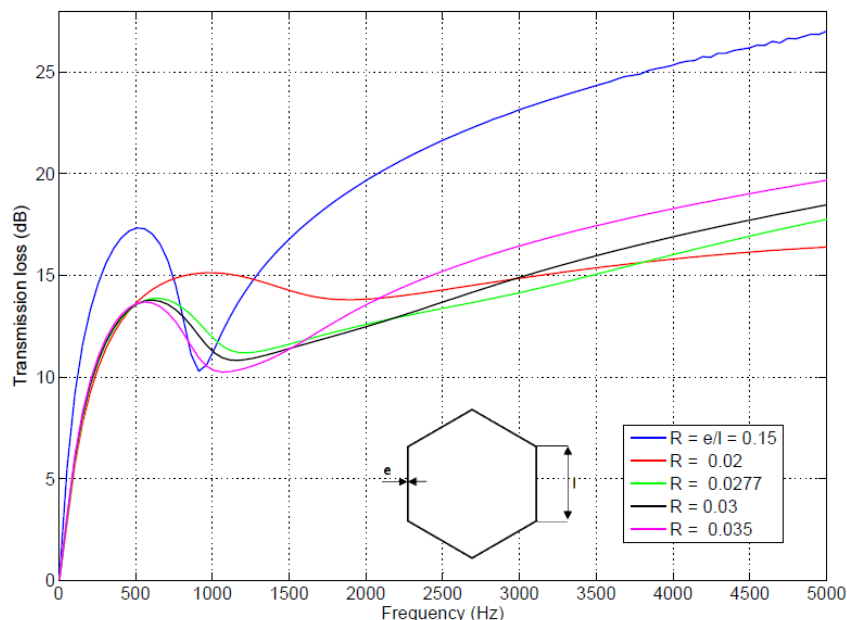


Figure 8. Effect of the cell size l and the thickness of the walls e on the transmission loss.

In Figure 8, a parametric study of the ratio e/l the walls' thickness e with respect to the cell size l is presented. The study indicates that the more the walls' thickness of the cell increases the more the critical frequency shifts until the curve becomes smooth. However, The sound transmission loss curve decreases when the ratio e/l increases.

4 CONCLUSION

The presented vibro-acoustic parametric analysis used the meso-macro approach, based on the wave finite element method (WFE), showed clearly that the geometrical and material properties of the periodic unit cell of the panel has a significant influence on the sound transmission loss (TL) as well as on the shifting of the critical frequency. In the present vibro-acoustic study, when changing two parameters at the same time, the criteria was to maintain the mass constant. Subsequently, This vibro-acoustic parametric analysis will facilitate the next step which is the optimization study. This later will permit to define the optimal design parameters of the honeycomb sandwich panel.

REFERENCES

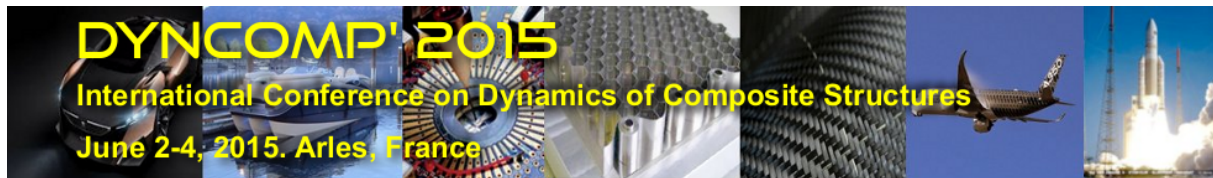
- [1] Erickson L. L. Modal density estimates for sandwich panels: theory and experiment. NASA technical note D-5771, September 1970.
- [2] Clarkson B. L. and Ranky M. F. Modal density of honeycomb plates. *Journal of Sound and Vibration*, 91(1):103–118, 1983.

- [3] Renji K. Sound transmission loss of unbounded panels in bending vibration considering transverse shear deformation. *Journal of Sound and Vibration*, 283:478–486, 2005.

COPYRIGHT NOTICE

Copyright ©2015 by the authors. Distribution of all material contained in this paper is permitted under the terms of the Creative Commons license Attribution-NonCommercial-NoDerivatives 4.0 International (CC-by-nc-nd 4.0).





THE SOUND TRANSMISSION LOSS USING THE STOCHASTIC WAVE FINITE ELEMENT METHOD

M. A. BEN SOUF^{1,3*}, D. Chronopoulos², M. N. ICHCHOU¹, O. BAREILLE¹ and M. HADDAR³

¹Laboratoire de Tribologie et de Dynamique des Systemes
École Centrale de Lyon, Ecully, FRANCE
Email: bensouf.mohamedamine@gmail.com

²Division of Mechanics, Materials and Structures, The University of Nottingham, University Park, Nottingham, NG7 2RD, United Kingdom

³Laboratoire de recherche de Mécanique, Modelisation et Productique
École Nationale d'Ingénieur de Sfax, TUNISIA

ABSTRACT

Anisotropic and sandwich structures are used in many engineering areas such as aerospace and automotive constructions. These types of structures are often used because of their high stiffness to mass ratios. However these structures oftentimes present a compromise between their mechanical and vibro-acoustic behaviour. The vibro-acoustic study for the anisotropic and sandwich structures is well developed during the last years.

There are many methods which allow the computation of the wavenumbers for isotropic and anisotropic structures. Analytical formulas exist to calculate the wavenumbers of anisotropic plates based on the Classical Laminate Plate Theory. To take into account shear deformation, Whitney suggested the formulation of the First-order Shear Deformation Theory (FSDT). A model for an infinite sandwich panel by including the description of symmetric and antisymmetric motions was developed. Leppington expressed the radiation efficiency of a rectangular panel as well as the vibroacoustic response under a reverberant field of thin orthotropic panels.

To deal with the wave characteristics in periodic structures, the Wave Finite Element Method (WFEM) is used. This spectral formulation is a result of a coupling between the conventional finite element method and the periodic structure theory. Its formulation starts with the discretization of the studied structure. An eigenvalue problem is then formulated using the periodicity of the structure. The general theory of the WFE is proposed by Mead and was improved by Zhong and Williams. This approach is then used for predicting the acoustic behavior of anisotropic plates. It investigates the evolution of radiation efficiency and sound transmission loss with frequency.

In all presented formulations, the input parameters are deterministic. However for layered structures, there is a high variability of mechanical parameters. The main novelty of this paper is investigating the effects of the uncertain mechanical parameters on the acoustic behaviour of anisotropic structures, especially in mid- and high frequencies.

This paper discusses the effect of uncertain parameters on vibro-acoustic behavior, especially on the Sound Transmission Loss (STL) of composite panels. The formulation presented is hybridization between spectral, energetic and uncertain methods. The Uncertain inputs parameters are represented using a parametric probabilistic approach which allows for the separation between the deterministic and the stochastic components in the process.

The second order stochastic parameters are developed using the generalized polynomial chaos expansion. In order to evaluate the outputs, there are two different methods: intrusive and non-intrusive methods. The efficiency of the approach is exhibited for isotropic panels.

1 INTRODUCTION

Anisotropic and sandwich structures are used in many engineering areas such as aerospace and automotive constructions. To deal with this type of structures in high frequencies, the Statistical Energy Analysis (SEA) is often used to predict the dynamic behavior of structures. The SEA method is based on the calculation of the energy quantities exchanged between the sub-systems. In the case of structural wave modelling, waves represent SEA subsystems, and the use of the SEA consist on evaluating the energy exchange between waves. Before using an SEA approach, the identification of the propagating waves is first investigated to obtain the spectrum of the wave dispersion characteristics. There are many methods which allow the computation of the wavenumbers for isotropic and anisotropic structures. Analytical formulas exist for the calculation of wavenumbers of anisotropic plates based on the Classical Laminate Plate Theory [1]. To take into account shear deformation, Whitney *et al.* [2] suggested the formulation of the First-order Shear Deformation Theory (FSDT). Dym and Lang [3] developed a model for an infinite sandwich panel by including the description of symmetric and antisymmetric motions. A Higher-order Shear Deformation Theory (HSDT), initially conceived in [4] is applied in [5] for expressing the vibroacoustic response of a structure within an SEA context. Leppington *et al.*[6] expressed the radiation efficiency of a rectangular panel as well as the vibroacoustic response under a reverberant field [7] of thin orthotropic panels.

This paper discusses the effect of uncertain parameters on vibro-acoustic behavior of composite panels. The formulation presented is a hybridization between spectral, energetic and uncertain methods. The Uncertain inputs parameters are represented using a parametric probabilistic approach which allows for the separation between the deterministic and the stochastic components in the process. The second order stochastic parameters are developed using the generalized polynomial chaos expansion. In order to evaluate the outputs, there are two different methods: intrusive and non-intrusive methods. The first one consists in projecting the process using a Galerkin approach to obtain a set of deterministic equations instead of the stochastic one. The second method is based on simulations of the deterministic model before an adequate post-processing to evaluate the uncertainty of the output parameters. In this paper, different methods are presented and discussed.

2 WAVE BASED PREDICTION OF THE VIBROACOUSTIC PERFORMANCE FOR A COMPOSITE STRUCTURE

2.1 Wave propagation analysis by a 2D Finite Element method

A rectangular periodic composite panel composed by N identical sub-structures is considered. The dimensions of the panel are : L_x , L_y and h its thickness(see fig.1). Using the conventional finite element method, a single periodic segment of the composite panel is modeled and the mass and stiffness matrices are extracted

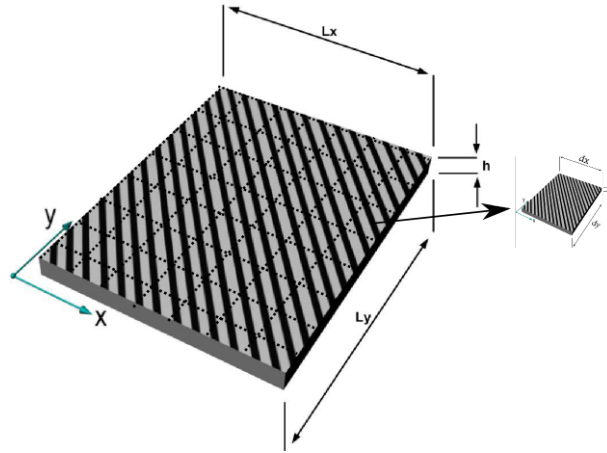


Figure 1. A periodic composite panel

The entries for each Degree of Freedom (DoF), of the nodes laying on the same edge of the segment, say edges Q, R, S and T, are organized in the mass and stiffness matrices so that the displacements can be written as: $\mathbf{u} = \{\mathbf{u}_Q \ \mathbf{u}_R \ \mathbf{u}_S \ \mathbf{u}_T\}^T$. Following the analysis presented in [8] the time-harmonic equation of motion of the segment assuming uniform and structural damping can be written as:

$$(\mathbf{K} (1 + \eta i) - \omega^2 \mathbf{M}) \mathbf{u} = \mathbf{F} \tag{1}$$

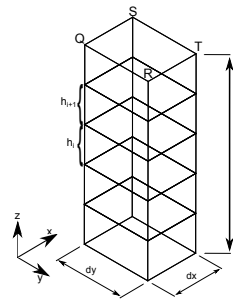


Figure 2. View of the modeled periodic segment with its edges Q, R, S and T

where η is the structural damping coefficient, ω is the angular frequency and \mathbf{F} the vector of the nodal forces. The dynamic stiffness matrix can be written as :

$$\mathbf{D} = \mathbf{K} (1 + \eta i) - \omega^2 \mathbf{M} \tag{2}$$

therefore equation (1) may be written as:

$$\begin{bmatrix} \mathbf{D}_{QQ} & \mathbf{D}_{QR} & \mathbf{D}_{QS} & \mathbf{D}_{QT} \\ \mathbf{D}_{RQ} & \mathbf{D}_{RR} & \mathbf{D}_{RS} & \mathbf{D}_{RT} \\ \mathbf{D}_{SQ} & \mathbf{D}_{SR} & \mathbf{D}_{SS} & \mathbf{D}_{ST} \\ \mathbf{D}_{TQ} & \mathbf{D}_{TR} & \mathbf{D}_{TS} & \mathbf{D}_{TT} \end{bmatrix} \begin{Bmatrix} \mathbf{u}_Q \\ \mathbf{u}_R \\ \mathbf{u}_S \\ \mathbf{u}_T \end{Bmatrix} = \begin{Bmatrix} \mathbf{F}_Q \\ \mathbf{F}_R \\ \mathbf{F}_S \\ \mathbf{F}_T \end{Bmatrix} \tag{3}$$

Using periodic structure theory for the modelled segment and assuming a time-harmonic response the displacements of each edge can be written as a function of the displacements at one single edge. Taking edge Q as the edge of reference we have:

$$\mathbf{u}_R = \lambda_x \mathbf{u}_Q, \ \mathbf{u}_S = \lambda_y \mathbf{u}_Q, \ \mathbf{u}_T = \lambda_x \lambda_y \mathbf{u}_Q \tag{4}$$

Using the same theory, the force vectors can be written as:

$$\mathbf{F}_R = \lambda_x \mathbf{F}_Q, \mathbf{F}_S = \lambda_y \mathbf{F}_Q, \mathbf{F}_T = \lambda_x \lambda_y \mathbf{F}_Q \quad (5)$$

With λ_x and λ_y the phase constants which are related to the wavenumbers k_x and k_y through the relation:

$$\lambda_x = e^{-ik_x d_x}, \lambda_y = e^{-ik_y d_y} \quad (6)$$

The displacement vector can therefore be written as:

$$\begin{Bmatrix} \mathbf{u}_Q \\ \mathbf{u}_R \\ \mathbf{u}_S \\ \mathbf{u}_T \end{Bmatrix} = \begin{Bmatrix} \mathbf{I} \\ \lambda_x \mathbf{I} \\ \lambda_y \mathbf{I} \\ \lambda_x \lambda_y \mathbf{I} \end{Bmatrix} \mathbf{u}_Q \quad (7)$$

Assuming no external excitation, the equilibrium conditions along edge Q implies that:

$$\left\{ \mathbf{I} \quad \lambda_y^{-1} \mathbf{I} \quad \lambda_x^{-1} \mathbf{I} \quad \lambda_x^{-1} \lambda_y^{-1} \mathbf{I} \right\} \begin{Bmatrix} \mathbf{F}_Q \\ \mathbf{F}_R \\ \mathbf{F}_S \\ \mathbf{F}_T \end{Bmatrix} = 0 \quad (8)$$

Eventually, substituting equation (7), (8) in equation (1) we end up with the eigenproblem:

$$\left\{ \mathbf{I} \quad \lambda_y^{-1} \mathbf{I} \quad \lambda_x^{-1} \mathbf{I} \quad \lambda_x^{-1} \lambda_y^{-1} \mathbf{I} \right\} \mathbf{D} \begin{Bmatrix} \mathbf{I} \\ \lambda_x \mathbf{I} \\ \lambda_y \mathbf{I} \\ \lambda_x \lambda_y \mathbf{I} \end{Bmatrix} \mathbf{u}_Q = 0 \quad (9)$$

2.2 Calculation of the modal density

Using the Courant's formula [9], the modal density of each propagating wave type w can be written for each angle ϕ as a function of the propagating wavenumber (obtained by the WFE 2D 2.1) and its corresponding group velocity c_g :

$$n_w(\omega, \phi) = \frac{A k_w(\omega, \phi)}{2\pi^2 |c_{g,w}(\omega, \phi)|} \quad (10)$$

where A is the area of the panel and the group velocity is expressed as:

$$c_g(\omega, \phi) = \frac{d\omega}{dk(\omega, \phi)} \quad (11)$$

The averaged modal density of the structure is eventually given as:

$$n_w(\omega) = \int_0^\pi n_w(\omega, \phi) d\phi \quad (12)$$

2.3 Calculation of the radiation efficiency

In order to calculate the radiation efficiency $\sigma(k(\omega))$ for each propagating wave type, the set of asymptotic formulas given in [6] can be used in order to compute $\sigma(k(\omega))$. Within an SEA context, energy equipartition amongst the resonant modes is assumed so that the radiation efficiency is expressed as:

$$\sigma_{rad}(\omega) = \frac{1}{n(\omega)} \int_0^\pi \sigma(k(\omega, \phi)) n(\omega, \phi) d\phi \quad (13)$$

For a periodic discontinuous structure assuming sinusoidal mode shapes is no longer valid; therefore the radiation efficiency should be computed directly from the WFEM derived wave mode shapes. The radiation efficiency expression given in [10] can be employed for this purpose.

3 EMPLOYING THE GENERALIZED POLYNOMIAL CHAOS EXPANSION (GPCE) WITHIN THE VIBROACOUSTIC RESPONSE MODELLING

The polynomial chaos expansion is an efficient tool for describing uncertainty propagation in mechanical systems. It consist on separating between the stochastic components of a random function and its deterministic components. This theory, developed by Wiener [11], helps to expand any second order process u (with finite variance) in a series of orthogonal polynomials as:

$$u = u_0 H_0 + \sum_{i_1=1}^{\infty} u_{i_1} H_1(\xi_{i_1}) + \sum_{i_1=1}^{\infty} \sum_{i_2=1}^{i_1} u_{i_1 i_2} H_2(\xi_{i_1}, \xi_{i_2}) + \sum_{i_1=1}^{\infty} \sum_{i_2=1}^{i_1} \sum_{i_3=1}^{i_2} u_{i_1 i_2 i_3} H_3(\xi_{i_1}, \xi_{i_2}, \xi_{i_3}) + \dots \quad (14)$$

where $H_p(\xi_{i_1}, \dots, \xi_{i_p})$ represents orthogonal polynomial (chaos polynomials) of order p . In practice, the polynomial chaos expansion is truncated to a finite number of terms. In a compact form, equation (14) can be expressed as:

$$u \approx \sum_{i=0}^P u_i \Psi_i(\xi) \quad , \quad G = \sum_{k=0}^p C_{M+k-1}^k = \frac{(M+p)!}{M!p!} \quad (15)$$

where $\xi = [\xi_{i_1}, \dots, \xi_{i_p}]^T$, and M denoting the number of the uncertain parameters.

Since in most applications the stochastic input variables are not normal, Xiu and Karniadakis [12] proposed a generalized form of Hermite polynomial chaos expansion using other orthogonal polynomials in terms of non-Gaussian random variables called wiener-askey. Table 1 resumes usual random variables and their orthogonal polynomials.

	Random variable ξ	Winer-Askey chaos $\Psi(\xi)$	Support
Continue distributions	Gaussian	Hermite	$(-\infty, +\infty)$
	Uniform	Legendre	$[a, b]$
	Gamma	Laguerre	$[0, \infty)$
	Beta	Jacobi	$[a, b]$
Discrete distribution	Poisson	Charlier	$\{0, 1, \dots, \}$
	binomial	Krawtchouk	$\{0, 1, \dots, N\}$

Table 1: Correspondence between the choice of polynomial and given distribution of usual random variables

When the input parameters have not a non-Gaussian behavior, the parametrization of the problem is quite difficult. Rosenblatt [13] proposed a simple transformation of non-Gaussian distributions to Gaussian ones. Some analytical transformations are mentioned in the following table:

Distribution	Transformation
Uniform (a, b)	$a + (b - a) (0.5 + 0.5 \operatorname{erf}(\xi/\sqrt{2}))$
Normal (μ, σ)	$\mu + \sigma \xi$
Lognormal (μ, σ)	$\exp(\mu + \sigma \xi)$
Gamma (a, b)	$ab \left(\xi \sqrt{\frac{1}{9a} + 1 - \frac{1}{9a}} \right)^3$
Exponential (λ)	$-\frac{1}{\lambda} \log \left(\frac{1}{2} + \frac{1}{2} \operatorname{erf}(\xi/\sqrt{2}) \right)$

Table 2. Random variables and their transformations

$$\text{with } \operatorname{erf}(x) = \frac{2}{\sqrt{\pi}} \int_0^x e^{-t^2} dt.$$

4 NUMERICAL VALIDATIONS

This section deals with numerical validations of the proposed formulation. As presented above, the formulation is a hybridization of an energy based approach, the wave finite element method and a parametric probabilistic approach. The objective of the approach is identifying the effects of uncertain parameters on the acoustic and vibro-acoustic behaviour of panels.

4.1 Isotropic honeycomb panel

In order to validate the suggested models, the first case study is evaluating the acoustic parameters for an isotropic honeycomb panel. The mechanical properties of facesheets and the core are mentioned in Table 3:

	E (Pa)	ρ (kg/m ³)	thickness (m)	Poisson's ratio	Structural damping
Facesheets	$49 \cdot 10^9$	1600	$5 \cdot 10^{-4}$	0.15	1 %
Core	$1.951 \cdot 10^8$	160	$6.3 \cdot 10^{-3}$	0.15	1 %

Table 3. Mechanical characteristics of facesheets and the core for the isotropic panel

The structure dimensions are : $L_x = 0.84$ m and $L_y = 0.42$ m. Regarding the periodicity of the panel, only one periodic segment with $d_x = 0.02$ (m) and $d_y = 0.005$ (m) is discretized using the conventional finite element method. The mass and stiffness matrices are then extracted in order to formulate the polynomial eigenvalue problem exhibited above. Knowing that the structure is an isotropic one, suggests that the wave properties are the same in all propagation directions in the structure. Therefore solving the eigenproblem for only one direction of propagation will suffice for capturing the entirety of the wave propagation data for the panel.

In order to apply the stochastic process, the mechanical parameters are assumed to be uncertain with different evolution. Table 4 summarizes the different stochastic parameters and their distributions. The choice of the Lognormal distribution is used regarding the positivity of the uncertain parameters.

Random variables	Type of distribution	Mean	Standard deviation
Young modulus of facesheets (Pa)	Lognormal	$49 \cdot 10^9$	5%
Density of facesheets (kg m^{-3})	Lognormal	1600	5%
Young modulus of core (Pa)	Lognormal	$1.951 \cdot 10^8$	10%
Density of core (kg m^{-3})	Lognormal	160	10%
Damping	Uniform	0.01	5%

Table 4. Random variables

In this stochastic calculations step, the isoprobabilistic transformations are used to move from a non-Gaussian distribution to a Gaussian one. Then, the Latin Hypercube Sampling is performed to apply the stochastic process with lower computation effort.

The wavenumber values for the first flexural wave of the isotropic sandwich structure are presented in Fig.3. In the same figure the envelope representing the min-max wavenumber due to the input stochastic parameters, as well as the standard deviation of the wavenumber values are also exhibited. It should be noted that the out of plane structural motion of the flexural wave is responsible for transmitting the vast majority of acoustic energy, therefore this will be the main wave type taken into account during the subsequent analysis. It is observed that the effect of parametric uncertainties on the flexural wavenumber is small for low frequencies (< 1000 Hz) with a maximum deviation of approximately 1.5%. With an increasing frequency the effect of the structural parametric uncertainties on the wavenumber becomes more evident, with the maximum deviation from the mean value being equal to 13.4% at the highest frequency of the analysis (10 kHz). Considering the standard deviation of the flexural wavenumber values a piece-wise linearity is observed. The first low frequency region is observed up to frequencies of 1000 Hz while for higher frequencies a second linear region of a higher gradient is exhibited. With regard to both the results of the wavenumber as well as its standard deviation values an excellent agreement is observed between the presented approach and the Monte Carlo simulation results. It is noted that 4000 samples were considered during the Monte Carlo simulation.

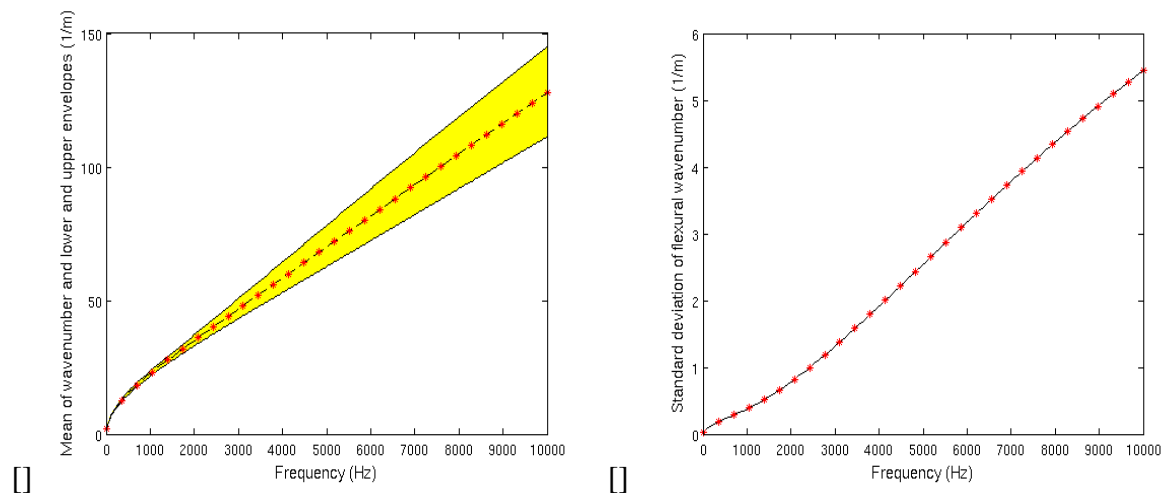


Figure 3: Wavenumber : (a) mean and min-max envelop, (b) Standard deviation, (-) WFE-Chaos, (*) Monte Carlo

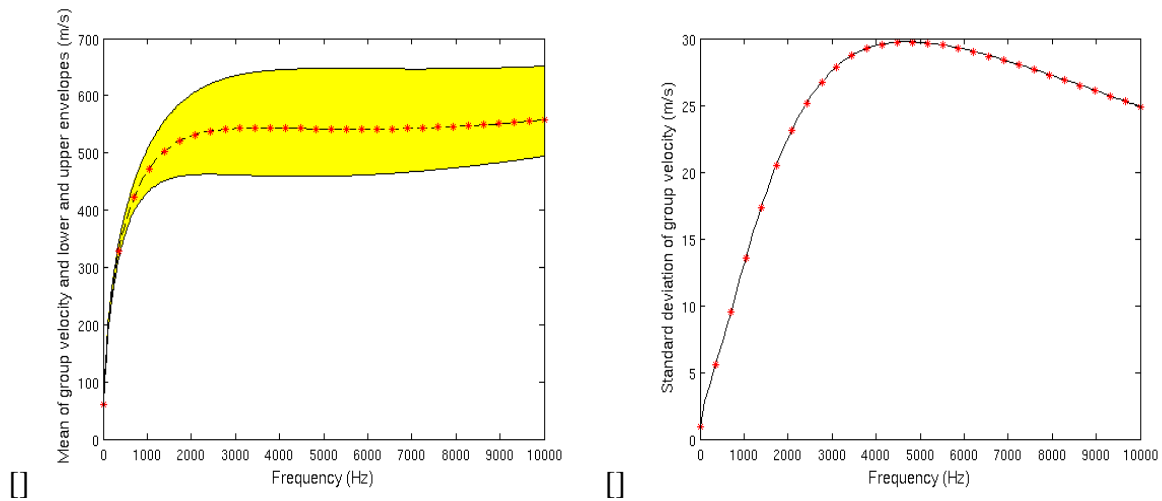


Figure 4: Group velocity : (a) mean and min-max envelop, (b) Standard deviation, (-) WFE-Chaos, (*) Monte Carlo

The group velocity results for the first flexural wave of the isotropic sandwich structure are presented in Fig.4. In the same figure the envelope representing the min-max group velocity values due to the input stochastic parameters, as well as the standard deviation of the group velocity are also presented. As with the wavenumber results it can be observed that for low frequencies (< 800 Hz) the impact of parametric uncertainties on the group velocity values of the flexural wavenumber is insignificant. For higher frequencies the effect of the structural parametric uncertainties on the group velocity results becomes important, with the maximum deviation from the mean value being equal to 19.2% at 5 kHz. With regard to the standard deviation of the flexural wavenumber group velocity it can be observed that it increases up to a certain frequency where it attains a maximum value; that is at approximately 5000 Hz. Again, as with the wavenumber results an excellent agreement is observed between the exhibited approach and the Monte Carlo simulation results.

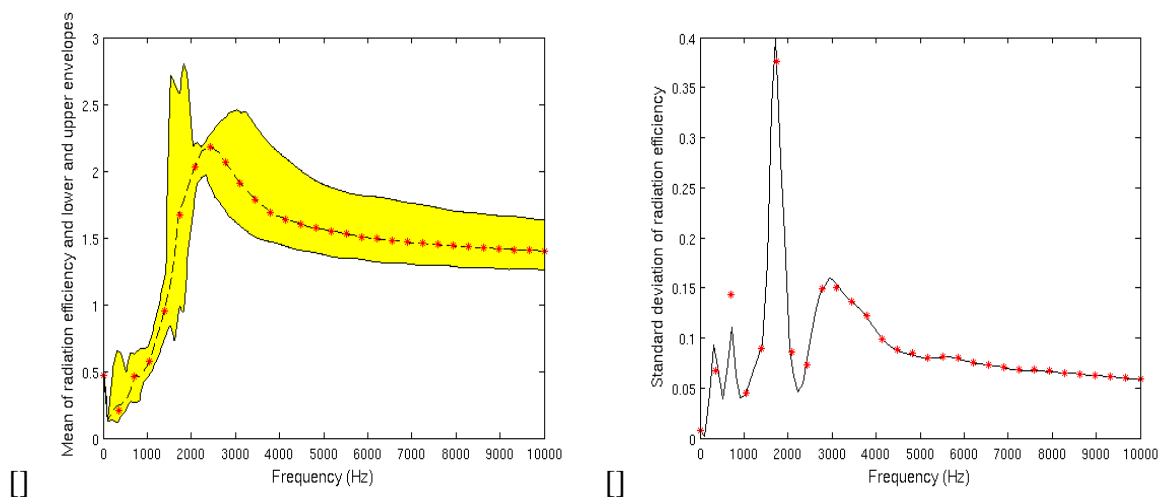


Figure 5: Radiation efficiency :: (a) mean and min-max envelop, (b) Standard deviation, (-) WFE-Chaos, (*) Monte Carlo

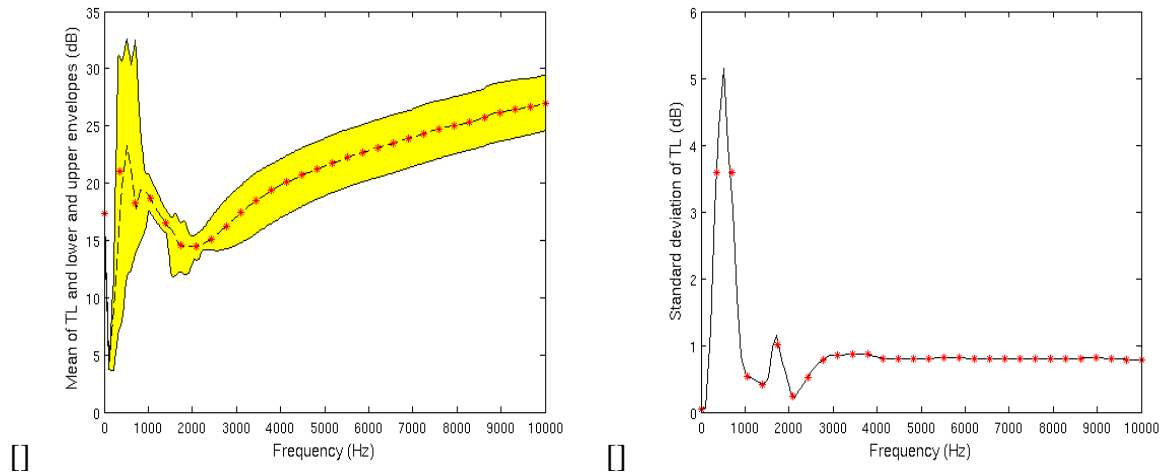


Figure 6: Transmission Loss: (a) mean and min-max envelop, (b) Standard deviation, (-) WFE-Chaos, (*) Monte Carlo

5 CONCLUSIONS

The modelling of the vibro-acoustic behaviour of composite layered structures with uncertain parameters was considered in this paper. The presented approach is a combination of a wave based SEA approach and a parametric probabilistic approach. The first method consists in evaluating the wave propagation characteristics within composite structures. A spectral method, based on the periodicity of the structure studied is presented. Then, the SEA can be applied to identify the evolution of energy quantities between different sub-structures. In our case, all waves are considered as substructures. This approach leads to obtain vibro-acoustic indices such as the radiation efficiency and the sound transmission loss for each considered wave type.

ACKNOWLEDGMENTS

Funding for this project was provided by a grant from la Région Rhône-Alpes.

REFERENCES

- [1] J. N. Reddy. *Mechanics of laminated composite plates: theory and analysis*, volume 1. CRC press Boca Raton, 1997.
- [2] J. Whitney and N. Pagano. Shear deformation in heterogeneous anisotropic plates. *A Appl Mech Trans ASME*, 37 Ser E(4):1031–1036, 1970.
- [3] C. L. Dym and M. A. Lang. Transmission of sound through sandwich panels. *Journal of the Acoustical Society of America*, 56(5):1523–1532, 1974.
- [4] JN Reddy. A refined nonlinear theory of plates with transverse shear deformation. *International Journal of Solids and Structures*, 20(9):881–896, 1984.
- [5] VS. Sokolinsky and SR. Nutt. Consistent higher-order dynamic equations for soft-core sandwich beams. *AIAA Journal*, 42(2):374–382, 2004.

- [6] F. G. Leppington, E. G. Broadbent, and K. H. Heron. Acoustic radiation efficiency of rectangular panels. In *Proceedings of The Royal Society of London, Series A: Mathematical and Physical Sciences*, volume 382, pages 245–271, 1982.
- [7] F. G. Leppington, K. H. Heron, and E. G. Broadbent. Resonant and non-resonant transmission of random noise through complex plates. *Proceedings of the Royal Society A: Mathematical, Physical and Engineering Sciences*, 458(2019):683–704, 2002.
- [8] B.R. Mace and E. Manconi. Modelling wave propagation in two-dimensional structures using finite element analysis. *Journal of Sound and Vibration*, 318(4-5):884–902, 2008.
- [9] R. Courant and D. Hilbert. *Methods of mathematical physics*, vol. 1. *New York: John Wiley*, 1989.
- [10] V. Cotoni, R. S. Langley, and P. J. Shorter. A statistical energy analysis subsystem formulation using finite element and periodic structure theory. *Journal of Sound and Vibration*, 318(4-5):1077–1108, 2008.
- [11] N. Wiener. The homogeneous chaos. *American Journal of Mathematics*, 60:897–936, 1938.
- [12] D. Xiu and G. E. Karniadakis. The wiener-asky polynomial chaos for stochastic differential equations. *SIAM Journal on Scientific Computing*, 24 (2):619–644, 2002.
- [13] M. Rosenblatt. Remarks on a multivariate transformation. *The Annals of Mathematical Statistics*, 23(3):470–472, 1952.



WAVE BASED DESIGN OPTIMISATION OF COMPOSITE STRUCTURES OPERATING IN DYNAMIC ENVIRONMENTS

D. Chronopoulos¹, S. Leerungruang¹, M. Collet², and M. Ichchou³

¹Division of Materials, Mechanics and Structures
University Park, The University of Nottingham, NG7 2RD, UK
e-mail: dimitrios.chronopoulos@nottingham.ac.uk

²LTDS, UMR-CNRS 5513
36 Avenue Guy de Collongue, 69130 Ecully, France
e-mail: manuel.collet@ec-lyon.fr

³Ecole Centrale de Lyon
36 Avenue Guy de Collongue, 69130 Ecully, France
e-mail: mohamed.ichchou@ec-lyon.fr

ABSTRACT

The optimal mechanical and geometric characteristics for layered composite structures subject to vibroacoustic excitations are derived. A Finite Element description coupled to Periodic Structure Theory is employed for the considered layered panel. Structures of arbitrary anisotropy as well as geometric complexity can thus be modelled by the presented approach. Initially, a numerical continuum-discrete approach for computing the sensitivity of the acoustic wave characteristics propagating within the modelled periodic composite structure is exhibited. The first and second order sensitivities of the acoustic transmission coefficient expressed within a Statistical Energy Analysis context are subsequently derived as a function of the computed acoustic wave characteristics. Having formulated the gradient vector as well as the Hessian matrix, the optimal mechanical and geometric characteristics satisfying the considered mass, stiffness and vibroacoustic performance criteria are sought by employing Newton's optimisation method.

1 INTRODUCTION

Layered and complex structures are nowadays widely used within the aerospace, automotive, construction and energy sectors with a general increase tendency, mainly because of their high stiffness-to-mass ratio and the fact that their mechanical characteristics can be designed to suit the particular purposes. Unluckily however, this high stiffness-to-mass ratio being responsible for the increased mechanical efficiency, at the same time induces high acoustic transmission through the structure. The need for simultaneously optimising an industrial structure of minimum mass and maximum static stiffness, while attaining satisfactory dynamic response performance levels is a challenging task for the modern engineer; especially when considering acoustic transmission through a layered structure which depends on the mechanical and geometric characteristics of each individual layer, resulting in a great number of design parameters to be optimised.

In this work an established wave based SEA approach is employed in order to predict the vibroacoustic performance of a composite layered panel. The novelty of the work focuses on the derivation of the first and second order sensitivity of the acoustic transmission coefficient expressed through SEA with respect to the structural design characteristics of the modelled structure. The considered design parameters include the entirety of the mechanical characteristics, the density as well as the thickness of each individual structural layer. Non conservative structural systems are also modelled by the exhibited approach. Employing a three dimensional FE description of the modelled structure allows for capturing the entirety of the sound transmitting propagating structural waves, while employing a PST formulation allows for drastically reducing the computational cost related to calculating the SEA parameters and the Hessian matrix for each configuration. Although not discussed in this work, the method is straightforward to apply to curved structures by expressing the FE structural matrices and wave propagation properties in polar coordinates.

2 ACOUSTIC WAVE SENSITIVITY

2.1 Formulation of the PST for an arbitrary structural segment

A periodic segment of a panel having arbitrary layering is hereby considered (see Fig.1) with L_x , L_y its dimensions in the x and y directions respectively. The segment is modelled using a conventional FE software. The mass, damping and stiffness matrices of the segment \mathbb{M} , \mathbb{C} and \mathbb{K} are extracted and the DoF set \mathbf{q} is reordered according to a predefined sequence such as:

$$\mathbf{q} = \{\mathbf{q}_I \ \mathbf{q}_B \ \mathbf{q}_T \ \mathbf{q}_L \ \mathbf{q}_R \ \mathbf{q}_{LB} \ \mathbf{q}_{RB} \ \mathbf{q}_{LT} \ \mathbf{q}_{RT}\}^T \quad (1)$$

corresponding to the internal, the interface edge and the interface corner DoF (see Fig.1). The free harmonic vibration equation of motion for the modelled segment is written as:

$$[\mathbb{K} + i\omega\mathbb{C} - \omega^2\mathbb{M}]\mathbf{q} = \mathbf{0} \quad (2)$$

The analysis then follows as in [1] with the following relations being assumed for the displacement DoF under the passage of a time-harmonic wave:

$$\begin{aligned} \mathbf{q}_R &= e^{-i\varepsilon_x} \mathbf{q}_L, \quad \mathbf{q}_T = e^{-i\varepsilon_y} \mathbf{q}_B \\ \mathbf{q}_{RB} &= e^{-i\varepsilon_x} \mathbf{q}_{LB}, \quad \mathbf{q}_{LT} = e^{-i\varepsilon_y} \mathbf{q}_{LB}, \quad \mathbf{q}_{RT} = e^{-i\varepsilon_x - i\varepsilon_y} \mathbf{q}_{LB} \end{aligned} \quad (3)$$

with ε_x and ε_y the propagation constants in the x and y directions related to the phase difference between the sets of DoF. The wavenumbers k_x , k_y are directly related to the propagation

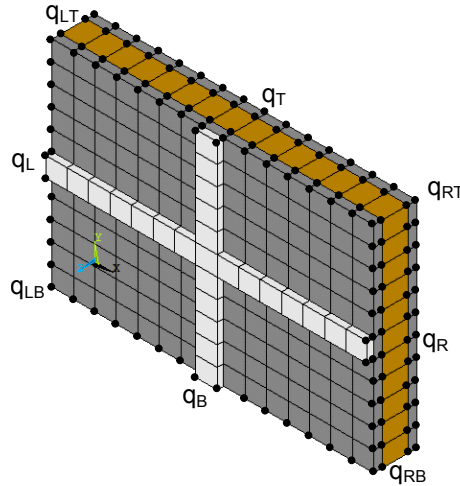


Figure 1. Caption of a FE modelled composite layered panel

constants through the relation:

$$\varepsilon_x = k_x L_x, \quad \varepsilon_y = k_y L_y \quad (4)$$

Considering Eq.3 in tensorial form gives:

$$\mathbf{q} = \begin{bmatrix} \mathbf{I} & \mathbf{0} & \mathbf{0} & \mathbf{0} \\ \mathbf{0} & \mathbf{I} & \mathbf{0} & \mathbf{0} \\ \mathbf{0} & \mathbf{I}e^{-i\varepsilon_y} & \mathbf{0} & \mathbf{0} \\ \mathbf{0} & \mathbf{0} & \mathbf{I} & \mathbf{0} \\ \mathbf{0} & \mathbf{0} & \mathbf{I}e^{-i\varepsilon_x} & \mathbf{0} \\ \mathbf{0} & \mathbf{0} & \mathbf{0} & \mathbf{I} \\ \mathbf{0} & \mathbf{0} & \mathbf{0} & \mathbf{I}e^{-i\varepsilon_x} \\ \mathbf{0} & \mathbf{0} & \mathbf{0} & \mathbf{I}e^{-i\varepsilon_y} \\ \mathbf{0} & \mathbf{0} & \mathbf{0} & \mathbf{I}e^{-i\varepsilon_x - i\varepsilon_y} \end{bmatrix} \mathbf{x} = \mathbf{R}\mathbf{x} \quad (5)$$

with \mathbf{x} the reduced set of DoF: $\mathbf{x} = \{\mathbf{q}_I \quad \mathbf{q}_B \quad \mathbf{q}_L \quad \mathbf{q}_{LB}\}^\top$. The equation of free harmonic vibration of the modelled segment can now be written as:

$$[\mathbf{R}^* \mathbf{K} \mathbf{R} + i\omega \mathbf{R}^* \mathbf{C} \mathbf{R} - \omega^2 \mathbf{R}^* \mathbf{M} \mathbf{R}] \mathbf{x} = \mathbf{0} \quad (6)$$

with * denoting the Hermitian transpose. The most practical procedure for extracting the wave propagation characteristics of the segment from Eq.6 is injecting a set of assumed propagation constants $\varepsilon_x, \varepsilon_y$. The set of these constants can be chosen in relation to the direction of propagation towards which the wavenumbers are to be sought and according to the desired resolution of the wavenumber curves. Eq.6 is then transformed into a standard eigenvalue problem and can be solved for the eigenvector \mathbf{x} which describe the deformation of the segment under the passage of each wave type at an angular frequency equal to the square root of the corresponding eigenvalue $\lambda = \omega^2$. It is noted that the computed angular frequency quantities $\omega = \omega_r + i\omega_i$ will have $|\omega_i| > 0$ implying complex values for the wavenumbers of the propagating wave types, otherwise interpreted as spatially decaying motion and from which the loss factor of each computed wave type w can directly be determined.

A complete description of each passing wave including its x and y directional wavenumbers and its wave shape for a certain frequency is therefore acquired. It is noted that the periodicity condition is defined modulo 2π , therefore solving Eq.6 with a set of $\varepsilon_x, \varepsilon_y$ varying from

0 to 2π will suffice for capturing the entirety of the structural waves. Further considerations on reducing the computational expense of the problem are discussed in [1]. It should be noted that only propagating waves will be considered in the subsequent analysis.

2.2 Parametric sensitivity

For an undamped structural segment the sensitivity of the real eigenvalues λ_p can be written as

$$\frac{\partial \lambda_p}{\partial \beta_i} = \mathbf{x}_p^\top \left(\frac{\partial \mathbf{K}}{\partial \beta_i} - \lambda_p \frac{\partial \mathbf{M}}{\partial \beta_i} \right) \mathbf{x}_p \quad (7a)$$

$$\begin{aligned} \frac{\partial^2 \lambda_p}{\partial \beta_j \partial \beta_i} = & \mathbf{x}_p^\top \left(\frac{\partial^2 \mathbf{K}}{\partial \beta_j \partial \beta_i} - \lambda_p \frac{\partial^2 \mathbf{M}}{\partial \beta_j \partial \beta_i} - \frac{\partial \lambda_p}{\partial \beta_j} \frac{\partial \mathbf{M}}{\partial \beta_i} - \frac{\partial \lambda_p}{\partial \beta_i} \frac{\partial \mathbf{M}}{\partial \beta_j} \right) \mathbf{x}_p \\ & + \mathbf{x}_p^\top \left(\frac{\partial}{\partial \beta_j} \left[\mathbf{K} - \lambda_p \mathbf{M} \right] \right) \frac{\partial \mathbf{x}_p}{\partial \beta_i} + \mathbf{x}_p^\top \left(\frac{\partial}{\partial \beta_i} \left[\mathbf{K} - \lambda_p \mathbf{M} \right] \right) \frac{\partial \mathbf{x}_p}{\partial \beta_j} \end{aligned} \quad (7b)$$

with the sensitivity of the real mode shapes $\frac{\partial \mathbf{x}_p}{\partial \beta_j}$ to be calculated by the approach exhibited in [2]. The global mass and stiffness matrices \mathbf{M} , \mathbf{K} of the structural segment are formed by adding the local mass and stiffness matrices of individual FEs. Eq.7 can be written as

$$\frac{\partial \lambda_p}{\partial \beta_i} = \mathbf{x}_p^\top \left(\mathbf{R}^* \frac{\partial \mathbf{K}}{\partial \beta_i} \mathbf{R} - \lambda_p \mathbf{R}^* \frac{\partial \mathbf{M}}{\partial \beta_i} \mathbf{R} \right) \mathbf{x}_p \quad (8a)$$

$$\begin{aligned} \frac{\partial^2 \lambda_p}{\partial \beta_j \partial \beta_i} = & \mathbf{x}_p^\top \left(\mathbf{R}^* \frac{\partial^2 \mathbf{K}}{\partial \beta_j \partial \beta_i} \mathbf{R} - \lambda_p \mathbf{R}^* \frac{\partial^2 \mathbf{M}}{\partial \beta_j \partial \beta_i} \mathbf{R} - \mathbf{R}^* \frac{\partial \lambda_p}{\partial \beta_j} \frac{\partial \mathbf{M}}{\partial \beta_i} \mathbf{R} - \mathbf{R}^* \frac{\partial \lambda_p}{\partial \beta_i} \frac{\partial \mathbf{M}}{\partial \beta_j} \mathbf{R} \right) \mathbf{x}_p + \\ & \mathbf{x}_p^\top \left(\frac{\partial}{\partial \beta_j} \left[\mathbf{R}^* \mathbf{K} \mathbf{R} - \lambda_p \mathbf{R}^* \mathbf{M} \mathbf{R} \right] \right) \frac{\partial \mathbf{x}_p}{\partial \beta_i} + \mathbf{x}_p^\top \left(\frac{\partial}{\partial \beta_i} \left[\mathbf{R}^* \mathbf{K} \mathbf{R} - \lambda_p \mathbf{R}^* \mathbf{M} \mathbf{R} \right] \right) \frac{\partial \mathbf{x}_p}{\partial \beta_j} \end{aligned} \quad (8b)$$

For the conservative system it is known however that $\frac{\partial \lambda_p}{\partial \beta_i} = \frac{\partial(\omega_p^2)}{\partial \beta_i}$, therefore

$$\frac{\partial \lambda_p}{\partial \beta_i} = \frac{\frac{\partial(\omega_p^2)}{\partial \beta_i}}{\frac{\partial \omega_p}{\partial \beta_i}} = 2\omega_p \frac{\partial \omega_p}{\partial \beta_i} \Leftrightarrow \frac{\partial \omega_p}{\partial \beta_i} = \frac{1}{2\omega_p} \frac{\partial \lambda_p}{\partial \beta_i} \quad (9a)$$

$$\frac{\partial^2 \lambda_p}{\partial \beta_j \partial \beta_i} = 2 \frac{\partial \omega_p}{\partial \beta_j} \frac{\partial \omega_p}{\partial \beta_i} + 2\omega_p \frac{\partial^2 \omega_p}{\partial \beta_j \partial \beta_i} \Leftrightarrow \frac{\partial^2 \omega_p}{\partial \beta_j \partial \beta_i} = \frac{1}{2\omega_p} \left(\frac{\partial^2 \lambda_p}{\partial \beta_j \partial \beta_i} - 2 \frac{\partial \omega_p}{\partial \beta_j} \frac{\partial \omega_p}{\partial \beta_i} \right) \quad (9b)$$

with ω_p the angular frequency at which the set of $\varepsilon_x, \varepsilon_y$ is true for the p wave type described by the \mathbf{x}_p deformation. For the wavenumber sensitivity $\frac{\partial k_p}{\partial \beta_i}$ the following is true

$$\frac{\partial k_p}{\partial \beta_i} = - \frac{\partial k_p}{\partial \omega_p} \frac{\partial \omega_p}{\partial \beta_i} = - \frac{1}{c_{g,p}} \frac{\partial \omega_p}{\partial \beta_i} \quad (10a)$$

$$\frac{\partial^2 k_p}{\partial \beta_j \partial \beta_i} = \frac{1}{c_{g,p}^3} \frac{\partial c_{g,p}}{\partial k_p} \frac{\partial \omega_p}{\partial \beta_j} \frac{\partial \omega_p}{\partial \beta_i} - \frac{1}{c_{g,p}} \frac{\partial^2 \omega_p}{\partial \beta_j \partial \beta_i} \quad (10b)$$

with $c_{g,p} = \frac{\partial \omega_p}{\partial k_p}$ the group velocity associated with the wave type p at frequency ω_p and the quantities $c_{g,p}, \frac{\partial c_{g,p}}{\partial \omega_p}$ to be evaluated by the solution of the baseline structural design.

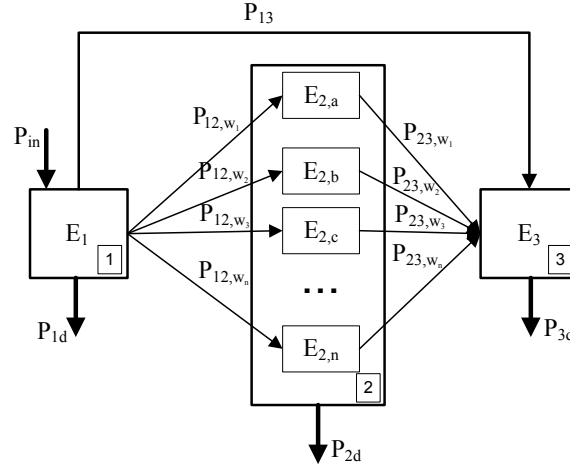


Figure 2: A schematic representation of the SEA power exchanges and energies for the modelled system.

3 SEA SENSITIVITY ANALYSIS

3.1 The employed SEA model

The impact of the parametric alterations on the vibroacoustic performance of the structure under investigation is exhibited in this section by deriving expressions for the sensitivity of the SEA results with respect to the propagating acoustic waves.

The total acoustic transmission coefficient τ is one of the most important indices of the vibroacoustic performance of a structure. The system to be modelled comprises one acoustically excited chamber (subsystem 1) and one acoustically receiving chamber (subsystem 3) separated by the modelled composite panel (subsystem 2). It is considered that each wave type is excited and transmits acoustic energy independently from the rest, therefore each considered wave type $w = w_1, w_2 \dots w_n$ propagating within the composite panel is considered as a separate SEA subsystem. No flanking transmission is considered in the SEA model. The energy balance between the subsystems as it is considered within an SEA approach (see [3]) is illustrated in Fig.2, in which E_1, E_3 stand for the acoustic energy of the source room and the receiving room respectively and E_2 for the vibrational energy of the composite panel. Moreover P_{in} is the injected power in the source room, P_{1d}, P_{2d} and P_{3d} stand for the power dissipated by each subsystem and P_{13} is the non-resonant transmitted power between the rooms.

The derivation of an expression for the total acoustic transmission coefficient τ of the composite structure by merely accounting for its structural dynamic behaviour is exhibited in [4] and reads

$$\tau = \sum_{w=w_1}^{w_n} \tau_w + \frac{P_{13}}{P_{inc}} \quad (11)$$

with τ_w being the transmission coefficient of the wave type w given as

$$\tau_w = \frac{8\rho^2 c^4 \pi \sigma_{rad,w}^2 n_w}{\rho_s \omega^2 A (\rho_s \omega \eta_w + 2\rho c \sigma_{rad,w})} \quad (12)$$

The non resonant transmission coefficient $\tau_{nr} = P_{13}/P_{inc}$ for a diffused acoustic field

can be written as in [5]:

$$\tau_{nr}(\omega) = \frac{1}{\pi(\cos^2 \theta_{min} - \cos^2 \theta_{max})} \int_0^{2\pi} \int_0^{\theta_{max}} \frac{4Z_0^2}{|i\omega\rho_s + 2Z_0|^2} \sigma(\theta, \phi, \omega) \cos^2 \theta \sin \theta d\theta d\phi \quad (13)$$

in which θ and ϕ are the incidence angle and the direction angle of the acoustic wave respectively and $Z_0 = \rho c / \cos \theta$ is the acoustic impedance of the medium. The term θ_{max} stands for the maximum incidence angle, accounting for the diffuseness of the incident field. It is hereby considered that $\theta_{max} = \pi/2$ for all the results presented in the current work. The term $\sigma(\theta, \phi, \omega)$ is the corrected radiation efficiency term. It is used in order to account for the finite dimensions of the panel and it is calculated using a spatial windowing correction technique presented in [6].

Eventually the STL of the panel can be expressed as

$$STL = 10 \log_{10} \left(\frac{1}{\tau} \right) \quad (14)$$

by definition.

3.2 Parametric sensitivity of the total acoustic transmission

In order to formulate the expression of the Hessian matrix describing the variation of the vibroacoustic performance of the structure with respect to its design parameters, the second order derivative of τ with respect to the considered set of parameters should be derived and expressed as

$$\frac{\partial \tau}{\partial \beta_i} = \sum_{w=w_1}^{w_n} \frac{\partial \tau_w}{\partial \beta_i} + \frac{\partial \tau_{nr}}{\partial \beta_i} \quad (15a)$$

$$\frac{\partial^2 \tau}{\partial \beta_j \partial \beta_i} = \sum_{w=w_1}^{w_n} \frac{\partial^2 \tau_w}{\partial \beta_j \partial \beta_i} + \frac{\partial^2 \tau_{nr}}{\partial \beta_j \partial \beta_i} \quad (15b)$$

while the sensitivity of the STL index can directly be expressed with regard to τ as

$$\frac{\partial(STL)}{\partial \beta_i} = \frac{d(STL)}{d\tau} \frac{\partial \tau}{\partial \beta_i} = -\frac{10}{\ln(10)\tau} \frac{\partial \tau}{\partial \beta_i} \quad (16a)$$

$$\begin{aligned} \frac{\partial^2(STL)}{\partial \beta_j \partial \beta_i} &= \frac{\partial^2(STL)}{\partial \tau^2} \frac{\partial \tau}{\partial \beta_j} \frac{\partial \tau}{\partial \beta_i} + \frac{\partial(STL)}{\partial \tau} \frac{\partial^2 \tau}{\partial \beta_j \partial \beta_i} \\ &= \frac{10}{\ln(10)\tau^2} \frac{\partial \tau}{\partial \beta_j} \frac{\partial \tau}{\partial \beta_i} - \frac{10}{\ln(10)\tau} \frac{\partial^2 \tau}{\partial \beta_j \partial \beta_i} \end{aligned} \quad (16b)$$

In the following sections the evaluation of Eq.15 is discussed.

3.3 Modal density sensitivity

Using Courant's formula [7], the modal density of each wave type w can be written at a propagation angle ϕ as a function of the propagating wavenumber and its corresponding group velocity c_g :

$$n_w(\omega, \phi) = \frac{Ak_w(\omega, \phi)}{2\pi^2 |c_{g,w}(\omega, \phi)|} \quad (17)$$

The angularly averaged modal density of the structure is therefore given as

$$n_w(\omega) = \int_0^\pi n_w(\omega, \phi) d\phi \quad (18)$$

Thanks to the chain differentiation rule the first and second order derivatives of the modal density for each wave type with respect to design variables β_i, β_j can be expressed as

$$\frac{\partial n_w(\omega, \phi)}{\partial \beta_i} = \frac{\partial n_w(\omega, \phi)}{\partial k_w(\omega, \phi)} \frac{\partial k_w(\omega, \phi)}{\partial \beta_i} + \frac{\partial n_w(\omega, \phi)}{\partial c_{g,w}(\omega, \phi)} \frac{\partial c_{g,w}(\omega, \phi)}{\partial \beta_i} \quad (19a)$$

$$\begin{aligned} &= \frac{A}{2\pi^2 |c_{g,w}(\omega, \phi)|} \frac{\partial k_w(\omega, \phi)}{\partial \beta_i} - \frac{A k_w(\omega, \phi) \operatorname{sgn}(c_{g,w}(\omega, \phi))}{2\pi^2 |c_{g,w}(\omega, \phi)|^2} \frac{\partial c_{g,w}(\omega, \phi)}{\partial k_w(\omega, \phi)} \frac{\partial k_w(\omega, \phi)}{\partial \beta_i} \\ \frac{\partial^2 n_w(\omega, \phi)}{\partial \beta_j \partial \beta_i} &= \frac{\partial^2 n_w(\omega, \phi)}{\partial k_w(\omega, \phi)^2} \frac{\partial k_w(\omega, \phi)}{\partial \beta_j} \frac{\partial k_w(\omega, \phi)}{\partial \beta_i} + \frac{\partial n_w(\omega, \phi)}{\partial k_w(\omega, \phi)} \frac{\partial^2 k_w(\omega, \phi)}{\partial \beta_j \partial \beta_i} \\ &+ \frac{\partial^2 n_w(\omega, \phi)}{\partial c_{g,w}(\omega, \phi)^2} \frac{\partial c_{g,w}(\omega, \phi)}{\partial \beta_j} \frac{\partial c_{g,w}(\omega, \phi)}{\partial \beta_i} + \frac{\partial n_w(\omega, \phi)}{\partial c_{g,w}(\omega, \phi)} \frac{\partial^2 c_{g,w}(\omega, \phi)}{\partial \beta_j \partial \beta_i} \\ &= \frac{A}{2\pi^2 |c_{g,w}(\omega, \phi)|} \frac{\partial^2 k_w(\omega, \phi)}{\partial \beta_j \partial \beta_i} + \frac{A k_w(\omega, \phi) \operatorname{sgn}(c_{g,w}(\omega, \phi))}{\pi^2 |c_{g,w}(\omega, \phi)|^3} \left(\frac{\partial c_{g,w}(\omega, \phi)}{\partial k_w(\omega, \phi)} \right)^2 \frac{\partial k_w(\omega, \phi)}{\partial \beta_j} \frac{\partial k_w(\omega, \phi)}{\partial \beta_i} \\ &- \frac{A k_w(\omega, \phi) \operatorname{sgn}(c_{g,w}(\omega, \phi))}{2\pi^2 |c_{g,w}(\omega, \phi)|^2} \left(\frac{\partial^2 c_{g,w}(\omega, \phi)}{\partial k_w(\omega, \phi)^2} \frac{\partial k_w(\omega, \phi)}{\partial \beta_j} \frac{\partial k_w(\omega, \phi)}{\partial \beta_i} + \frac{\partial c_{g,w}(\omega, \phi)}{\partial k_w(\omega, \phi)} \frac{\partial^2 k_w(\omega, \phi)}{\partial \beta_j \partial \beta_i} \right) \end{aligned} \quad (19b)$$

while for the spatially averaged modal density

$$\frac{\partial n_w(\omega)}{\partial \beta_i} = \int_0^\pi \frac{\partial n_w(\omega, \phi)}{\partial \beta_i} d\phi \quad (20a)$$

$$\frac{\partial^2 n_w(\omega)}{\partial \beta_j \partial \beta_i} = \int_0^\pi \frac{\partial^2 n_w(\omega, \phi)}{\partial \beta_j \partial \beta_i} d\phi \quad (20b)$$

suggesting that the modal density sensitivity can be expressed merely by

- The sensitivity of the characteristics of the waves travelling within the considered structure with respect to the structural design (already determined in Sec.2).
- The sensitivity of the modal density with respect to the characteristics of the waves travelling in it.

A similar approach can be followed for computing all the remaining necessary SEA quantities.

3.4 Radiation efficiency sensitivity

In order to avoid the computationally inefficient frequency and directional averaging of the modal dependent radiation efficiency sensitivity $\frac{\partial \sigma_{rad,w}(\omega, \phi)}{\partial \beta_i}$, it is practical to employ expressions introducing a direct wavenumber dependence of $\sigma_{rad,w}$ such as the ones exhibited in [1, 8, 9]. For a generic periodic structure including discontinuities the assumption of sinusoidal mode shapes is no longer valid, therefore the radiation efficiency should be calculated directly from the PST derived wave mode shapes. The radiation efficiency expression as derived in [1] can therefore be employed. For continuous structures, mode shapes of sinusoidal form can be assumed in order to avoid any FE discretization errors in the solution. The set of asymptotic

formulas given in [9] can be used for computing the averaged wavenumber dependent radiation efficiency of the panel as

$$\sigma_{rad,w} = \frac{1}{\sqrt{1-\mu^2}} \quad \mu < 0.90 \quad (21a)$$

$$\sigma_{rad,w} = \frac{L_x + L_y}{\pi \mu \kappa L_x L_y \sqrt{\mu^2 - 1}} \left(\ln \left(\frac{\mu + 1}{\mu - 1} \right) + \frac{2\mu}{\mu^2 - 1} \right) \quad \mu > 1.05 \quad (21b)$$

$$\sigma_{rad,w} = (0.5 - 0.15 \min(L_x, L_y) / \max(L_x, L_y)) \sqrt{k \min(L_x, L_y)} \quad \mu = 1 \quad (21c)$$

with $\mu = \left(\frac{k_x^2 + k_y^2}{\kappa^2} \right)^{1/2}$, where $\kappa = \omega/c$ is the acoustic wavenumber. In the region $0.90 < \mu < 1.05$ a shape preserving Hermite interpolation function is employed assuring the continuity and double differentiability for the entire spectrum of the $\sigma_{rad,w}$ expression. The sensitivity expressions for the radiation efficiency of the panel can therefore be derived as a function of the propagating flexural wavenumbers by Eq.21, while the interpolation function is used for expressing the sensitivity of $\sigma_{rad,w}$ for the remaining spectrum.

4 NUMERICAL CASE STUDIES

In order to validate the exhibited optimisation approach, an asymmetric sandwich panel comprising two facesheets and a core is modelled in this section. The lower facesheet has a thickness $h_1=1\text{mm}$ and is made of a material having $\rho_{m,1}=3000\text{e}^{-9}\text{kg/mm}^3$, $E_1 = 70\text{GPa}$ and a Poisson's ratio $\nu_1=0.1$. The upper facesheet has a thickness equal to $h_3=2\text{mm}$ and is made of the same material as the lower facesheet. The core has a thickness $h_2=10\text{mm}$ and is made of a material with $\rho_{m,2}=50\text{e}^{-9}\text{kg/mm}^3$, $E_2 = 0.07\text{GPa}$ and $\nu_2=0.4$. Three FEs are used in the sense of thickness in order to model the structure. All computations were conducted using the R2013a version of MATLAB[®].

4.1 Structural design optimisation of the layered structure

As discussed in Sec.2, the criteria to be considered within the optimisation process of the mechanical and geometric characteristics of the panel are its mass, stiffness and vibroacoustic performance. The surface mass of the panel ρ_s is chosen as a representative mass index, the total acoustic transmission coefficient τ is selected as the vibroacoustic performance index, while with regard to the structural stiffness and for the sake of simplicity we will hereby assume that we are solely interested in the sum of the static flexural stiffnesses of the panel D_{xx} , D_{yy} expressed in the case of an isotropic composite panel as

$$d_s = \frac{2}{3} \sum_{l=l_1}^{l_{max}} (Q_l(z_l^3 - z_{l-1}^3)) \quad (22)$$

with z_l the coordinate of the upper surface of layer l in the thickness direction. The design cost functions, employed in order to decide the relation between ρ_s , τ and d_s and the corresponding induced design cost are exhibited in Fig.3.

Additional constraints (e.g. minimum axial and/or flexural stiffness, maximum surface mass e.t.c) can be considered. The constrained optimization problem is solved using Newton's method.

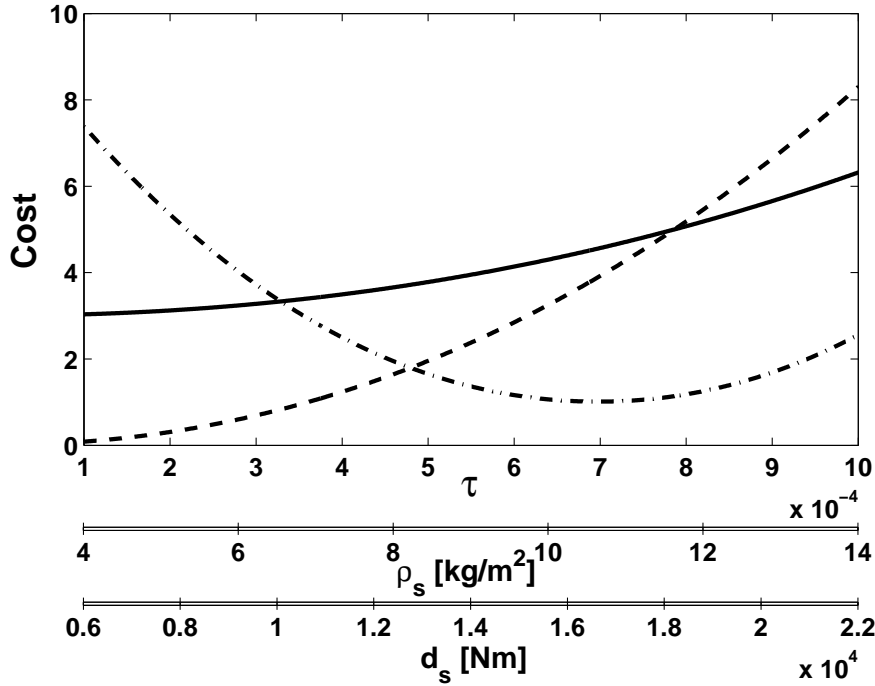


Figure 3: Representation of the cost functions employed within the current optimisation process. Cost function corresponding to: The acoustic transmission coefficient τ (—), The surface mass density ρ_s (---), The flexural stiffness d_s of the panel (- · -)

4.2 Optimal parameters and discussion on the computational efficiency

The optimisation problem is solved for $k = 0.13\text{rad/mm}$, and the optimal material and geometric parameters that minimise the sum of the costs as presented in Fig.3 are computed as follows

$$E_1 = 80.9\text{GPa}, v_1 = 0.12, h_1 = 1.19\text{mm}, \rho_{m,1} = 1647\text{kg/m}^3$$

$$E_2 = 110\text{MPa}, v_2 = 0.37, h_2 = 10.53\text{mm}, \rho_{m,2} = 14.6\text{kg/m}^3$$

$$E_3 = 58.3\text{GPa}, v_3 = 0.19, h_3 = 1.74\text{mm}, \rho_{m,3} = 1500\text{kg/m}^3$$

It is noted that the only quantities laying on the limits of the predefined constraints which could potentially further improve the overall structural performance are the Young's modulus of the core layer E_2 as well as the mass density of the upper layer $\rho_{m,3}$. Optimising the structure in a broadband frequency range can be done by averaging the optimal parameters over the frequency range of interest or by introducing a weighting average for the frequency bands that are considered more important (e.g. frequency of the external acoustic excitation). The optimisation process was completed in 8 iterations each of which lasted approximately 78 seconds, resulting in a total computation time of 630s. This suggests that a broadband structural optimisation is feasible within a few hours, even with a conventional computing equipment.

5 CONCLUSIONS

In this work, the optimal mechanical and geometric characteristics for layered composite structures subject to vibroacoustic excitations were derived in a wave SEA context. The main conclusions of the paper are summarised as:

(i) An intense frequency dependent variation of the sensitivity of the propagating wave characteristics has been observed as a function of the design of the composite structure. This

also implies frequency dependence of the optimal design parameters.

(ii) Expressions for the first and second order sensitivities of the SEA quantities, namely the modal density and the radiation efficiency of the composite panel were derived. The design parametric sensitivity for each of the SEA quantities, as well as of the acoustic transmission coefficient were found to be highly frequency dependent. The impact of the design alteration on the vibroacoustic response was maximised in the vicinity of the acoustic coincidence range for most parameters.

(iii) The suggested optimisation process is computationally efficient, allowing for a broadband structural optimisation of a layered structure in a rational period of time, even with the use of a conventional computing equipment.

REFERENCES

- [1] V. Cotoni, R. S. Langley, and P. J. Shorter. A statistical energy analysis subsystem formulation using finite element and periodic structure theory. *Journal of Sound and Vibration*, 318(4-5):1077–1108, 2008.
- [2] Richard B Nelson. Simplified calculation of eigenvector derivatives. *AIAA journal*, 14(9):1201–1205, 1976.
- [3] RH Lyon. *Statistical energy analysis of dynamical systems: theory and applications*. MIT press Cambridge, 1975.
- [4] D Chronopoulos, M Ichchou, B Troclet, and O Bareille. Computing the broadband vibroacoustic response of arbitrarily thick layered panels by a wave finite element approach. *Applied Acoustics*, 77:89–98, 2014.
- [5] Sebastian Ghinet, Nouredine Atalla, and Haisam Osman. The transmission loss of curved laminates and sandwich composite panels. *The Journal of the Acoustical Society of America*, 118(2):774–790, 2005.
- [6] Jean Allard and Nouredine Atalla. *Propagation of Sound in Porous Media: Modelling Sound Absorbing Materials 2e*. John Wiley & Sons, 2009.
- [7] Richard Courant and David Hilbert. *Methoden der mathematischen Physik, vol. 1*, volume 2. Berlin, 1931.
- [8] Gideon Maidanik. Response of ribbed panels to reverberant acoustic fields. *the Journal of the Acoustical Society of America*, 34(6):809–826, 1962.
- [9] F. G. Leppington, E. G. Broadbent, and K. H. Heron. Acoustic radiation efficiency of rectangular panels. In *Proceedings of The Royal Society of London, Series A: Mathematical and Physical Sciences*, volume 382, pages 245–271, 1982.



VISCOELASTIC CHARACTERISATION OF ADHESIVES USING INVERSE TECHNIQUES

L. Rouleau^{1*}, J.-F. Deü¹ and A. Legay¹

¹ Structural Mechanics and Coupled Systems Laboratory,
Cnam Paris, 2 Rue Conté, 75003 Paris, FRANCE

Email: lucie.rouleau@cnam.fr, jean-francois.deu@cnam.fr, antoine.legay@cnam.fr

ABSTRACT

Active or passive damping treatments are usually applied to vibrating structures for noise and vibration control by means of an adhesive layer. There is a high number of environmental parameters, such as temperature or frequency, which may influence the behaviour of the bonding layer and modify the damping efficiency of the treatment. Therefore it is desired to take into account the behaviour of that layer in the model.

The goal of this work is to present a procedure to characterise and model the adhesive layer. To that purpose, an experimental-numerical method for inverse characterisation of the frequency dependent properties of the glue is presented. The proposed inverse approach is a two-step gradient-based method (BFGS) based on a fractional derivative viscoelastic model whose parameters are identified by minimising the difference between the simulated and the measured dynamic response of a multi-layered structure assembled by bonding. In the finite element model used for the inverse approach, the bonding layer is modelled by interface finite elements, i.e. by bi-dimensional elements representative of the three-dimensional behaviour of the bonding layer. The identification procedure is applied to the characterisation of a double coated tape.

1 INTRODUCTION

Noise and vibration control is a major concern in several industries and a lot of work has been dedicated to the design of efficient active or passive damping treatments. Such treatments are usually applied to the vibrating structure by means of an adhesive layer. Being generally made of polymers, adhesive layers may have their properties influenced by a number of environmental parameters, such as temperature or frequency. For instance, Figure 1 evidences the viscoelastic behaviour of a double coated tape used for the assembly of sandwich structures, while the epoxy adhesive has little influence on the dynamic behaviour of the assembled structure. A consequence of the viscoelastic behaviour of the adhesive layer is that it may modify the dynamics of the structure and affect the damping efficiency of the active or passive treatment applied (see Figure 2 and [1]). In some cases, the adhesive layer must be modelled to have a predictive model of the treated structure [2]. Therefore, there is a need for a characterisation procedure to identify to frequency-dependent properties of the adhesive. DMA (Dynamical Mechanical Analysis) measurements are classically used to determine the viscoelastic properties of a material [3]. However, the bonding process generally has an important influence on the mechanical behaviour of the bonding layer, which makes inverse characterisation a more appropriate way of identifying the dynamic properties of the adhesive.

The goal of this work is to present a methodology to characterise and model the adhesive layer. To that purpose, an experimental-numerical method for inverse characterisation of the frequency dependent properties of the adhesive layer is applied. The proposed inverse approach is based on a fractional derivative model whose parameters are identified by minimising the difference between the simulated and the measured dynamic response of a multi-layered structure assembled by bonding. The fractional derivative model presents the advantage of describing accurately the viscoelastic behaviour of many polymers with only four parameters. In the finite element model used for the inverse method, the adhesive layer is modelled by interface finite elements, i.e. by bi-dimensional elements representative of the three-dimensional behaviour of the bonding layer.

The proposed characterisation and modelling procedure is applied to dynamic measurements of a structure assembled with a double coated tape.

2 INVERSE CHARACTERISATION PROCEDURE

In this work, a four-parameter fractional derivative model is used to describe the frequency dependency of the complex shear modulus of the adhesive:

$$G^*(\omega) = \frac{G_0 + G_\infty(i\omega\tau)^\alpha}{1 + (i\omega\tau)^\alpha} \quad (1)$$

where G_0 and G_∞ are respectively the relaxed and unrelaxed moduli, τ is the relaxation time, and α is a fractional parameter comprised between 0 and 1 which corresponds to the non-integer order of derivation in the $\sigma(t) - \epsilon(t)$ relationships [4].

The goal of the inverse method is to identify the parameters of this viscoelastic model by minimising a cost function which is defined as the normalised mean square error between a measured and a simulated response. At each step of the optimisation, the simulated response is computed from a finite element model with updated viscoelastic parameters. Consequently, if the model contains a lot of degrees of freedom or if the optimisation procedure requires a lot of iterations to converge, the inverse procedure may be time-consuming. The former occurs when the thin adhesive layer is modelled with three-dimensional elements since it would require a very fine mesh to avoid numerical problems related to the aspect ratio of the elements. Therefore, interface finite element are used to model the thin adhesive layer. These elements, initially

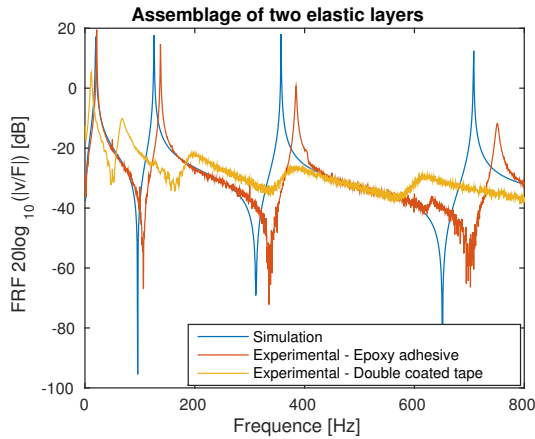


Figure 1: Measured frequency response functions of an assemblage of two $0.26\text{m} \times 0.026\text{m} \times 1\text{mm}$ steel beams realised by application of an epoxy adhesive (red) or a double coated tape (orange), compared to the simulated response computed by a finite element model neglecting the adhesive layer (blue).

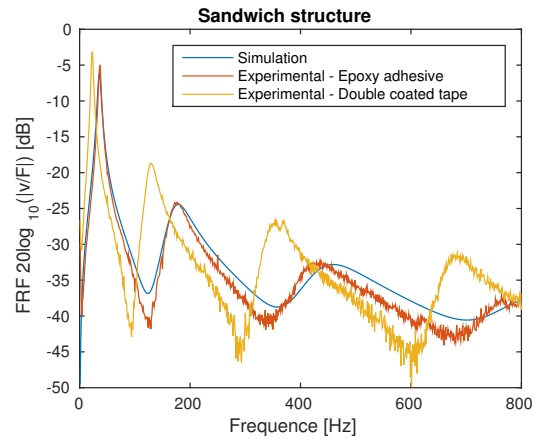


Figure 2: Measured frequency response functions of a sandwich beam with a viscoelastic core assembled by an epoxy adhesive (red) or a double coated tape (orange), compared with the simulated response computed by a finite element model neglecting the adhesive layer (blue).

developed for the modelling of thin constrained viscoelastic layers, consist of a mean surface and a fictive thickness, assumed constant [5]. Moreover, in order to keep the overall number of cost function evaluations reasonable, a gradient-based method (BFGS) is used to update the viscoelastic model's parameters and the gradient of the cost function is evaluated by a direct differentiation approach [6]. Since the problem to be solved is not convex, an initialisation step is introduced. It consists in optimising the model's parameters by minimising a cost function representing the difference between the measured and the simulated resonant frequencies of the structure. In this way, the risk of converging towards a local minimum is reduced.

3 APPLICATION AND RESULTS

The previously described inverse identification method is applied to dynamic measurements of a steel assemblage for the characterisation of a double coated tape (see Figure 1). Figure 3 shows the experimental response compared to the frequency response function computed with the optimised parameters of the viscoelastic model:

$$G_0 = 2.53 \cdot 10^4 \text{ Pa}, \quad G_\infty = 1.51 \cdot 10^8 \text{ Pa}, \quad \tau = 1.32 \cdot 10^{-6} \text{ s} \quad \alpha = 0.88, \quad (2)$$

The corresponding master curves of the adhesive are plotted in Figure 4. The identified properties of the double coated tape allow a good representation of the dynamic behaviour of the assembled structure. The slight overestimation of the damping on some modes may be due to the fact that a four-parameter fractional derivative model may not be the most appropriate model to describe the frequency dependency of the adhesive's properties.

4 CONCLUSION

The inverse characterisation technique presented in this paper aims at determining the parameters of a fractional derivative model which describes the frequency-dependent mechanical properties of adhesives. This can be used to improve the accuracy of a finite element model of a damped structure by taking into account the assembly procedure, and thus better predict the efficiency of the damping treatment.

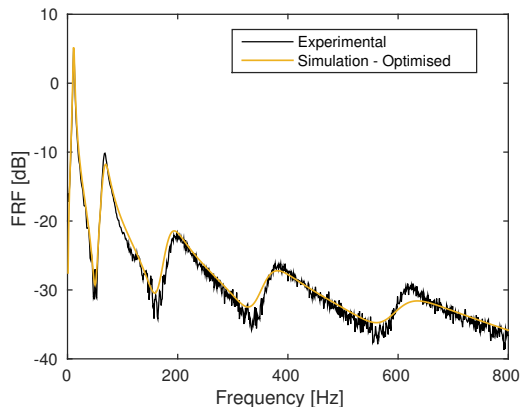


Figure 3: Measured frequency response functions of an assemblage of two $0.26\text{m} \times 0.026\text{m} \times 1\text{mm}$ steel beams realised by application of a double coated tape compared to the simulated response computed with the identified properties of the adhesive.

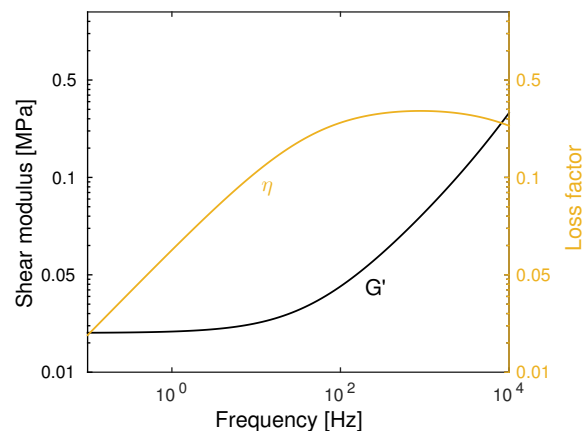


Figure 4: Master curves of the double coated tape, after inverse characterisation, at $T = 20^\circ\text{C}$.

REFERENCES

- [1] O. Rabinovitch and J.R. Vinson. Adhesive layer effects in surface-mounted piezoelectric actuators. *Journal of Intelligent Material Systems and Structures*, 13:689–704, 2002.
- [2] A. Sénéchal. Réduction de vibrations de structure complexe par shunts piézoélectriques - application aux turbomachines. PhD Thesis, Cnam Paris, 2011.
- [3] M. Martinez-Agirre, S. Illesca, and M.J. Elejabarrieta. Characterisation and modelling of prestrained viscoelastic films. *International Journal of Adhesion and Adhesives*, 50:183–190, 2014.
- [4] R.L. Bagley and P.J. Torvik. A theoretical basis for the application of fractional calculus to viscoelasticity. *Journal of Rheology*, 27:201–210, 1983.
- [5] L. Rouleau, J.-F. Deü, A. Legay, and F. Le Lay. Characterization and modeling of viscoelastic interfaces. Proceedings of the 12th International Conference on Computational Plasticity. Fundamentals and Applications, Barcelona, Spain, 2013.
- [6] L. Rouleau, B. Pluymers, and W. Desmet. Characterization of viscoelastic layers in sandwich lightweight panels through inverse techniques. Proceedings of NOVEM, Dubrovnik, Croatia, 2015.

COPYRIGHT NOTICE

Copyright ©2015 by the authors. Distribution of all material contained in this paper is permitted under the terms of the Creative Commons license Attribution-NonCommercial-NoDerivatives 4.0 International (CC-by-nc-nd 4.0).





Sound transmission characterisation: application to a sandwich composite space structure.

A. Cyprien LE PLENIER,

Airbus Defence and Space

Dépt. TSOEM523, 66 route de Verneuil, 78133 Les Mureaux cedex BP 3002
cyprien.le-plenier@astrium.eads.net

ABSTRACT

Acoustic insulation represents a very important issue in many fields of acoustic engineering. This issue is generally assessed through one characteristic named sound insulation parameter or noise reduction level (NR).

Research for materials with high mechanical-resistance-to-weight ratio promotes sandwich composite structures, but these ones present lower acoustic insulation performances than metallic homogeneous structures. Thus, the correct identification and assessment of the main transmission loss factor drivers for sandwich composite structures are essential to improve their acoustic isolation efficiency.

In space industry, acoustic characterization of sandwich composite structures, such as launcher fairing, is a key point for payload and equipment acoustic comfort assessment, when facing severe broadband environment during lift-off phase.

In this paper, the overall approach of acoustic specification to payload is detailed with a particular attention given to the noise reduction level estimation of the fairing structure. The first part will present the Vibroacoustic logic used for acoustic specification. Then, the method employed for fairing exterior acoustic field prediction will briefly be described. Next, the modelling of the composite structure depending on the frequency domain is studied. Finally, the methods used for Vibroacoustic computations as well as comparison with measurements are exposed.

KEY WORDS: *Vibroacoustic LF/HF, Composite structure, Noise Reduction.*

1 INTRODUCTION

In the spatial industries, the launch vehicles are subjected at lift-off and during flight ascent to severe acoustic and aero acoustic environment. This environment is broadband and random and covers a large band of frequency, in the low and high frequency regimes (15-2800 Hz). Electronic equipment and satellites are consequently excited and the induced vibrations must be predicted before flights, in order to be sure that they can endure the induced loads without any damage.

This is why, it is essential to have methods that compute the equipment vibroacoustic response over all frequency ranges of concern. The fairing noise reduction level is an important parameter for payload comfort.

The first part is dedicated to present the logic used to cover the two frequency domains.

2 VIBROACOUSTIC LOGIC

Acoustics covers several dynamic environment of the launcher's life:

- Engine generated acoustic loads during lift-off,
- Aerodynamic loads during ascent,
- Specific acoustic noise excitations (like venting).

The spectra of acoustic environments cover a wide frequency range. Predicted environments are generally limited to frequencies below 10 kHz for manned structures and below 2800 Hz for general structures.

For the fairing, payload acoustic environment is defined up to 2800 Hz.

This wide frequency range load can damage structures in low frequency regime, large area structures directly impacted by acoustics and equipment items that generally have their first modes in Mid/High Frequency. Thus it is necessary to compute the System response all along the frequency range.

Vibroacoustic analyses are divided into two domains along the frequency spectrum:

- Low Frequency [15-200Hz], where the modal density of a given component (number of mode per octave band) is quite low (less than 7 modes per octave band). FEM method can be performed while the number of Eigen modes is quite low,
- High Frequency [50-2800Hz], where the modal density of a given component is too important to look at each Eigen mode in particular. In this frequency range, a statistic method must be used. This method is based on transfer of energy between the components (Statistical Energy Analysis, see [2]).

Vibroacoustic overall logic for computation of response of sub-components is defined according these two approaches with an overlap between the two domains on the frequency range [50-200Hz], when possible. It is possible in the case of big launchers Fairing of sandwich construction, as many modes are present in the 125 Hz octave bands. This overlap is used to cross-check the two methodologies in order to validate the modelling.

With the Maximum Expected Environment computed with these two approaches and a Qualification Margin policy applied, a standard Random Qualification level is chosen to envelope those levels.

Acoustic logic can be summarized with the following diagram:

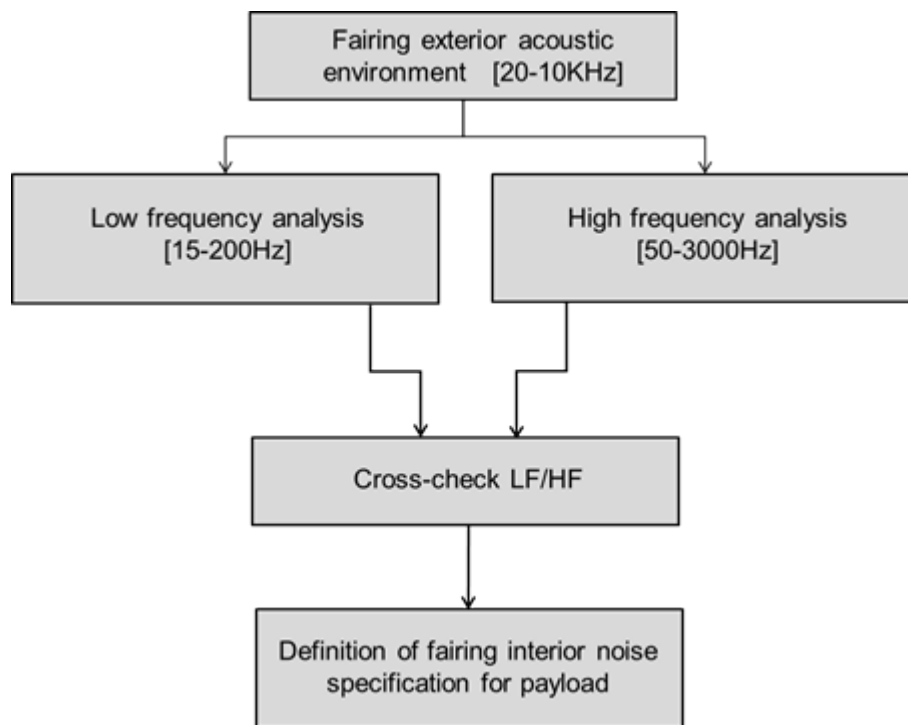


Figure 1. Vibroacoustic logic for payload interior noise specification

3 PREDICTION OF FAIRING EXTERIOR ACOUSTIC ENVIRONMENT

The acoustic loads predictions on space vehicle generated by the interaction of jet thrusters with the launch pad require models base on experimental data, as numerical methods are not available for predicting supersonic jet noise in the presence of waterfall. Simulations are generally validated using reduce scale tests.

In that frame, Airbus Defence and Space homemade software “BRUITJET” based on tests realised in Russia at TSNIIMASH enables to predict wide range acoustic environment during lift-off phase, see [3].

3.1 Method

To represent this interaction, different noise regions are identified. Each of these regions is represented by a system of independent acoustic sources with their own acoustic power and spectrum. The launcher is not modelled, only the free field is computed.

The acoustic field is computed in the symmetrical plan of the duct and the jet. The overall level as well as the spectrum features of the field is obtained by summation of contributions of the different sources.

Hiding and reflections conditions of sources due to the geometry of the duct are established by geometrical conditions. Their power, radiation and directivity come from many experimental data and literature, [3].

Finally, the entrance data for the computation are geometrical data of the studied launch pad configuration and the thermodynamic properties of the jet at exit nozzle.

The Ariane 5 launch pad is presented in the following figure. It is composed of two closed duct to evacuate boosters’ jet as well as on closed duct for the Vulcain engine.

Closed duct enable to put away jet sources to reduce acoustic environment on the launcher. Water injection systems on the launch pad table and inside ducts are also present ignition phase



Figure 2. Ariane 5 launch pad

3.2 Theoretical aspects

To solve the acoustical problem, the jet is decomposed in different regions as shown in the figure here below, ref [3].

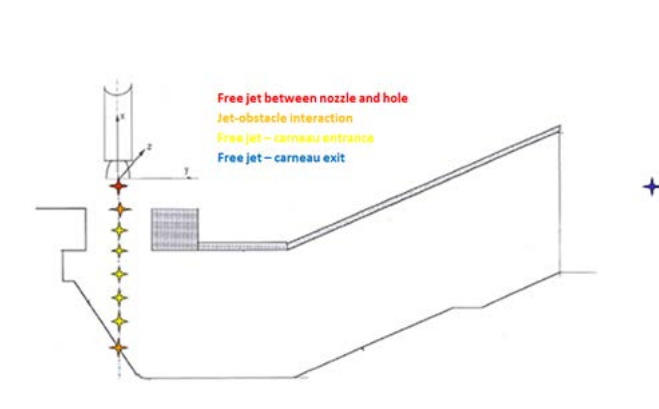


Figure 3. Sketch principal [closed duct]

The regions for the acoustic field computation are detailed here below:

- Free jet region (between exit nozzle and hole) : the acoustic field is modelled as punctual sources,
- Region of strong interaction with the hole,
- Region of the duct entrance (between hole and deflector) : the acoustic field is modelled by a distribution of decorrelated sources,
- Region of the duct exit,
- Reflected acoustic field modelled through the images sources method (inside duct, deflector, for open duct).

There are different types of noise through the frequency ranges:

- Low frequency noise generated in the region of the duct exit,
- Mid frequency noise mainly coming from the jet/ground interaction,
- High frequency noise coming from free jet and acoustic waves reflections on the launch pad.

4 FAIRING VIBROACOUSTIC CHARACTERISATION

The vibroacoustic characterisation of the fairing is done by two computations. One performed for the low frequency domain using modal basis and one for the high frequency domain using SEA (Statistical Energy Analysis).

The low frequency study is mainly used here to understand the PSD of acoustic pressure dispersion inside the cavity. Otherwise, for internal noise specification inside the fairing at the beginning of a new launcher definition, SEA method is used, ref [4].

4.1 5.1 Low frequency domain

The analysis is performed in two steps. First, the modal basis is computed with MSC-NASTRAN FEM software and then Airbus D&S Low Frequency vibroacoustic software LASCAR BF is used.

The FEM model used for vibroacoustic study is the same as the one used for static analysis with mass data added. Fairing sandwich composite structure is then modelled in detailed with NASTRAN PCOMP card that defines the properties of an n-ply composite material laminate. The sandwich of the fairing is composed of carbon and aluminium mainly due to weight constraints.

A picture of the FEM model is shown in the following picture. Payloads volumes are included under the fairing. Tetrahedral elements are used for fluid meshing.

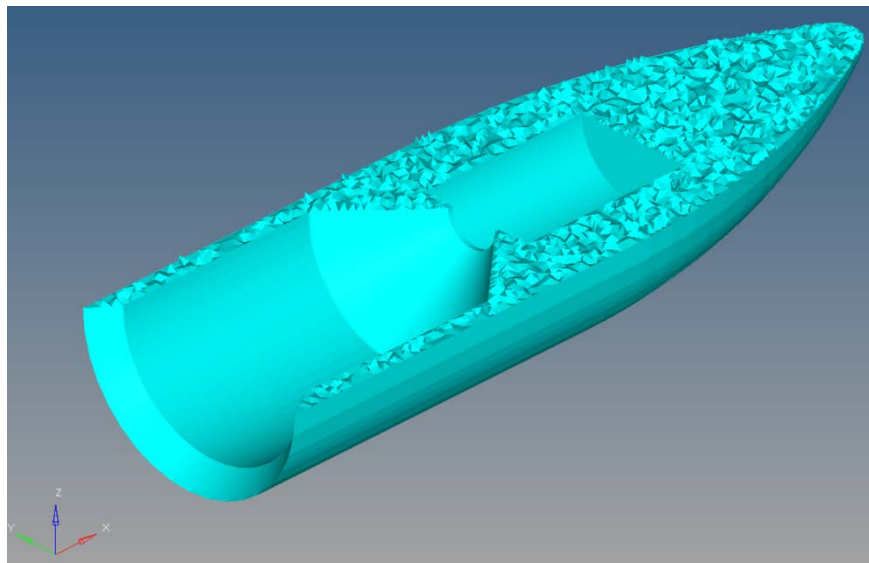


Figure 4. Fairing FEM model

The fairing low vibroacoustic analysis was done with the Airbus D&S software LASCAR BF up to 200Hz using a critical damping loss factor of 2% for the structure and experimental data using reverberation time so as to infer an equivalent modal damping factor for the fluid to take into account the acoustic protection. The acoustic excitation is supposed to be defined as a diffuse field excitation.

LASCAR BF computes the response of a structure under a random excitation using a modal basis coming from NASTRAN (sol 103) and an acoustic excitation matrix in Pa²/Hz, [4].

The PSD excitation is assumed to be homogeneous on the wetted area so as the excitation matrix can be decomposed as a product of an auto spectrum function simply depending of the noise entrance level and a correlation function depending of the type of excitation applied to the structure.

The excitation can be written as followed,

$$S_{PP'}(|P - P'|; \omega) = C(|P - P'|; \omega) \sqrt{S_{pp}(P, \omega) \cdot S_{pp}(P', \omega)} \quad (1)$$

Since the excitation is assumed to be homogeneous, it can be simplified in,

$$S_{PP'}(|P - P'|; \omega) = C(|P - P'|; \omega) \cdot S_{pp}(\omega) \quad (2)$$

where the correlation function C in the case of a diffuse field is analytically known as,

$$C(|P - P'|; \omega) = \frac{\sin\left(\frac{|P - P'| \omega}{c}\right)}{\frac{|P - P'| \omega}{c}} \quad (3)$$

At the highest frequency of study, 200Hz, the distance of the diffuse field correlation is two meters supposing that two points are correlated if the correlation function is at least equal to 0.1. This hypothesis enables to increase the size of the acoustic excitation meshing compared to the structural meshing, hence reduce times computations.

Joint-acceptance function is calculated following,

$$j_{rs}^2(\omega) = \frac{1}{A^2} \sum_i \sum_j S_{p_i p'_j}(\omega) \cdot \Phi_{ir} \Phi_{js} \cdot \Delta S_i \Delta S_j \quad (4)$$

with :

A : the total wetted area,

Φ_{ir} : the modal shape of the mode r at node i,

ΔS_i : the equivalent area associated with node i, $\Delta S_i = \frac{A}{N}$,

N : number of excitation nodes,

$S_{p_i p'_j}(\omega)$: the pressure power spectral density between nodes i and j at frequency ω .

This function simply described the efficiency of the acoustic field on the structural modes.

Finally, the response of the structure is computed. For root mean square acceleration, the equation can be written as followed,

$$\gamma_i^{-2} = \int \sum_r \sum_s \Phi_{ir} \Phi_{is} \cdot \omega^4 H_r(\omega) H_s^*(\omega) \cdot A^2 j_{rs}^2(\omega) d\omega, \quad (5)$$

with :

Φ_{ir} the modal displacement of the mode r at node i,

$H_r(\omega) = \frac{1}{\omega_r^2} \cdot \frac{1}{1 - \frac{\omega^2}{\omega_r^2} - i\eta_r \frac{\omega}{\omega_r}}$, the transfer function of the mode r supposing that modes

are normalised by the generalised mass.

In the case of effort and stress, equations are similar; the modal displacement is simply replaced by modal effort and modal stress.

The synoptic of LASCAR BF software is summed up in the following sketch.

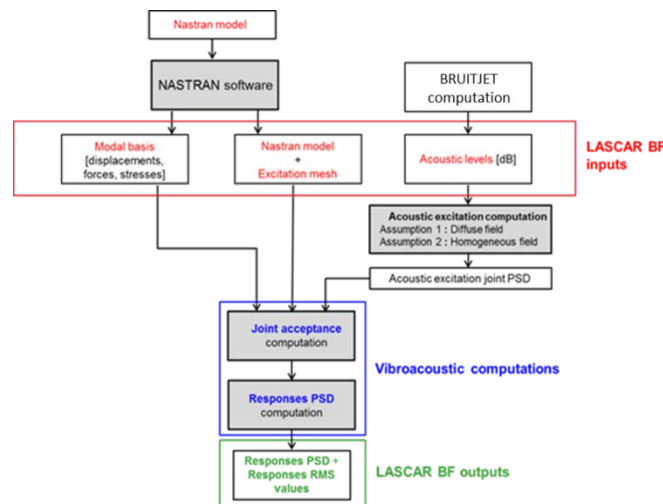


Figure 5. Synoptic of LASCAR BF

4.2 High frequency domain

In the High Frequency domain, the acoustic level is estimated by the SEA (Statistical Energy Analysis) with the in-house Airbus DS software SEALASCAR, ref [4].

SEA is a statistical method based on the exchange of energy between sub-components. A sub-component is a sub-division of the structure and the geometry of each sub-component is approximated by a simplified geometric shape (plate, cylinder, cavity etc...).

This method can be applied when the modal density of the structures and cavities is high (7 modes per octave band at least).

SEA method is not used to provide absolute acoustic levels, but in order to characterize the impact of a design change in the launcher.

The SEA method is based on a statistical analysis on transferred energy between sub-systems. There is no dumping like in FEM method but energy dissipation by the sub-systems, called dumping loss factor.

For structures, the dumping loss factor can be expressed either by a fixed value (for instance 1%) or by the following empirical relation. It yields, ref [4]:

$$\frac{A_0}{f^{B_0}}, \quad (6)$$

where f is the central frequency of the considered octave band. A_0 and B_0 are coefficients different in the case of equipped or non-equipped structures and coming from flights and acoustic tests experience.

In SEALASCAR, the calculation of the modal density of sandwich structures is based on the theory of Erickson, where the shear of the core is taken into account, [5].

For cavities, the damping loss factor is :

$$\eta_c = \frac{C_0 S \alpha}{4 \omega V}, \quad (7)$$

where C_0 , S and V are respectively the sound speed, the surfaces and the volume. α is the Sabine absorption coefficient, given by test. In the computations, experimental data using reverberation time so as to infer an equivalent modal damping factor for the fluid is used. After having described the different approaches Airbus D&S used to compute the noise inside the fairing, NR levels are compared with ground test and flight measurements.

5 COMPARISON OF SIMULATIONS WITH FLIGHT AND GROUND TEST MEASUREMENTS

5.1 Comparison of simulations with ground test measurement – Empty fairing

This section is dedicated to the comparison of results coming from low/high frequency simulations with results of ground test performed at the reverberant chamber of ESTEC regarding the “Noise Reduction” NR in dB per octave band.

The NR is computed as the difference between the external noise and the internal noise inside the fairing.

The internal noise reduction level is calculated as the average of acoustic power inside the overall fairing volume.

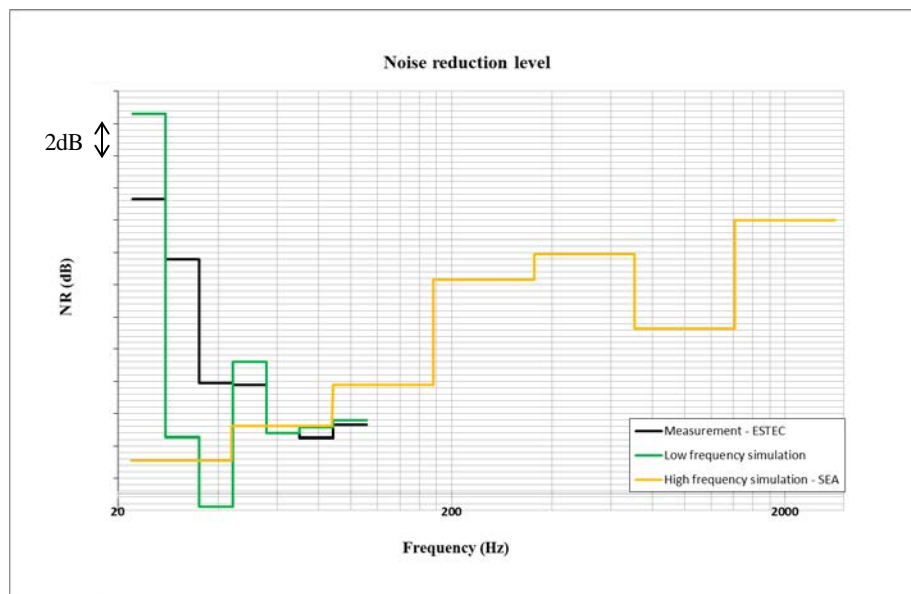


Figure 6. Comparison between simulation and ground test

Measurements and simulations are well correlated after 40Hz. Low frequency estimation and high frequency one have an overlap in the frequency range [40-100Hz] with maximum differences of 2dB.

Added to this, differences observed before 40Hz are mainly due to the assumption of diffuse field which is not respected in measurements due to cutting frequency of the reverberant room (modal behaviour).

After having compared simulation with reverberant room measurements for empty fairing, flight configuration is studied.

5.2 Comparison of simulations with flight measurement – Fairing with payloads volumes

The objective of this section is to compare noise reduction levels computed by simulations with measurements coming from flight 215 L570 [fairing with payloads] and ground test presented before [empty fairing].

The following figure presents the upper part configuration for the flight 215 (570) composed of a long fairing and a SYLDA family D. The fairing is covered by an acoustic protection. The payloads inside were manufactured by Space Systems / LORAL and I.S.R.O.

The fairing internal pressure during flight is measured by two sensors. For the external noise a sensor located on a tour on the launch pad one for each Ariane 5 flight is used.

However, to better represent the external noise that load the fairing; acoustic field has been measured during the experimental Ariane 5 flight 164 L521 using sensors outside the fairing.

To take into account exterior noise dispersion between flight 570 and 521 a correction computed as the ratio between sensors located on the tour is applied.

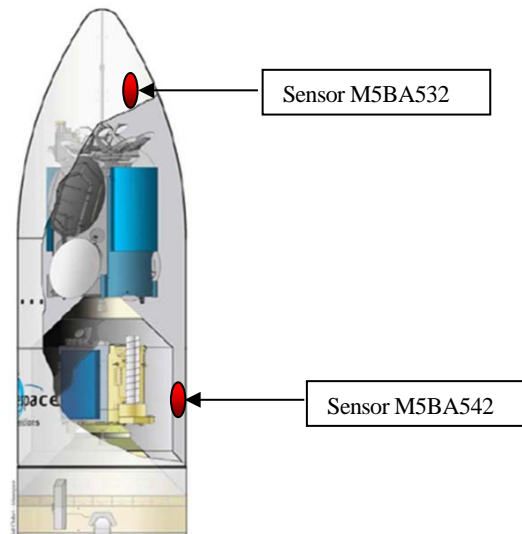


Figure 7. Fairing configuration for flight 215 L570

The next plot present the noise reduction level estimated during with flight measurements to see the influence of the payload volume inside the fairing.

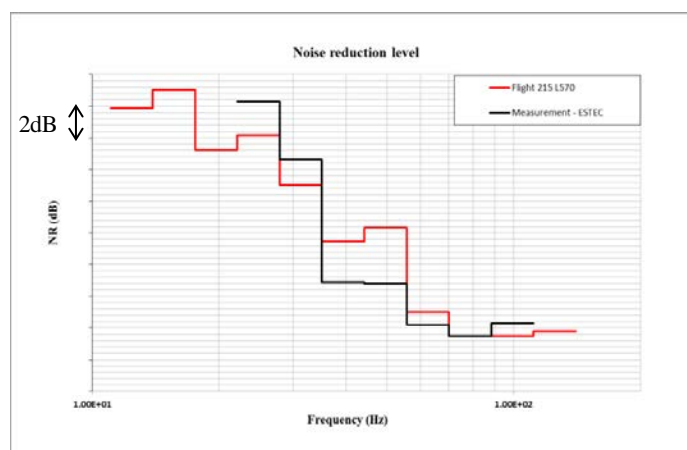


Figure 8. Comparison between flight and ground test measurements

The following plot compares low frequency simulations with flight. The two measurements fit quiet well. Differences are not only due to the payload volume that modify modal behaviour of the fluid but also due to fairing excitation.

The next plot shows that using two types of correlation, simulations can covered the noise reduction measured in flight.

The blue curve represents the noise reduction level coming from low frequency simulation using a rocket engine noise correlation instead of a diffuse field one. This correlation is coming from [1] and can be seen as a progressive wave coming from jet engine noise in longitudinal and radial direction.

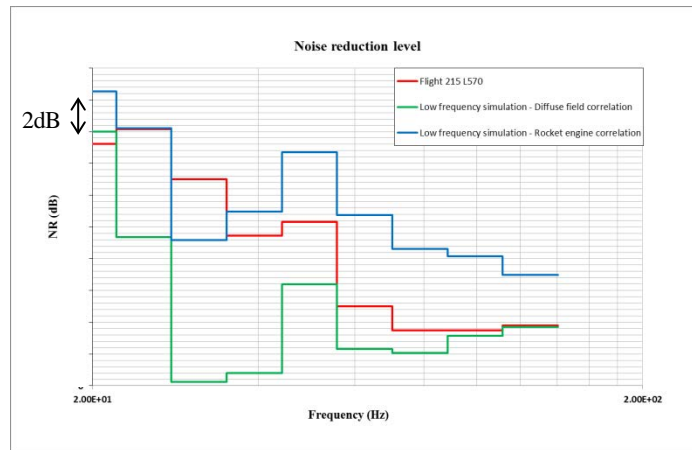


Figure 9. Comparison between flight and simulations (for two type of correlation)

Engine rocket noise correlation match well with flight in low frequency ($f < 30\text{Hz}$) and for frequency superior to 30Hz , diffuse field correlation fit well with flight. The flight noise reduction level is framed with simulations.

6 CONCLUSION

This paper is focus on our capability to predict noise reduction level for a space sandwich structure of major importance for payload comfort.

It has been firstly shown that low frequency method using finite elements and high frequency ones are able to well represent the sandwich structure and fit with reverberant room measurements for an empty fairing.

Then, noise reduction level measured in flight has been compared to low frequency simulations for configuration flight fairing. It has been shown that two types of correlation, the rocket engine noise for frequencies less than 30Hz and diffuse field for frequencies above are able to frame the flight. Indeed, rocket noise correlation during lift-of phase can be seen as a mix between progressive waves added with a diffuse field.

Work is still in progress on that topic to understand what is the part of those two correlations model is in order to improve low frequency simulations and payloads acoustic environment for new launcher.

REFERENCES

- [1] NASA-HDBK-7005. *NASA Technical Handbook – Dynamic Environmental Criteria*. Publisher, 2001.
- [2] Lyon R. H. *Statistical Energy Analysis of Dynamic Systems. Theory and Applications*. MIT press 1984.
- [3] Dementjev V. C., Rybak S. P., Koudriavtsev V. V., Safronov A. V., Troclet B. Technique for predicting the acoustical environment resulting from a launch vehicle engine jets interaction with a launch pad. *Proceedings of First European Conference on Launcher Technology. Launch Vehicle Vibrations*, December 14- 17, Toulouse, pp 169- 178 1999.
- [4] Troclet B. Low and High Frequency Prediction of the Vibroacoustic Response of Launch Vehicles and Aircrafts. *New Advances in Modal Synthesis of Large Structures*. A. A Balkema/Rotterdam/Brookfield, pp. 279- 290, 1997.
- [5] Erickson L. L. Modal densities of Sandwich Panels: Theory and Experiment. *Shock and Vibration bulletin n°39, Part 3* pp 1-16, 1969.



DELAMINATION AND DEBONDING PREDICTIONS FOR TYRE IMPACT ONTO COMPOSITE A/C COMPONENTS

Dr Michel Fouinneteau¹

¹Airbus Operation S.A.S, 316 route de Bayonne, 31060 Toulouse Cedex 09, France

Email: Michel.fouinneteau@airbus.com

ABSTRACT

Tire debris impact is a recurring event in the aircraft lifetime, which can potentially affect its structural integrity. In this work, delamination and debonding failure mechanisms are investigated in order to define a robust modeling method applicable at aircraft subcomponent level.

A standard cohesive element available in the explicit code Abaqus is used to represent ply interface and bondline failure. Due to finite element model size limitation driven by industrial operability, relatively large cohesive element size was used. A calibration exercise based on an existing knock-down method was conducted to insure correlation at coupon levels such as DCB, ENF and MMB. The calibrated methodology confidence was assessed upon three different levels of structural complexity ranging from skin panel to wing box lower skin based on Airbus building block approach philosophy.

Numerical predictions for delaminated and debonded areas have shown a satisfying level of correlation to test in terms of predicted damage and overall structural behavior. Such methodology can be used to have a general assessment on post-impact structure integrity.





SENSITIVITY ANALYSIS OF TRANSMISSION LOSS THROUGH COMPOSITES WITH ACOUSTIC TREATMENT

J.-L. Christen¹, M. Ichchou¹, B. Troclet², O. Bareille¹, M. Ouisse³

¹LTDS

École centrale de Lyon, cully, FRANCE
Email: jean-loup.christen@ec-lyon.fr

²Airbus Defence and Space
Route de Verneuil, Les Mureaux, FRANCE

³Femto-st
Chemin de l'Épitaphe, Besançon, FRANCE

ABSTRACT

Composite materials are widely used in the aerospace industry, for their low mass and high stiffness, however, these characteristics tend to increase noise transmission. Sound protection must therefore be added, in the form of porous material layers. Uncertainties may affect both the structural and sound package parameters. It is therefore important to assess the influence of these uncertain parameters on the sound transmission properties of the assembly. The sound transmission loss through a composite plate-foam assembly is first computed with the transfer matrix method. The effect of uncertainty of several parameters such as the porosity, flow resistivity and mechanical parameters is then analysed with the FAST (Fourier amplitude sensitivity test) method. The effect of adding a thin screen at the interface between the porous and air is also investigated.

1 INTRODUCTION

Noise transmission is often a major concern in the industry. Composite structures are known to have lower acoustic performance than their metallic counterparts, but their high stiffness to mass ratio makes them more and more used in aerospace applications. One of the most frequently used construction is the sandwich one, with stiff skins constraining a softer, shearing core. Analytical models of sound transmission have been proposed in the literature [1, 2]. Some kind of acoustic treatment is then needed to enhance the transmission loss. Porous materials such as fibreglass are commonly employed for this purpose, which can be modelled with the Biot model [3, 4]. Sometimes a thin screen can be glued to the porous material to protect it on the transmission side.

Some variability always occur when modelling the transmission loss of structures with noise treatment, due either to uncertainty in the parameter measurement, or to design latitudes allowing for optimisation. It is therefore of utmost importance to assess the effect of this variability on the model output, and estimate the sensitivity of it with respect to each uncertain parameter. Several methods have been proposed for this purpose, one of the most popular being the evaluation of Sobol indices [5]. The Fourier Amplitude Sensitivity Test (FAST) method [6] has been proposed to accelerate the computation of these indices and already used successfully for acoustic and poroelastic applications [7].

We propose here to use the (FAST) method to investigate the effect of several parameters of a plate-porous assembly such as the one shown on figure 1. This paper is structured as follows. The FAST method is first presented in section 2. A model of transmission loss through infinite plane assemblies of composite a porous materials based on the transfer matrix method is presented in section 3. Finally some results are discussed in section 4.

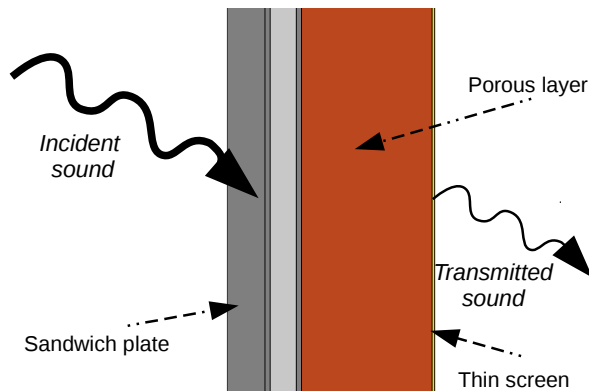


Figure 1: View of the studied configuration. The influence of the presence of a limp screen on the transmission side is studied

2 GLOBAL SENSITIVITY ANALYSIS: THE FAST METHOD

In the analysis of variance technique, a parameter's influence on the model output is quantified by the impact it has on the variance in the given design range. In the following development, a generic mathematical model is considered. A model is a real valued function f defined over K^n , where $K = [0, 1]$. With appropriate scaling and translations, any model defined over continuous ranges of parameters can be represented that way.

For a given model f linking input parameters $\mathbf{x} = (x_1, \dots, x_n)$ to a scalar output $y = f(\mathbf{x})$,

there exists a unique partition of f so that

$$y = f(x_1, x_2, \dots, x_n) = f_0 + \sum_{i=1}^n f_i(x_i) + \sum_{i<j} f_{ij}(x_i, x_j) + \dots + f_{1\dots n}(x_1, \dots, x_n) \quad (1)$$

provided that each function f_I involved in the decomposition has zero mean over its range of variation. The decomposition given by equation 1 is called the Hoeffding decomposition or high order model representation (HDMR) [8].

For a given set of indices $I = \{i_1, \dots, i_n\}$, the partial variance is therefore the variance of f_I

$$D_I = \int_{K|I} f_I(x_I)^2 dx_I \quad (2)$$

the sensitivity index relative to the set I is expressed as the ratio of the variance of the function f_I to the total variance of the model:

$$SI(I) = \frac{D_I}{D}. \quad (3)$$

The computation of all the 2^n sensitivity indices is needed to represent completely the model, however this becomes quickly a very costly task in terms of computational time, as they have to be evaluated by numerical integration. However, most information about a parameter's influence can be found in the first-order sensitivity index and the total sensitivity index, which can be computed more efficiently with the FAST method.

For a given parameter $i \in [1, n]$, the main effect (ME) is then the sensitivity index relative to the 1-dimensional function f_i .

The first-order index represents the share of the output variance that is explained by the considered parameter alone. Most important parameters therefore have high ME, but a low ME does not mean the parameter has no influence, as it can be involved in interactions.

The idea of the FAST method is to avoid the evaluation of the n -dimensional integrals needed for the computation of the f_i functions, and replace them by a single 1-dimensional integral along a *space-filling* curve in the design space. This curve is defined so as to be periodic with different periods relative to each parameter. Saltelli [9] propose the sampling function defined by:

$$x_i = \frac{1}{2} + \frac{1}{\pi} \arcsin(\sin(\omega_i s + \varphi_i)) \quad (4)$$

The frequencies ω_i are integers chosen so as to minimize interference between parameters[10]. The frequencies are said to be free of interference up to order M if all linear combinations

$$\sum_{i=1}^n \alpha_i \omega_i \neq 0 \quad (5)$$

where $\alpha_i \in \mathbb{Z}$ and $\sum_{i=1}^n |\alpha_i| < M$.

As all frequencies are integers, the resulting function is 2π -periodic with respect to variable s . The sampling is then done using $N > 2\omega_n + 1$ samples in the $[0, 2\pi]$ interval. Calling $y_k = f(x_k)$ the model output on each sample, the discrete Fourier transform \hat{y}_k can be computed.

The total variance of the function in the design space is computed with Parseval's theorem as

$$D = \int_K f^2(x) - f_0^2 dx \approx \sum_{k=1}^N y_k^2 = \sum_{k=1}^N \hat{y}_k^2 \quad (6)$$

The contribution of parameter i will then be:

$$D_i = \sum_{k=1}^M \hat{y}_{k\omega_i} \quad (7)$$

3 THE SIMPLIFIED TRANSFER MATRIX METHOD

The sound transmission loss through a multilayered structure composed of plates, air gaps and poroelastic materials can be computed with the transfer matrix method (TMM). This method was first proposed by Brouard *et al.* [11] and extended by Allard and Atalla [4]. We shall use here a simplified version presented by Hu [12] valid for limp poroelastic materials. The acoustic behaviour of the structure can be represented with only the fluid pressure p and normal velocity v as state variables. These two variables are defined in each point in the fluid layers, and on each side of the solid layers. Each layer can be represented by a 2×2 matrix linking the state variables on one side to those on the other side, and a global transfer matrix can be obtained by multiplying all these matrices together. The transfer equation then reads:

$$\begin{pmatrix} p_L \\ v_L \end{pmatrix} = \begin{pmatrix} T_{11} & T_{12} \\ T_{21} & T_{22} \end{pmatrix} \begin{pmatrix} p_R \\ v_R \end{pmatrix}, \quad (8)$$

where indices R and L stand for right and left sides of the structure. Waves on each side can be decomposed in positive- and negative-going waves, which can be written :

$$p_R = p_R^+ + p_R^- \quad \text{and} \quad p_L = p_L^+ + p_L^- \quad (9)$$

According to the pressure-displacement relation in the fluid, the normal velocities are:

$$v_R = Y_0(p_R^+ - p_R^-) \quad \text{and} \quad v_L = Y_0(p_L^+ - p_L^-), \quad (10)$$

where $Y_0 = \cos \theta / \rho_0 c_0$ is the characteristic admittance of the surrounding fluid.

This leads to rewriting equation 8 as

$$\begin{cases} p_L^+ + p_L = T_{11}(p_R^+ + p_R^-) + Y_0 T_{12}(p_R^+ - p_R^-) \\ p_L^+ - p_L = \frac{T_{21}}{Y_0}(p_R^+ + p_R^-) + T_{22}(p_R^+ - p_R^-) \end{cases} \quad (11)$$

We will be studying transmission of a plane wave incident from the left side, whose interaction with the structure creates a reflected wave into the left side, and a transmitted wave into the right side. In that case, no negative-going wave will propagate in the right side. The acoustic transparency is defined as the ratio of transmitted to incident acoustic intensities, which reduces to

$$\tau = \left| \frac{p_R^+}{p_L^+} \right|^2 \quad (12)$$

in the case of identical fluids on each side of the structure. Solving the system in equation 11, we get

$$\tau(\omega, \theta) = \frac{1}{4} \left| T_{11} + T_{12} Y_0 + \frac{T_{21}}{Y_0} + T_{22} \right|^2 \quad (13)$$

The diffuse field transmission loss is then obtained by performing a weighted average of the transparency over an angular range. The full range $[0; \pi/2]$ is retained here. In that case, we get the diffuse field transparency:

$$\tau_d(\omega) = 2 \int_0^{\pi/2} \tau(\omega, \theta) \sin \theta \cos \theta d\theta. \quad (14)$$

The transmission loss (TL) is then defined as

$$TL = -10 \log_{10} \tau_d. \quad (15)$$

The transfer matrices for a sandwich plate and a limp poroelastic material are derived in the following subsections. Due to the forced nature of the excitation, the transverse wavenumber $k_t = \frac{\omega}{c} \sin \theta$ and the pulsation of the incident wave ω are conserved across the whole system.

3.1 Transfer matrix of a sandwich plate

The transfer matrix of a general plate can be obtained from its constitutive equation in presence of forced loads. When excited by a plane wave with frequency ω , the plate will vibrate and radiate one acoustic wave on each side, respectively reflected and transmitted. The constitutive equation can be put under the general form

$$Zv = p_L - p_R, \quad (16)$$

where Z , a linear operator, is the impedance of the plate. The sound field on the left side of the plate is p_L and on the right side it is p_R .

The continuity of normal speed between the surrounding fluids and the plate imposes $v_L = v_p$, hence

$$\begin{pmatrix} p_L \\ v_L \end{pmatrix} = \begin{pmatrix} 1 & Z \\ 0 & 1 \end{pmatrix} \begin{pmatrix} p_R \\ v_R \end{pmatrix} \quad (17)$$

For a sandwich plate, the constitutive equation is given by Mead [1], with five main parameters, namely skin bending stiffness D_t , overall bending stiffness B , damping η , surface mass m and shear stiffness g . After minor corrections, this reads:

$$D_t(1+i\eta)\nabla^6 w - g(D_t+B)(1+i\eta)\nabla^4 w + m\frac{\partial^2 w}{\partial t} - \frac{mB}{N}\frac{\partial^2}{\partial t^2}\nabla^2 w = (\nabla^2 - g)(p_L - p_R), \quad (18)$$

where $w = v/i\omega$ is the normal displacement of the plate. In the considered frame where a forced wave is imposed on the plate with a wavenumber $k_t = \frac{\omega}{c} \sin \theta$, the spatial derivative operator ∇ can be replaced by $-ik_t$. This leads to the following expression of the impedance

$$Z(\omega, \theta) = \frac{D_t k^6 + g(D_t + B)k^4 - m\omega^2 k^2 - mg\omega^2(1 - \nu^2)}{i\omega(k^2 + g)}. \quad (19)$$

For sandwiches made of isotropic materials and identical skins, the skin bending stiffness is $D_t = \frac{Eh_s^3}{6(1-\nu^2)}$ the overall bending stiffness is $B = Eh_c^2 h_s (1 + \frac{h_s}{h_c})^2 / 2$ and the shear stiffness is $g = Gh_c \left(1 + \frac{h_s}{h_c}\right)^2$. This expression is equivalent to that of a thin plate if the shear stiffness is infinite.

3.2 Limp poroelastic model

Poroelastic materials can be modelled with the Biot-Allard model, taking into account wave propagation in the fluid and solid phases. However, if the material is especially limp, like fibreglass, it can be possible to neglect the solid part and model it as an equivalent fluid with complex and frequency dependent parameters. The wave propagation equation in the porous layer reduces to one scalar equation[4]

$$\Delta p + \frac{\tilde{\rho}^{limp}}{\tilde{K}_{eq}} \omega^2 p = 0, \quad (20)$$

where $\tilde{\rho}_{limp}$ is the equivalent density and \tilde{K}_{eq} the equivalent bulk modulus of the fluid representing the porous material. These two quantities are complex and frequency dependent. Their expression is given in chapter 5 of reference [4]:

$$\tilde{K}_{eq} = \frac{\gamma P_0}{\phi \left(\gamma - \frac{\gamma-1}{K} \right)} \quad (21)$$

$$(22)$$

$$\tilde{\rho}_{limp} = - \frac{\rho_0^2 - \frac{1}{\phi^2} (\rho_1 + \phi \rho_0) \left(\frac{iB}{\omega} + \alpha_\infty \phi \rho_0 \right)}{\rho_1 - 2\rho_0 + \phi \rho_0 + \frac{1}{\phi^2} \left(\frac{iB}{\omega} + \alpha_\infty \phi \rho_0 \right)} \quad (23)$$

where the coefficients K and B can be expressed as

$$K = 1 + \frac{8\mu_0}{i\omega \text{Pr} \Lambda_{therm}^2 \rho_0} \sqrt{1 + i\omega \frac{\text{Pr} \Lambda_{therm}^2 \rho_0}{16\mu_0}} \quad (24)$$

$$(25)$$

$$B = \sigma \phi^2 \sqrt{1 + 4i\omega \frac{\alpha_\infty^2 \mu_0 \rho_0}{(\sigma \Lambda_{visc} \phi)^2}}. \quad (26)$$

The parameters Pr, μ_0 , P_0 and ρ_0 are respectively the Prandtl number, the dynamic viscosity, the bulk modulus and the density of air, whose reference values at 20°C are given in table 1.

The porous material is described by six characteristic parameters, namely the porosity ϕ , the flow resistivity σ , the static tortuosity α_∞ , the viscous and thermal dissipation characteristic lengths Λ_{visc} and Λ_{therm} , and the *in vacuo* skeleton density ρ_1 .

Parameter	description	unit	value
Pr	Prandtl number	-	0.71
μ_0	dynamic viscosity	Pa.s	$1.845 \cdot 10^{-5}$
ρ_0	density	kg.m ⁻³	1.21
P_0	reference pressure	Pa	101325

Table 1. Reference parameters for air at 20°C.

The complex wavenumber of the wave propagating in the equivalent fluid is, according to equation 20:

$$k = \omega \sqrt{\frac{\tilde{\rho}_{limp}}{\tilde{K}_{eq}}}, \quad (27)$$

and the normal component is $k_n = \sqrt{k^2 - k_t}$.

The transfer equation between two points inside the equivalent fluid separated by a distance h then writes:

$$\begin{pmatrix} p_L \\ v_L \end{pmatrix} = \begin{pmatrix} \cos(k_n h) & i\omega \frac{\tilde{\rho}_{limp}}{k_n} \sin(k_n h) \\ i \frac{k_n}{\omega \tilde{\rho}_{limp}} \sin(k_n h) & \cos(k_n h) \end{pmatrix} \begin{pmatrix} p_R \\ v_R \end{pmatrix}. \quad (28)$$

The previous equation is valid for the wave inside the fluid. When coupled to another medium, the continuity of normal speed should account for the porosity of the material. If the other material is a plate or the surrounding air, this conditions reads

$$\phi v_{poro} = v_m, \quad (29)$$

where v_m is the normal velocity inside the other medium. The complete transfer matrix of the porous layer then writes:

$$T_{poro} = \begin{pmatrix} 1 & 0 \\ 0 & \phi \end{pmatrix} T_p \begin{pmatrix} 1 & 0 \\ 0 & \frac{1}{\phi} \end{pmatrix}. \quad (30)$$

4 RESULTS

The transmission loss of a system composed of a honeycomb panel and a fibreglass layer has been studied. This was modelled with the analytical model described in section 3, where the global transfer matrix is

$$T_{bare} = T_{sandwich} T_{poro}, \quad (31)$$

where $T_{sandwich}$ is given in equation 17 and T_{poro} in equation 30. A second configuration in which a thin limp screen is glued to the porous layer at the interface with the receiving cavity is studied. In this case, the transfer matrix is

$$T_{screen} = T_{bare} \begin{pmatrix} 1 & i\omega m_{screen} \\ 0 & 1 \end{pmatrix}. \quad (32)$$

In both cases, the diffuse field transmission loss is computed with equation 15 between 100Hz and 10kHz. All constant parameters are summarised in table 2. We would like to study the effect of five parameters on the overall transmission loss in the two configurations, namely 2 parameters of the sandwich, core shear modulus and damping coefficient, and 3 parameters of the fibreglass layer, its porosity ϕ_0 , flow resistivity σ and viscous characteristic length Λ_{visc} . The two characteristic lengths Λ_{visc} and Λ_{therm} are usually correlated, which will be taken into account by taking $\Lambda_{therm} = 2\Lambda_{visc}$. The variation ranges of these five parameters are shown in table 3. They are chose as realistic considering both uncertainty in measurement and some latitude in design.

Results of the FAST analysis are presented in figure 2 for the bare case and 3 for the case with a screen. The sensitivity indices of each parameter are presented as proportions of the standard deviation. Some conclusions can be drawn for both cases: none of the considered parameters is important in low frequency, while the dominant parameter in HF is the viscous length, which accounts also for the thermal characteristic length, as they are considered proportional. The parameters of the structure (G and η) have no significant incidence on the transmission loss in their considered variation ranges. This is due to the fact that the considered frequency range is well below the coincidence frequency, which occurs around 19kHz.

The transmission loss variation range is shown for the two cases in figure 4 for the two cases. It can be seen that the addition of a thin screen reduces the loss in low frequency, but improves in much more in high frequency. A mass-fluid-mass resonance phenomenon appears in both cases, where the TL is lower around 500Hz for the screen case, and around 1kHz for the bare case. In both cases, flow resistivity σ is the dominant parameter between 1000 and 1500Hz. This phenomenon is due to the mechanical resonance of the cavity filled of porous, analogous to what happens in a double-plate system.

The main difference between the two cases in terms of sensitivity is the preponderance of porosity between 400 and 1200 Hz when a screen is placed after the porous material. The overall effect of the screen is globally to increase the transmission loss above 650 Hz, and reduce the variability of the TL with respect to the investigated parameters.

5 CONCLUSION

A model of transmission loss through composite sandwich plates with attached limp poroelastic materials based on the transfer matrix method has been proposed in this paper. Its sensitivity

Parameter	description	unit	value
E	Skin Young modulus	GPa	47
ν	Poisson ratio	–	0.1
h_{skin}	Skin thickness	mm	1
h_{core}	Core thickness	mm	12.7
m	Sandwich surface density	kg.m ⁻²	8
α_{∞}	Tortuosity	–	1.25
ρ_1	Porous <i>in vacuo</i> density	kg.m ⁻³	5.5
Λ_{therm}	Thermal characteristic length	μm	$2\Lambda_{visc}$
h_{poro}	Porous thickness	mm	50
m_{screen}	Screen surface density	kg.m ⁻²	0.2

Table 2. Constant parameters considered in this study

Parameter	description	unit	min. value	max. value
G	Shear modulus of the sandwich's core	MPa	20	40
η	Structural damping	–	10^{-3}	10^{-2}
ϕ_0	Porosity	–	0.85	0.99
σ	Flow resistivity	kN.m ⁻⁴ .s	10	30
Λ_{visc}	Viscous characteristic length	μm	25	75

Table 3. Variable parameters considered in this study

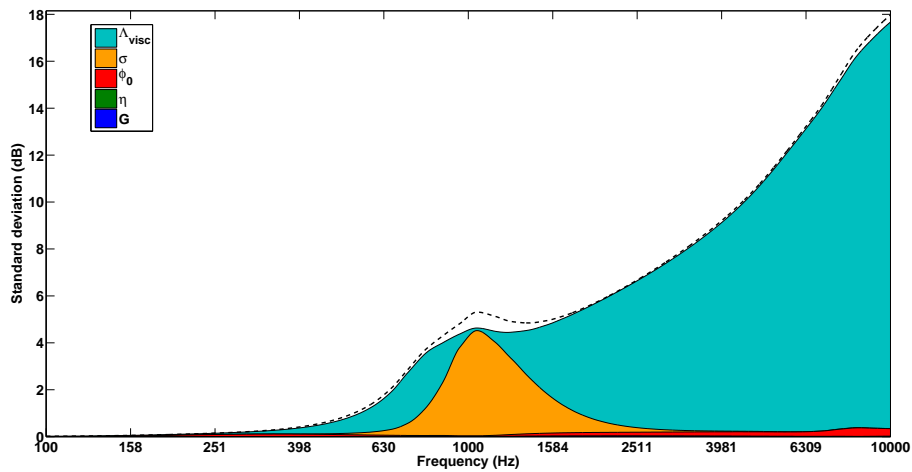


Figure 2. Sensitivity indices in the bare configuration

to several parameters is studied with the FAST method, which allows to efficiently estimate the sensitivity indices of parameters subjected to uncertainty in a model. However the uncertainty level of the parameters should be known before the analysis, in the form of a variation range or a probability distribution.

In the considered case, it has been found that the most important parameters in high frequency are the viscous and thermal characteristic lengths, as well as the flow resistivity in an intermediate frequency range around the mass-fluid-mass resonance. The presence of a light thin screen on the transmission side allows to efficiently increase the TL in high frequency, though lowering the mass-air-mass resonance, which leads to slightly reduced performance in

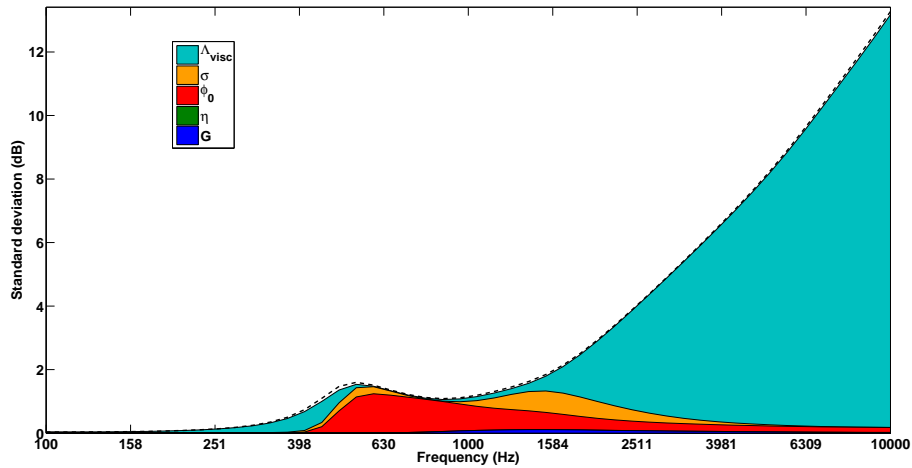


Figure 3. Sensitivity indices in the screen configuration

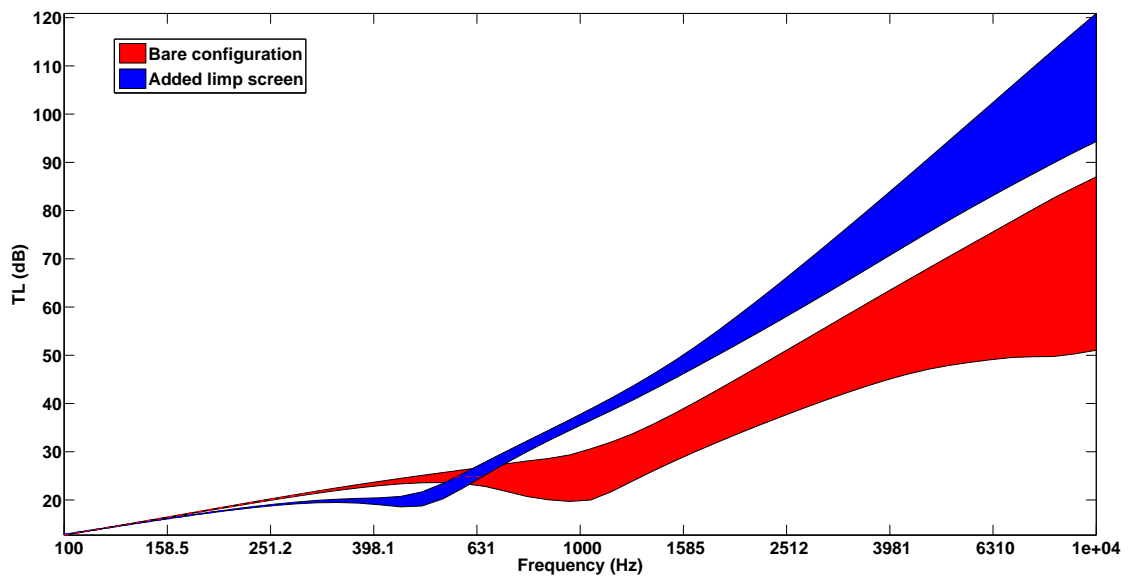


Figure 4: Transmission loss variability in the two configurations (average value \pm standard deviation). Red: bare case ; blue: thin screen.

low frequency. In low frequency, the overall variability of the parameters stays low, well below 1dB, because none of the investigated parameters have an effect on the mass of the system, and the effect of poroelastic materials is usually rather weak in low frequencies.

ACKNOWLEDGEMENT

The authors would like to gratefully acknowledge Airbus Defence and Space for their financial support. This project is part of the international cooperation project CRIAQ ACOU504_INTL.

REFERENCES

- [1] D. J. Mead and S. Markus. The forced vibration of a three-layer damped sandwich beam with arbitrary boundary conditions. *Journal of Sound and Vibration*, 10:163–175, 1969.
- [2] K. Renji. Sound transmission loss of unbounded panels in bending vibration considering transverse shear deformation. *Journal of Sound and Vibration*, 283:478–486, 2005.
- [3] M. A. Biot. Theory of propagation of elastic waves in a fluid saturated porous solid. i. low frequency range. II. higher frequency range. *Journal of the Acoustical Society of America*, 28(2), 1956.
- [4] J. F. Allard and N. Atalla. *Propagation of sound in porous media*. John Wiley & Sons, Ltd., 2009.
- [5] I. M. Sobol. Sensitivity analysis for nonlinear mathematical models. *Mathematical modeling and computational experiment*, 1:407–414, 1993.
- [6] R. I. Cukier, C. M. Fortuin, K. E. Shuler, A. G. Petschek, and J. H. Schaibly. Study of the sensitivity of coupled reaction systems to uncertainties on rate coefficients. I. Theory. *Journal of Chemical Physics*, 59(8).
- [7] M. Ouisse, M. Ichchou, S. Chedly, and M. Collet. On the sensitivity analysis of porous material models. *Journal of Sound and Vibration*, 331:5292–5308, 2012.
- [8] W. Hoeffding. A class of statistics with asymptotically normal distribution. *The annals of Mathematical Statistics*, 19:293–325, 1948.
- [9] A. Saltelli, S. Tarantola, and K. P.-S. Chan. A quantitative model-independent method for global sensitivity analysis of model output. *Technometrics*, 41(1):39–56, 1999.
- [10] G. J. McRAE, J. W. TILDEN, and J. H. SEINFELD. Global sensitivity analysis –a computational implementation of the fourier amplitudesensitivity test (FAST). *Computers and chemical engineering*, 6(1):15–25, 1982.
- [11] B. Brouard, D. Lafarge, and J.-F. Allard. A general method of modelling sound propagation in layered media. *Journal of Sound and Vibration*, 183(1):129–142, 1995.
- [12] Ying Hu. *Development of hybrid passive/active panels for acoustics*. PhD thesis, École Centrale de Lyon, 2010.

COPYRIGHT NOTICE

Copyright ©2015 by the authors. Distribution of all material contained in this paper is permitted under the terms of the Creative Commons license Attribution-NonCommercial-NoDerivatives 4.0 International (CC-by-nc-nd 4.0).





ANALYSIS OF THE STIFFNESS CONTRAST OF A MECHANICAL STRUCTURE MADE OF COMPOSITE MATERIALS

M. Nobou Dassi^{1,2}, A. Gaudin¹, Z. Abbadi¹, L. Gagliardini¹, C. Pézerat² and F. Gautier²

¹PSA Peugeot Citroën, Direction de la Recherche et de l'Ingénierie Avancée
Route de Gisy, 78140 Vlizey-Villacoublay - France
Email: martial.noboudassi@mpsa.com

²Laboratoire d'Acoustique de l'Université du Maine
Rue Aristote, 72085 Le Mans cedex 9 - France

ABSTRACT

In the context of lightening automotive vehicles to reduce the greenhouse gas emissions, one solution considered is to use composite materials. The introduction of such orthotropic materials can yet significantly modify the automotive design due to the new distribution of local stiffness. These modifications may result in very different vibro-acoustic behaviours and therefore different NVH performances. Indeed, the panels can participate more greatly to the overall stiffness of the car, reducing the ratio of frame in the architecture and therefore the number of assemblies. The objective of this work is to bring out the concept of structural contrast and define the associated indicator. This indicator suitable to any kind of material ensures the level of performance requested by the stakeholders.

Several strategies can be used to highlight the vibrational contrast of a mechanical structure made of frame and panels. In this work, this concept is investigated by using an analytical model made of a plate and five rectangular section beams. This model allows an easy introduction of the detailed coupling expressions at the interface between a frame and panels. The system is studied using a modal approach. The computations of point mobilities allow building maps which are representative of the vibrational behaviour of the structure. On such a map, the areas corresponding to the presence of stiffeners (frame) can be identified. A histogram containing the values of point mobilities is then build and allows the definition of different classes of behaviour. The latter define the stiffness contrast of the structure, which is evaluated by a contrast indicator.

An extension of this approach is presented on two industrial cases of roof panels. The first case is based on a steel roof, with conventional design architecture (frame and panels). The second case is based on an innovative roof, made of composite materials. The developed approach allows to locate the stiffeners and to highlight their contribution to the overall stiffness of the structure. Moreover, the contrast indicator identifies the areas requiring an addition of stiffeners to ensure the required level of performance. Thus, for several frequency ranges the calculated contrast allows one to assess the vibrational performance of a mechanical structure, whatever the used material.



EFFECT OF TREATED ZONE GEOMETRY ON THE DYNAMIC PLASTIC BUCKLING OF STEEL COMPOSITE THIN TUBULAR STRUCTURES

A. Ahmed-Ali¹, R. Baleh^{1,2}, D. Razafindramary^{1,3} and A. Abdul-Latif^{1,3}

¹Laboratoire d'Ingénierie des Systèmes Mécaniques et des Matériaux (LISMMA)
Supméca, 3, rue Fernand Hainaut - 93407 St Ouen Cedex, France

²La Salle Passy-Buzenval, 50 avenue Otis Mygatt 92500 Rueil-Malmaison, France

³Université Paris 8, France

Email: r.baleh@passy-buzenval.com

ABSTRACT

Thin tubes made from steel composite are experimentally investigated showing their energy absorption capacity during dynamic plastic buckling. In fact, steel-steel composite cylindrical tubes are characterized by a specific outer surface heat treatment. Only 15% of tubes outer surface are heat treated for a certain depth along the tube thickness with different geometrical shapes. The patented idea aims to enhance the impact resistance of tubular structures not only through the treated area but especially through its geometry.*

A key point emerging from this study is that the structure impact response (i.e., the plastic flow mechanism and the absorbed energy) is influenced by the loading rate coupled with the heat treated configuration. To study the geometry effect of carburizing treated zone, several shapes are tested :three different ring-shape configurations (2, 4 and 6 rings), a configuration with three uniformly distributed vertical strips parallel to the axis of the tube and finally one treated helically case with tilt angle of 45°. All the experimental tests are carried out using a dynamic drop mass bench of a maximum impact velocity of 10 m/s.

The obtained results show the enhancement in the energy absorption, notably in the case of 4-ring (and then helically case with a tilt angle of 45°) is higher than 78% in comparison with the non-treated tube.

Keywords: plastic buckling; surface heat-treatment, dynamic loading; energy absorption

*Patent submitted in France: INPI No. 1400843, Inventor : Akrum ABDUL-LATIF

1 INTRODUCTION

Adopted since several decades by different transport vehicles, the thin-walled tubular structures are widely used as a fundamental tool in developing a passive safety concept, i.e., energy dissipating devices based on large plastic deformations (e.g., Abramowicz and Jones, 1986; Johnson and Reid, 1986, Jones, 1998; Al-Ghamdi, 2001; Abdul-Latif, 2000; Baleh and Abdul-Latif, 2007, Abdul-Latif and Baleh, 2008, Abdul-Latif, 2011; Menouer et al., 2014).

Understanding the behavior of collapsed structures and the materials behavior is essential to assess the energy absorption. Different studies reveal that the crushing process remains sensitive to several key parameters like magnitude, type and method of application of loads, strain rates, deformation or displacement patterns and material properties (Baleh and Abdul-Latif, 2007; Karagiozova and Jones, 2000; 2001).

Under dynamic loading, the axial crushing of cylindrical tube is an effective shock absorber device and is highly dependent on inertial effects of strain rate (Karagiozova, 2000, 2001; Jones, 2003). As a main subject of this work, the plastic buckled tubes can dissipate a large amount of energy due to the available long stroke per unit mass and stable average load in the entire collapse process (Yasui, 2000). The bending and stretching strains combination and its progress along the buckled tube guarantees the participation of material in the absorption of energy by plastic work. Three collapse modes of tubular structures have been shown in the literature survey: axisymmetric mode, diamond mode, and mixed one. The main geometrical parameters controlling these modes during plastic buckling are: the η ($=R/t$) ratio of diameter (R) to thickness (t) and the λ ($=R/L$) ratio of diameter to length (L) (Karagiozova, and Jones, 2002; Bouchet et al., 2002; Al Galib and Limam, 2004; Baleh, 2004; Abdul-Latif et al., 2005). Note that the mean collapse load is the most important parameter in evaluating the absorbed energy.

From the energy point of view, the limit of the performance of axially crushed tubes can be enhanced using an innovated idea. This is based on the generation of complex loading conditions through the combination of local heterogeneities dictated by the steel-steel composite and the external load. Hence, 15% of tubes outer surface is heat treated proposing different shapes. A key point that emerges from this study is that the response of the structure (i.e., plastic flow mechanism and the energy absorbed) is largely influenced by the treated shape and the loading rate. To study the geometry effect of carburizing treated zone, seven different distinct shapes are tested: three different ring-shape configurations (2, 4 and 6 rings), a configuration with three uniformly distributed vertical strips parallel to the axis of the tube and finally a helically treated case with tilt angle of 45° . The behavior of the crushed materials demonstrates the dependence of the plastic buckling on the composite type and loading rate.

2 EXPERIMENTAL PROCEDURE

2.1 Originality and experimental methodology

This actual investigation is based on a patented concept (Abdul-Latif, 2014), where the first results show the importance of this new methodology. Enhancement of the energy absorption capacity through the coupling of the steel-steel composite configuration and the loading rate is considered.

In fact, the basic idea is to make a steel-steel composite (i.e., increase the tube wall strength in certain zones) via the heat treatment of a given area. The definition of the targeted area is based on its form within the treated structure which requires special attention.

The originality of this technique consists of partially coating the outer surface of the tube with a thin layer of a specific paint before the heat-treatment. Therefore, the coated area should resist against any change in phase during treatment. This allows keeping its initial mechanical behavior. This study is addressed to study the mechanical behavior of tubular steel-steel composite structures under quasi-static and dynamic regime. The material of the structure is subjected to an important stress conditions enhancing the energy dissipation capacity. Thus, the influence of the loading rate and the shape and layout of the heat treated area is investigated.

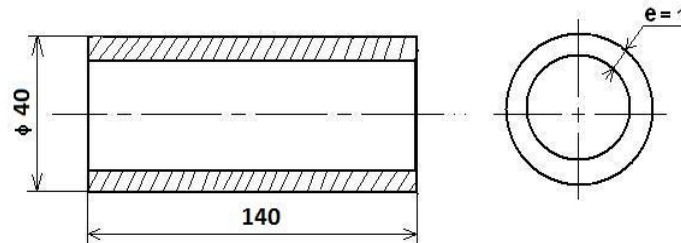


Figure 1. Initial geometry of the used samples

2-2. Material, geometry and heat treatment

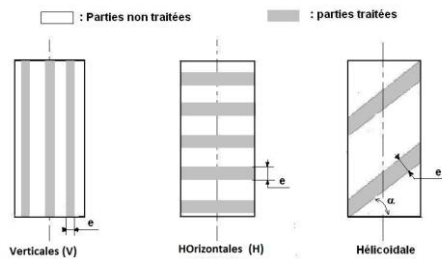
The investigation focuses on several cases using tubes of 40mm diameter and 1mm thickness and an initial length of 140 mm (Fig. 1).

The choice of this mild steel is evidently based on the ability of the metal to receive a particular heat treatment. Indeed, after a few trials subcontracted by a specialized company (Bodycoat) nitriding, carburizing and carbonitriding, it turned out that it provided better leverage to control appropriately the depth of treatment.

The opportunity is therefore to give a judicious choice in controlling the geometrical parameters (the shape and the depth of the treated zone). The carburizing heat treatment can suitably control the depth of treatment by 0.4 mm to set this important geometrical factor. To study the geometry effect of carburized zone with only 15% of tubes outer surface, different shapes are tested which are three different ring-shape configurations (2, 4 and 6 rings), a configuration with three uniformly distributed vertical strips parallel to the axis of the tube and finally a helically treated case with a tilt angle of 45° .

2-3. Samples Preparation

After machining, several operations are performed before the heat-treatment which are cleaned and degreased. Tubes are then painted by immersion in a paint solution (LUISO W36 for gas carburizing) that can provide protection for non-hardened parts up to 6mm in depth, at temperatures around 970°C . Furthermore, the different types of area (or shapes) that are tested can be classified into three categories (fig. 2) noted by (nH nV and nHe) where n indicates the number of bands, H horizontal positioning, vertical V and helical He. The first three configurations are: 2H, 4H and 6H having a ring form arranged equidistantly over the entire length of the tube. The second category deals with longitudinal strips over the entire length of the tube and arranged regularly and parallel to the tube axis. The third category is based on helical strips with a helicoidal angle $\text{He}45^\circ$.



(a)



(b)

Figure 2. (a) Scheme of proposed configurations, (b) view of the geometry of the patterns of 2V configurations, 4H and 2He before heat treatment

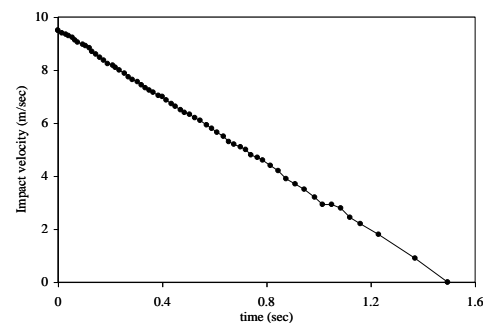
All tests were performed under the same experimental conditions using a free-ends mode. In the case of quasi-static regime, tests are conducted using a universal testing Instron machine type 5582. It has a maximum load capacity of 100 kN with a range of cross-head speeds varying from 0.001 to 500 mm/min. Furthermore, the obtained quasi-static strain rate is a parameter that has no significant influence on the material behavior. Therefore only a speed of 5 mm/min is employed for this study.

3 IMPACT APPARATUS

All the experimental tests are carried out using a dynamic drop mass bench of a maximum impact velocity of 10 m/s and of a maximum kinetic energy of 2.5 kJ. It is equipped with a dynamic load cell of 20 tons, a 5000g accelerometer, and a laser beam displacement transducer (series M5L of international Bullier) for a measurement bracket of 100mm. These instruments are connected to a rapid acquisition chain (2.5MHz), which ensures the simultaneous recording of these experimental data: force, acceleration and displacement.



(a)



(b)

Figure 2: (a) overview of the drop mass bench; (b) changes in the impact speed

Tests are conducted under initial impact velocity of about 9.5 m/s use a maximum masse of 45.5 kg. As a typical example, the rate of change of the impact velocity during crushing process is obviously illustrated in figure (2).

In order to ensure the experimental results accuracy, each test is repeated three times under the same experimental conditions (applied velocity and temperature). If the differences between the three responses exceed 5%, then another test should to be performed.

4 RESULTS AND INTERPRETATION

It is now known that the absorbed energy is controlled by the plastic hinges and localized areas of plasticity which differs from one deformation mode to another. Thus, three issues are mainly considered: local hardness (micro-hardness) before crushing, deformation mode and the crushing load (and the energy dissipated by plastic buckling).

4.1 Behavior of treated specimens

Figure 3 analyzes the effect of heat treatment on the tube wall behavior by comparing the non heat-treated and treated samples. Several Vickers micro-hardness tests are made.

Figure 3 shows micro-hardness evolution of 8 traces of the cross section of the wall starting from the outer radius to the inner one. Unlike the wall of the non treated specimen, which shows a relatively constant Vickers hardness over the whole thickness, the treated specimen demonstrates a remarkable increase in hardness from 180 HV to 780 HV, i.e., 300%. This decreases substantially linearly to 200 HV at trace 5, and in a constant evolution until the inner end of the wall.

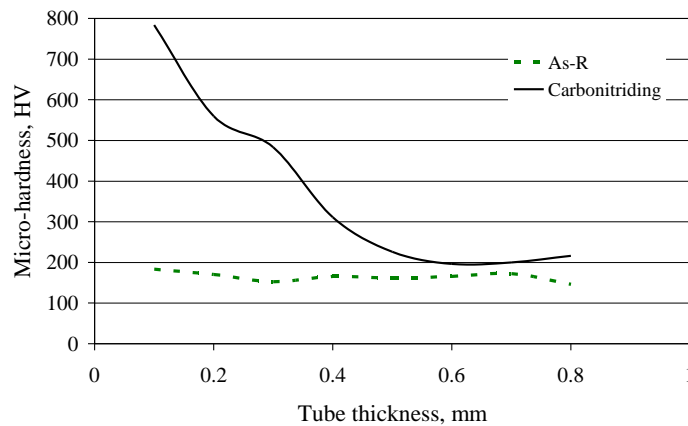


Figure 3: Effect of the carburizing on the hardness of the tube wall.

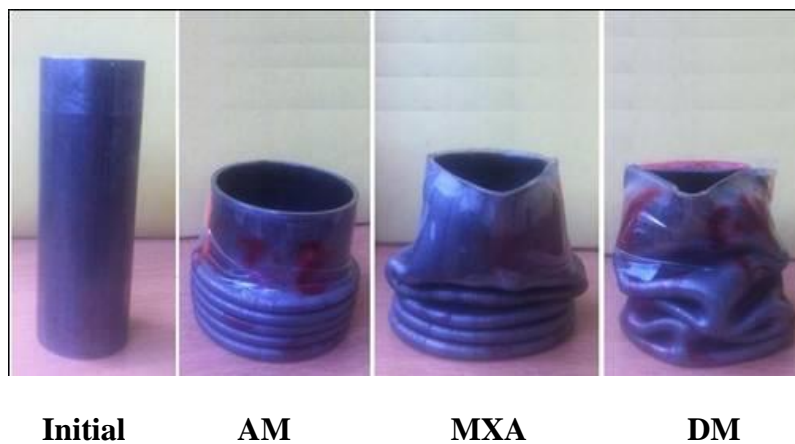


Figure 4. Specimen before and after plastic buckling

Concerning the collapse mode of tubes, it is obvious that whatever the loading configuration (quasi-static or dynamic), three modes of deformation are generated: axisymmetric mode (AM), diamond mode (DM), and mixed mode (XM). However, it is noted that in terms of proportion is the mixed mode axisymmetric dominant (MXA) that appears frequently, particularly in quasi-static due to a better centering of the applied load. An examination of the tested tubes at the end of collapse (figure 4) reveals that their plastic buckling where the three different modes are captured.

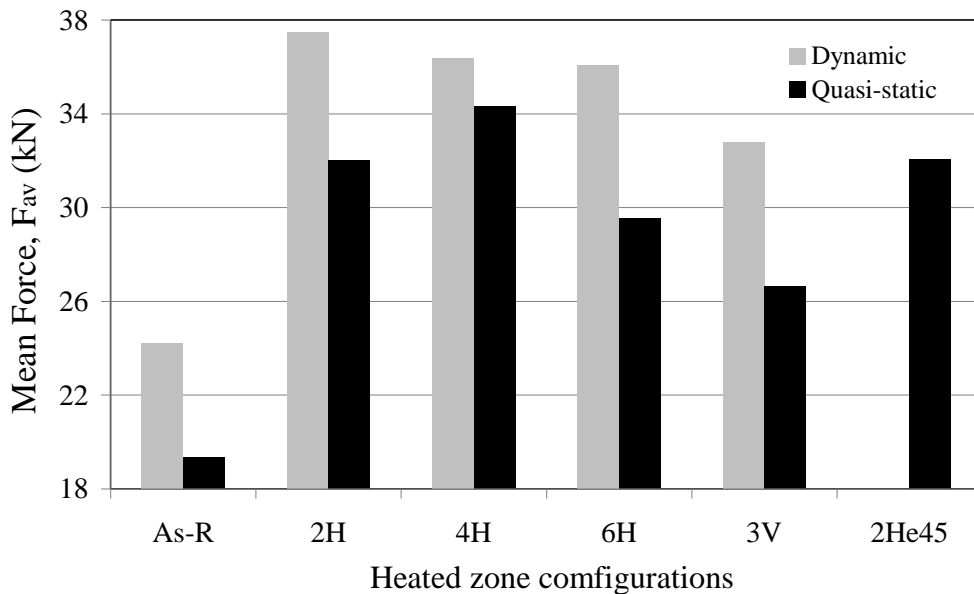


Figure 5. Comparison showing the variation of crushing mean load depending on the heat treated zone configuration and crushing regime

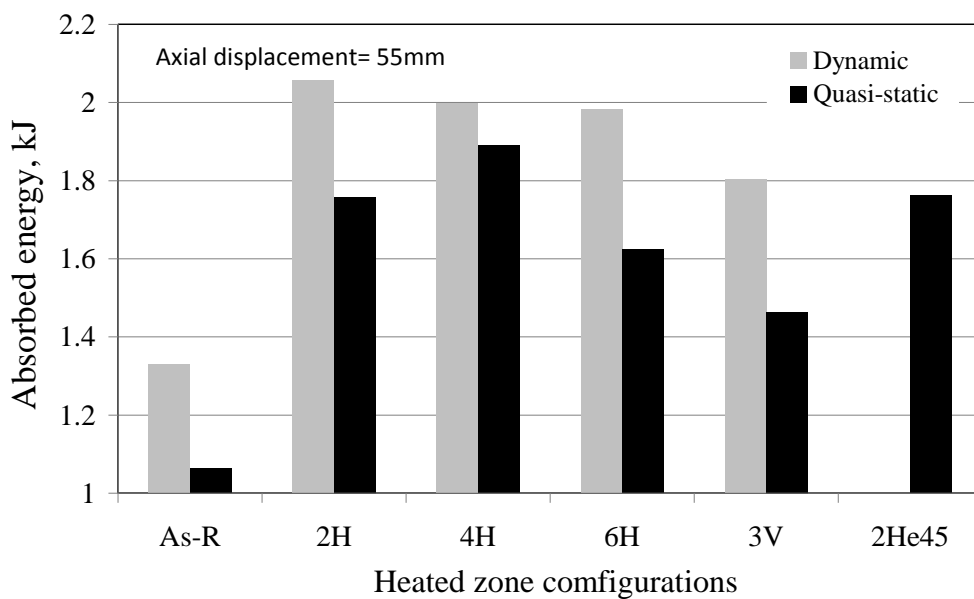


Figure 6. Comparison regarding the variation of energy absorbed controlled by the heat treated zone configuration and the speed of loading for an axial displacement of 55mm

The influence of the heat-treated zone configuration on the mean crushing load (F_{av}) is presented in figure (5). This figure obviously shows the effect of this zone and its shape on the absorbed energy. The enhancement of the absorbing capacity is determined with respect to the as-received tube (not heat-treated tube, noted As-R), where its mean collapse load (F_{av}) is compared to the other cases. Under quasi-static load, enhancements in the F_{av} are: 77.7% for 4H against 65.3%, 52.8%, 66.3%, and 37.8% for 2H, 6H, He45° and 3V cases, respectively.

As far as the energy absorption is concerned, figure (6) illustrates a clear enhancement in the energy dissipated. In fact, this figure shows the evolution of energy absorbed versus the five treated configurations for a given axial crushed length of 55mm under quasi-static and dynamic loading. As an example, for this axial displacement under quasi static condition, the best enhancement regarding the energy absorbed is captured in the case of 4H with a value of 1.9 kJ. However, another evolution is recorded at dynamic loading, which gives us a best energy absorbed in the case of 2H with a value of 2 kJ. So, the best enhancements are: 78% for 4H and then 67% for 2He45° in quasi static with respect to the As-R case against 55% for 2H and 51% for 4H under dynamic loading. The best variation in the heated configuration which absorbs the highest amount of energy seems to be controlled by the loading speed. However, this conclusion will require further investigation to be confirmed.

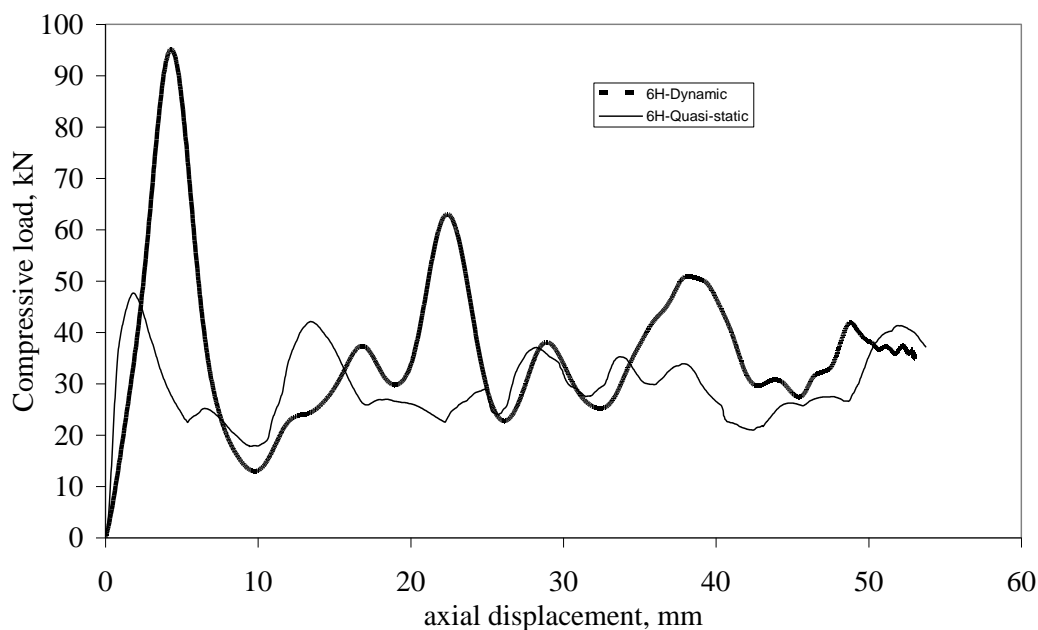


Figure 7. Loading rate effect on the collapse loading evolution versus the axial deflection for a case of 6H

Figure 7 shows a typical example of the crushing load evolution versus axial displacement in the case of 6H, with a compressive speed of 5 mm/min in quasi-static regime and 9.5m/sec as initial impact velocity for the dynamic regime. These two loading conditions point out a remarkable increase in the maximum dynamic load of 104% before the beginning of plastic deformation. It is recognized also that the general trend of their evolution provides: $F_{va} = 36.3$ kN for dynamic loading against 27 kN for quasi-static one. This result confirms a noticeable sensitivity of the structure to the employed strain rate range.

5 CONCLUDING REMARKS

In this work, the energy absorbing device that includes a thin-walled tube is tested under dynamic and quasi-static compressive loads. On the outer surface of the tube, different heat-treated zones of 15% are proposed. To study the geometry effect of carbonitriding treated zone, several shapes are tested: 3 ring-shape configurations of 2, 4 and 6 rings, a three uniformly distributed vertical strips and a helically with tilt angle of 45°. All the tests are carried out using a dynamic drop mass bench of a maximum impact velocity of 10 m/s and an Instron tension-compression universal testing machine of 5 mm/min for quasi-static loading condition.

The obtained results show the enhancement in the energy absorption, notably in the case of 4-ring (and then helically case with a tilt angle of 45°) is higher than 78% for quasi-static loading and 55% for dynamic loading compared to the non-treated tube. Whatever, the heat-treated zone configuration, the obtained results confirm a noticeable sensitivity of the used structure to the strain rate range.

REFERENCES

- Abdul-Latif, A., 2000, "On the Lateral Collapse of an Identical Pair of Cylinders," *International journal of Solids and Structures*, vol. 37, 1955-1973
- Abdul-Latif, A., R. Baleh and Aboura, Z., 2006, "Some improvements on the energy absorbed in axial plastic collapse of Hollow cylinders," *International Journal of Solids and Structures*, vol.43, 1543-1560.
- Abdul-Latif, A. and Baleh, R., 2008, "Dynamic biaxial plastic buckling of circular shells," *ASME, Journal of Applied Mechanics*, vol. 75, issue 3, 031013
- Abdul-Latif, A., 2011, "Experimental Comparison of Several Energy Absorbing Devices," *ASM, Journal of Materials Engineering and Performance*, vol. 20, pp. 1392-1400
- Abdul-Latif, A., 2014, "Système d'absorption d'énergie à organe en composite métallique déformable plastiquement," INPI No. BT 890/1400843, France.
- Abramowicz, W., and Jones, N., 1986, "Dynamic progressive buckling of circular and square tubes," *Int. J. Impact Engineering*, 4, pp. 243-270.
- Al Galib, D., and Limam, A., 2004, "Experimental and numerical investigation of static and dynamic axial crushing of circular aluminum tubes," *Thin-Walled Structures*, 42, pp. 1103-1137.
- Al-Ghamdi, A. A. A., 2001, "Collapsible impact energy absorbers: an overview, *Thin-walled structures*," 39, pp. 189-213.
- Baleh R., 2004, "Flambage plastique quasi-statique et dynamique de structures tubulaires métalliques sous sollicitations simple et complexe –système d'absorption d'énergie-via un nouveau dispositif expérimental," Thèse de Doctorat, UTT.
- Baleh, R., and Abdul-Latif, A., 2007, "Uniaxial-biaxial transition in quasi-static plastic buckling used as an energy absorber," *ASME, Journal of Applied Mechanics*, vol.74, pp. 628-635
- Bouchet, J., Jacquelin, E., and Hamelin, P., 2002, "Dynamic Axial Crushing of Combined Composite Aluminum Tube: the Role of Both Reinforcement and Surface Treatments," *Composite Structures*, 56, pp. 87-96.
- Johnson, W. and S. R. Reid, 1986, Update to "Metallic energy dissipating systems," *Appl. Mech. Rev.* 31, 277-288 (1978); *Appl. Mech.*, pp. 315-319.
- Jones, N., 1998, "Some Recent Developments and Future Trends in Thin-Walled Sections for Structural Crashworthiness," *Thin-Walled Structures*, 32, pp. 231-233.
- Jones, N., 2003, "Several Phenomena in Structural Impact and Structural Crashworthiness," *European J. of Mechanics A/Solids*, 22, pp. 693-707.

- Karagiozova, D., and Jones, N., 2000, "Dynamic Elastic-Plastic Buckling of Circular Cylindrical Shells under Axial Impact," *International Journal of Solids and Structures*, 37, pp. 2005-2034.
- Karagiozova, D., and Jones, N., 2001, "Dynamic Effects on Buckling and Energy Absorption of Cylindrical Shells under Axial Impact," *Thin-Walled Structures*, 39, pp. 583-610.
- Karagiozova, D., and Jones, N., 2002, "On Dynamic Buckling Phenomena in Axially Loaded Elastic-Plastic Cylindrical Shells," *Int. J. of Non-Linear Mechanics*, 37, pp. 1223-1238.
- Menouer A., Baleh R., Djebbar A. and Abdul-Latif A., 2014, "New generation of energy dissipating systems based on biaxial buckling," *Journal of Thin-Walled Structures*, vol. 85, pp. 456-465.
- Yasui, Y., 2000, "Dynamic Axial Crushing of Multi-layer Honeycomb Panels and Impact Tensile Behavior of the Component Members," *Int. J. Impact Engineering*, 24, pp. 659-671.



DYNAMIC MECHANICAL ANALYSIS OF CARBON-CERAMIC COMPOSITES

A. Teresa Gumula^{1,2*}, B. Francisco José Carrión-Vilches³, C. María Dolores Bermúdez³

¹AGH University of Science and Technology, Faculty of Materials Science and Ceramics
Al. Mickiewicza 30, 30-059 Krakow, POLAND
Email: tgumula@agh.edu.pl

²Centro Universitario de la Defensa, Academia General del Aire
Calle Coronel López Peña, s/n, 30720 Santiago de la Ribera, Murcia, SPAIN
Email: teresa.gumula@ud.upct.es

³Grupo de Ciencia de Materiales e Ingeniería Metalúrgica, Departamento de Ingeniería de Materiales y Fabricación, Universidad Politécnica de Cartagena
Campus de la Muralla del Mar, C/Doctor Fleming, s/n. 30202-Cartagena, SPAIN
Email: mdolores.bermudez@upct.es, fjc.vilches@upct.es

ABSTRACT

The aim of this work is to compare mechanical behavior of phenol-formaldehyde resin-derived CC (carbon) composite with CC/ceramic (carbon/ceramic) composites obtained by the impregnation of CC composite with commercially available polysiloxane-based solutions of preceram and their subsequent heat treatment at 1000 °C, 1500 °C and 1700 °C. CC/ceramic composites heat treated at 1000 °C and 1500 °C contain silicon oxycarbide [2] and CC/ceramic composite heat treated at 1700 °C contains silicon carbide [2]. As a reinforcement HTS 5131 carbon fibers (Tenax) in a form of roving were used. Phenol-formaldehyde resin (Organika-Sarzyna, Poland) and Lukosil 901 polysiloxane substrate (Lucebni zavody, Czech Republic) used in this experiments were inexpensive (cost about 10\$/kg).

Dynamic mechanical analysis (DMA) in three-point clamping mode was carried out. All tests were carried out in air at 450 °C at an oscillatory frequency of 20 Hz. A multifrequency-strain mode was set up under a strain of 80 μm . CC composite was used as a reference.

In comparison to the reference CC composite, CC/ceramic composites exhibited up to 10 times longer lifetime.

1 INTRODUCTION

Carbon fibres-reinforced carbon composites (CC composites) are candidate materials for advanced structures, which could work under dynamic load at elevated temperature. Their mechanical properties are retained even until 2000 °C, and due to low values of the coefficients of thermal expansion (CTE) and high heat of sublimation they have good ablation resistance.

Additionally, CC composites exhibit thermal shock resistance and chemical resistance in non-oxidizing atmosphere.

However, application of CC composites in high temperature structures is limited due to the potential oxidation damage and erosion in air above 400 °C [1]. Much effort is done in order to protect CC composites against air – oxidation. Several methods have been developed to improve oxidation resistance: chemical vapor deposition (CVD) coatings, multilayer coatings, impregnation of CC composite with organosilicon compounds, i.e. polysiloxanes and heat treatment [1]. A cross-linked polysiloxane resin during pyrolysis up to 1000 °C can be transformed into a silicon oxycarbide (structure containing Si-C-O bonds, blackglass), and during pyrolysis up to 1700 °C silicon carbide crystallizes [2]. Our previous work indicate that depending on the structure of polysiloxane resins it is possible to obtain ceramic samples with high ceramic yield, i.e. from 82 to 86 wt % at 1000 °C and from 61 to 70 wt % at 1700 °C [2].

The aim of this work is to compare dynamic mechanical properties of phenol-formaldehyde resin-derived CC (carbon) composite with CC/ceramic (carbon/ceramic) composites obtained by the impregnation of CC composite with commercially available polysiloxane-based solutions of preceram and their subsequent heat treatment up to 1700 °C. As a reinforcement carbon fibers in a form of roving were used. Phenol-formaldehyde resin and polysiloxane substrate used in this experiments were inexpensive (cost about 10\$/kg).

2 MATERIALS AND METHODS

As a reinforcement HTS 5131 carbon fibers (Tenax) in a form of roving were used. To prepare the unidirectional fiber prepreg tapes the carbon fibers were impregnated with phenol-formaldehyde resin (Organika-Sarzyna, Poland). The tapes were dried and cut to obtain 15 cm long laminates and unidirectionally stacking laminates were placed in a metallic mold. The stacked layup was heated up to 140 °C in air atmosphere under a pressure of 10 MPa. Then, the composite samples were heated to 1000 °C in an argon atmosphere to obtain CC composite. C/C composites obtained in such a way were impregnated with Lukosil 901 polysiloxane (PS) resin (Lucebni zavody, Czech Republic). Impregnated composite samples were subjected to subsequent thermal treatment in an inert argon atmosphere. CC/ceramic composites heat treated at 1000 °C and 1500 °C contain silicon oxycarbide [2] and CC/ceramic composite heat treated at 1700 °C contains silicon carbide [2]. Samples in a form of bars were prepared (1mm x 4mm x 35mm). Types of prepared CC/ceramic composites are presented in Table 1, the characteristics of the composites are presented in Table 2 and their mechanical properties are presented in Table 3.

	Composite	Description	Matrix
Reference	CC composite	CC	C
Sample 1	CC/ceramic composites	CC + PS, HT 1000 °C	C+SiCO _a
Sample 2		CC + PS, HT 1500 °C	C+SiCO _b
Sample 3		CC + PS, HT 1700 °C	C+SiC

Table 1. Types of prepared composites

Composite	Aparent density [g/cm ³]	Specific density [g/cm ³]	Porosity [%]
Reference	1.18	1.53	23
Sample 1	1.39	1.75	14
Sample 2	1.33	1.63	20
Sample 3	1.19	1.56	21

Table 2. Microstructure of composites

Composite	Bending strength [MPa]	Young's modulus [GPa]	Deflection [mm]	ILSS [MPa]
Reference	300 ± 20	91 ± 6	0.73 ± 0.15	14 ± 2
Sample 1	287 ± 11	71 ± 7	0.85 ± 0.15	15 ± 1
Sample 2	289 ± 15	74 ± 14	0.82 ± 0.02	14 ± 1
Sample 3	279 ± 32	78 ± 14	0.55 ± 0.02	15 ± 1

Table 3. Mechanical properties of composites

Dynamic mechanical analysis (DMA) in three-point clamping mode was carried out with TA Q800 DMA analyzer equipped with a TA Universal Analysis 2000 software. The span between supports was 20 mm. All tests were carried out in air at 450 °C at an oscillatory frequency of 20 Hz. A multifrequency-strain mode was set up under a strain of 80 µm. CC composite was used as a reference.

3 RESULTS AND DISCUSSION

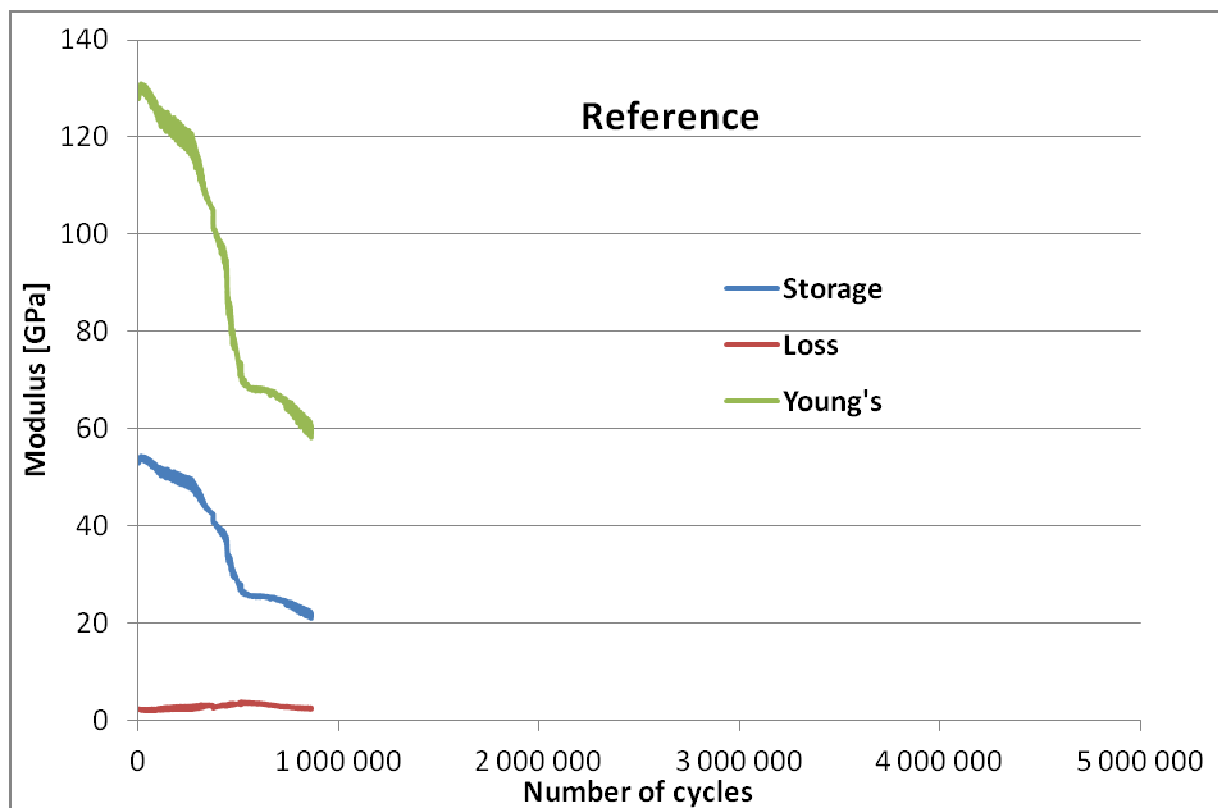


Fig. 1. Results of DMA for reference sample

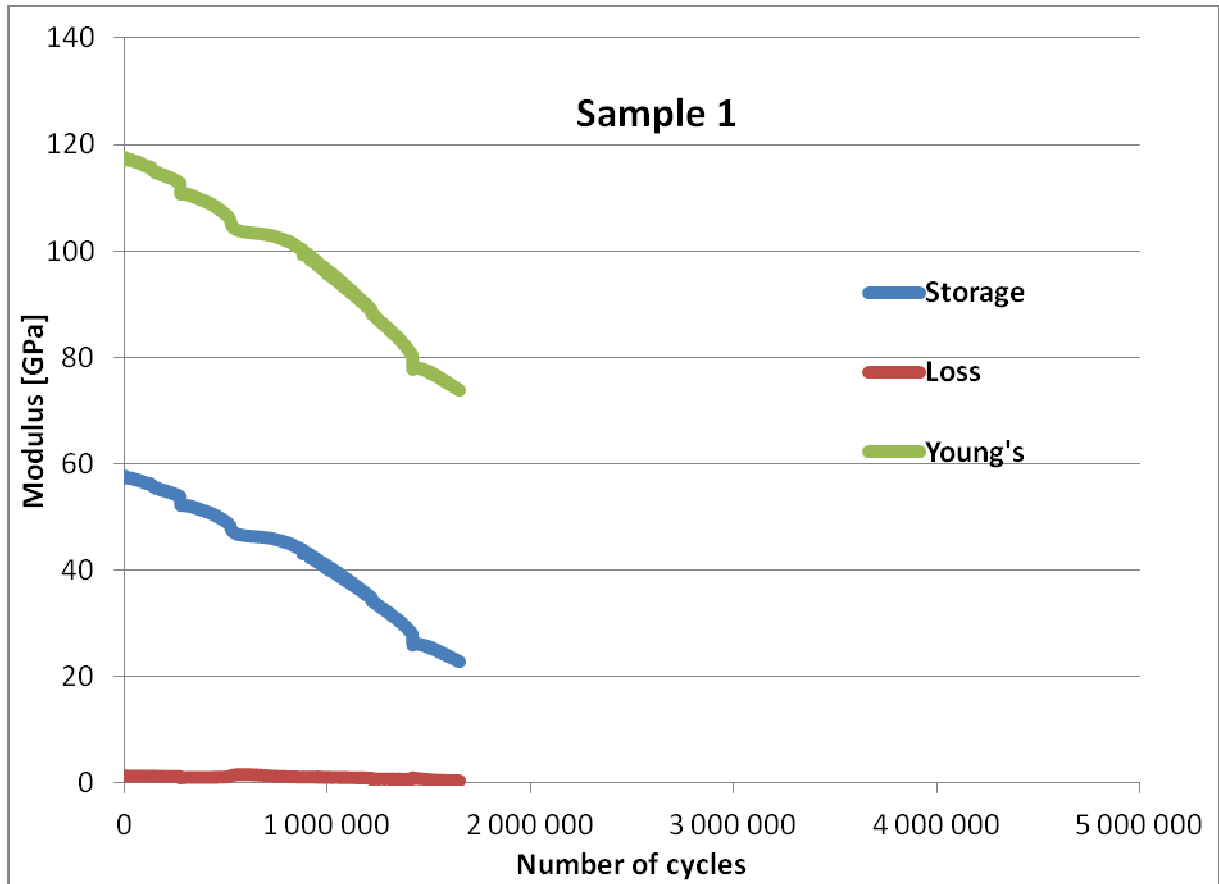


Fig. 2. Results of DMA for sample 1

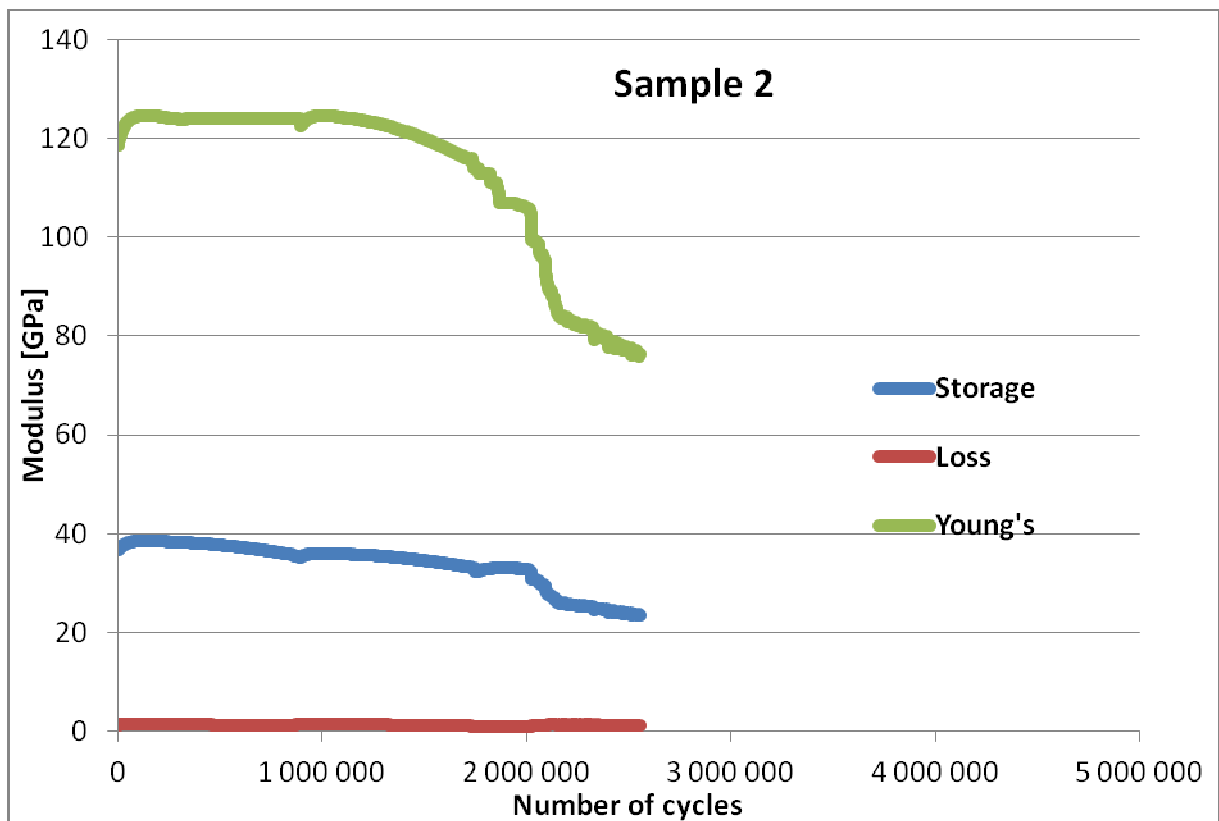


Fig. 3. Results of DMA for sample 2

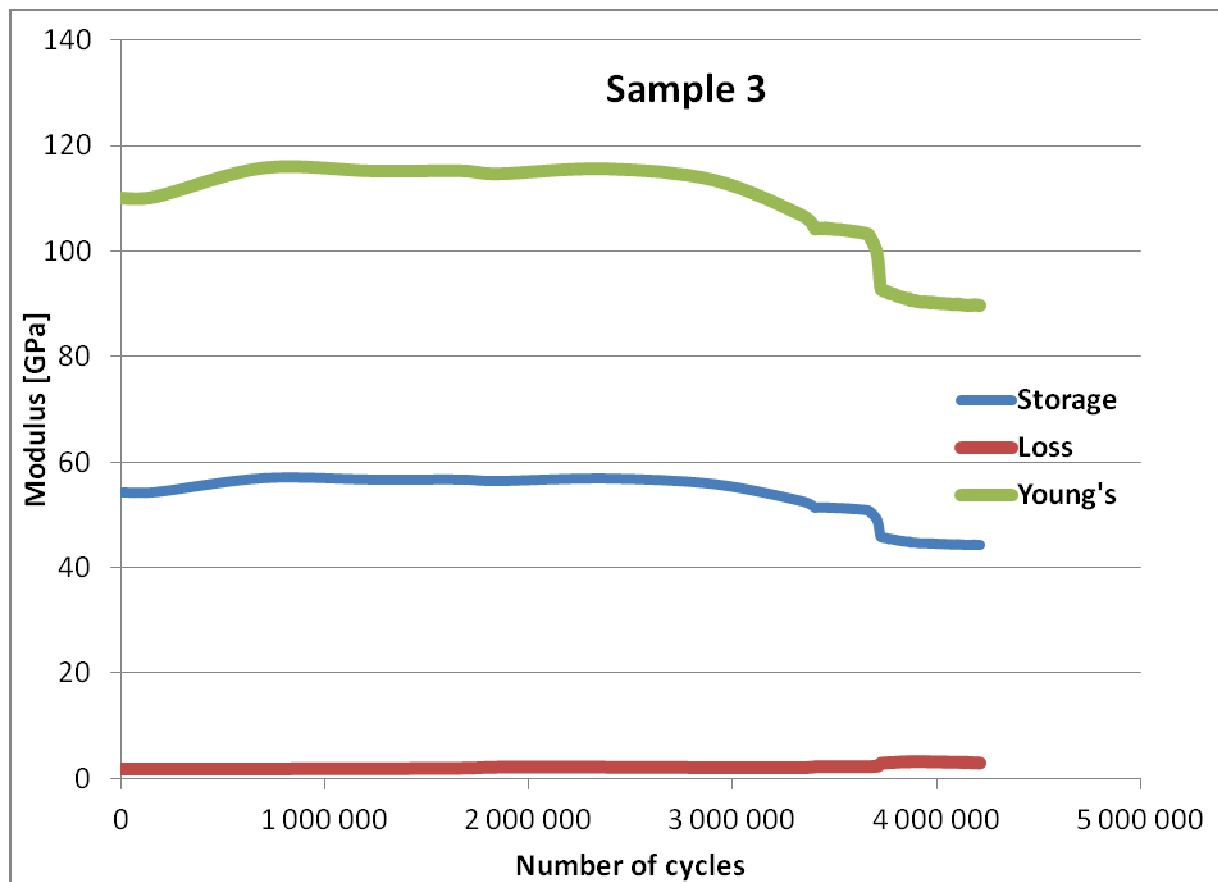


Fig. 4. Results of DMA for sample 3

Figure 1-4 represents modulus-number of cycles relationships registered during DMA analysis. It is possible to observe differences in dynamic properties of investigated samples. Table 4 gathers the numbers of cycles corresponding to the losses of 20% of the Young's modulus and storage modulus. It is possible to note that all CC/ceramic composites represents better dynamic properties in comparison with the CC reference. CC/ceramic composite obtained at 1000 °C (Sample 1) shows at least 2 times better fatigue life, while CC/ceramic composite obtained at 1500 °C (Sample 2) shows 5 times better fatigue life respect to the CC reference. CC/ceramic composite obtained at 1700 °C (Sample 3) exhibits 10 times longer lifetime in comparison to the CC reference.

Composite	Number of cycles when the loss of 20% of the Young's modulus was registered	Number of cycles when the loss of 20% of the storage modulus was registered
Reference	373 000	358 000
Sample 1	1 100 000	767 000
Sample 2	2 020 000	2 042 000
Sample 3	4 050 000	4 120 000

Table 4. Number of cycles when the loss of 20% of the Young's and storage modulus was observed

4 CONCLUSIONS

The aim of this work was to compare dynamic mechanical properties of CC (carbon) composite with CC/ceramic (carbon/ceramic) composites obtained by the impregnation of CC composite with commercially available polysiloxane-based solutions of preceram and their subsequent heat treatment up to 1700 °C. The results shows that at elevated temperature, CC/ceramic composite obtained at 1700 °C exhibit the best fatigue properties in an oxidative atmosphere. This results from the presence of silicon carbide that protect carbon fibres and carbon matrix against oxidation.

5 ACKNOWLEDGEMENTS

This work was supported by the National Science Centre, grant No. 2011/01/B/ST8/07451, decision No. DEC-2011/01/B/ST8/07451.

REFERENCES

- [1] G. Savage, *Carbon – carbon composites*. Chapman and Hall, London, 1992.
- [2] T. Gumula, C. Paluszkiewicz, S. Blazewicz, Study on thermal decomposition processes of polysiloxane polymers – from polymer to nanosized silicon carbide. *Journal of Analytical and Applied Pyrolysis*. 86: 375-380, 2009.

1 INTRODUCTION

Model calibration methods improve the correlation between finite element models (FEM) and measured data. The aim is to obtain the most predictive analytical model despite their incompleteness to describe exactly the underlying physics: most of the parameters should be considered as uncertain rather than nominal values due to manufacturing and experimental variability. In this case, a stochastic calibration method should be use.

On the other hand, the calibration convergence can be wrong due to physical compensating effects which lead to fidelity-equivalent solutions. The info-gap theory provides a way to ensure that the system remains reliable even under these unknown compensating effects. This paper presents an approach to enhance the robustness of a stochastic calibration method using the info-gap theory.

2 ROBUST CALIBRATION

2.1 Calibration performances

We wish to compare experimental data results to simulated outputs. A common metric to evaluate deterministic calibration performances is the normed Euclidean distance D_E :

$$D_E = \sum_{i=1}^n \frac{\sqrt{(v_{a_i} - v_{m_i})^2}}{v_{m_i}} \quad (1)$$

v_m is a vector containing the nominal eigenfrequencies measured (n outputs) and v_a the corresponding vector containing the nominal analytical responses and the same number of outputs.

Parameters may be considered as uncertain and defined by probability density functions. In this case, the model now provides uncertain outputs and can be calibrated using stochastic approaches such as covariance adjustment [?], Gibbs sampling [?] and Metropolis-Hasting algorithm [?]. The Euclidean distance is not suitable to compare two unknown distributions whereas Bhattacharya distance D_B is relevant to evaluate multivariate features [?]. This metric takes into account both the mean-difference and the covariance difference between the two distributions :

$$D_B = \frac{1}{8}(\bar{v}_a - \bar{v}_m)^T \Sigma^{-1}(\bar{v}_a - \bar{v}_m) + \frac{1}{2} \ln\left(\frac{\det(\Sigma)}{\sqrt{\det \Sigma_a \det \Sigma_m}}\right) \quad (2)$$

with \bar{v}_m the vector containing the measured eigenfrequencies mean values and \bar{v}_a the mean vector of the mean analytical responses. The pooled matrix Σ is given by the combination of Σ_m the covariance of the experimental eigenfrequencies and Σ_a the covariance of the analytical outputs as $\Sigma = \frac{\Sigma_a + \Sigma_m}{2}$.

2.2 Info-gap theory

Info-gap theory has its origins in Ben-Haim [2] studying the reliability of mechanical systems. Since, this approach has been use on a wide range of applications such as climate models [3] and medical researches [4]. The purpose of info-gap is to provide tools for decision-makers in order to assess risks and opportunities of a model in light of the analysis of severe lack of information.

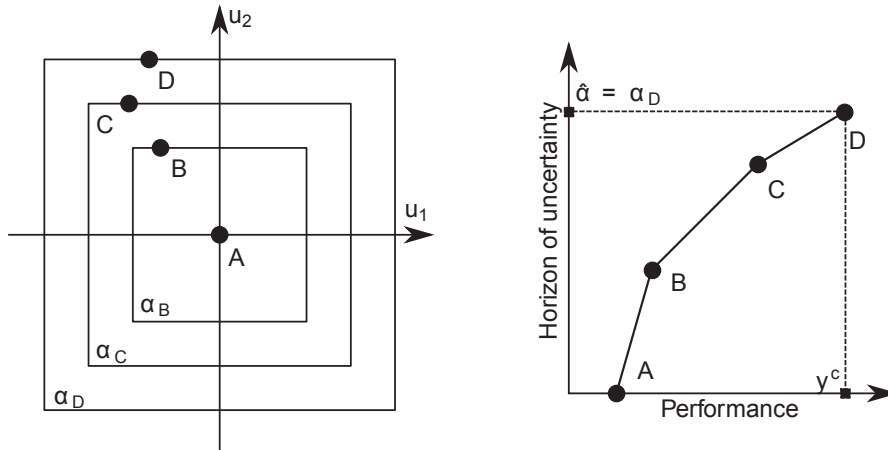


Figure 1. Nested subsets (left) - Robustness curve (right).

In practice, important modeling information may be lacking due to an incomplete understanding of the underlying physics. Hence, probability density functions are not generally suitable alone to describe severely uncertain parameters θ .

We introduce the horizon of uncertainty characterized by α . The larger α , the greater the range of unknown parameter variations i.e. a bigger space is available for uncertain parameters. Numerical model performances are commonly defined by a function which assess the quality of the response fidelity. Consequently, a catastrophic failure may appear for one set of uncertain parameters sampled from the previous space.

Let's consider several horizons of uncertainty α_i , the function that yields the worst case model predictions for a given horizon α is called \hat{R} and calculated as follow [5] :

$$\hat{R}(\alpha) = \max_{\theta \in U(\alpha, \tilde{\theta})} R(\theta) \tag{3}$$

$\tilde{\theta}$ is the calibrated best-estimate parameter values of the simulation model. The robustness function expresses the greatest level of uncertainty at which performance remains acceptable.

$$\hat{\alpha} = \max\{\alpha : \hat{R}(\alpha) \geq R_c\} \tag{4}$$

with $\hat{\alpha}$ the maximum horizon to which info-gap uncertainty model is allowed to expand as long as minimal requirements R_c are satisfied.

The figure 1 explains in a schematic way the method to compute robustness curve [6]. The unknown parameters are u_1 and u_2 . At the first step α_A , we consider no uncertainty thus the space contains a single point A which is necessarily the worst case. The respective performance $R(u_{1A}, u_{2A})$ is noted on the robustness curve on the right. Second step, the horizon of uncertainty is increased to α_B . In the space defined by α_B , the worst case can be found using a factorial design or by optimization [7]. The algorithm returns the worst case B and report it on the robustness curve. The procedure can be repeated for as much nested subsets required.

3 NUMERICAL APPLICATION

A new generation of ceramic matrix composite (CMC) turbine blades have been developed [8]. These materials show high resistance to extremely high temperature (1000°C), low density and a good fracture toughness compared to conventional metallic alloys.

The approach developed previously is applied to a CMC plate perfectly clamped with a progressively reducing thickness. The plate is itself divided into three isotropic material parts to represent physical heterogeneity due to the industrial process. Differences between the experimental results and the numerical outputs will be analyzed through the first three eigenfrequencies of the structure.

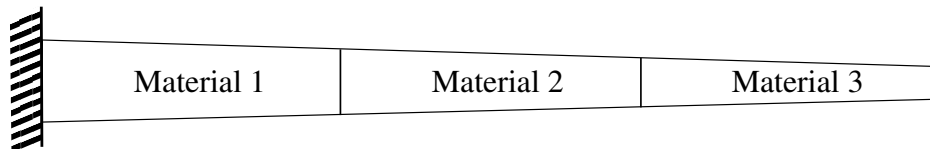


Figure 2. Material properties distribution.

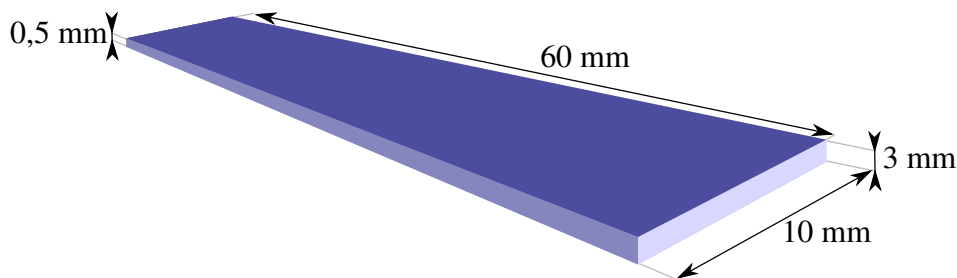


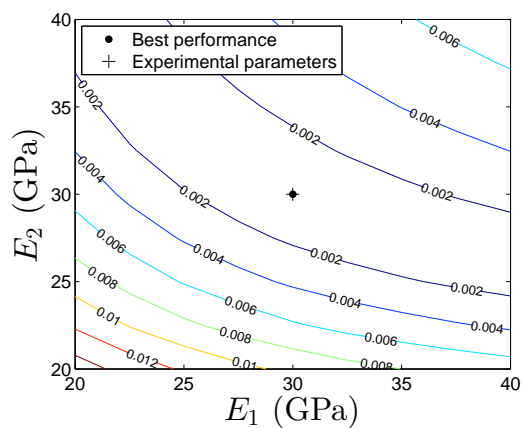
Figure 3. Plate dimensions.

The system is studied through material 1 and material 2 Young's Modulus, noted respectively E_1 and E_2 . The range of parameters E_1 and E_2 values is [20 GPa;40 GPa], divided into a 20×20 grid. Thus, 300 Monte-Carlo sampling are achieved with NASTRAN for each combination of parameters using these values as mean. The parameters variance are defined as 10% of the corresponding mean values.

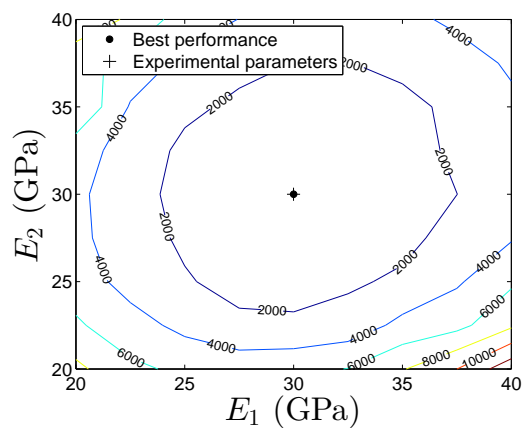
For the simulated test data, 500 experiments are sampled in the same way with $E_1 = E_2 = 30$ GPa and their variances $\sigma_{E_1} = \sigma_{E_2} = 3$ GPa. No model form error is added between the two samples. The nominal exact outputs are $\nu_1 = 18.15$ Hz, $\nu_2 = 50.64$ Hz and $\nu_3 = 78.25$ Hz.

The error surface responses are plotted in the space of the two parameters (Figure 4). The contours illustrate fidelity-equivalent solutions and define satisfying boundaries. The best performance marker stands for the global minimal distance found in the discrete space. As expected, this marker totally coincides with the experimental parameters marker for both distance metrics. In this case, the corresponding couple of parameters provides exact and optimal solutions.

In Figure 4(a), there is a slender space where the error remains below 0.2%. It means that deterministic calibrating algorithms can find acceptable set of parameters quite far from the actual experimental parameters. These compensating effects are inevitable even in the absence of bias in the model prediction. In Figure 4(b), the isocontours create nested circles which the lowest error is located in the center. In this case, stochastic calibration should provide relevant updated parameters.



(a) Euclidean isocontour.



(b) Bhattacharya isocontour.

Figure 4. Euclidean and Mahalanobis distances.

4 CONCLUSION

This paper proposes a framework to motivate the robust calibration process. In the case study, material parameters have been considered uncertain and the compensating effects between them as a lack of knowledge. Successful updating provides parameters which minimize the error between simulated experiments and analytical outputs while taking into account unavoidable compensating effects. Two calibration metrics have been investigated, in particular a deterministic euclidean error as well as the statistical Bhattacharyya error.

REFERENCES

- [1] Y. Govers and M. Link. Stochastic model updating - Covariance matrix adjustment from uncertain experimental modal data. *Mechanical Systems and Signal Processing*, 24(3):696–706, April 2010.
- [2] Yakov Ben-Haim. *Info-gap decision theory: decisions under severe uncertainty*. Academic Press, 2006.
- [3] Jim W. Hall, Robert J. Lempert, Klaus Keller, Andrew Hackbarth, Christophe Mijere, and David J. McInerney. Robust Climate Policies Under Uncertainty: A Comparison of Robust Decision Making and Info-Gap Methods: **A Comparison of Robust Decision Making and Info-Gap Methods**. *Risk Analysis*, 32(10):1657–1672, October 2012.
- [4] Y. Ben-Haim, M. Zacksenhouse, C. Keren, and C.C. Dacso. Do we know how to set decision thresholds for diabetes? *Medical Hypotheses*, 73(2):189–193, August 2009.
- [5] Sez Atamturktur, Zhifeng Liu, Scott Cogan, and Hsein Juang. Calibration of imprecise and inaccurate numerical models considering fidelity and robustness: a multi-objective optimization-based approach. *Structural and Multidisciplinary Optimization*, August 2014.
- [6] Emmanuel Pillet. *Méthodologies d'aide à la décision en conception robuste*. PhD thesis, Université de Franche-Comté, 2008.
- [7] Antoine Kuczkowiak. *Modèle hybride incertain pour le calcul de réponse en fonctionnement d'un alternateur*. PhD thesis, Université de Franche-Comté, 2014.
- [8] SNECMA and HERAKLES. Aube de Turbomachine en Matériau Composite et Procédé pour sa Fabrication - Brevet. *WO 2011/080443 A1*, July 2011.

COPYRIGHT NOTICE

Copyright ©2015 by the authors. Distribution of all material contained in this paper is permitted under the terms of the Creative Commons license Attribution-NonCommercial-NoDerivatives 4.0 International (CC-by-nc-nd 4.0).





A NEW EXPERIMENTAL SETUP TO CHARACTERIZE THE DYNAMIC MECHANICAL BEHAVIOR OF BALLISTIC YARNS

C. Chevalier^{*1}, N. Faderl¹, C. Kerisit¹, F. Boussu² and D. Coutellier³.

¹ French-German Research Institute of Saint-Louis (ISL)
5 rue du général Cassagnou _ BP 70034 _ 68301 Saint-Louis Cedex _ FRANCE
Email : *caroline.chevalier@isl.eu, norbert.faderl@isl.eu, christophe.kerisit@isl.eu

² Ecole Nationale Supérieure des Arts et Industries Techniques (ENSAIT)
2 Allée Louise et Victor Champier _ 59100 Roubaix _ FRANCE
Email : francois.boussu@ensait.fr

³ LAMIH UMR CNRS 8201 ENSIAME University of Valenciennes
Campus Mont Houy _ 59313 Valenciennes Cedex 9 _ FRANCE
Email : daniel.coutellier@univ-valenciennes.fr

ABSTRACT

In order to improve our knowledge about the dynamic behavior of composite materials used in ballistic protection, it is necessary to characterize first the mechanical behavior of single ballistic yarns, part of these fibrous structures, which will help to predict their impact behavior.

To respond to this yarn characterization, we have developed a new device, the Tensile Impact Test of Yarn (TITY), in order to test yarns under dynamic uniaxial tension and determine their mechanical behaviors in the longitudinal direction. During the test, we measure the displacement of the flying mass when it applies a longitudinal tension on the yarn which undergoes a strain up to its rupture.

After data treatment, we obtain the evolution of the velocity of the flying mass versus time which depends on the mechanical behavior of the yarn (evolution of the stress vs. strain, ultimate stress and strain). Thanks to an analytical approach proposed to model these two phases, we could estimate the longitudinal Young modulus of the yarn under dynamic loading. These results also provide us information about the specific energy absorbed by the yarn and what could be failure mechanisms of yarns under a dynamic tension. This knowledge about dynamic behavior of yarns would then be considered for improving future numerical models.

1 INTRODUCTION

Composite materials with fibrous reinforcement are widely present in ballistic protection and offer both high protection level and lightweight to armored structures. However, these materials could potentially still be improved with a better understanding of the influence of the composite material properties on ballistic performances. During an impact, the mechanical behavior of the composite material is mainly controlled by the dynamic mechanical behavior of its components (matrix and reinforcement). For ballistic protection materials, the fibrous reinforcement can be a woven, a unidirectional or a nonwoven structure, itself composed of a multitude of yarns intertwined, or layered in the case of a unidirectional structure. Among several inner parameters like the number of filaments, the linear density or the nature of the fiber, the mechanical behavior of these complex structures depends on the mechanical behavior of these single yarns. Few studies have been done on the characterization of ballistic yarn mechanical behavior in dynamic load at the three scales: the filament scale [1, 2], the yarn scale [3, 4] and the fabric scale [5, 6]. Thus, characterizing the mechanical behavior of single ballistic yarns can widely help to predict the impact behavior of these fibrous structures.

In this paper, a method for testing aramid yarns in dynamic uniaxial tension using a new experimental device is presented. Then, a description of the measurement device associated is done with the different curves obtained after data treatments. In a third part, we discuss about the experimental results obtained.

2 EXPERIMENTAL TESTS

2.1 The Tensile Impact Test for Yarn (TITY) device

To respond to this yarn characterization, we have developed a new device, the Tensile Impact Test for Yarn (TITY), in order to test yarns under dynamic uniaxial tension and determine their mechanical behaviors in the longitudinal direction. The TITY device consists of three main parts: the support, the projectile and the yarn sample which is maintained by its two ends to the support and the projectile (Figure 1).

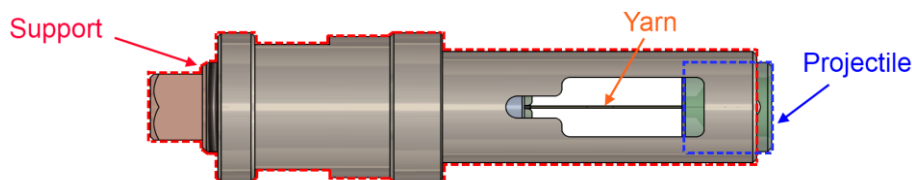


Figure 1. TITY device

A gas gun is used to propel the TITY device at an initial velocity v_{initial} from 20 to 40 m/s. Aramid yarns (Twaron 336Tex) are tested and two different sample lengths are used (5 mm and 20 mm) to reach initial strain rates within the range from 1000 to 4000 s^{-1} . So, the whole device (support, yarn and projectile) is propelled at a velocity v_{initial} through the gas gun up to its muzzle where the support is suddenly stopped caused by a cross-section diminution. The working mass keeps its initial velocity v_{initial} and applies a dynamic uniaxial tension on the yarn sample (Figure 2).

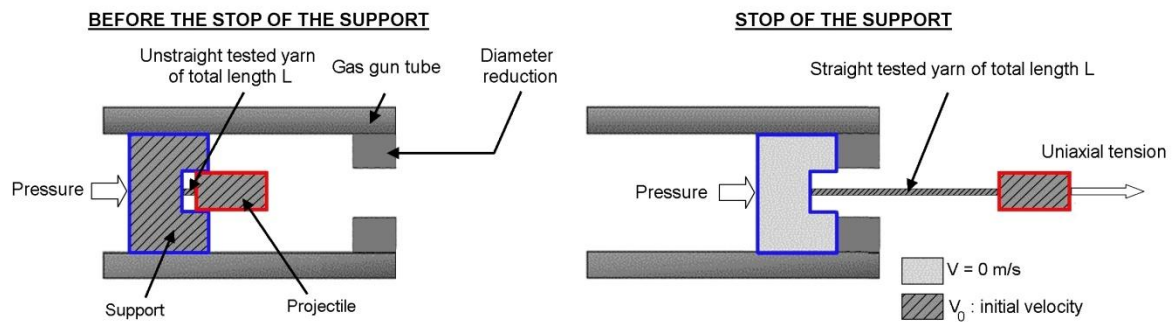


Figure 2. Principle of the TITY device.

Criteria had to be taken into account in order to realize tensile tests in good conditions:

- Firstly, the yarn has to be maintained straight along the TITY device in order to apply a longitudinal tension with the projectile without transversal component.
- Secondly, any slide of the yarn inside the support or the projectile has to occur during tensile tests. It results in an energy absorption provided by the projectile to the yarn. The yarn rupture and the data obtained are thus misrepresented.
- Moreover, the rupture of the yarn has to occur in the effective length, between the edge of the support and the edge of the projectile.
- At least, the projectile weight has to be adapted to the tested yarn. The energy provided by the projectile to the yarn has to be superior to the rupture energy of the yarn but it also doesn't have to be so important in order to observe elongation and rupture phenomena of the yarn.

2.2 The laser measurement device

During the test, we measure the light intensity variation of a homogeneous laser beam with a photo detector. This variation is due to the motion of the projectile in front of the homogeneous laser beam when it applies a longitudinal tension on the yarn which undergoes an elongation up to its rupture. From this light intensity variation, the photo detector provides us a voltage variation versus time.

In order to define a relationship between the coverage of the laser line and the position of the projectile, a second discontinuous laser line with five markers is superposed to the homogeneous laser beam (Figure 3).

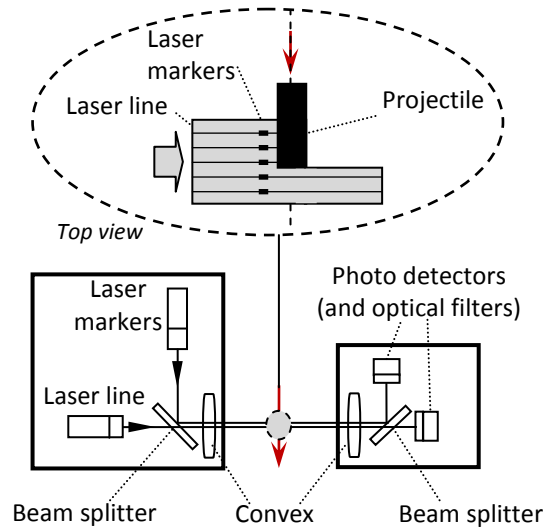


Figure 3. Sketch of the double laser device.

During the passage of the projectile in front of the homogeneous laser beam, we can identify several phases among which four ones interest us. The first phase corresponds to a constant displacement of the projectile at a velocity $v_{initial}$, the second phase to the strain of the yarn, the third phase to a gradual rupture of the yarn and a fourth phase to a constant displacement of the projectile at a velocity $v_{residual}$ (Figure 4). The times t_1 , t_2 and t_3 are identified with the use of an ultra high speed camera during tests.

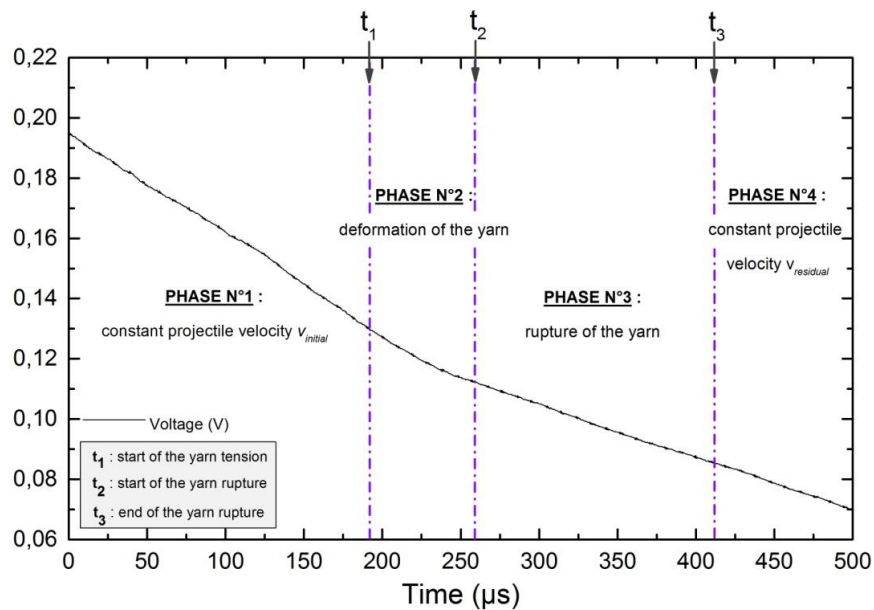


Figure 4. Test on aramid yarn (Twaron 336Tex) on 2 cm at $v_{initial} = 20$ m/s: Identification of the four phases on the voltage curve.

In order to obtain the projectile displacement from the voltage, a calibration of the laser measurement device is necessary. Then, adapted mathematical data treatments of the projectile displacement provide us the projectile velocity (Figure 5).

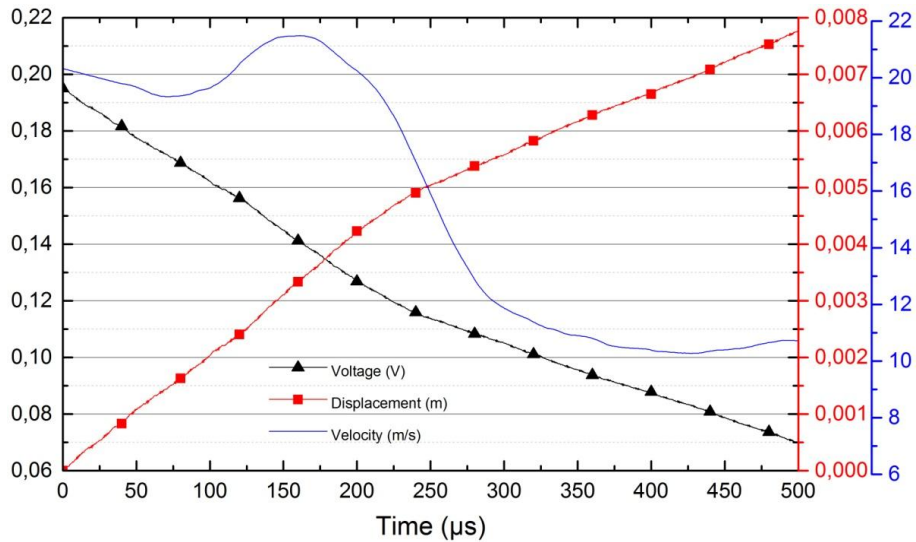


Figure 5. Test performed on aramid yarn (Twaron 336Tex) of 2 cm at $v_{initial} = 20$ m/s: black (triangular shape) left scale: Voltage-time curve, red (square shape) first right scale: projectile displacement-time curve and blue second right scale: projectile velocity-time curve.

2.3 Validation of the laser measurement device

In order to validate our laser measurement device, we realized a campaign of tests with both our device and a Photon Doppler Velocimeter (PDV). The PDV device can provide us directly a measurement of the velocity by measuring the difference of frequency between the incident (f_0) and the reflected lasers light (f_d) (Figure 6).

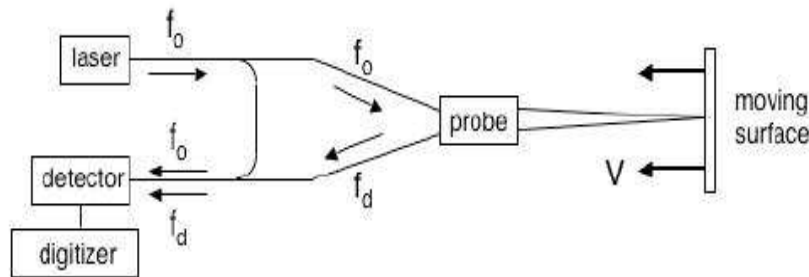


Figure 6. Principle of the PDV device.

A set of 16 tests have been performed on yarn samples (Twaron _ 336Tex) of 2 cm length at $v_{initial} = 31$ m/s. For each test the PDV device curve and our laser device curve are superimposed, principally during the phases of the yarn strain (phase n°2) and the yarn rupture (phase n°3) what allows validating our new experimental device and the laser measurement device (Figure 7).

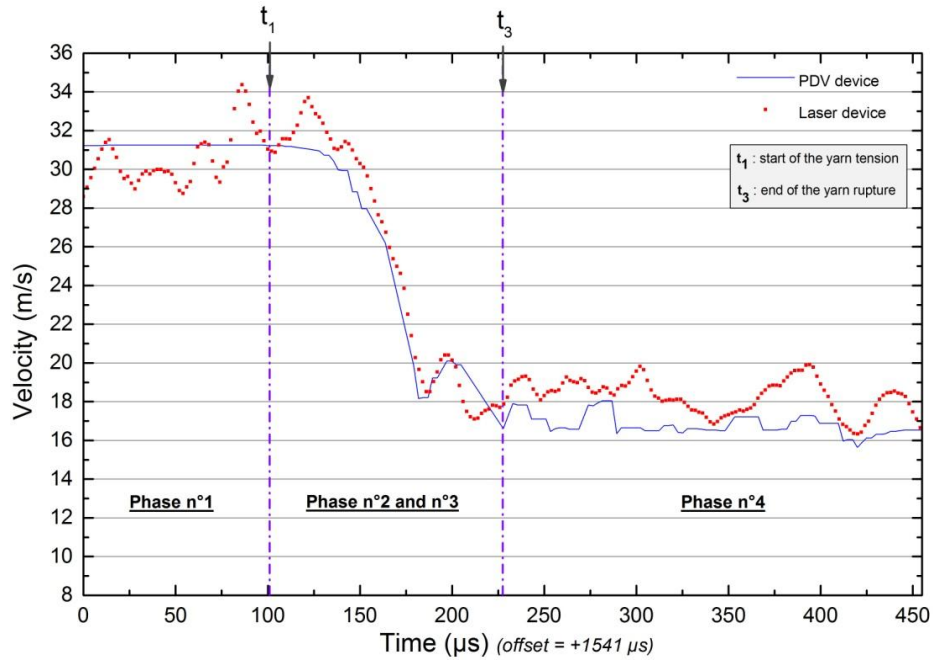


Figure 7. Validation of the laser measurement device with the PDV device.

3 RESULTS

A set of ten tests with the TITY device has been performed on aramid yarn (Twaron 336Tex) of 2 cm length at $v_{initial} = 20$ m/s. We can evaluate the initial strain rate at 1000 s^{-1} . The projectile velocity variation is obtained from the voltage measured thanks to the calibration and the adapted mathematical data treatments. We can identify the four phases including those with the deformation and the rupture of the yarn (Figure 8).

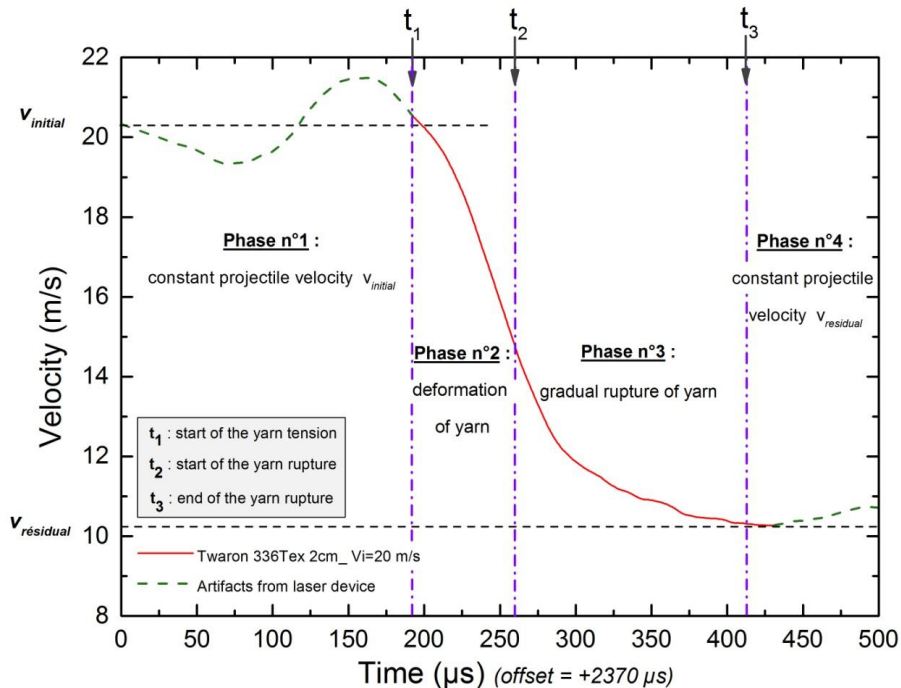


Figure 8. Identification of the four phases on the projectile velocity-time curve for tests performed on aramid yarn (Twaron 336Tex) of 2 cm length.

The yarn deformation phase is of about $70 \mu\text{s}$ and is followed by a gradual yarn rupture phase of about $150 \mu\text{s}$. This characteristic evolution of the projectile velocity versus time depends on the mechanical properties of the tested yarn. Reproduce the shape of this characteristic curve with an analytical approach will allow us determining the longitudinal mechanical parameters of the yarn in dynamic load.

The laser measurement device lets appear artifacts during the phases of constant velocity but the discontinuous laser light with the five markers allows measuring the initial and residual velocities and visualizing the complete shape of the projectile velocity-time curve during the phases $n^{\circ}1$ to $n^{\circ}4$.

The residual velocity measured is 10 m/s . With a projectile of $2,6 \text{ g}$ mass, the kinetic energy variation ΔE_c is equal to $0,390 \text{ J}$. By assuming that the whole yarn volume is a part of the absorption of the energy provided by the projectile, the specific energy absorbed by the yarn E_{abs} is equal to $83,5 \text{ MJ/m}^3$. In order to compare this data between a dynamic load and a quasi-static load, tests have been performed on the same yarn sample at a strain rate of $0,001 \text{ s}^{-1}$ (Figure 9).

The specific energy absorbed by the yarn under quasi-static load ($0,001 \text{ s}^{-1}$) is equal to $67,5 \text{ MJ/m}^3$. From these two results of the specific energy absorbed by the yarn, we can suppose that the rupture mechanisms in dynamic load are different and need more energy than that in quasi-static load (Figure 9).

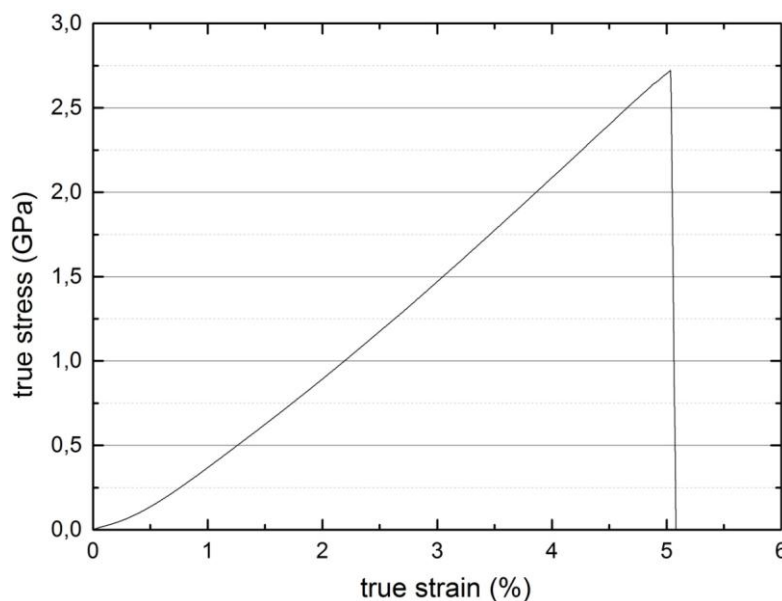


Figure 9. Quasi-static tests performed on aramid yarn (Twaron 338Tex) of 15 cm at $0,001 \text{ s}^{-1}$.

4 CONCLUSION

We have developed a new device to test yarn in dynamic uniaxial tension, the Tensile Impact Test for Yarn (TITY), in function of several criteria in order to respect good test conditions. A measurement device is used to obtain the variation of the projectile displacement thanks to a homogeneous laser light.

After several data treatments, we obtain the evolution of the projectile velocity versus time which depends on the mechanical behavior of the yarn (evolution of the stress vs. strain, ultimate stress and strain). The comparison of our results with ones of a Photon Doppler Velocimeter allows validating this new dynamic uniaxial tension device and the associated laser measurement device. Four phases are defined on the velocity versus time curve. Among

them, we identify two important phases which are the yarn elongation and the progressive yarn rupture.

Thanks to an analytical approach proposed to model these two phases, we could estimate the longitudinal Young modulus of the yarn under dynamic loading. These results allow us assuming that the rupture mechanisms in dynamic load are different and need more energy than that in quasi-static load. Thus, this new test on yarns under dynamic loading gives promising results and, with further work, could lead to a better knowledge of ballistic yarns. This knowledge about dynamic behavior of yarns would then be considered for improving future numerical models.

5 REFERENCES

1. Lim, J., et al., *Effects of gage length, loading rates, and damage on the strength of PPTA fibers*. International Journal of Impact Engineering, 2011. 38(4): p. 219-227.
2. Hudspeth, M., X. Nie, and W. Chen, *Dynamic failure of Dyneema SK76 single fibers under biaxial shear/tension*. Polymer, 2012. 53(24): p. 5568-5574.
3. Tan, V.B.C., X.S. Zeng, and V.P.W. Shim, *Characterization and constitutive modeling of aramid fibers at high strain rates*. International Journal of Impact Engineering, 2008. 35: p. 1303-1313.
4. Zhu, D., et al., *Strain rate and gage length effects on tensile behavior of Kevlar 49 single yarn*. Composites Part A: Applied Science and Manufacturing, 2012. 43(11): p. 2021-2029.
5. Chocron Benloulou, I.S., et al., *Dynamic tensile testing of aramid and polyethylene fiber composites*. International Journal of Impact Engineering, 1997. 19(2): p. 135-146.
6. Shim, V.P.W., C.T. Lim, and K.J. Foo, *Dynamic mechanical properties of fabric armour*. International Journal of Impact Engineering, 2001. 25(1): p. 1-15.



Optimization of the vibro-acoustic indicators of honeycomb panels

O. BAHO^{1,2*}, M. Ichchou¹, B. Harras² and R. Benamar³

¹Ecole central de lyon\ LTDS
36 Avenue Guy de Collongue, 69134 Écully
Email: omar.alich@gmail.com, mohamed.ichchou@ec-lyon.fr

²Faculté des sciences et techniques de Fès
B.P. 2202 – Route d'Imouzzer – FES – MAROC
Email: harrasbilal@yahoo.fr

³Ecole Mohammadia d'ingénieurs
Avenue Ibn Sina, Rabat, Maroc
Email: rhali.benamar@gmail.com

ABSTRACT

Modern design in the aerospace industry requires the use of lightweight structures, ensuring security and comfort and responding adequately to the environmental demands. In particular, a great deal of interest is focused on the question of noise reduction, because lightweight structures have generally poor sound insulation properties.

The aim of the present work is to find a periodic optimal geometry of the honeycomb core. The suggested design strategy reported here is an optimization procedure involving two scales: the meso-scale for the unit cell of the honeycomb panel and the macro-scale for the whole panel. To this purpose, an analytical homogenization technique was developed to determine the effective properties of the honeycomb structure along with a comparison with existing models. Also, a sensitive analysis in terms of the geometrical parameters of the unit cell has been conducted. Then, the modal density of honeycomb panel was predicted using the macro homogenized parameters.

1 INTRODUCTION

Honeycomb core sandwich panels are widely used in designing the structure of the aerospace industry. These panels typically feature orthotropic alveolar cores bonded to high modulus laminate skins. Generally, commercial varieties of honeycomb core sandwich panels are optimized for mechanical and weight constraints. As a result of this, a sandwich panel can be lightweight and designed to carry high mechanical loads. However, it tends to be poor when it comes to acoustic attenuation. To address this issue, several attempts have been made to identify the optimal sandwich plans that balance mechanical and acoustic properties. Among these attempts, the following references [1-3] have developed a methodology in order to maximize the transmission loss of these types of panels.

In the present paper, an optimization methodology was proposed to reduce the modal density (n) for the honeycomb sandwich panels. The modal density was predicted by using the analytical model established by Renji [4], which takes into account the shearing effect of the core structure. To predict the modal density, the effective properties of the honeycomb sandwich structure are required. For this purpose, the effective properties were obtained by analytical homogenization techniques by exploiting the meso-scale for the unit cell of the honeycomb panel and the macro-scale of the whole panel. Thereafter, a sensitivity analysis in terms of the geometrical and material parameters of the unit cell has been conducted.

1. FORMULATION OF THE PROBLEM

1.1 Optimization Model Formulation

The modal density of honeycomb sandwich panels is investigated in a large number of papers. Among the first formulation of the modal density for isotropic sandwich panels is developed by Wilkinson [5]. Later, a study was carried out by Erickson [6] to investigate the effect of the anisotropy of the core on the modal density. The theories suggested by the latter two authors are compared to experiments by Clarkson [7].

Experimental and analytical modal density for honeycomb sandwich panels, used in some applications, have been reported in the reference [4]. The study done in the reference [8], a summary of different theories for the modal density behavior of honeycomb sandwich panels has been reported.

The expression for the modal density of a honeycomb panel with an isotropic face sheet is written as follows:

$$n(f) = \frac{\pi ab M_p f}{N} \left\{ 1 + \left(M_p^2 \omega^4 + \frac{4 M_p \omega^2 N^2}{D} \right)^{-\left(\frac{1}{2}\right)} \left(M_p \omega^2 + \frac{2 N^2}{D} \right) \right\} \quad (1)$$

Where:

- $a b$ is the panel surface area
- D is the section bending stiffness,
- M_p is the build-up panel mass/area
- N is the shear stiffness

1.2 Optimization Model Formulation

Optimization methods are mainly used in engineering design activities to achieve a competitive design, which optimize (i.e. either minimize or maximize) a certain objective by satisfying a number of constraints. The first step in an optimal design is to formulate the problem by writing the

mathematical functions relating to the objective and constraints [9]. For this study, the optimization problem is defined in the following form:

$$\begin{aligned}
 & \text{Minimize} && f(x) \\
 & \text{subject to} && g_i(x) \geq 0, && i = 1, 2, \dots, I; \\
 & && h_j(x) = 0, && j = 1, 2, \dots, J; \\
 & && x_k^l \leq x_k \leq x_k^u, && k = 1, 2, \dots, N.
 \end{aligned}
 \tag{2}$$

Where $f(x)$ is the objective function. $g_i(x)$ is the equality constraint. $h_j(x)$ is the inequality constraints. While x is the variable vector, represents a set of variables x_i .

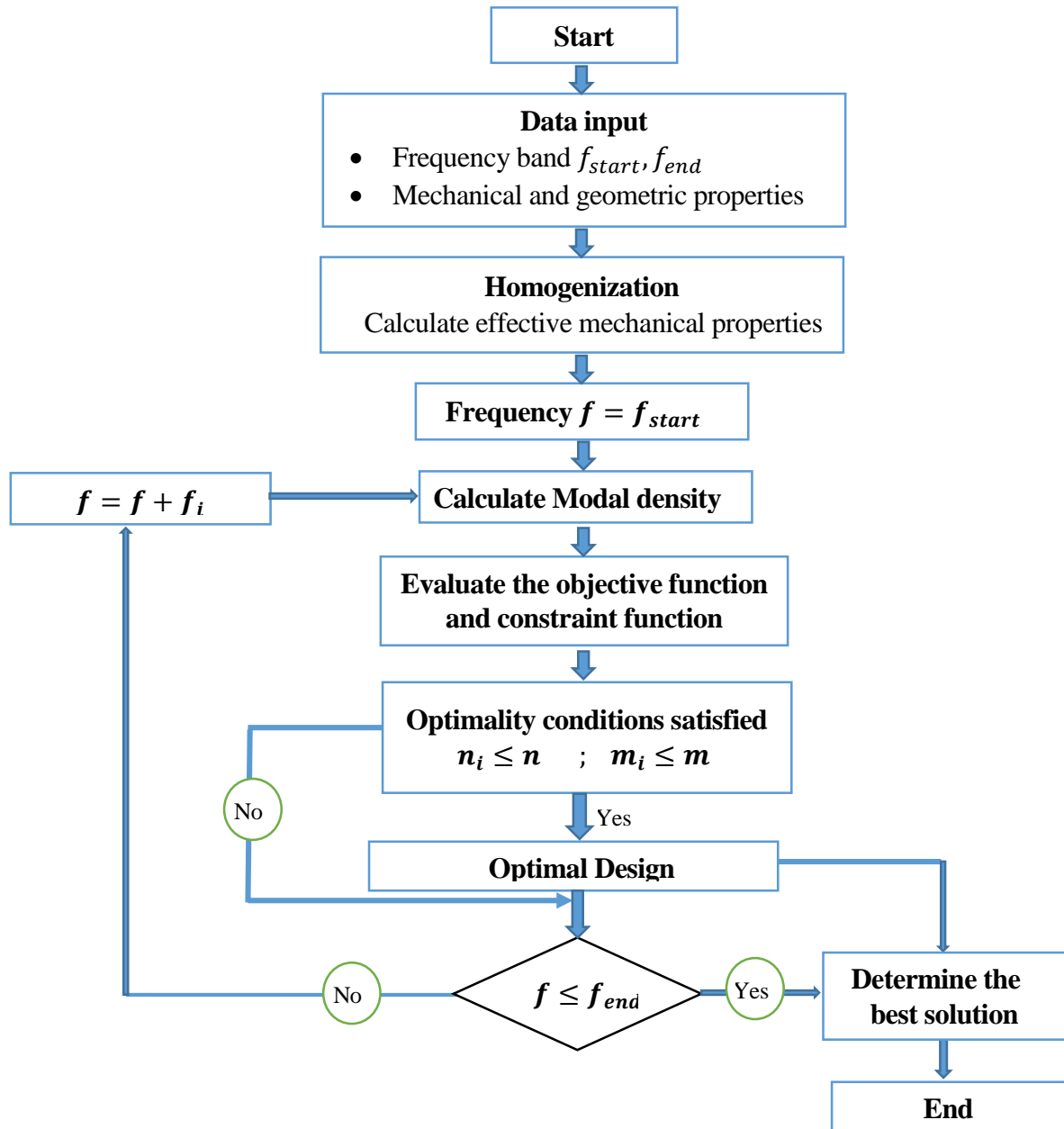


Figure 1. The current optimization methodology of the honeycomb modal density.

2 RESULTS

For the analyses of the present study, the hexagonal-cell core sandwich panel is considered, as illustrated in the figure (1). The honeycomb core is made of Nomex, whose properties and

dimensions are summarized in the table (1). On the other side, the face-sheet material is made of Aluminum, whose properties are $E = 72,5 \text{ GPa}$, $\nu = 0.33$, and the skin thickness $t_f = 0.076 \text{ mm}$.

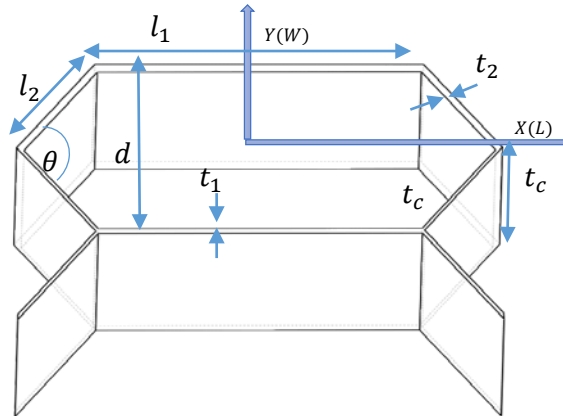


Figure 2. The geometrical parameters of the honeycomb cell.

Core: Nomex honeycomb core	
Core density	$1,38 \cdot 10^3 \text{ kg/m}^3$
Core thickness	20 mm
$t_2, t_1,$	0,079 mm, 0,159 mm
l_1, l_2, θ	4,9 mm, 1,63 mm, $\frac{\pi}{12} \text{ rad}$

Table 1. The geometrical core values of the honeycomb cell.

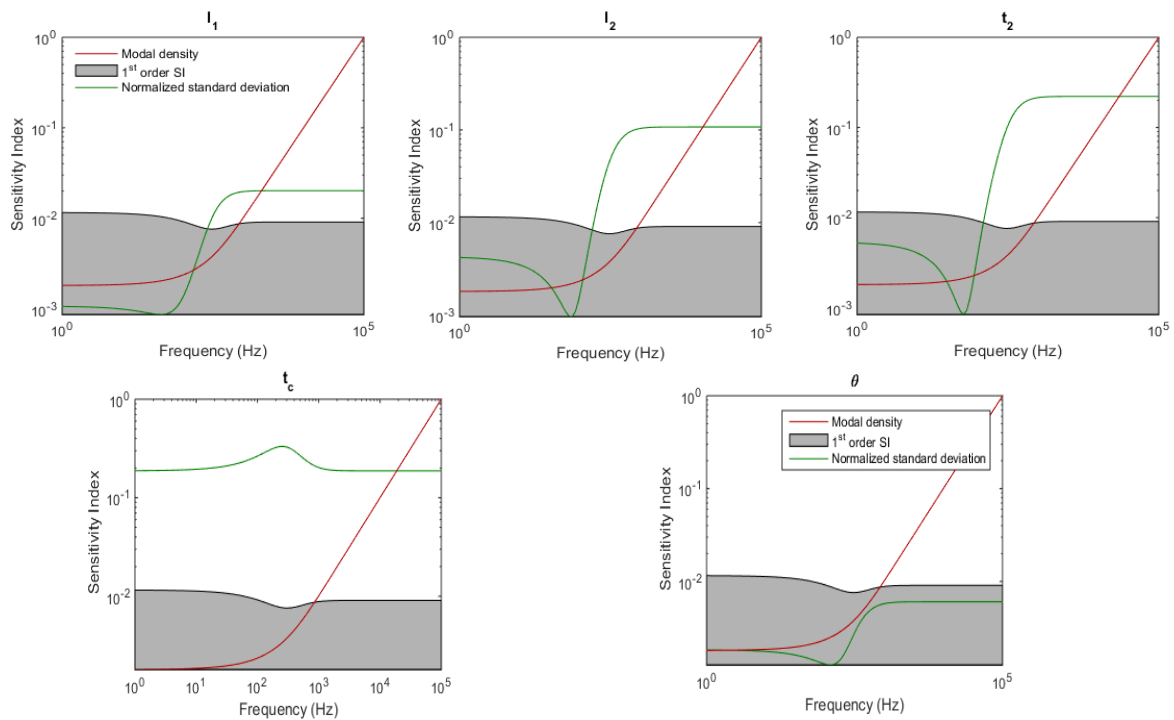


Figure 3. The sensitivity results of geometrical honeycomb panel

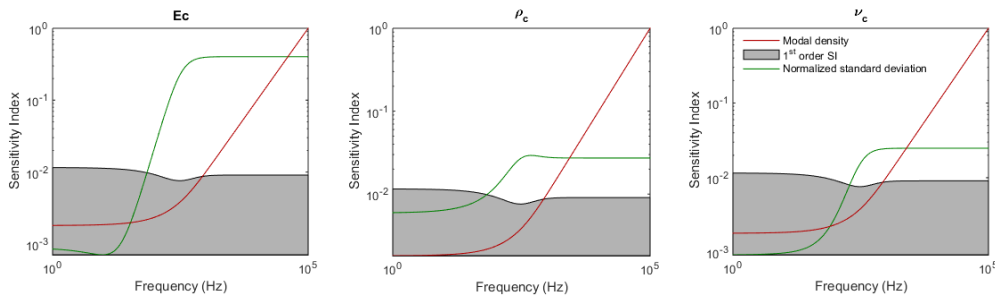


Figure 4. The sensitivity results of material honeycomb panel

The figures (3) and (4) represent the sensitivity analysis done for a honeycomb sandwich panel illustrated in the figure (1). The study shows that for 1% of variation of each honeycomb properties, in the medium and high frequency, the effect of the properties is very considerable with respect to the low frequency.

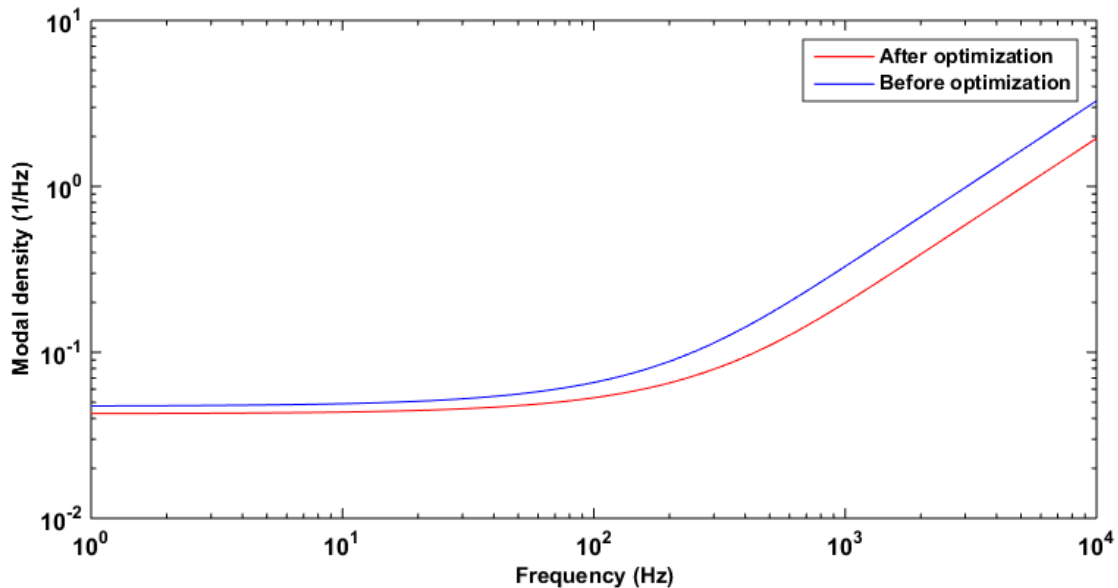


Figure 5. The comparison between the optimal modal density and the original modal density

By following the optimization methodology presented in the figure (1), a comparison of the non-optimal and optimal modal density is depicted in the figure (5). The optimization study is done under two constraints the mass and the stiffness of the honeycomb panel. These two constraints have to remain constant after the optimization study. The red modal density curve in the figure (5) presents the minimum modal density obtained by the optimal variable design.

3 CONCLUSION

The present optimization study was based on the modal density predicted by Renji’s model. This modal density takes into account the transverse shear effect. The sensitivity analysis of the honeycomb sandwich panel showed that the effective properties of the panel, obtained by different homogenization techniques, have considerable influence on the modal density whether in the medium or the high frequency range. This sensitivity study allows us to identify the most sensitive properties which we should focus on them. The optimization of these sensitive core parameters resulted a minimum modal density with respect to the previous one.

4 REFERENCES

- [1] M. A. Lang and C. L. Dym. Optimal acoustic design of sandwich panels. *Journal of the Acoustical Society of America*. 57: 1481-1487, 1975.
- [2] R. Hooke and T. A. Jeeves. Direct search solution of numerical and statistical problems. *J. Assoc. Comput. Mach.* 8: 212-219, 1961.
- [3] S. E. Makris, C. L. Dym, and J. M. Smith. Transmission loss optimization in acoustic sandwich panels. *Journal of the Acoustical Society of America*, 79 (6):1833-1843, 1986.
- [4] K. Renji. P.S. Nair and S. Narayanan. Modal density of composite honeycomb sandwich panels. *Journal of Sound and Vibration*, 195(5):687-699, 1996.
- [5] J. P. D. Wilkinson. Modal densities of certain shallow structural elements. *J. Acoust. Soc. Am.*, Vol. 43(2):245-251, 1968.
- [6] L. L. Erickson. Modal densities of sandwich panels: theory and experiment. *The Shock and Vibration Bulletin*, 39(3): 1-16, 1969.
- [7] B. L. Clarkson and Ranky M.F. Modal density of honeycomb plates. *Journal of Sound and Vibration*, 91:103-118, 1983.
- [8] S. Ghinet and Atalla N. Vibro-acoustic behaviors of flat sandwich composite panels. *Transactions of Canadian Soc. Mech. Eng J.* 30(4), 2006.
- [9] K. Deb. *Optimization for engineering design: Algorithms and examples*. New Delhi: Prentice-Hall, 1995.

5 COPYRIGHT NOTICE

Copyright ©2015 by the authors. Distribution of all material contained in this paper is permitted under the terms of the Creative Commons license Attribution-Non Commercial-No Derivatives 4.0 International (CC-by-nc-nd 4.0).





A TWO STEPS DAMAGE LOCALIZATION METHOD BASED ON WAVELET PACKET DECOMPOSITION. APPLICATION TO MULTI-LAYER COMPOSITE STRUCTURES

A. Boumrar, A. Bouazzouni* and M. Dahmane

Laboratoire de Mécanique, Structures et Energétique

Université Mouloud Mammeri de Tizi-Ouzou,

BP17 RP, Tizi-Ouzou 15000, ALGERIA

tak_gm@hotmail.fr, abouazzouni@yahoo.com, dahmani_merzak@yahoo.fr

ABSTRACT

In this work, we propose a two steps method for localizing damages in multi-layer composite structures. The signals of the dynamic responses of the healthy and damaged structures are initially decomposed using the analysis into wavelet packages and then rebuilt. Then, energies of these last signals are used to define an indicator of variation of energy called Wavelet Packages based Energy Variation Index (WPEVI). The robustness of this damage localization index is tested in the case of composite beams with respectively two and three damages.

To ascertain the quality of the results, the sensitivity of the proposed method to structural damage is studied. In this respect, we define the threshold sensibility of a damage vibration indicator based on wavelet package decomposition of structural vibration responses before and after the occurrence of structural damage. Each of these structural vibration responses is decomposed to the j^{th} order wavelet package sub-signals. The structure is subdivided into a certain number of finite elements. For a structure with one particular finite element perturbed to a certain rate, the damage indicator is then defined as the maximum of all energy variations of the wavelet package sub-signals of the structural vibration response before and after the occurrence of some structural damage. The indicator is called maximum energy variation (MEV). For the same mono-excitation, this indicator is then evaluated for all the elements of the discretization with the same perturbation rate. The values of this indicator are then represented on a graph in terms of the number of the finite element. Once we have determined the element whose damage indicator value is minimum, further trials are carried out in order to draw the curve representing the indicator in terms of the different rates of damage. From the graph, we determine the least detectable damage rate using the wavelet package decomposition of structural response. A mapping of the structure is carried out as to the least detectable damaged element of the structure. With this tool in hand, we may ascertain or not each of the damage localization results.

1 INTRODUCTION

The aim of this work is to develop a damage detection-localization procedure as well as a global damage threshold indicator, both based on the wavelet packet decomposition.

The projected damage detection procedure is to use temporal response function data. The method is in particular based on sub-signals of a certain level in the decomposition process of a signal in wavelet packets. The property of wavelet packets decomposition for denoizing signals is certainly of great help particularly in the case of laminated composite structures.

Another part of the undertaken work consists in establishing a global threshold damage indicator. Many research works have dealt with damage detection in composite structures but few of these have been concerned with the minimum of the magnitude of the damage that can be detected. Yam and al [1] use the wavelet packet analysis for the detection of damage in composite laminate plates. In their work, they define a damage indicator named "Maximum Energy Variation" (MEV). To establish this, they consider a structure with one particular finite element perturbed to a certain rate. Then, they calculate successively the energy of each sub-signal in the wavelet packets decomposition of the dynamical response of the damaged structure as well as that of the corresponding sub-signal corresponding of the healthy structure. The difference of these respective energies is then calculated and divided by the total energy of the sub-signals of the considered level of wavelet decomposition. The maximum of these normalized variations constitutes the so-called MEV damage indicator.

Our contribution consists in finding a global threshold damage indicator rather than a particular one for a defined position of the damaged element in the structure as did Yam and al. This global threshold damage indicator is useful to help ascertain whether results of the localization process are reliable or not.

In our work, we are interested in using this damage indicator in the case of a layered beam structure. For the purpose of analysis, a finite element model of this structure is built. For the same excitation and damage rate, a graph representing the indicator in terms of the perturbed element number is drawn to determine the element for which this has the lowest value. Different graphs of the MEV indicator in terms of damage rate may be drawn for different damaged element positions along the structure, and a damage detection threshold is established.

Before presenting the damage detection method and the global threshold damage indicator, first let us define the SI20 beam finite element.

2 FINITE ELEMENT SI20

The finite element model we use in this study is based on the theory of the zigzag movement of the first order. The finite element [2] is composed of three layers in symmetrical stackings sequences. Thus, the displacement at an arbitrary point of the beam can be expressed by a longitudinal displacement $u_1(x)$ along the beam axis and a transverse $u_3(x)$ along the z axis and a rotation $\gamma_x(x)$ characterizing the rotation about the y axis (see FIG. 1).

Displacements are given by:

$$\left. \begin{aligned} u_1(x) &= u(x) + z \gamma_x(x) \\ u_3(x) &= w(x) \end{aligned} \right\} \quad (1)$$

where u is the longitudinal displacement at $z = 0$ and w is the deflection of the beam axis.

The rigidity matrix is obtained from the strain energy of the element:

$$U_e = \sum_{k=1}^3 \frac{1}{2} \int_0^l \varepsilon^{(k)T} D^{(k)} \varepsilon^{(k)} dx = \sum_{k=1}^3 \frac{1}{2} \int_0^l v_e^{(k)T} B^{(k)T} D^{(k)} B^{(k)} v_e^{(k)} dx \quad (2)$$

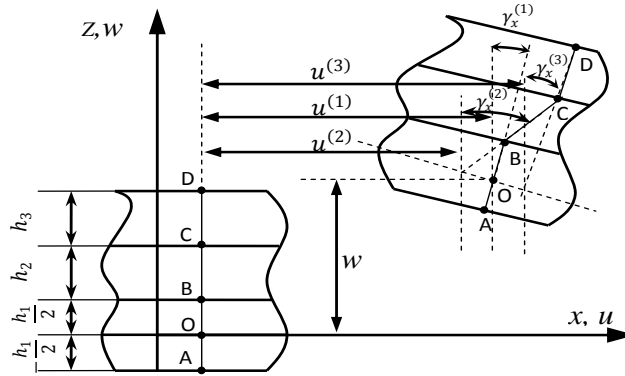


FIG. 1– Initial and deformed SI20 element

where k : layer number. $k = 1, 2$ et 3 . l : length of the element. D : elasticity matrix of the element.

B : deformation matrix. $v_e = [u^{(k)}, w^{(k)}, \gamma_x^{(k)}]^T$: nodal displacement vector.

Similarly, we may write the kinetic energy of the element in order to derive the mass matrix:

$$T_e = \sum_{k=1}^3 \frac{1}{2} \int_0^l \dot{u}^{(k)T} R_0^{(k)} \dot{u}^{(k)} dx = \sum_{k=1}^3 \frac{1}{2} \int_0^l \dot{v}_e^{(k)T} N^T R_0^{(k)} N \dot{v}_e dx \quad (3)$$

where: \dot{v}_e : the nodal velocity vector. N : the shape function matrix. R_0 : Matrix bulk densities.

$$R_0 = \begin{bmatrix} \rho_0 & 0 & \rho_1 \\ 0 & \rho_0 & 0 \\ \rho_1 & 0 & \rho_2 \end{bmatrix}$$

Generalized densities are given by:

$$\rho_0 = b \sum_{k=1}^K \rho_k [z_k - z_{k-1}] \quad \rho_1 = \frac{1}{2} b \sum_{k=1}^K \rho_k [z_k^2 - z_{k-1}^2] \quad \rho_2 = \frac{1}{3} b \sum_{k=1}^K \rho_k [z_k^3 - z_{k-1}^3] \quad (4)$$

Once the elementary matrices of rigidities and masses are obtained, they will be assembled to build the global stiffness matrices and weight of the individual system:

$$M = \sum_{i=1}^n M_i^{(e)} \quad \text{and} \quad K = \sum_{i=1}^n K_i^{(e)} \quad (5)$$

Having obtained the analytical model of the beam structure, in the case of a sine wave excitation, the equation of forced motion can be easily derived.

3 ENERGY CHANGE INDICATOR

Let $y(t)$ the signal of the dynamic response of a structure. This signal is decomposed by wavelets packets in a sum of subsignals $y_j^i(t)$, at the i^{th} level, as follows:

$$y(t) = \sum_{i=1}^{2^j} y_j^i(t) \tag{6}$$

The energy U stored in a sub-signal is given by:

$$U_j^i = \int_{-\infty}^{+\infty} y_j^i(t)^2 dt \tag{7}$$

Thus, the total energy U of the signal is defined as being the sum of the energies of these sub-signals

$$U = \sum_{i=1}^{2^j} U_j^i \tag{8}$$

We consider the responses of the two structures healthy indexed h and damaged indexed d . For each structure, we define respectively the vectors V_h and V_d whose components are each the ratio of the sub-signal energy to the total energy of the signal at the level selected of wavelet package decomposition.

$$V_h = \{C_{h_j}^1, C_{h_j}^2, C_{h_j}^3, \dots, C_{h_j}^{2^j}\} = \left\{ \frac{U_{h_j}^1}{U_h}, \frac{U_{h_j}^2}{U_h}, \frac{U_{h_j}^3}{U_h}, \dots, \frac{U_{h_j}^{2^j}}{U_h} \right\} \tag{9}$$

$$V_d = \{C_{d_j}^1, C_{d_j}^2, C_{d_j}^3, \dots, C_{d_j}^{2^j}\} = \left\{ \frac{U_{d_j}^1}{U_d}, \frac{U_{d_j}^2}{U_d}, \frac{U_{d_j}^3}{U_d}, \dots, \frac{U_{d_j}^{2^j}}{U_d} \right\} \tag{10}$$

From these last two vectors we define the relative energy variation vector as follows:

$$EV = \left\{ \left(\frac{C_{h_j}^1 - C_{d_j}^1}{C_{h_j}^1} \right), \left(\frac{C_{h_j}^2 - C_{d_j}^2}{C_{h_j}^2} \right), \left(\frac{C_{h_j}^3 - C_{d_j}^3}{C_{h_j}^3} \right), \dots, \left(\frac{C_{h_j}^{2^j} - C_{d_j}^{2^j}}{C_{h_j}^{2^j}} \right) \right\} \times 100\% \tag{11}$$

The MEV is defined as the maximum of the absolute relative energy variations (EV).

4 NUMERICAL SIMULATION TEST CASES

The composite beam structure represented in FIG.2 is composed of 3 layers glass/époxy, disposed in the following configuration $[0^\circ/90^\circ/0^\circ]$. The beam is subdivided into 60 finite elements SI20 [3].

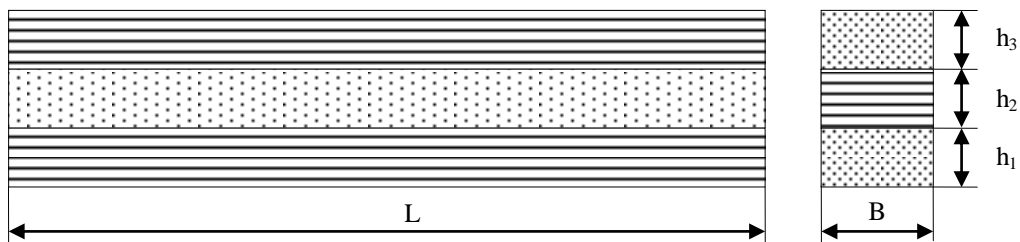


FIG. 2 – Stratified composite beam

The mechanical properties of the material are : $E_1 = 47.518$ GPa; $E_2 = 4.588$ GPa; $G_{12} = 2.201$ GPa; $\mu_{12} = 0.0419$; $\mu_{21} = 0.434$; $\rho = 1850$ kg/m³. Its geometry is characterized by : $L = 360$ mm, $h_1 = h_2 = h_3 = 4$ mm, $B = 30$ mm.

We consider two types of boundary conditions: a cantilever and a simply-simply supported beam. The damaged beam is simulated by reducing the longitudinal Young's modulus E_2 of the middle layer of the finite element.

For the first type of boundary conditions, the excitation is applied at its first node from the free end and for the second case of boundary conditions it is applied at the 25th node. The excitation force consists of three components and it is applied normally to the beam at the node previously indicated:

$$F_e(t) = A_0(\sin(\omega_1 t) + \sin(\omega_2 t) + \sin(\omega_3 t))$$

The measurement frequency band must contain as many eigenmodes as possible, and the exciting force must be chosen to excite the maximum number of these. The temporal responses signals of healthy and damaged structures are decomposed by «db4» wavelets packets to the 5th level.

5 HOW TO DETERMINE DAMAGE THRESHOLD OF A STRUCTURE

The strategy for determining damage threshold is highlighted through the stratified composite beam defined above in two cases of boundary conditions.

5.1 CANTILEVER BEAM CASE

To begin, we damage by 40% successively each element of the structure and we draw the MEV curve in terms the element number of the structure (FIG. 3).

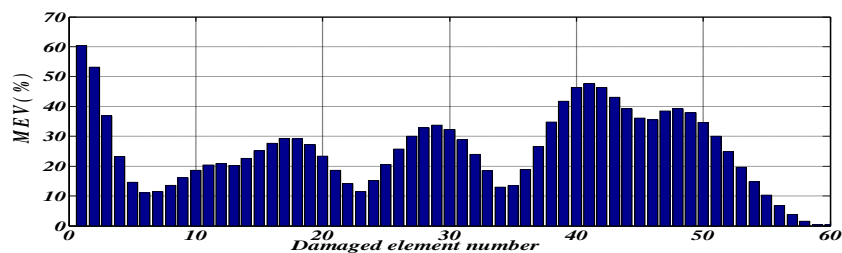


FIG. 3 – Cantilever beam : Histogram of MEV – 40% damaged beam element number.

The sensitivity of this indicator is variable according to the location of the defect. We choose on the FIG.3 element 6 which has the lowest value of MEV. We damage it at various rates and we seek in the waveband a combination of components of the exiting force which gives us the curve representative of MEV according to the rate of damage. This shape of the curve enables us to fix a priori a threshold of detectability of damages at the selected position (FIG. 4). The threshold is fixed just under the point of inflection of the curve at 60% and the smallest rate of detectable damage of element 6 is thus approximately 22%.

We obtain the same shape of the MEV-damage rate curve each time we change the position of the damaged element, the structure being always subjected to the same excitation as in the case of the damage of element 6, while varying the extent of the damage. This makes it possible to fix a threshold for each selected position of the damaged element. We represent above for some elements the graphs of MEV according to the damage rate of the element.

We maintain the same threshold of 60% for all the damaged elements and we take note of the smallest rate of detectable damage (FIG.5a). For element 12 for example, the smallest detectable rate is 20%; for element 18 it is 14%; for element 38 it is 12%.

5.2 SIMPLY-SIMPLY SUPPORTED BEAM CASE

Let us consider the case of the simply-simply supported beam. In the same manner as we proceeded in the preceding case, we start by damaging by 40% successively each element of the structure. The histogram representing the MEV according to the damaged element number is given by the FIG. 4.

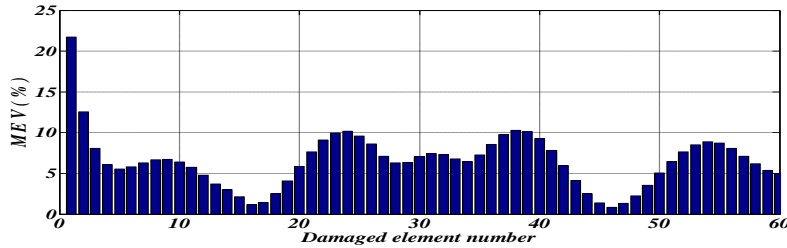


FIG. 4 – Simply-simply supported beam : MEV histogram in terms of 40% damaged beam element number

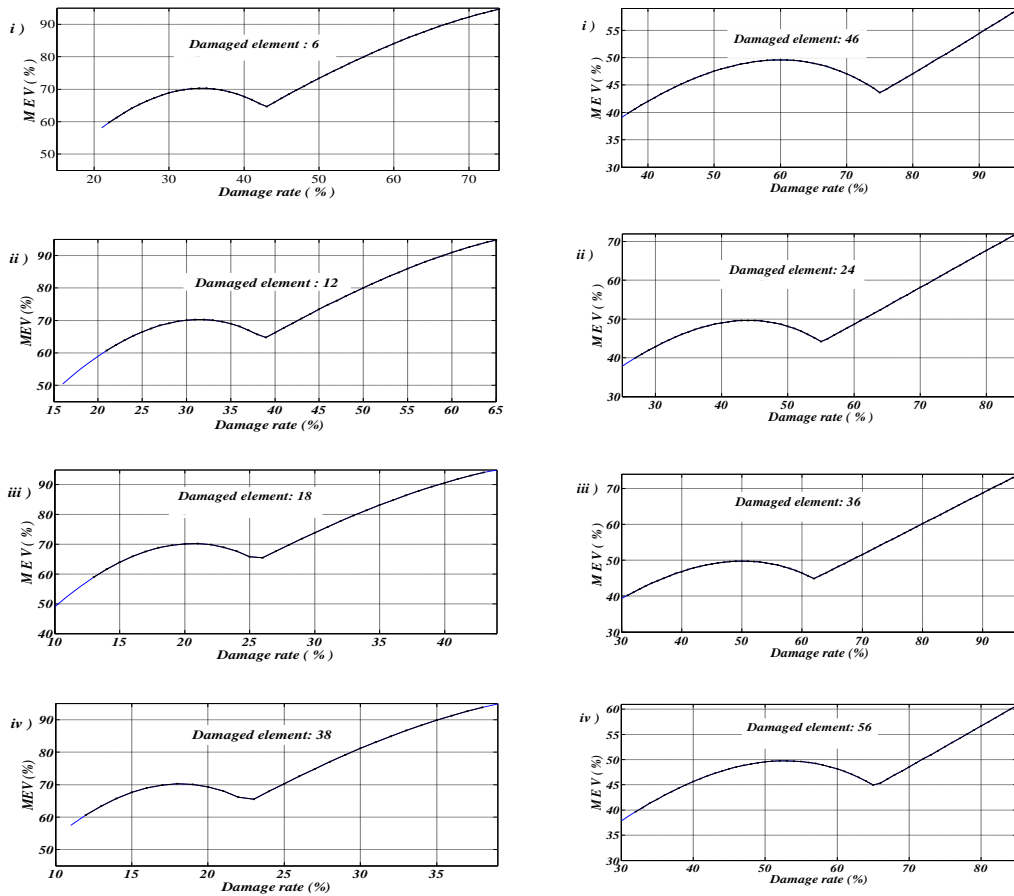


FIG.5a - : Cantilever beam

FIG.5b : Simply-simply supported beam

FIG. 5 –Variation of MEV according to the damage rate.

On FIG. 4 we choose element 46 and seek the good combination of the components of the exciting force giving the representative MEV curve. The threshold is fixed here at 40% and the smallest damage is located at approximately of 40%.

For all the structures the threshold of MEV is fixed at 40%. Of each curve we take note of the minimum detectable rate of damage. Some curves are presented in FIGS.5.b. The threshold of

detectability is 35% for element 6; 38% for element 10; 44% for element 12 and 46 for the 56ème damaged element.

FIG.5 give us detailed information about the variation of MEV according to the size of the defect for each case of structure with different damaged element, and help us locate the threshold of detectability for each one of them. We notice a correspondence between the data of the histograms and those of FIGS.5, i.e. the elements having low values of MEV on the histograms have a detectability threshold higher and vice versa. For example, on histogram 3, the value of MEV for element 12 is 20% and for element 28 it is 35%. On FIG.5, the damage is detectable from the value of MEV of 12% if the damaged element is the 38ème while it is detectable only from a MEV value of 20% for the élément12. The application of the method on the two types of boundary conditions gives us similar results.

6 DAMAGE DETECTION-LOCALIZATION METHOD

6.1 PRESENTATION OF THE METHOD OF DETECTING AND LOCALIZING DAMAGE IN STRUCTURES.

Let $y(t)$ be the dynamic response signal of the structure rebuilt after wavelet packet decomposition, according to formula (6). Its total energy U is given by the formula (8). Total energy structures, healthy and damaged, are designated by U^h and U^d respectively.

First, we define $VEPO_{nq}$ by the absolute value of the relative change between the total energy of the healthy structure U^e and that of the damaged structure U^e , measured from the nq^{th} node.

$$VEPO_{nq}(\%) = \frac{|U^h - U^d|}{U^h} = \frac{\left| \sum_{j=1}^{2^k} U_k^{j(h)} - \sum_{j=1}^{2^k} U_k^{j(d)} \right|}{\sum_{j=1}^{2^k} U_k^{j(h)}} \times 100\% \quad (12)$$

where U_k^j is the energy of the j^{th} sub-signal in the decomposition of the structure of the response by the k^{th} wavelet packet level.

The response of the structure is measured in a single DOF. The principle of this procedure is to calculate the $VEPO_{nq}$ for two DOF belonging to the same element, and calculating the relative difference between them.

Among the 20 DOFs of the SI20 finite element, we chose the two vertical DOFs of the ends of each element to measure the $VEPO_{nq}$. The $VEPO$ value estimated at the first DOF defining element q is affected by the index q and the second by the index $q+1$ (Fig. 6).



Fig. 6. Numbering of vertical DOF of the structure

We then calculate, for each q element, an IVEPO indicator (Energy change indicator based on Wavelets Packets) defined by:

$$IVEPO(\%) = \left| \frac{VEPO_{nq+1} - VEPO_{nq}}{VEPO_{nq}} \right| \times 100(\%) \quad (12)$$

The application of our indicator for fault location on a structure requires as many sensors as the number of discretization elements. This, from a practical point of view, is a cumbersome burden for the structure and causes expensive implementation costs. An alternative to these constraints is to use a method for optimizing the number of sensors used and their positioning on the structure. In this work, the method of H. Amdriambolona [3] for selecting DOF sensors and reconstituting the unobserved DOF is used.

6.2 NUMERICAL SIMULATION TEST CASE

We consider the composite beam structure of graphite/epoxy in Figure 7 having the configuration. It is discretized into 40 finite elements SI20, numbered 1 to 40 from the left to the right.

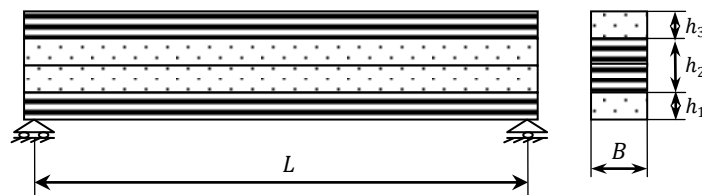


Fig. 7. Doubly simply supported layered $[0^\circ/(90^\circ)_2/0^\circ]$ beam.

The mechanical characteristics of the beam material are given by:

$E1 = 144,8\text{GPa}$; $E2 = 9,65\text{GPa}$; $G13 = 4,14\text{GPa}$; $G23 = 3.45\text{ GPa}$; $\mu12 = 0.25$; $\rho = 1390\text{ kg / m}^3$.

Its geometry is characterized by:

$L = 15\text{m}$; $h1 = h3 = 0.25\text{m}$; $h2 = 0.5\text{ m}$; $B = 1\text{m}$.

In the numerical simulation tests that follow, we examine the sensitivity of the indicator in the case of the presence of two and three defects.

In all tests, we adopt the same approach:

- the simulation of damage to a component is performed by a 20% reduction of the longitudinal Young's modulus of the second layer ($E2$) and 5% of its transverse shear modulus ($G23$).
- we excite all the structures in the same position (vertical excitation in the 20th node from the right end) with a single exciting force of the form. The dynamic response is calculated for the two structures, healthy and damaged.

Among the 40 vertical translational DDL, we selected 23 sensors positions. For the simulation, we added random noise to simulate responses of both healthy and damaged structures using model: $YBT\ y = (1 + gn \times \text{rand})$.

Then, the responses of healthy and damaged structures are then decomposed by wavelet packet of order Daubechies 4 "db4" the 5th level. Then we calculate the IVEPO for each element and we represent IVEPO-number of the element of each test curves.

A. Case of two damages

We examine three cases of structures: each containing two damaged components: The first structure has its elements 23 and 24 damaged; the second is damaged in the elements 11 and 33 and the third is damaged in elements 6 and 37. Representative histograms are shown in Figures above.

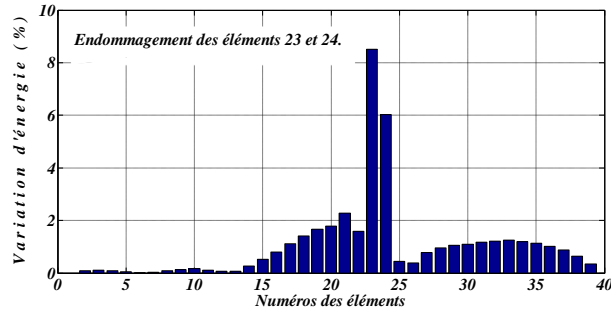


Fig.8. Histogram IVEPO-number of the element in the case of damaged items 23 and 24

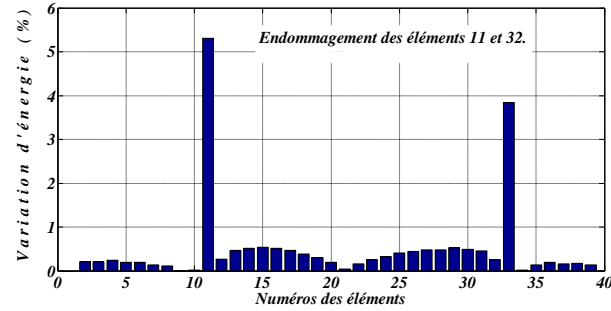


Fig.9. Histogram IVEPO-number of element in the case of damage to the elements 11 and 32

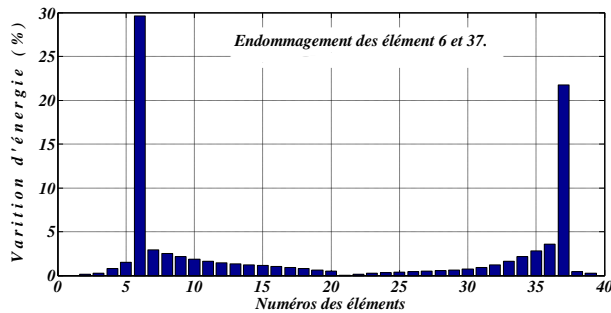


Fig.10. Histogram IVEPO-number of element in the case of damage to the elements 6 and 37

B. Case of three damages

As in the first case, we simulate three damaged structures having each three damages. For the first, it is damaged in its elements 10, 13 and 22; the second, items 7, 10 and 35, and finally the third, we simulate damage to the 11th, 14th and 32nd element. The results of these tests are shown in the following figures.

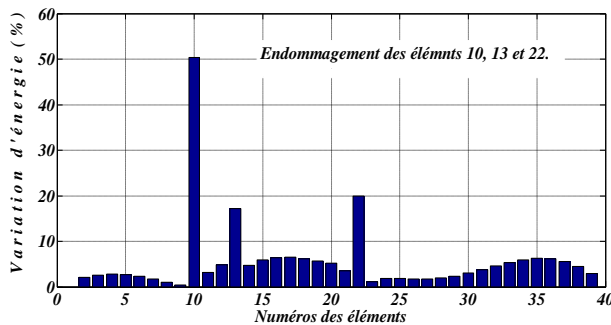


Fig. 11. Histogram IVEPO-element number in the case of damage to elements 10, 13 and 22

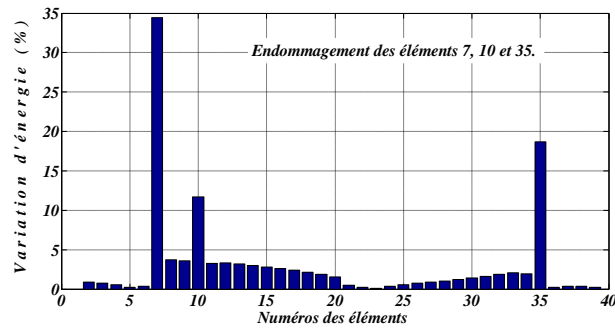


Fig. 12. Histogram IVEPO-number in the case of damage to elements 7, 10 and 35

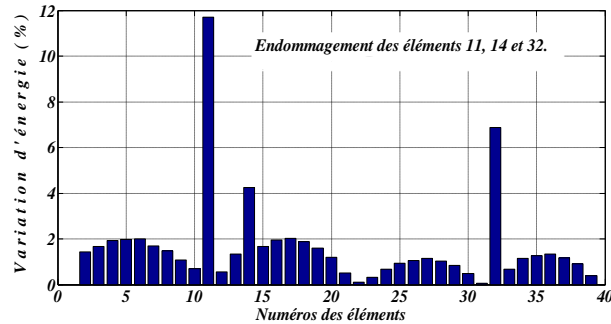


Fig. 13 Histogram IVEPO-element number in the case of damage to elements 11, 14 and 32

7 CONCLUSION

In this work, we propose a damage indicator based on the decomposition of wavelet packet responses to locate damage in composite beam structures in their first stage of development. This indicator is the relative difference between the total energy of the sub-signals of the healthy structure response and that of the corresponding ones of the damaged structure response. A resembling indicator proposed by Jian-Gang Han [4] is defined differently. The latter is equal to the sum of all relative energy differences of corresponding sub-signals of healthy and damaged responses included in the wavelet packets decomposition.

The property of wavelet packets decomposition for denoizing signals is certainly of great help particularly in the case of laminated composite structures.

As for the global threshold damage indicator is concerned, our contribution consists in finding a global threshold damage indicator rather than a particular one for a defined position of the damaged element in the structure as did Yam and al. This global threshold damage indicator is useful to help ascertain whether results of the localization process are reliable or not.

8 REFERENCES

- [1] Y. J. Yan, L. H. Yam. Detection of delamination damage in composite plates using energy spectrum of structural dynamic responses decomposed by wavelet analysis. [J] computers and structures 82 (2004) 347-358
- [2] Rolands Rikards. Analysis of laminated structures course of lectures. Riga T. University 1999
- [3] H. Amdriambolona. Optimization registration trials structural models. PhD in engineering sciences, University of Franche-Comté, Besançon 1990.
- [4] Jian-Gang Han, Wei-Xin Zeng Ren and Shou-Sun " Wavelet Packet based damage identification of beam structures', International journal of solids and structures, vol. 42, 2005, pp. 6610-6627.



HYPERVELOCITY IMPACTS ON COMPOSITE OVERWRAPPED PRESSURIZED VESSELS

J.HASSIN^{1*}, K.PFAAB¹, C.PUILLET¹, J.LIMIDO², J-L. LACOME² and P.HEREIL³

¹Centre National d'Etudes Spatiales, 18 avenue Edouard Belin 31400 Toulouse, France

Email: jeremie.hassin@cnes.fr, kilian.pfaab@cnes.fr, christian.puillet@cnes.fr

²IMPETUS AFEA, 6 rue du Gers 31330 Grenade sur Garonne, FRANCE

Email: jerome@impetus-afea.com, jll@impetus-afea.com

³THIOT INGENIERIE, Route Nationale 46130 Puybrun, FRANCE

Email: hereil@thiot-ingenierie.com

ABSTRACT

In the framework of its R&T activities, French Space Agency CNES has entrusted the study of the consequences of high velocity impact on a composite overwrapped pressurized vessels to two SMEs THIOT INGENIERIE and IMPETUS AFEA. The general context of this project is to study the vulnerability of a pressurized tank onboard spacecraft impacted by a projectile at high velocity. Tanks selected for this study are commercially available that consist of an aluminum liner and four composite layers made of carbon fibers and silica fibers. The impact tests, performed by THIOT INGENIERIE, were instrumented with suitable metrology in the field of shock to identify the main physical phenomena associated to the hypervelocity impact of a few grams aluminum ball on a pressurized tank. Numerical simulations of these impact configurations were performed with IMPETUS AFEA solver which is based on innovative and advanced numerical methods: High order Finite Elements, meshless method called γ SPH. This unique approach has been fully implemented in 3 dimensions and represents the real geometry of the tanks (as opposed to 2D axisymmetric simulations). Performing comparison with experiment, numerical simulation reproduces the main physical phenomena identified in the experiments, as the 3D cracking failure modes. Although some items would need to be improved to better reproduce the physical mechanisms, the reliability of these calculations is sufficient to extrapolate these first results in a range of more representative impact operational applications (impact velocity > 15 km / s). Thus a method for analyzing such impact configurations is set to address the risk of tank loss or explosion and space debris generation. The proposed method to answer this question is to implement in a coordinated way, tests of impact on tanks, load calculations and material behavior characterization in the ranges encountered in these extreme impacts configurations.

1 INTRODUCTION

Vulnerability of spacecraft to debris impacts is a burning issue which has led to many Research & Development actions in CNES, especially since the *Loi relative aux Opérations Spatiales* has entered into force in 2009. Indeed, hypervelocity impacts on satellite structure could lead to exponential increase of space debris which, in the worst scenario, would not allow to use anymore orbits for spacecraft operations. In that frame, CNES has started to study modelling of HVI on pressurized vessels since many years [1]. Even if tests could be done, modelling is not a small matter when dynamic reaches several km/s for impacts, coupled with hydrodynamic effects due to pressurized gas and with an appropriate model for composite behavior. Aim of this study was to work out a methodology to model these effects and to correlate with dedicated tests. In order to reduce costs and to concentrate on phenomenon rather than on a specific part, tanks selected for this study are commercially available and not tanks dedicated for space applications. They consist of an aluminum liner and four composite layers made of carbon fibers and silica fibers. Approach is to build a general method that could be suitable to reproduce expected and observed effects. This method has to be usable in an industrial context and should be later implemented to extrapolate results for different velocity range and different pressure vessels configuration. The objective is to better assess risks of explosion of a tank submitted to different size of high velocity debris.

2 SIMULATION APPROACH

Finite elements methods widely spreaded in industrial simulation codes are limited to predict large deformations behaviors or phenomena localization. IMPETUS AFEA looked for new modeling solutions to be able

to simulate a hypervelocity impact of an aluminum ball of few grams on a pressurized tank made up of aluminum liner and CFRP composite. IMPETUS AFEA solver is based on two innovative and advanced numerical methods:

- **High Order Solid Finite Elements**
- **Meshless method called γ SPH (Smoothed Particle Hydrodynamics)**

Originally developed to simulate gas and fluid behaviors, SPH method is used for impact simulation since 1996 [2]. This method is particularly adapted to hypervelocity impact on axisymmetric structure or small nonsymmetrical structure. SPH method drawback is a long calculation time and instability for high tensile stress. A full SPH approach is therefore limited to 2D case study and is not able to evaluate intermediate states between perforation, cracking and total explosion. IMPETUS AFEA focused on a more robust approach to predict large deformation and pressurized tank cracking: a third order solid finite elements formulation (64 integration points). γ SPH [3] method remains the relevant method for the tank gas/fluid modeling.

2.1 High order finite elements

IMPETUS AFEA has developed a high order finite element approach for transient dynamics. The main features obtained are the following:

- High precision for large deformation and plasticity.
- Low finite elements sensitivity to a poor aspect ratio
- No zero energy deformation mode (exact integration)
- Simulation of inter elements cracks (node splitting)

Given these characteristics IMPETUS AFEA approach is perfectly adapted to tanks modeling.

2.2 IMPETUS AFEA simulation approach for hypervelocity impacts on pressurized tank.

An innovative approach that couple γ SPH and high order finite elements is proposed and illustrated in Figure 1.

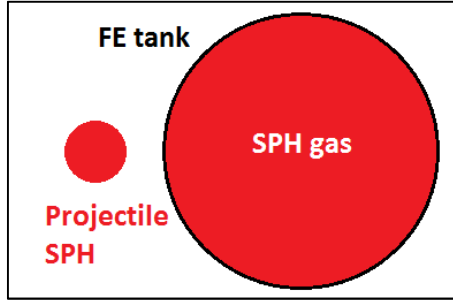


Figure 1. Modeling approach

The projectile is described by the γ SPH method to keep its exact mass and simulate a “cloud” generation.

Internal gas or fluid modeling is also based on a γ SPH formulation to take properly into account interactions between fragments in the fluid and the propagation of the shock wave generated by the impact.

Tank structure model is based on a high order finite elements approach. This approach enables to simulate advanced mechanisms like aluminum cracks and composite damages and delamination.

2.3 Composite structure modeling

2.3.1 Intra lamina modeling

IMPETUS AFEA solver uses an advanced method to predict damage evolution in the fibre reinforced plastic (CFRP) structure. This method is based on unidirectional lamina damage functions derived from Hashin criteria [4], damage variables growth rates governed by a damage rule suggested by [5], a damage coupling functions described hereafter, a node-splitting formulation to enable crack propagation and a strain-rate dependent functions for the elastic moduli.

Three damage functions are used for fiber failure, one in tension/shear, one in

compression, and another one in crush under pressure. They are chosen in terms of quadratic strain forms as follows.

- Tension/Shear:

$$f_1 - r_1^2 = \left(\frac{E_a \langle \epsilon_a \rangle}{\sigma_{aT}} \right)^2 + \left(\frac{G_{ab}^2 \epsilon_{ab}^2 + G_{ca}^2 \epsilon_{ca}^2}{\sigma_{FS}^2} \right) - r_1^2 = 0 \quad (1)$$

- Compression:

$$f_2 - r_2^2 = \left(\frac{E_a \langle \epsilon'_a \rangle}{\sigma_{aC}} \right)^2 - r_2^2 = 0 \quad (2)$$

$$\epsilon'_a = -\epsilon_a - \frac{\langle -E_c \epsilon_c - E_b \epsilon_b \rangle}{2E_a} \quad (3)$$

- Crush:

$$f_3 - r_3^2 = \left(\frac{E_c \langle -\epsilon_c \rangle}{\sigma_{FC}} \right)^2 - r_3^2 = 0 \quad (4)$$

Where a, b, c are the fiber direction, transverse direction and out of plane direction, $\langle \cdot \rangle$ are Macaulay brackets, σ_{aT} and σ_{aC} are the tensile and compressive strengths in the fiber direction, and σ_{FS} and σ_{FC} are the layer strengths associated with the fiber shear and crush failure, respectively.

Matrix mode failures must occur without fiber failure, and hence they will be on planes parallel to fibers. Two matrix damage functions are chosen:

- Transverse compression mode:

$$f_4 - r_4^2 = \left(\frac{E_b \langle -\epsilon_b \rangle}{\sigma_{bC}} \right)^2 - r_4^2 = 0 \quad (5)$$

- Perpendicular matrix mode:

$$f_5 - r_5^2 = \left(\frac{E_b \langle \epsilon_b \rangle}{\sigma_{bT}} \right)^2 + \left(\frac{G_{bc} \epsilon_{bc}}{\sigma_{bc0} + \sigma_{SRB}} \right)^2 + \left(\frac{G_{ab} \epsilon_{ab}}{\sigma_{ab0} + \sigma_{SRB}} \right)^2 - r_5^2 = 0 \quad (6)$$

where σ_{bT} is the transverse tensile strength, σ_{ab0} and σ_{bc0} are the shear strength values of the corresponding tensile modes $\epsilon_b > 0$ or $\epsilon_c > 0$). Under compressive transverse strain ($\epsilon_b < 0$ or $\epsilon_c < 0$), the damaged surface is considered to be “closed”, and the damage strengths are assumed to depend on the compressive normal strains based on the Mohr-Coulomb theory:

$$\sigma_{SRB} = E_b \tan(\varphi) \langle -\epsilon_b \rangle \quad (7)$$

Where Φ is a material constant as $\tan(\phi)$ is similar to the coefficient of friction.

The damage thresholds, $r_j, j = 1,2,3,4,5$ have the initial values equal to 1 before the damage initiated, and are updated due to damage accumulation in the damage modes.

A set of damage variables $\bar{\omega}_i$ with $i = 1, \dots, 6$, are introduced to relate the onset and growth of damage to stiffness losses in the material. The compliance matrix [S] is related to the damage variables as [5]:

$$[S] = \begin{bmatrix} \frac{1}{(1-\bar{\omega}_1)E_a} & \frac{-\nu_{ba}}{E_b} & \frac{-\nu_{ca}}{E_c} & 0 & 0 & 0 \\ \frac{-\nu_{ab}}{E_a} & \frac{1}{(1-\bar{\omega}_2)E_b} & \frac{-\nu_{cb}}{E_c} & 0 & 0 & 0 \\ \frac{-\nu_{ac}}{E_a} & \frac{-\nu_{bc}}{E_b} & \frac{1}{(1-\bar{\omega}_3)E_c} & 0 & 0 & 0 \\ 0 & 0 & 0 & \frac{1}{(1-\bar{\omega}_4)G_{ab}} & 0 & 0 \\ 0 & 0 & 0 & 0 & \frac{1}{(1-\bar{\omega}_5)G_{bc}} & 0 \\ 0 & 0 & 0 & 0 & 0 & \frac{1}{(1-\bar{\omega}_6)G_{ca}} \end{bmatrix} \quad (8)$$

The stiffness matrix C is obtained by inverting the compliance matrix.

As suggested in Matzenmiller et al. [5], $\bar{\omega}_i$ is governed by the damage rule:

$$\bar{\omega}_i = \max \{ \dot{\phi}_j q_{ij} \} \quad (8)$$

where the scalar functions $\dot{\phi}_j$ control the amount of growth and the vector-valued functions $q_{ij} (i=1,\dots,6, j=1,\dots,5)$ provide the coupling between the individual damage variables (i) and the various damage modes (j). Five damage modes are taken into consideration in this model.

$$\dot{\phi}_j = 1 - \exp \left(\frac{1}{m_j} \left(1 - r_j^{m_j} \right) \right) \quad (9)$$

Equation (9) gives $\dot{\phi}_j$ evolution law. m_j is a material constant for softening behavior.

The damage coupling functions q_{ij} are considered for the unidirectional and fabric models as:

$$q_{ij}^{UD} = \begin{bmatrix} 1 & 1 & 1 & 0 & 0 \\ 0 & 0 & 1 & 1 & 1 \\ 0 & 0 & 1 & 0 & 0 \\ 1 & 1 & 1 & 1 & 1 \\ 0 & 0 & 1 & 1 & 1 \\ 1 & 1 & 1 & 0 & 0 \end{bmatrix} \quad (10)$$

2.3.2 Inter lamina modeling

Cohesive links method is used to simulate delamination. Cohesive links are implemented between each composite plies and between the first composite ply and the aluminum liner.

3 TEST FACILITY AND INSTRUMENTATION PLAN

3.1 Existing facilities and previous works

Based on IADC works, hypervelocity phenomenon is defined for a velocity higher than typically 1km/s. With this velocity, projectile and the target are severely damaged in impacted areas. Some works have been previously achieved performing HVI on tanks, among them NASA laboratories (USA) and EMI (G) have performed HVI tests ($V_p \sim 6.5$ km/s) on metallic tanks (aluminum and Titanium) pressurized up to 25 bars, with high-velocity camera. HVI up to 8 km/s could be reached by double-stages laboratory launcher using gas, without damaging the projectile. Other technologies like 3-stages launchers or explosive launchers could reach velocities higher than 8 km/s but most of the case without keeping integrity of projectiles.

For this tests campaign, the double stage launcher HERMES in THIOT INGENIERIE has been used.

3.2 Phenomena to be characterized

HVI effects on tanks could be depicted in 3 phases:

- **Hydrodynamic:** energy transmitted by the target and contained by the projectile will diffuse, creating a shock wave which will allow transfer kinetic energy from

projectile to target. Hemispheric crater arises and ejection of material starts.

- **Shock damage:** the spherical shock will propagate, with attenuation, which leads to damage the target: plastification or fragmentation, depending on ductility or fragility of the material.
- **Damage by reflected shock wave:** propagation and reflection of shock waves could even lead to plastification of thin targets under high velocity conditions, near free surface.

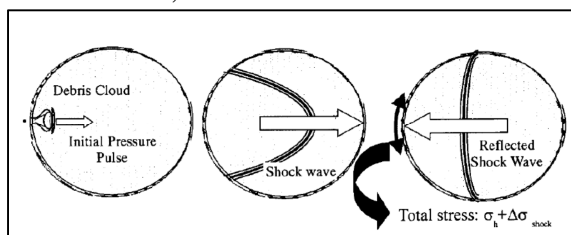


Figure 2. Illustration of impact phenomena

3.3 Instrumentation plan

In order to bring out the different steps and associated parameters, following metrology has been implemented:

- Velocity laser barrier to record impact velocity
- Deformation gauge to characterize CFRP tank deformation.
- Interferometer (PDV or VH system) to measure local material velocity
- Flash X-Ray 150 keV to characterize post impact cloud of fragments.

Instrumentation has been changed between the first two trials and the five remaining in order to improve information recorded relative to fragments cloud and to guarantee a sufficient number of measurement points.

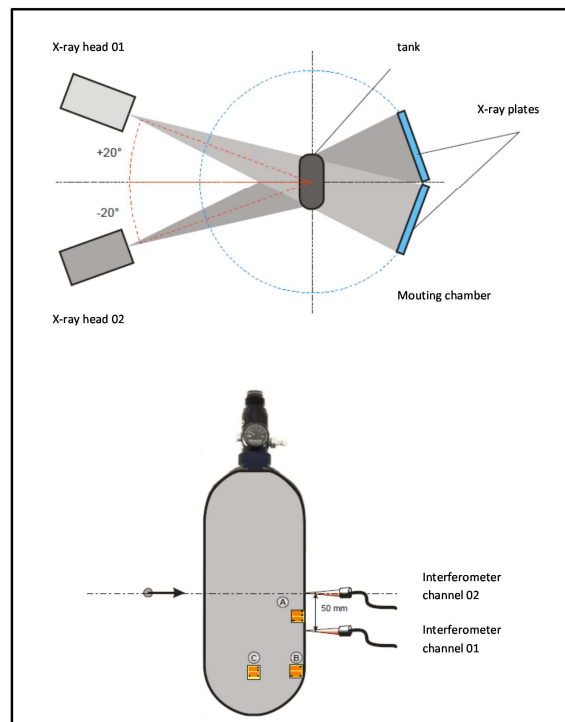


Figure 3. Instrumentation used for end of test campaign

3.4 Test plan

Test campaign has been based on 7 impact trials and one quasi-static trial without HVI. Hereafter are described the parameters associated to each trial.

Test ID	Projectile velocity (m/s)	Nitrogen pressure (bar)
#HE0183	4334±60	1
#HE0184	4425±60	200
#HE0187	4322±60	250
#HE0188	4310±60	300
#HE0208	4638±120	1 bar Water
#HE0212	No HVI : quasi-static explosion	687
#HE0213	4341±40	400
#HE0214	4410±40	500

Table 1. Trial parameters

Used projectile is a 8mm diameter aluminum ball, projected with velocities around 4350 m/s and a normal incidence. Internal pressure is varying from one trial to the other, in order to determine if there is a threshold beyond which the impact leads not to perforation but to an explosion of the CFRP tank.

3.5 Test results

3.5.1 Quasi-static burst pressure test (#HE0212)

This reference test, performed to rescale the tank model, has led to a burst pressure determination of 687 bar. Nonlinear behaviour of the tank has been highlighted with a non-homogeneous deformation of the tank when pressure exceeds 300 bar. To explain this phenomenon, following assumptions have been made:

- Local strain of supports on which were glued the gauge (external coating and CFRP plies)
- Non homogenous strain of CFRP plies
- Pre-stresses of CFRP lies with non-uniform thicknesses on metallic liner which could also have variable thickness.

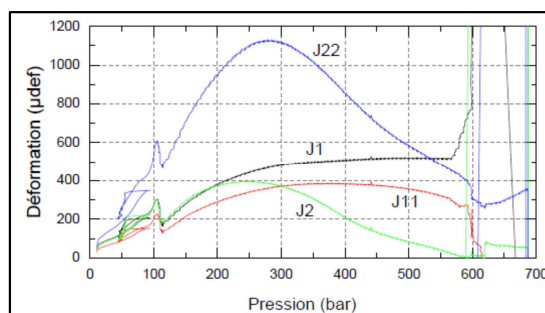


Figure 4. Strain vs. Pressure

3.5.2 Impact tests

First test has been performed without pressure in the tank to start with a reference configuration. Pressure has been progressively increased for the following trials, until 500 bars. Only one trial has been performed with the CFRP tank filled with 1bar water, in order to increase shock pressure effects in fluid with respect to structural deformation. This trial has led to a simple perforation of the tank with a hole diameter higher than with gaseous configurations. However shockwave could not be characterized under this condition, due to water density not compatible with instrumentation.



Figure 5. Perforation of tank with large mushrooming for trial with water #HE0208

After impact tests on Nitrogen pressure tanks, they are splitted in 3 or 4 main pieces, with numerous fragments of fiber composite. Whereas the tanks have been deeply damaged, they have not exploded. Shock wave in pressurized gas has been highlighted.

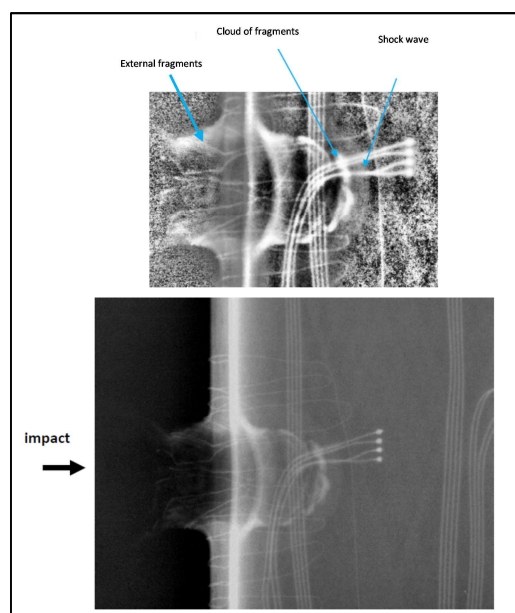


Figure 6. X-Ray diagnosis for trial #HE0184 at 200 bars

This wave foreruns the cloud of fragments and attenuates progressively along its propagation. Moreover, it has been shown that cloud of fragments generated by HVI is slow down by pressurized gas. No fragment has reached opposite surface to impact point except for trial #HE0184 at 200 bars. In velocity diagram for test #HE0184, origin of

diagram is taken as impact of the ball on the tank, thus compression wave is observed at 84 μ s.

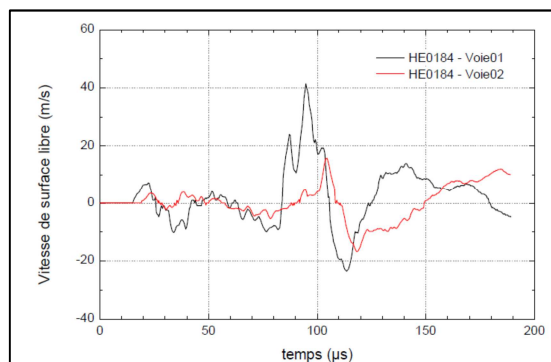


Figure 7. Velocity diagram of rear face for trial #HE0184

3.5.3 TEST CAMPAIGN SYNTHESIS

When comparison is performed between relevant trials on rear face velocity reached perpendicular to impact point, same events are observed at the same time.

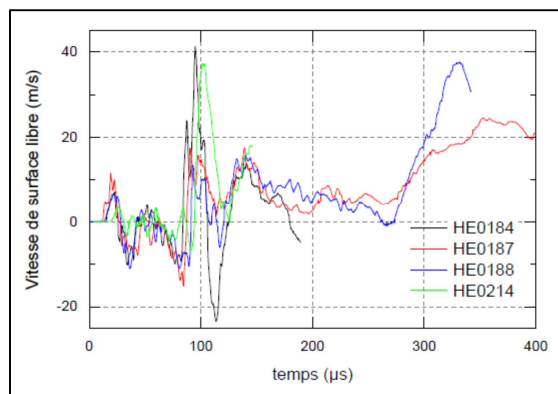


Figure 8. Free surface velocity vs. time

First two oscillations correspond to structural deformation due to compression/relaxation waves. Then around 85 μ s, higher oscillations are highlighted which could be linked to creation of shock wave transmitted in pressurized gas.

It is worth to notice that damage state of tank after impact is deeply correlated to pressure level. Preload of metallic liner by composite winding under pressure drives mainly the failure mode of the tank.

		Nb of pieces	Central fragment width
HE0184		1	40 mm
HE0187		1	35 à 70 mm
HE0188		2	55 mm
HE0213		2	80 mm
HE0214		2	105 mm

Figure 9. Overview of highly pressurized tanks after HVI

The ball perforates CFRP layers (also metallic liner) and near the impact, preload of the liner decreases due to damage of the CFRP which was sustaining the pressure loads. Finally it leads to inject high stress directly on the liner which causes its breakdown.

4 MODEL SET UP AND SIMULATION RESULTS

4.1 Model set up

To model hypervelocity impact on a pressurized tank, a strong gas/tank coupling has to be taken into account. Several issues that lead the model set up can be described below.

4.1.1 Impact behavior with a 1 bar pressurized tank.

A first 3D model has been developed to validate the qualitative behavior of a hypervelocity impact on an empty tank (3 order high order finite elements model). The main simulation difficulties of this model are:

- The very large deformations
- Free edges creation (fragmentations or cracking)
- Simulation stability

The model predicts well the tank fragmentation, its energetic balance is relevant. Figure 10 shows simulation and experimental results.

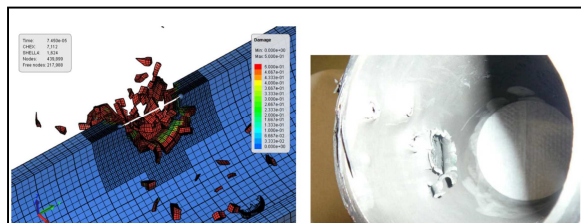


Figure 10. Simulation and experimental results.

4.1.2 Tank pressure initialization

Next step is to validate the quasi-static state before tank impact. Tank pressure initialization is fulfilled through a 3D model coupling High order(tank) and γ SPH(gas) methods. A relaxing dynamic method (damping) is used to obtain a steady state. The pressurized tank steady state is validated comparing the coupled model obtained with a simple finite element model (linear static without gas).

4.1.3 Full fluid/structure coupling for impact simulation.

A full coupled 3D model SPH/EF based on the first 3D model presented in 4.1.1 is done to validate the SPH/EF methods coupling. Simulation shows a hypervelocity impact behavior as well as the tank fragmentation

and the gas shock wave qualitatively representative of the physical phenomena.

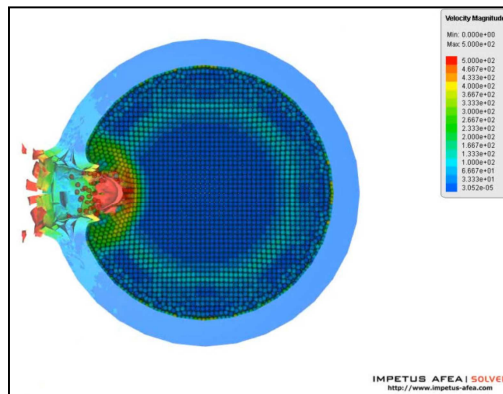


Figure 11. Cut view of a simplified coupled model SPH/EF.

4.1.4 Prestressed quasi-static state

Aluminum liner is prestressed during the composite layering. This prestressed state is taken into account adding a thermal load on aluminum liner that induces 80% of aluminum yield strength at 300 bars. To define this initial state a full 3D coupled model is developed. This model is used later for 3D impact simulations.

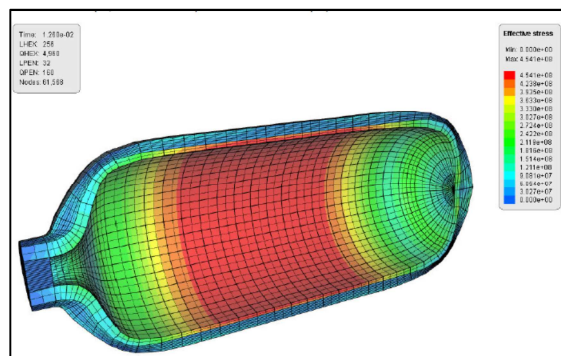


Figure 12. Tank prestress initialization.

4.1.5 2D simulations

2D plane models are developed:

- To set experimental parameters (projectile size, velocity and mass) to obtain the desired failure mode (tank explosion)
- To identify a relevant mesh size for the 3D model (particularly for SPH elements) to simulate properly gas/structure coupling and to value precisely the

coupled method representativeness from a qualitative point of view.

Figure 13. illustrates 2D model results.

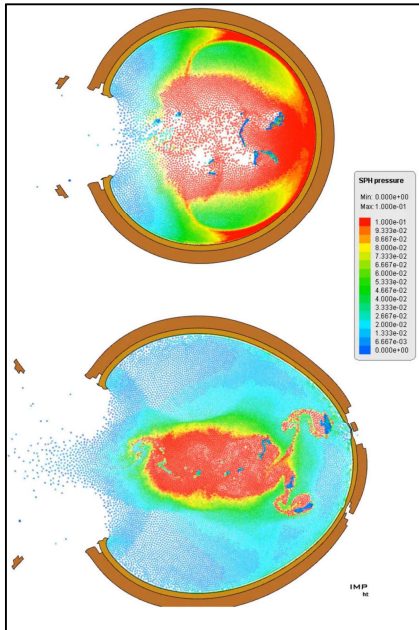


Figure 13. 2D model simulation of the tank explosion.

Such 2D models enable to simulate several cases in a reasonable time scale.

4.1.6 Damage parameters calibration

Damage models parameters have been identified thanks to literature data.

Full 3D model is readjusted through 2 impact tests (Case 1: 8mm ball, 4500m/s speed and 1 bar pressure, see trial #HE0183. Case 2: 8mm ball, 4500m/s speed and 300 bar pressure, see trial #HE0188). This approach limits the model predictability. A complete identification phase should be performed for industrial use.

4.2 3D Simulation results

Main failure mechanisms are well predicted by IMPETUS AFEA 3D model (cloud propagation and shock wave). Figure 14 show a predicted wave front delay. This delay is not observed at $t=13\mu s$ (left part of Figure 14) but at $28\mu s$ (right part of Figure 14). Two factors could explain this delay: a

too rough SPH elements meshing or/and a state equation not precise enough.

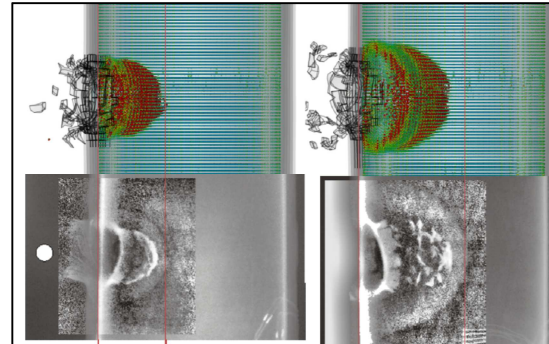


Figure 14. Simulation vs. test wave front comparison.

Failure modes of experimental cases that led to a simple tank perforation without a total explosion are well predicted in simulations. Figure 15 and 16 show that coupling between aluminum ductile behavior and composite fragile behavior that leads for the highest energy cases to a longitudinal cracks until bifurcation points and a total tank explosion is well simulated as well.

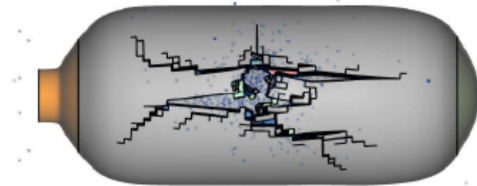


Figure 15. 300bars, 20000m/s, $t=100 \mu s$.

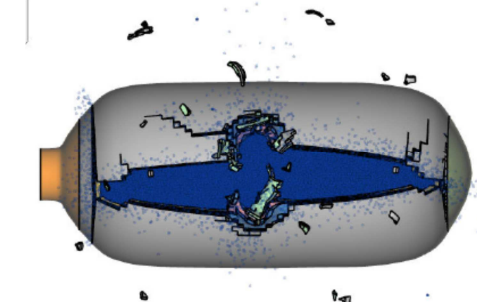


Figure 16. 300bars, 4500m/s, $t=200 \mu s$.

Mean computational time is 12 hours (1CPU+1GPU). The development of an axisymmetric SPH approach on a GPU (Graphics Processing Unit) should reduce computational time to 1h.

Simulations show total energy conservation.

5 CONCLUSION

Simulations performed by IMPETUS AFEA software have shown that using innovative methodologies (Lagrangian and γ SPH) is appropriate to model properly the physical phenomena identified during experiments performed by THIOT INGENIERIE:

- Perforation of front face of the tank and mushrooming correlated to pressure level.
- Generation of a cloud of fragments which will be progressively slow down by the gas, depending on pressure level
- Generation of a shock wave in pressurized gas, which foreruns the cloud of fragments
- Generation of a structural deformation wave in the tank
- Damage and fragmentation of the tank correlated to the pressure level.

Total energy conservation has been respected. Time calculations while important (~ 12h) are realistic from an industrial point of view and can be significantly reduced using a SPH axisymmetric method.

IMPETUS AFEA simulation method has the potential to well assess risks of tank explosions submitted to different kind of high velocity debris, efforts have to be done on its predictability. A complete damage and material parameters identification has to be fulfilled for any industrial use.

Next step would be to consider a typical spacecraft tank which characteristics are slightly different from the tank considered here, particularly in term of structure (thinner liner, thicker composite).

6 REFERENCES

- [1] IADC Protection Manuel, Version 7.0, Sept. 2014.
- [2] T. Rabcuck, T. Belytchko. SPH for high velocity impact. *Computer methods in applied mechanics and engineering*, vol. 139, p.347-373, 1996.
- [3] M. Clayer, J.L. Lacombe, J. Limido, J.P. Vila, Pressure evaluation improvement for Euler isentropic SPH scheme, in: Proc. 9th International SPHERIC Workshop, Paris, France, June 2–5, 2014
- [4] Z. Hashin. Failure criteria for unidirectional fiber composites. *Journal of applied mechanics*, 47:329, 1980.
- [5] A. Matzenmiller, J. Lubliner and R.L. Taylor. A constitutive model for anisotropic damage in fiber-composites. *Mechanics of Materials*, 20:125-152, 1995.
- [6] CNES contract n°130124. *Action R&T R-12/PF-0002-044 : Modélisation d'impacts hyper-vitesse sur réservoir sous pression*
- [7] P. L. Héreil, J. Mespoulet , “Behaviour of high pressure vessels under an hypervelocity impact” *European Conference on Spacecraft Structures, Materials and Environmental Testing*, Braunschweig, Germany, April 2014
- [8] P. L. Héreil, J. Mespoulet, F. Plassard “Hypervelocity impact of aluminum projectiles against pressurized aluminum-composite vessel” 13th Hypervelocity Impact Symposium, Boulder, US, 2015

7 COPYRIGHT NOTICE

Copyright ©2015 by the authors. Distribution of all material contained in this paper is permitted under the terms of the Creative Commons license Attribution-NonCommercial-NoDerivatives 4.0 International (CC-by-nc-nd 4.0).



HIGH FREQUENCY DYNAMIC MECHANICAL ANALYSIS ON SHAPE MEMORY POLYMERS

P. Butaud^{1*}, F. Renaud², G. Chevallier¹, M. Ouisse¹ and E. Foltête¹

¹FEMTO-ST Applied Mechanics, UMR 6174, CNRS-UFC-ENSMM-UTBM,
24, rue de l'Épitaphe, FR-25000 Besançon
Email: pauline.butaud@femto-st.fr

²LISMMA Institut Supérieur de Mécanique de Paris
3, rue Fernand Hainaut, FR-93400 Saint-Ouen
Email: franck.renaud@supmeca.fr

ABSTRACT

This work deals with experimental measurements of the viscoelastic properties of a Shape Memory Polymer (SMP). The material has been previously analyzed using Dynamic Mechanical Analysis in the [0.1 – 180]Hz frequency range and the [0 – 90] °C temperature range. In this work, the measurement has been extended to the [200 – 3000]Hz frequency range and [20 – 80] °C temperature range thanks to a High Frequency Viscoanalyzer (HFV). Among the major novelties of this work, this is the first time that this viscoanalyzer is used over the ambient temperature for a full measurement campaign ; the SMP properties have been found over a large frequency and temperature bandwidth without time-temperature superposition (TTS) assumption. Finally a plate with aluminum skins and a SMP core has been designed from the knowledge of the core's behavior, and the model has been experimentally validated. This campaign highlights the uncertainties on the damping properties of the material especially for the lowest loss factor values. It seems that, in these conditions, modal tests combined with identification, might improve the results.

1 INTRODUCTION

Composite structures are designed to ensure several functions such as stiffness, damping, resistance, mass reduction, thermal or acoustic insulation, etc. To achieve these multiple functionalities, the use of "exotic" materials can be helpful. Shape memory polymers (SMPs) are "smart" materials which have the remarkable ability to recover their primary shape from a temporary one under an external stimulus. SMPs encounter a growing interest over the past ten years, in particular because of their eventual bio-compatibility. They also present many benefits because of their controllable damping property. In this study, the chosen polymer is the tBA/PEGDMA, a chemically cross-linked thermoset. It is synthesized via photo polymerization (UV curing) of the monomer tert-butyl acrylate (tBA) with the crosslinking agent poly(ethylene glycol) dimethacrylate (PEGDMA) and the photoinitiator 2,2-dimethoxy-2-phenylacetophenone (DMPA) [1].

In a previous work, the dynamic mechanical characterization of this SMP has been performed using a Dynamic Mechanical Analyzer (DMA50) from Metravib-ACOEM Company on the $[0.1 - 180]$ Hz frequency range and $[0 - 90]$ °C temperature range. This first experimental campaign highlights promising damping properties controllable by the frequency of the mechanical loadings and the temperature field, see P. Butaud et al. [2]. In order to design a sandwich structure composed of two aluminum skins and a SMP core, the properties have to be extended to larger frequency and temperature domains. This has been first done thanks to the time-temperature superposition (TTS) assumption.

To validate this hypothesis and to improve our knowledge about the SMP properties, a High Frequency Viscoanalyzer (HFV), see F. Renaud et al. [3], has been used to measure the shear properties of the SMP on the $[200 - 3000]$ Hz frequency range and $[20 - 80]$ °C temperature range. The SMP properties are first identified using a lumped-mass model of the HFV system thanks to Least Mean Square minimization between the test and the simulation results. This allows comparing the results obtained from the DMA and the HFV. Since their operating conditions are different, there are only few couples of temperature-frequency values available, thus the TTS is also used to extend the comparison.

To follow, the SMP datas are used to simulate the behavior of a composite plate constituted with aluminum skins and a SMP core. This sandwich plate has been manufactured and tested in modal analyses. The comparison between tests and simulations highlights distances between the experimental and the simulated modal damping. The updating of the loss factor values is discussed, in section 3.

As a perspective of this work and in order to extend the measurement frequency range of the HFV, one can use a more realistic model that accurately takes into account the eigenmodes. This opportunity is discussed in the paper. To conclude the talk, the design of the HFV and the post-processing improvements will be discussed.

2 SET-UP DESCRIPTION

The High Frequency Viscoanalyzer (HFV), developed by the F. Renaud et al. [3] aims at providing frequency dependent properties of viscoelastic materials over a large frequency bandwidth. This bandwidth starts between $[100 - 200]$ Hz and stops between $[2000 - 5000]$ Hz according to the stiffness of the specimen.

To measure the viscoelastic properties of the materials, two kinds of setups can be used. Oberst-like setups are based on the analysis of the Frequency Response Function (FRF) of a normalized specimen. This procedure is defined in ASTM-1998 [4] or in ISO-1994 [5]. The latter is generally a multi-layered beam or a multilayered plate constituted with weak viscoelastic layers and stiff elastic layers. The damping properties of the specimen are post-processed

from the FRF; its stiffness properties are deduced from the resonance frequency. Unfortunately this method is really efficient if a model, that allows to compute the strain field all over the specimen, is available. Moreover, even if this model is available, it is impossible to ensure an homogeneous strain field in the viscoelastic layer. Thus this method is mainly used to measure the linearized properties. Furthermore, as the signal-to-noise ratio is better close to the resonance frequency, this method only provides confident datas around resonance frequency.

The second kind of setup aims at measuring variations in material properties versus temperature, excitation frequency and imposed strains. It is based on quasi-static excitation, which means that no controllable vibration eigenmodes belongs to the frequency bandwidth of the test. Due to this specificity, it is strongly different to Oberst-like setups. Metravib, MTS or Bose Dynamic Mechanical Analyzer use hydraulic or electromagnetic actuators to load a specimen dedicated to pure traction, compression, shear. The specimen has to be loaded thanks to specific test fixtures dedicated to each kind of test. Our purpose has been to miniaturize such kind of testing device, see Figure 1. The actuators has been replaced by piezo-actuators provided by PhysikInstrumenteTM. The test fixture is dedicated to pure shear loading ; to achieve this goal, the setup has three symmetry planes and four specimens, see Dion et al. [6]. Moreover, a bolt is used to preload the setup along the transverse direction. This allows to perform shear measurements according to transverse preload. Six accelerometers are used to measure the accelerations. From these datas, the strain of the specimens are post-processed; two load sensors are used to measure the dynamic shear loading applied to the specimens.

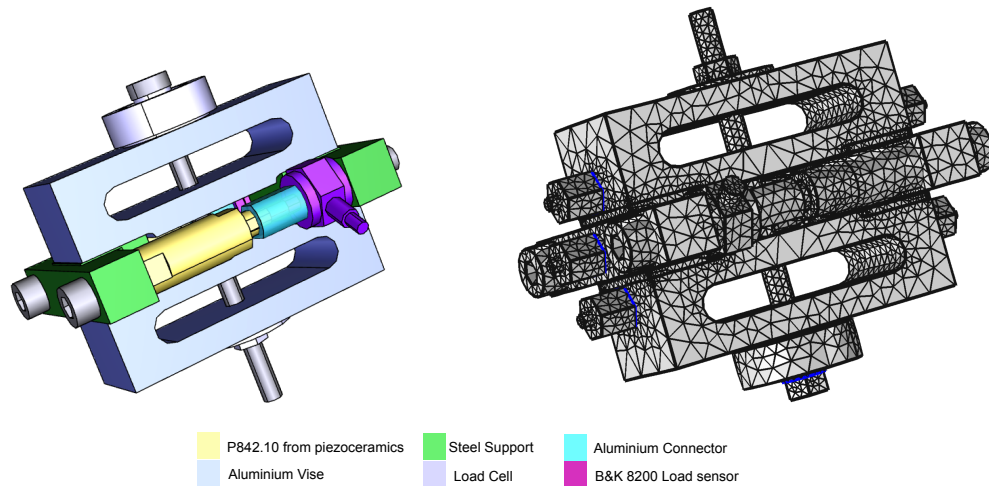


Figure 1: **Left** : 3D CAD view of the HF-DMA. **Right** : Finite Element mesh of the setup : around 10^5 tetrahedron quadratic elements (T10).

2.1 Post-processing of the test

The stress-strain ratio, i.e. the shear modulus, might be computed thanks to the following relationships. If the shear stress σ_{12} is supposed to be uniform in the specimen, it is defined by :

$$\sigma_{12} = \frac{F}{S}, \quad (1)$$

where F is the effective load applied to the steel support, see Figures 1 and 2 and S is the section in the plane orthogonal to the shear plane. Assuming that the shear strain ε_{12} and the distortion γ are also uniform in the specimen, one has:

$$2\varepsilon_{12} = \gamma = \frac{u}{t}, \quad (2)$$

where u is the effective displacement of each support and t is the thickness of the specimen, see Figure 2.

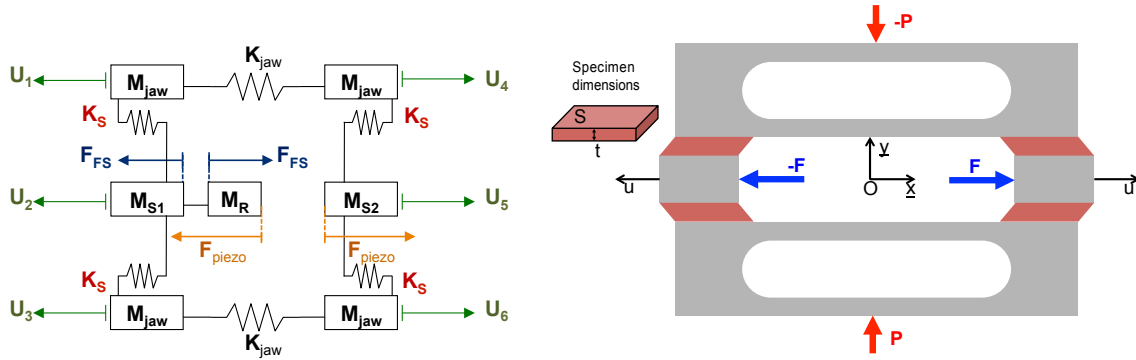


Figure 2: **Left** : Lumped Mass Model of the HFV. **Right** : Dimensions of the specimens. Schema of the test fixture.

The shear modulus is defined as the ratio between the shear stress and the distortion:

$$G = \frac{\sigma_{12}}{\gamma} = \frac{F t}{u S} . \tag{3}$$

However, the shear modulus can not be estimated from the sensors signals processed using Equation (3), because of inertial load effects due to the equipment. The Newton equation applied on the sensor leads to the expression of the stiffness of the specimen:

$$K_S = \frac{\omega^2((M_{S1} - M_R)\hat{u}_2 + M_{S2}\hat{u}_5) - 2\hat{F}_{FS}}{2\hat{u}_2 + 2\hat{u}_5 - \hat{u}_1 - \hat{u}_3 - \hat{u}_4 - \hat{u}_6} , \tag{4}$$

where \hat{u}_i is the Fourier Transform of the i^{th} accelerometer divided by the excitation angular frequency ω . Using the previous definitions, the shear modulus is defined according to accelerometers and load sensors measurements:

$$G = K_S \frac{t}{S} . \tag{5}$$

This post-processing can be done at each frequency of excitation in order to build the frequency dependence of the complex shear modulus $G^*(\omega)$. As shown in Figure 3, the signal is rather good between 200 Hz and 2500 Hz. Below this frequency bandwidth, the acceleration are not large enough and the accelerometers are not sensitive enough, thus the signal is noisy. Above this bandwidth, the first excitable eigenmode (2500 Hz) is visible and prevents direct reading of the phase and modulus.

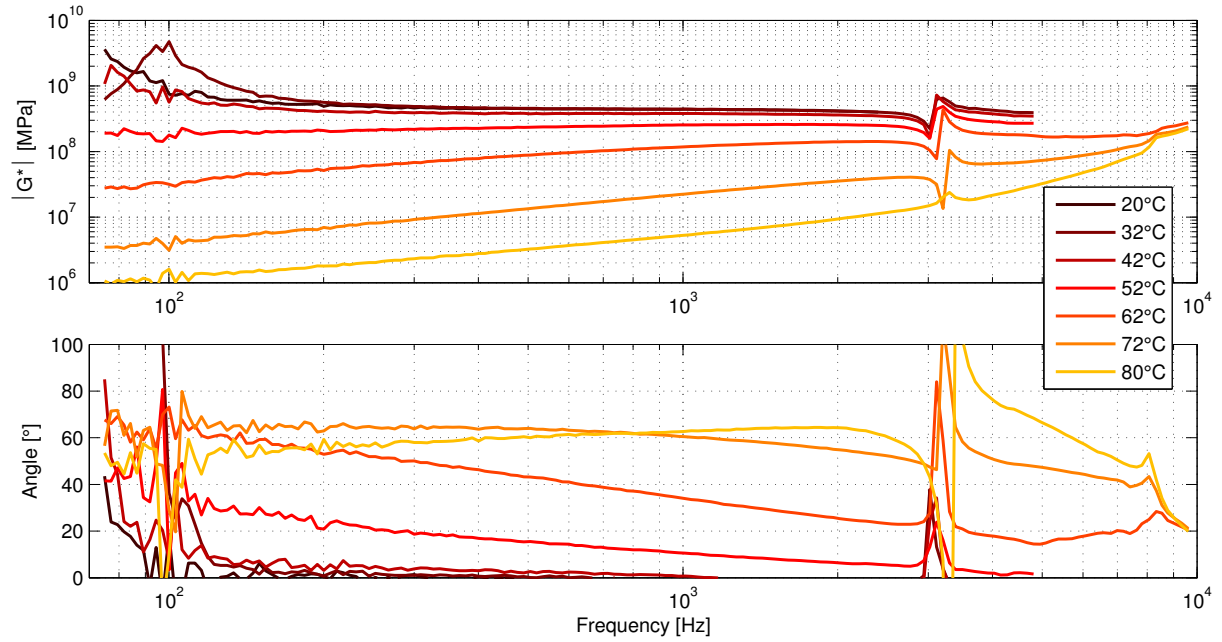


Figure 3: HFV results : absolute value and angle of the complex shear modulus of the tBA/PEGDMA according to the frequency.

A comparison has been done between these HFV measures and those obtained using a Dynamic Mechanical Analyzer (DMA50). The elastic modulus of the HFV results is directly deduced from the shear modulus thanks to the Poisson's ratio of 0.37 determined in a previous study [7] using a quasi-static test:

$$E^*(\omega) = E\hat{h}^*(\omega) = 2G^*(\omega)(1 + \nu) = 2G\hat{h}^*(\omega)(1 + \nu), \quad (6)$$

where \hat{h}^* is the constitutive parameter of the viscoelastic model that translate into the frequency dependence of the material. This direct relation could be discussed because of the possible frequency dependence of the Poisson's ratio which is common for polymeric materials [8]. The use of compression measurement and shear measurement in the same frequency bandwidth may answer to this question. Unfortunately, the actual results have been obtained at different frequencies. Figure 4 shows the comparison between the two measurements methods through the master curve obtained by the TTS principle, used to extend the comparable frequency band. These results highlight the fact that both campaigns (DMA-TTS and HFV) provide close results. Looking to the master curves more carefully, we detect the 2500 Hz eigenmode on the right and the noise on the left which make the master curve growing up for each temperature. These artificial values are always in the same frequency ranges and can be easily removed. Moreover, there is a distance between the curves because, for both DMA and HFV tests, it is quite hard to stabilize the temperature. This leads to uncertainties on the storage modulus and on the loss factor, especially when the loss factor variation are really important, around $f.a_T = 10^3$ Hz.

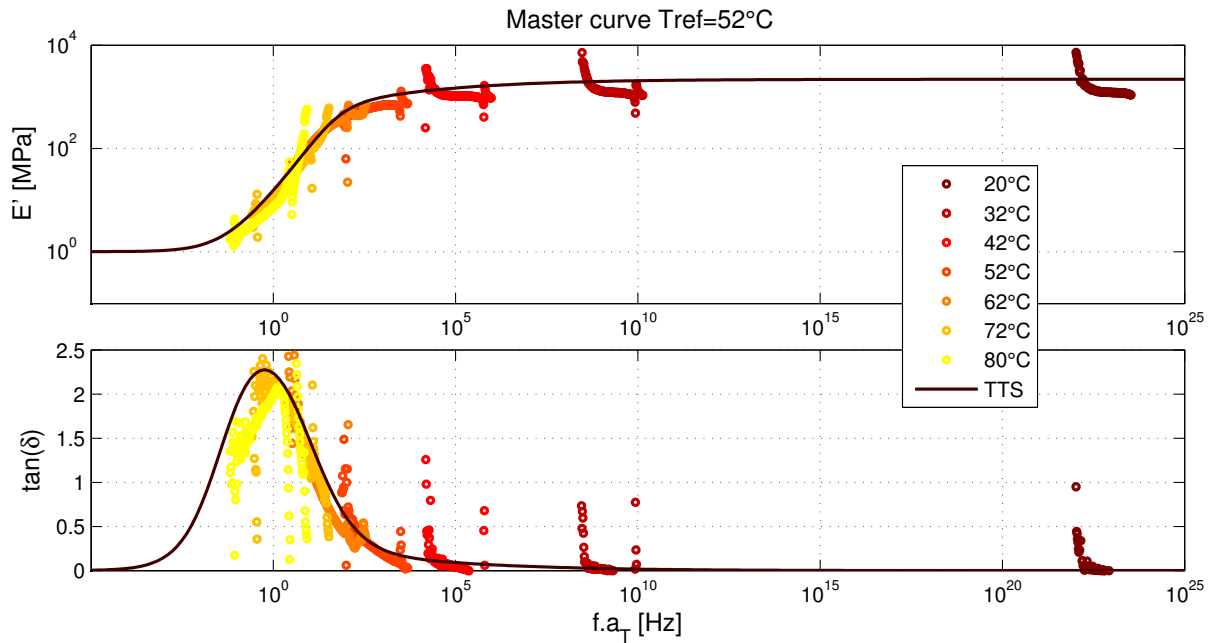


Figure 4: Comparison through the master curve between the HFV results and those obtained by the DMA.

3 MODAL ANALYSIS AS CHARACTERIZATION TEST

In a previous study, it has been shown that a modal analysis is interesting to characterize a SMP in high frequency but it is limited in temperature because of the very low stiffness of the material near the glass transition temperature [9]. An alternative technique is proposed here, by performing modal analysis on a SMP composite structure.

The structure which has been tested is shown in Figure 5. This composite sandwich has been experimentally and numerically studied. The sandwich was in free-free conditions, a broadband random excitation was applied on [100 – 10000] Hz frequency range. The details of the elaboration of the SMP core sandwich and the experimental tests can be found in [10].

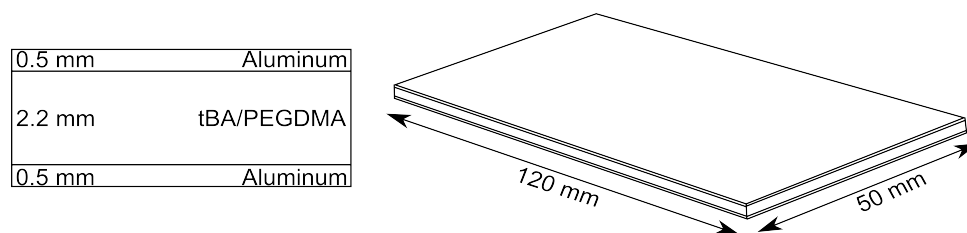


Figure 5. Sandwich structure used in numerical simulation and in experimental tests.

The composite sandwich has been tested between 0 and 130 °C every 10 °C (± 1 °C). Thanks to the aluminum skins which strengthen the structure, the measurements near the glass transition temperature (between 45 °C and 75 °C according to the frequency) have therefore been possible. Results are obtained experimentally but also through numerical simulations. The simulation parameters are detailed in [10]: the expression of the SMP complex modulus comes from a 2S2P1D model [11] based on the DMA TTS; the mechanical properties of the aluminum

skins ($E = 70000$ MPa and $\eta = 10^{-4}$) are taken from the literature [12]. The results of four representative temperatures are presented on Figure 6.

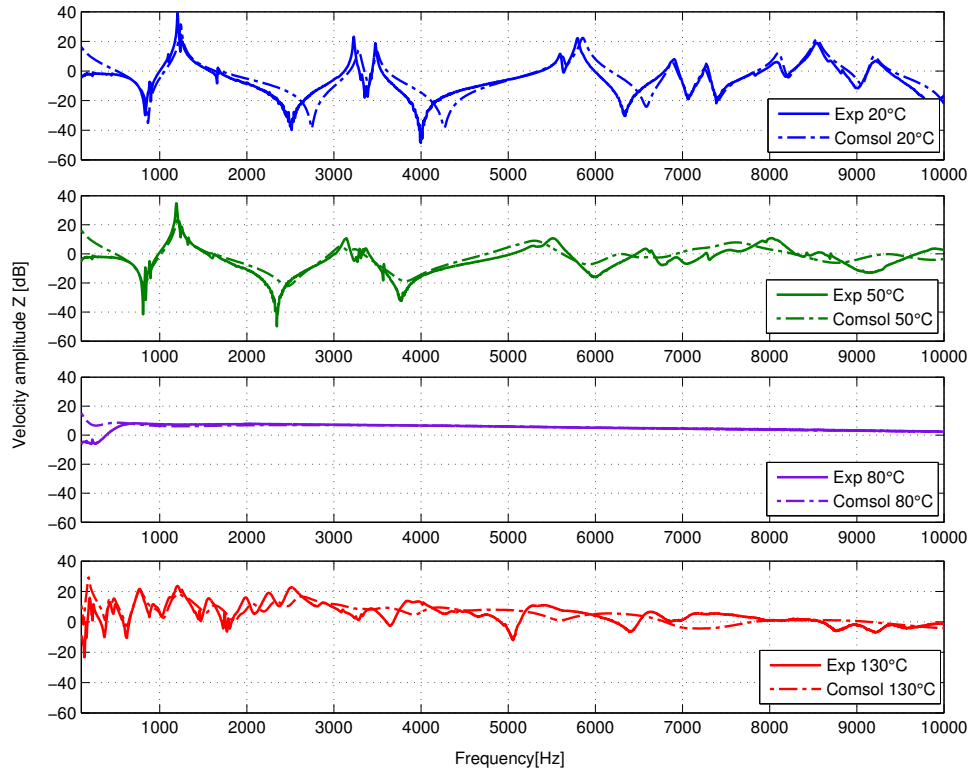


Figure 6. Experimental and simulation results at 20 ° C, 50 ° C, 80 ° C and 130 ° C.

Given the uncertainties on the thickness of the sandwich and on the gluing skins, a good correlation is obtained. A relative distance ε defined by

$$\varepsilon = \frac{1}{n} \sqrt{\sum_{k=1}^n \left(\frac{f_k^{simu} - f_k^{exp}}{\frac{f_k^{simu} + f_k^{exp}}{2}} \right)^2}, \quad (7)$$

with n the number of eigenfrequencies measured, is evaluated at 20, 50 and 130 ° C; firstly on the eigenfrequencies, and secondly on the modal damping ratios obtained using a classical modal identification technique. This evaluation was not performed for 80 ° C because of the impressive damping capacities of the SMP which smooths all the resonances. The relative distance on the eigenfrequencies is less than 1% at 20 ° C, and around 3% at 50 and 130 ° C, the Finite Element model with the material datas is so quite representative concerning the stiffness properties of the composite sandwich. The relative distance on the modal damping ratio is less than 10% at 20 ° C but up to 70% for high temperatures. These significant errors on the damping properties can be explained by the large uncertainties on the SMP loss factor values implemented in the FE model. The loss factor values obtained by DMA-TTS are precise at around 50% which is problematic near the glass transition temperature where the loss factor variation are really important; such uncertainties on the loss factor, implemented in the finite element model, permits to bound the modal damping values.

The main conclusions of the comparison between modal tests and simulation based results with DMA datas is that: stiffness is quite well identified from both experimental techniques; damping is harder to identify. To our opinion, the DMA techniques are more suitable

in order to identify high loss factors, whereas modal tests are more suitable for lowest loss factors. In order to improve the results, a FEM-based post-processing can be used to identify the material.

4 CONCLUSION

This paper shows results from measurements of viscoelastic properties coming from classical DMA analysis, HFV analysis and Oberst-like analysis. Each device is able to provide temperature dependent results. This is a novelty for the HFV. Let's notice that for the HFV, the temperature range would be extended by the uses of specific piezo actuators. Each device provides interesting results in a specific domain. DMA is able to give results by direct analysis at low frequency. Its results may be extended using TTS. HFV give direct results at higher frequency. Modal analysis can give complementary results for the lowest and highest reduced frequency when the loss factor is small. An ongoing work is to extend the frequency range and reduce the uncertainties by using FEM-based post-processing.

REFERENCES

- [1] Christopher Michael Yakacki, Robin Shandas, Craig Lanning, Bryan Rech, Alex Eckstein, and Ken Gall. Unconstrained recovery characterization of shape-memory polymer networks for cardiovascular applications. *Biomaterials*, 28(14):2255 – 2263, 2007.
- [2] Pauline Butaud, Morvan Ouisse, Vincent Placet, and Emmanuel Foltête. Experimental investigations on viscoelastic properties of a shape memory polymer. In *ASME Conference on Smart Materials, Adaptive Structures and Intelligent Systems*, pages V001T01A029–V001T01A029. American Society of Mechanical Engineers, 2014.
- [3] F. Renaud, G. Chevallier, J. L. Dion, and R. Lemaire. Viscoelasticity measurement and identification of viscoelastic parametric models. In *ASME International Design Engineering Technical Conferences and Computers and Information in Engineering Conference*, pages 701–708, Washington DC, 2011.
- [4] ASTM E 756-9 : Standard test method for measuring vibration-damping properties of materials, 1998.
- [5] ISO 6721-3 : Plastics - determination of dynamic mechanical properties - part 3 - flexural vibration - resonance-curve method, 1994.
- [6] JL Dion, G Chevallier, O Penas, and F Renaud. A new multicontact tribometer for deterministic dynamic friction identification. *Wear*, 300(1):126–135, 2013.
- [7] Pauline Butaud, Anne Maynadier, Nicolas Brault, Vincent Placet, Morvan Ouisse, Emmanuel Foltete, and Cécile Rogueda-Berriet. Static and dynamic thermo mechanical characterization of a bio-compatible shape memory polymer. In *ICAST 2013, The 24th International Conference on Adaptive Structures Technologies*, pages 1–10, 2013.
- [8] Roberto Caracciolo and M Giovagnoni. Frequency dependence of poisson's ratio using the method of reduced variables. *Mechanics of materials*, 24(1):75–85, 1996.
- [9] P. Butaud, V. Placet, J. Klesa, M. Ouisse, E. Foltete, and X. Gabrion. Investigations on the frequency and temperature effects on mechanical properties of a shape memory polymer (veriflex). *Mechanics of Materials*, 2015 doi:10.1016/j.mechmat.2015.04.002.

- [10] Butaud Pauline, Ouisse Morvan, Foltete Emmanuel, and Rogueda-Berriet Cecile. Smp-based solution for structural damping. In *Conference on Noise and Vibration NOVEM2015*, 2015.
- [11] Nur Izzi Md Yusoff, Damien Mounier, Ginoux Marc-Stéphane, Mohd Rosli Hainin, Gordon D Airey, and Hervé Di Benedetto. Modelling the rheological properties of bituminous binders using the 2s2p1d model. *Construction and Building Materials*, 38:395–406, 2013.
- [12] F Orban. Damping of materials and members in structures. In *Journal of Physics: Conference Series*, volume 268, page 012022. IOP Publishing, 2011.



ENERGY FLOW PREDICTION IN PIEZOELECTRIC COMPOSITE STRUCTURES THROUGH A HYBRID FINITE ELEMENT/WAVE AND FINITE ELEMENT APPROACH

Y. Fan¹, M. Collet¹, M. Ichchou^{1*}, O. Bareille¹ and Z. Dimitrijevic²

¹Laboratoire de Tribologie et Dynamique des Systèmes (LTDS)
Ecole Centrale de Lyon, 69134 Ecully Cedex, FRANCE
Email: mohamed.ichchou@ec-lyon.fr, yu.fan@ec-lyon.fr

²PSA Peugeot-Citroën
F-78943 Vélizy Villacoublay Cedex, FRANCE
Email: zoran.dimitrijevic@mpsa.com

ABSTRACT

The vibration and noise of a structure can be mitigated by controlling the power exchange between the excitation and the remote parts. An implementation is to integrate piezoelectric materials into the host structure and to design the associated electric impedance in order to control the energy flow. In this work, built-up structures with periodical piezoelectric shunts are considered. Major efforts are devoted to develop a rapid and accurate numerical tool for the evaluation of the energy flow in this kind of built-up structures. In this method, Wave and Finite Element Method (WFEM) is employed to model the periodic substructures while Finite Element Method (FEM) is used to capture the non-periodic substructures. A modal reduction technique is introduced to WFEM accelerate the wave basis calculation. Validations are presented, attesting the accuracy of the proposed method. An application is given, where energy flow of a infinite structure with resistive piezoelectric waveguide is presented.

1 INTRODUCTION

To control the energy transmission through the excitation to the remote parts, one method is to periodically distribute piezoelectric patches with identical circuits between the source (termed *near-field* substructure) and the remote parts (termed *far-field* substructure), shown in figure 1. This idea was considered in [1] and [2] to reduce the vibration in rotational components in aero-engine. It has been shown that periodically distributed piezoelectric shunts can control the localized vibration in near-periodic structures [2] and also can reduce the response to the engine order excitation in periodic structures [1]. Alternatively, the wave perspective was considered in [3, 4], where the functions of piezoelectric patches are to reflect the injected waves or to welcome the waves and dissipate them. To evaluate the performance of the piezoelectric waveguide as a component in a built-up structure, a numerical tool for the forced response and energy flow in these built-up structures are required.

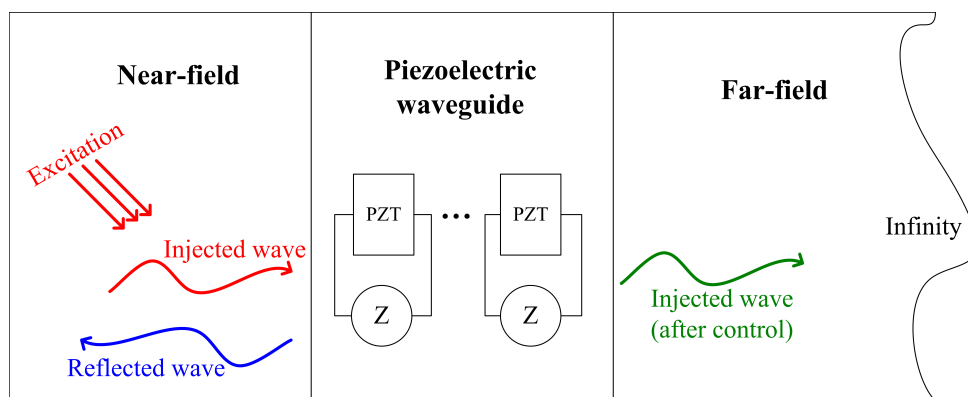


Figure 1: Illustration of the considered piezoelectric-based built-up structures

In this work, a hybrid finite element method (FEM) /wave and finite element method (WFEM) is developed to determine the forced response and energy flow of built-up structure with periodic piezoelectric patches. The near-field is supposed to be non-periodic so it is modeled by FEM. The piezoelectric substructure and the far-field are regarded as waveguide and they are modeled by WFEM. By WFEM, the dynamics of the periodic waveguide would be analyzed by only considering one segment of it, hence the computation time is saved. The engineering example is shown in figure 2 where a car chassis is considered. The domain near the engine can be regarded as near-field while the car body connected to the frame can be treated as far-field. Piezoelectric patches can be periodically bonded to the frame so that it can be treated as a periodic waveguide.

Specifically, a modal reduction approach is introduced into the WFEM to accelerate the wave basis calculation. It is useful especially when the DOFs of the cross-section are numerous. Moreover, only the DOFs of the FE modeled near-field will be kept while the ones of the waveguides will be eliminated eventually. Then the response and energy flow can be obtained by post-processing in a multi-scale manner. The far-field substructure can be both finite and infinite, so this method is applicable in both mode-dominated (low frequency) cases [5] and the wave-dominated (mid- and high frequencies) cases [6].

In the following sections, firstly the enhanced WFEM is briefly introduced. Then the way to adapt the WFEM modeled waveguides into the FEM modeled near-field is presented. A validation is presented where finite far-field substructures are considered and each piezoelectric

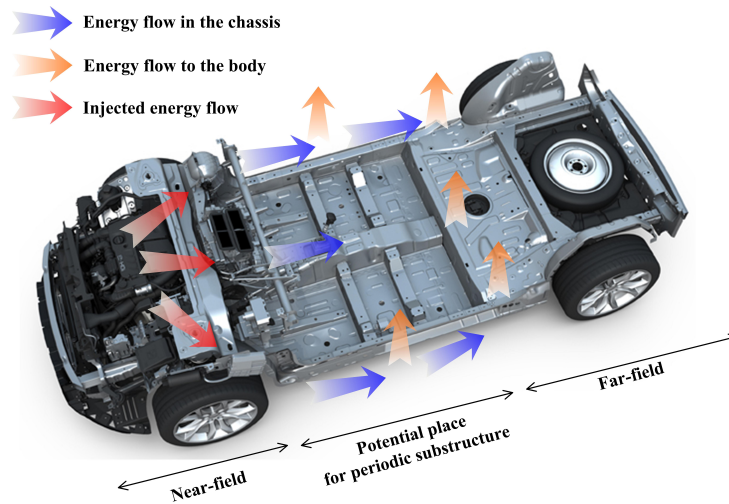


Figure 2: An engineering example of the considered structures

patch is shunted by an identical Resistor-inductor circuit. At the end an application is presented where the energy flow to a infinite far-field is presented.

2 ENHANCED WAVE AND FINITE ELEMENT METHOD

2.1 Modal condensation of a unit cell

In WFEM, the dynamics of the whole periodic waveguide can be described only by analyzing one unit cell of the waveguide thanks to Bloch theorem. The dynamics equations of a unit cell in the periodic waveguide can be formed by any existed FEM package and they write

$$\begin{bmatrix} \mathbf{H}_{ii} & \mathbf{H}_{ib} \\ \mathbf{H}_{bi} & \mathbf{H}_{bb} \end{bmatrix} \begin{pmatrix} \mathbf{q}_i \\ \mathbf{q}_b \end{pmatrix} = \begin{pmatrix} \mathbf{0} \\ \mathbf{f}_b \end{pmatrix} \quad (1)$$

where superscripts i and b respectively refer to the internal and the boundary DOFs. Splitting boundary DOFs on left (subscript L) and right (subscript R) interfaces, it gives $\mathbf{q}_b = (\mathbf{q}_L^T \ \mathbf{q}_R^T)^T$ and $\mathbf{f}_b = (\mathbf{f}_L^T \ \mathbf{f}_R^T)^T$. The terms are illustrated in figure 3. Then the internal DOFs would be condensed so that equation (1) becomes

$$\mathbf{D}\mathbf{q}_b = \mathbf{f}_b \quad (2)$$

where

$$\mathbf{D} = \mathbf{H}_{bb} - \mathbf{H}_{bi}\mathbf{H}_{ii}^{-1}\mathbf{H}_{ib} \quad (3)$$

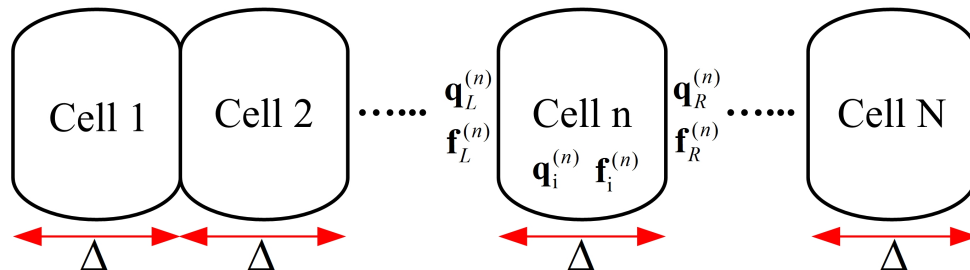


Figure 3: Illustration of the unit cells in a waveguide

Searching for the inverse of \mathbf{H}_{ji} might be time consuming once the number of the internal DOFs is large. Alternatively, it is better to firstly reduce the dimension of the matrices before the condensation as proposed by [7]. In their work, the Craig Bampton method for modal reduction was employed on all the internal DOFs. Here the major concern is that not all the DOFs in \mathbf{q}_i is suitable to be transferred to modal space and be reduced. The DOFs associated with the electric field are better not to be transferred into the modal space. There are two reasons. Firstly the impedance of the electric circuits need to be changed in the calculations so as to evaluate the performance under different parameters. If they are transferred to the modal space it would be difficult to change the corresponding modal impedance for each retained modes [3]. Otherwise the modal transformation need to be performed once again, after each electric impedance modification. Secondly, if electric impedance are considered in the shunted circuits, the dynamic stiffness matrix can no longer be diagonalized by the open-circuit or close-circuit modal shapes. Consequently the modal coordinates might be coupled with each other due to non-diagonal damping terms, then simply remove the modes with higher natural frequencies might induce unexpected errors.

For these reasons, we rewrite array \mathbf{q}_i into $(\mathbf{q}_c^T \quad \mathbf{q}_n^T)^T$ where \mathbf{q}_c represents all the mechanical DOFs and \mathbf{q}_n for the electric ones. Then only the DOFs in \mathbf{q}_c are transferred into the modal coordinates \mathbf{y} by

$$\begin{pmatrix} \mathbf{q}_i \\ \mathbf{q}_b \end{pmatrix} = \begin{pmatrix} \mathbf{q}_c \\ \mathbf{q}_n \\ \mathbf{q}_b \end{pmatrix} = \begin{bmatrix} \Psi & -\mathbf{K}_{cc}^{-1}\mathbf{K}_{cn} & -\mathbf{K}_{cc}^{-1}\mathbf{K}_{cb} \\ \mathbf{0} & \mathbf{I} & \mathbf{0} \\ \mathbf{0} & \mathbf{0} & \mathbf{I} \end{bmatrix} \begin{pmatrix} \mathbf{y} \\ \mathbf{q}_n \\ \mathbf{q}_b \end{pmatrix} \quad (4)$$

where $\Psi = [\psi_1 \quad \psi_2 \quad \cdots \quad \psi_l]$. ψ_k is the k th natural mode of the unit cell with all rest DOFs fixed ($\mathbf{q}_b = \mathbf{0}$ and $\mathbf{q}_n = \mathbf{0}$) and the corresponding natural frequencies is ω_k . Specifically, ψ_k and ω_k with $k = 1, 2, \dots, l$ are obtained as the eigenvectors and eigenvalues of

$$(\mathbf{K}_{cc} - \omega_i^2 \mathbf{M}_{cc}) \psi_i = \mathbf{0} \quad (5)$$

Only l modes are kept in Ψ , and the number is less than that of \mathbf{q}_c . The criterion for the selection of the retained modes is $\omega_k < 3\omega_m$ where ω_m is the maximum excitation frequency to be considered. Introduce the transformation (4) into equation (1), the dynamical equations can be reduced to

$$\begin{bmatrix} \hat{\mathbf{H}}_{cc} & \hat{\mathbf{H}}_{cn} & \hat{\mathbf{H}}_{cb} \\ \hat{\mathbf{H}}_{nc} & \hat{\mathbf{H}}_{nn} & \hat{\mathbf{H}}_{nb} \\ \hat{\mathbf{H}}_{bc} & \hat{\mathbf{H}}_{bn} & \hat{\mathbf{H}}_{bb} \end{bmatrix} \begin{pmatrix} \mathbf{y} \\ \mathbf{q}_n \\ \mathbf{q}_b \end{pmatrix} = \begin{pmatrix} \mathbf{f}_y \\ \mathbf{f}_n \\ \mathbf{f}_b \end{pmatrix} \quad (6)$$

where

$$\hat{\mathbf{H}}_{cc} = \begin{bmatrix} \ddots & & & \\ & 1 - \omega_k^2 + 2j\xi_k\omega_k & & \\ & & \ddots & \\ & & & \ddots \end{bmatrix} \quad (7)$$

Then the electromechanical coupling is already integrated into matrix \mathbf{H} in the FEM procedure. While the electric impedance matrix \mathbf{Z} can be introduced by adding relation $\mathbf{f}_n = -\mathbf{Z}\mathbf{q}_n$ in equation (6). Eliminating \mathbf{y} and \mathbf{q}_n in equation (6) when no external forces are applied to the internal DOFs ($\mathbf{f}_y = \mathbf{0}$ and $\mathbf{f}_n = \mathbf{0}$), we can also obtain the same form as shown in equation (2) by

$$\mathbf{D} = \hat{\mathbf{H}}_{bb} - \hat{\mathbf{H}}_{bi} \hat{\mathbf{H}}_{ii}^{-1} \hat{\mathbf{H}}_{ib} \quad (8)$$

where

$$\hat{\mathbf{H}}_{ii} = \begin{bmatrix} \hat{\mathbf{H}}_{cc} & \hat{\mathbf{H}}_{cn} \\ \hat{\mathbf{H}}_{nc} & \hat{\mathbf{H}}_{nn} + \mathbf{Z} \end{bmatrix} \quad (9)$$

Less computational cost are required because $\hat{\mathbf{H}}_{ii}$ is a sparse matrix with a much smaller size in comparison with \mathbf{H}_{ii} .

2.2 Wave basis: a selected set of characteristic waves

According to Bloch theory, the free wave of the form $e^{j\omega t - kx}$ that travels in the periodic structure should satisfy the condition

$$\mathbf{q}_R^{(n)} = \lambda \mathbf{q}_L^{(n)} \tag{10}$$

while the equilibrium implies that

$$\mathbf{f}_R^{(n)} = -\lambda \mathbf{f}_L^{(n)} \tag{11}$$

where $\lambda = e^{-jk\Delta}$ describes the amplitude and phase change when the wave propagates from the left side to the right side of a unit cell. k is the wavenumber and Δ is the length of a unit cell. Introduce equation (10) and (11) into (2) and eliminate \mathbf{f}_L and \mathbf{f}_R , leads to

$$\left(\begin{bmatrix} \mathbf{0} & \sigma \mathbf{I} \\ -\mathbf{D}_{RL} & -\mathbf{D}_{RR} \end{bmatrix} - \begin{bmatrix} \sigma \mathbf{I} & \mathbf{0} \\ \mathbf{D}_{LL} & \mathbf{D}_{LR} \end{bmatrix} \right) \begin{pmatrix} \mathbf{q}_L \\ \mathbf{q}_R \end{pmatrix} = \mathbf{0} \tag{12}$$

Assembling the displacement and force eigenvectors in the matrix form we obtain the wave basis

$$\Phi = \begin{bmatrix} \Phi_q^+ & \Phi_q^- \\ \Phi_f^+ & \Phi_f^- \end{bmatrix} \tag{13}$$

where superscript + and - refer to the data belong to positive and negative going waves respectively. It is not necessary to consider all the N waves, because those strong evanescent waves nearly have no contribution to the overall response while they cause numerical issues [8, 9]. The m kept waves are those propagating ($|\lambda| = 1$) and less decaying ($|\lambda| > \tau$), where τ is a given factor, here is $\tau = 0.01$ is used. Because of the wave selection, the number of waves to be kept can be different in different frequencies.

3 DYNAMIC STIFFNESS MATRIX OF THE BUILT-UP STRUCTURE

Concerning the analysis of the complete assembled structure, there are 3 major steps, as shown in figure 4: 1) model the near-field completely by FEM, with no reduction or simplification; 2) model the far-field waveguide by WFEM and obtained the equivalent reflection matrix; and 3) model the piezoelectric waveguide and obtain the equivalent mechanical impedance matrix.

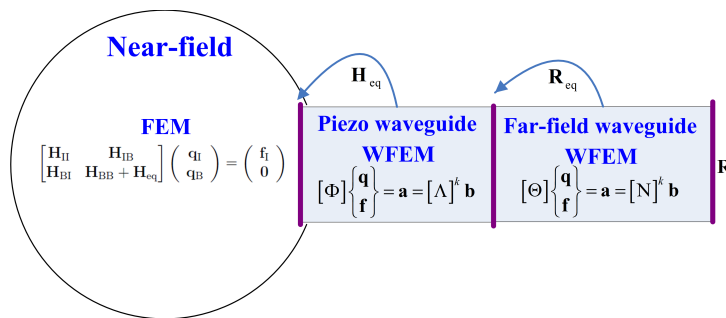


Figure 4: Illustration of the modeling process of the proposed method.

After these steps, all the DOFs of the waveguides would be condensed so that the final dimension of the dynamics stiffness matrix of the built-up structure is equal to the near field

one. The governing equations then write

$$\begin{bmatrix} \mathbf{H}_{II} & \mathbf{H}_{IB} \\ \mathbf{H}_{BI} & \mathbf{H}_{BB} + \mathbf{H}_{eq} \end{bmatrix} \begin{pmatrix} \mathbf{q}_I \\ \mathbf{q}_B \end{pmatrix} = \begin{pmatrix} \mathbf{f}_I \\ \mathbf{0} \end{pmatrix} \quad (14)$$

where subscripts **I** and **B** indicate the internal DOFs of the near-field and the DOFs connected to the waveguides respectively. \mathbf{H}_{eq} is the equivalent mechanical impedance of piezoelectric waveguide and it is

$$\mathbf{H}_{eq} = [\Phi_f^+ + \Phi_f^- (-\Lambda^{-L_p/\Delta_p} \cdot \mathbf{R}_{eq} \cdot +\Lambda^{L_p/\Delta_p})] [\Phi_q^+ + \Phi_q^- (-\Lambda^{-L_p/\Delta_p} \cdot \mathbf{R}_{eq} \cdot +\Lambda^{L_p/\Delta_p})]^{-1} \quad (15)$$

where \mathbf{R}_{eq} is the equivalent reflection matrix of the far-field substructure. Specifically, it is

$$\mathbf{R}_{eq} = -(\Phi_q^- - \mathbf{Y}\Phi_f^-)^{-1} (\Phi_q^+ - \mathbf{Y}\Phi_f^+) \quad (16)$$

and

$$\mathbf{Y} = [\Theta_q^+ + \Theta_q^- (-\mathbf{N}^{-L_f/\Delta_f} \cdot \mathbf{R} \cdot +\mathbf{N}^{L_f/\Delta_f})] [\Theta_f^+ + \Theta_f^- (-\mathbf{N}^{-L_f/\Delta_f} \cdot \mathbf{R} \cdot +\mathbf{N}^{L_f/\Delta_f})]^{-1} \quad (17)$$

where \mathbf{R} is the reflection matrix at the boundary of far-field substructure. For infinite case it is a zero matrix. $+\Lambda$ and $-\Lambda$ are diagonal matrices consisted of wavenumbers associated to positive-going and negative-going waves in piezoelectric waveguide respectively. $+\mathbf{N}$ and $-\mathbf{N}$ have the same meaning but they are for far-field waveguide. Φ and Θ represent the wave basis for piezoelectric waveguide and far-field waveguide respectively.

4 VALIDATIONS

A finite solid-element meshed structure is considered, shown in figure 5. It is constructed by bonding 10 groups of co-located piezoelectric patches onto a uniform host structure excited at the center. 5 groups of piezoelectric patches are periodically distributed at the right side of the excitation while five other groups are located on the other side. The structure is clamped on the right top and free at the left end.

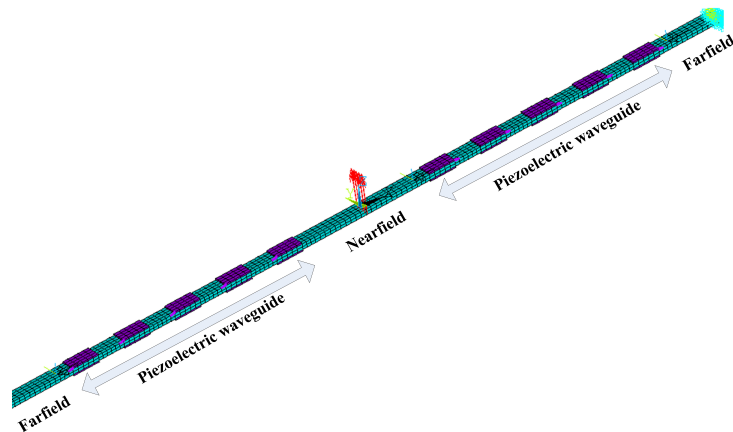


Figure 5: The calculation layout of the finites piezoelectric structure

To establish the wave basis of the piezoelectric waveguides, the proposed modal reduction approach is employed. All the internal mechanical DOFs have been transferred into modal coordinates and only 10 modal DOFs are retained. While all the electric DOFs remain in the

reduced dynamic stiffness matrix. Figure 6 compares the stiffness matrix of a unit cell before and after the modal reduction in the form $\log_{10}(| \cdot |)$. It can be seen in figure 6a that, before the reduction, the matrix is sparse and large (722×722). While after the reduction it tends to be dense and with a much smaller size (102×102). In the condensation process, 90 boundary DOFs are retained, which means only a 12×12 matrix of the internal DOFs needs to be inverted after the reduction, otherwise the inverse of a 632×632 matrix of the internal DOFs will be searched.

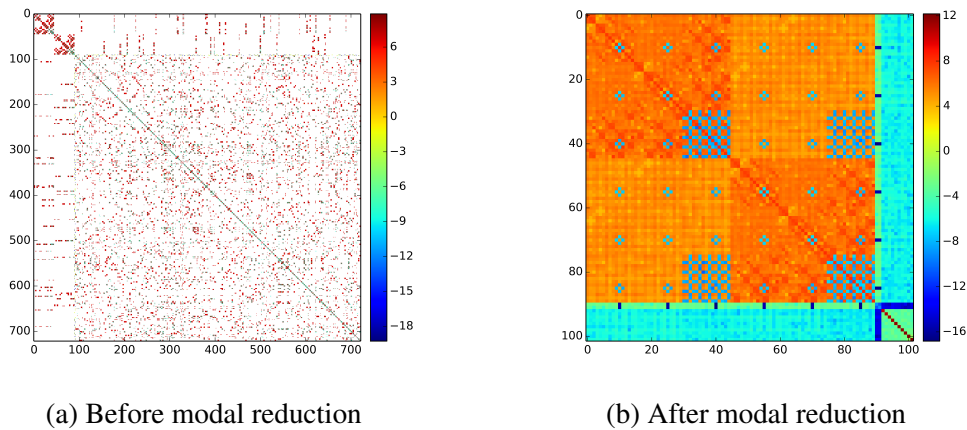


Figure 6: Illustration of stiffness matrix of a unit cell

The dispersion curves of the piezoelectric waveguides are shown in figure 7a. Overall 6 waves are observed after the identification, in which 4 waves (wave index 0, 1, 4 and 5) are propagating and 2 waves (wave index 2 and 3) are evanescent. Their wave shapes indicate that wave 0 and 2 are propagating (figure 7b) and evanescent flexural waves in z direction respectively, wave 1 and 3 are the propagating and evanescent flexural waves in y direction, wave 4 is the torsional wave and wave 5 is the longitudinal wave.

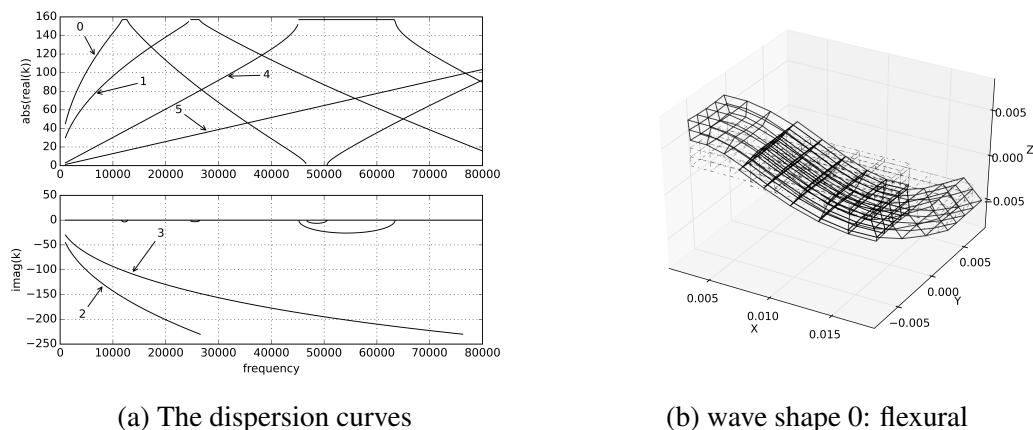
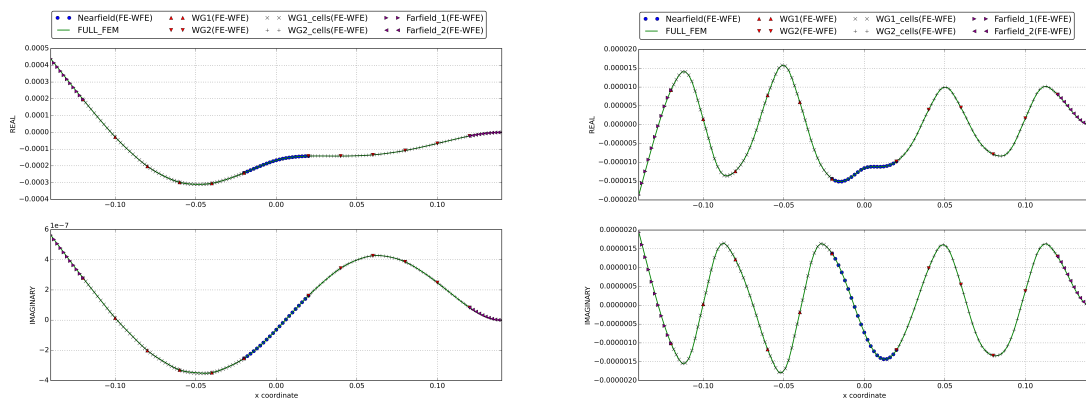


Figure 7: Wave modal results of the piezoelectric waveguide

With the reduced wave bases of the piezoelectric and far-field waveguides, the proposed method can be employed to analyze the forced response of the structure. The validation data come from the full FE model of the whole assembled structure. Two circuits are considered: 1)

resistor $R = 1 \times 10^5 \Omega$; and 2) resistor-inductor $R = 10 \Omega$ and $L = 2.945 \text{ H}$. The response is compared between full FE model and the proposed hybrid model, shown in figure 8. The results of the proposed method are first obtained only on the near-field DOFs. Then the response of the waveguides are obtained progressively by post-processing. Good agreements can be seen in both figures. It should be noted that two reduction have been made on different stages. To obtain the wave basis, a structural-modal reduction was conducted in order to accelerate the calculation. Additionally, in forced response analysis, a wave-modal reduction was employed to avoid ill-conditioning. In this validation case, 10 of the overall 632 structural modes are retained in the first reduction and concerning the later reduction only 6 of the overall 45 waves in the piezoelectric waveguides and 42 waves of the overall 45 waves in far-field waveguides are kept. The agreement with the full model results indicate that these reductions are accurate and the proposed method is applicable to solid-element modeling case.



(a) With resistive circuit at 400 Hz

(b) With resistor-inductor circuit at 3120 Hz

Figure 8: Validation of the proposed method with full FEM results: displacement of u_z DOF of all the middle line nodes

5 APPLICATION

The proposed numerical tool also enables one to analyze the energy flow and forced response in open structural system constructed by a near-field and several periodic waveguides. Here an application is briefly presented. The considered open structural system is obtained by changing the far-field of the closed structural system used in the validation to infinite. The material properties, the geometric of near-field and the parameters of a single unit cell of the waveguides remain the same. Each piezoelectric patch is shunted by an identical resistive circuit, where resistance $R = 1 \times 10^4 \Omega$. The excitation is applied in the center of the near-field, still as same as it was considered in the validation.

Forced response and energy flow are obtained by the proposed method and presented in figure 9, where only the data in positive x coordinates are presented due to the symmetry of the structure. The contribution to the displacement of the evanescent waves can be seen in the near-field. In the Far-field, propagating waves dominate the response where the phase varies linearly in space. Through the results of energy flow, the dissipation caused by the piezoelectric waveguide are clearly illustrated.

To find the desired design of the piezoelectric waveguide, one needs to choose a patten of

the electric circuit and calculate the power flow with different parameters. Sometimes maybe a optimization process will be connected. Due to the dual condensation condensations considered in this method, it is suitable for this kind of repetitive calculation.

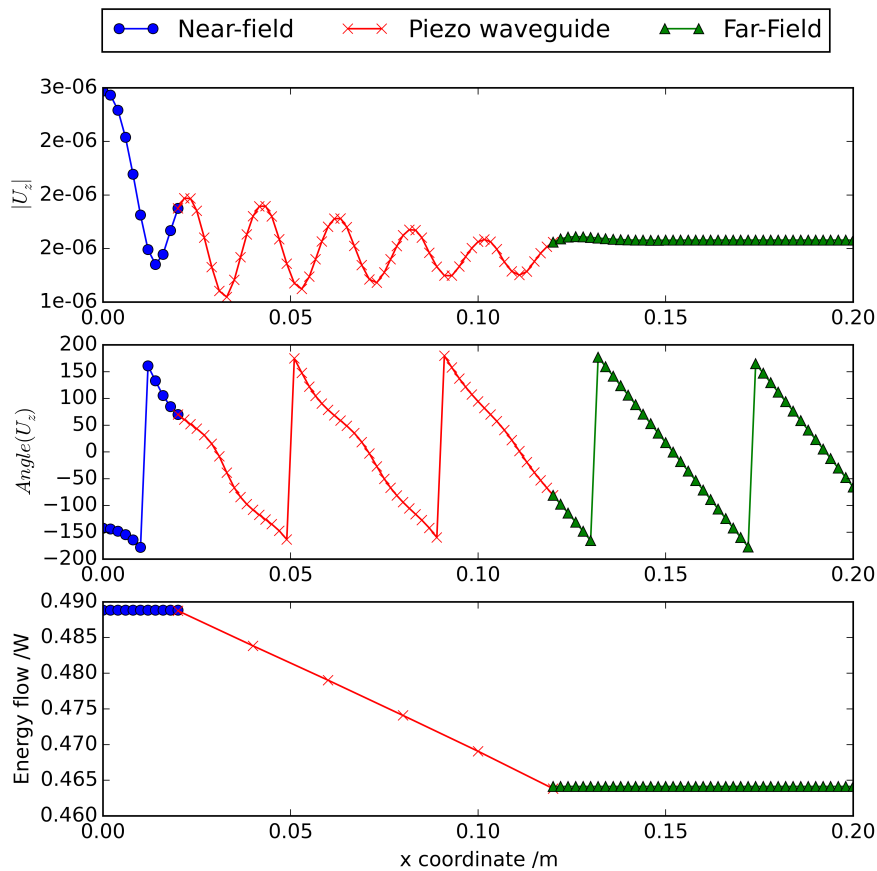


Figure 9: Forced response and energy flow in the structure

6 CONCLUDING REMARKS

A multi-scale numerical tool for the forced response and energy flow for piezoelectric-based structures are proposed in this paper. By means of this approach, the designed 1D piezoelectric waveguides can be evaluated by considering them as components of a built-up structure. The major modeling strategy is to model the non-periodic near-field by FEM and the waveguides by an enhanced WFEM, and then adapt the models of the substructures. The correlation with full FEM results attests that the proposed method is also accurate to simulate mode-dominated finite structures. With the advantage in the calculation speed, this method is applicable in the design process where the calculation is required on numerous sets of parameters.

REFERENCES

- [1] Yu Fan and Lin Li. Vibration Dissipation Characteristics of Symmetrical Piezoelectric Networks With Passive Branches. In *ASME Turbo Expo 2012: Turbine Technical Conference and Exposition, Volume 7: Structures and Dynamics, Parts A and B*, pages 1263–1273. ASME, June 2012.

- [2] Hongbiao Yu and K. W. Wang. Vibration Suppression of Mistuned Coupled-Blade-Disk Systems Using Piezoelectric Circuitry Network. *Journal of Vibration and Acoustics*, 131(2):021008, 2009.
- [3] M. Collet, K.a. Cunefare, and M.N. Ichchou. Wave Motion Optimization in Periodically Distributed Shunted Piezocomposite Beam Structures. *Journal of Intelligent Material Systems and Structures*, 20(7):787–808, October 2008.
- [4] O Thorp, M Ruzzene, and a Baz. Attenuation and localization of wave propagation in rods with periodic shunted piezoelectric patches. *Smart Materials and Structures*, 10(5):979–989, 2001.
- [5] Lin Li and Peiyi Wang. Evaluation of High-Order Resonance of Blade Under Wake Excitation. In *ASME Turbo Expo 2010: Power for Land, Sea, and Air; Volume 6: Structures and Dynamics, Parts A and B*, pages 995–1001. ASME, October 2010.
- [6] H.G.D. Goyder and R.G. White. Vibrational power flow from machines into built-up structures, part III: Power flow through isolation systems. *Journal of Sound and Vibration*, 68(1):97–117, January 1980.
- [7] Changwei Zhou. *Wave and modal coupled approach for multi-scale analysis of periodic structures*. Phd thesis, Ecole Centrale de Lyon, 2014.
- [8] Y. Waki, B.R. Mace, and M.J. Brennan. Free and forced vibrations of a tyre using a wave/finite element approach. *Journal of Sound and Vibration*, 323(3-5):737–756, June 2009.
- [9] W.J. Zhou and M.N. Ichchou. Wave propagation in mechanical waveguide with curved members using wave finite element solution. *Computer Methods in Applied Mechanics and Engineering*, 199(33-36):2099–2109, July 2010.

COPYRIGHT NOTICE

Copyright ©2015 by the authors. Distribution of all material contained in this paper is permitted under the terms of the Creative Commons license Attribution-NonCommercial-NoDerivatives 4.0 International (CC-by-nc-nd 4.0).





GEOMETRICALLY NON-LINEAR FREE AND FORCED VIBRATION OF FULLY CLAMPED LAMINATED COMPOSITE SKEW PLATES

H. Moulay Abdelali^{1*}, B. Harras² and R. Benamar¹

¹ERSIM, Ecole Mohammadia D'ingénieurs
University Mohammed V Agdal, Ecole Mohammadia D'ingénieurs, Avenue Ibn Sina, B.P.765,
Agdal, Rabat, MOROCCO
Email: h.moulay1983@gmail.com, rbenamar@emi.ac.ma

²FST B.P.2202- Route D'Imouzzer Fes, MOROCCO
Email: harrasbilal@yahoo.fr

ABSTRACT

In this paper, a theoretical model based on Hamilton's principle and spectral analysis is used to obtain the geometrically non linear free and steady state forced response of a laminated skew plate at large vibration amplitudes. Such a structure is analyzed regarding the influence of different parameters: the intensity of the excitation force, the ply properties, the plate aspect ratio and skew angle. The solution of the amplitude equation is obtained in each case using the explicit analytical approach previously developed. The results showed, as may be expected due to the membrane forces induced by the large vibration amplitudes, a non linearity of the hardening type with a shift to the right of the bent frequency response function, in the neighborhood of the fundamental mode. The effects of the various parameters mentioned above have been examined and the comparison between the results obtained and those available in previous studies showed a good agreement.

1 INTRODUCTION

Field like Aerospatiale, mechanical and civil engineering are commonly used the thin laminated composite skew plates on their applications. Generally, such structures are supported a forces, and vibrating in high amplitude, inducing a new behavior in the lamina constituted the composite material. Analytical methods are interesting to understand the influence of different parameters on the response of the structure, and complete the numerical methods as a basic reference tool. A lot of studies are concerned by analytical and numerical method. Kadiri and Benamar [1-3] has developed a semi analytical method based on Hamilton's principle and spectral analysis, for determination of the geometrically non-linear free and forced response of thin straight structures. Two models for non-linear vibration of beam and plate have been proposed. These two models were based on the linearization of the nonlinear algebraic equations, written in the modal basis, in the neighbourhood of each resonance. The first formulation leads to explicit analytical expressions for higher mode contribution coefficients to the i th non linear mode shape of the structure considered, as functions of the amplitude of vibration, the mass, rigidity, and non linearity tensors. This first model was shown to be applicable to finit amplitude of vibration, up to 0.8 times the beam thickness, and 0.5 times the plate thickness. The second formulation was leaded to similar results for higher amplitudes of vibration, up to 2.3 time the beam thickness, and once the plate thickness via solution of reduced linear systems. Das and al analysed [4] the static behaviour of thin isotropic skew plates under uniformly distributed load with the geometric nonlinearity using a variational method based on total potential energy. Duan and Mahendran [5] analysed the large deflection behavior of skew plate with various skew angles, length to width ratios, thicknesses and supported edges under uniformly distributed and concentrated loads using a new hybrid/mixed shell element. Also, published works devoted to the forced vibration of composite plates was found in literature. Han and Petyt [6] investigated the forced vibration of symmetrically laminated plates using the hierarchical finit element method (HFEM). Nguyen-Van and al [7] presented an improved finite element computational model using a flat four-node element with smoothed strains for geometrically nonlinear analysis of composite plate/shell structures. The Von-Karman's large deflection theory and the total Lagrangian approach are employed in the formulation of the element to describe small strain geometric nonlinearity with large deformations using the first-order shear deformation theory (FSDT). Harras and Benamar [8, 9] investigated theoretical and experimental of the non-linear behavior of various fully clamped rectangular composite panels at large vibration amplitudes. Ribeiro and Petyt [10] has applying the principle of virtual work and the HFEM for studying the steady state, geometrically non-linear, forced vibration of isotropic and composite laminated rectangular plates under harmonic external excitation.

This work presents an explicit analytical model for the steady state, geometrically non linear, periodic forced vibration of fully clamped thin skew composite plates, under harmonic external excitation. The theoretical model developed in [1-3] was adapted here. Comparison was made between the iterative method and the approximate explicit method. The frequency response curves have been obtained at the plate centre, for various levels of loading, various skew angles and various aspect ratios. It appeared that the method works well, since excellent agreement was found between the result of the present model and those published in the literature.

2 EXPLICIT ANALYTICAL FORMULATION FOR THE GEOMETRICALLY NONLINEAR LAMINATED SKEW PLATE EXCITED HARMONICALLY BY CONCENTRATED OR DISTRIBUTED FORCES

Consider the skew plate with a skew angle θ shown in Figure 1. For the large vibration amplitudes formulation developed here, it is assumed that the material of the plate is elastic, isotropic and homogeneous. The thickness of the plate is considered to be sufficiently small so as to avoid the effects of shear deformation. The skew plate has the following characteristics: a, b, S : length, width and area of the plate; x - y : plate co-ordinates in the length and the width directions; ξ - η , H : Skew plate co-ordinates and plate thickness; E, ν : Young's modulus and Poisson's ratio; D, ρ : plate bending stiffness and mass per unit volume.

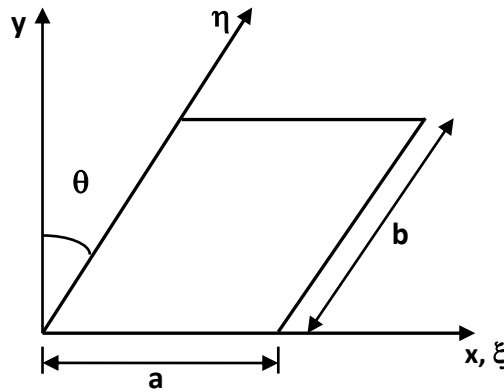


Figure 1 Skew plate in x - y and ξ - η co-ordinate system

For the classical plate laminated theory, the strain-displacement relationship for large deflections are given by:

$$\{\varepsilon\} = \{\varepsilon^0\} + z \{k\} + \{\lambda^0\}. \tag{1}$$

In which $\{\varepsilon^0\}$, $\{k\}$ and $\{\lambda^0\}$ are given by:

$$\{\varepsilon^0\} = \begin{bmatrix} \frac{\partial U}{\partial x} \\ \frac{\partial V}{\partial y} \\ \frac{\partial U}{\partial y} + \frac{\partial V}{\partial x} \end{bmatrix}; \{k\} = \begin{bmatrix} k_x \\ k_y \\ k_{xy} \end{bmatrix} = \begin{bmatrix} -\frac{\partial^2 W}{\partial x^2} \\ -\frac{\partial^2 W}{\partial y^2} \\ -2 \frac{\partial^2 W}{\partial xy} \end{bmatrix}; \{\lambda^0\} = \begin{bmatrix} \lambda_x^0 \\ \lambda_y^0 \\ \lambda_{xy}^0 \end{bmatrix} = \begin{bmatrix} \frac{1}{2} \left(\frac{\partial W}{\partial x}\right)^2 \\ \frac{1}{2} \left(\frac{\partial W}{\partial y}\right)^2 \\ \frac{\partial W}{\partial x} \frac{\partial W}{\partial y} \end{bmatrix}. \tag{2}$$

U, V and W are displacements of the plate mid-plane, in the x, y and z directions respectively. For the laminated plate having n layers, the stress in the K th layer can be expressed in terms of the laminated middle surface strains and curvatures as:

$$\{\sigma_k\} = [\bar{Q}]_k \{\varepsilon\}. \tag{3}$$

In which $\{\sigma\}_k^T = [\sigma_x \sigma_y \sigma_{xy}]$ and terms of the matrix $[\bar{Q}]$ can be obtained by the relationships given in reference [11]. The in-plane forces and bending moments in a plate are given by:

$$\begin{bmatrix} \mathbf{N} \\ \mathbf{M} \end{bmatrix} = \begin{bmatrix} \mathbf{A} & \mathbf{B} \\ \mathbf{B} & \mathbf{D} \end{bmatrix} \begin{bmatrix} \{\varepsilon^0\} + \{\lambda^0\} \\ \{k\} \end{bmatrix}. \quad (4)$$

A, B and D are the symmetric matrices given by the following Equation 5. $[\mathbf{B}] = 0$ for symmetrically laminated plates [12].

$$(A_{ij}, B_{ij}, D_{ij}) = \int_{-H/2}^{H/2} Q_{ij}^{(k)}(1, z, z^2) dz. \quad (5)$$

Here the $Q_{ij}^{(k)}$ are the reduced stiffness coefficients of the k th layer in the plate co-ordinates. The transverse displacement function W may be written as in reference [10] in the form of a double series:

$$W = \{A_k\}^T \{W\} \sin k\omega t. \quad (6)$$

Where $\{A_k\}^T = \{a_1^k, a_2^k, \dots, a_n^k\}$ is the matrix of coefficients corresponding to the k th harmonic, $\{W\}^T = \{w_1, w_2, \dots, w_n\}$ is the basic spatial functions matrix, k is the number of harmonics taken in to account, and the usual summation convention on the repeated index k is used. As in reference [13], only the term corresponding to $k=1$ has been taken into account, which has led to the displacement function series reduced, to only one harmonic: i.e.,

$$W = a_i w_i(x, y) \sin \omega t. \quad (7)$$

Here the usual summation convention for the repeated indexes i is used. i is summed over the range 1 to n , with n being the number of basic functions considered. The expression for the bending strain energy V_b , axial strain energy V_a and kinetic energy T are given in reference (Harras 2001) in the rectangular co-ordinate (x, y) . The skew co-ordinates are related to the rectangular co-ordinate (ξ, η) by: $\xi = x - y \tan \theta$; $\eta = y / \cos \theta$. So, the strain energy due to bending V_b , axial strain energy V_a and kinetic energy T are given in the ξ - η co-ordinate system. In the above expressions, the assumption of neglecting the in plane displacements U and V in the energy expressions has been made as for the fully clamped rectangular isotropic plates analysis considered in reference [13]. Discretization of the strain and kinetic energy expressions can be carried out leading to:

$$V_b = \frac{1}{2} \sin^2(\omega t) a_i a_j k_{ij}; V_a = \frac{1}{2} \sin^4(\omega t) a_i a_j a_k a_l b_{ijkl}; T = \frac{1}{2} \omega^2 \cos^2(\omega t) a_i a_j m_{ij}. \quad (8)$$

In which m_{ij} , k_{ij} and b_{ijkl} are the mass tensor, the rigidity tensor and the geometrical non-linearity tensor respectively. Non-dimensional formulation of the non-linear vibration problem has been carried out as follows.

$$w_i(\xi, \eta) = H w_i^* \left(\frac{\xi}{a}, \frac{\eta}{b} \right) = H w_i^*(\xi^*, \eta^*). \quad (9)$$

Where ξ^* and η^* are non-dimensional co-ordinates $\xi^* = \frac{\xi}{a}$ and $\eta^* = \frac{\eta}{b}$ one then obtains:

$$k_{ij} = \frac{aH^5 E}{b^3} k_{ij}^*; b_{ijkl} = \frac{aH^5 E}{b^3} b_{ijkl}^*; m_{ij} = \rho H^3 ab m_{ij}^*. \quad (10)$$

Where the non-dimensional tensors m_{ij}^* , k_{ij}^* and b_{ijkl}^* are given in terms of integrals of the non-dimensional basic function w_i^* , non-dimensional extensional and bending stiffness coefficient A_{ij}^* and D_{ij}^* , skew angle θ and aspect ratio α .

Upon neglecting energy dissipation, the equation of motion derived from Hamilton's principle is:

$$\delta \int_0^{2\pi} (V - T) = 0. \quad (11)$$

Where $V=V_a+V_b$. Insertion of Equations 8 into Equation 11, and derivation with respect to the unknown constants a_i , leads to the following set of non-linear algebraic equations:

$$2a_i k_{ir}^* + 3a_i a_j a_k b_{ijkr}^* - 2\omega^* a_i m_{ir}^* = 0. \quad (12)$$

Where $r=1, \dots, n$. These have to be solved numerically. To complete the formulation, the procedure developed in [8] is adopted to obtain the first non-linear mode. As no dissipation is considered here, a supplementary equation can be obtained by applying the principle of conservation of energy, leads to the equation:

$$\omega^{*2} = \frac{a_i a_j k_{ij}^* + (3/2) a_i a_j a_k a_l b_{ijkl}^*}{a_i a_j m_{ij}^*}. \quad (13)$$

This expression for ω^{*2} is substituted into Equation 12 to obtain a system of n non-linear algebraic equations leading to the contribution coefficients a_i , $i=1$ to n . ω and ω^* are the non-linear frequency and non-dimensional non-linear frequency parameters related by:

$$\omega^2 = \frac{D}{\rho b^4 \cos^4 \theta} \omega^{*2}. \quad (14)$$

To obtain the first non-linear mode shape of the skew plate considered, the contribution of the first basic function is first fixed and the other basic functions contributions are calculated via the numerical solutions of the remaining $(n-1)$ non-linear algebraic equations.

In this section, a fully clamped laminate skew plate excited by a concentrated harmonic force F^c applied at the point (ξ_0, η_0) ; or by a distributed harmonic uniform force F^d , distributed over the surface of the plate S are considered. F^c and F^d may be written using the Dirac function δ as:

$$F^c(\xi, \eta, t) = F^c \delta(\xi - \xi_0) \delta(\eta - \eta_0) \sin \omega t. \quad (15)$$

$$F^d(\xi, \eta, t) = F^d \sin \omega t \quad \text{if } (\xi, \eta) \in S. \quad (16)$$

$$F^d(\xi, \eta, t) = 0 \quad \text{if } (\xi, \eta) \notin S. \quad (17)$$

The corresponding generalized forces $F_i^c(t)$ and $F_i^d(t)$ in the beam function basis (BFB) are given by:

$$F_i^c(t) = F^c w_i(x_0, y_0) \sin \omega t = f_i^c \sin \omega t. \quad (18)$$

$$F_i^d(t) = F^d \sin \omega t \int_{\Omega} w_i(x, y) dx dy = f_i^d \sin \omega t. \quad (19)$$

The explicit analytical method has been successively applied in references [1-3] to non-linear free and forced vibrations, occurring at large displacements amplitudes, of rectangular plate. The purpose of this paper is to apply the explicit simple formulation to non-linear forced vibrations of laminated skew plate, then, make comparison of the new results with those found by the iterative method and with the previous ones available in the literature in order to determine exactly the limit of validity of this formulation. Analytical details are given in this section for the first non-linear mode shape of a forced fully clamped laminated skew plate. As it was noticed that the contribution a_1 remains significantly higher than a_2 to a_n , denoted in what follows as $\varepsilon_2, \varepsilon_3, \dots, \varepsilon_{18}$, the main idea of the approach presented in references [1-3] was to simplify the non-linear expression $a_i a_j a_k b_{ijk}$ in Equation 12, which involves summation for the repeated indices i, j, k over the range $\{1, 2, \dots, n\}$, by neglecting both first and second order terms with respect to ε_i , i.e. terms of the type $a_i^2 \varepsilon_k b_{11kr}$ or of the type $a_i \varepsilon_j \varepsilon_k b_{1jkr}$ so that the only remaining term is $a_1^3 b_{111r}^*$. The Equation 12 becomes:

$$(k_{ir}^* - \omega^{*2} m_{ir}^*) \varepsilon_i + \frac{3}{2} a_1^3 b_{111r}^* = f_r^*, \quad r = 2, 3, \dots, 18. \quad (20)$$

Where f_i^{*c} and f_i^{*d} corresponding, respectively to the dimensionless generalized concentrated force F^c at point (ξ_0, η_0) ; and to the uniformly distributed force F^d over the surface Ω of the plate; The expressions obtained are:

$$f_i^{*c} = F^c \frac{b^3}{aEH^4} w_i^*(\xi_0^*, \eta_0^*). \quad (21)$$

$$f_i^{*d} = F^d \frac{b^4}{EH^4} \iint_{\Omega} w_i^*(\xi^*, \eta^*) d\xi^* d\eta^*. \quad (22)$$

As mentioned in reference [3], the above system permits one to obtain explicitly the basic function contributions $\varepsilon_2, \varepsilon_3, \dots, \varepsilon_{18}$ of the second and higher functions, corresponding to a given value of the assigned first basic function contribution a_1 if k_{ir}^* , for $i \neq r$, is assumed to be negligible compared to k_{rr}^* , and direct solution was as follows:

$$\varepsilon_r = \frac{f_r^* - \frac{3}{2} a_1^3 b_{111r}^*}{k_{rr}^* - \omega^{*2} m_{rr}^*}, \quad r = 2, 3, \dots, 18. \quad (23)$$

It was shown in Reference [3] that the accurate explicit analytical solution corresponding to the non-linear free and forced vibration cases can be obtained only in the normal modes basis of the fully clamped plate considered (MFB). So, the problem of non linear forced laminated skew plate will also be formulated in this appropriate basis, using the notation of Reference [3].

The simplified theory presented in this subsection focuses on non-linear vibrations of plates using a multi-mode approach and taking into account the coupling between the higher vibration modes. The solution obtained in Equation (23) makes it possible to get directly the non-linear frequency response function in the neighbourhood of the first mode. This gives not only the displacement at the centre of the plate, as is usually the case, as a function of the non-linear

frequency, but also the plate response spatial distribution on its whole area, for each level of excitation. The results obtained by this approach, are in good agreement with the experimental results in Reference [14].

3 RESULTS AND DISCUSSION

The aim of this section is to apply the theoretical model presented above to analyze the geometrical non-linear free and forced dynamic response of skew fully clamped symmetrically laminated plates in order to investigate the effect of non-linearity on the non-linear resonance frequencies and non-linear fundamental mode shape at large vibration amplitudes. Convergence studies are carried out, and the results are compared with those available from the literature through a few examples of laminated composite skew thin clamped plates with different fibre orientation and aspect ratio. The material properties, used in the present analysis are: Isotropic plate and composite laminated plate (graphite/epoxy) has five layers symmetrical angle-ply ($45^\circ, -45^\circ, 45^\circ, -45^\circ, 45^\circ$); $E_L=173 \text{ GN/m}^2$; $E_T=E_L/15.4$ $G_{LT}/E_T = 0.79$; $\nu_{LT} = 0.3$.

Where E , G and ν are Young's modulus, shear modulus and Poisson's ratio. Subscripts L and T represent the longitudinal and transverse directions respectively with respect to the fibres. All the layers are of equal thickness. Calculation was made by using 18 functions corresponding to three symmetric beam functions in the ξ direction and three symmetric beam functions in the η direction, and three anti-symmetric beam functions in the ξ direction and three anti-symmetric beam functions in the η direction. Table 1 shows the non linear results for a fully clamped isotropic square plate subjected to harmonic distributed force $f_1^{*d}=104.45$ ($F^d=873.82\text{N/m}^2$) obtained using a multimode approach. It can be seen a good convergence with results presented in reference [3].

W_{\max}^*	Reference [3]	Present result	Error %
+0.2	0.1475	0.1487	0.81
-0.2	1.4218	1.4220	0.01
+0.4	0.7661	0.7671	0.13
-0.4	1.2596	1.2602	0.05
+0.6	0.9285	0.9304	0.20
-0.6	1.2364	1.2377	0.11
+0.8	1.0476	1.0507	0.30
-0.8	1.2639	1.2665	0.21
+1	1.1588	1.1632	0.38
-1	1.3202	1.3240	0.29

Table 1. Forced vibration frequency ratio ω/ω_1 for a fully clamped square plate subject to harmonic distributed force $f_1^{*d}=104.45$ ($F^d=873.82\text{N/m}^2$).

The variation of non-dimensional nonlinear frequency ratio ω_{nl}/ω_1 with respect to non dimensional maximum amplitude w_{\max}/h is evaluated for different skew angle subjected to uniform harmonic load is shown in figure 2. The nonlinearity is reduced with increasing skew angle. It can be noticed multivalued regions corresponding to the jump phenomena occurring in non-linear vibration.

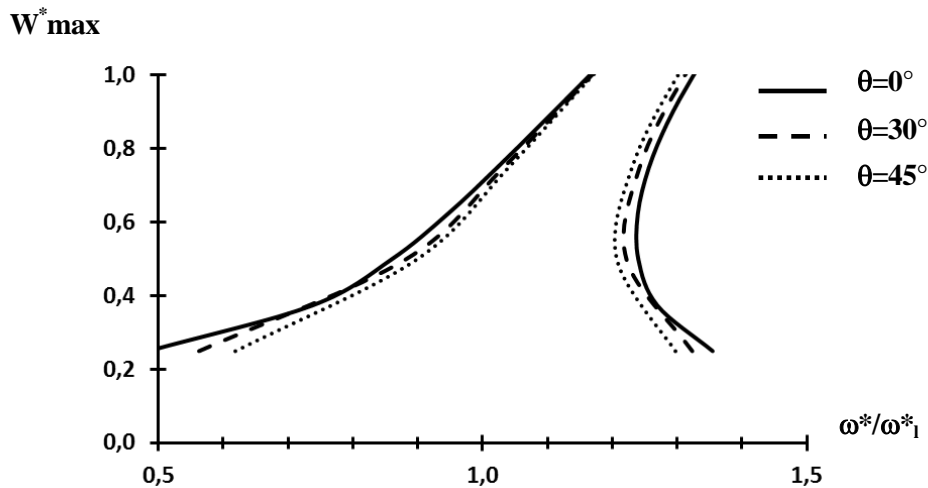


Figure 2. Comparison of the Forced response of a fully clamped isotropic square plate subjected to harmonic distributed force $f_1^{*d}=104.45$ ($F^d=873.82\text{N/m}^2$) for different skew angle.

A comparison between results obtained by the explicit model with those obtained using the single mode approach for fully clamped laminated composite plate excited by a harmonic distributed forces $f_1^{*d}=10$ ($F^d=124.7\text{N/m}^2$) was presented in Figure 3. It can be seen a reasonable estimate for the amplitude at the centre of the plate.

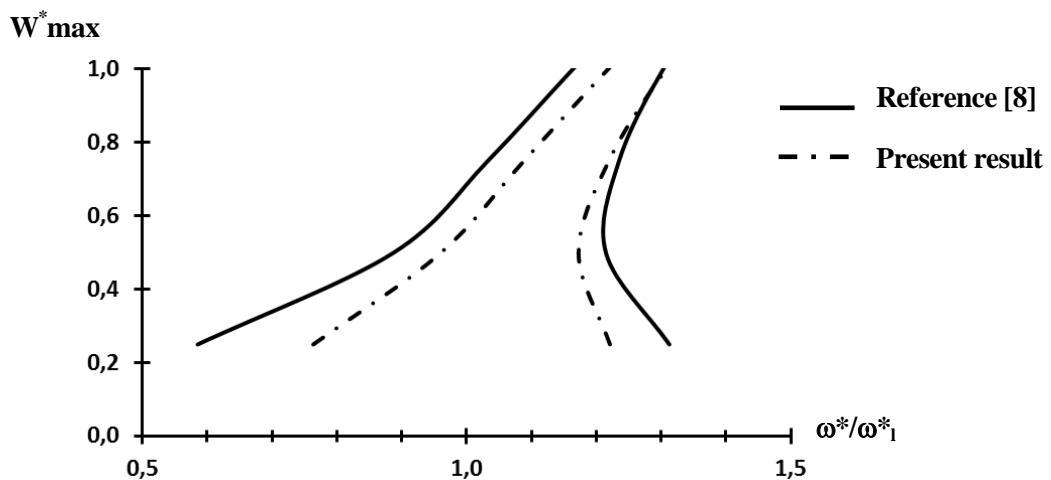


Figure 3. Comparison of the forced response of a fully clamped composite square plate subjected to harmonic distributed force $f_1^{*d}=10$ ($F^d=124.7\text{N/m}^2$) obtained with explicit method with reference [8].

In the case of fully clamped composite skew plate subjected to harmonic distributed force $f_1^{*d}=10$ ($F^d=124.7\text{N/m}^2$) with aspect ratio equal to 1, the effect of increasing skew plate on the nonlinearity was clearly exhibited in figure 4. The nonlinearity decreases with increases skew angle. For skew angle $\theta=45^\circ$ it decreases about 10% compared with the rectangular case.

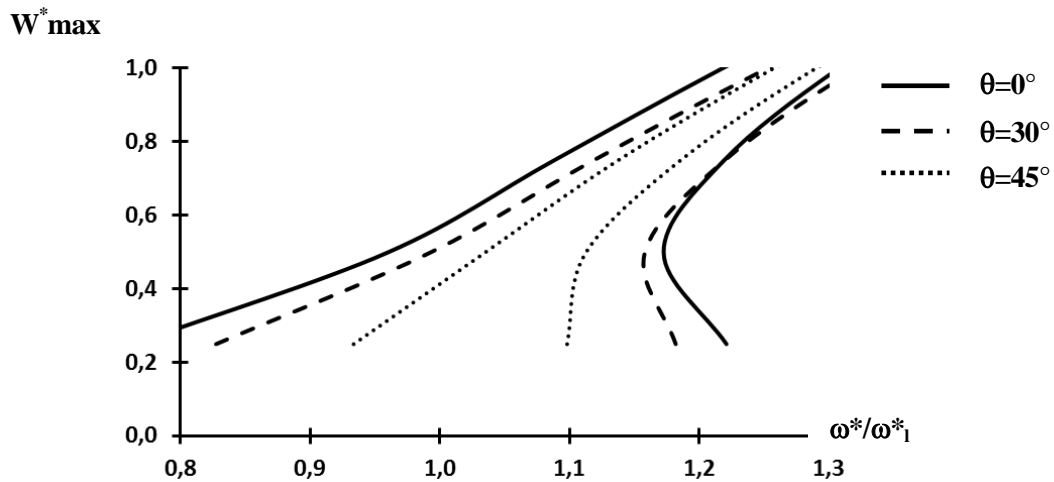


Figure 4. Comparison of the Forced response of a fully clamped composite plate subjected to harmonic distributed force $f_1^{*d}=10$ ($F^d=124.7\text{N/m}^2$) for different skew angle and $\alpha=1$.

The figure 5 shows the effect of the aspect ratio on the fully clamped composite skew plate. It can be seen that the increasing of aspect ratio; reduced the non-linearity of the plate.

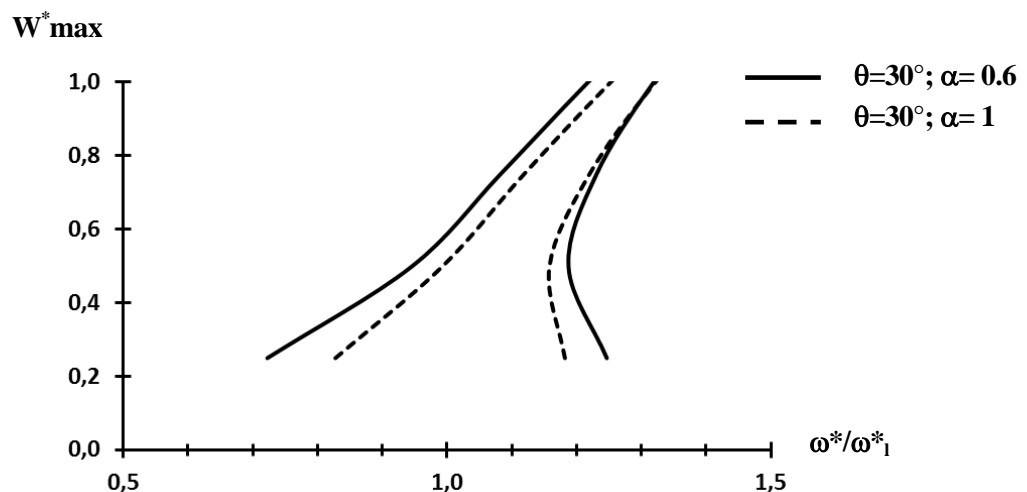


Figure 5. Comparison of the forced response of a fully clamped composite skew plate subjected to harmonic distributed force $f_1^{*d}=10$ ($F^d=124.7\text{N/m}^2$) for different aspect ratio α and $\theta=30^\circ$.

4 CONCLUSION

A model using a semi analytical approach based on lagrange's equations, and the harmonic balance method are successively applied for geometrical non-linear, steady state, periodic forced vibration of composite laminated skew plates. Good results were found using a single and multimode approach to determine the amplitude frequency dependence in the centre of the plate by varying skew angle and aspect ratio. It can be seen that the skew angle reduce the effect of the nonlinearity, also the increasing aspect ratio decrease the nonlinearity. Good agreement between the present results and those found in literature has been achieved.

REFERENCES

- [1] M. EL Kadiri, R. Benamar, and R. G. White. Improvement of the semi-analytical method, based on Hamilton's principle and spectral analysis, for determination of the

geometrically non-linear free response of thin straight structures. Part II: Application to the first and second non-linear mode shapes of fully clamped rectangular plates. *Journal of Sound and Vibration*. 257: 16-62, 2002.

[2] M. EL Kadiri, and R. Benamar. Improvement of the semi-Analytical Method, for Determining the Geometrically non-linear Response of Thin Straight Structures. Part I: Application to Clamped-Clamped and Simply Supported Clamped Beams. *Journal of Sound and vibration*. 249: 263-305, 2002.

[3] M. El Kadiri, and R. Benamar. Improvement of the semi-analytical method, based on Hamilton's principle and spectral analysis, for determination of the geometrically non-linear response of thin straight structures. Part III: steady state periodic forced response of rectangular plates. *Journal of Sound and Vibration*. 264: 1-35, 2003.

[4] D. Das, P. Sahoo, and K. Saha. A variational analysis for large deflection of skew plates under uniformly distributed load through domain mapping technique. *International Journal of Engineering, Science and Technology*. 1(1): 16-32, 2009.

[5] M. Duan, and M. Mahendran. Large deflection analyses of skew plates using hybrid/mixed finite element method. *Computers and Structures*. 81:1415-1424, 2003.

[6] W. Han, and M. Petyt. Linear vibration analysis of laminated rectangular plates using the hierarchical finite element method-II: Forced vibration analysis. *Computers and Structures*. 61 (4):713-724, 1996.

[7] H. Nguyen-Van , N. Nguyen-Hoai, T. Chau-Dinh, and T. Nguyen-Thoi. Geometrically nonlinear analysis of composite plates and shells via a quadrilateral element with good coarse-mesh accuracy. *Composite Structures*. 112: 327-338, 2014.

[8] B. Harras. Theoretical and Experimental Investigation of the non-Linear Behaviour of various Fully Clamped Rectangular Composite Panels at large Vibration Amplitudes. *Ph.D. thesis, University Mohammed V-Agdal*. 2001.

[9] B. Harras, R. Benamar, and R.G. White. Investigation of non-linear free vibrations of fully clamped symmetrically laminated carbon-fibre-reinforced PEEK (AS4/APC2) rectangular composite panels. *Composites sciences and technology*. 62: 719-727, 2002.

[10] P. Ribeiro, and M. Petyt. Geometrical non-linear, steady state, forced, periodic vibration of plates. Part I: Model and convergence studies. *Journal of Sound and Vibration*. 226 (5): 955-983, 1999.

[11]S. Timoshenko, S. Weinsowsky-Krieger, and R.M. Jones. *Mechanics of Composite Materials, 51*. International Student Edition, McGraw-Hill Kogakusha, Ltd. Tokyo, 1975.

[12]P.K. Mallick. *Fibre-reinforced composites: Materials, Manufacturing and Design, 152*. New York: Marcel Dekker, Inc., second edition revised and expanded, 1993.

[13]R. Benamar, M.M.K. Bennouna, and R.G. White. The effects of large vibration amplitudes on the fundamental mode shape of thin elastic structures. Part II fully clamped rectangular isotropic plates. *Journal of Sound and Vibration*. 164: 295-316, 1993.

[14] R. Benamar, M.M.K. Bennouna, and R.G. White. The effects of large vibration amplitudes on the mode shapes and natural frequencies of thin elastic structures. Part III: fully clamped rectangular isotropic plates-measurment of the mode shape amplitude dependence and spatial distribution of harmonic distortion. *Journal of sound and vibration*. 175: 377-395, 1991.



HIGH-ORDER WAVE DIFFUSION IN A SANDWICH PLATE WITH BONDED COUPLING ELEMENT

Droz C.^{1,2*}, J.-P. Lainé² and M.N. Ichchou²

¹Airbus Helicopters
Aéroport Inter. Marseille-Provence, 13725 Marignane Cedex, FRANCE

²Ecole Centrale de Lyon
36 Avenue Guy de Collongue, 69134 Ecully Cedex, FRANCE
Email: christophe.droz@ec-lyon.fr

ABSTRACT

In this paper, a numerical method is employed to determine high-order waves dispersion characteristics in a sandwich waveguide. Then, wave reflection is examined through a coupling element involving an elastic layer deposited on the waveguide's surface. The influence of structural loss factor on the reflection coefficients of propagating waves is evaluated. Then, high-order waves reflections are compared for several layer's thicknesses and distributions, in order to determine whether further informations can be gathered on a given structural alteration by using high-order waves.

1 INTRODUCTION

In the context of structural health monitoring (SHM) of composite structures, an increasing research effort was developed in recent years. The motivation is, among others, the development of non-destructive inspection techniques providing maximum information on the structural state of a structure, as well as the possible defects localization and sizing. For this purpose, systems based on guided waves revealed very promising and are currently used for numerous applications.

Yet, designing wave-based SHM systems requires effective tools for analysing and predicting the various types of elastic waves propagating in the considered structure. These waves can propagate with different group velocities, wavenumbers and spatial attenuations, and require specific actuation and measurement systems. For example, Lamb waves, originally defined for thin isotropic plates with stress-free surfaces, are now extensively used in SHM for anisotropic, multi-layered or other composite structures. Accordingly, waveguides involving complex or heterogeneous cross-sections can produce numerous wave types, whose dispersion characteristics prediction may require advanced numerical simulation. For such applications, the Wave Finite Element Method (WFEM) uses Bloch's theorem [1] to significantly reduce of the modelling effort. It combines Periodic Structures Theory (PST) with commercial finite element (FEM) packages. The wave dispersion characteristics can be determined by solving a quadratic eigenvalue problem obtained with a finite element model of the waveguide's cross-section [2].

In order to describe the wave transmission, reflection and coupling effects occurring when the aforementioned waves propagate through a defect, join or other type of coupling element, the Diffusion Matrix Model (DMM) was developed to connect two waveguides with an elastic coupling element [3]. This method was extensively employed for defining reflection coefficients in order to localize and evaluate cracks in pipelines [4]. The DMM is used to identify, among the different propagating wave types [5], the waves which exhibit the highest sensitivity towards structural perturbation, such as reduced mass or stiffness induced by imperfection, defect or erosion.

This work is concerned with the diffusion of high-order waves through a coupling element involving added mass and stiffness, bonded on the surface of a sandwich plate. In this example, the structural perturbation is made of an elastic layer modelled using FEM. The propagation of high-order plane waves in the sandwich plate made of transverse isotropic honeycomb core surrounded by fiber-reinforced skins is investigated. High-order waves are discriminated according to their dispersion characteristics and wave shapes. Finally, their sensitivity to localized structural perturbations is discussed.

2 WAVE PROPAGATION AND DIFFUSION THROUGH A COUPLING ELEMENT

2.1 Wave finite element method

A waveguide is considered as a straight elastic structure made of N of identical substructures of same length d , connected along the direction x . The state vector is described in figure 1. Nodal displacements and forces are denoted \mathbf{q} and \mathbf{f} , where the subscripts 'L' and 'R' describe the cell's left and right faces. Both edges have the same number n of degrees of freedom. Mesh compatibility is assumed between the cells. The governing equation in a cell at frequency ω is written :

$$(-\omega^2\mathbf{M} + \mathbf{K})\mathbf{q} = \mathbf{f} \quad (1)$$

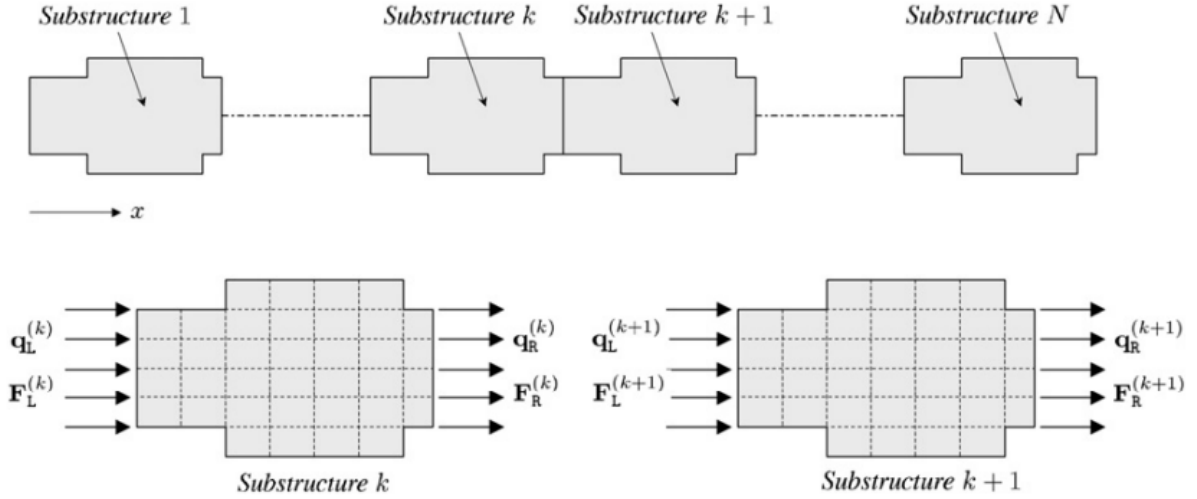


Figure 1. Illustration of a waveguide and the state vector of a unit cell.

where \mathbf{M}, \mathbf{K} are the mass and complex stiffness matrices, respectively. A dynamic condensation of the inner DOFs can be required if the structure is periodic. The governing equation can be written by reordering the DOFs :

$$\begin{bmatrix} \mathbf{K}_{LL} & \mathbf{K}_{LR} \\ \mathbf{K}_{RL} & \mathbf{K}_{RR} \end{bmatrix} - \omega^2 \begin{bmatrix} \mathbf{M}_{LL} & \mathbf{M}_{LR} \\ \mathbf{M}_{RL} & \mathbf{M}_{RR} \end{bmatrix} \begin{Bmatrix} \mathbf{q}_L \\ \mathbf{q}_R \end{Bmatrix} = \begin{Bmatrix} \mathbf{f}_L \\ \mathbf{f}_R \end{Bmatrix} \quad (2)$$

where \mathbf{M}_{ii} and \mathbf{K}_{ii} are symmetric, $\mathbf{M}_{LR}^t = \mathbf{M}_{RL}$ and $\mathbf{K}_{LR}^t = \mathbf{K}_{RL}$. $\lambda = e^{-jkd}$ is the propagation constant, describing wave propagation over the cell length d and k is the associated wavenumber, considering force equilibrium $\lambda \mathbf{f}_L + \mathbf{f}_R = 0$ in a cell and Bloch's theorem, $\mathbf{q}_R = \lambda \mathbf{q}_L$ into Eq. (2), it yields the following spectral eigenproblem :

$$\mathbf{S}(\lambda, \omega) = (\lambda \mathbf{D}_{LR} + (\mathbf{D}_{LL} + \mathbf{D}_{RR}) + \frac{1}{\lambda} \mathbf{D}_{RL}) \Phi = 0 \quad (3)$$

where the solutions Φ stand for the wave shape associated with the displacements \mathbf{q}_L of the waveguide's cell. In damped waveguides, complex wavenumbers are associated to decaying waves. Defining the state vector : $\Phi = [(\Phi_q)^t, (\Phi_f)^t]^t$, the spectral problem can be written using the symplectic transfer matrix \mathbf{T} .

$$\mathbf{T}\Phi = \begin{bmatrix} \mathbf{D}_{LR}^{-1} \mathbf{D}_{LL} & \mathbf{D}_{LR}^{-1} \\ \mathbf{D}_{RL} - \mathbf{D}_{RR} \mathbf{D}_{LR}^{-1} \mathbf{D}_{LL} & -\mathbf{D}_{RR} \mathbf{D}_{LR}^{-1} \end{bmatrix} \begin{Bmatrix} \Phi_q \\ \Phi_f \end{Bmatrix} = \lambda \begin{Bmatrix} \Phi_q \\ \Phi_f \end{Bmatrix} \quad (4)$$

Here, the waves associated with positive wavenumber are travelling in the positive x -direction and the negative wavenumbers describe propagation in the negative x -direction. Therefore the wave solutions can be ordered as follows :

$$\Phi = \begin{bmatrix} \Phi_q^{\text{inc}} & \Phi_q^{\text{ref}} \\ \Phi_f^{\text{inc}} & \Phi_f^{\text{ref}} \end{bmatrix}, \quad (5)$$

where *inc* refers to the incident waves and *ref* denotes the reflected waves and $\Phi_q^{\text{inc}}, \Phi_q^{\text{ref}}, \Phi_f^{\text{inc}}, \Phi_f^{\text{ref}}$ are $n \times n$ matrices. The displacements $u_L^{(k)}$ and $u_R^{(k)}$ of any substructure k can be written using the wave solutions $\{\Phi_i\}_{i=1, \dots, 2n}$:

$$u_L^{(k)} = \Phi \mathbf{Q}^{(k)}, \quad u_R^{(k)} = \Phi \mathbf{Q}^{(k+1)} \quad (6)$$

where the vector \mathbf{Q} stands for the wave amplitudes, and is written :

$$\mathbf{Q} = \begin{pmatrix} \mathbf{Q}^{\text{inc}} \\ \mathbf{Q}^{\text{ref}} \end{pmatrix}. \quad (7)$$

2.2 Wave diffusion through a coupling element

Consider the two waveguides connected with an elastic coupling element in figure 2. The substructures are connected, assuming compatible mesh at the interfaces Γ_1 and Γ_2 and no external forces are applied on the coupling element.

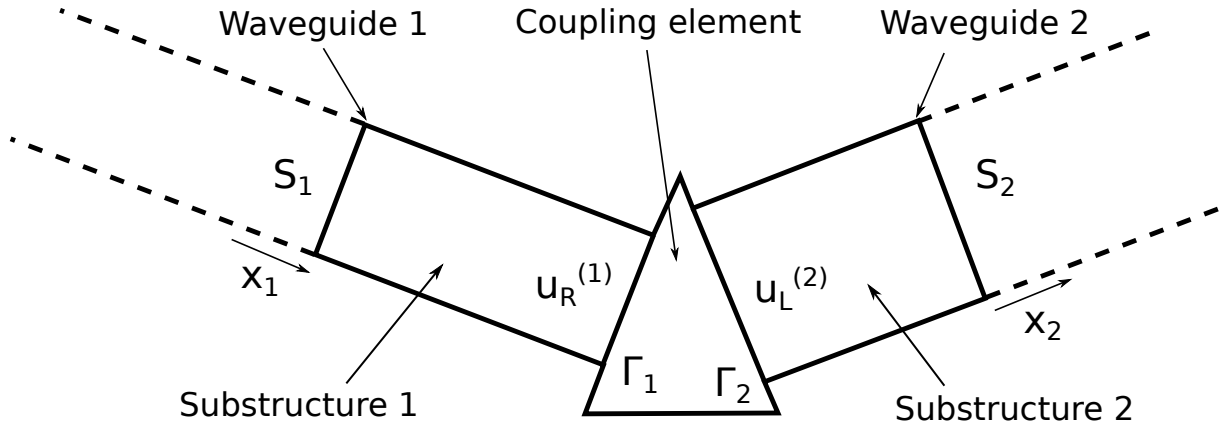


Figure 2. Illustration of two coupled waveguides.

This part is concerned with the determination of transmitted and reflected waves amplitudes through the coupling element. Denoting \mathbb{D}_c^* the condensed dynamical stiffness of the coupling element, the governing equation can be written :

$$\mathbb{D}_c^* \begin{pmatrix} \mathbf{q}_1^c \\ \mathbf{q}_2^c \end{pmatrix} = \begin{pmatrix} \mathbf{F}_1^c \\ \mathbf{F}_2^c \end{pmatrix}, \quad (8)$$

Considering the relations between the displacements $(\mathbf{q}_R^{(1)}, \mathbf{q}_L^{(2)})$ and the forces $(\mathbf{F}_R^{(1)}, \mathbf{F}_L^{(2)})$ applied on the surfaces Γ_1 and Γ_2 :

$$\begin{pmatrix} \mathbf{F}_R^{(1)} \\ \mathbf{F}_L^{(2)} \end{pmatrix} = - \begin{pmatrix} \mathbf{F}_1^c \\ \mathbf{F}_2^c \end{pmatrix}, \quad \begin{pmatrix} \mathbf{q}_1^c \\ \mathbf{q}_2^c \end{pmatrix} = \begin{pmatrix} \mathbf{q}_R^{(1)} \\ \mathbf{q}_L^{(2)} \end{pmatrix}, \quad (9)$$

the coupling relation between the two waveguides can be written :

$$\mathbb{D}^{c*} \begin{pmatrix} \mathbf{q}_R^{(1)} \\ \mathbf{q}_L^{(2)} \end{pmatrix} = \begin{pmatrix} \mathbf{F}_R^{(1)} \\ \mathbf{F}_L^{(2)} \end{pmatrix}. \quad (10)$$

In this context, the dynamical behaviour of the coupled waveguide can be described using the incident $((\Phi_q^{\text{inc}(i)})^T (\Phi_F^{\text{inc}(i)})^T)^T$ and reflected $((\Phi_q^{\text{ref}(i)})^T (\Phi_F^{\text{ref}(i)})^T)^T$ waves. Therefore, in can be shown in reference [3] that the incident and reflected wave amplitudes $(\mathbf{Q}^{\text{inc}(1)}, \mathbf{Q}^{\text{inc}(2)})$ can be related through a diffusion matrix \mathbb{C} :

$$\begin{pmatrix} \mathbf{Q}^{\text{ref}(1)} \\ \mathbf{Q}^{\text{ref}(2)} \end{pmatrix} = \mathbb{C} \begin{pmatrix} \mathbf{Q}^{\text{inc}(1)} \\ \mathbf{Q}^{\text{inc}(2)} \end{pmatrix}, \quad (11)$$

where

$$\mathbb{C} = - [\mathbb{D}^{c*} \Psi_q^{\text{ref}} + \Psi_F^{\text{ref}}]^{-1} [\mathbb{D}^{c*} \Psi_q^{\text{inc}} + \Psi_F^{\text{inc}}] \quad (12)$$

and the matrices Ψ_q^{inc} , Ψ_q^{ref} , Ψ_F^{inc} and Ψ_F^{ref} are expressed in terms of incident and reflected wave solutions described in Eq.(5) :

$$\Psi_q^{\text{inc}} = \begin{bmatrix} \Phi_q^{\text{inc}(1)} & \mathbf{0} \\ \mathbf{0} & \Phi_q^{\text{inc}(2)} \end{bmatrix}, \quad \Psi_q^{\text{ref}} = \begin{bmatrix} \Phi_q^{\text{ref}(1)} & \mathbf{0} \\ \mathbf{0} & \Phi_q^{\text{ref}(2)} \end{bmatrix} \quad (13)$$

$$\Psi_F^{\text{inc}} = \begin{bmatrix} \Phi_F^{\text{inc}(1)} & \mathbf{0} \\ \mathbf{0} & \Phi_F^{\text{inc}(2)} \end{bmatrix}, \quad \Psi_F^{\text{ref}} = \begin{bmatrix} \Phi_F^{\text{ref}(1)} & \mathbf{0} \\ \mathbf{0} & \Phi_F^{\text{ref}(2)} \end{bmatrix}.$$

In the following section, the diffusion matrix \mathbb{C} is determined to provide the transmission t and reflection r coefficients of high-order waves in a sandwich waveguide exhibiting a layer of epoxy deposit.

3 WAVE DISPERSION IN THE SANDWICH WAVEGUIDE

The rectangular sandwich waveguide is composed of a 8 mm thick homogenised honeycomb core surrounded by 1 mm thick fiber-reinforced skins. The 400 mm width cross-section is modelled using 360 linear block elements having 8-nodes and 3 degrees of freedom (DOF) per node. A detailed description of the materials is given in tables 1, 2 and 3.

Material	Density (kg.m ⁻¹)	Young Modulus (Pa)	Shear Modulus (Pa)
Nomex	24	$E_x = 5 \times 10^6$ $E_y = 5 \times 10^6$ $E_z = 46.6 \times 10^6$	$G_{xy} = 1 \times 10^6$ $G_{xz} = 10.13 \times 10^6$ $G_{yz} = 10.13 \times 10^6$

Table 1. Material properties of honeycomb core

Material	Density (kg.m ⁻¹)	Young Modulus (Pa)	Shear Modulus (Pa)
TC skin	1451	$E_x = 81 \times 10^9$ $E_y = 81 \times 10^9$ $E_z = 3.35 \times 10^9$	$G_{xy} = 2.5 \times 10^9$ $G_{xz} = 2.8 \times 10^9$ $G_{yz} = 2.8 \times 10^9$

Table 2. Material properties of fiber-reinforced skins

Material	Density (kg.m ⁻¹)	Young Modulus (Pa)	Shear Modulus (Pa)
Aggregate	2000	$E = 20 \times 10^9$	$G = 7.7 \times 10^9$

Table 3. Material properties of the deposit layer

The wave dispersion characteristics of the sandwich structure are given in figure 3. Continuous lines describe first-order waves while dashed lines represent high-order propagating waves, associated with deformed cross-sections. In the considered waveguide, high-order waves appearing in the frequency range $[0, 5000]$ are propagating waves with sinusoidal deformation of their cross-section. These waves are referred as high-order flexural waves since they share the same asymptotic group velocity of the first-order flexural and torsional waves.

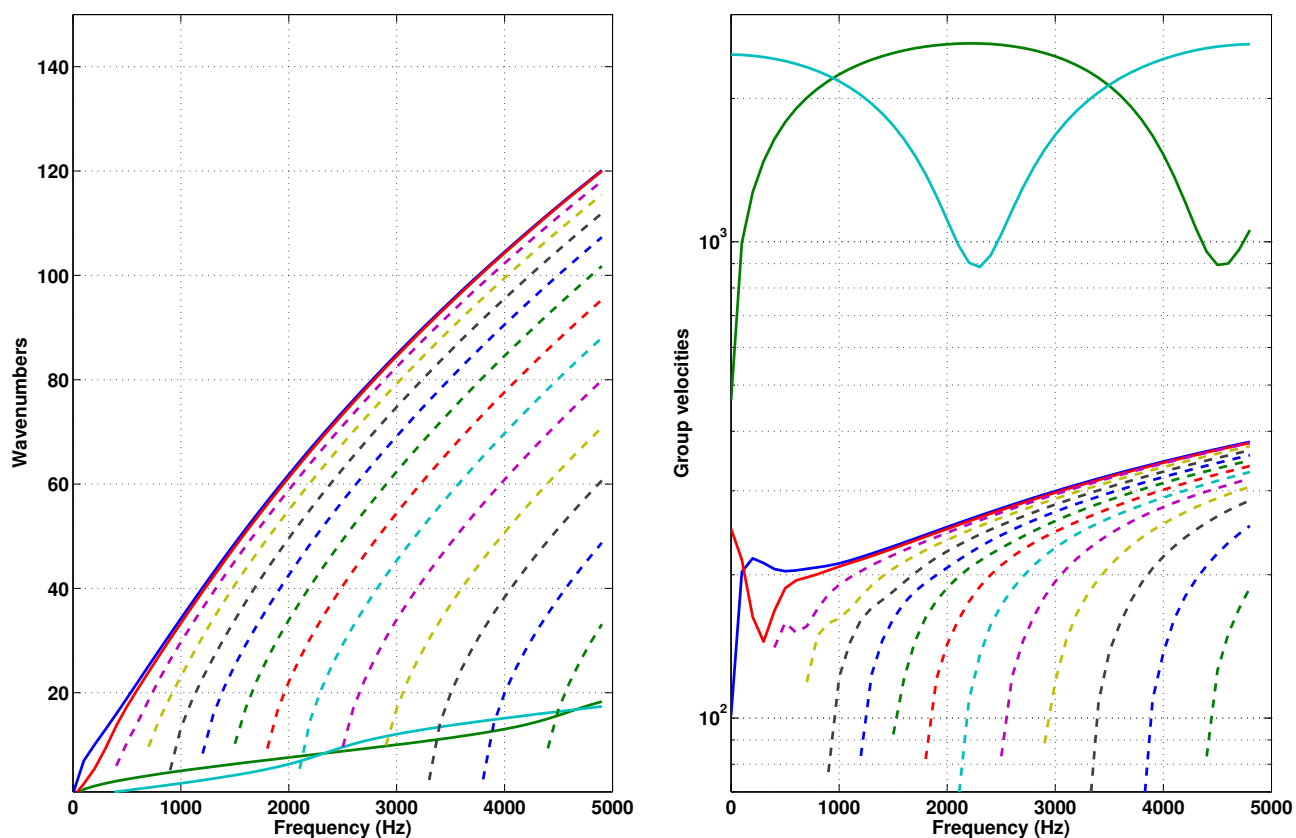


Figure 3: Wavenumbers and group velocities of propagating, positive-going waves along the main direction y .

4 REFLECTION OF PROPAGATING WAVES ON THE COUPLING ELEMENT

In this section, the wave reflection coefficients are examined for the aforementioned waveguide assuming different types of coupling element. A representation of the coupled structure is shown in figure 4.

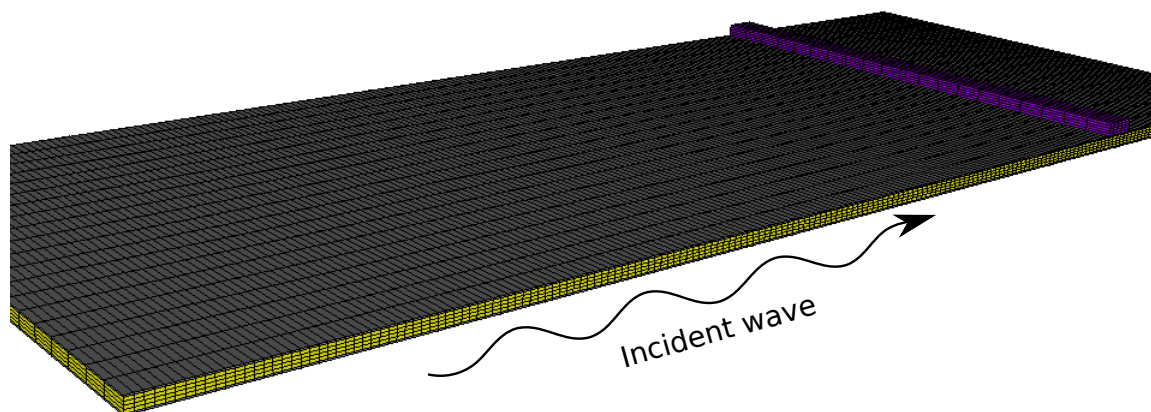


Figure 4: Description of the sandwich waveguide with coupling element involving a deposit layer of finite dimensions.

The influence of the structural loss factor μ in the waveguide is described in figure 5 for the propagating waves. Although minor differences can be noticed in the higher frequencies, the difference between undamped, moderately damped ($\mu = 0.05$) and highly dissipative waveguides is not significant on the frequency range $[0, 5000]$. Noteworthy, the high-order waves exhibit a low reflection coefficient close to their cut-on frequency, slightly exceed the first-order waves after 3000 Hz.

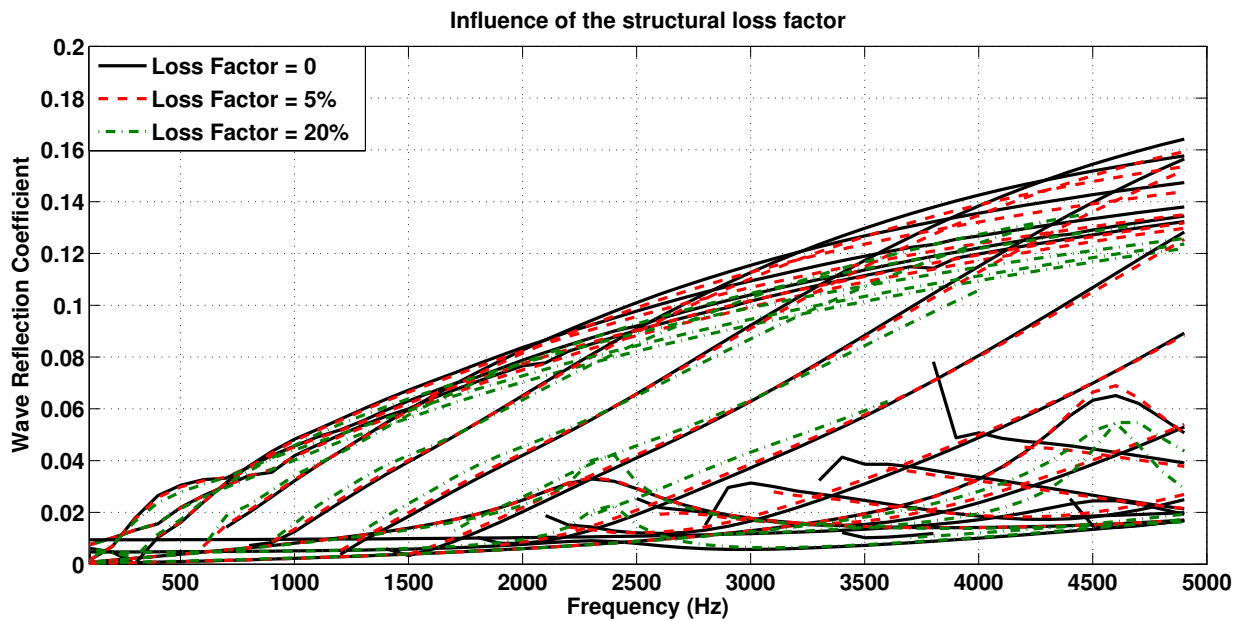


Figure 5: Comparison of different structural loss factors on the reflection coefficients of propagating waves.

This work being concerned with the sensitivity of high-order waves to different types of bonded deposits, the wave reflection is studied for two layers involving the same mass of aggregate, with different shapes. The thick layer (figure 6.a) has a thickness $h_c = 5$ mm and a length $l_c = 1$ mm while the long layer (figure 6.b) is defined by $h_c = 1$ mm and a length $l_c = 5$ mm.

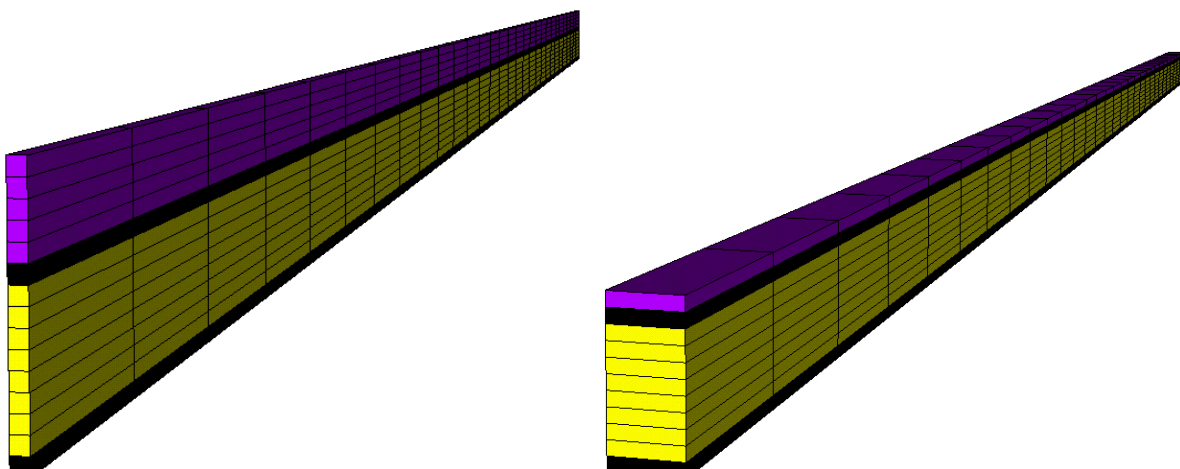


Figure 6: Coupling elements involving the same amount of deposit distributed : (a) in thickness. (b) : in length.

The wave reflections for the two layers are split between first-order and high-order propagating waves. In figure 7.a, the first-order waves exhibit close reflection coefficients, meaning that both coupling elements are expected to produce similar waves reflection. In figure 7.b, the reflections of the 2nd (\square), 3rd (\times), 6th (∇) and 8th ($-$) wave orders are compared for both long and thick layers. Noteworthy, the difference on the reflections is small for the 2nd order wave and increases after the 3rd order. The difference increases with the wave orders and becomes important for the 6th and 8th orders. Thus, the two layer's profiles can be discriminated using higher orders of flexural waves in the considered waveguide.

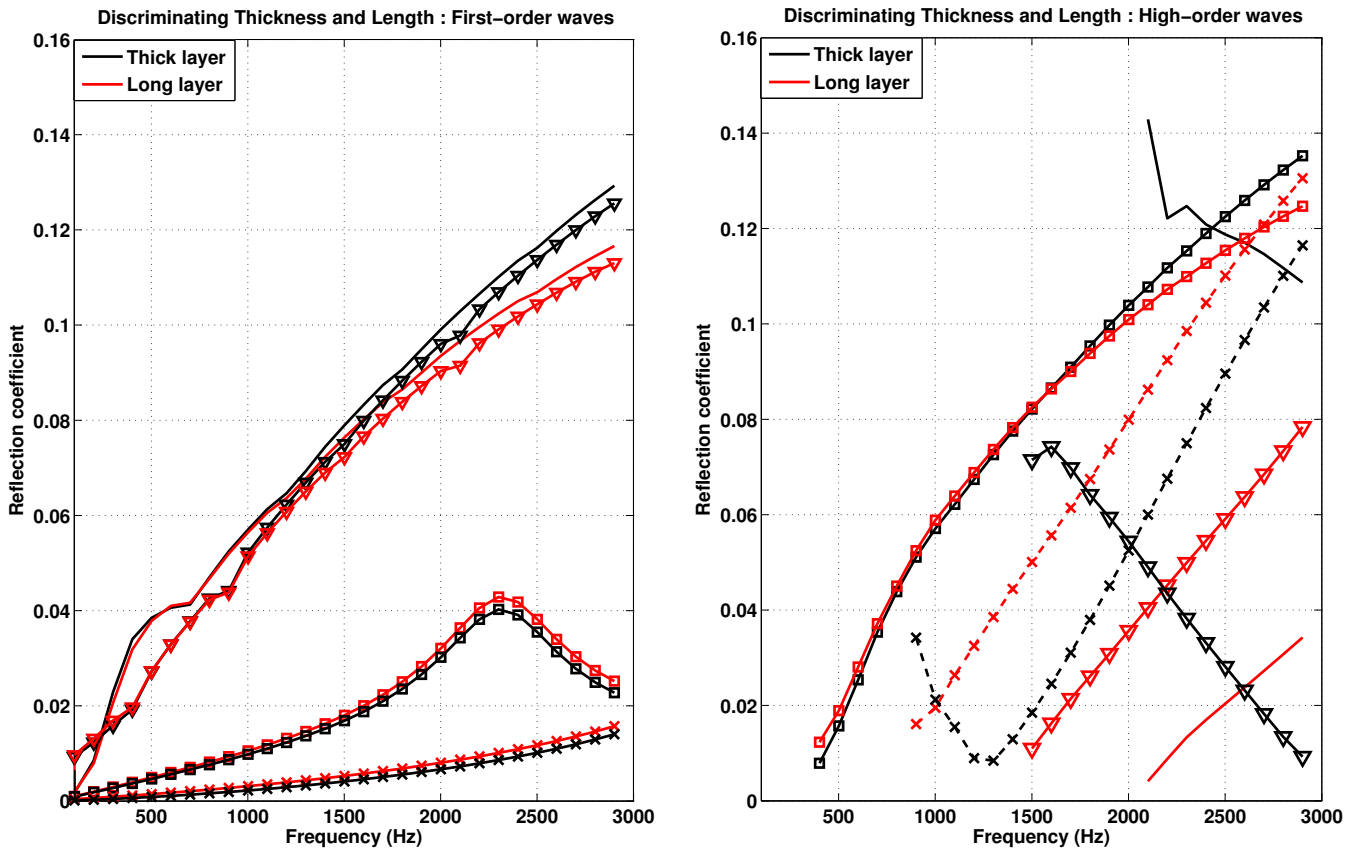


Figure 7: Influence of the deposit layer's shape on the low-order (a) and high-order (b) waves reflection coefficients.

5 DISCUSSIONS

The sandwich waveguide considered in this work exhibits numerous high-order waves associated with sinusoidal mode shapes of the cross section. Although these waves are associated with slightly higher spatial attenuations, they propagate through heterogeneous or composite waveguides with similar dispersion characteristics than first-order waves. The effect of the waveguide's structural loss factor on wave reflection coefficients was examined, since the determination of this parameter is often a concern when considering heterogeneous or composite waveguides. Important changes on the loss factor produced weak variations of the wave reflections. Still, loss factor rules the waves spatial attenuations, hence is a critical information for large-scaled waveguides.

Then, the sensitivity of high-order waves to the deposit surface distribution was exhibited, while such differentiation could not be provided by the reflection coefficients of first-order waves. Indeed, the deposit layer's thickness produced a reflection gap, associated with phase shift of the complex reflection coefficients. Therefore, it is hoped that such waves can usefully be employed for further characterization of localized defects in heterogeneous, structurally advanced or composite waveguides.

ACKNOWLEDGEMENTS

The authors would like to gratefully acknowledge Airbus Helicopters for their financial support.

REFERENCES

- [1] Felix Bloch. Über die quantenmechanik der elektronen in kristallgittern. *Zeitschrift für physik*, 52(7-8):555–600, 1929.
- [2] B. R. Mace, D. Duhamel, M. J. Brennan, and L. Hinke. Finite element prediction of wave motion in structural waveguides. *J. Acous. Soc. Am.*, 117:2835–2843, 2005.
- [3] M.N. Ichchou, J.-M. Mencik, and W. Zhou. Wave finite elements for low and mid-frequency description of coupled structures with damage. *Computer methods in applied mechanics and engineering*, 198(15):1311–1326, 2009.
- [4] O. Bareille, M. Kharrat, W. Zhou, and M. N. Ichchou. Distributed piezoelectric guided-t-wave generator, design and analysis. *Mechatronics*, 22:544–551, 2012.
- [5] C. Droz, M.N. Ichchou, and J.P. Laine. Numerical prediction of dispersion characteristics for high-order waves in composite waveguides. *Proceedings of ISMA2014*, pages 4203–4216, 2014.



MEASUREMENT OF THE VIBROACOUSTIC INDICATORS OF SANDWICH COMPOSITE STRUCTURES

A. Raef Cherif¹, B. Nouredine Atalla^{1*} and C. Andrew Wareing²

¹GAUS

University of Sherbrooke, Sherbrooke (Québec), CANADA

Email: Raef.Cherif@usherbrooke.ca, Nouredine.Atalla@usherbrooke.ca

²Bombardier Aerospace,

123 Garratt Blvd, North York M3K 1Y5, Ontario, CANADA

Email: Andrew.Wareing@aero.bombardier.com

ABSTRACT

This paper discusses the measurement of the vibroacoustic indicators of two sandwich-composite structures over a large frequency band. Several indicators are investigated including the structural wavenumber, modal density, damping loss factor, radiation efficiency, and sound transmission loss. For the first four indicators several direct and indirect measurements techniques are presented and compared. Moreover, the measured indicators are compared to analytical predictions. Results show that all measured indicators are in good agreement with theory for the studied constructions.

1 INTRODUCTION

Composite sandwich panels are used in several applications due to their favorable stiffness to weight ratios. Such panels are composed of thin composite face sheets and a shearing core. Unfortunately, these panels do not provide suitable sound insulation or good vibration damping characteristics. Indeed, they may depict a wide area of acoustic coincidence, starting at low frequencies, leading to increased radiation efficiency, which can lead in some instances to higher interior noise levels [1]. Hence, noise reduction and vibration suppression in sandwich panels pose major challenges for future aircraft design. Large numbers of references have been devoted to the prediction of the vibroacoustic behavior of such panels. A description and comparison of various analytical methods can be found in Refs. [2-3]. In comparison, there are few published studies on the experimental validation of these models [4]. The objective of this paper is to present the measurement of the various vibroacoustic indicators of two sandwich-composite structures over a large frequency band. The investigated indicators include the structural wavenumber, modal density, damping loss factor, radiation efficiency, and sound transmission loss. For the first four indicators several direct and indirect measurements techniques are presented and compared. Moreover, the measured indicators are also compared to an analytical general laminate model (GLM) [3] and to an equivalent orthotropic panel [4] predictions.

2 DESCRIPTION OF THE MEASUREMENTS

This section describes the measurement of the structural and acoustical properties of the studied panels. They consist of the wavenumber, modal density, damping loss factor, radiation efficiency and the TL. The analysis is performed in a large frequency band starting from 100 Hz to 10 kHz. A comparison between the measured parameters and the presented models are given in Section 3. A thick and a thin flat sandwich-composite panel with a Honeycomb (HC) core construction are studied (Figure 1). They are representative of an aircraft skin and trim panel, respectively. Both panels have a surface area equal to 1.5 m^2 ($L_x = 1.5\text{m}, L_y = 1\text{m}$). The thicknesses of the thick and the thin flat panels are 26.4 mm and 6.8 mm, respectively.

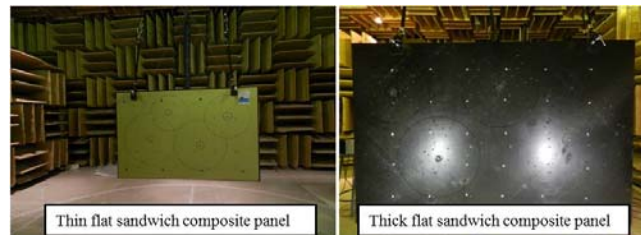


Figure 1. A thin and a thick flat sandwich composite panels.

2.1 Wavenumber measurements

Experimental tests are performed in order to determine the bending wavenumber of the composite plates using both the phase difference [5] and correlation [6] techniques. The phase difference method is based on the measurement of the phase difference φ between accelerometers located at two positions r_1 and r_2 as shown in Figure 2.a.

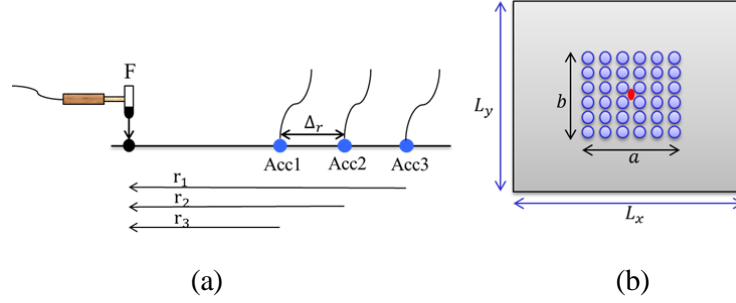


Figure 2. Measurement setup of: (a) the phase difference technique, (b) the Fourier Transform technique.

The bending wavenumber k_b is given by [5]:

$$\varphi(\text{Acc1}, \text{Acc2}) = k_b (r_2 - r_1). \quad (1)$$

This method assumes the panel flat and of infinite extent and thus doesn't take into account the reflections on the edges of the test panel. The flexural wavenumber was also measured using the correlation technique [5]. This approach is based on the calculation of the two-dimensional space Fourier transform of the surface normal velocity field. For this, the panels were freely hung in a quiet room (semi-anechoic) using flexible chords (Figure 1). A shaker was attached at the centre of the panel through a stringer and was driven by a broadband white noise signal. A scanning laser vibrometer was used to measure the velocity over a surface mesh. The used scan area was 1m by 0.75 m and consisted of 80 points along the X direction and 80 along the Y direction for a total of 6400 measurement points. A schematic is given in Figure 2.b. Measuring the plate normal velocity field, $w(x_p, y_q, \omega)$, at each point of the scanning area and using the transition to the wavenumber space leads to the flexural wavenumber [6]:

$$\hat{W}(k_x, k_y, \omega) = \frac{L_x L_y}{N^2} \sum_{p=1}^N \sum_{q=1}^N w(x_p, y_q, \omega) e^{-jk_x x_p} e^{-jk_y y_q}. \quad (2)$$

The technique is restricted by the size of the physical scan area, requires equally spaced measurement and is very sensitive to noise in the data. It is still used here to corroborate the results of the classical phase difference method.

2.2 Damping loss factor

The damping loss factor (DLF) of the panels is experimentally derived from the half-power bandwidth method (3dB method), the decay rate method (DRM) and the steady state power input method (PIM). The first technique refers to modal damping which is valid only at low frequency; when possible it is used in the current work as a validation for the other two methods. In the other two methods, the primary property of interest is the band-averaged loss factor. The DRM is based on the logarithmic decrement of the transient structural response, which is obtained from measurement of the decay of accelerometers placed on the structure's surface after the excitation is cut off. Here damping is assumed to follows an exponential decay and all modes in a third-octave band have the same damping. Hence, the damping loss factor is given, for a third-octave band of centre frequency f and slope of the decay DR in units of decibel/second, by the following expression [7]:

$$\eta_i = \frac{DR}{27.3f}. \quad (3)$$

The third method (PIM) is directly derived from Statistical Energy Analysis (SEA) power balance equation. The damping loss factor is obtained from the measurement of the power supplied to the structure and the spatially averaged square velocity produced. In steady state conditions, the average power input is equal to the average power dissipated and then the average loss factor is [8]:

$$\eta_i = \frac{P_i}{\omega E_i}. \quad (4)$$

2.3 Modal Density

The modal density of the panels is measured with the panel freely suspended inside an anechoic room to minimize radiation coupling between the panel and the room. It is obtained from the measurement of the spatially averaged input mobility following [9]:

$$n(f) = 4MRe(Y_p), \quad (5)$$

where M is the mass of the panel and $Re(Y_p)$ is the real part of the panel's input mobility $Y_p = G_{Fv}/G_{FF} \cdot G_{Fv}$ is the cross-spectrum between the force and the velocity signals at the excitation location and G_{FF} is the autospectrum of the force signal. Mass corrections must be considered when making shaker-based frequency response measurement on a lightweight structure because of the added mass coming from the impedance head [10]. In consequence, a corrected admittance Y_c was rather used in Eq.(6). It is obtained using the admittance of the impedance head Y_M , which is measured by exciting the impedance head without the driven plate:

$$Y_c = Y_p \left/ 1 - \frac{Y_p}{Y_M} \right. \quad (6)$$

The modal densities of the panels were obtained by averaging the modal densities measured at the same four locations used for the measurement of the damping loss factor. The modal densities were also estimated from the measured wavenumbers using [4]:

$$n(\varphi, \omega) = \frac{A_p}{2\pi^2} \frac{k_s(\varphi, \omega)}{|c_g(\varphi, \omega)|}, \quad (7)$$

where $n(\varphi, \omega)$ is the angular distribution of the modal density and $c_g(\varphi, \omega) = d\omega/dk$ is the group velocity. The results of both measurement methods will be compared to predictions in section 3.

2.4 Radiation efficiency

There are several methods to measure the radiation efficiency of the panels. In this work, an indirect method based on an experimental SEA model of the panel freely hanged in a reverberant room was used. It is obtained by studying energy flow relations between the structure and the reverberation room. The method is based on solving a two subsystems SEA equation where the tested panel is defined as subsystem 1 and the reverberant room as subsystem 2, respectively:

$$\omega \begin{bmatrix} \eta_1 + \eta_{12} & -\eta_{21} \\ -\eta_{12} & \eta_2 + \eta_{21} \end{bmatrix} \begin{Bmatrix} E_1 \\ E_2 \end{Bmatrix} = \begin{Bmatrix} P_1 \\ P_2 \end{Bmatrix}, \quad (8)$$

where η_{ij} is the coupling loss factor (CLF) between subsystems i and j (with $j \neq i$) and η_i is the damping loss factor of subsystem i .

The radiation efficiency σ is related to the CLF between the tested panel and the reverberant room. Assuming both faces of the panel to radiate equally, $\eta_{12} = 2\eta_{rad}$ is thus twice the radiation coupling and in consequence [6]:

$$\sigma = \frac{1}{2} \frac{\omega M}{\rho_0 c_0 A_p} \eta_{12}. \quad (9)$$

In the presented results, the CLF η_{12} is obtained from the inversion of the SEA matrix:

$$\omega \begin{bmatrix} \eta_{11} & -\eta_{21} \\ -\eta_{12} & \eta_{22} \end{bmatrix} = \begin{bmatrix} A_{11} & A_{12} \\ A_{21} & A_{22} \end{bmatrix}^{-1}, \quad (10)$$

where coefficients A_{ij} denote the ratio of the energy (response) of subsystem i to the input power to (excitation of) subsystem j and $\eta_{11} = \eta_1 + \eta_{12}$; $\eta_{22} = \eta_2 + \eta_{21}$. The radiation efficiency of the panel when freely hanged in a semi-anechoic room was also measured for cross validation purposes. It is derived from the measurement of the spatially averaged squared velocity $\langle v^2 \rangle$ and the radiated sound power. The radiation efficiency is defined as the proportionality between radiated sound power P_{rad} and the spatially averaged squared velocity $\langle v^2 \rangle$ over radiation surface A_p :

$$\sigma = \frac{P_{rad}}{\rho_0 c_0 A_p \langle v^2 \rangle}. \quad (11)$$

2.5 Transmission loss

The TL tests were performed in a semi-anechoic–reverberant transmission loss suite. The measurement follows ISO 15186-1:2000 standard [11]. The panels are clamped in a frame between a reverberant and a semi-anechoic room. White noise was generated in the reverberant room using six loudspeakers and the average sound power is captured using a rotating microphone. On the semi-anechoic side, the sound intensity is measured using an intensity probe with a 6 mm spacer between two 1/4-in microphones. The transmission loss of the structure is given by [4]:

$$TL = L_p - L_i - 6. \quad (12)$$

L_p is the average SPL in the source room. L_i is the averaged intensity level over the measurement surface in the receiving room.

3 RESULTS AND DISCUSSION

Comparison between the prediction and experiments are presented and discussed in this section. Damping loss factor, wavenumber, modal densities, and the radiation efficiency are measured for thin and thick composite panels and compared to analytical (general laminate model, equivalent orthotropic panel) predictions.

3.1 Wavenumber

Wavenumber results of the thick and thin composite sandwich panels are shown in Figure 3, respectively. For each panel, the wavenumber curves measured along X and Y directions using the phase difference and correlation techniques are compared. Note that in Figure 3, the acoustic wavenumber (straight line) is also presented to show the acoustic coincidence zone of the panels.

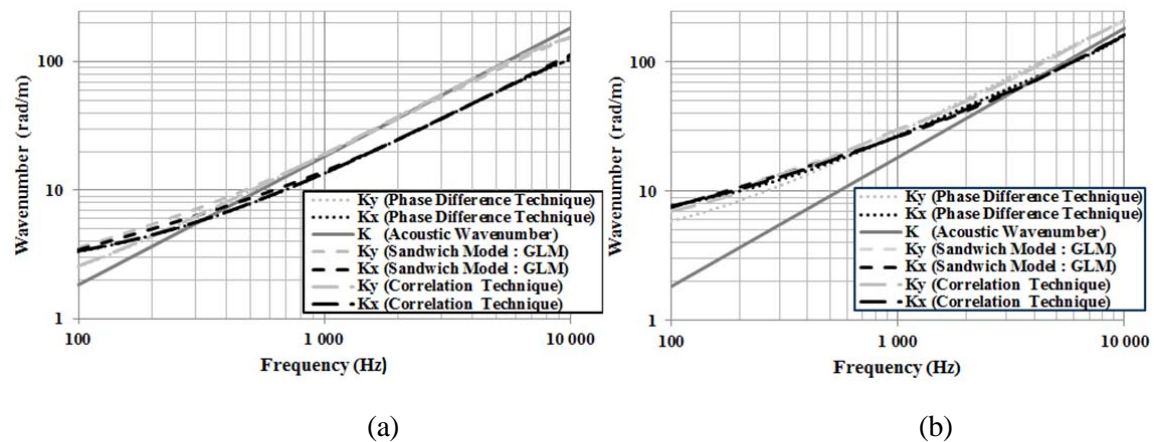


Figure 3. Measured vs. predicted wavenumbers of: (a) the thick panel, (b) the thin sandwich panel.

Overall, the comparisons between the experimental and analytical results are good for both methods. At high frequency, the correlation technique gives a better estimation due to fine mesh used in the scan. However, the method seems less accurate at low frequencies, especially for the thick panel where an overestimation is observed.

3.2 Damping loss factor

Damping loss factor results using the half-power bandwidth method (-3dB), the decay rate method and the power input method are shown in Figure 4. The half-power bandwidth method (-3dB) results are used only as a validation tool when applicable.

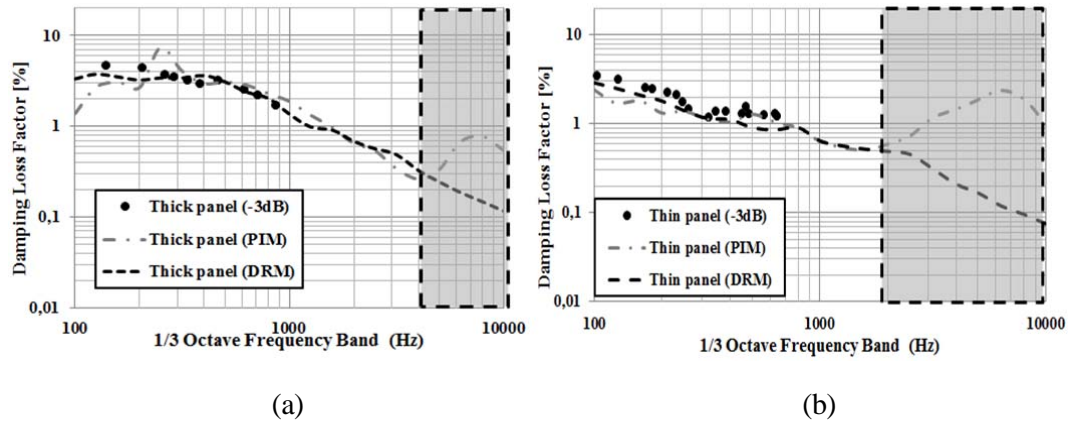


Figure 4. Measured damping loss factor of: (a) the thick panel, (b) the thin sandwich panel.

For both panels, it is observed that the DRM and the PIM agree well at mid frequencies. However, at low frequency [100–300 Hz], the damping loss factor is better predicted by the DRM compared to the PIM, the reason being the low mode count of the two panels. At high frequency, damping loss factor is also well predicted by the DRM. Meanwhile, the PIM fails (Gray area in Figure 4). The cause was related to an experimental limitation in injecting power into the system in this frequency region. In consequence, in the prediction of the transmission loss, the DRM results will be used.

3.3 Modal Density

Figure 5 shows comparisons of the modal density predicted by the GLM model to measurements (using Eq. (5) for the Input Mobility method and Eq. (7) for the Wavenumber method) for the thick and thin composite sandwich panels, respectively.

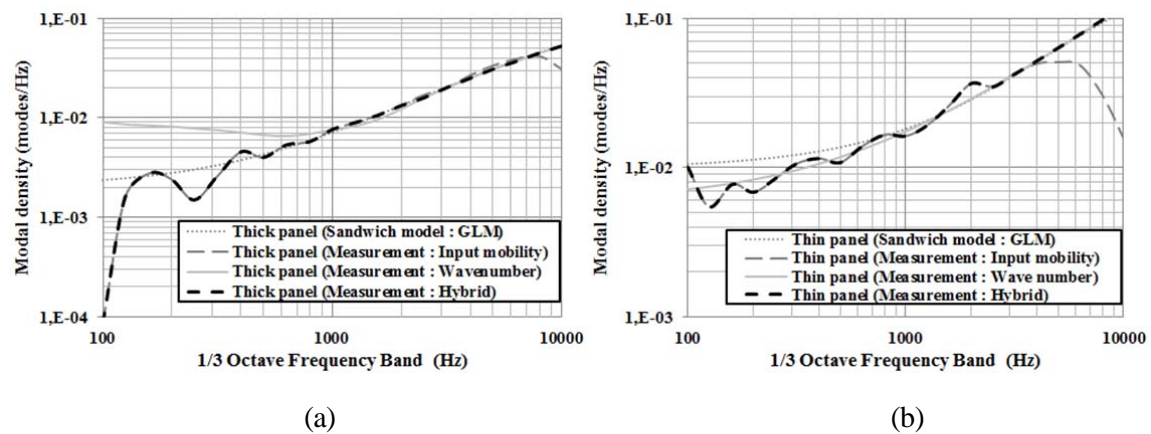


Figure 5. Measured vs. predicted modal densities of: (a) the thick panel, (b) the thin sandwich panel.

At low and mid frequency, the predicted modal density compares well with measurements using the Input Mobility method for both panels. At higher frequencies, the measurement fails, a consequence again of the difficulty in injecting the power to the panels with the used shaker. On the other hand, good comparison is obtained for both panels at these high frequencies using the wavenumber method. This is logical because a fine scan is used. However, a difference between the measurement and theoretical values are observed at low frequencies, especially for the thick

panel where an overestimation is observed. The cause was related to the previously mentioned limitation in measuring the wavenumber. In consequence, better results are obtained using a Hybrid method which combine the Input Mobility method at low frequency and the Wavenumber method at mid and high frequency (black dotted line in the Figure 5). The Hybrid method results agree well with theory over a large frequency band [200Hz to 10 kHz].

3.4 Radiation efficiency

Fig. 6 shows the comparisons between predictions using the GLM model and measurements for the thick and thin panels, respectively. As discussed before, measurement using both the classical method [Eq.(11)] and experimental SEA [Eq.(9)] were performed and are compared in the two figures.

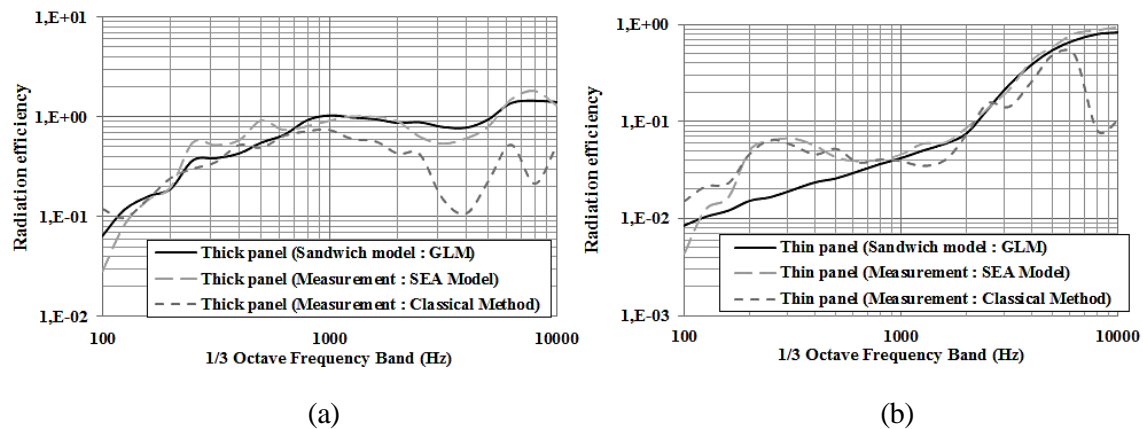


Figure 6. Measured vs. predicted radiation efficiency of: (a) the thick panel, (b) the thin sandwich panel.

Overall, it is observed that the comparison is fair for both panels between prediction and measurements using the SEA based measurement method. However, the SEA based methodology is limited at low frequencies due to the low mode count. On the other hand, and for both panels, the classical measurement method diverges at high frequencies. The cause was related again to an experimental limitation in injecting power to the system in this frequency region.

3.5 Transmission loss

The comparison between tests and predictions is shown in Figure 7. Two prediction methods are shown. In the first, the surface impedance of the panel calculated using the GLM model is used to estimate the TL. In the second, an equivalent orthotropic panel model is used. For both cases, to account for the damping added by the installation of the panels in the test window, the damping loss factor measured using the decay rate method with the panels mounted in the window was used in the predictions.

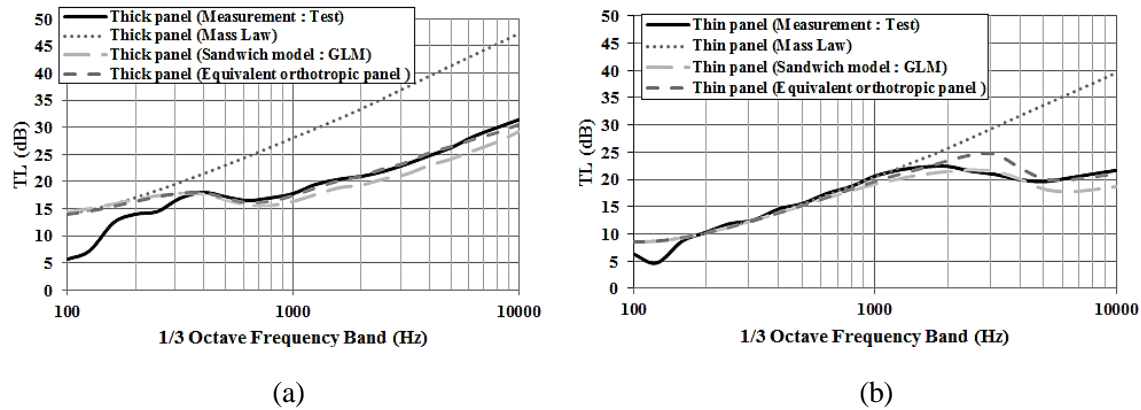


Figure 7. Measured vs. predicted transmission loss of: (a) the thick panel, (b) the thin sandwich panel.

Figure 7.a shows that the TL prediction of the thick sandwich panel using the equivalent orthotropic panel correlates well with the test results. Predictions using both the measured and predicted wavenumbers leads to the same results. However, the use of the full GLM model underestimates the TL, by approximately 2 dB, starting at the onset of the coincidence region (around 500 Hz). For the thin sandwich panel (Figure 7.b), both models are in good agreement with measurements in the mass-law region. Sandwich model predict well the critical frequency region (around 4000 Hz), while the equivalent panel model overestimates this region. At much high frequencies, the sandwich model tends to underestimate the TL. For this panel, all the above discussed discrepancies are traced to the uncertainties in the measurement of the panel's damping loss factor.

4 CONCLUSION

This paper discusses the measurement of the vibroacoustics indicators of two sandwich-composite structures over a large frequency band. Various experimental methods were used and compared to analytical predictions. It is shown that the GLM model predict very well the wavenumber (dispersion curves), the modal density and the radiation efficiency of the two tested panels. The prediction of the TL while acceptable was however found less satisfactory for the thick panel. The paper also shows that a simple equivalent orthotropic panel model predict with accuracy the transmission loss of the two studied sandwich panels.

ACKNOWLEDGEMENTS

This work was supported by grants-in-aid from the Natural Sciences and Engineering Research Council of Canada (N.S.E.R.C.). Bombardier Aerospace is acknowledged for contributing panels and materials for the tests.

REFERENCES

- [1] U. Orrenius. Prediction and control of sound transmission through honeycomb sandwich panels for aircraft fuselage and train floors. 17th International Congress on Sound and Vibration, Cairo, Egypt, 117-124, 2010.
- [2] T. Wang, V.S. Sokolinsky, S. Rajaram, and S. Nutt. Assessment of sandwich models for the prediction of sound transmission loss in unidirectional sandwich panels. *Applied Acoustics*. 66: 245-262, 2005.
- [3] S. Ghinet, and N. Atalla. Modeling thick composite laminate and sandwich structures with linear viscoelastic damping. *Computers and Structures*. 89:1547-1561, 2011.
- [4] R. Cherif, and N. Atalla. Experimental investigation of the accuracy of a sandwich model. *Journal of the Acoustical Society of America*. 137(3):1541, 2015.
- [5] J. H. Rindel. Dispersion and absorption of structure-borne sound in acoustically thick plates. *Applied Acoustics*. 41(2):97-111, 1994.
- [6] A. N. Thite, and N. S. Ferguson. Wavenumber Estimation: Further Study of the Correlation Technique and Use of SVD to Improve Propagation Direction Resolution. ISVR Technical Memorandum, 2004.
- [7] R. H. Lyon, and R. G. DeJong. Theory and application of statistical energy analysis. Butterworth-Heinemann, Boston, second edition edn, 1995.
- [8] D. A. Bies, and S. Hamid. In situ determination of loss and coupling loss factors by the power injection method. *Journal of Sound and Vibration*. 70(2):187-204, 1980.
- [9] B. L. Clarkson. The derivation of modal densities from point impedances. *Journal of Sound and Vibration*. 77(4):583-588, 1981.
- [10] K. Renji, and M. Mahalakshmi. High frequency vibration energy transfer in a system of three plates connected at discrete points using statistical energy analysis. *Journal of Sound and Vibration*. 296(3):539-553, 2006.
- [11] ISO 15186-1:2000. Acoustics – “Measurement of sound insulation in buildings and of building elements using sound intensity” – Part 1: Laboratory measurements. 1-25, 2000.



LOW VELOCITY IMPACT ON LAMINATE COMPOSITE WITH THERMOPLASTIC RESIN

C. Bouvet¹, P. García Pérez^{2*}, F. Dau² and P. Peres³

¹Université de Toulouse; ICA (Institut Clément Ader)
ISAE (Institut Supérieur de l'Aéronautique et de l'Espace), 31055 Toulouse Cedex, FRANCE
Email: christophe.bouvet@isae.fr

² I2M (Institut de Mécanique et d'Ingénierie)
ENSAM (École Nationale Supérieure d'Arts et Métiers), 33405 Talence Cedex, FRANCE
Email: pablo.garcia-perez@ensam.eu, frederic.dau@ensam.eu

³ Airbus Defence and Space, Établissement d'Aquitaine
BP 20011, 33165 Saint-Médard-en-Jalles Cedex, FRANCE
Email: patrick.peres@astrium.eads.net

ABSTRACT

Composite materials have been increasingly used in airframe and space applications because of their advantageous mechanical properties. Nevertheless, during the structure's life, damage induced by low velocity impact, such as matrix cracks, fiber breakage and delamination can drastically decrease the residual mechanical characteristics of the structure. There is a strong current trend towards a greater use of high-performance thermoplastics in composites structures for damage tolerance reasons. In this study, unidirectional carbon/PEEK laminate has been subjected to impact and the damage has been studied using C-scan investigations. The experimental results show higher delaminated area than expected. The damage morphology presents high delaminated interfaces situated at mid-thickness of the plate. These delaminations have also the characteristic to be asymmetric whereas the boundary conditions are symmetric. Afterwards, this paper shows that a "discrete ply model" is able to simulate the complex three-dimensional damage patterns in composite laminates with PEEK resin subjected to low velocity impact. Nevertheless, it is necessary to use low rate on the mode II interlaminar fracture toughness to recover the experimental results. The objective is together to simulate the impact damage and to better understand the unclassical damage morphology observed during impact with thermoplastic material.

1 INTRODUCTION

Nowadays the use of composite materials is fastly growing in potential applications in aerospace and automotive industries. Nevertheless, impact damage in composite structures may lead to significant reduction in structure compressive strength and this damage may remain unnoticed below the Barely Visible Impact Damage threshold. Damage in composite materials and structures involves multiple failure modes such as fibre breakage, fibre pullout, delamination between plies, matrix cracking, fibre-matrix debonding, etc.

Many computational methods and experimental characterization techniques are developed in the impact prediction of composite materials to measure the impact resistance and thereby to explain the failure criteria. Impact damage behaviors are very difficult to predict because they depend on many parameters. IM7/PEEK is a carbone fibre reinforced thermoplastic composite unidirectional laminate. It presents inherently nonlinear material properties with greater residual strength after impact, higher toughness, better delamination resistance and can absorb a greater quantity of energy in an impact and crash than using carbone fibre reinforced thermosetting composite.

In the current paper, a 3D damage and failure model of composite laminates subjected to low-velocity impact damage is described. The modelling of impact damage and its validation for IM7/PEEK laminate composite plate are presented.

2 IMPACT DAMAGE MODEL

To capture the effects of progressive damage and failure on laminated composite structures, failure modes in both the fibre and matrix resin must be considered. The model presented here considers fibre failure in tension and compression, matrix cracking taking into account permanent indentation and delamination. It is based on the use of cohesive zone models to capture delamination between plies of different orientation and transverse matrix cracking in cross-ply. The model is developed and implemented into Explicit/Dynamic Abaqus code with a VUMAT subroutine. The damage and failure model of composite laminates subjected to low-velocity impact is now presented.

A damage criterion for the fibre failure is derived from the energy balance based on crack band theory to dissipate a constant energy release rate per unit area in the 3D continuum element [1]. This energy-based criterion defines a stiffness degradation model that is introduced both in tension and compression. The linear relationships between stresses and strains in the volumic element represents the evolution of the damage in the fibre [2].

The fibre compressive failure behavior is more complicated than in tension. Crack initiation in compression is due to kink band followed by the crushing of fibres packages. Therefore, a compressive mean crushing stress is applied as a plateau to complete the law. Moreover, during the plateau, plasticity is also taken into account to prevent compressive strain from returning to zero to unloaded state [3].

Matrix cracking refers to the onset of damage at a material point which is based on Hashin's theory. The Hashin criteria is calculated in the neighboring volume elements of the zero-thickness cohesive element. This criterion is assessed at each time increment: the interface stiffness between two volume elements becomes zero if the criterion is reached and otherwise, it remains intact.

Permanent indentation is an important prognostic indicator of occurred impact. It reflects a non-closure of crack which is the result of the formation of debris inside matrix cracking. In this model, a pseudo-plasticity law has been used in order to predict the permanent indentation. It is experimentally observed that the permanent indentation remains approximately 30 % of maximum crack opening in both transversal and out-of-plane directions [4].

A failure mode which is widely observed in laminate composites is delamination between adjacent layers or plies of different orientation. This mode is commonly modeled with a cohesive interface elements based on fracture mechanics. Zero-thickness 3D cohesive elements are used to joint lower and upper ply volume elements. A failure criterion of interface element under mixed mode condition is introduced in the model. An exponential softening law is chosen to avoid the shock of the final fracture by introducing a complex state variable to track the extent of damage accumulated at the interface.

3 EXPERIMENT AND SIMULATION

In order to validate the impact damage model described above, an experimental low-velocity impact test was carried out. Postmortem evaluation of the damage delamination is performed through C-scan inspection and visual inspection of the permanent indentation.

Impact test was performed using a drop tower system with a 2,028 kg mass and 16 mm spherical impactor. Composite laminate plates of 150x100 mm² with 4,4 mm thick were made from carbon fiber/PEEK resin prepreg using an unidirectional symmetrical stacking sequence [0₂/45₂/90₂/-45₂]_{2S}. The detailed material properties of the composite plate are summarized in Table 1.

E_l^t (GPa)	Tensile Young's modulus in fibre direction	150
E_l^c (GPa)	Compressive Young's modulus in fibre direction	140
E_t (GPa)	Transverse Young's modulus	9
G_{lt} (GPa)	Shear modulus	5
S_{nt} (MPa)	Transverse failure stress	60
S_{tt} (MPa)	Shear failure stress	160
X_{crush} (MPa)	Longitudinal compressive mean crushing stress	250
ν_{lt}	Poisson's ratio	0.3
ε_0^t	Tensile strain in fibre direction at damage initiation	0.0167
ε_0^c	Compressive strain in fibre direction at damage initiation	-0.0096
G_I^t (N mm ⁻¹)	Fracture toughness for mode I in traction	80
G_I^c (N mm ⁻¹)	Fracture toughness for mode I in compression	40
G_I^d (N mm ⁻¹)	Interface fracture toughness for opening mode (I)	0.5 → 1
G_{II}^d (N mm ⁻¹)	Interface fracture toughness for shear mode (II and III)	2 → 0.4

Table 1. Material properties of carbon fiber/PEEK laminate for numerical simulations

Firstly, a numerical simulation of 20 J impact was performed with $G_I^d = 1 \text{ N mm}^{-1}$ and $G_{II}^d = 2 \text{ N mm}^{-1}$ but the results are not accurate with respect to the experiment. A second simulation was performed with interface fracture toughness values of $G_I^d = 0,5 \text{ N mm}^{-1}$ and $G_{II}^d = 1 \text{ N mm}^{-1}$. Figure 1 shows the comparison of the delaminated areas through the thickness obtained from the experimental test (a) and impact damage model (b). The model under-predicts the delaminated areas.

It has been reported the effects of shear displacement rate on the mode II interlaminar fracture toughness in graphite/PEEK laminates [5]. It is shown that the PEEK material exhibits ductile crack growth at low rates and brittle crack growth at high rates. The change on fracture mechanism resulted in a decrease from 1,9 to 0,4 N mm⁻¹.

Keeping G_I^d to 1 N mm⁻¹ and decreasing G_{II}^d to 0,4 N mm⁻¹ as explained, the shape and distribution of delaminated areas are in better agreement between experimental and numerical results, as shown in Figure 1 (a) et (c). The difference between numerical results is mostly associated with the energy required to propagate the delamination in mode II. The model is able to predict the asymmetrical area and principal orientations of the delamination without introducing the asymmetric damage mode in the constitutive equations.

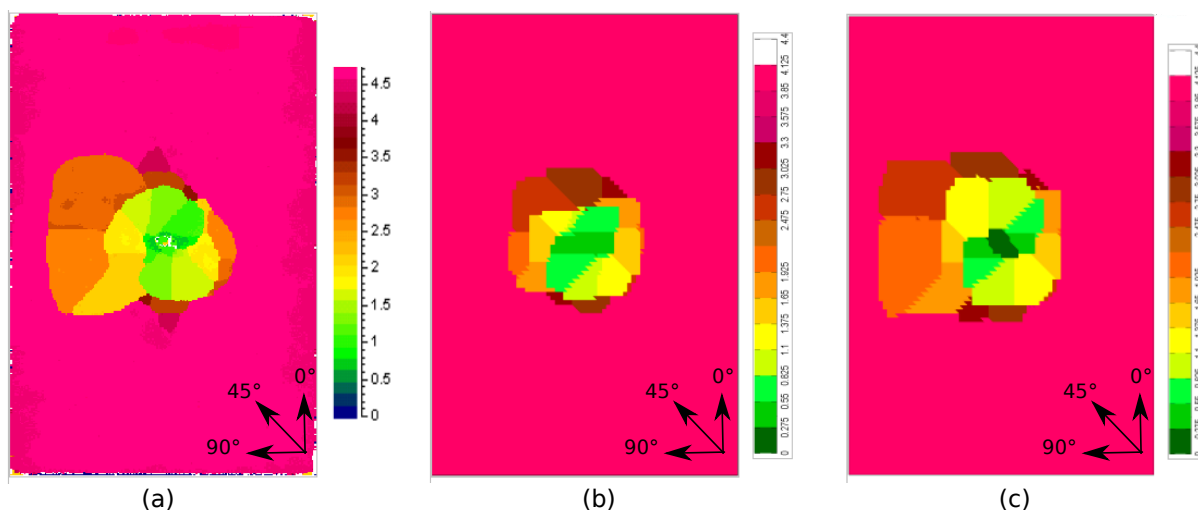


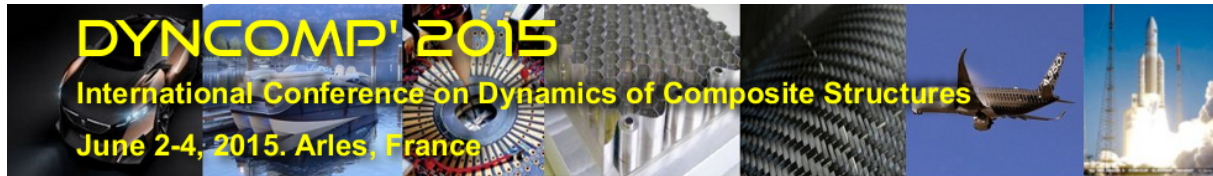
Figure 1: C-scan delamination area from impacted side: (a) experiment (b) simulation with $G_{II}^d = 1 \text{ N mm}^{-1}$ et (c) simulation with $G_{II}^d = 0,4 \text{ N mm}^{-1}$

4 CONCLUSION

The capability of a cohesive-based impact damage model is investigated to predict more complex three-dimensional damage patterns induced by impact. The numerical simulations were validated against experimental results. The proposed formulation has shown a good ability to predict the low-velocity impact behavior of IM7/PEEK composite laminates. The results reported in [5] are verified through two simulations with different constant values of G_{II}^d . In order to capture the main differences between the predictions and experiments, the observed Ultrasonic C-Scan delamination size and shape at interfaces are reported and discussed. Further investigations are needed to clarify the main reasons of the discrepancies.

REFERENCES

- [1] Bazant Z.P. and OH D.H. Crack band theory for fracture of concrete. *Materials and Structures*, 16:155–177, 1983.
- [2] Samuel Rivallant, Christophe Bouvet, and Natthawat Hongkarnjanakul. Failure analysis of CFRP laminates subjected to compression after impact: FE simulation using discrete interface elements. *Composites Part A: Applied Science and Manufacturing*, 55:83–93, 2013.
- [3] Benjamin Ostré, Christophe Bouvet, Clément Minot, and Jacky Aboissière. Edge impact modeling on stiffened composite structures. *Composite Structures*, 2015.
- [4] N. Hongkarnjanakul, S. Rivallant, C. Bouvet, and A. Miranda. Permanent indentation characterization for low-velocity impact modelling using three-point bending test. *Journal of Composite Materials*, 48(20):2441–2454, August 2013.
- [5] A.J. Smiley and R.B. Pipes. Rate sensitivity of mode II interlaminar fracture toughness in graphite/epoxy and graphite/PEEK composite materials. *Composites Science and Technology*, 29:1–15, 1987.



COUPLING PHENOMENA ON HEAVY VEHICLES: MEDIUM FREQUENCY EXPERIMENTAL ANALYSIS AND NUMERICAL APPLICATIONS

A.R. Tufano^{1,2*}, E. Laligant¹, M. Ichchou¹, O. Bareille¹, C. Braguy², and N. Blairon²

¹Laboratoire de Tribologie et Dynamique des Systèmes
Ecole Centrale de Lyon, 36 avenue de Collongue, F-69134 Ecully, FRANCE
Email: anna-rita.tufano@doctorant.ec-lyon.fr, anna.rita.tufano@volvo.com

²Noise and Vehicle Dynamics, Volvo Group Trucks Technology
99 route de Lyon, F-69800 St Priest, FRANCE

ABSTRACT

Driveline vibrations of a truck are a cause of strong discomfort for drivers, and have to be investigated in early design stages. In order to develop analytical and numerical tools for the prediction of vibration of such a heterogeneous and composite structure, a deep knowledge of the physical phenomena involved is imperative. Few experimental studies have been performed on truck vibrations, and they mostly concerned single components of a vehicle. Therefore an Experimental Modal Analysis (EMA) of a complete truck has been performed in order to observe vibratory phenomena and determine influencing parameters involved in the vibration transmission. Low Frequency and High Frequency ranges were located, and the so called Medium Frequency range was determined. In the latter, interesting transition and interaction phenomena take place, which are thought to have a first order influence on vibration transmission over trucks.

The results of the test campaign are used to validate a pre-design Finite Element model of the complete vehicle, which is subsequently used to investigate the phenomena observed in the experimental phase.

1 INTRODUCTION

Experimental Modal Analysis ([1], [2]), one of the best known techniques to characterize the dynamic behaviour of a structure, is commonly applied in the heavy vehicle industry ([3], [4], [5]). Though, studies usually focus on the dynamics of single parts of a vehicle and no EMA of a whole truck exists, to the authors' knowledge, in the literature; that is why a test campaign was launched, with a twofold objective: give a preliminary idea of the dynamic phenomena found in a heavy vehicle and provide an experimental reference for the validation of a numerical model.

The numerical model will be used for assessments on vibratory performance estimators. The need for a numerical model to perform this kind of assessments is of primary importance for truck analysis, due to the large variability in truck configurations, which makes the study of every specimen unachievable.

Along with EMA, another test campaign has been launched, to perform the so called Operational Modal Analysis, or output-only Modal Analysis. Results were not promising, both from the point of view of their quality and from the point of view of the comparison with modal parameters identified through hammer tests. This bias can originate from incorrect hypotheses formulated on the current excitation, or from modifications that the structure encompasses when excited in its real operating conditions. The authors decided to rely only on hammer test results in view of future exploitation for numerical models validation.

2 TEST SETUP AND CONFIGURATIONS

A heavy vehicle is roughly made up of a chassis, a cabin, a powertrain, axles, and elements suspended to the chassis (Fig. 1). It appears as a composite structure, from the point of view of the architecture and of the dynamic couplings among its components, in other words, it is a composite structure on a macroscopic scale (opposed to the microscopic scale where the composite nature of some materials shows up).

The chassis constitutes the main transfer path for vibration originating from the powertrain. This is the reason why the current analysis focuses on the chassis; all the elements suspended to the chassis are also considered important, because of the way they are supposed to modify the dynamic stiffness of the former. The test campaign has been performed on a Medium duty truck, having a Gross Vehicle Weight (GVW) of 12 tonnes.

Two configurations have been studied:

- Configuration A: unloaded truck;
- Configuration B: truck loaded with superstructure.

The superstructure is used to simulate the truck payload; it is a welded frame that approximately reproduces the torsional stiffness of common truck payloads. The superstructure has been tested itself in free-free boundary conditions, to determine its modal properties.

Impact testing is performed on these two configurations, and respective modal parameters are then compared; comparison between configurations A and B allows drawing conclusions on the effect of chassis stiffness modifications and mass addition.

The truck has been tested while lying on its tyres; indeed, it is assumed that free-free boundary conditions are not attainable (based on the rule of thumb stating that rigid body frequencies should be below 10% of the first flexible mode, [1], [2]), thus the boundary conditions are rather chosen to fit the numerical model conditions. As a matter of fact, testing a massive structure on its suspensions is a common practice in Ground Vibration Testing of aircrafts.

The structure is excited through an impact hammer, heavy enough to inject a sufficient amount of energy into the structure. Measurements are performed on the frequency range [0 Hz

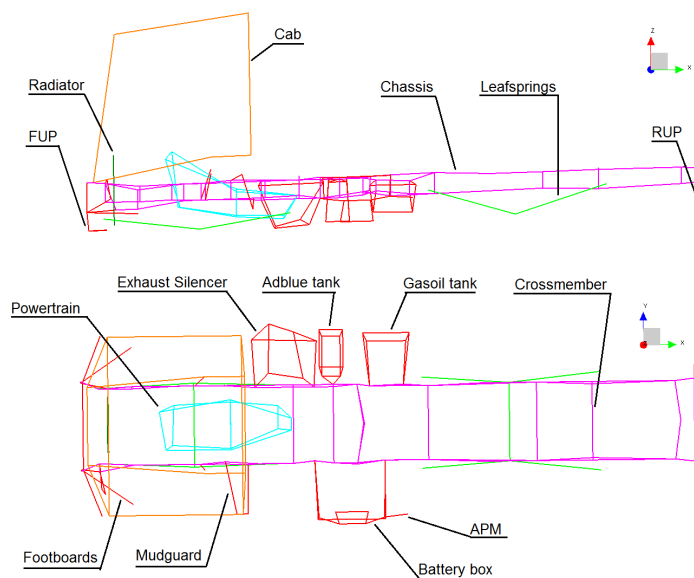


Figure 1: Truck geometry

- 256 Hz]. Pre-test check of input excitation allows limiting the validity of Frequency Response Function's (FRF) to the frequency range [0 Hz - 160 Hz]: a drop of 10 dB in the power spectrum of the injected force highlights the value of this limiting frequency, based on a common rule of thumb ([1], [2]).

A compromise between testing time and testing accuracy leads to choose a frequency step of 0.25 Hz for all acquisitions, thus causing a limitation with respect to the estimation of damping at low frequencies; the authors evaluate that a damping ratio of 1% (a realistic value for such a structure) could be estimated with sufficient accuracy only above 25 Hz. Thus the damping estimation is affected by a certain degree of inaccuracy.

The structure is impacted at two reference points so as to excite the highest possible number of modes. Additional measurements are also performed with input forces on several suspended elements: these sets of measurements serve to inject energy specifically to these components, thus estimating their dynamic characteristics in a boundary condition correspondent to the attachment to the chassis; this boundary condition is intermediate between a fixed interface, and a free interface.

FRF's were acquired by roving tri-axial accelerometers over 143 points (most of whose lied on the chassis). Mass loading from accelerometers was considered to be negligible, because of the lightness of accelerometers (ICP sensors weighting 10 g are used) with respect to the test object.

Modal parameters are identified through the commercial software LMS[®] Tes.Lab, and a poly-reference Least-Squares Complex Frequency-domain (LSCF) estimation method (PolyMax) is exploited, [6]. The sum of all the measured FRF's and Complex Mode Indicator Functions (CMIF) are fed to the PolyMax algorithm, and physical resonances are detected thanks to a stabilization diagram.

3 DYNAMIC CHARACTERIZATION OF THE UNLOADED TRUCK

The analysis of the sum of all FRF's brings to light a fundamental information: in the frequency range considered, the structure presents well separated behaviours that are typical of the Low Frequency (LF) and High Frequency (HF) ranges. Besides, a transition range commonly called

Medium Frequency (MF) range is observable (Fig. 2). The LF behaviour is characterized by the presence of rigid body modes of the vehicle and of its main suspended constituents (cabin, powertrain); modal density is quite high. The MF behaviour is dominated by elastic deformation modes of the chassis, coupled with all the other components; modal density is lower than in the LF range, while damping is increasingly high. The HF behaviour is characterized by a sort of structural diffuse field; here only local deformation shapes are visible, and modal density is extremely low.

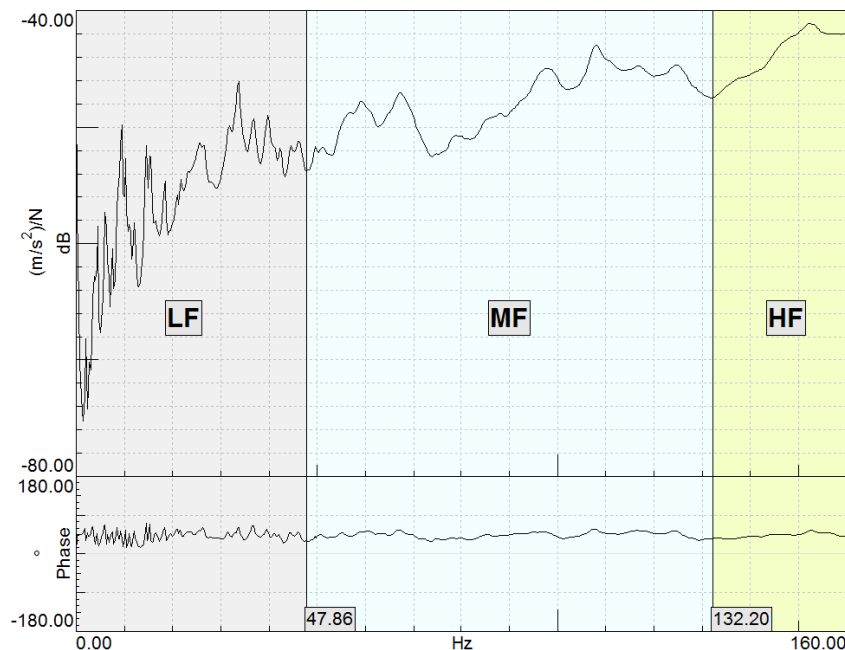


Figure 2: Sum of all the measured FRF's and characteristic frequency ranges.

Two main conclusions can be drawn, these being:

- to study whole-body vibrations of a complete truck in an early design stage, all the information can be found in the frequency range [0 Hz - 160 Hz]; phenomena at higher frequency are barely an extension of the HF behaviour, or local phenomena that attain to the analysis of limited parts of the truck;
- a transition frequency can be defined, lying at about 50 Hz, where the behaviour of the structure changes from global to local.

The transition from global to local behaviour, or equivalently from long wavelength to short wavelength wave propagation, happens in the MF domain; here, the interaction between stiffer and more flexible components (the suspended elements and the chassis) is thought to drive the said transition. A number of studies on the said interaction is found in the literature, but they are rather analytic or applied to academic structures. Thus further analyses are needed to highlight the causes and physics of the behaviour for the case at hand; they can be better carried out with numerical tools, as the models that are the final objective of this study.

3.1 Modal parameters estimation

A table of modes (natural frequencies, modal damping and corresponding deformation shapes) is constructed; both global and local modes are identified, depending on the frequency range considered (Figs. 3a, 3b and 3c).

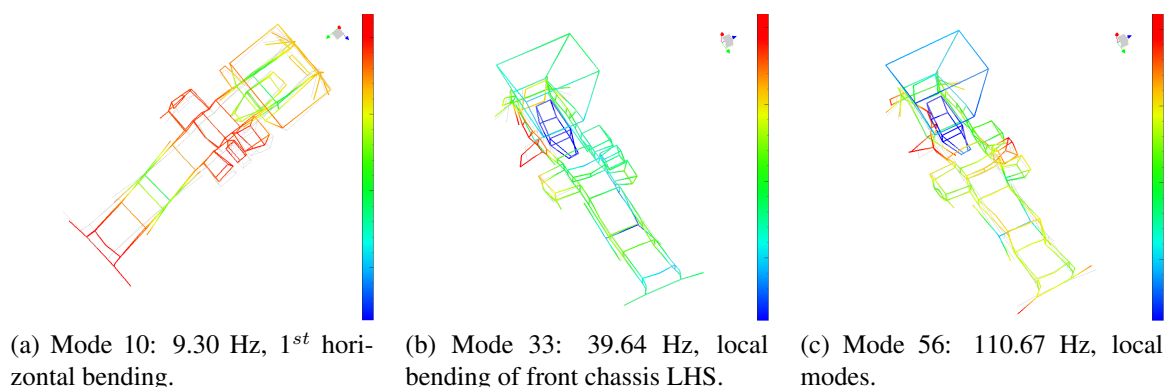


Figure 3: Some estimated mode shapes.

A check on the quality of modal parameter estimation shows that modal data are better identified in the low and mid frequency ranges (up to approximately 50 Hz), where identified modes have mostly real deformation shapes.

3.2 Influence of payload on the dynamic behaviour

The dynamic behaviour of the superstructure can be determined with a high degree of accuracy, due to its low modal density. Nevertheless, it is interesting to analyze how the superstructure influences the modes of the complete structure, when lying on it. The superstructure lies on the chassis, and their connection is made through a wooden interface and clamping bars: the transmission of forces turns out to be distributed along a line, instead of concentrated on discrete points.

As one could expect, the main consequence of adding the superstructure to the complete vehicle is a frequency shift (the superstructure represents 30% of the mass of the unloaded vehicle), Fig. 4. Nonetheless, this frequency shift changes at each mode (natural frequencies increase in certain cases and decrease in others, when going from configuration A to configuration B) due to the fact that the added mass has its own dynamics. It is interesting to see the effects on deformed mode shapes: this is done synthetically by calculating the Modal Assurance Criterion (MAC) matrix for the modal shapes of the two configurations.

4 NUMERICAL MODELS

A Finite Element (FE) model has been assembled for a complete truck; it comprises all the main components of the tested truck, with different levels of detail, Fig. 5.

This model must be validated for dynamic calculations. Due to the differences between numerical and experimental meshes, and having experimented some bias when calculating MAC matrices [7], the authors decided to update the FE model based on frequency response, instead of mode shapes; the target of the model update is to match both natural frequencies and response amplitudes.

The comparison of measured and calculated frequency responses is promising, since orders of magnitude and trends of frequency response functions are well predicted. Besides, the calculation confirms that impact test results, instead of operational test data, should be used for comparison with numerical data. Current work aims at updating the numerical model.

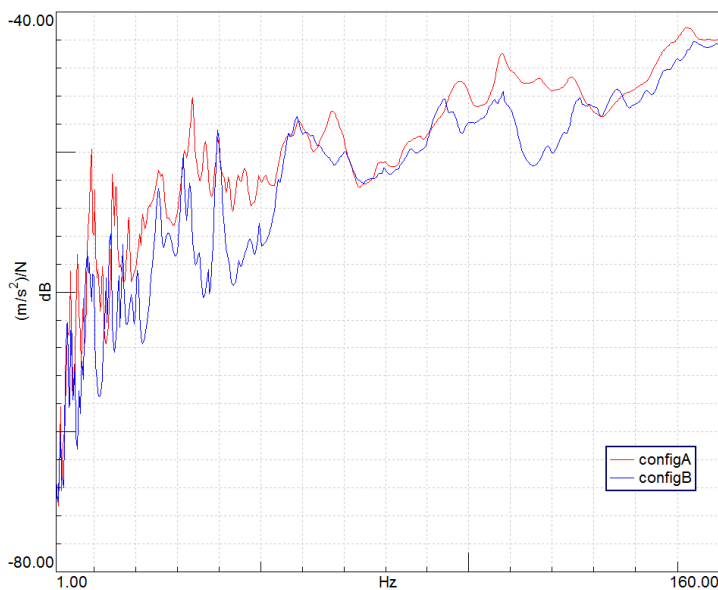


Figure 4: Comparison of the sum of FRF's measured for configurations A and B.

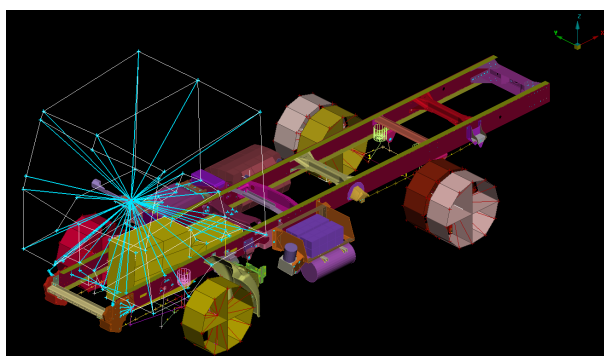


Figure 5: Complete Vehicle Model.

4.1 Applications of the FE model

Once validated, the presented FE model is used to make assessments on the physical phenomena found in the experimental phase.

One interesting application consists in the evaluation of the interface conditions between chassis and suspended elements; possible estimators for the interface conditions are:

- displacements at points of the interface;
- forces transmitted between the chassis and suspended elements at the interface;
- normal modes of the suspended elements in different boundary conditions (free-free, fixed, screwed on a siderail).

Interesting conclusions can also be done by comparing the computed natural frequencies for suspended elements and assemblies. Fig. 7 shows modes of the chassis and of the main elements suspended to the latter; modes of the chassis and suspended elements assembly and of the complete vehicle are also shown. What is shown is barely the mode count, that helps to identify the frequency ranges spanned by each component.

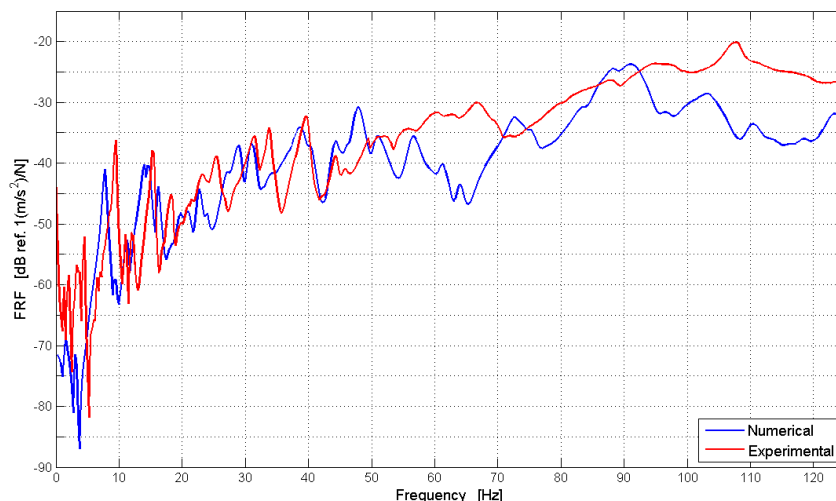


Figure 6: Point FRF's on a selected point of chassis: comparison between experimental and measured curves.

One can see that the first modes of the chassis appear at quite low frequency, while the first modes of the suspended elements appear at high frequency. One thus observes the interaction between a flexible component (the chassis) and stiffer ones (suspended elements), that has been mentioned in Section 3, the notion of stiff and flexible being here intended to be iso-mass. By deeply inspecting mode shapes related to the shown natural frequencies, one is able to understand how coupled modes originate.

4.2 Future developments for numerical models

The objective of the project which is the framework of this study is the development of numerical tools for the prediction of vibro-acoustic estimators in truck cabins. The named tools should be used at an early design stage, so one should be able to perform rapid calculations thank to these tools. Conventional Finite Element is seemingly not the most adapted technique to fulfill the aimed task, so the authors identified better methodologies to develop the said tools: the Wave Finite Element method ([8]), in conjunction with suitable reduction techniques, will be employed to build reduced models for the calculation of the frequency response of a simplified structure representing the vehicle. The FE model presented here will represent a reference for the reduced models.

5 CONCLUDING REMARKS

An experimental modal campaign on an industrial vehicle is described and the estimation of modal parameters carried on. Physical phenomena linked to the onset of the so called Mid-frequency range are highlighted thanks to the measurements. The results of the experimental campaign can serve as a reference for comparisons with numerical models developed in the truck industry, most of all when concerning frequency ranges and expected physical phenomena. Measurements allow identifying local vibration phenomena, and investigating the influence of mass and stiffness changes.

The estimated modal parameters are used as a basis for modal update of a FE model. First correlations are promising, but an effort has to be made to further improve the predictability of the numerical model. One possible application of the numerical model is showed, and its usefulness in interpreting the experimental phenomena is illustrated. Future reduced numerical

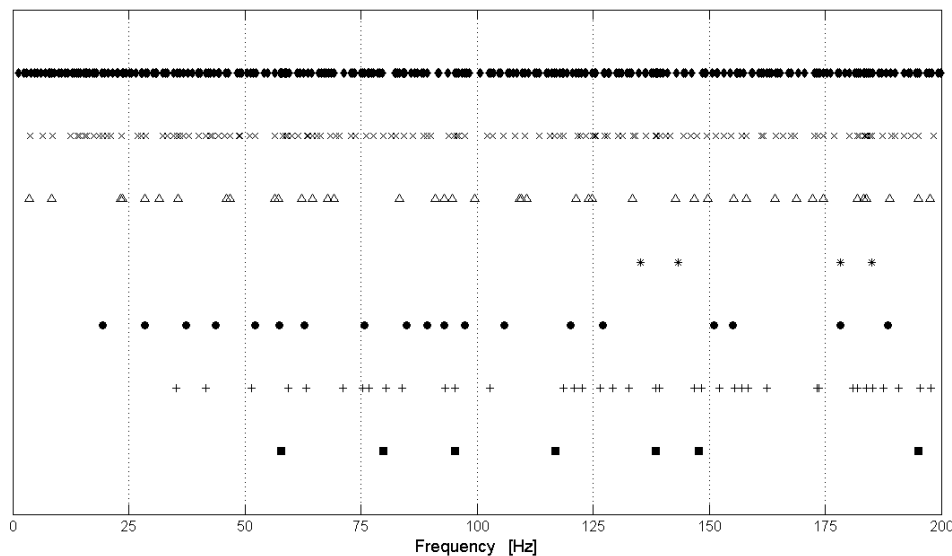


Figure 7: Mode count for components and assemblies. $\square + \circ *$: suspended elements in free-free BC, \triangle : frame in free-free BC \times : frame assembly in free-free BC, \diamond : complete vehicle lying on its tires

models are briefly introduced and their relationship with the FE model explained.

REFERENCES

- [1] W. Heylen, S. Lammens, and P. Sas. *Modal Analysis Theory and Testing*. KULeuven Press, 1997.
- [2] D. J. Ewins. *Modal testing, theory, practice, and application*. Research Studies Press, 1986.
- [3] I. Z. Bujang and R. A. Rahman. Dynamic analysis, updating and modification of truck chassis. In *Regional Conference on Engineering, Mathematics, Mechanics, Manufacturing & Architecture*, 2007.
- [4] Q. Xiaomin, D. Fang, and X. Dezhang. Modal sensitivity analysis and structural optimization of the cab of light truck. In *Proceedings of the International Conference on Mechanical Engineering and Material Science, MEMS*, 2012.
- [5] A. Viswanathan and E. Perumal. Deciding isolator and mounting points of a truck's exhaust system based on numerical and experimental modal analysis. In *Proceedings of the 16th International Congress on Sound and Vibration*, 2009.
- [6] P. Guillaume, P. Verboven, S. Vanlanduit, H. Van der Auweraer, and B. Peeters. A poly-reference implementation of the least squares complex frequency-domain estimator. In *Proceedings of the 21st IMAC*, 2003.
- [7] R. J. Allemang. The modal assurance criterion - twenty years of use and abuse. In *Proceedings of the 20th IMAC*, 2002.
- [8] J.-M. Mencik and M.N. Ichchou. Multi-mode propagation and diffusion in structures through finite elements. *European Journal of Mechanics A/Solids*, 24:877–898, 2005.

COPYRIGHT NOTICE

Copyright ©2015 by the authors. Distribution of all material contained in this paper is permitted under the terms of the Creative Commons license Attribution-NonCommercial-NoDerivatives 4.0 International (CC-by-nc-nd 4.0).





OPTIMIZATION IN THE COMPOSITION OF LAMINATED COMPOSITE STRUCTURES

M. Jaber^{1*}, H. Schneeweiss¹, J. Bös², T. Melz²

¹Structural Dynamics and Analysis
BMW Group, Munich, GERMANY
Email: mariam.jaber@bmw.de, helmut.schneeweiss@bmw.de

²System Reliability and Machine Acoustics SzM
Technische Universität Darmstadt, Darmstadt, GERMANY
Email: boes@szm.tu-darmstadt.de, melz@szm.tu-darmstadt.de

ABSTRACT

Composite materials are often used in the automotive industry to reduce acoustic vibrations and the sound pressure in a car by the use of damping patches or changing car part fabrication. The material make-up of these composites plays a big role in the effectiveness of damping treatments and is therefore a large focus in the vehicle design process. In this study, a genetic algorithm (GA) is used to test the different configurations of laminated composite structures and is compared with the results of a particle swarm optimization (PSO) and gradient-based algorithms that are performed with the same design variables. Aiming at producing a composite structure containing a high modal loss factor, the design variables are considered as: 1) viscoelastic material thickness, 2) fiber orientation angle, and 3) carbon layer thickness. The ultimate goal of the designed composite structure is to create the optimal balance between minimum vibrations and a minimum mass of the structure.

1 INTRODUCTION

The automotive industry often faces the problem of high vibrations in vehicle structures due to large excitation forces on the body. Fiber-reinforced composites are frequently used in lightweight structures due to their high strength-to-weight ratio as well as good fatigue and corrosion properties versus those of metal alloys. These composites provide better damping properties than those of steel or aluminum but must be paired with a viscoelastic layer to provide more efficient damping. This combination can have a stacking sequence similar to a sandwich, with two composite structures surrounding a viscoelastic layer. This viscoelastic core exhibits high shearing during deformation and, therefore, dissipates vibratory energy more effectively than the composites alone. Mead and Markus [1] developed the theoretical models for the axial and bending vibrations of sandwich beams with viscoelastic cores. Two possible applications exist for these kinds of composite structures: constrained layer damping (CLD) treatment patches and car part fabrication. Car part fabrication is easier to be used in industry than the patches and is the focus in this paper. The laminate is not limited to only three layers, fortunately, and is thus able to be optimized for the best damping configuration. Optimal design of these constrained layer damping treatments has long been a subject of high focus for reducing vibrations in structures by means of the maximization of modal damping ratios and reduction of modal strain energies. This maximization and reduction are achieved by determination of the best material, layer sequence, and laminate make-up, while also aiming at reducing the mass of the treatment.

This paper aims at maximizing the modal loss factor of sandwich structures comprised of varying laminas with respect to their mass as well as to the improvement of their noise, vibration, and harshness (NVH) performance. Multiple optimization algorithms are used to determine the most efficient laminate make-up for damping purposes, as well as the modal strain energy method to calculate strain energies stored and dissipated in the composite layers, and finally these optimization algorithms calculate the modal loss factor for the complete structure, which utilizes a dynamic response in terms of the undamped natural frequencies. A complex modulus approach is used to evaluate the viscoelastic material layers in the given frequency range due to the material experiencing dynamic loading. A comparison between the effectiveness of the different optimization algorithms will also be carried out. Based on the selected best algorithm, the optimal created design will be applied to a vehicle structure in order to validate the efficiency for acoustically problematic automobile parts.

2 OPTIMIZATION ALGORITHM SELECTION

To determine the best optimization algorithm, an extensive literature review was conducted and each different algorithm will be compared based on the results of the literature. The first algorithm is the genetic algorithm (GA) [2] due to its ability to work with large and complicated variable problems. A GA is an evolutionary optimization technique modeled after Darwin's theory of "survival of the fittest" in order to improve each population of solutions. Fortunately, the GA will not be stuck in a local optimum if the population size is significantly large. Araújo et al. [3] maximized the modal loss factor of a structure using single and multiobjective optimizations based on GA. The design variables that they used were fiber orientation angles of laminate face layers and thickness design. Their results showed that this algorithm can substantially improve the modal loss factor for simply supported sandwich beams and plates. Focusing on rectangular plates, Montemurro et al. [4] maximized the first N modal loss factors of the laminate structure through the use of a GA. Their design variables included the number of layers, layer thickness, and fiber orientation, and the results proved GA to be very flexible and applicable as well as able to reach a suitable optimum. According to Rahul et al. [5] the optimization of composite

structures using an island model parallel GA method produces a good convergence and a lower processing time, i.e., one tenth of the time of sequential GA.

Gradient-based methods [6], abbreviated to GB for this paper, based on the gradients of the constraints and objectives, can approximate solutions when mathematical closed-form expressions are not available. Therefore, these solutions are only local optima, but the advantage is a faster convergence rate. The research of Araújo et al. [3] proved that the use of GB methods had a computation time fifteen times faster than those of GA for the case of damping maximization of laminated sandwich composite structures. Their design variables were layer thickness and fiber orientation angle. Moita et al. [7] significantly increased the modal loss factor of triangular plates by optimizing fiber orientation angles and layer thicknesses, the design variables, by use of a GB optimization algorithm.

The third optimization algorithm investigated in this paper is the particle swarm optimization (PSO) algorithm [8]. This algorithm is population-based and stochastic, modeled after the flocking behavior of birds. Each solution in the search space of this method is called a particle, resembling one bird out of a flock. The position of this particle in the search space changes based on the best solution in its individual history, resembling the bird's own flying experience, as well as the best solution among all of the particles, i.e., the flying experience of the other birds. From these adjustments, PSO has an optimal potential to benefit from parallel computing. Suresh et al. [9] utilized the PSO method to optimally design a composite box beam for a helicopter rotor blade. They concluded that the use of PSO produced closer results to the optimum values than those produced by GA because PSO produced greater damping values for five different simulations in comparison with GA. However, the computational times were similar with PSO converging after 32.34 minutes and GA after 42.35 minutes. Kathiravan et al. [10] also used PSO in comparison to GB methods for the maximization of failure strength in thin-walled composite box beams. They found that PSO gave superior or equivalent results to the GB methods. The PSO was also used by Bargh and Sadr [11] for the optimization of the lay-up design of laminated composite plates. It was seen that the performance of the PSO was more efficient than the GA. Manjunath and Rangaswamy [12] optimized a ply stacking sequence with the use of PSO. They compared the results from PSO to those of GA and found that PSO produced better results. Fortunately, the PSO algorithm does not need to begin from different initial points as seen in GB methods.

3 VISCOELASTIC MATERIALS: PROPERTIES AND CHARACTERIZATION

Viscoelastic materials can be highly effective in controlling the dynamics of structures in noise control applications. The structural vibrations and the underlying noise radiation can be reduced and controlled by using these materials, whose properties are dependent on the room temperature and the frequency of the applied cyclic load. These characteristics are significant to accurately model viscoelastic materials in numerical simulations. The complex modulus of the behavior of viscoelastic materials was deeply investigated by Jones [13]. For the purpose of this paper, only the frequency dependency is to be taken into account. Also, the properties of viscoelastic materials are defined in a complex domain, having both real and imaginary components. The real component is associated with the elastic behavior of the material and is called the storage modulus E' , while the imaginary component is associated with the viscous material behavior and is called the loss modulus E'' . These properties can be modeled using the following equation:

$$E^* = E' + E'' , \quad (1)$$

Various measurement methods exist in which mechanical properties of materials can be determined. For example, dynamic mechanical analysis (DMA) [14] provides the characteristics of

viscoelastic materials over a large range of temperatures and frequencies. As previously stated, only the frequency dependency is analyzed in this paper.

4 MODAL STRAIN ENERGY METHOD

Throughout literature, the established damping model of fiber-reinforced composites, first developed by Adams and Ni [15], has been adopted by additional authors to improve the analysis of different composite structures with embedded viscoelastic layers [16]. This method is called the modal strain energy method and is used in this paper to simulate the damping in a laminated composite structure with embedded viscoelastic layers. This method defines the damping characteristics of a structure by the ratio of dissipated energy to stored energy during a stress cycle. The total structural damping loss factor can be expressed as

$$\eta = \frac{\sum_k \eta_{ij}^k U_{ij}^k}{\sum_k U_{ij}^k} \quad (i, j = 1, 2, 3), \quad (2)$$

where η_{ij}^k and U_{ij}^k are the damping loss factors for the layer k of the composite materials and strain energy stored in the layer k , and U_{ij}^k is the summation of U_{ij}^e , where e represents each element in a layer, related to the stress component σ_{ij}^e [17]. This relationship with respect to stress and strain [18] can be written as

$$U_{ij}^e = \frac{1}{2} \int \sigma_{ij}^e \epsilon_{ij}^e dV^e. \quad (3)$$

Figure 1 defines the fiber directions, where number 1 is in the fiber direction, 2 is transverse to this direction, and 3 is through the thickness direction. Theta represents the angle between the x-axis and the fiber direction.

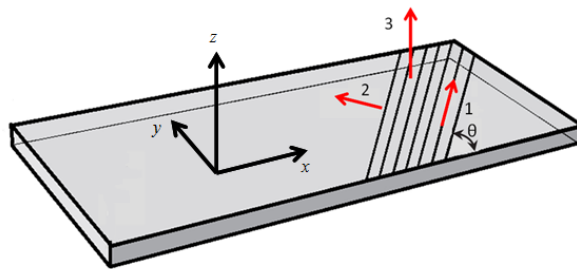


Figure 1. Fiber directions

The modal strain energy method can also be applied for the case of composite materials with embedded viscoelastic layers by considering that the viscoelastic material loss factor can be represented by

$$\eta(f) = \frac{E''}{E'} \quad , \quad (4)$$

where E' and E'' are the storage and loss modulus of the viscoelastic material, respectively, and can be integrated into Eq. 2 for η_{ij}^k when k is the number of the corresponding viscoelastic layer. This η represents the material loss factor for all directions, as the viscoelastic material is isotropic. See Eqs. 6 and 7 for the loss and storage modulus equations.

5 OPTIMAL DESIGN FORMULATION

A common goal in the automotive industry is to improve acoustic performance in vehicles without sacrificing structural dynamic stiffness. One means of improving this acoustic performance is through the use of CLD patches. Another method consists of the development of materials suitable for car body manufacturing, aiming at reducing poor acoustic performance. This paper focuses on the development of efficient composite structures made of fiber-reinforced composite and viscoelastic layers. In order to efficiently design these automobile parts, the design variables are taken as: layer thickness and fiber orientation based on mechanical properties. The objective by means of various optimization algorithms is to improve the acoustic performance of structures. The first improvement can be made through the increase in damping capabilities of the composite structure in order to minimize the resonance vibrations of the vehicle. The optimization work flow can be seen in Figure 2. The pre-processor ANSA is utilized to change the

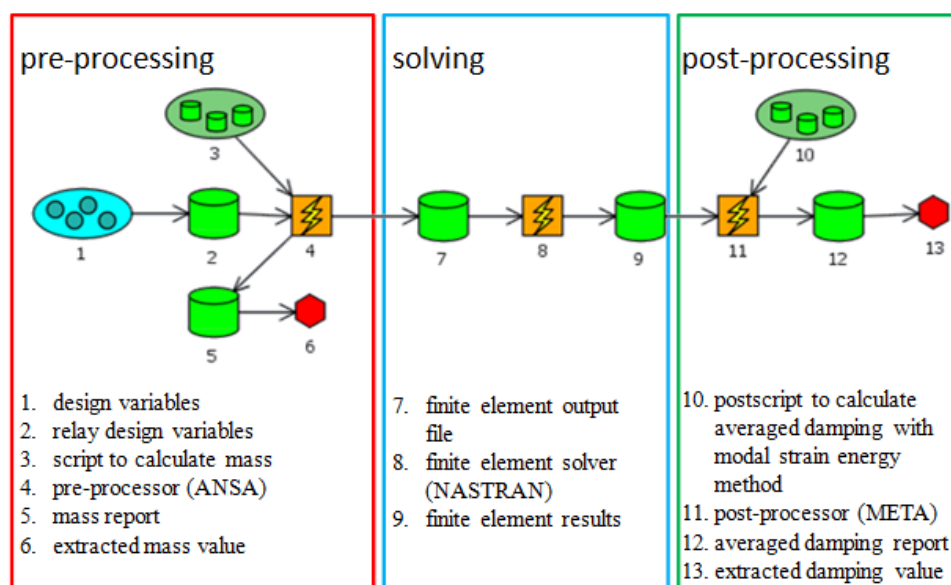


Figure 2. Optimization work flow for one objective value function.

design variables of the optimization and calculate the mass, NASTRAN is used as the solver, and Meta is used to calculate the damping via a post-script. This post-script was developed to calculate the loss factor at a faster rate by reading all of the stresses and strains of every single layer simultaneously.

In a literature review on the effect of damping layers in the laminate, Zhang and Chen [19] found that a laminate sequence of viscoelastic layers between layers of carbon composites had the highest modal loss factor. They found that the shear deformation in the viscoelastic layers is maximized when a central carbon composite layer is inserted between two viscoelastic layers. This, in turn, increases the modal loss factor of the structure. The layer sequence will behave better than one viscoelastic layer inserted between two composite laminates.

The laminate sequence scenario 2 will then be used in several optimization problems with the design variables and the constraints remaining the same. The problem that is solved through these optimizations is the maximization of damping, averaging the damping values at the natural frequencies between 30 and 200 Hz, as well as the minimization of the composite mass. The reason for this low frequency range is that automobile acoustic issues are mainly induced by the automobile panels' vibrations in this range. The damping values were averaged over the natural frequencies in the frequency range to improve the damping of all mode shapes.

However, the damping is dependent on the frequency, and the increase in damping will not be equivalent between all mode shapes. Averaging the damping resolves this issue and allows for a better treatment of mode shapes for all frequencies.

6 MODEL VALIDATION

To validate the implementation of an in-house strain energy model a test is developed and compared for glass fiber composites. The strain energy model, previously described, is able to calculate the damping of any geometry and for any boundary conditions through the use of FEM based on the parent material specific damping capacity information resulting from measurement on a cantilever beam. This was described by Berthelot [16]. The specific damping capacities, ψ , and material properties of the layers are taken from Adams and Maheri [20]. The test involves a cantilever beam with one clamped boundary experiencing an excitation at a point near the clamped edge. The material of the beam is considered a glass fiber/epoxy laminate with $E_{11} = 41.5$ GPa, $E_{22} = 10.9$ GPa, $G_{12} = 4.91$ GPa, $\nu_{12} = 0.32$, $\psi_{11} = 1.61\%$, $\psi_{22} = 6.7\%$, and $\psi_{12} = 7.3\%$, where E represents the Young's modulus, G represents the shear modulus of the material, ν represents Poisson's ratio of the material, and ψ represents the material's specific damping capacity in the directions of tangential and transverse directions, 1 and 2, respectively. The relationship between specific damping capacities, ψ , and modal loss factors, η , [17] is:

$$\eta = \frac{\psi}{2\pi}. \quad (5)$$

The frequency is fixed at 50 Hz to test the effects of the fiber orientation on loss factors. The beam consists of eight unidirectional layers, each of which has a thickness of 0.5 mm, and the width-to-length ratio of the beam is 1:17. The loss factor is tested for various fiber orientations between 0° and 90° . The results will then be compared with those of Bilups and Cavali [21] to show agreement between the results gathered in this test with those of previously developed methods, resembling the curve resulting from the Ni/Adams equation [15].

7 APPLICATIONS

The first application in this paper involves a cantilever beam made from eight symmetric layers of carbon HMS 209. The mechanical properties of the carbon composite is as follows: $E_1 = 189$ GPa, $E_2 = 6.08$ GPa, $G_{12} = 2.72$ GPa, $\nu_{12} = 0.3$, $\psi_1 = 0.64\%$, $\psi_2 = 6.9\%$, and $\psi_{12} = 10\%$. The aspect ratio of this cantilever beam is 1:17 and the cantilever exhibits a boundary condition of one clamped edge close to the excitation point. The design variables in this scenario involved the fiber orientation angles. The mass is kept constant, 0.1925 kilograms, and the specific damping capacity is averaged over all of the natural frequencies between 30 and 200 Hz and is considered as the objective function to be maximized. The results can be seen in Figure 3.

A validation also to be carried out in this paper, before optimizations, is a simulation and comparison of the stack-up sequence and their damping effectiveness. The first scenario is made of a viscoelastic material with a thickness of 4 mm embedded between two composite material layers of 3 mm. The viscoelastic material exhibits the following mechanical properties [19]

$$E'(f) = 0.0041 + 0.0322 \log(f) \quad (6)$$

and

$$E''(f) = 0.0077 + 0.0433 \log(f) \quad (7)$$

in GPa, where E' and E'' are the storage and loss modulus of the viscoelastic material, respectively.

The second scenario is comprised of a composite material of thickness 2 mm, a viscoelastic material 2 mm thick, another composite material with a thickness of 2 mm, another viscoelastic layer of 2 mm, and lastly, a composite material layer of thickness 2 mm. An improvement of 6% from the original percentage is observed for the second scenario with respect to the specific damping capacity percentage.

Based on the results of this application, the best layer stack-up sequence proved to be the second scenario. This layer sequence is further developed to optimize its damping capabilities for a roof based on the problem solution described in the previous section. In this test, the fiber orientation was chosen to vary between 0° and 90° , and the fiber orientations of the first and last layer were considered as one design variable to be changed similarly in order to guarantee that the laminate would be symmetric. The thicknesses of the various layers were varied between 0.6 mm and 1.4 mm, and the thicknesses of the different carbon composite layers were considered as one design variable to be equally changed together, as it was found in Zhang and Chen [19] that this configuration produced a maximum loss factor. The real-life application is then carried out in this paper for the automotive industry. In one part of the automobile, in this case a car roof, the material is optimized based on the problem solution previously described, with clamped boundary conditions. The results of each optimization solution will then be evaluated for the best material make-up for this roof. The solution will then be applied in the entire roof, and the structure will be coupled with fluid inside the vehicle to compare the sound pressure at the driver's ear position. Lastly, a comparison between each different optimization algorithm will be carried out with respect to convergence time and the performance quality of the optimal result obtained for each algorithm.

8 RESULTS AND DISCUSSIONS

The two previously described optimization algorithms, GA and PSO, were utilized to optimize the damping of a cantilever beam and the GB method for the damping of a car roof. The results of the cantilever beam can be seen in Fig. 3, where the blue dots represent the objective function evaluations, and the red dot shows the optimal result of the PSO algorithm. This simulation

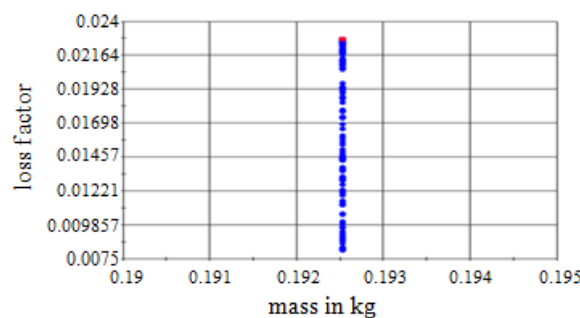


Figure 3. Beam damping maximization using PSO method.

has shown that changing only the fiber orientation, between 0° and 90° , while keeping a similar mass, can improve the loss factor by a factor of approximately 2.9. The optimal fiber orientation, seen in red and coming from PSO, consisted of a fiber orientation of $[90, 7, 90, 90]_2$, starting at layer one, with a loss factor of 0.023. The loss factor as a function of the carbon fiber orientation can be seen in Fig. 4a and Fig. 4b. It can be seen in Fig. 4a that the high loss factor is obtained when the fiber orientation of layers 1, 3, 5, 6, and 8 are oriented at 90° and in Fig. 4b when

layers 2 and 7 are oriented at 7° . The high damping value of the optimal design configuration obtained by use of PSO can be explained by the high Young's modulus in the second direction. This high Young's modulus will produce a high strain energy stored in this second direction. As the specific damping capacity of the material, $\psi_2 = 6.9\%$, is much higher in the second direction than the first direction, $\psi_1 = 0.64\%$, a high composite loss factor will be produced, based on Equation 1. By adding the layer with a fiber orientation of 7° between the layers, the inter-laminar strain energies were increased, meaning that the strain energy in the direction 1,2 increased and produced a higher loss factor as the specific damping capacity of the material is very high in this direction, $\psi_{12} = 10\%$. The second beam configuration, from GA, for the cantilever beam consisted of a fiber orientation of $[44, 44, 44, 44]_2$ and a loss factor of 0.018. The results of this GA can be seen in Fig. 4c. The highest loss factor from these results are obtained for all layers oriented at 44° , as seen in the graph. However, for GA, the Young's modulus in the second direction was not high due to the fiber orientation 44° , which produced a loss factor less than that produced by PSO. The PSO converged after 10 iterations with a total of 200 objective function evaluations and the GA after 16 iterations with 340 total objective function evaluations.

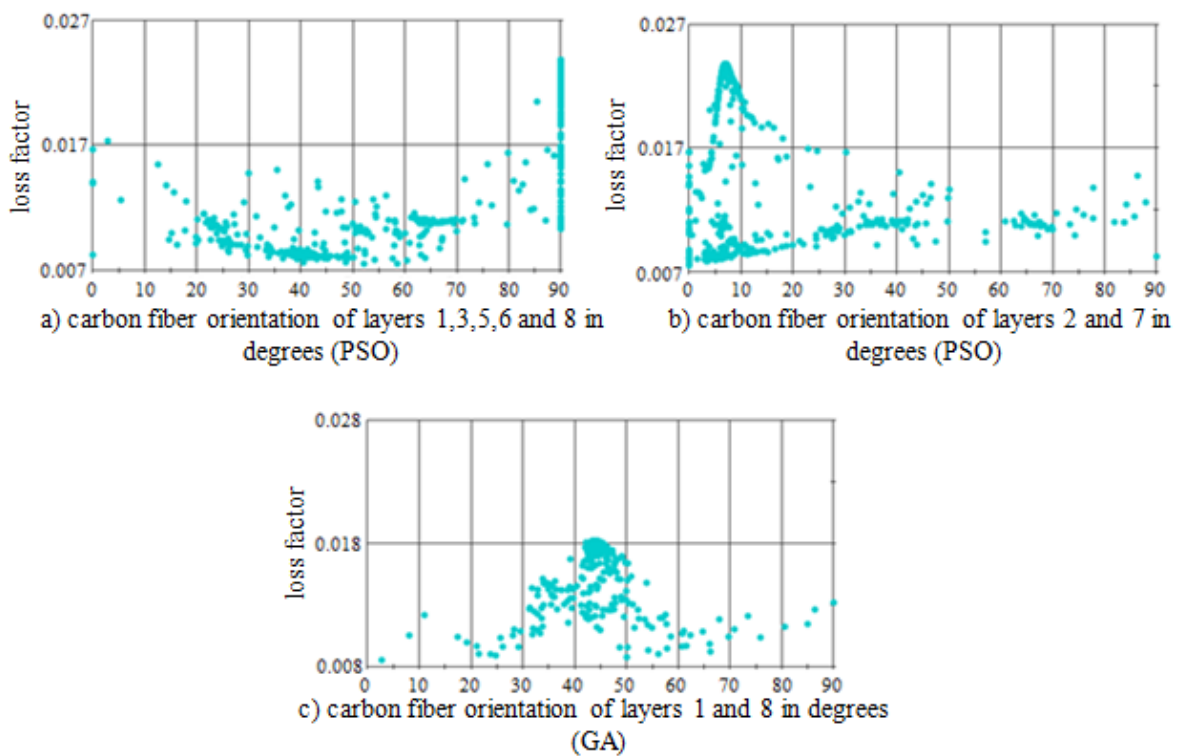


Figure 4. Loss factor as a function of fiber orientation.

The same procedure is applied to the roof of a car. By constraining the mass between 11 and 13 kg, the averaged damping over the natural frequencies between 30 and 200 Hz was considered as the objective function to be maximized in the optimization process. The PSO algorithm converged to the best damping value, the GA converged second best, followed by the GB method. The results can be seen in Fig. 5. Also, the GA optimization required many more iterations than the GB optimization method, while the GA and PSO were similar and required more iterations than the GB method.

The green dots in Fig. 5 are the accepted objective function evaluations and the pink dots are the rejected objective function evaluations due to the mass constraint defined by the user.

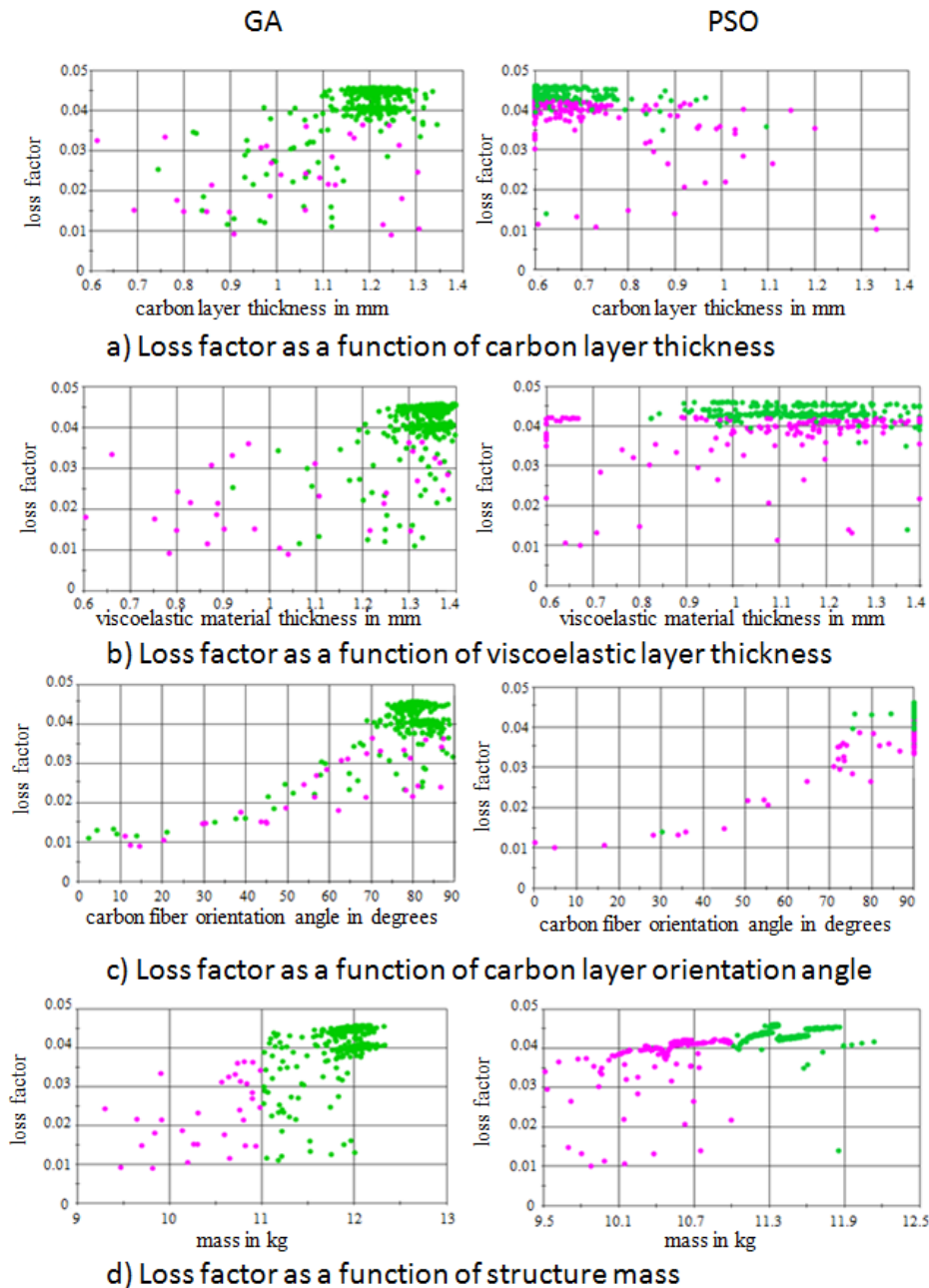


Figure 5. PSO and GA optimization results for the composite roof structure.

Each algorithm performed in different ways. The carbon layer thickness converged to 1.2 mm in GA, shown in Fig. 5a, left, and the PSO carbon layer thickness converged to the minimum allowable thickness, 0.6 mm, in Fig. 5a, right. The viscoelastic layer thickness converged to 1.35 mm in GA, shown in Fig. 5b, left, and the PSO viscoelastic layer thickness started to converge at 0.9 mm, in Fig. 5b, right. In terms of fiber orientation angles, the GA converged to 85°, Fig. 5c, left, while the PSO fiber orientation angles converged to 90°, Fig. 5c, right. The GA converged to a mass of 12 kg while the PSO converged to a mass of 11.3 kg, Fig. 5c left and right, respectively. This difference of mass is a result of the fact that the PSO carbon composite thickness converged to a lower value, as the carbon is heavier than the viscoelastic material. All convergences were considered as the thickness, angle, or mass that produced the highest loss factor value.

To compare the performance of each optimization method, the results of each method are recorded and are displayed in Table 1.

Table 1: Layer properties and loss factor of optimization results for the composite roof structure.

	carbon angles 1 and 6	carbon angle 3	carbon layer thicknesses	first viscoelastic layer thickness	second viscoelastic layer thickness	loss factor percentage
PSO	90°	90°	0.60 mm	1.34 mm	0.98 mm	4.6%
GA	85°	81°	1.22 mm	1.39 mm	1.23 mm	4.5%
GB	81°	70°	0.8 mm	1.4 mm	1.3 mm	4.4%

In addition to these results, the objective function evaluations, which occur within each iteration, were observed. The PSO was observed to have the best convergence performance in terms of reaching their optimum values, followed by GA and GB, respectively. The difference between the PSO optimum value and the GB optimum was only around 0.2%. However, the GB converged with 3.2 times fewer objective function evaluations in comparison with PSO. PSO converged after 300 objective function evaluations over 15 iterations, GA performed with 250 objective function evaluations over the course of 9 iterations, and lastly, the GB optimization performed with 94 objective function evaluations over the course of 10 iterations.

A mass of 11.8 kg was further considered to be able to compare two different results for the same mass. The optimal of PSO observed an averaged damping of 0.046, and a similar-mass scenario observed an averaged damping of 0.013. The two different layer compositions can be seen in Table 2. The layer thicknesses are more or less the same, with the only differences being the carbon fiber orientation angles, which performed best for 90°. This best performance for 90° comes from the fact that a high strain energy is stored in the material in the second direction, which is produced by a high Young's modulus in the second direction, in conjunction with the high specific damping capacity of the material in this direction and agrees with the results found in [19] for their study performed on beam structures. According to Zhang and Chen [19] the fiber orientation angles of compliant layers played a crucial role in improving the dissipation capacity of the complete composite. They observed that the stiffer the constraining layers were, the higher the shear deformation in the viscoelastic layers will be and the higher the loss factor of the composite. The second design has more energy stored in the first direction, causing a lower total loss factor due to the lower specific damping capacity of the material in this direction.

Table 2. Comparison for same-mass and optimal PSO design results.

	carbon angles 1 and 6	carbon angle 3	carbon layer thicknesses	first viscoelastic layer thickness	second viscoelastic layer thickness	loss factor percentage
optimal design	90°	90°	0.62 mm	1.39 mm	1.16 mm	4.5%
same-mass design	2°	30°	0.62 mm	1.37 mm	1.18 mm	1.4%

Considering these two scenarios, the averaged strain energy between 30 and 200 Hz was calculated for the roof of the car. As expected, the strain energy values were efficiently reduced in the optimal composite in comparison with the composite of similar mass but less damping.

The strain energy was used in this case to compare two different roof configurations, as it has been previously proven by Jaber et al. [22] that placing damping treatments on locations of high strain energy is able to greatly reduce the vibratory energy in an automobile part. The optimal design has a minimum strain energy value and shows that it does not require any further damping treatment.

The strain energy on the roof of the car for the two scenarios, along with a reference strain energy of the aluminum roof, can be seen in Figure 6. Through optimization, the laminate roof caused an reduction of the strain energy in the structure, even with the most poorly performing objective function evaluation from PSO. Moreover, the strain energy was better reduced by the optimum objective function evaluation laminate structure make-up created by the PSO method.

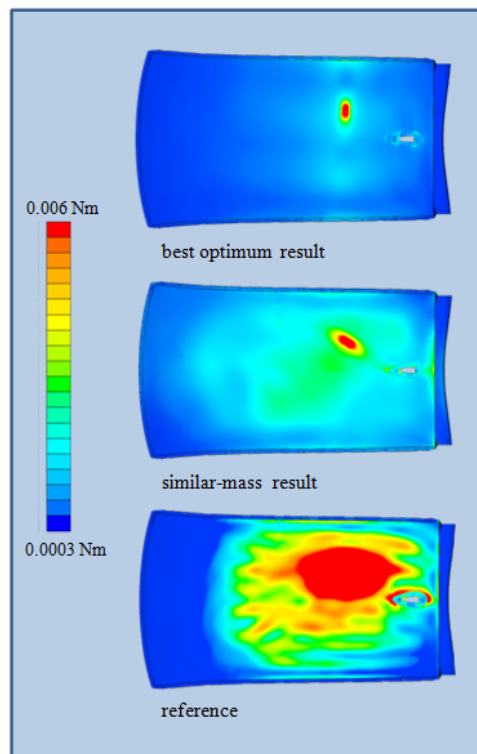


Figure 6. Strain energy comparison for PSO results with the same mass.

In order to better illustrate these damping solutions in a real-life application, the newly designed roof was put in place of the original aluminum roof of a car. The structure was coupled with the fluid within the vehicle chassis, and the sound pressure was calculated at the driver's ear position. The results can be seen in Figure 7.

Observed from these results, the sound pressure at the driver's ear position was reduced by around 5 dB (SPL) for some frequencies. The reduction was not similar for all frequencies due to the fact that the increase in the damping is not similar over all frequencies due to its dependance on the mode shape of the structure. This reduction shows that this optimization of the material make-up of the structure itself is able to effectively improve the NVH performance of an automobile and provides a more feasible solution than using CLD treatments because the part is previously controlled in terms of acoustic issues through production, rather than cutting and placing CLD treatments after production. Furthermore, the mass of the automobile roof was effectively reduced from 14.17 kg to 12 kg. It is suggested that further studies be conducted to investigate if this newly designed roof will affect other testing requirements such as crash testing and dynamic stiffness testing, as well as a cost comparison between designs should be

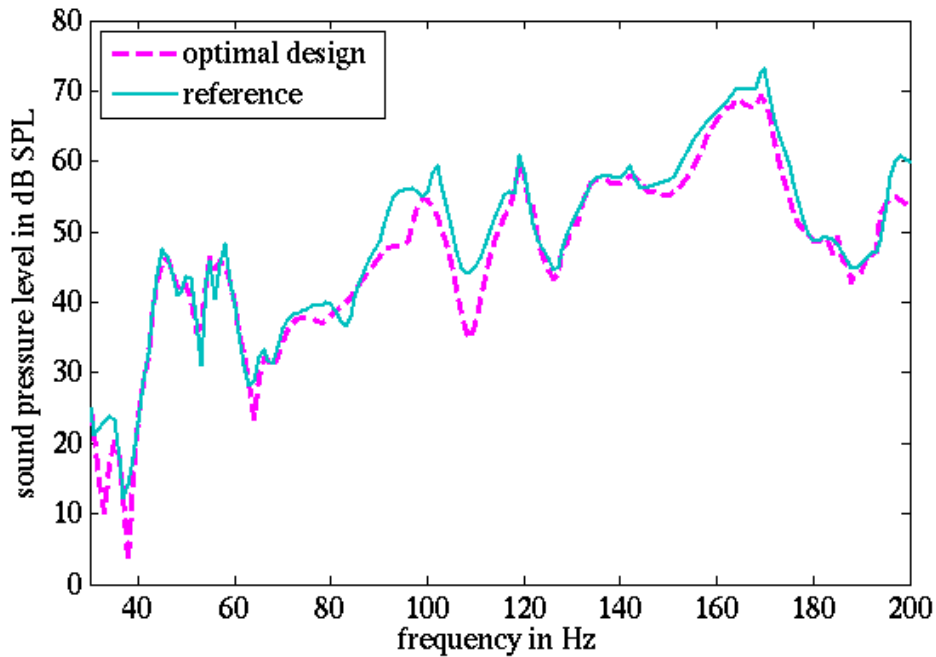


Figure 7. Sound pressure level comparison at driver's ear position.

conducted.

9 CONCLUSIONS

In order to design a vehicle with a good lightweight structure, carbon composite materials with embedded viscoelastic layers can be a potential solution to improve NVH performance levels. Unfortunately, carbon composites do not always have a reliable performance and require a very accurate design. Many parameters, such as fiber orientation, layer thickness, and laminate stack-up sequence, can play a crucial role in the design of these NVH-improving, lightweight structures. The modal strain energy method has been used to predict the loss factor of carbon composites with embedded viscoelastic layers in conjunction with optimization algorithms, and as well the frequency dependence of the viscoelastic material has been taken into account. Optimization algorithms can be an efficient way to optimize the design of these structures, such as GA and PSO. The PSO proved to be more efficient and faster than the GA, followed by GB optimization algorithms. It has been shown that changing the composition of a car roof can effectively reduce the strain energies of said roof as well as reduce the sound pressure at the driver's ear position within a vehicle chassis. For this PSO, the damping value was calculated as improving by a factor of four when compared between the best and worst optimization results for the same mass. Also, the GB optimization method is a better optimization method in situations of large automobile parts due to the optimum varying only slightly from the PSO optimum, and is observed to converge at a faster rate than that of PSO. Changing the material itself in structural parts of an automobile can provide an effective means of improving the acoustic behavior of cars, as well as create a more efficient car part fabrication for passive control purposes. Further investigations should be carried out to verify other requirements during design, such as crash testing and dynamic stiffness testing.

ACKNOWLEDGEMENTS

The authors gratefully acknowledge the European Commission for its support of the Marie Curie program through the ITN EMVeM project (GA 315967). The authors acknowledge Ainsley Baum for her participation in this work.

REFERENCES

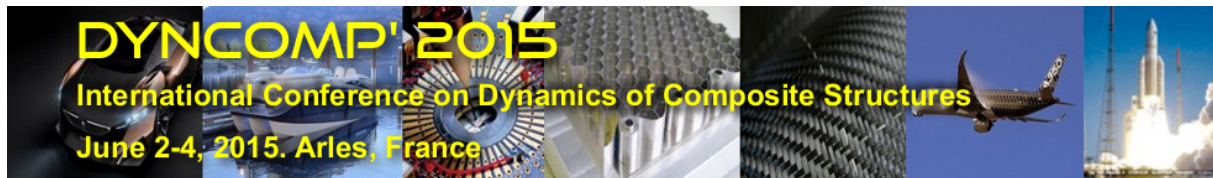
- [1] Mead, D.J. and Markus, S. The forced vibration of a three-layer, damped sandwich beam with arbitrary boundary conditions. *Journal of sound and vibration*, 10(2):163–175, 1969.
- [2] Davis, L. *Handbook of genetic algorithms*, volume 115. Van Nostrand Reinhold New York, 1991.
- [3] Araújo, A., Martins, P., Mota Soares, C.M., Mota Soares, C.A., and Herskovits, J. Damping optimization of viscoelastic laminated sandwich composite structures. *Structural and Multidisciplinary Optimization*, 39:569–579, 2009.
- [4] Montemurro, M., Koutsawa, Y., Belouettar, S., Vincenti, A., and Vannucci, A. Design of damping properties of hybrid laminates through a global optimisation strategy. *Composite Structures*, 94:3309–3320, 2012.
- [5] Chakraborty, D., Dutta, A., and Chakraborty, D. Optimization of frp composites against impact induced failure using island model parallel genetic algorithm. *Composites science and technology*, 65(13):2003–2013, 2005.
- [6] Snyman, J. *Practical mathematical optimization: an introduction to basic optimization theory and classical and new gradient-based algorithms*, volume 97. Springer Science & Business Media, 2005.
- [7] Moita, J., Araújo, A., Mota Soares, C.M., and Mota Soares, C.A. Finite element model for damping optimization of viscoelastic sandwich structures. *Advances in Engineering Software*, 66:34–39, 2013.
- [8] Trelea, I.C. The particle swarm optimization algorithm: convergence analysis and parameter selection. *Information processing letters*, 85(6):317–325, 2003.
- [9] Suresh, S., Sujit, P., and Rao, A. Particle swarm optimization approach for multi-objective composite box-beam design. *Composite Structures*, 81:598–605, 2007.
- [10] Kathiravan, R. and Ganguli, R. Strength design of composite beam using gradient and particle swarm optimization. *Composite Structures*, 81:471–479, 2007.
- [11] Bargh, H. and Sadr, M. Stacking sequence optimization of composite plates for maximum fundamental frequency using particle swarm optimization algorithm. *Meccanica*, 47:719–730, 2012.
- [12] Manjunath, K. and Rangaswamy, T. Ply stacking sequence optimization of composite driveshaft using particle swarm optimization algorithm. *International Journal for Simulation and Multidisciplinary Design Optimization*, 5:A16, 2014.
- [13] Jones, D.I.G. *Handbook of viscoelastic vibration damping*. John Wiley & Sons, 2001.

- [14] Menard, K.P. *Dynamic mechanical analysis: a practical introduction*. CRC press, 2008.
- [15] Ni, R. and Adams, R. The damping and dynamic moduli of symmetric laminated composite beamstheoretical and experimental results. *Journal of Composite Materials*, 18:104–121, 1984.
- [16] Berthelot, J.M. *Composite materials: mechanical behavior and structural analysis*. Springer Science & Business Media, 1999.
- [17] Luersen, M. and Lopez, R. A genetic algorithm for optimization of hybrid laminated composite plates. In *Optimization of Structures and Components*, pages 49–71. Springer, 2013.
- [18] Jaber, M., Schneeweiss, H., Bös, J., and Melz, T. Vibrational energy flow in carbon composite structures. In *INTER-NOISE and NOISE-CON Congress and Conference Proceedings*, volume 249, pages 4636–4652. Institute of Noise Control Engineering, 2014.
- [19] Zhang, S. and Chen, H. A study on the damping characteristics of laminated composites with integral viscoelastic layers. *Composite Structures*, 74:63–69, 2006.
- [20] Maheri, M. and Adams, R. Finite-element prediction of modal response of damped layered composite panels. *Composites science and technology*, 55:13–23, 1995.
- [21] Billups, E. and Cavalli, M. 2d damping predictions of fiber composite plates: Layup effects. *Composites Science and Technology*, 68:727–733, 2008.
- [22] Jaber, M., Schneeweiss, H., Bös, J., and Melz, T. Efficient damping treatment for structure-borne noise reduction in vehicles. In *Proceedings of Novem 2015: Noise and Vibration - Emerging Technologies*, pages 49859–1 – 49859–13, April 13-15 2015.

COPYRIGHT NOTICE

Copyright ©2015 by the authors. Distribution of all material contained in this paper is permitted under the terms of the Creative Commons license Attribution-NonCommercial-NoDerivatives 4.0 International (CC-by-nc-nd 4.0).





EXPERIMENTAL AND NUMERICAL INVESTIGATION OF THE MECHANICAL BEHAVIOUR OF AN OPEN-CELL CERAMIC FOAM UNDER MULTIAXIAL LOADINGS

O. Kraiem ^{1*}, M. Houillon ², N. Schmitt¹ and H. Zhao¹

¹LMT-Cachan UMR 8535
ENS Cachan, CNRS, Université Paris Saclay
Bâtiment Léonard de Vinci
61 avenue du Président Wilson
94230 Cachan

Email: kraiem@lmt.ens-cachan.fr, schmitt@lmt.ens-cachan.fr, zhao@lmt.ens-cachan.fr

² TN International
1 Rue des Hrons, 78180 Montigny-le-Bretonneux
Email: marie.houillon@areva.com

ABSTRACT

In this study, an experimental and numerical investigation regarding the mechanical behavior of open-cell ceramic-like foam (OCCF) was carried out. The aim was to identify a continuum model able to predict the mechanical response under complex path loadings. Uniaxial and true triaxial tests have been done to investigate the compression behavior of OCCF. Elastic-brittle behavior is observed under uniaxial unconfined compression loading while a crushing plateau with high-energy absorption capacity is exhibited under uniaxial confined compression. Limited strain rate dependence is found. The experimental results are discussed and correlated with degradation mechanisms identified by X-ray computed tomography observation. Tested under multiaxial loadings, the OCCF exhibits slightly transversely isotropy. Also its yield surface has been well described by a Deshpande-Fleck yield criterion. The Deshpande-Fleck model for foam has been modified by introducing a dependence of the plastic Poisson's coefficient with the plastic volumetric strain to improve the prediction of the radial expansion. It has been implemented into the finite-element code LS-Dyna via a usermat subroutine. Numerical results are in close agreement with the experimental results.

1 INTRODUCTION

In recent years, Open-Cell Ceramic-like Foams (OCCF) are widely used in many industrial applications thanks to their physical and thermo-mechanical properties such as low density, low thermal conductivity, high compressive strength to weight ratio and high fire resistance [1],[2],[3]. Due to its ability to accommodate large deformation, OCCF is a promising candidate for energy absorption engineering applications, provided that foam parts are encapsulated by a ductile housing to avoid mass loss during the crushing. In that case foams can be subjected to complex multiaxial stress states. Consequently, performing simple uniaxial compression tests without or with lateral confinement at different strain rates is not sufficient to identify a mechanical model. It is therefore necessary to characterize the behavior under multiaxial loadings.

The mechanical characterization of brittle foams under complex loadings is scarcely found in the literature unlike that of ductile foams. To understand the compressive behavior and estimate the failure envelope of polymeric and metallic foams, Deshpande et al. [4],[5] have developed two high-pressure triaxial systems allowing to apply a particular multiaxial loading paths on cylindrical and cubic samples. Canto [6], developed a true triaxial compaction device composed of six sliding blocks to study the triaxial behavior of very compressible materials and powders allowing to explore more complex triaxial loading paths and for very large strains [7][8].

In this research, the mechanical response of low density OCCF has been characterized at room temperature under uniaxial and multiaxial loadings and notably its yield surface has been identified. Thanks to X Rays Computer Tomography observation on samples subjected to oedometric compression test stopped a different load, the mechanisms of degradation has also been identified and correlated to the change in behavior noted on the Force - displacement curves. An extension of Deshpande Fleck criterion[4] is proposed to predict the OCCF experimental data. The identified model has been implemented as a user-defined material model in the finite element code LS-DYNA[9], and numerical simulations of crushing tests were carried out in order to validate this model.

2 EXPERIMENTAL CHARACTERIZATION

2.1 Material : microstructure, specimens geometry and procedures

The OCCF foams used in this experimental study was manufactured by direct carbonization of a polymeric foam. The apparent bulk density of the OCCF material is about $\rho_a = 250 \text{ kg.m}^{-3}$ and its porosity is equal to $n = 82 \%$. A typical microstructure is shown in Fig. 1. Like most foams, it is characterized by cells, empty pores and ligaments connecting cells together. The characteristic cell-size ranges from $50 \mu\text{m}$ to $150 \mu\text{m}$. Small-pores, the size of which being lower than $10 \mu\text{m}$, are also observed on the wall of the cells. Due to the manufacturing process, the microstructure of this material is slightly elongated in the foaming direction (Fig 1b) and explains the slightly anisotropy observed during the tests.

Quasi-static compression tests with and without lateral confinement were conducted on cubical ($a = 40 \text{ mm}$) and cylindrical specimens ($D = 30 \text{ mm}$, $H = 30 \text{ mm}$) by using an Universal hydraulic testing machine Instron. A Split Hopkinson Pressure Bar (SHPB) system was used to study the strain rate sensitivity of the OCCF foams. Cylindrical samples ($D = 22 \text{ mm}$, $H = 9 \text{ mm}$) were used for that analysis. Ex-situ quasi-static compression tests with X-ray computed tomography analysis were performed on cylinders ($D = 30 \text{ mm}$, $H = 30 \text{ mm}$) to investigate their failure mechanisms. Triaxial tests were conducted on cubes to study the multiaxial behavior by using Cantos compaction device (Fig. 2a) installed in the triaxial testing

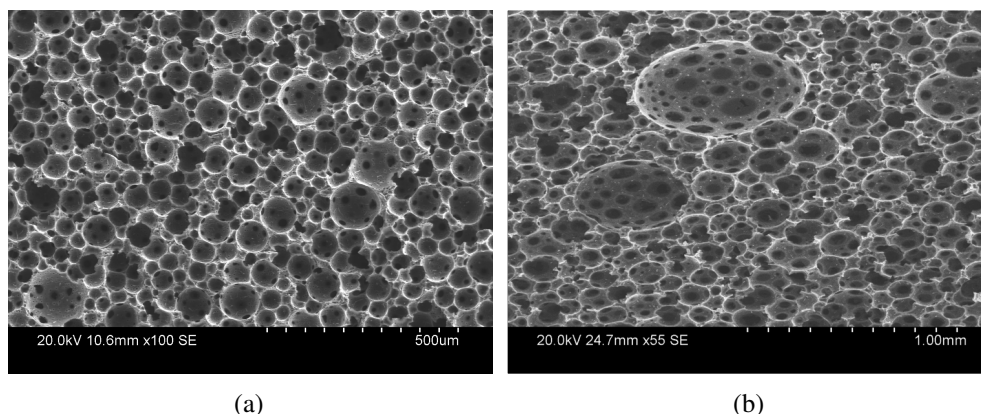


Figure 1. SEM micrographs of the OCCF foam

machine ASTREE. ASTREE comprises six independent actuators paired up along the three perpendicular directions pushing the blocks to reduce the hole, each one sliding relative to the others. During the triaxial tests, the imposed displacements on the cubical specimen in each direction were measured by laser displacement sensors (Fig. 2b).

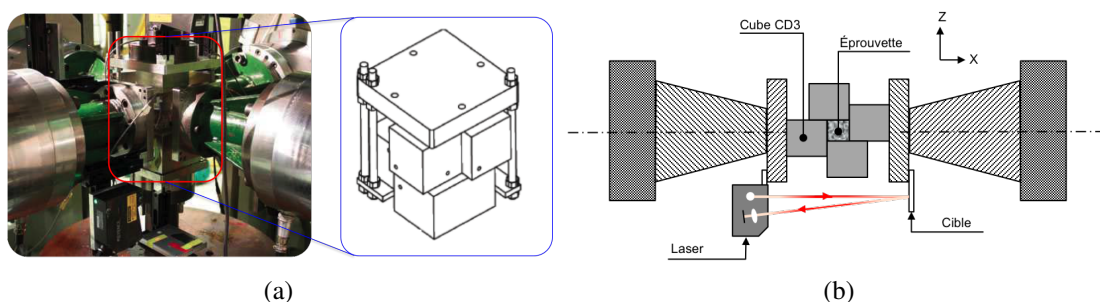


Figure 2: Triaxial compression test: a) compaction device installed in the ASTREE testing machine b) Actuators displacement measurement with a laser sensor

2.2 Experimental results

Typical compressive stress-strain curves of an OCCF subjected to quasi-static loading ($V = 5 \text{ mm} \times \text{min}^{-1}$) with and without lateral confinement, is shown in Fig. 3. The stress-strain curve obtained during unconfined compression test reveals the elastic-brittle behavior of that the foam has an elastic-brittle behaviour (Fig. 3a). When lateral displacement is prevented under confined conditions the compression behavior is significantly different (Fig. 3b). Three zones can be highlighted: first a short elastic range with a brittle failure, then a crushing plateau and finally a densification with an increase in stiffness and stress. Fig. 3c shows the slightly anisotropic compressive response when the OCCF specimens are loaded in three directions (i.e., for angles 0, 45 and 90). The dynamic stress-strain curves of OCCF under confined conditions are shown in Fig. 3d. Comparing the dynamic compressive and confined behavior to those obtained under quasi-static conditions permits to show the responses are close to each other (elastic regime, plateau and densification) and confirms a low sensibility of the mechanical behavior to the applied strain rate compared with other cellular materials the compressive properties look good for structural applications, notably its ability to absorb a large amount of energy under impact loadings.

To understand the damage mode and the crush mechanisms of the brittle ceramic foams under impact, an ex-situ compression test was performed on a confined cylindrical sample. The test

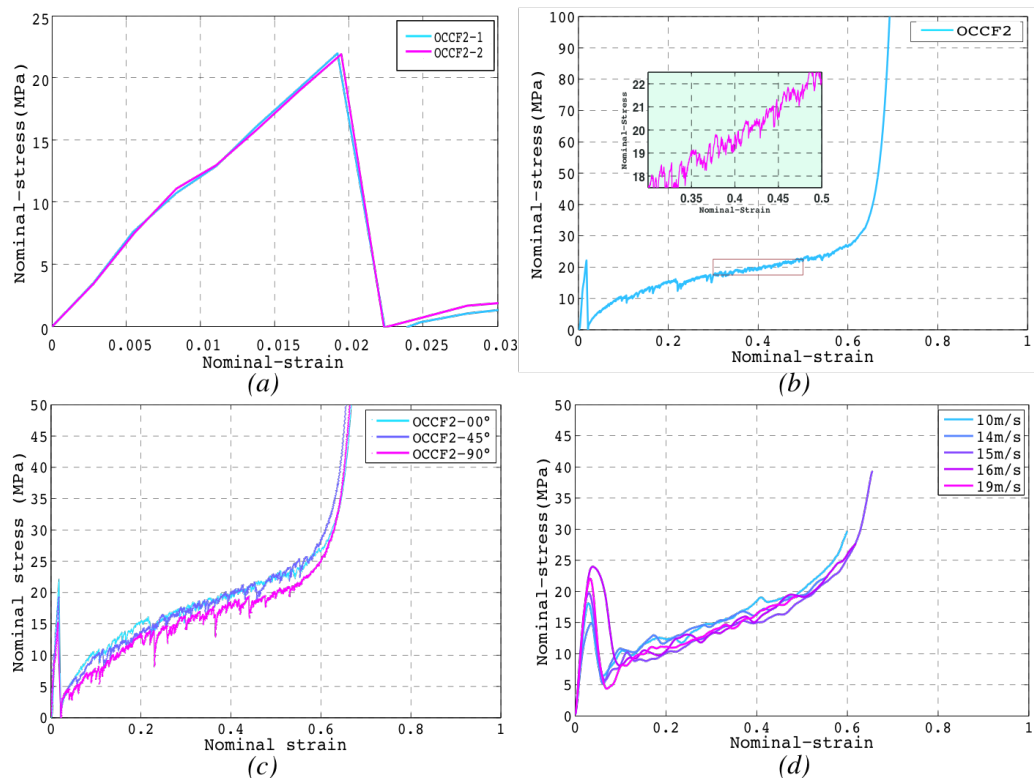


Figure 3: Uniaxial compression stress-strain curves: a) static compression behavior without confinement, b) static compression behavior with lateral confinement, c) Static anisotropic compression behavior with lateral confinement in three loading directions and d) dynamic compression behavior

was interrupted at different strain levels and scans were taken with a X-rays CT tomograph at each step. Analysis of the 3D images has enable tracking the mechanisms of deformation during the test. They have shown that the non linear deformation of the OCCF are controlled by the appearance of crushing bands in the sample which lead to the fragmentation of foam into parts becoming more and more smaller until it has been transformed into powder at the end of the densification. Figure 4 shows the force-displacement curve registered during the ex-situ compression test and cross-sectional tomography images at each step.

Triaxial compression tests were performed with a triaxial testing machine "ASTREE" to characterize the OCCF multiaxial behavior. Iso-displacement compaction pression loading, oedometric compression loading and more complex triaxial compression loading with variable confining pressure were carried out under quasi-static conditions ($5 \text{ mm} \times \text{min}^{-1}$). In these tests, the samples inside the compacting device have been oriented along in such way that their foaming direction was parallel to the vertical axis of the ASTREE machine *axis 3*. Under iso-displacement compression loading (i.e., same compression loading rate applied along the three perpendicular directions), the material exhibits a slightly transversely isotropic behavior (stress-volumetric strain curves drawn on Fig. 5a). The compressive strength in the rise foaming direction *axis 3* is higher than that in perpendicular directions (*axis 1* and *axis 2* directions). In another triaxial test the foam sample was compressed by applying the same displacement rate in the three directions until the first brittle failure was reached and then it was loaded axially (uniform compression force rate in direction *axis 3*) while keeping constant the confining pressure in the perpendicular directions *axis 1* and *axis 2*. These experiments exhibit clearly the influence of the lateral confinement on the mechanical response of OCCF. Figure 5b shows the variation of the curves stress-volumetric strain when varying lateral confinement from 5KN to 25KN.

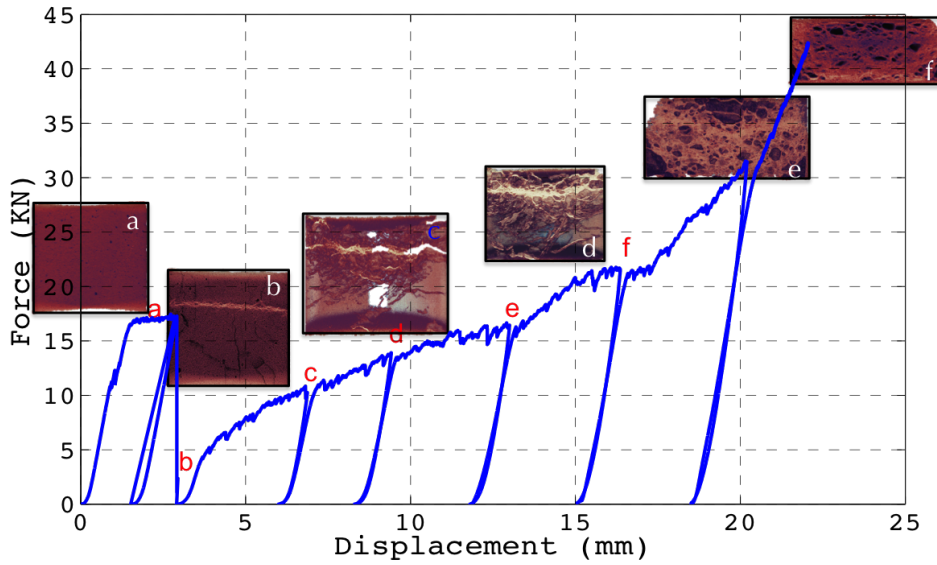


Figure 4: Force versus displacement curve and microstructural change obtained by tomographic analysis of the OCCF from the ex-situ confined compression test

Experimental data have been used to identify the yield surface of the brittle ceramic foam. The

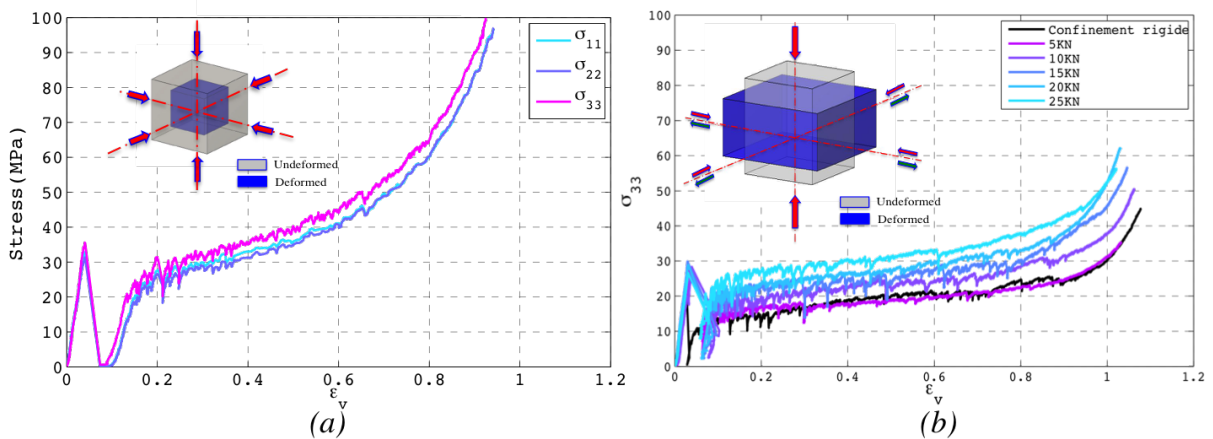


Figure 5: Triaxial compression tests on OCCF samples: a) response of the material under a hydrostatic loading, b) Effect of the lateral confining pressure on the response of the material

failure surfaces and its evolution were constructed in mean stress ($\sigma_m = -\frac{1}{3}(\text{tr}\sigma)$) versus deviatoric stress ($\sigma_d = \sqrt{\frac{3}{2} \mathbf{s} : \mathbf{s}}$) space for various levels of volumetric strain. The obtained behavior seems to be adjusted by an elliptic yield criterion in the compressive zone of the space $\sigma_m - \sigma_d$ defined by :

$$\Phi = \hat{\sigma}^2 - Y^2 = \frac{1}{[1 + (\frac{\alpha}{3})^2]} [\sigma_e^2 + \alpha^2 \sigma_m^2] - Y^2 \quad (1)$$

This relationship corresponds to the Deshpande Fleck criterion. To account for a good description of the hardening of the material during the densification, the initial Deshpande & Fleck model has been improved to predict the radial anelastic expansion in the plastic domain (called MDF model). Where σ_e is the von Mises effective stress and σ_m is the hydrostatic stress. The parameter α defines the shape of the yield surface given by

$$\alpha = \frac{9}{2} \frac{1 - 2\nu^p}{1 + \nu^p} \quad (2)$$

where ν^p is the plastic coefficient defined as a function of the plastic volumetric strain.

Figure 6.b shows the evolution of the OCCF yield surfaces fitted by the Modified Deshpande & Fleck (MDF) yield surface.

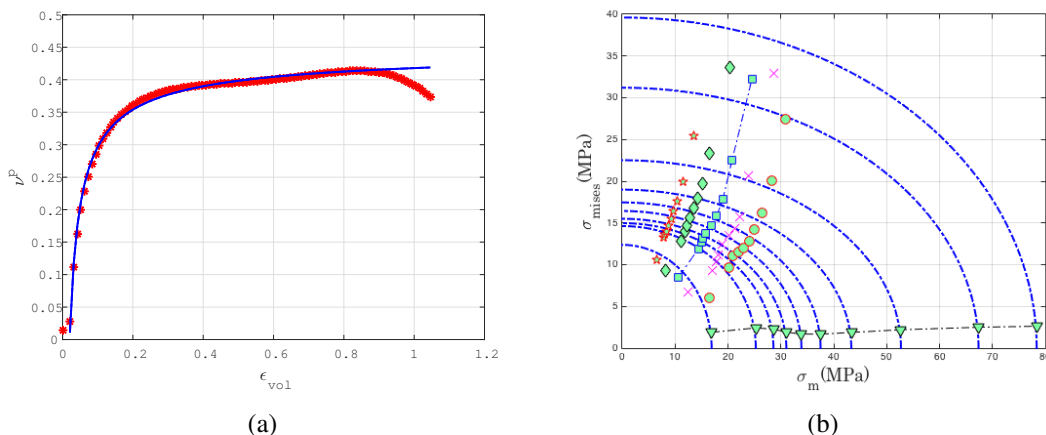


Figure 6: Identification of the MDF parameters model for the OCCF: a) variation of the plastic Poisson’s Ratio b) Yield surface in mean stress-deviatoric stress space

3 NUMERICAL SIMULATION

The MDF model has been implemented via an usermat subroutine in the finite element code LS-DYNA. In order to validate the behavior model and to verify its applicability to simulate crushing tests in quasistatic conditions. The crushing test consists to apply an inclined (15°) on a cylindrical OCCF part enclosed in a metallic jacket where behavior is described by the piecewise-linear-plasticity material model. Fig.7a shows the deformation map obtained at the last step of the loading. For each test the overall force ? overall displacement curve was recorded. A comparison of the force versus displacement curves from testing and simulation are shown in Fig.7b. Comparison between the simulation model from the inclined test showed that the MDF model gives a realistic description of the test.

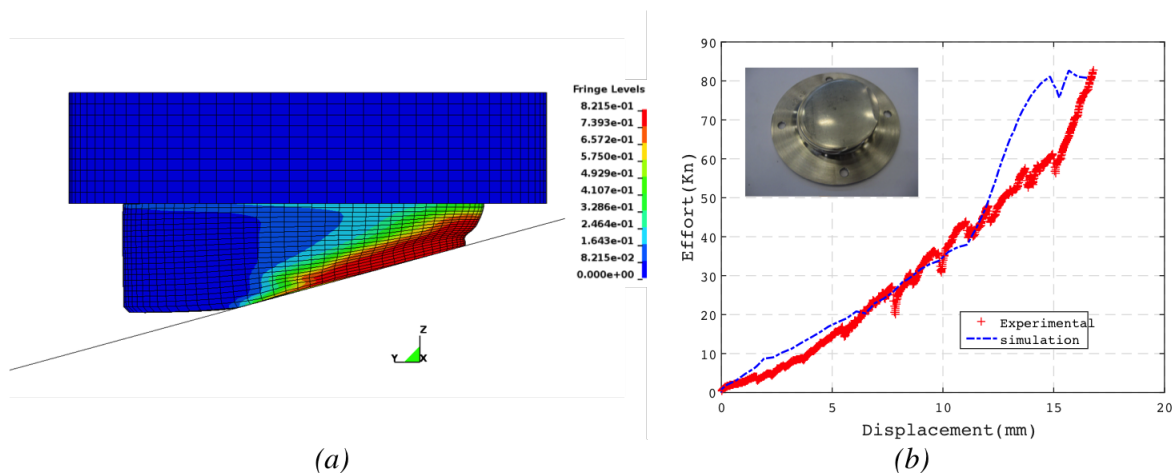


Figure 7: Finite element simulation of crushing test: a) residual deformation of the structure at the end of loading and equivalent plastic strain distribution on the OCCF part. b) comparison of experimental and numerical force-displacement curves from inclined crushing test.

4 CONCLUSIONS

In this work a exhaustive characterization of the brittle ceramic foam (OCCF) has been presented. A slightly modified Deshpande and Fleck model is identified in which both the slightly transversely isotropy due to the manufacturing process and slightly time dependence are not taken into account in this first model. First analysis of the experimental data permitted to identify an elliptic yield criterion depending on the level of volumetric plastic strain. The constitutive equations have been implemented into LS-Dyna FE code. First numerical results shows a good agreement compared to the experimental results. Further investigation is required to model the transversely isotropically behavior of the OCCF foam and the strong tension-compression assymetry that is observed for this material.

REFERENCES

- [1] Paolo Colombo Michael Scheffler. *Cellular Ceramics: Structure, Manufacturing, Properties & Applications*. Weinheim: Wiley-VCH, 2005.
- [2] J.M. Gmez de Salazar, M.I. Barrena, G. Morales, L. Matesanz, and N. Merino. Compression strength and wear resistance of ceramic foams-polymer composites. *Materials Letters*, 60(13-14):1687 – 1692, 2006.
- [3] M.Houillon. Shock-absorbing protection element for packaging for the transport and/or temporary storage of radioactive materials, 2015.
- [4] V.S. Deshpande and N.A. Fleck. Isotropic constitutive models for metallic foams. *Journal of the Mechanics and Physics of Solids*, 48(67):1253 – 1283, 2000.
- [5] V.S Deshpande and N.A Fleck. Multi-axial yield behaviour of polymer foams. *Acta Materialia*, 49(10):1859 – 1866, 2001.
- [6] Rodrigo Bresciani Canto. *Theoretical and experimental study of the compaction and sintering processes of polytetrafluoroethylene (PTFE)*. Theses, École normale supérieure de Cachan - ENS Cachan, August 2007.
- [7] Carole Frdy, Rodrigo B. Canto, Nicolas Schmitt, Stphane Roux, and Ren Billardon. Modelling of the mechanical behaviour of two pure ptfe powders during their compaction at room temperature. *AIP Conference Proceedings*, 1542(1), 2013.
- [8] Omar Kraiem, Nicolas Schmitt, and Han Zhao. Experimental investigation of mechanical behaviour of brittle foam under multiaxial loading. ICEM16, 2014.
- [9] J.O.Hallquist. *Ls-dyna theoretical manual*. May 1998.

COPYRIGHT NOTICE

Copyright ©2015 by the authors. Distribution of all material contained in this paper is permitted under the terms of the Creative Commons license Attribution-NonCommercial-NoDerivatives 4.0 International (CC-by-nc-nd 4.0).





MECHANICAL PROPERTIES OF LIGHT WEIGHT HYBRID THERMOPLASTIC BASED COMPOSITES

Réda Ourahmoune, Michelle Salvia

Laboratoire de tribologie et dynamique des systèmes
Ecole Centrale de Lyon, Ecully, France

Email: reda-el-hak.ourahmoune@ec-lyon.fr, michelle.salvia@ec-lyon.fr

ABSTRACT

Combination of thermoforming process of thermoplastic laminates reinforced with continuous fibers associated with injection molding of discontinuous reinforced thermoplastic in order to add stiffeners or specific functions at precisely defined locations is increasingly used for applications which require structural lightweight parts. This technique is well suitable to use in substituting metals and thermosetting composite materials by thermoplastics based composites particularly in automotive industries allowing to the various advantages which can offer thermoplastics composites like: lightness (compared to metals), toughness and recyclability (compared to thermosets).

In this study which is made in the framework of FUI project ARIZONA, complex shaped components were fabricated from thermoplastic prepreg combined with injected composite based on PA6 matrix. The prepreg lay-up was consolidated as a plate, pre-heated with an IR heating system, and put inside the mold. The plate was then thermoformed by closing the mold and over-molded in one step.

The objective of this study was to characterize the thermal-mechanical and mechanical properties of the laminate, injected and over-molded zones in relation with the processing parameters for different environments use (temperature and moisture). Thermal-mechanical properties were investigated by the Mechanical Dynamical Analysis (DMA) in range of temperature between -130°C to 200°C and dynamical frequency was varied from 0.1 to 30 [Hz]. Three-point bending and tensile tests were used to investigate the mechanical properties. Micro-tomography was realized to investigate in 3D reinforcement architecture and failure scenarii. The results show clearly the influence of the moisture absorption on the mechanical properties of each composite.

1 INTRODUCTION

In recent decades, the automotive industry has experienced considerable technological development, according to a demand for more and more challenging. Today, due to the globalization car manufacturers are innovating every day, in a sense of growing competition in the market by introducing vehicles more comfortable, safe, economic and environmentally friendly throughout.

In this way the choice of materials became an important step in the eco-conception, which can contribute significantly in environment preservation. Composite materials with organic matrix can be good alternative to replacement of classical metallic materials. During the last century, the introduction of advanced composite materials in various industries (aerospace, aerospace, automotive ...) was a striking success. The strengths of these materials reside in: their lightness, their chemical stability and their implementation facilities.

However, the physical properties of these materials vary depending on several factors: the nature of the matrix and the reinforcement, the architecture and the reinforcement rate ... etc. In an economic context the use of mid-range materials is preferred in automotive mass production. In this context, the thermoplastic matrix based composites reinforced with glass fiber are good candidates. Recyclability of thermoplastics is one of their various advantages. In addition, these materials are characterized by their low density which gives a considerable lightness in comparison to metallic materials. This significant weight saving has a direct impact on the surrounding, by the considerable decrease of emission of non-desirable gases such as (CO₂).

One of these materials materials that are used increasingly in automotive field is polyamide-6 (PA-6), which is a semi crystalline polymer characterized by acceptable mechanical properties, good resistance to fatigue, chemicals and hydrocarbons. However, it has poor resistance to water and its implementation requires drying [1]. The use of this material as matrix constitutes an ideal candidate for the manufacture of thermoplastic composites reinforced with glass fibers for the automotive industry.

However, at thickness and shape equivalent composite materials based on PA-6 reinforced with glass fibers are not equivalent to steels in terms of overall rigidity.

In order to overcome this difficulty, a new technique of composite manufacture has been developed; this technique is composite over-molding.

This study is made in the framework of FUI project ARIZONA, which consists in a new methodology of composite manufacturing from thermoplastic prepreg combined with injected composite based on PA6 matrix

The objective of this work is to characterize thermal-mechanical and mechanical properties of different zones of the composite part: laminate, injected and over-molded zones in relation with the processing parameters and moisture content.

2 MATERIALS & METHODES

2.1 Materials

The materials used in this study were three Polyamide PA6 based composites:

- Continuous glass fibers reinforced PA6, commercially named Tepex Dynalyte 102 RG 600(2); the reinforcement of this material is a balanced fabric with 0° and 90° oriented made from two plies of 0.5 mm oriented at [0°, 90°] given a total thickness of 1mm. The reference of the material in this study is CGFR-PA6. Fiber weight fraction is about 64% (cf. fig.1.1).

- Injected composite reinforced by discontinuous glass fibers with a nominal length of 250 μ m; this material is made with the same grade of PA6 and commercially named Durethan BKV 60 characterized by fiber weight fraction of 62% (cf. fig.1.2). The reference of the material in this study is DGFR-PA6.
- Over-molded composite which is a bi-layered composite between continuous and discontinuous fiber reinforced composite.

All materials were supplied by Bond-Laminates GmbH[®] and Lanxess[®].

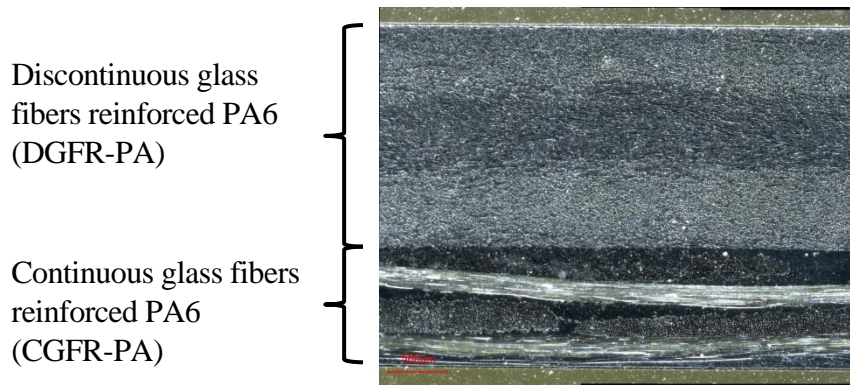


Fig.1. Numerical optical micrograph showing over-molded composite layers.

In the aim to characterize the effect of process manufacturing parameters, a prototype part with a complex shape was designed in ARIZONA project. The design was carried out by Mecaplast[®] after shape optimization given by LTDS. The mold was realized by Compose[®]. All prototype parts were manufactured at the PEP[®]. The prepreg lay-up was consolidated as a plate, pre-heated with an IR heating system, and put inside the mold. The plate was then thermoformed by closing the mold and over-molded by injecting the DGFR-PA6 (Fig.1.b) in one step.

Temperature of pre-heating was varied as follow: 250, 270, 285 and 295°C. Mold temperature was 110°C.

All specimens were obtained by water jet cutting from prototypes.

2.2 Thermomechanical analysis

Rheological characteristics of materials were performed with the use of DMA50 0.1dB from METRAVIB on rectangular (20mm×2mm× thickness mm) specimens in the tension/compression mode at controlled alternating strain. The temperature range was -130°C to 200°C with a heating rate of 1°C/min and the frequency was varied from 0.1 to 30 Hz.

2.3 Tree point bending test

The three point bending loadings were carried out using an INSTRON 4206 electromechanical machine with load cells of 100 kN and cross head speed was 2.5 mm/min. The radius of the load roller was 5 mm and the distance between supports was 60 mm. Experimental procedure was made according to the International standard ISO 14125 at room temperature ($T=23\pm 1^\circ\text{C}$, $\text{RH} = 40\pm 5\%$). CGFR-PA6 samples have the following dimensions: 100 mm long, 25 mm wide and 1 mm thick. In the case of DGFR-PA6 and over-molded composite the samples dimensions are 100 mm long, 15 mm wide and 3 mm thick.

The apparent flexural elastic modulus (E_f) and the ultimate stress (σ_{\max}) were the mechanical properties evaluated.

Figure (fig.2) shows an example of three point bending curves of DGFR-PA6 composite. The linear part corresponds to the elastic behavior and the maximum recorded stress is considered as an ultimate flexural stress.

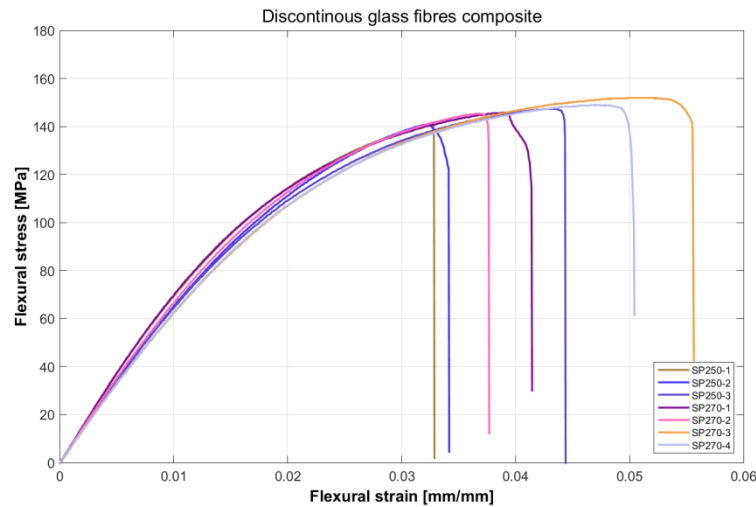


Fig.2. Flexural stress vs flexural strain curve (three bonding test): Discontinuous glass reinforced PA6.

2.4 Computed tomography analysis

The computed tomography is a non-destructive method based in the 3D X ray scan which allows three-dimensional structure information of materials without contact. The micro-tomograph used is Nanotm[®] research edition manufactured by General Eclectic inspection Technology. It allows analysis of samples size: height from 1 mm to 120 mm, maximum 100 mm width and sample acquisition in aqueous medium. The X-ray source is an open tube GE Phoenix nano-focus, providing a maximum voltage of 180 kV and a maximum power of 15 W. The voltage range operates between 10 and 180 kV. The apparatus detector is a digital detector with dimensions 115 mm x 115 mm, with a pixel size of 50 microns x 50 microns (2300 x 2300 matrix px). It provides submicron resolution (minimum pixel size of 0.5 microns). However the pixel resolution is highly dependent on the specimen size.

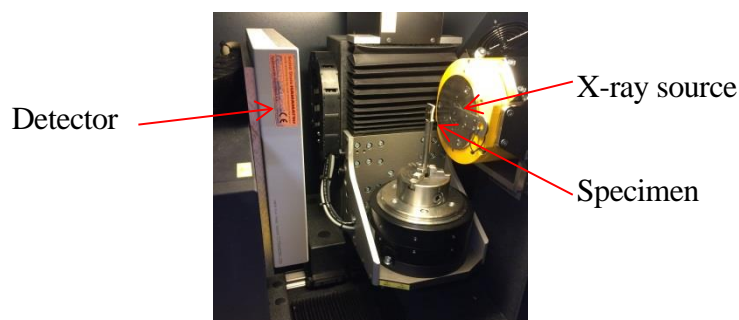


Fig.3. Micro-tomography device.

The test parameters used in this study are as follows: sample dimensions 15 mm long, 15 mm width and 4 mm thick and the beam operated at 80 keV and 120 μ A. According to the sample size the voxel resolution achieved in this study was 8 μ m. The result obtained by X-ray tomography was a stack of slices in 3 directions which includes about 2400 images. These slices were analysed using VG-studio and ImageJ to generate 3D representation of the specimens.

3 RESULTS & DISCUSSIONS

3.1 Materials conditioning

Effect of moisture content on PA6 based composite on mechanical properties were investigated. Specimens were dried for 8 days in stove at 60°C, in the objective to remove all residual moisture due to air conditioning and transportation. After surface polishing of sample the absorption of water was achieved by immersion in distilled water at room temperature ($T = 23^{\circ}\text{C} \pm 2^{\circ}\text{C}$). Uptake moisture of specimens was measured by differential weighting using an electronic balance of accuracy 10^{-5} g. Difference between the weight of dried specimens and the weight after water immersion was calculated. Supposing that in the composite only the matrix PA6 uptakes water, the moisture content $M(t)$ absorbed by each specimen was calculated from its initial weight (w_0) of dried matrix PA6 and its weight after absorption (w_t) as follows:

$$w_0 = w_{0c} \cdot (1 - X_f) \tag{eq.1}$$

$$w_t = w_{tc} - w_{0c} \tag{eq.2}$$

Where, (w_{0c}) is the initial weight of the composite, (X_f) is the weight fraction of the fiber (0.64%) and (w_{tc}) the weight of conditioned composite at the instant t .

$$M(t) = 100 \cdot \left(\frac{w_t - w_0}{w_0} \right) \tag{eq.3}$$

Figure VI.1 shows the weight gain $M(t)$ as a function of the square root of time ($t^{1/2}$) during ageing in distilled water for the studied composites. Three specimens were studied for each case and the presented water uptakes are average values.

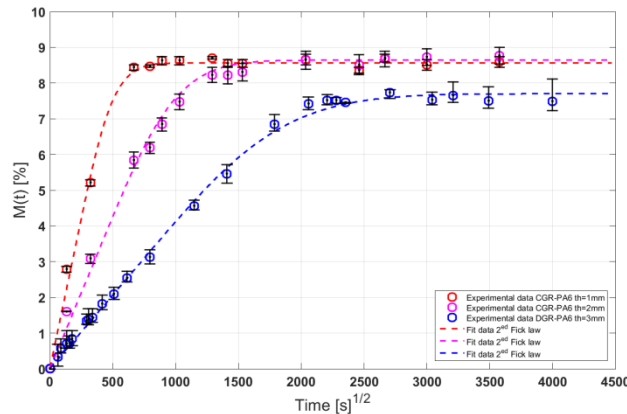


Fig.4. Moisture content evolution as a function of time for the three composites CGFR-PA6 1 mm thick, CGFR-PA6 2 mm thick and CGFR-PA6 3 mm thick

All composite curves showed similar profiles and one can distinguish the presence of two zones. The first one is linear corresponding to a rapid increase of moisture content. The second region corresponds to a plateau at which the aged material reaches saturation. In this case, and for all studied composites the kinetics of water diffusion follow the one-dimensional Fick's second law. The coefficient of diffusion of water can be calculated from the slope (S) of the linear part of the last curves as follows [2]:

$$D = \pi \left(\frac{h}{4M_{\infty}} \right)^2 (S)^2 \tag{eq.4}$$

By considering the coefficients D and M_m , the moisture content as a function of time $M(t)$ can be expressed according to the following equation [3]:

$$\frac{M(t)}{M_{\infty}} = 1 - \sum_{n=0}^{\infty} \frac{8}{\pi^2(2n+1)^2} \exp\left(-\frac{D(2n+1)^2\pi^2 t}{h^2}\right) \quad (\text{eq.5})$$

where M_{∞} is the moisture content at saturation, D is the apparent diffusion coefficient, t is the aging time and h is the sample thickness.

The apparent diffusion coefficient and the maximum moisture content vary with the nature of composite. The continuous glass reinforced PA-6 composites achieved moisture saturation at 8.7% with an apparent coefficient of water diffusion equal to $7.01 \text{ e-}7 \text{ mm}^2/\text{s}$ whereas the discontinuous glass reinforced PA-6 composite (DGFR-PA6) showed better hygrothermal properties since the water diffusivity and the moisture content at saturation were lower than for the CGFR-PA6 ($M_{\infty} = 7.7\%$ and $D = 5.1 \text{ e-}7 \text{ mm}^2/\text{s}$).

3.2 Dynamical mechanical analysis

The storage moduli (E') and the loss factor ($\tan \delta$) as a function of the temperature and frequency for all composites were measured by DMA.

In order to determine different relaxation temperatures, CPGR-PA6 composite were oriented at $\pm 45^\circ$ according to the direction of loading. Figure 3 shows an example of the evolution of storage modulus (E') and damping factor ($\tan(\delta)$) as a function of temperature and frequency for CPGR-PA6. These figures compare two moisture content states: dried and wet at saturation.

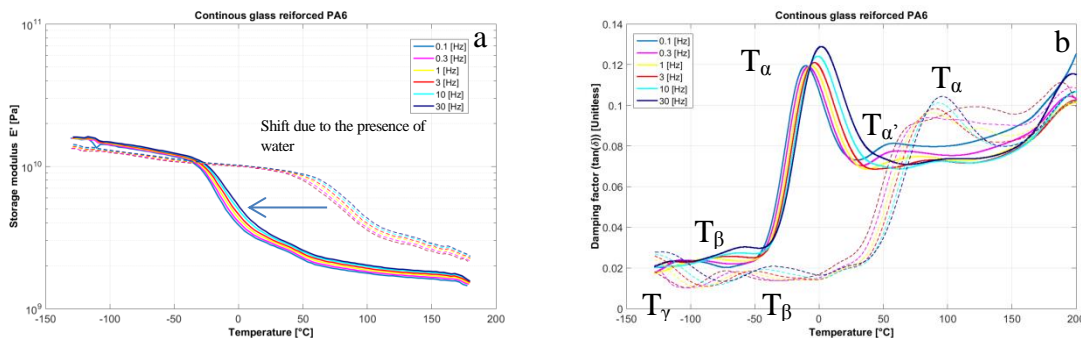


Fig. 5. Evolution of viscoelastic properties of CGFR-PA6 oriented at $\pm 45^\circ$ measured by DMA as versus temperature and frequency : a) Storage modulus E' b) damping factor ($\tan(\delta)$).
(----) dried composite (—) wet composite.

In the range of temperature studied ($-130 - 200 \text{ }^\circ\text{C}$) a decrease of storage modulus is observed with temperature increase. The structural change occurring in polymeric materials is a result of the molecular mobility at different time scales. These motions are known as molecular relaxations. In the case of dried composites three clear relaxations can be distinguished:

- the main relaxation or relaxation- α corresponding to the drastically decrease of the storage modulus and the highest peak of the $\tan(\delta)$; this relaxation is associated to the glass transition, and corresponds to the coordinated motion of relatively long chain segments by debonding of low energy bonds (hydrogen bonds) [4]. This relaxation occurs approximately at $T_{\alpha} = 80 - 90^\circ\text{C}$ depending on frequency.
- two sub- T_g relaxations [5-6]: the relaxation- β and relaxation- γ corresponding to the motions of small chain segments or molecular functions. The relaxation- β involves the rotation of the amide functions and occurs in the range of $-80 / -40^\circ\text{C}$ approximately; the

relaxation- γ corresponds to the vibrational motions of the methylene functions in the chains and it occurs at around -130°C .

After conditioning the composites by water immersion, the DMA results show that the presence of water in the PA6 matrix involves a shift of mechanical molecular relaxations to low temperature as observed in fig.5. In fact, the T_{α} decreases from 80°C in dried composite to -10°C for wet composite at 1Hz as shown in Figure (fig.6).

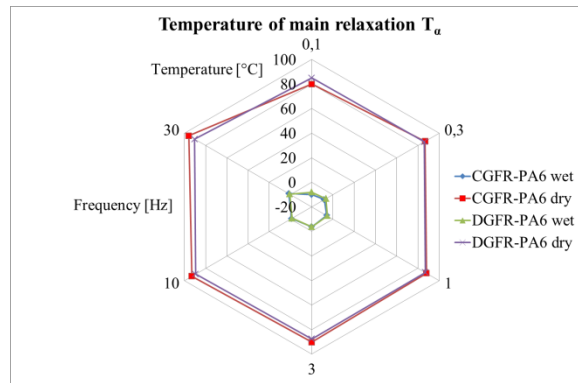


Fig.6. Temperature of main relaxation versus moisture content for different loading frequencies.

In the case of the main relaxation (α) the shift of temperature is due to the fact that the presence of water increases the local volume by separating the polymer chains [11, 12].

3.3 Three-point bending tests

Mechanical properties of all composites according to the process conditions and moisture content were studied using 3-point bending test. The apparent flexural modulus was taken as a main mechanical property discriminant between different composites.

Figures (fig.7.a & fig.7.b) compare the flexural properties of Continuous GFR-PA6 and Discontinuous GFR-PA6 respectively for different processing conditions and sampling zones. Prepreg heating was varied from 250 to 295 °C. In all cases the composite failure occurred on the tensile side.

The results show there is not a significant variation in the apparent flexural modulus for the two composites whatever the processing conditions. Nevertheless there is a large modulus range for discontinuous fiber reinforced composite (7-16 GPa) due to the fiber architecture which varies with sampling zone.

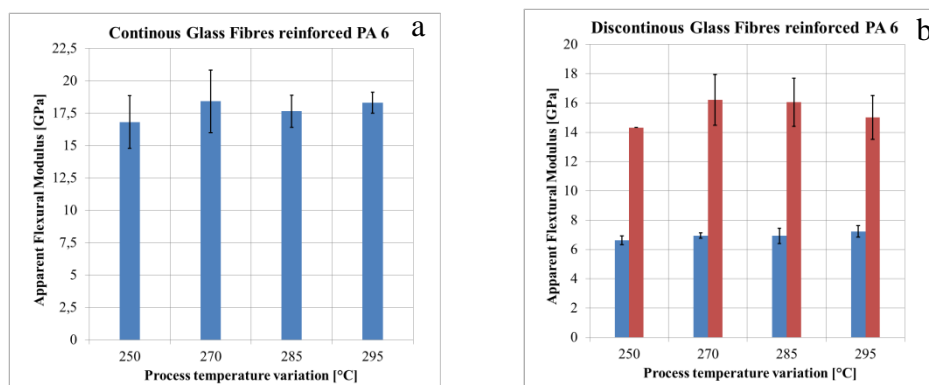


Fig.7. Evolution of apparent flexural modulus according to the temperature process variation: a) CGFR-PA6 and b) DGFR-PA6 (zone1 blue & 2 red).

Figures (Fig.8.a & Fig.8.b) compare the flexural properties of over-molded composites for different processing temperatures. Due to the multi-layering feature of these composites, two bending configurations were investigated: in the first, continuous glass fibers on tensile side and in the second on compressive side.

Fig.8.a and Fig.8.b show the homogenized apparent flexural modulus and the ultimate flexural strength respectively.

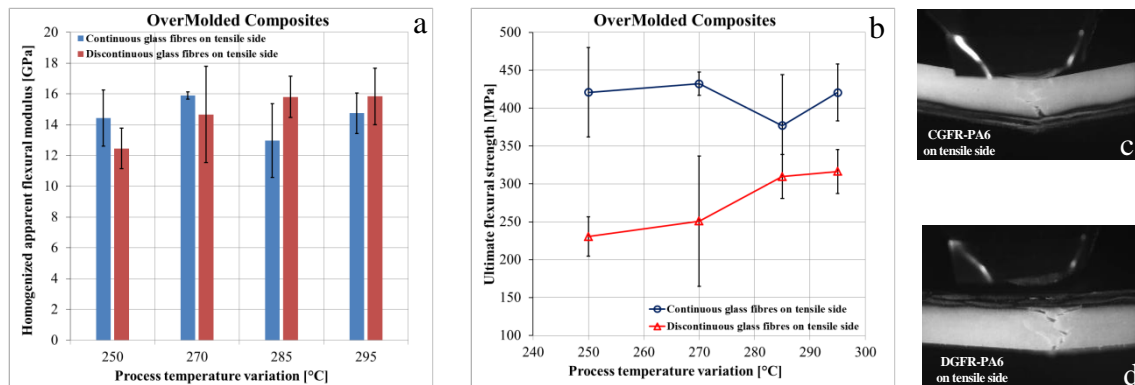


Fig.8. Evolution of flexural properties for the over-molded composite: a) apparent flexural modulus b) Ultimate flexural strength c) and d) illustration of different bending configurations and failure features.

The results show that there is no clear tendency concerning the apparent flexural modulus according to the temperature processing and bending configuration. This behavior is probably associated to the complex fiber architecture according to sampling zone (fig.8.a). The ultimate flexural strength evolution according to the different mode of bending is shown in figure (fig.8.b). When the CGFR-PA6 is on the tensile side the flexural strength is the highest and quasi-stable whatever the processing conditions. For the system with the discontinuous fibers on the tensile side the ultimate stress increases with the processing conditions probably due to a better interface between the two composites. The computed tomography technique was used to investigate failure mode of the over-molded systems. Fig.9 shows an example of 3D reconstitution computed from X-ray slices for continuous glass fibers on the tensile side (Fig.9.a) and discontinuous glass fibers on the tensile side (Fig.9.b). These figures show typical failure features. In the case when CGFR-PA6 is on the tensile side the failure grows through the two composites (Fig.9.a). However, in the second case (discontinuous fibers on the tensile mode) the failure occurs through the discontinuous glass fiber composite and at the interface between the two materials (Fig.9.b).

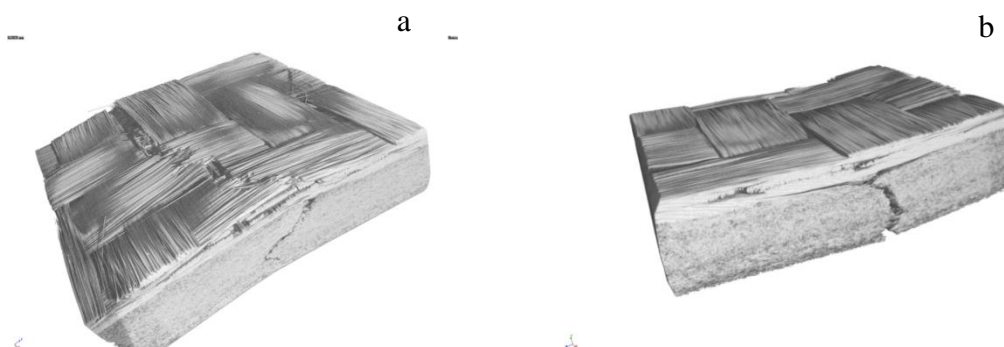


Fig.9. 3D micro-tomography representation of over-molded composite after 3-point bending test: a) CGFR-A6 on the tensile side and b) DGFR-A6 on the tensile side.

This analysis confirms that the scattering of the results is due to the fiber architecture of the injected composite. In fact, the injection flow makes the fiber orientation: in some cases the skin/core morphology is dominant with high thickness of skin layer and with fibers oriented principally in longitudinal direction, leading to a higher strength. Figure (fig.10) shows two over-molded composites with the same process parameters but presenting different ultimate flexural strength (a : $\sigma_{max} = 190$ MPa, b: $\sigma_{max} = 312$ MPa).

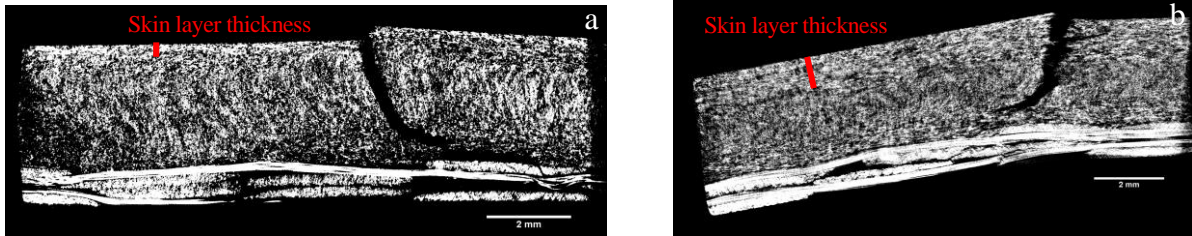


Fig.10. Micro-tomography slices showing discontinuous fibers orientation for the same process conditions but different sampling zones.

Effect of moisture on flexural properties

Figure (fig.11) illustrates the evolution of apparent flexural modulus (fig.11.a) and ultimate flexural strength (fig.11.b) as a function of moisture content for all studied composites for a given sampling zone.

The results show a sharp decrease in the flexural modulus as well as in the ultimate flexural strength. The continuous glass fibres reinforced PA6 observes a decrease of 50% in apparent flexural modulus and the ultimate flexural strength for the moisture saturation state. At 5% of moisture content the decrease of flexural modulus is about 50% and the flexural strength was reduced of about 36%.

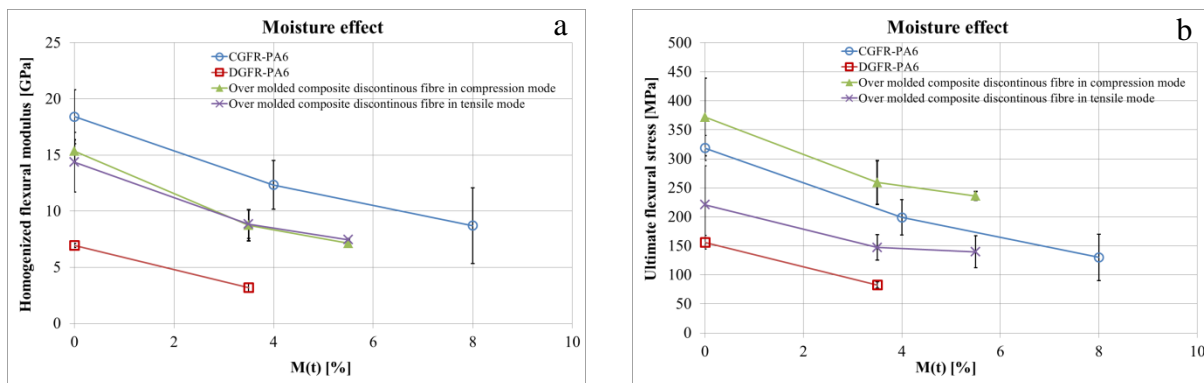


Fig.11. Evolution of flexural properties according to the moisture content for all composites: a) Apparent flexural modulus and b) ultimate flexural stress.

As shown previously with DMA, the absorbed water decreases the main relaxation of PA6 due to the plasticizing action of water molecules. This phenomenon leads to a drop of the modulus of the matrix at room temperature, and therefore to a decrease of the composite one (mixture law). Moreover, the increase in molecular mobility of the wet matrix reduces the yield stress and increases the ductility and elongation at break of the composite.

4 CONCLUDING REMARKS

In this study the thermomechanical and mechanical properties of PA6 composites was investigated. This work demonstrates that the conditioning history and environment conditions are important parameters to be taken into account in design of structural part composites based on PA6. The PA6 matrix is very sensitive to humidity; the sorption of water can decrease drastically the thermal and mechanical properties of glass fiber reinforced PA6 composites. The over-molding of prepreg composite can be a solution to enhance the rigidity and therefore the mechanical properties of composite parts by a local addition of discontinuous glass fiber reinforced composite.

5 ACKNOWLEDGEMENTS

The authors would like to acknowledge all the partners of ARIZONA project, Guillaume Huguet from Mecaplast®, Mathieu Schwander from PEP®, Guillaume Salaun from Compose® and Jean-Marie Olive from Lanxess® and our colleagues in ECL for their help: Jerome Laborde, Jean-Michel Vernet and Benoit Ponsard.

6 REFERENCES

- [1] L. Monson, M. Braunwarth, and C.W Extrand, Moisture absorption by various polyamides and their associated dimensional changes, *Journal of Applied Polymer Science*, (107): 355-363, .2008.
- [2] C.H. SHEN, G.S. SPRINGER, Moisture Absorption and Desorption of Composite Materials, *Journal of Composite Materials*, (10) : 2-20, 1976
- [3] W. Jost, Diffusion in Solids, Liquids, Gases. New York: Academic Press, 1960.
- [4] A. Owen, R. Bonart, Cooperative relaxation processes in polymers, *Polymer*, (26):1034, 1985.
- [5] Y. Park, J. Ko, T-K. Ahn, and S. Choe, Moisture Effects on the Glass Transition and the Low Temperature Relaxations in Semiaromatic Polyamides, *J. Polym. Sci. Part B: Polym. Phys.*, (35): 807, 1997.
- [6] G. Rotter and H. Ishida, Dynamic Mechanical Analysis of the Glass Transition: Curve Resolving Applied to Polymers, *Macromolecules*, (25): 2170, 1992.
- [7] N.S. Murthy, Hydrogen Bonding, Mobility, and Structural Transitions in Aliphatic Polyamides, *J. Polym. Sci. Part B: Polym. Phys.*, (44):1763, 2006.
- [8] S. Rastogi, A.E. Terry, and E. Vinken, Dissolution of Hydrogen-Bonded Polymers in Water: A Study of Nylon-4,6, *Macromolecules*, (37): 8825, 2004.
- [9] E. Vinken, A.E. Terry, O. van Asselen, A.B. Spoelstra, R. Graf, and S. Rastogi, Role of superheated water in the dissolution and perturbation of hydrogen bonding in the crystalline lattice of polyamide 4,6, *Langmuir*, 24, 6313 (2008).
- [10] Abacha et al. – eXPRESS Polymer Letters, (3) 4 : 245–255, 2009.
- [11] N. S. Murthy, M. K. Akkapedi, Analysis of lamellar structure in semicrystalline polymers by studying the absorption of water and ethylene glycole in nylons small angle neutron scattering, *Mocromelecules*, (3): 142-152, 1998.

[12] A. Bergeret, L. Ferry, P. Ienny. Vieillessement hygrothermique des composites thermoplastiques renforcés par des fibres de verre, *Revue des composites et des matériaux avancés*, (18)1: 33-49, 2008.

COPYRIGHT NOTICE

Copyright ©2015 by the authors. Distribution of all material contained in this paper is permitted under the terms of the Creative Commons license Attribution-NonCommercial-NoDerivatives 4.0 International (CC-by-nc-nd 4.0).



1 INTRODUCTION

The use of numerical simulation techniques has become an indispensable part of the industrial design process of innovative constructions for vibration performances. The Galerkin Finite Element Method (FEM) [1] is a well-established tool, which is commonly used for the analysis of vibration problems. However, as it uses continuous, piecewise polynomial shape functions, it often leads to huge numerical model. As a consequence, in practice, its use is restricted to low-frequency range applications. Trefftz methods [2] have been proposed as a means to bypass this limitation. They differ from the FEM in the expansion of the field variables, as they use shape functions that are exact solutions of the governing differential equations. Compared to the FEM, Trefftz methods often lead to a considerable reduction in model size and computational effort. Some examples of such methods are: a special version of the partition of unity method [3], the ultra weak variational method [4], the plane wave discontinuous Galerkin method [5], the least-squares method [6], the discontinuous enrichment method [7], the element-free Galerkin method [8], the wave boundary element method [9] and the wave-based method [10]. The Variational Theory of Complex Rays (VTCR), first introduced in [11] for steady-state vibration problems and in [12] for 3-D acoustics problems, also belongs to that category. The main differences between these methods lie essentially in the treatment of the transmission conditions at the boundaries of the elements or substructures.

The VTCR uses a specific weak formulation of the problem, which enables the approximations within the substructures (the shape functions that verify the governing equations) to be a priori independent of one another. Thus, any type of shape function can be used within a given substructure provided it satisfies the governing equation, thus giving the approach great flexibility. In this work, we introduce extensions of the classical VTCR formulation: the constraint, which imposes the verification of the governing equation, is weakened. This leads to a new numerical method, which can be called the weak Trefftz discontinuous Galerkin method. These extensions allow one to easily couple different types of numerical models and then get hybrid models: the FEM and the classic VTCR models used together, for example. As a consequence, they lead to new approaches to the resolution of engineering problems where composite structures have to be faced.

2 DEVELOPMENT OF HYBRID METHODS

Our hybrid method will be presented on a Helmholtz vibration problem. Then, consider a standard problem defined on a domain Ω with boundaries $\partial\Omega = \partial_1\Omega \cup \partial_2\Omega$ (see Figure 1): find $u \in H^1(\Omega)$ such that

$$\begin{cases} (1+i\eta)\Delta u + k^2 u + r_d = 0 & \text{over } \Omega \\ u = u_d & \text{over } \partial_1\Omega \\ (1+i\eta)\partial_n u + hiku = g_d & \text{over } \partial_2\Omega \end{cases}$$

where $\partial_n u = \text{grad } u \cdot n$, (n being the outward normal). k is the wave number; h is a constant related to the vibration impedance; r_d and g_d are prescribed sources. The damping coefficient η is positive. The data are supposed to be sufficiently regular to have a unique solution.

Let us introduced the VTCR variational formulation for this problem. To do this, the domain Ω is divided into subdomains Ω_E . The interface between two subdomains E and E' is denoted $\Gamma_{EE'}$. The VTCR is a Trefftz approach which uses the affine space $U = \{u / u \in U_E \text{ on } \Omega_E\}$ with

$$U_E = \{u_E / u_E \in V_E \subset H^1(\Omega_E); (1 + i\eta)\Delta u_E + k^2 u_E + r_d = 0 \text{ on } \Omega_E\}$$

The vector spaces (with $r_d = 0$) associated with U and U_E are denoted U_0 and $U_{E,0}$. We also denote $\{u\}_{EE'} = (u_E + u_{E'})_{\Gamma_{EE'}}$ and $[u]_{EE'} = (u_E - u_{E'})_{\Gamma_{EE'}}$. Denoting $q_u = (1 + i\eta)grad u$, the VTCR formulation can be written: find $u \in U$ such that

$$\begin{aligned} & \text{Re} \left(-ik \left(\sum_{E,E'} \int_{\Gamma_{EE'}} \left(\frac{1}{2} \{q_u \cdot n\}_{EE'} \{\bar{v}\}_{EE'} - \frac{1}{2} [\bar{q}_v \cdot n]_{EE'} [u]_{EE'} \right) dS \right. \right. \\ & \quad \left. \left. - \sum_E \int_{\Gamma_{EE} \cap \partial_1 \Omega} \bar{q}_v \cdot n (u - u_d) dS \right. \right. \\ & \quad \left. \left. + \sum_E \int_{\Gamma_{EE} \cap \partial_2 \Omega} \frac{1}{2} (-\bar{q}_v \cdot n (u + (q_u \cdot n - g_d) / (hik)) + \bar{v} (q_u \cdot n + hiku - g_d)) dS \right) \right) \\ & = 0 \quad \forall v \in U_0 \end{aligned}$$

where the over line represents the complex conjugate part, and “Re” the real part. It is proven that this variational formulation is equivalent to the reference problem. All that has to be done to get an approximation is to replace U_E by the finite dimension subspace U_E^h in the variational formulation, for example spanned by N_E propagative waves $e^{ik(\theta).x}$ regularly reparted on the θ -polar $[0; 2\pi[$ range for 2-D examples.

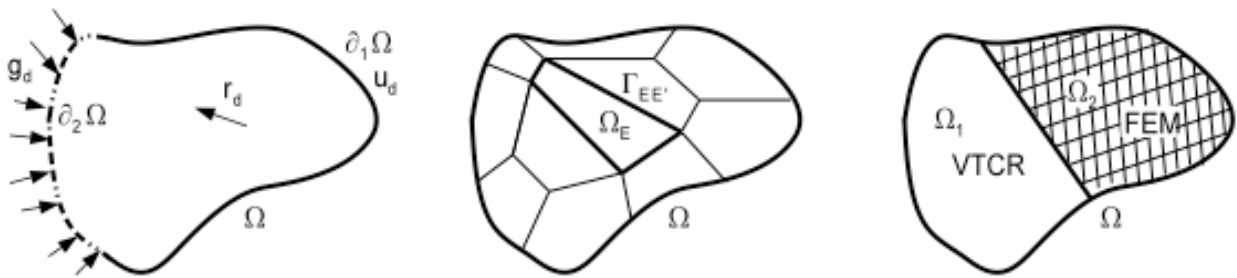


Figure 1: Left: definition of the computational domain. Middle: definition of the subdomains. Right: coupling of the FEM and VTCR descriptions for hybrid models.

However, one constraint with the VTCR is the need for verifying the governing equation (also called the Trefftz constraint): $u \in U$. As a consequence, FEM shape functions can not be used directly. Then, in order to develop hybrid methods, which mix VTCR and FEM approximations, one has to weaken this constraint (then leading to the definition of weak Trefftz methods). To do this, it is necessary to modify the variational formulation. The new variational formulation is now: find $u \in U$ (with now no constraint on U) such that:

$$\begin{aligned} & \operatorname{Re} \left(-ik \left(\sum_{E,E'} \int_{\Gamma_{EE'}} \left(\frac{1}{2} \{q_u \cdot n\}_{EE'} \{\bar{v}\}_{EE'} - \frac{1}{2} [\bar{q}_v \cdot n]_{EE'} [u]_{EE'} \right) dS \right. \right. \\ & \quad \left. \left. - \sum_E \int_{\Gamma_{EE} \cap \partial_1 \Omega} \bar{q}_v \cdot n (u - u_d) dS \right. \right. \\ & \quad \left. \left. + \sum_E \int_{\Gamma_{EE} \cap \partial_2 \Omega} \frac{1}{2} (-\bar{q}_v \cdot n (u + (q_u \cdot n - g_d) / (hik)) + \bar{v} (q_u \cdot n + hiku - g_d)) dS \right. \right. \\ & \quad \left. \left. + \sum_E \int_{\Omega_E} (\operatorname{div} q_u + k^2 u + r_d) \bar{v} d\Omega \right) \right) = 0 \quad \forall v \in U_0 \end{aligned}$$

As one can see, the difference between this formulation and the last one is just the add of a new term which weakens the governing equation. Again, it can be demonstrated that this formulation is equivalent to the reference problem. As no constraint is needed for the definition of the space U , FEM approximation can be used anywhere it is needed. We can also mix the approximations by using the VTCR approximation in a partition Ω_1 and the FEM approximation in another partition Ω_2 (see Figure 1). As a consequence, a great flexibility is provided by such an approach, especially on composite structures, where VTCR or FEM can be used (see [13] for the VTCR).

3 NUMERICAL ILLUSTRATION

We here consider the example described in Figure 2 for the illustration of hybrid methods. The problem is considered to be homogeneous, and restricted to a 2-D L-curve shape domain. The wave numbers of the fluids a and b are $k_a = 6.5 \text{ m}^{-1}$ and $k_b = 29.4 \text{ m}^{-1}$. The damping coefficients are $\eta_a = \eta_b = 0.001$. The boundary conditions are Robin condition with $h = 0.001$ and $g_d = 0$ or 1 m^{-1} .

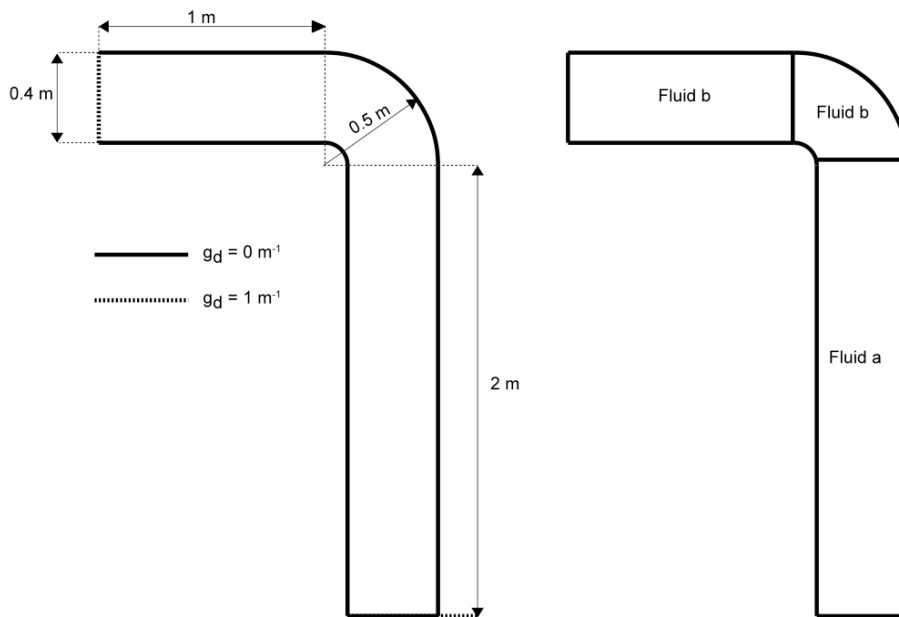


Figure 2: Definition of the computational domain for the illustration example used in Section 3.

The selected subdomaining for computing the problem can be seen in Figure 3. The FEM approximation has been used in Ω_1 , where the wavelength is the smallest. Its mesh uses 10 elements along the x-axis and 40 elements along the y-axis, leading to a mesh with 451 DOFs. The VTCR approximation has been used in the subdomains Ω_E with $E \in \{2..13\}$. In each of these subdomains, the number N_E of the regularly oriented used rays satisfies $N_E = \lceil 2.k.diam(\Omega_E) \rceil$ where $\lceil \square \rceil$ stands for the integer part, k stands for the wavenumber and $diam(\Omega_E)$ stands for the diameter of Ω_E . With such a choice, we are sure that the VTCR subdomains contains enough DOFs to get a good solution (see the heuristic criterion in [12]). The corresponding result can be seen on Figure 3. One can see that, globally, the solution looks like the FEM reference solution visible in Figure 3, and computed with a very refined mesh. Indeed, almost all the vibration peaks are located at the right location and have the right amplitude. Then, this example validates the proposed approach and shows that the hybrid method can solve this very complex numerical example, which mixes different kind of approximation with different kind of physics.

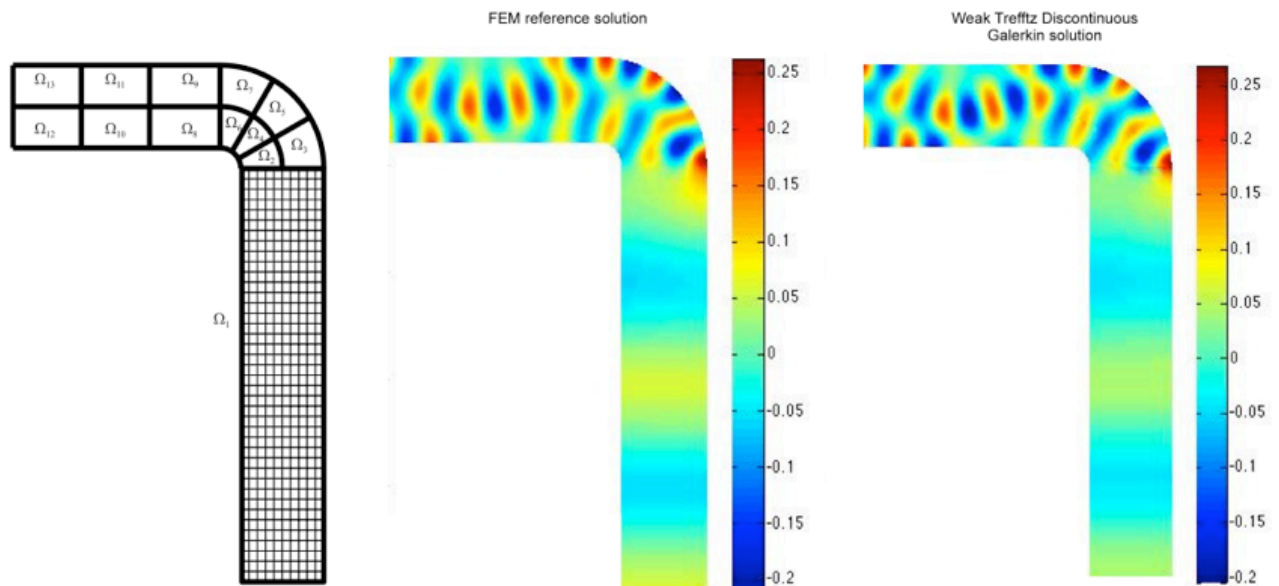


Figure 3 Left: selected subdomaining and modeling for computing the problem of Section 3, defined in Figure 2. Middle: FEM reference solution. Right: numerical result obtained with the proposed hybrid approach.

4 CONCLUSION

In the VTCR proposed in [11], [12] and [13], the solution of a vibrational problem is tough in an approximated space spanned by exact solutions of the governing equation (i.e. propagative waves). Their continuities along the interface between the subdomains are ensured thanks to a dedicated variational formulation. Here, this variational formulation is extended in such a way that any kind of approximation can be used: exact solutions of the governing equation, or not. Then, hybrid approximation mixing VTCR and FEM approximation can be used. This has been illustrated on an example, which mixes two types of fluid. Waves are used to approximate the

vibrational response of the fluid which contains the smallest wavelength. Polynomial FEM shape functions are used to approximate the response the fluid which contains the largest wavelength. As a consequence, this work is dedicated to the definition of a new generation of computational strategy, able to easily mix different kind of approximations, which is useful for the prediction of the vibrational performances of composite structures.

REFERENCES

- [1] Zienkiewicz OC: The Finite Element Method. McGraw-Hill 1977.
- [2] Trefftz E: Ein gegenstück zum ritzschen verfahren. Second International Congress on Applied Mechanics 1926, 131–137.
- [3] Strouboulis T, Hidajat R: Partition of unity method for Helmholtz equation: q-convergence for plane-wave and wave-band local bases. Applications of Mathematics 2006, 51:181–204.
- [4] Cessenat O, Despres B: Application of an ultra weak variational formulation of elliptic pdes to the two-dimensional helmholtz problem. SIAM Journal on Numerical Analysis 1998, 35:255–299.
- [5] R. Hiptmair, A. Moiola, I. Perugia, Plane wave discontinuous Galerkin methods for the 2D Helmholtz equation: analysis of the p-version, SIAM Journal on Numerical Analysis 2011, 49:264–284.
- [6] Monk P, Wang D: A least-squares method for the Helmholtz equation. Computer Methods in Applied Mechanics and Engineering 1999, 175:121–136.
- [7] Farhat C, Tezaur R, Toivanen J: A domain decomposition method for discontinuous Galerkin discretizations of Helmholtz problems with plane waves and Lagrange multipliers. International journal for numerical methods in engineering 2009, 78(13):1513–1531.
- [8] Bouillard P, Suleaub S: Element-Free Galerkin solutions for Helmholtz problems: fomulation and numerical assessment of the pollution effect. Computer methods in applied mechanics and engineering 1998, 162:317–335.
- [9] Perrey-Debain E, Trevelyan J, Bettess P: Wave boundary elements: a theoretical overview presenting applications in scattering of short waves. Engineering Analysis with Boundary Elements 2004, 28:131–141.
- [10] Van Genechten B, Atak O, Bergen B, Deckers E, Jonckheere S, Lee JS, Maressa A, Vergote K, Pluymers B, Vandepitte D, et al.: An efficient Wave Based Method for solving Helmholtz problems in three- dimensional bounded domains. Engineering Analysis with Boundary Elements 2012, 36:63–75.
- [11] Ladevèze P: A new computational approach for structure vibrations in the medium frequency range. Comptes Rendus Académie des Sciences Paris 1996, 332(2b):849–856.
- [12] Kovalevsky L, Ladevèze P, Riou H, Bonnet M: The Variational Theory of Complex Rays for three- dimensional Helmholtz problems. Journal of Computational Acoustics 2012, 20(04).
- [13] Kovalevsky L., Riou H., Ladevèze P.: A Trefftz approach for medium-frequency vibrations of orthotropic structures. Computers & Structures 2014, 143:85-90.

COPYRIGHT NOTICE

Copyright ©2015 by the authors. Distribution of all material contained in this paper is permitted under the terms of the Creative Commons license Attribution-NonCommercial-NoDerivatives 4.0 International (CC-by-nc-nd 4.0).



Title: **Accounting for manufacturing effects in composites virtual prototyping.**

Authors: A. Trameçon and Dr Patrick de Luca

Abstract

The presentation will review several examples of the effects of the manufacturing process and of the means to incorporate them, directly or indirectly, in the simulation of the shock or crash events. The use of the virtual material characterization is a key ingredient in addressing these issues (effects of manufacturing and new textile architectures) and it will be presented.

1. Introduction

It is generally felt that the numerical simulation of composite materials has not reached the required level to fully support the long-time promised explosion of the use of composite materials. One of the reasons is that the effects of the manufacturing and assembly processes are not taken into account in the assessment of the mechanical performance of the composite structures (statics, strength and crash). The manufacturing effects include the fiber reorientation, the thickness variations, the local fiber content variations, the fiber waviness, the micro and macro porosities, the degree of cure and of crystallization, the degree of intimate contact, the tows sections deformations, etc. Another reason is the lack of modelling tools for the ever increasing textile architectures put on the market. Because of these large domains of incomplete control of the knowledge and technology, the industry relies on large safety margins, at best involving statistical tools, that lead to add plies and therefore mass, hindering the full fruition of the lightness of the composite materials.

2. Effects of preforming onto dry reinforcement impregnation

In this section, one will start by reporting about the effects of the preforming onto the reinforcement impregnation.

a. Example of the impregnation of a hemisphere.

This example is one of the first example reported, it traces back to the 2002 german SAMPE (1) and is due to a team of the Institut für Verbundwerkstoffe at Kaiserlautern, Germany. The figure 1 shows the RTM (Resin Transfer Molding) impregnation of a dry fabric placed in an hemispherical mold using a pole injection and the finite element simulation based on the Darcy equation using a uniform permeability (one can see a filling time contour plot showing a circular radial flow front evolution). One reminds that the Darcy equation relates the flow front velocity (V) through a porous medium to the pressure (P) gradient

using the resin viscosity (μ) and the preform permeability ($[k]$) material properties:

$$V = [k] / \mu \cdot \text{grad}(P)$$

One can observe a clear discrepancy between the experimental results and the numerical simulation results.

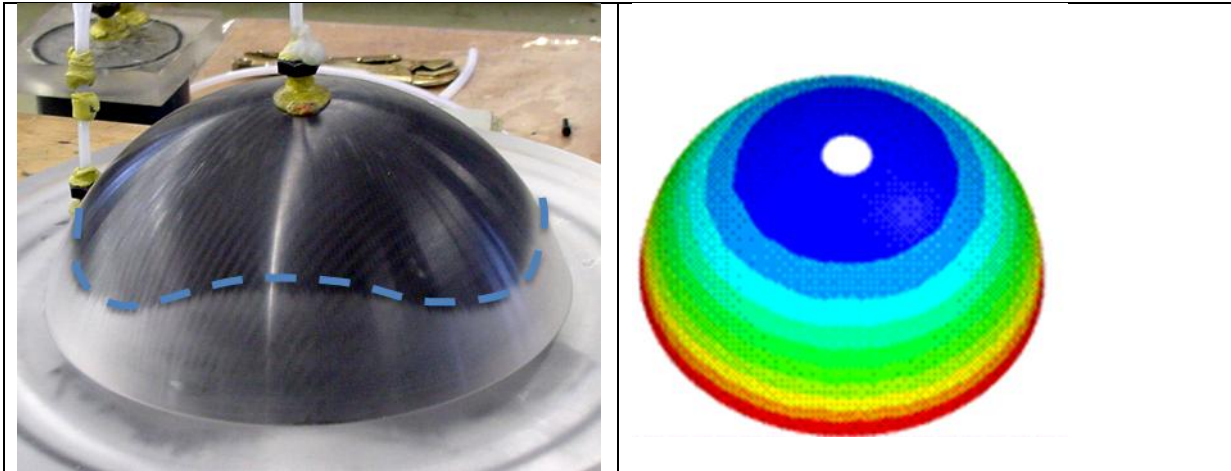


Figure 1: RTM injection of an hemisphere: experiment and simulation

Actually, the permeability is not a number but a tensor and one must use the permeabilities of the warp and of the weft direction. But this is not sufficient to obtain a correct simulation. During the preforming of the dry preform, there is a reorientation of the fibers that happens and significant shearing up to nearly 40° can be observed over the preform as can be seen on the figure 2.

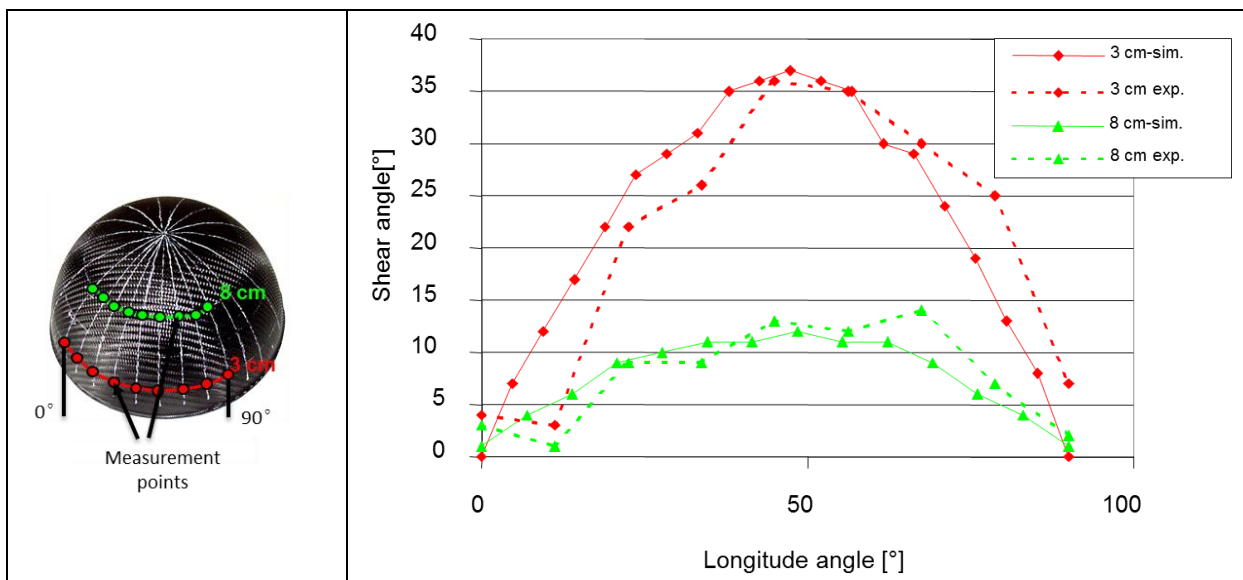


Figure 2: Experimental measurements of the shearing angle along two parallels.

Indeed, using a permeability field varying with the shearing angles and using the contour map of the shearing using a finite element simulation (PAM-

FORM), IVW was able to get a good correlation between the experiment and the simulation – see figure 3.

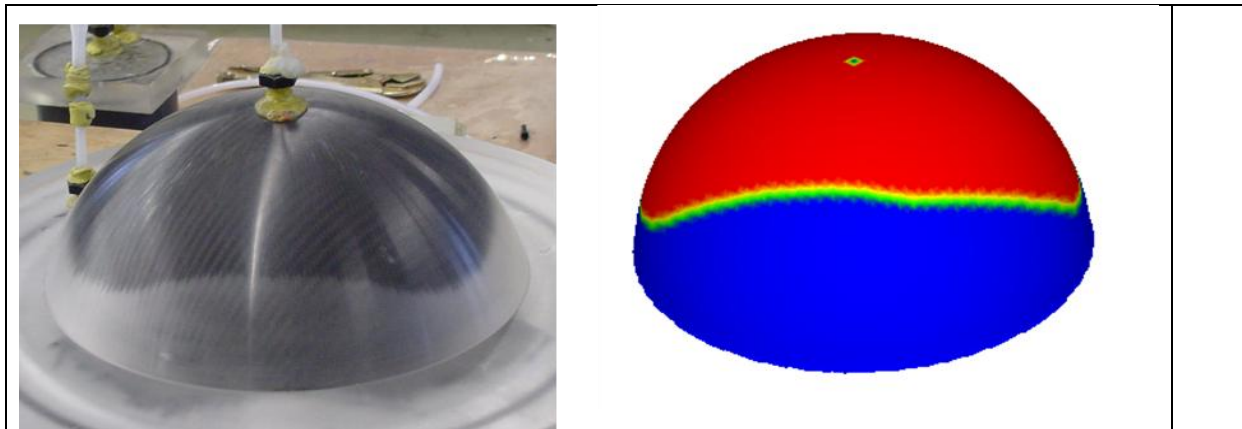


Figure 3: Comparison of the injection experiment and of the simulation based on actual shearing and associated permeability.

These phenomena are now well understood and can be taken into account in commercial software. The description of the fiber reinforcement reorientation may come from geometric but also directly from the machine creating the preform in case of fiber placement (AFP process, AFP standing for Automatic Fiber Placement) or braiding machines.

Note that additional material data are needed to be able to run such an injection simulation, namely the permeability as a function of the shearing angle of the woven preform.

b. Volume fiber content (V_f) variations around a radius

The permeability is obviously strongly dependent on the fiber volume content: one can refer for example to one of the first model: the Kozeny Carman model (2). Looking at a typical section of the fiber distribution in a radius, one can see again a preforming effect onto the reinforcement impregnation.



Figure 4: Section of a laminate around a radius showing the higher V_f close to the inner radius and the free space left for an easy resin flow close to the outer radius.

In this section, we only focused on the impregnation consequences of the dry preform. One will see in section 6 that actually the mechanical properties are modified according to the flow velocity and therefore according to the preforming.

3. Effects of textile processing onto subsequent forming steps

In this section, one will cover some additional effects of the textile technology used in the manufacturing.

a. Example of deviations of the fiber paths in the braiding process

For the braiding process, there is no possible direct transfer of machine commands to a full description of the fiber paths to be used in the mechanical simulation tools. One option is the use of analytical formulae. The figure 5 shows a comparison of a specific yarn path using analytical analysis and FE simulation (3). It shows that a full FE simulation is needed if one needs accurate fiber paths.

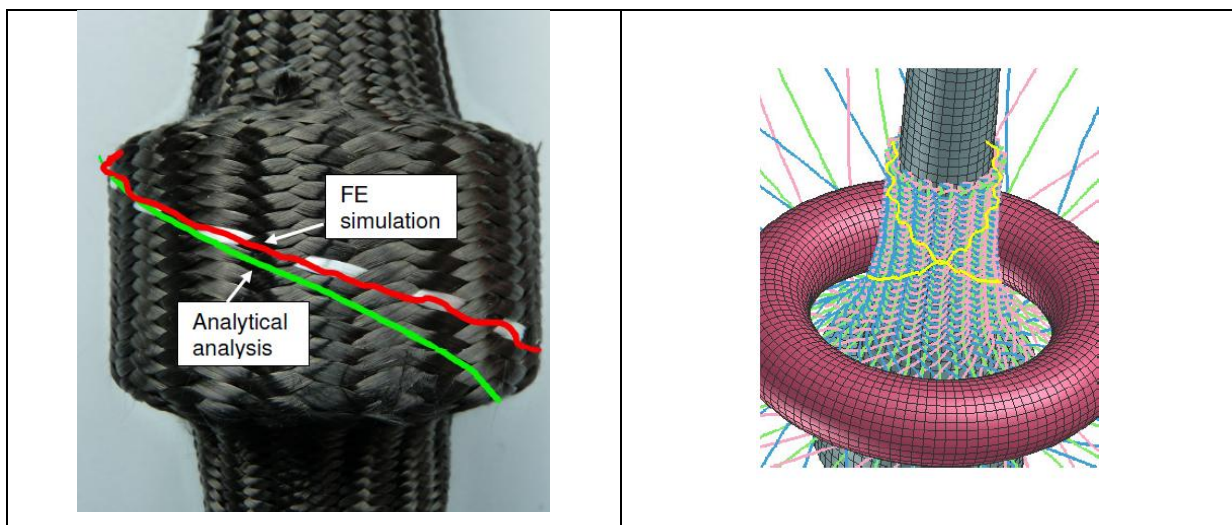


Figure 5: LHS: Manufactured braided preform and a comparison of analytical and FE prediction of a particular yarn path. RHS: view of a braiding simulation.

The last remark can be extended to AFP and ATL (Automatic Tape Laying) because when the curvature of the part needs steering, gaps and overlay appear in the preform that depart from the targeted ideal design definition of the reinforcement.

b. Example of tows section modifications in the braiding process

Up to now, we have only considered the fiber paths themselves, but the textile technology also modifies the tows sections during the processing and creation of the fabrics or the braid. One can see on figure 6 a micrograph of a braided preform; to really account for this state of yarns deformations, a FE simulation is necessary.

This kind of result needs to be appreciated with in mind the way this kind of phenomena is handled in the industry and in the academic world. Usually, *a priori* distribution of fibers is assumed or mathematical tools are used to provide some fiber distribution or these variations are accounted for through stochastic methods.

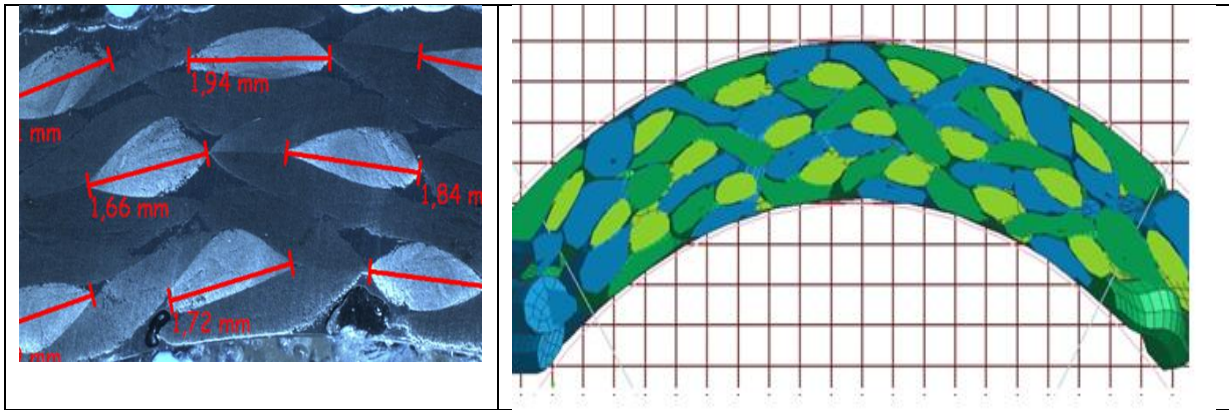


Figure 6: LHS: Micrograph of a braided preform. RHS: section of the associated braiding simulation.

Note that we do not pretend that it is possible to ask to the simulation to provide a comprehensive description of the reinforcement and of the composite itself in a fully deterministic way. But we claim that manufacturing simulation should be used in order to provide a first realistic description of the composite part and that one should start tackling the various variabilities involved in a composite part earlier in the part manufacturing. That is the variability should be addressed at the yarn level and at the manufacturing process parameters variations level and not at design stage.

4. Effects of preforming onto mechanical performance

In this section, one will report some examples of fiber reorientation onto the mechanical performance.

a. Effect of fiber reorientation on first ply failure analysis

The work reported here was performed in the European FP7 FALCOM project. A four points bending test of an aeronautical frame was performed by EADS/M at Ottobrunn, Germany. Simulations were conducted using the design definition of the fiber orientations and using the fiber orientations coming from a draping simulation. Using commercial software based on idealized fiber orientation and a classical failure criterion like the Tsai-Hill criterion, one calculates a failure at the axis of symmetry. One can see a better prediction of the failure location on the figure 8. This improved result is obtained using the fiber orientation coming from a preliminary simulation of the draping operation (4).

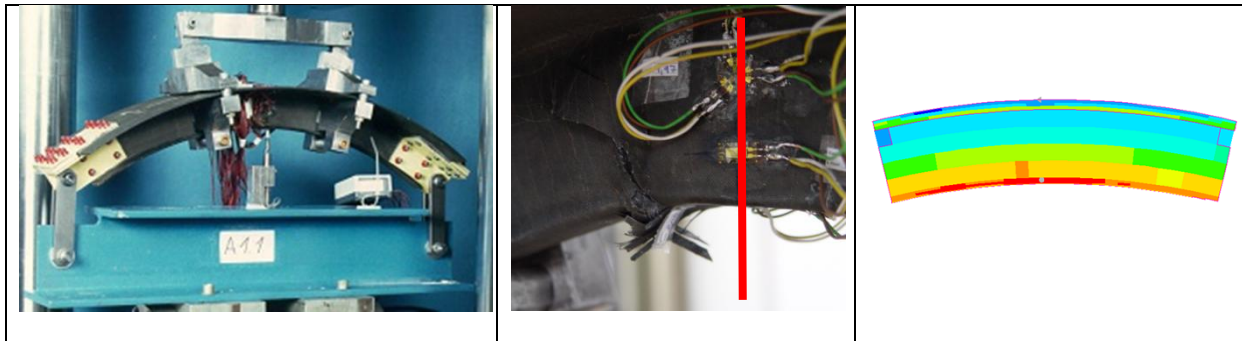


Figure 8: View of the test setting; view of the offset of the failure w.r.t. the (red) axis of symmetry; Tsai-Hill contour plot based on simulated fiber orientation.

b. Effect of fiber reorientation on progressive damage simulation

The effects of the manufacturing process on catastrophic failure seen in the last section are the result of the evolution of damage in the composite part. One reports here the effects of the manufacturing process onto the progressive damage evolution itself. The mathematical model of the damage used in this example is the popular Ladevéze model(5). In the works of L. Greve and A.K. Pickett (6), the material characterization tests usually run to be able to simulate with the Ladevéze model are done not only for the undeformed coupon from the roll but also for pre-sheared sample, that is at the four following pre-shearing values, $+10^\circ$, -10° , $+170^\circ$ and -17° . The characterization is used to punch various deformable discs with various pre-shearing values and the results are seen on the figure 9 extracted from (6).

Note again that additional material testing is required if one wants to simulate the actual composite discs.

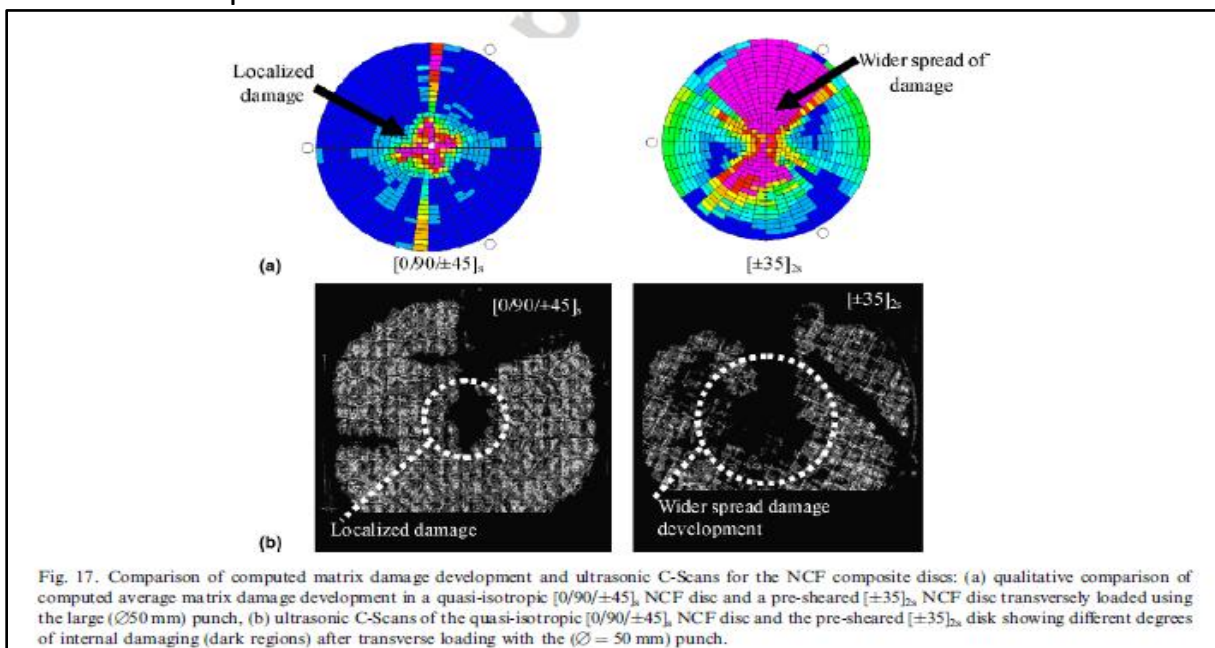


Figure 9: Results of progressive damage analysis on two punched pre-sheared composite discs.

5. Effects of textile processing onto mechanical performance

Having the objective to use the manufacturing results in mechanical performance simulation, generating the manufacturing process simulation results is not enough to improve the mechanical performance assessment. In this section, one would like to stress the need for having mechanical simulation software that can actually use these simulation results.

In the following example an additional ingredient is introduced in the modeling. The part studied is a composite mudguard (7). But, at the difference of the approach used for the aeronautical frame described in section 3, the stiffness modification is not restricted to a modification of the fiber direction and rotations of the stiffness matrices. Here, all the elastic stiffness coefficients are calculated again using TEXCOMP (8). That enables to take into account the intra-tow deformations resulting from the shearing and from the interactions between the warp fibers and the weft fibers.

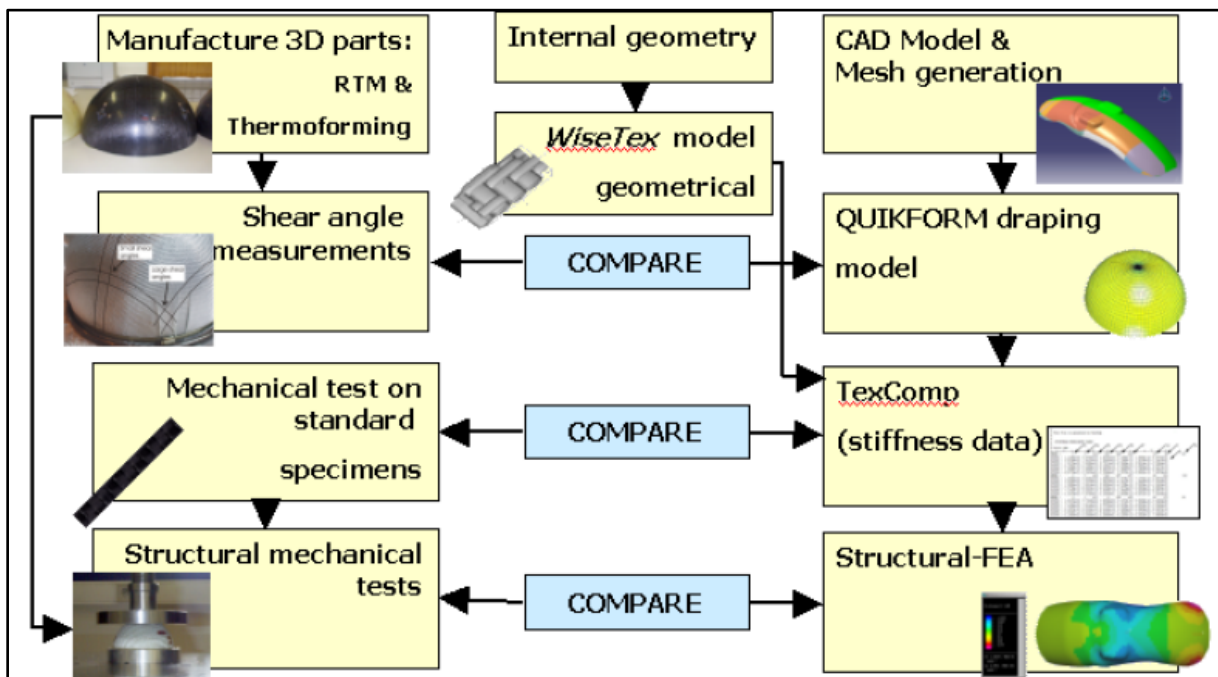


Figure 10: Mechanical analysis integrating local stiffness variations accounting for local tow deformations

6. Effects of RTM process conditions onto mechanical performance

As announced in the section 2, one reports here a few information about the effects of the impregnation onto the final content of porosities and therefore onto the final mechanical part performance. E. Ruiz is one of the first author to report a comprehensive work covering both the prediction of micro and macro-porosities (that is intra and inter-yarn porosities) occurring in the RTM manufacturing of composite parts and also the effects of the porosities onto

the stiffness and strength – see the figure 10 from (9). A main outcome of this work is that there is an optimal flow velocity that minimizes the micro-voids (due to too high flow front velocity) and the macro-voids (due to too low flow front velocity). This is a useful observation for process engineers in order to optimize the process. This information can also be used by designers: assuming the knowledge of the stiffness and strength as a function of micro/macro-voids, the designer can run simulations using a contour of mechanical properties calculated from the map of porosities obtained at the end of the RTM process simulation.

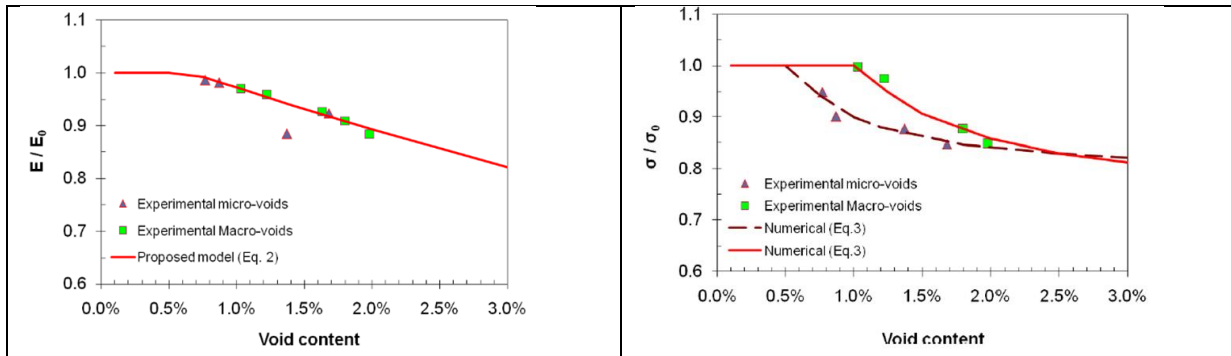


Figure 11: Variations of young modulus and strength with macro/micro-porosities(9)

7. Virtual Material Characterization

As noticed in all the examples afore mentioned, accurate mechanical behavior of a composite structure requires not only the description from the manufactured part but also an enriched material characterization. Not only the standard mechanical properties (elastic stiffness, strength, strain energy release rate, etc.) obtained by testing the purchased material must be available for the mechanical simulations but the properties must also be available as a function of the parameters modified during the various stages of the manufacturing process. The list includes the fiber reorientation, the thickness variations, the local fiber content variations, the fiber waviness, the micro and macro porosities, the degree of cure and of crystallization, the degree of intimate contact, the tows sections deformations, etc.

This requirement represents a significant additional burden to the simulation activity. In this section one report about active explorations of the virtual material characterization that could provide an alternative to expensive physical coupon testing.

The permeability prediction has been shown to be an effective technique as demonstrated for example by the Nottingham University works. The idea is simply to start from a representative unit cell of the studied reinforcement, to inject (numerically) resin from one side (using a CFD software like the FPM

method) and using the Darcy equation one can recover the permeability from the pressure drop – see (10) for more details.

Drapeability prediction in order to simulate the draping operation has been tackled through meso-mechanical modeling of individual tows and stitching yarns in (11).

The prediction of elastic properties is now done more or less on a regular basis, at least in academic world. The prediction of damage properties requires more attention. A recent work shows significant progress in this direction[??]. The figure 11 shows the simulation process used in this work: filament winding simulation, extraction of mechanical properties and final use in a crash tube simulation.

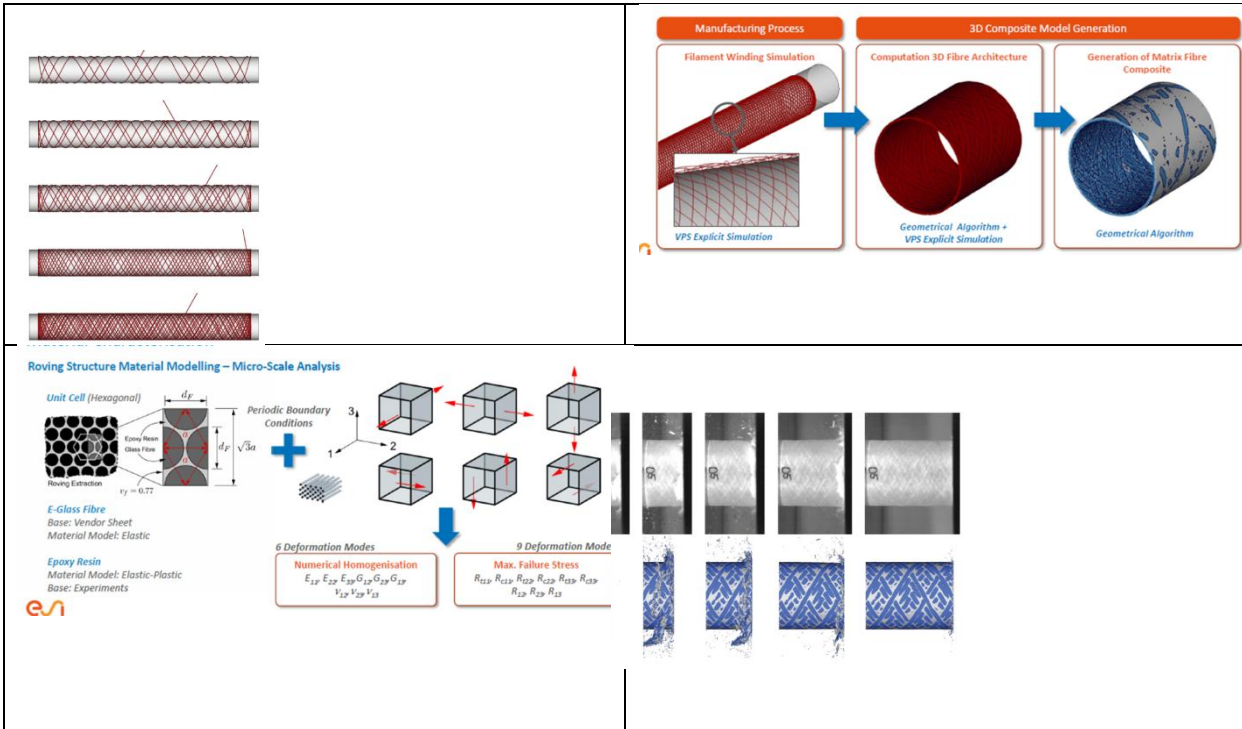


Figure 11: Material prediction and crash simulation: a global approach (12)

8. Conclusion and challenges for E2E composites simulation

This paper has presented an overview of current attempts to develop simulation tools contributing to the accounting of manufacturing effects in the mechanical design of composite parts. Additional tools will be necessary in order to make this complete (end-to-end or E2E) simulation of composite parts a routine activity. We can mention for example tools to map results from one simulation into a different simulation tool using different numerical techniques and physics. The related statistic and reliability analysis tools will need integrating the variability of the material and of the manufacturing process. The composite part development process will iterate over a large loop ranging from material design, process design and

part design. The resulting robustness and full control gained over the product development process will enable to decrease the safety margins and eventually really take advantage of the benefits of composite materials.

References

- [1] Louis, M.; Huber, U.; Maier M.: Harzinjektionssimulation unter Berücksichtigung des Einflusses der Drapierung auf die Permeabilität, 8. nationales Symposium SAMPE Deutschland e.V., 7.-8. März 2002, Kaiserslautern.
- [2] Carman, P.C. 1956. Flow of Gases Through Porous Media. New York City: Academic Press Inc
- [3] A. Pickett; A. Erber; T. von Reden; K. Drechsler, Comparison of analytical and finite element simulation of 2D braiding, *Plastics, Rubber and Composites*, Volume 38, Issue 9-10 (01 December 2009), pp. 387-395
- [4] P. de Luca, Y. Benoit, E. Berthé, M. Cabin, L. Dufort, M. Ziane, Predicting Mechanical performance of composite parts through manufacturing simulations, SAMPE Europe 2006, Paris, Proceedings, pp. 519-525.
- [5] Ladevéze P., Le Dantec E., Damage modelling of the elementary ply for laminated composites, *Compos. Sci. Techno.* 1992(43):257-67
- [6] Greve L., Pickett A.K., Modelling damage and failure in carbon/epoxy non-crimp fabric composites including effects of fabric pre-shear, *Composites: Part A*, 37 (2006) 1983-2001.
- [7] B. Van Den Brouke, F. Tümer, S. Lomov, I. Verpoest, P. de Luca, L. Dufort, Micro-macro structural analysis of textile composite parts: case study, SAMPE Europe Conference proceedings, Paris, 2004.
- [8] S.V. Lomov, G. Huysmans, A. Podromou, I. Verpoest, *Composites A*, 32 (2001) 1379-1394.
- [9] Leclerc JS, Ruiz E, Porosity reduction using optimized flow velocity in Resin Transfer Molding, *Composites: Part A*, Volume 39, Issue 12, December 2008, Pages 1859-1868 (2008), doi:10.1016/j.compositesa.2008.09.008
- [10] Alain Trameçon, Patrick de Luca, Christophe Binetruy, Jörg Kuhnert, "Finite Pointset Method (FPM): A Meshfree Approach for Incompressible Flow Simulations Applied to Composite Materials", FPCM8 proceedings, Douai(F), 2006.
- [11] A. Pickett, G. Greech, P. de Luca, Simplified and advanced simulation methods for prediction of fabric draping, *Revue Européenne de Mécanique Numérique*, anciennement *Revue Européenne des éléments Finis (1250-6559)*
- [12] A. Berger, T. Pyttel, F. Duddeck, Crash simulation of wound composite tubes based on multi-level modelling, *International Journal of Crashworthiness*, Vol. 20, Iss. 2, 2015



VIBRO-ACOUSTIC MODELING OF SANDWICH AND UNRIBBED OR RIBBED PANELS WITH THICK LAMINATE COMPOSITE SKIN USING STATISTICAL ENERGY ANALYSIS

Abderrazak Mejdji¹, Bryce Gardner¹ and Chadwyck Musser¹

¹ESI Group US R&D, 12555 High Bluff Dr. Suite 175, San Diego, California, 92130, USA

Email: amj@esi-group.com

ABSTRACT

This paper investigates the vibro-acoustic response of stiffened and unstiffened laminate composite structures and sandwich structures based on a Statistical Energy Analysis (SEA) approach. SEA is a modeling procedure which uses energy flow relationships for the theoretical estimation of the dynamic response as well as the sound transmission through structures in resonant motion. The accuracy of SEA is related to the accurate estimates of its parameters (modal density, Damping Loss Factor (DLF) and the Coupling Loss Factor (CLF)). Wave and modal based approaches are developed to predict the SEA parameters for both stiffened and unstiffened composite panels and sandwich panels. For composite structures each layer is assumed to be a thick laminate with orthotropic orientation. Moreover, rotational inertia and transversal shearing, membrane and bending deformations are accounted for. First order shear deformation theory is used. The developed approach handles symmetrical and asymmetrical constructions of an unlimited number of transversal incompressible layers. Moreover, for the case of a ribbed panel with thick composite skin, the effect of variable spacing of the ribs is accounted for. The sandwich model uses a discrete displacement field for each layer and allows for out-of-plane displacements and shearing rotations. The accuracy of this modeling approach is confirmed through comparison to measured test data and alternate validated theoretical results. The advantages of the new developed models compared to the classical models are also investigated. Representative examples of aircraft interior noise predictions for typical load cases are shown and the use of SEA models as a tool for guiding construction of multi-layer lightweight structures to meet acoustic performance and weight targets and optimize designs are presented. Conclusions about the overall applications and improvements offered by these approaches, current limitations, and future work to extend and improve these approaches are given.

1 INTRODUCTION

Nowadays there is an increasing use of sandwich and laminate composite panels due to their light weight and higher stiffness. The ability to accurately predict the dynamic structural properties of such structures is essential in order to accurately predict the corresponding interior noise and structural vibration levels for many industrial applications including aerospace vehicles. Unlike the vibro-acoustic response of simple continuous structures, a detailed analysis of wave motions for stiffened plates is often difficult to achieve because of the complexity of the structural configuration and the uncertainty of the boundary conditions. Most of the previous research focused on the modelling of ribbed panels with regular spacing between stiffeners [1]-[2]. In practice ribbed panel construction is always accompanied with non-uniform, statistically variable spacing between stiffeners even when uniform spacing is intended. Little previous research was developed to account for this stiffener spacing uncertainty.

The Statistical Energy Analysis (SEA) technique is commonly used at higher frequencies to predict airborne and structure borne noise transmission for many industrial applications. Being able to properly characterize complex ribbed and unribbed multi-layer lightweight structures and derive the modal density and coupling loss factors (CLF) is essential. A large number of researchers have studied these parameters for single-layer structures but only a limited amount of work has been carried out to determine these parameters for sandwich panel and ribbed or unribbed panels with thick composite skin. For instance, Zhou and Crocker [3] analysed the sound transmission of sandwich panels where the classical sandwich formulation is used to predict the modal density and the coupling loss factor is measured. Other researchers modelled the laminate composite as a two-dimensional problem wherein the displacement field in each lamina is based on Kirchhoff's hypothesis [4]-[6]. Moreover, most of the existing models neglect the shear and the inplane contributions as well as the rotational inertia that strongly influence the high-frequency behavior of these structures. More accurate results are provided by a first-order shear deformation theory [7]-[9] or other higher order shear deformation theories [10]. The first-order shear deformation theory based on Reissner–Mindlin-type assumptions takes the transverse shear deformation into account. However, it requires shear correction factors to compensate for errors resulting from the approximation of the shear-strain distribution. For instance, Ghinet and Atalla [11]-[12] used Reissner–Mindlin-type assumptions in a Transfer Matrix Method (TMM) context. For ribbed panels, the stiffener spacing uncertainty effect was always ignored in the modelling of these structures. Only a few researchers studied this effect; for instance, Mejdí and Atalla [13] developed a semi analytical model to analyse ribbed panels with evenly and unevenly stiffened composite laminate flat structure. Langley [14] derived the modal density of periodically stiffened beam and plate structures in terms of phase constants, which were associated with propagating wave motion. In his analysis he assumes that the modal density is not affected by the imperfection in the attachment.

In this paper, a wave and modal based approach are developed to model both sandwich and ribbed or unribbed panels with thick composite skins in an SEA context. The effect of shear deformation and the in-plane / bending coupling effects are employed to improve the vibro-acoustic response prediction of multilayer structures. Moreover, for ribbed panels, the stiffeners spacing uncertainty effect is accounted for. SEA prediction using classical models are compared to the presented models using thick plate theory. The latter are found more suitable for both low- and high- frequency analysis. The stiffeners spacing uncertainty has an important effect on the dynamic response of ribbed panels.

2 THEORY

2.1 Thick composite model

The laminate panels considered here have a symmetric or an asymmetric configuration. The panel is assumed infinite. For a point M belonging to the laminated composite shell, the displacement field is defined by the Mindlin type assumption where both bending and transverse shear effects are considered:

$$\begin{aligned} U(x, y, z) &= U_0(x, y) + z\varphi_x(x, y) \\ V(x, y, z) &= V_0(x, y) + z\varphi_y(x, y) \\ W(x, y, z) &= W_0(x, y) \end{aligned} \tag{1}$$

U, V and W are the in-plane and the transversal displacements and φ_x, φ_y are the rotational displacements in x and y directions, respectively and z is the layer's point position from lamina mid-plane. Geometrically, the shell is considered to be of infinite extent in the axial (x) direction and thus the origin for both x and y is arbitrary. Nevertheless, the origin for the z axis is defined on a reference surface passing through the middle thickness of the shell.

The dynamic equilibrium relations of the unstiffened in-vacuum panel are given by integrating the stress continuity relation through the thickness of the lamina [13]:

$$\begin{aligned} \frac{\partial N_x}{\partial x} + \frac{\partial N_{xy}}{\partial y} &= (m_s) \frac{\partial^2 U}{\partial t^2} + (I_{z2}) \frac{\partial^2 \varphi_x}{\partial t^2} \\ \frac{\partial N_y}{\partial y} + \frac{\partial N_{xy}}{\partial x} &= (m_s) \frac{\partial^2 V}{\partial t^2} + (I_{z2}) \frac{\partial^2 \varphi_y}{\partial t^2} \\ \frac{\partial Q_x}{\partial x} + \frac{\partial Q_y}{\partial y} &= (m_s) \frac{\partial^2 W}{\partial t^2} \\ \frac{\partial M_x}{\partial x} + \frac{\partial M_{xy}}{\partial y} - Q_x &= I_z \left(\frac{\partial^2 \varphi_x}{\partial t^2} \right) + I_{z2} \left(\frac{\partial^2 U}{\partial t^2} \right) \\ \frac{\partial M_y}{\partial y} + \frac{\partial M_{xy}}{\partial x} - Q_y &= I_z \left(\frac{\partial^2 \varphi_y}{\partial t^2} \right) + I_{z2} \left(\frac{\partial^2 V}{\partial t^2} \right) \end{aligned} \tag{2}$$

where N_x, N_y, N_{xy} are the in plane forces and M_x, M_y, M_{xy} are the bending moments and Q_x, Q_y are the shearing forces. m_s and I_z, I_{z2} are the total mass per unit area and the total rotational inertia terms, respectively. Using the stress displacement relation and integrating the stress through the thickness, the constitutive relation between the forces and the displacements can be written as:

$$\begin{bmatrix} N_x \\ N_y \\ N_{xy} \\ M_x \\ M_y \\ M_{xy} \\ Q_x \\ Q_y \end{bmatrix} = \begin{bmatrix} A_{11} & A_{12} & A_{16} & B_{11} & B_{12} & B_{16} & 0 & 0 \\ A_{12} & A_{22} & A_{26} & B_{12} & B_{22} & B_{26} & 0 & 0 \\ A_{16} & A_{16} & A_{66} & B_{16} & B_{26} & B_{66} & 0 & 0 \\ B_{11} & B_{12} & B_{16} & D_{11} & D_{12} & D_{16} & 0 & 0 \\ B_{12} & B_{22} & B_{26} & D_{12} & D_{22} & D_{26} & 0 & 0 \\ B_{16} & B_{26} & B_{66} & D_{16} & D_{26} & D_{66} & 0 & 0 \\ 0 & 0 & 0 & 0 & 0 & 0 & F_{44} & F_{45} \\ 0 & 0 & 0 & 0 & 0 & 0 & F_{45} & F_{55} \end{bmatrix} \begin{bmatrix} \partial U / \partial x \\ \partial V / \partial y \\ \partial U / \partial y + \partial V / \partial x \\ \partial \varphi_x / \partial x \\ \partial \varphi_y / \partial y \\ \partial \varphi_x / \partial x + \partial \varphi_y / \partial y \\ \partial W / \partial x + \partial \varphi_x / \partial x \\ \partial W / \partial y + \partial \varphi_y / \partial y \end{bmatrix} \tag{3}$$

where A_{ij}, B_{ij} and D_{ij} are the extensional, extensional-bending and bending stiffness. The equations of motion can be obtained by introducing (3) into (2) and assuming a solution in the following form:

$$\{e\} = \{U, V, W, \varphi_x, \varphi_y\}^T \exp(jk_x x + jk_y y + j\omega t) \tag{3}$$

where k_x and k_y are the components of the structural wave number, k_p is defined as a function of the heading angle θ :

$$\begin{aligned} k_x &= k_p \cos(\theta) \\ k_y &= k_p \sin(\theta) \end{aligned} \tag{4}$$

Using Eqs. (2)-(4), we obtain the following compact matrix equation:

$$\{k_p^2 [A_3] - ik_p [A_2] - [A_1] - \omega^2 [M]\} \{e\} = 0, \quad (5)$$

For a wave-based approach, one can obtain the eigen solutions from Eq (6). The three smallest real positive solutions correspond to the bending, extension and shearing wavenumbers. The extensional and bending matrices can be obtained from the eigen solution and all the SEA parameters: CLF, DLF and modal density, can be obtained.

2.2 Ribbed panel with thick composite skin and periodic and variable stiffener spacing

2.2.1 Periodic ribbed panels

For ribbed panel, the stiffened effect could be accounted for by correcting the mass and stiffeners in the wavenumber domain. Indeed, Bremner [16] has explained the distinct behaviours in terms of wavenumbers of a flat ribbed plate of width L_x and height L_y stiffened with ribs and frames with spacing S_x and S_y between the ribs and frames. As the modal half-wavelength in the x and y directions goes below the L_x and L_y dimensions, the plate behaviour shifts from global behaviour, over the plate area (L_x, L_y), to periodic behaviour over areas delimited by (S_x, L_y), (L_x, S_y). Finally, when the modal half-wavelength goes below the rib and frame spacing S_x and S_y , the modal behaviour is determined by the behaviour of a flat uniform subpanel delimited by the ribs and frames (local behaviour). Those four conditions represent the four models required when fully describing the modal behaviour of a stiffened plate over a large frequency band. When a particular condition is met for periodic modes behaviour, the number of modes should be multiplied by the multiplicity factor μ .

For example, the mass and stiffness correction in region 1 where the bending wave numbers $k_m < \pi/S_x$ and $k_n < \pi/S_y$ and both x and y ribs smeared over surface (L_x, L_y) with a group of multiplicity $\mu_p = 1$, are given by:

$$\begin{aligned} m^{total} &= m^{skin} + \frac{m_{bx}}{S_x} + \frac{m_{by}}{S_y} \\ D_{11} &= D_{11}^{skin} + \frac{(EI)_{bx}}{S_x} + \frac{z^2(EA_x)}{S_x}; D_{22} = D_{22}^{skin} + \frac{(EI)_{by}}{S_y} + \frac{z^2(EA_y)}{S_y}; D_{33} = D_{33}^{skin} + 0.25 \frac{(G_x J_{bx})}{S_x} + 0.25 \frac{(G_y J_{by})}{S_y} \\ A_{11} &= A_{11}^{skin} + \frac{(EA)_{bx}}{S_x}; A_{22} = A_{22}^{skin} + \frac{(EA)_{by}}{S_y}; A_{33} = A_{33}^{skin} + \frac{(k_x G_x A_{bx})}{4S_x} + \frac{(k_y G_y A_{by})}{4S_y}; \\ B_{11} &= B_{11}^{skin} + \frac{z(EA)_{bx}}{S_x}; B_{22} = B_{22}^{skin} + \frac{z(EA)_{by}}{S_y}; B_{33} = B_{33}^{skin} + \frac{z(k_x G_x A_{bx})}{4S_x} + \frac{z(k_y G_y A_{by})}{4S_y} \\ F_{44} &= F_{44}^{skin} + \frac{(k_x G_x A_{bx})}{S_x}; F_{55} = F_{55}^{skin} + \frac{(k_y G_y A_{by})}{S_y} \end{aligned} \quad (7)$$

Where m denote the mass, E , G are the stiffener's young and shear modulus respectively, I and A are the stiffener's moment of intertie and cross section respectively.

Once the mass and stiffness are corrected, the modal frequency can be obtained by considering a simply-supported boundary condition and by solving Eq (6) for each mode order. Indeed, for a simply-supported boundary condition, the bending wavenumber is given by

$k_{mn} = \sqrt{(m\pi/L_x)^2 + (n\pi/L_y)^2}$ where m and n are the modal orders. Eq (6) can be rewritten as:

$$\{k_{mn}^2 [A_3] - ik_{mn} [A_2] - [A_1] - \omega_{mn}^2 [M]\} \{e\} = 0 \quad (8)$$

To account for any curvature and tension effects that may be acting on the structure, the modal frequency can be corrected as:

$$\omega_{mn_cor} = \omega_{mn} + C + T \quad (9)$$

where the terms C and T are the curvature and tension correction factors.

By solving Eq (8) for the modal frequency, the mode list can be obtained by evaluating the modal frequency regarding each bandwidth and in this manner all the SEA parameters can be obtained.

2.2.2 Variable spacing effect

To account for the uncertainties in the ribs spacing, a statistical process can be employed by considering an ensemble of i spacing varying by a certain percentage over the nominal rib spacing values. It is assumed that the spacing uncertainty can be computed as though it has a normal distribution as shown in Figure 1:

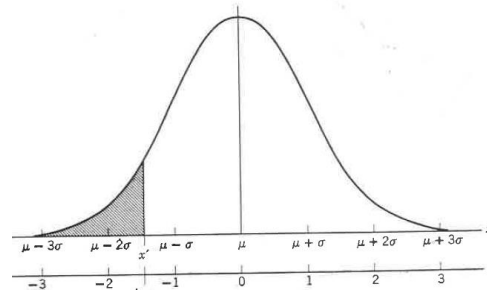


Figure 1: Graph of normal probability density function.

$$f = \frac{1}{\sqrt{2\pi}} e^{-\frac{z^2}{2}} \quad \text{where } z = [-3 \ -2 \ -1 \ 0 \ 1 \ 2 \ 3] \quad (10)$$

where f is the probability density function (pdf). The modal energy corresponding to each spacing could be computed using the power balance equation:

$$\pi_i = \omega \left[\eta(S_x^i, S_x^j) \right] E_i \Leftrightarrow E_i = \omega \left[\eta(S_x^i, S_x^j) \right]^{-1} \pi_i \quad \text{where } i = 1, 2, \dots, 7 \quad (11)$$

$\eta(S_x^i, S_y^i)$ is the SEA coupling matrix corresponding to a given spacing S_x^i, S_y^i . E_i and π_i are the corresponding modal energy and injected power respectively.

The average estimate of all the SEA parameters and vibro-acoustic responses can be obtained using the following formulation:

$$\langle V \rangle = \sum_{i=1}^7 \alpha_i V_i \quad \text{where } \alpha_i = \frac{f^i}{\sum_{i=1}^7 f^i} \quad (12)$$

V_i is an SEA parameter such as the modal density, CLF, DLF or injected power and f^i is the pdf given by $f^i = \frac{1}{\sqrt{2\pi}} e^{-z_i^2/2}$ for a given $z_i = [-3 \ -2 \ -1 \ 0 \ 1 \ 2 \ 3]$ as mentioned in Eq (10).

2.3 Sandwich model with composite skin

For a sandwich model, a Mindlin-type assumption is used to describe the displacement field of the core [12]. The skins are assumed to be thinner than the core and display bending behaviour. Their displacement field is built using the Love-Kirchhoff's assumptions but is corrected to account for the rotational influence of the transversal shearing in the core [12].

$$\begin{cases} u^k(x, y, z) = u_0^k(x, y) - z \frac{\partial w}{\partial x}(x, y) + r_{kx} \\ v^k(x, y, z) = v_0^k(x, y) - z \frac{\partial w}{\partial y}(x, y) + r_{ky} ; \quad k = 1; 3 \\ w^k(x, y, z) = w(x, y) \end{cases} \quad (13)$$

where r_{kx} and r_{ky} are the rotational coefficients.

Perfect bonding of the layers is assumed, so that the displacement field remains continuous throughout the interface between two consecutive layers.

The relations of stresses' dynamic equilibrium are written for each layer separately in order to develop the continuity of stress relations at the interface between the layers. These relationships are next integrated through the layer's thickness and the dynamic equilibrium relations along the x and y directions are obtained. For the top skin – core interface represented by the superscript ¹, the relations of continuity are written as follows:

$$\begin{aligned} \frac{\partial N_x^1}{\partial x} + \frac{\partial N_{xy}^1}{\partial y} - \tau_{xx}^1 - (I_{z1}^1 \frac{\partial w}{\partial x} - I_{z2}^1 \varphi_x) &= 0 \\ \frac{\partial N_y^1}{\partial y} + \frac{\partial N_{xy}^1}{\partial x} - \tau_{yz}^1 - (I_{z1}^1 \frac{\partial w}{\partial x} - I_{z2}^1 \varphi_x) &= 0 \end{aligned} \tag{14}$$

The panel's dynamic behaviour is governed by the dynamic equilibrium relations of the forces and moments along the x , y and z directions. The sandwich-type panel assumptions are considered; the membrane forces N_x , N_y and N_{xy} and the bending moments M_x , M_y and M_{xy} are computed through the thickness of the skins while the transversal shearing forces Q_x and Q_y are expressed through the core's thickness. Considering the stresses' continuity relations along the x , y , and z directions as well as the panel's incompressibility along the z direction and integrating through the panel thickness, the following equilibrium relations can be written:

$$\begin{aligned} \frac{\partial Q_x}{\partial x} + \frac{\partial Q_y}{\partial y} &= m_s \frac{\partial^2 W}{\partial t^2} \\ \frac{\partial M_x}{\partial x} + \frac{\partial M_{xy}}{\partial y} - Q_x &= I_{z-t} \left(\frac{\partial^2 U}{\partial t^2} \right) \\ \frac{\partial M_y}{\partial y} + \frac{\partial M_{xy}}{\partial x} - Q_y &= I_{z-t} \left(\frac{\partial^2 V}{\partial t^2} \right) \end{aligned} \tag{15}$$

The shearing forces Q_x and Q_y can be replaced in the last two equations to express the following relationship of motion:

$$\begin{aligned} \frac{\partial^2 M_x}{\partial x^2} + 2 \frac{\partial^2 M_{xy}}{\partial x \partial y} + \frac{\partial^2 M_y}{\partial y^2} - \\ I_{z_2} \left(\frac{\partial^2 U}{\partial t^2} \right) - I_{z_2} \left(\frac{\partial^2 V}{\partial t^2} \right) + (m_s) \frac{\partial^2 W}{\partial t^2} &= 0 \end{aligned} \tag{16}$$

The stresses' continuity relations compose the system of dynamic equilibrium equations of sandwich composite panels. This system can be expressed in a matrix form using the constitutive equation Eq (4) in the same solution form as in Eq (6):

$$\{k^4 [A] + jk^3 [B] + k^3 [C] + jk [D] + [E]\} \{e\} = 0 \tag{17}$$

As for the thick composite model, the eigenvalue problem can be solved and sorted out to find the three smallest real positive solutions. All the SEA parameters (CLF, DLF and modal density) can then be easily computed.

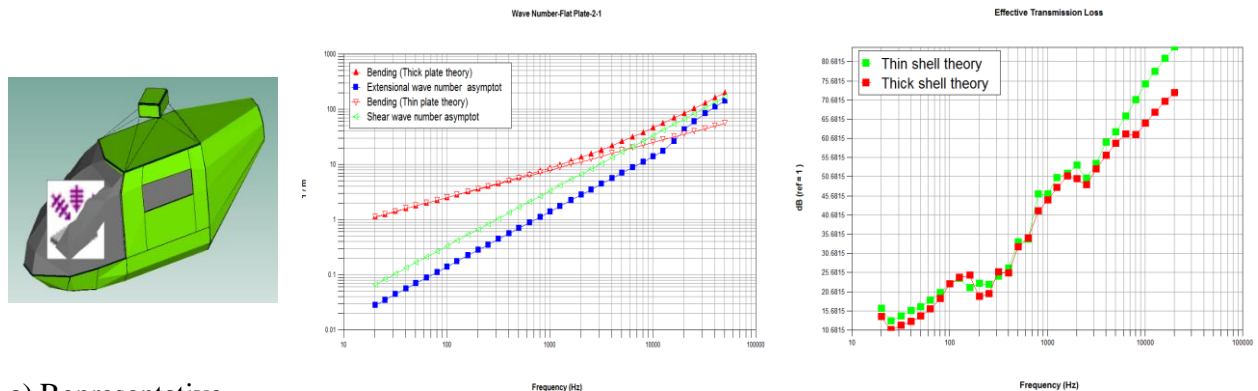
3 NUMERICAL RESULTS

Various numerical examples are given and validated by the VA One commercial software code. Both ribbed and unribbed panels with thick composite and uniform skin are analyzed. The effect of variable spacing between stiffeners reinforcing thick composite skin is also analysed. The accuracy of the modeling approach for sandwich panels in which the skin layers are made of composite materials is also analysed. In the following examples, both the wave and modal approach based predictions using the different models are examined by comparing various vibro-

acoustic indicators with experimental and existing models. Acoustic behavior under airborne and structure borne excitation is investigated. VA One capabilities and accuracy of the sound transmission prediction of various types of structures are checked by analyzing their effects.

3.1 Thick versus thin composite model

A representative model of helicopter with skin made up of ribbed panel with composite skin (Figure 2-a) is investigated in the following example. The skin is made up of three layers of Graphite/Epoxy. Each layer of the composite is 2.5mm thick. Both thick and thin shell theories are employed to predict the sound transmission loss (STL) between the cockpit and the cabin which are separated by the bulkhead which is an unstiffened composite shell having the same properties as the ribbed panel's skin. The structural wavenumber of the bulkhead is also predicted using both thick and thin shell theories. It is observed in Figure 2-b that the bulkhead has pure bending behaviour at low frequencies and pure shearing behaviour at high frequencies. In fact, the two theories give approximately the same STL until 1kHz. However, the latter is overestimated using the classical thin plate theory over 1kHz as shown in Figure 2- c. This is mainly due to the fact the shear deformation effect is ignored in thin shell theory. Also, the in-plane and out-of-plane coupling effect is ignored in the thin shell theory. The effects are usually negligible at low frequencies but must be included to model the physics of the structure at higher frequencies.



a) Representative helicopter model.

b) predicted wavenumber for unstiffened bulkhead example panel using thick and thin composite models

c) Comparison between predicted transmission loss using thick and thin composite models with reference [15]

Figure 2: predicted wave number and transmission loss of unstiffened bulkhead example panel using thick and thin shell theory.

3.2 Ribbed panel with thick composite skin and variable spacing

In order to analyze the variable spacing effect, a cylindrical shell with skin made up of 3 mm steel material is considered. The cylindrical skin is reinforced by eight stiffeners. The modal density is predicted for both evenly and unevenly spaced stiffeners. To account for the uncertainties in the rib spacing, a statistical process has been evolved by considering an ensemble of 7 spacing varying by 5% over the nominal values. It is observed that, the averaged estimation smoothens out the modal density curve, which is in very good agreement with experimental data compared to reference [17] and regular spacing prediction which show distinct, large peaks and valleys at certain frequencies for a periodic stiffened panel. This is mainly due to the periodicity characteristic of the panel. Indeed, in the case of periodic spacing with uniform spacing, all the stiffeners behave as pass band filter at the same frequencies, thus the energy is totally transmitted between sub panels. However, for uneven stiffener spacing, some of the stiffeners behave as pass

band filter while others behave as stop band filter and so the modal density results are averaged out more evenly in frequency as a result as can be seen in Figure 3.

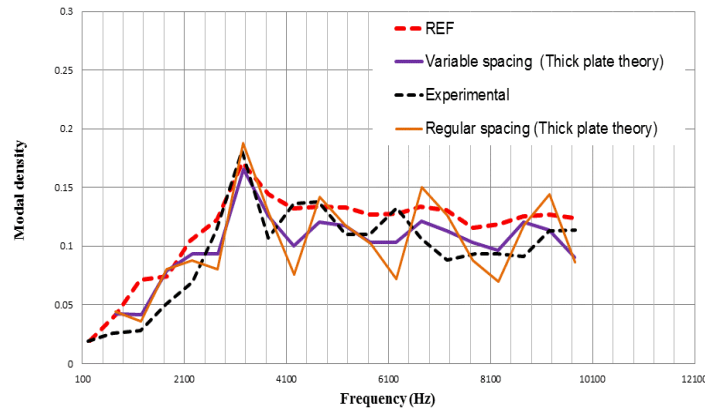


Figure 3: Comparison of ribbed panel modal density with even and uneven stiffener spacing versus experimental and Reference [17].

3.3 Sandwich model

In the following example, the accuracy of the sandwich model is examined by comparison with experimental results. A sandwich with honeycomb core and isotropic face with Density $\rho = 1716$ (kg/m³), Young’s modulus $E = 49$ GPa, Poisson’s ratio $\nu = 0.134$ and thickness $h_s = 5.84 \times 10^{-4}$ m. Experimental data is shown compared to a prediction using classical theory with thin plate assumptions versus the new approach using thick plate theory (Figure 4). Excellent agreement is found versus the experimental results when using the presented sandwich model. However, the classical sandwich model fails to correctly capture the physical behavior. Indeed, the SEA estimates provide unreasonable predictions for the sound transmission loss using the classical sandwich model at and over the coincidence frequency region which is predicted to occur about 300 Hz lower in frequency than the measurement. The prediction making use of the presented sandwich model does capture the correct coincidence frequency region in comparison to the measured data.

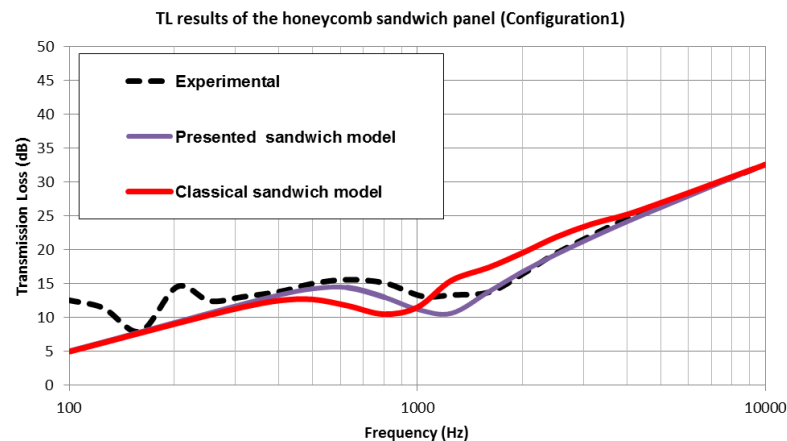


Figure 4: Comparison between predicted transmission loss using improved sandwich model and experimental result.

3.4 Material properties’ effect

In the following example, the structure borne excitation from the helicopter gearbox is simulated in VA One as a velocity constraint applied to the bottom face of the gear box (Figure 5-a). This excitation is transmitted to the helicopter skin through eight rectangular metallic beams. The pressure level inside the cockpit is predicted for two different configurations. In the first

configuration, the bulkhead wall separating the cockpit and the cabin is modeled as 3mm aluminum structure. In the second configuration, the bulkhead is modeled as sandwich with two 3mm aluminum skins and a 6.35 mm honeycomb core. The rest of the helicopter skin is made up of ribbed panels with composite skin made up of three layers of Graphite/Epoxy of 1 mm thickness each. It is observed that the pressure inside the cockpit has different level for the two configurations below the ring frequency at 200 Hz thought to be the ring frequency of the whole cockpit curved shell while between the ring frequency and the critical frequency at 3 kHz, the two configurations have also different level. This is mainly due to the fact that the sandwich has a pure bending behavior of the panel at low frequencies and core's shearing at mid frequencies as shown in the wave number plot in figure 5-b. The interior SPL levels are shown in Figure 5-c where it can be seen that above the critical frequency the sandwich and the aluminum bulkhead have the same pressure level. This is due to the fact that at high frequencies, the sandwich is controlled by a decoupled skin bending effect which has the same properties as the uniform panel as shown in figure 5-b.

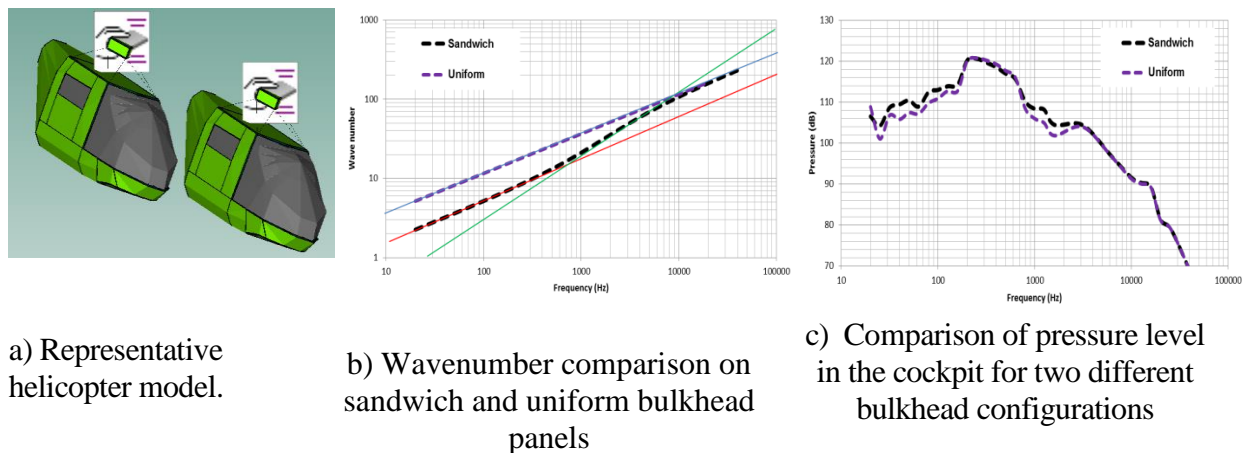


Figure 5: Wavenumber of bulkhead panels and pressure level in the cockpit due to structure born excitation

4 CONCLUSION

In this paper, a model for sandwich panel with composite face sheets for both ribbed and unribbed cases is developed. The ribbed panels' skin is assumed to be thick composite and the stiffeners may be modeled as unevenly spaced. The theories are developed in a wave and modal approach context. For the thick composite model, shear deformation and in-plane / out-of-plane motion coupling were both taken into account. For the sandwich model, the physical behavior of the panel is represented using a discrete lamina description. The acoustic transmission problem is represented within the SEA context and is successfully compared to experiments and to existing models. The SEA estimate provides reasonable results at low frequencies using the classical composite and classical sandwich models. However, they both fail to correctly capture the physical behavior at mid and high frequencies and the thick plate theory is needed to capture these high-frequency effects. The interior noise effect due to airborne and structure borne excitations were analysed and the effect of material properties was also investigated. It was found that the interior noise level is sensitive to the material properties and the excitation type. This work can be extended to model the ribbed panel stiffeners as composite material. The application of sandwich as a skin for ribbed panel constitutes another challenge.

REFERENCES

- [1] A. Mejdı and N. Atalla, Dynamic and acoustic response of bidirectionally stiffened panels with eccentric stiffeners subject to airborne and structureborne excitations, *J. Sound. Vib.* 329(21), 4422–4439 (2010).
- [2] Abderrazak Mejdı, Julien Legault and Nouredine Atalla, Transmission loss of periodically stiffened laminate composite panels: Shear deformation and in-plane interaction effects. *J. Acoust. Soc. Am.* 131 , 174 (2012)
- [3] Ran Zhou , Malcolm J.Crocker , Sound transmission loss of foam-filled honeycomb sandwich panels using statistical energy analysis and theoretical and measured dynamic properties. *J. Sound. Vib.* 329 (2010) 673–686.
- [4] R.S. Langley, The modal density and mode count of the thin cylinders and curved panels, *J. Sound. Vib* 169 (1994).
- [5] Roussos L. A., Powell C. A., Grosveld F. W. and Koval L. R., Noise Transmission Characteristics of advanced composite structural materials, *J. Aircraft*, vol. 21, no.7, 528-535, (1984).
- [6] J. P. D. Wilkinson, Modal densities of certain shallow structural elements, *J. Acoust. Soc. Am.*, Vol. 43, No. 2, 245-251, 1968.
- [7] Mindlin RD. Influence of rotatory inertia and shear on flexural motions of isotropic, elastic plates. *ASME J Appl Mech* 1951:1831–8.
- [8] Nosier A, Kapania RK. Free vibration analysis of laminated plates using a layer-wise theory. In: *AIAA/ASME/ASCE/AHS/ASC structures, structural dynamics, and materials conference no. 34, La Jolla, CA, ETATS-UNIS*, vol. 31 (12); 1993. p. 2335–46.
- [9] Michael P. Nemeth, A Treatise on Equivalent-Plate Stiffnesses for Stiffened Laminated-Composite Plates and Plate-Like Lattices, *Langley Research Center, Hampton, Virginia, NASA/TP-2011-216882*
- [10] Reddy JN. A simple higher-order theory for laminated composite plates. *ASME J Appl Mech* 1984;51(4):745–52.
- [11] Ghinet S, Atalla N. Diffuse field transmission into infinite sandwich composite and laminate composite cylinders. *J Sound Vib* 2006;289(4–5):745–78.
- [12] Ghinet S, Atalla N. Vibro-acoustic behaviours of flat sandwich composite panels. *Trans Can Soc Mech Eng* 2006;30(4):473–93.
- [13] A. Mejdı and N. Atalla, Vibroacoustic analysis of laminated composite panels stiffened by complex laminated composite stiffeners, *International Journal of Mechanical Sciences* 58 (2012) 13–26
- [14] R.S. Langely, On the modal density and energy flow characteristics of periodic structures, *J. Sound. Vib* 172 (1994) 491–511.
- [15] Shorter P. J., Wave propagation and damping in linear viscoelastic laminates, *J. Acoust. Soc. Am.*, 115(5), 1917–1925, (2004).
- [16] P.G. Bremner, Vibro-acoustics of ribbed structures – a compact modal formulation for SEA models, *Noise-Con 94*, Ft. Lauderdale, Florida (1994).
- [17] P. Ramachandran, S. Narayanan, Evaluation of modal density, radiation efficiency and acoustic response of longitudinally stiffened cylindrical shell, *J. Sound. Vib* 304 (2007) 154–174



MECHANICAL PROPERTIES IDENTIFICATION OF COMPOSITE MATERIAL USING FORCE ANALYSIS TECHNIQUE

Bertrand Lascoup¹, Frédéric Ablitzer², Charles Pézerat²

¹IRT Jules Verne

Chemin du Chaffault, 44340 Bouguenais, FRANCE

Email: bertrand.lascoup@irt-jules-verne.fr

²LUNAM, Université du Maine, CNRS UMR 6613, LAUM

Avenue Olivier Messiaen, 72085 le Mans Cedex 9, FRANCE

Email: frederic.ablitzer@univ.lemans.fr, charles.pezerat@univ-lemans.fr

ABSTRACT

This study concerns the implementation and the validation of an experimental method leading to determine the complex elastic properties (modules and coefficient of absorption) of an orthotropic material by a non-destructive method on a range of frequencies. Based on an inverse vibratory method, it requires the measurement of a transverse displacement field and is independent from boundary conditions. It can then be used in situ on complex structures. Besides, as regards a method using a field of measures, it is possible to determine local properties. The first results show an interesting potential of the method since it gives good results in medium and high frequency ranges where the structure has not a modal behavior. The proposed approach can then be seen as a complementary method to modal analysis approaches

1 INTRODUCTION

With the massive introduction of composite component in the industrial products, it becomes necessary to predict exactly the mechanical behaviour of these structures in order to limit the costs and the mass of the whole product. During the conception step, an extensive use of finite element models is made to predict the static, dynamic and vibro-acoustic behaviour. To achieve predictions as accurate as possible, the key challenge is to enter the material characteristics into the model.

The simplest way to define the properties of a material is to measure the characteristic engineer parameter by classical mechanical testing in static condition. But in the some cases (for example polymer materials), the behaviour determined at low strain rates is not able to report the viscous aspect which modifies these parameters.

Then because the stiffness and damping of composites may strongly vary with frequency, it is necessary to obtain material properties in a wide frequency range instead of extrapolating results obtained at low frequencies.

Then, it is not possible to characterize the material directly on the target structure itself: Experiments are generally carried out on specific test specimens, a precise knowledge of boundary conditions being crucial.

In consequence it is often necessary to measure the elastic and damping properties for the particular plate under study, if vibration predictions of any accuracy are needed.

In this paper, an approach to making such measurements is described. It is based on observing damping factors of orthotropic plates with free boundaries with respect to frequency.

2 THEORETICAL BACKGROUND

Let us consider a thin orthotropic plate (h is the thickness and X and Y are principal directions of the material) supposed to be in free boundary condition as presented in figure 1.

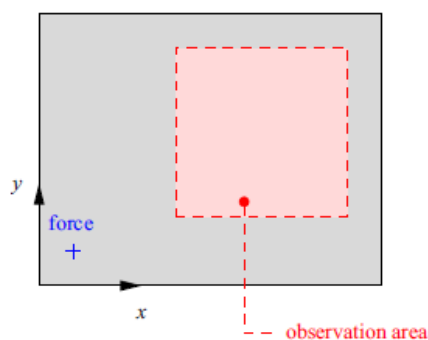


Figure 1. Geometry of the model and measurement set-up.

The general equation of motion of such orthotropic thin plate in the harmonic regime may be given by relation (1) considering an area on which no external force is applied [1]:

$$w(x,y) = \frac{h^2}{\rho\omega^2} \left[D_1 \frac{\partial^4 w}{\partial x^4} + (D_2 + D_4) \frac{\partial^4 w}{\partial x^2 \partial y^2} + D_3 \frac{\partial^4 w}{\partial y^4} \right] \quad (1)$$

where D_1 , D_2 , D_3 and D_4 are the flexural stiffness, ρ the density, h the thickness, ω the angular frequency, $w(x,y)$ the transverse displacement.

The flexural stiffness are given by equation (2) where the complex Young's moduli are considered to be complex $E(1+j\eta)$, j being the unit imaginary number and η denoting the structural damping coefficient, which characterizes material damping.

$$\begin{aligned} D_1 &= \frac{E_x}{12(1 - \nu_{xy}\nu_{yx})} \\ D_3 &= \frac{E_y}{12(1 - \nu_{xy}\nu_{yx})} \\ D_2 &= \frac{\nu_{xy}E_y}{6\nu_{xy}\nu_{yx}} = \frac{\nu_{yx}E_x}{6\nu_{xy}\nu_{yx}} \\ D_4 &= \frac{G_{xy}}{3} \end{aligned} \quad (2)$$

The transverse displacement at a given location may be easily obtained by using an accelerometer or a servimeter, its partial derivatives are less straightforward to obtain. They are approximated by using finite difference schemes thanks to several measurements of displacement on a regular mesh grid.

But the noise in the displacement field $w(x,y)$ is considerably amplified by the finite difference scheme and a regularization step must be conducted [2-4]. In order to eliminate high wavenumbers components, a low-pass filter in the wavenumber domain is applied to the displacement field and the partial derivatives.

First, each field is windowed by a bidimensional Tukey window. This preliminary step replaces the truncation of the field at the edges by a smooth variation from zero amplitude. Then, the windowed field is convolved by the finite spatial response of a low-pass filter with cut-off wavenumber k_c .

At this point, a cut-off wavenumber k_c should be chosen low enough to diminish the noise level in the partial derivatives of the transverse displacement field, but not too low in order to keep as much information as possible.

3 EXPERIMENTAL DEVICE

3.1 Material

The material of the study is a composite made up of UD glass fiber impregnated by a vinyl ester resin. Panel's size is 600 mm long and 400 mm width. A stacking of 8 layers (300 g/m² each) oriented at 0° compared to the length of the plate is impregnated by the resin using a LRI process. The fiber volume ratio is 60 %.



Figure 2. LRI process.

After manufacturing, the total thickness of the plate is 2mm which is constant on its surface. Any default such as bubbles or delamination has been identified. According to the direction of the higher length (i.e. direction of fibers), the Young modulus is estimated using the classical laminate's theory to be $E_1=20-25\text{GPa}$. In the lower length, it is of $E_2=5-10\text{GPa}$.

3.2 Experimental device

The test plate is suspended to a frame in order to be close to free boundary (see figure 3).

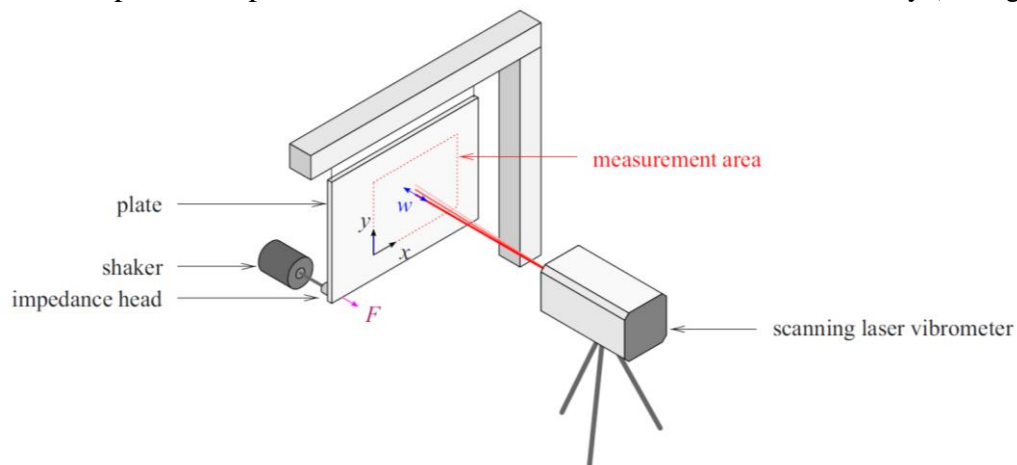


Figure 3. Global scheme of experimental device

A Polytec Scanning Vibrometer PSV 300 is used to measure the displacement field. The excitation is provided by a Brüel&Kjær 4810 shaker, supplied in power by a B&K 2718 amplifier. The excitation signal was a periodic chirp in the frequency range [8, 3200] Hz. Although no knowledge of excitation level is required by the method, a B&K 8001 impedance head is used to provide both phase reference and input force measurement, in conjunction with a B&K NEXUS conditioning amplifier.

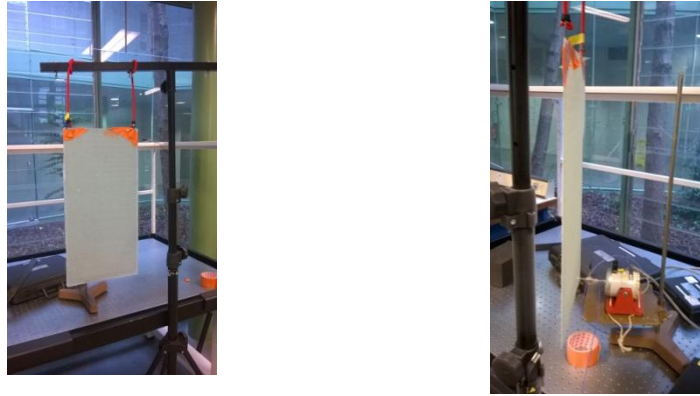


Figure 4. Specimen of the experimental device

Data collected from this experiment consists of out-of plane displacements of the specimen in its complex form for each frequency of the study (in our case between 8Hz and 3200Hz). The measurements (1000 points in a 200mmx400mm surface) are made on a regular meshgrid where the numerical treatment will be applied to determine the elastic performances of the material. The point of application of the mechanical excitation is outside of this zone.

4 RESULTS

Figure 5 shows the displacement field measured on our sample at one frequency in the study range. The elastic wave propagation starting at the application point at lower left corner of the plate can be visualised.

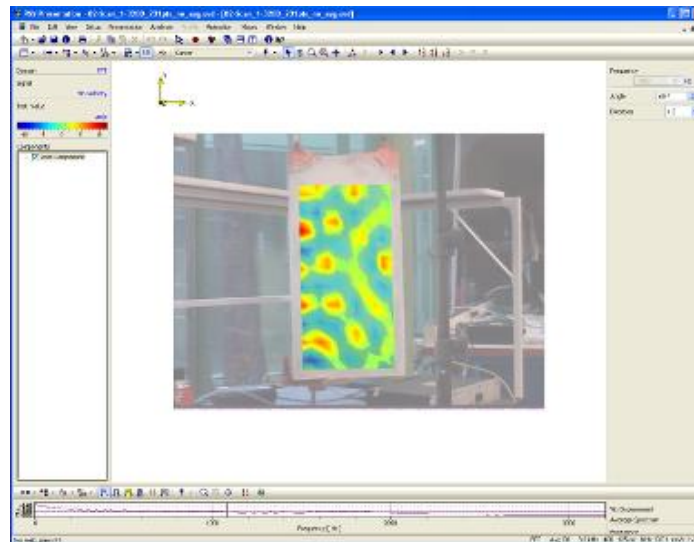


Figure 5. Experimental displacement field at 848Hz.

Using the analytical method as previously presented, the evolution of the rigidity in both directions according to the frequency can be determined as presented in the figure 6. Note that the orientations of axes where D_3 gives information onto E_x and D_1 on E_y .

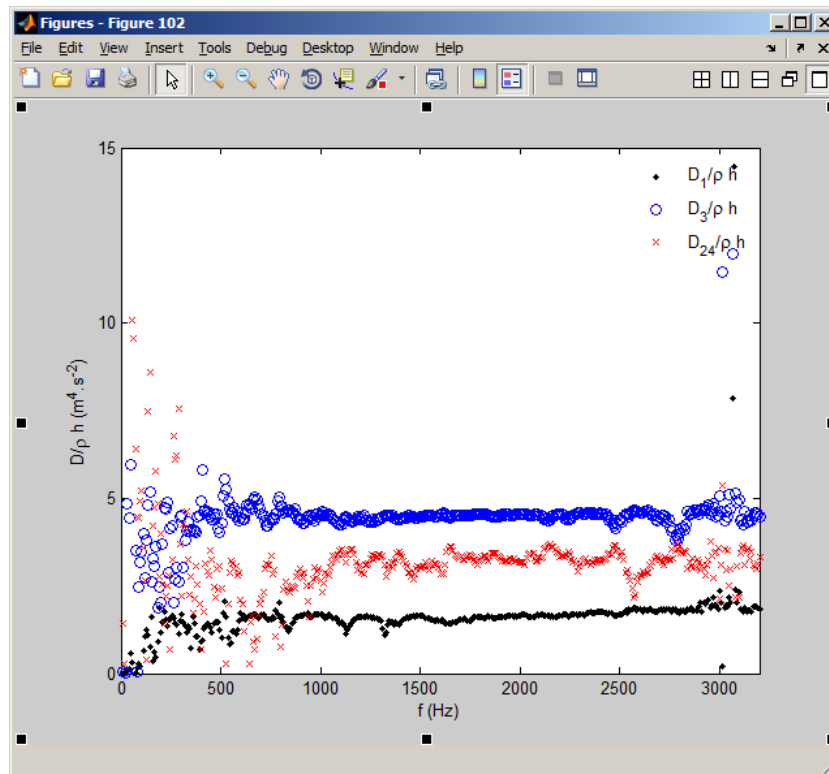


Figure 6. Evolution of elastic properties according to frequency.

Both rigidity of the main directions (D_1 and D_3) are in accordance with what can be deduce with the classical theory of laminate. Indeed using Poisson's ratio, the values of modulidetermined by the formulae 2 are in the range of the static value.

Globally, the evolution of the rigidity remains constant on the studied range of frequency of the study. The visco-elastic effects are so little marked as we could expect it with a thermosetting resin.

5 CONCLUSION

From a simple loading in a zone of a structure to be estimated and without any boundary conditions, the method presented here allows the determination of the rigidity of anorthotropic thin plate in its main directions.

Actual improvements of the method deal with a reliability increase: the filtering and the windowing steps, the improvement of the quality of the results in low frequencies and study on typical more viscous materials (thermoplastic for example). Finally a comparison with results from DMA will validate the accuracy of the calculated values.

REFERENCES

- [1] M. E. McIntyre, J. Woodhouse, On measuring the elastic and damping constants of orthotropic sheet materials, *Acta metall.* Vol. 36, No. 6, pp. 1397-1416, 1988
- [2] C. Pezerat, J.L. Guyader, Inverse methods for localization of external sources exciting a beam, *Acta Acustica* 3 (1995) 1–10.
- [3] C. Pezerat, J.L. Guyader, Force analysis technique: reconstruction of forced distribution on plates, *Acustica* 86 (2000) 322–332.
- [4] C. Pezerat, J.L. Guyader, Identification of vibration sources, *Applied Acoustics* 61(2000)309–324.

ACKNOWLEDGEMENT

This study is part of the COPERSIM-Vibro project managed by IRT Jules Verne (French Institute in Research and Technology in Advanced Manufacturing Technologies for Composite, Metallic and Hybrid Structures). The authors wish to associate the industrial and academic partners of this project; Respectively PSA Peugeot Citroen, Renault, Solvay, Plastic Omnium, CETIM, LAUM.

COPYRIGHT NOTICE

Copyright ©2015 by the authors. Distribution of all material contained in this paper is permitted under the terms of the Creative Commons license Attribution-NonCommercial-NoDerivatives 4.0 International (CC-by-nc-nd 4.0).





Wave propagation in phononic-crystal composites plates

S. ZOUARI^{1,2}, J-M. GENEVAUX², J. BROCAIL¹ and F. ABLITZER²

¹ Centre de Recherche de l'ESTACA, 2MCE
ESTACA Campus - Ouest, Laval, FRANCE

Email: sahar.zouari@estaca.fr, Julien.BROCAIL@estaca.fr

² LAUM

Université du Maine, Le Mans, FRANCE

Email: Jean-Michel.Genevaux@univ-lemans.fr, frederic.ablitzer@univ-lemans.fr

ABSTRACT

Composite structures have been introduced in the transportation industry to reduce vehicle mass and energy consumption. Composites have low internal damping which leads to higher levels of vibration and induced noise. To reduce the vibrations amplitude and thus the acoustic discomfort, damping elements placed in specific locations of the structure [1-2] are sometimes used. In this paper, the anti-vibration function is obtained by the introduction of periodic effect. This arrangement constitutes a phononic crystal that generates frequency ranges without free wave propagation [3-4], called band gap. The vibro-acoustic properties of the structure are thus improved.

This study focuses on periodic composite plates of glass/epoxy by defining elementary cells.

In a first part, when the periodicity is very smaller than the dimensions of the plate a finite element approach is proceed using Comsol Multiphysics ®4.4 software, to obtain the dispersion curves of an infinite periodic structure. The frequency associated to each wave vector which propagates through the elementary cell is calculating using Bloch-Floquet periodicity conditions on the boundaries. The dispersion curves around the edge of the irreducible Brillouin zone are obtained.

The study is focuses on the bidirectional periodic structures. One of the configurations studied is a plate composed of a periodic square of rubber inclusions embedded in a composite material with eight-layer of fiber glass. Unlike the band diagram of a composite reference plate, the band diagram obtained (Fig.1) shows that waves are blocked for frequencies around 2600 Hz, in all directions of the wave vector.

The second parts of the study concern the fabrication and characterization of unidirectional periodic plates, in order to take into account the technical limits of the production of periodic plates with composite materials. These plates are composed of a succession of strips, with a number of layers of glass fibers varying from one strip to another. This succession of strips provides directional bands gaps. To test these plates, an experimental protocol is chosen to

impose unidirectional wave propagation: the plate is attached in the middle between two aluminum beams enough rigid at low frequency. The lower beam is connected to a vibration exciter for exciting the structure. Several plates will be tested and compared to the numerical results.

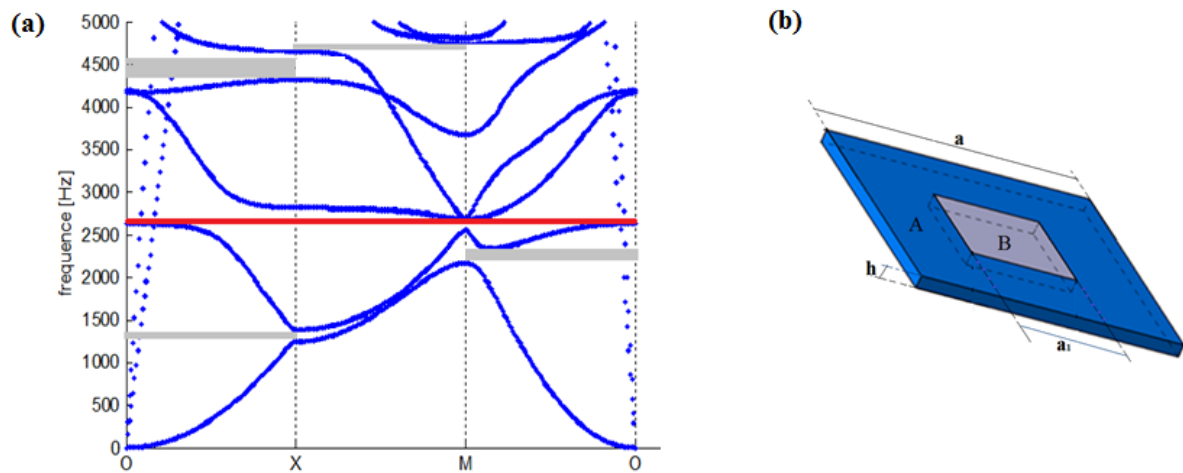


Figure 1. (a) Band diagram of a periodic composite plate with rubber inclusions, (b) Unit cell with inclusion.

REFERENCES

- [1] M. Assarar, A. El Mahi, J-M. Berthelot, “Damping Analysis of Sandwich Composite Materials”, *Journal of Composite Materials - J COMPOS MATER*, vol. 43, no. 13, pp. 1461-1485, 2009.
- [2] S. Assaf, “Finite element vibration analysis of damped composite sandwich beams”, *International Journal of Acoustics and Vibration*, Vol. 16, n°4, pp. 163-172, 2011.
- [3] L. Brillouin, “Wave propagation in periodic structures”, McGraw-Hill Book Company, New York, 1946.
- [4] C. Claeys, K. Vergote, P. Sas, W. Desmet, “On the potential of tuned resonators to obtain low-frequency vibrational stop bands in periodic panels”, *Journal of Sound and Vibration* 332, pp. 1418–1436, 2013.

COPYRIGHT NOTICE

Copyright ©2015 by the authors. Distribution of all material contained in this paper is permitted under the terms of the Creative Commons license Attribution-NonCommercial-NoDerivatives 4.0 International (CC-by-nc-nd 4.0).



